DASSAULT SYSTEMES

SIMULIA

ABAQUS 2016

EXAMPLE PROBLEMS GUIDE

VOLUME II: OTHER APPLICATIONS AND ANALYSES

3DEXPERIENCE®

Abaqus

Example Problems Guide

Volume II

Legal Notices

Preface

This section lists various resources that are available for help with using Abaqus Unified FEA software.

Support

Both technical software support (for problems with creating a model or performing an analysis) and systems support (for installation, licensing, and hardware-related problems) for Abaqus are offered through a global network of support offices, as well as through our online support system. Contact information for our regional offices is accessible from **SIMULIA→Locations** at www.3ds.com/simulia. The online support system is accessible by selecting the **SUBMIT A REQUEST** link at **Support - Dassault Systèmes** (http://www.3ds.com/support).

Online support

Dassault Systèmes provides a knowledge base of questions and answers, solutions to questions that we have answered, and guidelines on how to use Abaqus, Engineering Process Composer, Isight, Tosca, fe-safe, and other SIMULIA products. The knowledge base is available by using the **Search our Knowledge** option on www.3ds.com/support (http://www.3ds.com/support).

By using the online support system, you can also submit new requests for support. All support/service requests are tracked. If you contact us by means outside the system to discuss an existing support problem and you know the support request number, please mention it so that we can query the support system to see what the latest action has been.

Training

All SIMULIA regional offices offer regularly scheduled public training classes. The courses are offered in a traditional classroom form and via the Web. We also provide training seminars at customer sites. All training classes and seminars include workshops to provide as much practical experience with Abaqus as possible. For a schedule and descriptions of available classes, see the **Training** link at www.3ds.com/products-services/simulia (www.3ds.com/products-services/simulia) or call your support office.

Feedback

We welcome any suggestions for improvements to Abaqus software, the support tool, or documentation. We will ensure that any enhancement requests you make are considered for future releases. If you wish to make a suggestion about the service or products, refer to www.3ds.com/simulia. Complaints should be made by contacting your support office or by visiting **SIMULIA→Quality Assurance** at www.3ds.com/simulia (www.3ds.com/simulia).

Contents

Volume I

1. Static Stress/Displacement Analyses

Static and quasi-static stress analyses

Axisymmetric analysis of bolted pipe flange connections 1.1.1
Elastic-plastic collapse of a thin-walled elbow under in-plane bending and internal pressure 1.1.2
Parametric study of a linear elastic pipeline under in-plane bending 1.1.3
Indentation of an elastomeric foam specimen with a hemispherical punch 1.1.4
Collapse of a concrete slab 1.1.5
Jointed rock slope stability 1.1.6
Notched beam under cyclic loading 1.1.7
Uniaxial ratchetting under tension and compression 1.1.8
Hydrostatic fluid elements: modeling an airspring 1.1.9
Shell-to-solid submodeling and shell-to-solid coupling of a pipe joint 1.1.10
Stress-free element reactivation 1.1.11
Transient loading of a viscoelastic bushing 1.1.12
Indentation of a thick plate 1.1.13
Damage and failure of a laminated composite plate 1.1.14
Analysis of an automotive boot seal 1.1.15
Pressure penetration analysis of an air duct kiss seal 1.1.16
Self-contact in rubber/foam components: jounce bumper 1.1.17
Self-contact in rubber/foam components: rubber gasket 1.1.18
Submodeling of a stacked sheet metal assembly 1.1.19
Axisymmetric analysis of a threaded connection 1.1.20
Direct cyclic analysis of a cylinder head under cyclic thermomechanical loadings 1.1.21
Erosion of material (sand production) in an oil wellbore 1.1.22
Submodel stress analysis of pressure vessel closure hardware 1.1.23
Using a composite layup to model a yacht hull 1.1.24
Energy computations in a contact analysis 1.1.25

Buckling and collapse analyses

Snap-through buckling analysis of circular arches 1.2.1
Laminated composite shells: buckling of a cylindrical panel with a circular hole 1.2.2
Buckling of a column with spot welds 1.2.3
Elastic-plastic K-frame structure 1.2.4
Unstable static problem: reinforced plate under compressive loads 1.2.5
Buckling of an imperfection-sensitive cylindrical shell 1.2.6

Forming analyses

Upsetting of a cylindrical billet: quasi-static analysis with mesh-to-mesh solution mapping (Abaqus/Standard) and adaptive meshing (Abaqus/Explicit) 1.3.1
Superplastic forming of a rectangular box 1.3.2
Stretching of a thin sheet with a hemispherical punch 1.3.3
Deep drawing of a cylindrical cup 1.3.4
Extrusion of a cylindrical metal bar with frictional heat generation 1.3.5
Rolling of thick plates 1.3.6
Axisymmetric forming of a circular cup 1.3.7
Cup/trough forming 1.3.8
Forging with sinusoidal dies 1.3.9
Forging with multiple complex dies 1.3.10
Flat rolling: transient and steady-state 1.3.11
Section rolling 1.3.12
Ring rolling 1.3.13
Axisymmetric extrusion: transient and steady-state 1.3.14
Two-step forming simulation 1.3.15
Upsetting of a cylindrical billet: coupled temperature-displacement and adiabatic analysis 1.3.16
Unstable static problem: thermal forming of a metal sheet 1.3.17
Inertia welding simulation using Abaqus/Standard and Abaqus/CAE 1.3.18
Moldflow translation examples 1.3.19

Fracture and damage

A plate with a part-through crack: elastic line spring modeling 1.4.1
Contour integrals for a conical crack in a linear elastic infinite half space 1.4.2
Elastic-plastic line spring modeling of a finite length cylinder with a part-through axial flaw 1.4.3
Crack growth in a three-point bend specimen 1.4.4
Analysis of skin-stiffener debonding under tension 1.4.5
Failure of blunt notched fiber metal laminates 1.4.6
Debonding behavior of a double cantilever beam 1.4.7
Debonding behavior of a single leg bending specimen 1.4.8
Postbuckling and growth of delaminations in composite panels 1.4.9

Import analyses

Springback of two-dimensional draw bending 1.5.1
Deep drawing of a square box 1.5.2

2. Dynamic Stress/Displacement Analyses

Dynamic stress analyses

Nonlinear dynamic analysis of a structure with local inelastic collapse 2.1.1

Detroit Edison pipe whip experiment 2.1.2
Rigid projectile impacting eroding plate 2.1.3
Eroding projectile impacting eroding plate 2.1.4
Tennis racket and ball 2.1.5
Pressurized fuel tank with variable shell thickness 2.1.6
Modeling of an automobile suspension 2.1.7
Explosive pipe closure 2.1.8
Knee bolster impact with general contact 2.1.9
Crimp forming with general contact 2.1.10
Collapse of a stack of blocks with general contact 2.1.11
Cask drop with foam impact limiter 2.1.12
Oblique impact of a copper rod 2.1.13
Water sloshing in a baffled tank 2.1.14
Seismic analysis of a concrete gravity dam 2.1.15
Progressive failure analysis of thin-wall aluminum extrusion under quasi-static and dynamic loads 2.1.16
Impact analysis of a pawl-ratchet device 2.1.17
High-velocity impact of a ceramic target 2.1.18

Mode-based dynamic analyses

Analysis of a rotating fan using substructures and cyclic symmetry 2.2.1
Linear analysis of the Indian Point reactor feedwater line 2.2.2
Response spectra of a three-dimensional frame building 2.2.3
Brake squeal analysis 2.2.4
Dynamic analysis of antenna structure utilizing residual modes 2.2.5
Steady-state dynamic analysis of a vehicle body-in-white model 2.2.6

Eulerian analyses

Rivet forming 2.3.1
Impact of a water-filled bottle 2.3.2

Co-simulation analyses

Dynamic impact of a scooter with a bump 2.4.1

Volume II

3. Tire and Vehicle Analyses

Tire analyses

Symmetric results transfer for a static tire analysis	3.1.1
Steady-state rolling analysis of a tire	3.1.2
Subspace-based steady-state dynamic tire analysis	3.1.3
Steady-state dynamic analysis of a tire substructure	3.1.4
Coupled acoustic-structural analysis of a tire filled with air	3.1.5
Import of a steady-state rolling tire	3.1.6
Analysis of a solid disc with Mullins effect and permanent set	3.1.7
Tread wear simulation using adaptive meshing in Abaqus/Standard	3.1.8
Dynamic analysis of an air-filled tire with rolling transport effects	3.1.9
Acoustics in a circular duct with flow	3.1.10

Vehicle analyses

Inertia relief in a pick-up truck	3.2.1
Substructure analysis of a pick-up truck model	3.2.2
Display body analysis of a pick-up truck model	3.2.3
Continuum modeling of automotive spot welds	3.2.4

Occupant safety analyses

Seat belt analysis of a simplified crash dummy	3.3.1
Side curtain airbag impactor test	3.3.2

4. Mechanism Analyses

Resolving overconstraints in a multi-body mechanism model	4.1.1
Crank mechanism	4.1.2
Snubber-arm mechanism	4.1.3
Flap mechanism	4.1.4
Tail-skid mechanism	4.1.5
Cylinder-cam mechanism	4.1.6
Driveshaft mechanism	4.1.7
Geneva mechanism	4.1.8
Trailing edge flap mechanism	4.1.9
Substructure analysis of a one-piston engine model	4.1.10
Application of bushing connectors in the analysis of a three-point linkage	4.1.11
Gear assemblies	4.1.12

5. Heat Transfer and Thermal-Stress Analyses

Thermal-stress analysis of a disc brake	5.1.1

A sequentially coupled thermomechanical analysis of a disc brake with an Eulerian approach 5.1.2
Exhaust manifold assemblage 5.1.3
Coolant manifold cover gasketed joint 5.1.4
Conductive, convective, and radiative heat transfer in an exhaust manifold 5.1.5
Thermal-stress analysis of a reactor pressure vessel bolted closure 5.1.6
Coupled thermomechanical analysis of viscoelastic dampers 5.1.7

6. Fluid Dynamics and Fluid-Structure Interaction

Conjugate heat transfer analysis of a component-mounted electronic circuit board 6.1.1

7. Electromagnetic Analyses

Piezoelectric analyses

Eigenvalue analysis of a piezoelectric transducer 7.1.1
Transient dynamic nonlinear response of a piezoelectric transducer 7.1.2

Joule heating analyses

Thermal-electrical modeling of an automotive fuse 7.2.1

8. Mass Diffusion Analyses

Hydrogen diffusion in a vessel wall section 8.1.1
Diffusion toward an elastic crack tip 8.1.2

9. Acoustic and Shock Analyses

Fully and sequentially coupled acoustic-structural analysis of a muffler 9.1.1
Coupled acoustic-structural analysis of a speaker 9.1.2
Analysis of a speaker using Abaqus-Dymola co-simulation 9.1.3
Response of a submerged cylinder to an underwater explosion shock wave 9.1.4
Convergence studies for shock analyses using shell elements 9.1.5
UNDEX analysis of a detailed submarine model 9.1.6
Coupled acoustic-structural analysis of a pick-up truck 9.1.7
Long-duration response of a submerged cylinder to an underwater explosion 9.1.8
Deformation of a sandwich plate under CONWEP blast loading 9.1.9

10. Soils Analyses

Plane strain consolidation 10.1.1
Calculation of phreatic surface in an earth dam 10.1.2
Axisymmetric simulation of an oil well 10.1.3
Analysis of a pipeline buried in soil 10.1.4
Hydraulically induced fracture in a wellbore 10.1.5
Permafrost thawing–pipeline interaction 10.1.6

11. Structural Optimization Analyses

Topology optimization analyses

Topology optimization of an automotive control arm 11.1.1

Shape optimization analyses

Shape optimization of a connecting rod 11.2.1

Sizing optimization analyses

Sizing optimization of a gear shift control holder 11.3.1
Sizing optimization of a car door 11.3.2

Bead optimization analyses

Bead optimization of a plate 11.4.1

12. Abaqus/Aqua Analyses

Jack-up foundation analyses 12.1.1
Riser dynamics 12.1.2

13. Particle Methods Analyses

Mixing of granular media in a drum mixer 13.1.1

14. Design Sensitivity Analyses

Overview

Design sensitivity analysis: overview 14.1.1

Examples

Design sensitivity analysis of a composite centrifuge 14.2.1
Design sensitivities for tire inflation, footprint, and natural frequency analysis 14.2.2
Design sensitivity analysis of a windshield wiper 14.2.3
Design sensitivity analysis of a rubber bushing 14.2.4

15. Postprocessing of Abaqus Results

User postprocessing of Abaqus results files: overview 15.1.1
Joining data from multiple results files and converting file format: FJOIN 15.1.2
Calculation of principal stresses and strains and their directions: FPRIN 15.1.3
Creation of a perturbed mesh from original coordinate data and eigenvectors: FPERT 15.1.4
Output radiation view factors and facet areas: FRAD 15.1.5
Creation of a data file to facilitate the postprocessing of elbow element results: FELBOW 15.1.6
Translating Abaqus data to modal neutral file format for analysis in MSC.ADAMS 15.1.7

3. Tire and Vehicle Analyses

- “Tire analyses,” Section 3.1
- “Vehicle analyses,” Section 3.2
- “Occupant safety analyses,” Section 3.3

3.1 Tire analyses

- “Symmetric results transfer for a static tire analysis,” Section 3.1.1
- “Steady-state rolling analysis of a tire,” Section 3.1.2
- “Subspace-based steady-state dynamic tire analysis,” Section 3.1.3
- “Steady-state dynamic analysis of a tire substructure,” Section 3.1.4
- “Coupled acoustic-structural analysis of a tire filled with air,” Section 3.1.5
- “Import of a steady-state rolling tire,” Section 3.1.6
- “Analysis of a solid disc with Mullins effect and permanent set,” Section 3.1.7
- “Tread wear simulation using adaptive meshing in Abaqus/Standard,” Section 3.1.8
- “Dynamic analysis of an air-filled tire with rolling transport effects,” Section 3.1.9
- “Acoustics in a circular duct with flow,” Section 3.1.10

3.1.1 SYMMETRIC RESULTS TRANSFER FOR A STATIC TIRE ANALYSIS

Product: Abaqus/Standard

This example illustrates the use of symmetric results transfer and symmetric model generation to model the static interaction between a tire and a rigid surface.

Symmetric model generation ("Symmetric model generation," Section 10.4.1 of the Abaqus Analysis User's Guide) can be used to create a three-dimensional model by revolving an axisymmetric model about its axis of revolution or by combining two parts of a symmetric model, where one part is the original model and the other part is the original model reflected through a line or a plane. Both model generation techniques are demonstrated in this example.

Symmetric results transfer ("Transferring results from a symmetric mesh or a partial three-dimensional mesh to a full three-dimensional mesh," Section 10.4.2 of the Abaqus Analysis User's Guide) allows the user to transfer the solution obtained from an axisymmetric analysis onto a three-dimensional model with the same geometry. It also allows the transfer of a symmetric three-dimensional solution to a full three-dimensional model. Both these results transfer features are demonstrated in this example. The results transfer capability can significantly reduce the analysis cost of structures that undergo symmetric deformation followed by nonsymmetric deformation later during the loading history.

The purpose of this example is to obtain the footprint solution of a 175 SR14 tire in contact with a flat rigid surface, subjected to an inflation pressure and a concentrated load on the axle. Input files modeling a tire in contact with a rigid drum are also included. These footprint solutions are used as the starting point in "Steady-state rolling analysis of a tire," Section 3.1.2, where the free rolling state of the tire rolling at 10 km/h is determined and in "Subspace-based steady-state dynamic tire analysis," Section 3.1.3, where a frequency response analysis is performed.

Problem description

The different components of the tire are shown in Figure 3.1.1–1. The tread and sidewalls are made of rubber, and the belts and carcass are constructed from fiber-reinforced rubber composites. The rubber is modeled as an incompressible hyperelastic material, and the fiber reinforcement is modeled as a linear elastic material. A small amount of skew symmetry is present in the geometry of the tire due to the placement and $\pm 20.0°$ orientation of the reinforcing belts.

Two simulations are performed in this example. The first simulation exploits the symmetry in the tire model and utilizes the results transfer capability; the second simulation does not use the results transfer capability. Comparisons between the two methodologies are made for the case where the tire is in contact with a flat rigid surface. Input files modeling a tire in contact with a rigid drum are also included. The methodology used in the first analysis is applied in this simulation. Results for this case are presented in "Steady-state rolling analysis of a tire," Section 3.1.2.

The first simulation is broken down into three separate analyses. In the first analysis the inflation of the tire by a uniform internal pressure is modeled. Due to the anisotropic nature of the tire construction, the inflation loading gives rise to a circumferential component of deformation. The resulting stress field is fully three-dimensional, but the problem remains axisymmetric in the sense that the solution does not

vary as a function of position along the circumference. Abaqus provides axisymmetric elements with twist (CGAX) for such situations. These elements are used to model the inflation loading. Only half the tire cross-section is needed for the inflation analysis due to a reflection symmetry through the vertical line that passes through the tire axle (see Figure 3.1.1–2). We refer to this model as the axisymmetric model.

The second part of the simulation entails the computation of the footprint solution, which represents the static deformed shape of the pressurized tire due to a vertical dead load (modeling the weight of a vehicle). A three-dimensional model is needed for this analysis. The finite element mesh for this model is obtained by revolving the axisymmetric cross-section about the axis of revolution. A nonuniform discretization along the circumference is used as shown in Figure 3.1.1–3. In addition, the axisymmetric solution is transferred to the new mesh where it serves as the initial or base state in the footprint calculations. As with the axisymmetric model, only half of the cross-section is needed in this simulation, but skew-symmetric boundary conditions must be applied along the midplane of the cross-section to account for antisymmetric stresses that result from the inflation loading and the concentrated load on the axle. We refer to this model as the partial three-dimensional model.

In the last part of this analysis the footprint solution from the partial three-dimensional model is transferred to a full three-dimensional model and brought into equilibrium. This full three-dimensional model is used in the steady-state transport example that follows. The model is created by combining two parts of the partial three-dimensional model, where one part is the mesh used in the second analysis and the other part is the partial model reflected through a line. We refer to this model as the full three-dimensional model.

A second simulation is performed in which the same loading steps are repeated, except that the full three-dimensional model is used for the entire analysis. Besides being used to validate the results transfer solution, this second simulation allows us to demonstrate the computational advantage afforded by the Abaqus results transfer capability in problems with rotational and/or reflection symmetries.

Model definition

In the first simulation the inflation step is performed on the axisymmetric model and the results are stored in the results files (**`.res`**, **`.mdl`**, **`.stt`**, and **`.prt`**). The axisymmetric model is discretized with CGAX4H and CGAX3H elements. The belts and ply are modeled with rebar in surface elements embedded in continuum elements. The roundoff tolerance for the embedded element technique is used to adjust the positions of embedded element nodes such that they lie exactly on host element edges. This feature is useful in cases where embedded nodes are offset from host element edges by a small distance caused by numerical roundoff. Eliminating such gaps reduces the number of constraint equations used to embed the surface elements and, hence, improves performance. The axisymmetric results are read into the subsequent footprint analysis, and the partial three-dimensional model is generated by Abaqus by revolving the axisymmetric model cross-section about the rotational symmetry axis. The partial three-dimensional model is composed of four sectors of CCL12H and CCL9H cylindrical elements covering an angle of 320°, with the rest of the tire divided into 16 sectors of C3D8H and C3D6H linear elements. The linear elements are used in the footprint region. The use of cylindrical elements is recommended for regions where it is possible to cover large sectors around the circumference with a small number of elements. In the footprint region, where the desired resolution of the contact patch

dictates the number of elements to be used, it is more cost-effective to use linear elements. The road (or drum) is defined as an analytical rigid surface in the partial three-dimensional model. The results of the footprint analysis are read into the final equilibrium analysis, and the full three-dimensional model is generated by reflecting the partial three-dimensional model through a vertical line. The line used in the reflection is the vertical line in the symmetry plane of the tire, which passes through the axis of rotation. The model is reflected through a symmetry line, as opposed to a symmetry plane, to take into account the skew symmetry of the tire. The analytical rigid surface as defined in the partial three-dimensional model is transferred to the full model without change. The three-dimensional finite element mesh of the full model is shown in Figure 3.1.1–4.

In the second simulation a **datacheck** analysis is performed to write the axisymmetric model information to the results files. The full tire cross-section is meshed in this model. No analysis is needed. The axisymmetric model information is read in a subsequent run, and a full three-dimensional model is generated by Abaqus by revolving the cross-section about the rotational symmetry axis. The road is defined in the full model. The three-dimensional finite element mesh of the full model is identical to the one generated in the first analysis. However, the inflation load and concentrated load on the axle are applied to the full model without making use of the results transfer capability.

The footprint calculations are performed with a friction coefficient of zero in anticipation of eventually performing a steady-state rolling analysis of the tire using steady-state transport, as explained in "Steady-state rolling analysis of a tire," Section 3.1.2.

Since the results from the static analyses performed in this example are used in a subsequent time-domain dynamic example, the input files include a hyperelastic material that models the rubber directly using the Prony series parameters. This approach enables us to model viscoelasticity in the steady-state transport example that follows. As a consequence of defining a time-domain viscoleastic material property, the elastic properties specified in the hyperelasticity material behavior define the long-term behavior of the rubber. In addition, all static steps are defined to ensure that the static solutions are based upon the long-term elastic moduli.

Loading

As discussed in the previous sections, the loading on the tire is applied over several steps. In the first simulation the inflation of the tire to a pressure of 200.0 kPa is modeled using the axisymmetric tire model (tiretransfer_axi_half.inp) with a static analysis procedure. The results from this axisymmetric analysis are then transferred to the partial three-dimensional model (tiretransfer_symmetric.inp) in which the footprint solution is computed in two sequential static steps. The first of these static steps establishes the initial contact between the road and the tire by prescribing a vertical displacement of 0.02 m on the rigid body reference node. Since this is a static analysis, it is recommended that contact be established with a prescribed displacement, as opposed to a prescribed load, to avoid potential convergence difficulties that might arise due to unbalanced forces. The prescribed boundary condition is removed in the second static step, and a vertical load of $N = 1.65$ kN is applied to the rigid body reference node. The 1.65 kN load in the partial three-dimensional model represents a 3.3 kN load in the full three-dimensional model. The transfer of the results from the axisymmetric model to the partial three-dimensional model is accomplished by using symmetric results transfer. Once the static footprint solution for the partial three-dimensional model has been established, symmetric results transfer is used to transfer the solution

to the full three-dimensional model (tiretransfer_full.inp), where the footprint solution is brought into equilibrium in a single static increment. The results transfer sequence is illustrated in Figure 3.1.1–5.

Boundary conditions and loads are not transferred with the symmetric results transfer; they must be carefully redefined in the new analysis to match the loads and boundary conditions from the transferred solution. Due to numerical and modeling issues the element formulations for the two-dimensional and three-dimensional elements are not identical. As a result, there may be slight differences between the equilibrium solutions generated by the two- and three-dimensional models. In addition, small numerical differences may occur between the symmetric and full three-dimensional solutions because of the presence of symmetry boundary conditions in the symmetric model that are not used in the full model. Therefore, it is advised that in a results transfer simulation an initial step be performed where equilibrium is established between the transferred solution and loads that match the state of the model from which the results are transferred. It is recommended that an initial static step with the initial time increment set to the total step time be used to allow Abaqus/Standard to find the equilibrium in one increment.

In the second simulation identical inflation and footprint steps are repeated. The only difference is that the entire analysis is performed on the full three-dimensional model (tiretransfer_full_footprint.inp). The full three-dimensional model is generated using the restart information from a **datacheck** analysis of an axisymmetric model of the full tire cross-section (tiretransfer_axi_full.inp).

Contact modeling

The default contact pair formulation in the normal direction is hard contact, which gives strict enforcement of contact constraints. Some analyses are conducted with both hard and augmented Lagrangian contact to demonstrate that the default penalty stiffness chosen by the code does not affect stress results significantly. The augmented Lagrangian method can be invoked as part of the definition of the modified contact pressure-overclosure relationship. The hard and augmented Lagrangian contact algorithms are described in "Contact constraint enforcement methods in Abaqus/Standard," Section 38.1.2 of the Abaqus Analysis User's Guide.

Solution controls

Since the three-dimensional tire model has a small loaded area and, thus, rather localized forces, the default averaged flux values for the convergence criteria produce very tight tolerances and cause more iteration than is necessary for an accurate solution. To decrease the computational time required for the analysis, the solution controls can be used to override the default values for average forces and moments. The default controls are used in this example.

Results and discussion

The results from the first two simulations are essentially identical. The peak Mises stresses and displacement magnitudes in the two models agree within 0.3% and 0.2%, respectively. The final deformed shape of the tire is shown in Figure 3.1.1–6. The computational cost of each simulation is shown in Table 3.1.1–1. The simulation performed on the full three-dimensional model takes 2.5 times

longer than the results transfer simulation, clearly demonstrating the computational advantage that can be attained by exploiting the symmetry in the model using the symmetric results transfer.

Input files

tiretransfer_axi_half.inp	Axisymmetric model, inflation analysis (simulation 1).
tiretransfer_symmetric.inp	Partial three-dimensional model, footprint analysis (simulation 1).
tiretransfer_symmetric_auglagr.inp	Partial three-dimensional model, footprint analysis using augmented Lagrangian contact (simulation 1).
tiretransfer_full.inp	Full three-dimensional model, final equilibrium analysis (simulation 1).
tiretransfer_full_auglagr.inp	Full three-dimensional model, final equilibrium analysis using augmented Lagrangian contact (simulation 1).
tiretransfer_axi_full.inp	Axisymmetric model, **datacheck** analysis (simulation 2).
tiretransfer_full_footprint.inp	Full three-dimensional model, complete analysis (simulation 2).
tiretransfer_symm_drum.inp	Partial three-dimensional model of a tire in contact with a rigid drum.
tiretransfer_full_drum.inp	Full three-dimensional model of a tire in contact with a rigid drum.
tiretransfer_node.inp	Nodal coordinates for the axisymmetric models.
tiretransfer_axi_half_ml.inp	Axisymmetric model, inflation analysis (simulation 1) with Marlow hyperelastic model.
tiretransfer_symmetric_ml.inp	Partial three-dimensional model, footprint analysis (simulation 1) with Marlow hyperelastic model.
tiretransfer_full_ml.inp	Full three-dimensional model, final equilibrium analysis (simulation 1) with Marlow hyperelastic model.

Table 3.1.1–1 Comparison of normalized CPU times for the footprint analysis (normalized with respect to the total "No results transfer" analysis).

	Use results transfer and symmetry conditions	**No results transfer**
Inflation	0.005[(a)]+0.040[(b)]	0.347[(e)]
Footprint	0.265[(c)]+0.058[(d)]	0.653[(e)]
Total	0.368	1.0

(a) axisymmetric model
(b) equilibrium step in partial three-dimensional model
(c) footprint analysis in partial three-dimensional model
(d) equilibrium step in full three-dimensional model
(e) full three-dimensional model

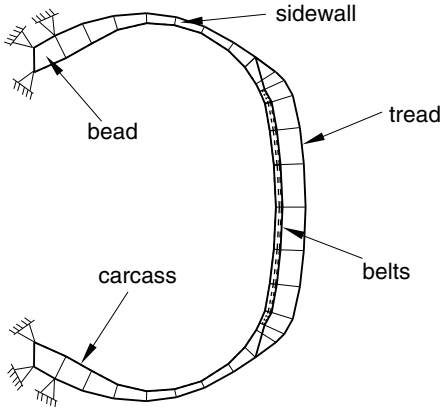

Figure 3.1.1–1 Tire cross-section.

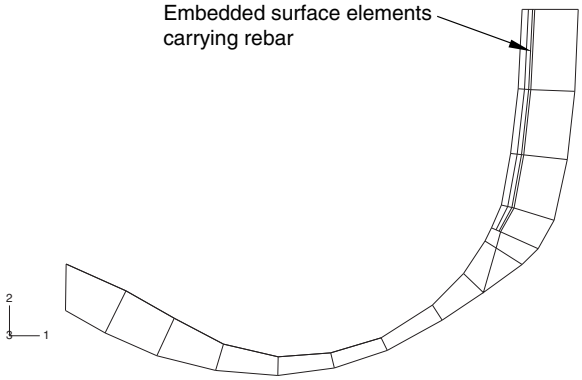

Figure 3.1.1–2 Axisymmetric tire mesh.

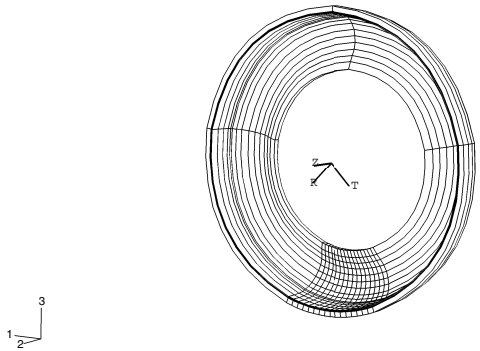

Figure 3.1.1–3 Partial three-dimensional tire mesh.

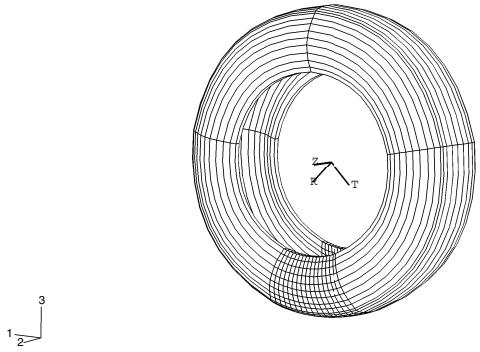

Figure 3.1.1–4 Full three-dimensional tire mesh.

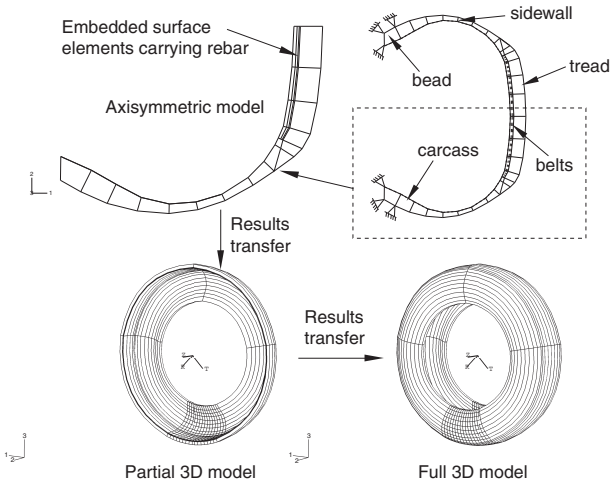

Figure 3.1.1–5 Results transfer analysis sequence.

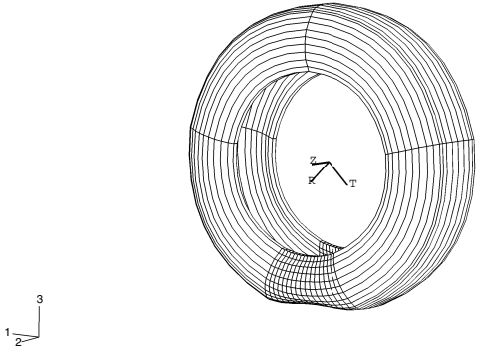

Figure 3.1.1–6 Deformed three-dimensional tire (deformations scaled by a factor of 2).

3.1.2 STEADY-STATE ROLLING ANALYSIS OF A TIRE

Product: Abaqus/Standard

This example illustrates the use of steady-state transport in Abaqus to model the steady-state dynamic interaction between a rolling tire and a rigid surface.

A steady-state transport analysis uses a moving reference frame in which rigid body rotation is described in an Eulerian manner and the deformation is described in a Lagrangian manner. This kinematic description converts the steady moving contact problem into a pure spatially dependent simulation. Thus, the mesh need be refined only in the contact region—the steady motion transports the material through the mesh. Frictional effects, inertia effects, and history effects in the material can all be accounted for in a steady-state transport analysis.

The purpose of this analysis is to obtain free rolling equilibrium solutions of a 175 SR14 tire traveling at a ground velocity of 10.0 km/h (2.7778 m/s) at different slip angles on a flat rigid surface. The slip angle is the angle between the direction of travel and the plane normal to the axle of the tire. Straight line rolling occurs at a 0.0° slip angle. For comparison purposes we also consider an analysis of the tire spinning at a fixed position on a 1.5 m diameter rigid drum. The drum rotates at an angular velocity of 3.7 rad/s, so that a point on the surface of the drum travels with an instantaneous velocity of 10.0 km/h (2.7778 m/s). Another case presented examines the camber thrust arising from camber applied to a tire at free rolling conditions. This also enables us to calculate a camber thrust stiffness.

An equilibrium solution for the rolling tire problem that has zero torque, T, applied around the axle is referred to as a free rolling solution. An equilibrium solution with a nonzero torque is referred to as either a traction or a braking solution depending upon the sense of T. Braking occurs when the angular velocity of the tire is small enough such that some or all of the contact points between the tire and the road are slipping and the resultant torque on the tire acts in an opposite sense from the angular velocity of the free rolling solution. Similarly, traction occurs when the angular velocity of the tire is large enough such that some or all of the contact points between the tire and the road are slipping and the resultant torque on the tire acts in the same sense as the angular velocity of the free rolling solution. Full braking or traction occurs when all the contact points between the tire and the road are slipping.

A wheel in free rolling, traction, or braking will spin at different angular velocities, ω, for the same ground velocity, $\mathbf{v_0}$. Usually the combination of ω and $\mathbf{v_0}$ that results in free rolling is not known in advance. Since the steady-state transport analysis capability requires that both the rotational spinning velocity, ω, and the traveling ground velocity, $\mathbf{v_0}$, be prescribed, the free rolling solution must be found in an indirect manner. One such indirect approach is illustrated in this example. An alternate approach involves controlling the rotational spinning velocity using user subroutine **UMOTION** while monitoring the progress of the solution through a second user subroutine **URDFIL**. The **URDFIL** subroutine is used to obtain an estimate of the free rolling solution based on the values of the torque at the rim at the end of each increment. This approach is also illustrated in this example.

A finite element analysis of this problem, together with experimental results, has been published by Koishi et al. (1997).

Related topics

- "Steady-state transport analysis," Section 6.4.1 of the Abaqus Analysis User's Guide

Problem description and model definition

A description of the tire and finite element model is given in "Symmetric results transfer for a static tire analysis," Section 3.1.1. To take into account the effect of the skew symmetry of the actual tire in the dynamic analysis, the steady-state rolling analysis is performed on the full three-dimensional model, also referred to as the full model. Inertia effects are ignored since the rolling speed is low ($v_0 = 10$ km/h).

As stated earlier, the steady-state transport capability in Abaqus uses a mixed Eulerian/Lagrangian approach in which, to an observer in the moving reference frame, the material appears to flow through a stationary mesh. The paths that the material points follow through the mesh are referred to as streamlines and must be computed before a steady-state transport analysis can be performed. As discussed in "Symmetric results transfer for a static tire analysis," Section 3.1.1, the streamlines needed for the steady-state transport analyses in this example are computed using the revolve functionality for symmetric model generation.

The incompressible hyperelastic material used to model the rubber in this example includes a time-domain viscoelastic component, which is specified directly using the Prony series parameters. A simple 1-term Prony series model is used. For an incompressible material a 1-term Prony series in Abaqus is defined by providing a single value for the shear relaxation modulus ratio, $\bar{g}_1^P$, and its associated relaxation time, τ_1. In this example $\bar{g}_1^P = 0.3$ and $\tau_1 = 0.1$. The viscoelastic—i.e., material history—effects are included in a steady-state transport step unless you are investigating the long-term behavior of the material. See "Time domain viscoelasticity," Section 22.7.1 of the Abaqus Analysis User's Guide, for a more detailed discussion of modeling time-domain viscoelasticity in Abaqus.

Loading

As discussed in "Symmetric results transfer for a static tire analysis," Section 3.1.1, it is recommended that the footprint analyses be obtained with a friction coefficient of zero (so that no frictional forces are transmitted across the contact surface). The frictional stresses for a rolling tire are very different from the frictional stresses in a stationary tire, even if the tire is rolling at very low speed; therefore, discontinuities may arise in the solution between the last static analysis and the first steady-state transport analysis. Furthermore, varying the friction coefficient from zero at the beginning of the steady-state transport step to its final value at the end of the steady-state transport step ensures that the changes in frictional forces reduce with smaller load increments. This is important if Abaqus must take a smaller load increment to overcome convergence difficulties while trying to obtain the steady-state rolling solution.

Once the static footprint solution for the tire has been computed, the steady-state rolling contact problem can be solved using steady-state transport. The objective of the first simulation in this example is to obtain the straight line, steady-state rolling solutions, including full braking and full traction, at different spinning velocities. We also compute the straight line, free rolling solution. In the second simulation free rolling solutions at different slip angles are computed. In the first and second simulations material history effects are ignored by specifying that the long-term behavior of the material is to be

used. The third simulation repeats a portion of the straight line, steady-state rolling analysis from the first simulation; however, material history effects are included if you do not specify a long-term material response. A steady ground velocity of 10.0 km/h is maintained for all the simulations. The objective of the fourth simulation is to obtain the free rolling solution of the tire in contact with a 1.5 m rigid drum rotating at 3.7 rad/s.

In the first simulation (rollingtire_brake_trac.inp) the full braking solution is obtained in the first steady-state transport step by setting the friction coefficient, μ, to its final value of 1.0 by changing friction properties and applying the translational ground velocity together with a spinning angular velocity that will result in full braking. An estimate of the angular velocity corresponding to full braking is obtained as follows. A free rolling tire generally travels farther in one revolution than determined by its center height, H, but less than determined by the free tire radius. In this example the free radius is 316.2 mm and the vertical deflection is approximately 20.0 mm, so $H = 296.2$ mm. Using the free radius and the effective height, it is estimated that free rolling occurs at an angular velocity between $\omega = 8.78$ rad/s and $\omega = 9.38$ rad/s. Smaller angular velocities would result in braking, and larger angular velocities would result in traction. We use an angular velocity $\omega = 8.0$ rad/s to ensure that the solution in the first steady-state transport step is a full braking solution (all contact points are slipping, so the magnitude of the total frictional force across the contact surface is μN).

In the second steady-state transport analysis step of the full model, the angular velocity is increased gradually to $\omega = 10.0$ rad/s while the ground velocity is held constant. The solution at each load increment is a steady-state solution to the loads acting on the structure at that instant so that a series of steady-state solutions between full braking and full traction is obtained. This analysis provides us with a preliminary estimate of the free rolling velocity. The second simulation (rollingtire_trac_res.inp) performs a refined search around the first estimate of free rolling conditions.

In the third simulation (rollingtire_slipangles.inp) the free rolling solutions at different slip angles are computed. The slip angle, θ, is the angle between the direction of travel and the plane normal to the axle of the tire. In the first step the straight line, free rolling solution from the first simulation is brought into equilibrium. This step is followed by a steady-state transport step where the slip angle is gradually increased from $\theta = 0.0°$ at the beginning of the step to $\theta = 3.0°$ at the end of the step, so a series of steady-state solutions at different slip angles is obtained. This is accomplished by prescribing a traveling velocity vector with components $v_x = v_0 \cos\theta$ and $v_y = v_0 \sin\theta$ in the prescribed translational motion, where $\theta = 0.0°$ in the first steady-state transport step and $\theta = 3.0°$ at the end of the second steady-state transport step.

The fourth simulation (rollingtire_materialhistory.inp) includes a series of steady-state solutions between full braking and full traction in which the material history effects are included.

The fifth simulation (rollingtire_camber.inp) analyzes the effect of camber angle on the lateral thrust at the contact patch under free rolling conditions.

The final simulation in this example (rollingtire_drum.inp) considers a tire in contact with a rigid rotating drum. The loading sequence is similar to the loading sequence used in the first simulation. However, in this simulation the translational velocity of the tire is zero, and a rotational angular velocity is applied to the reference node of the rigid drum. Since a prescribed load is applied to the rigid drum reference node to establish contact between the tire and drum, the rotation axis of the drum is unknown prior to the analysis. Abaqus automatically updates the rotation axis to its current position if the angular

velocity is defined. The rotational velocity of the rigid surface can also be defined. In that case the position and orientation of the axis of revolution must be defined in the steady-state configuration and, therefore, must be known prior to the analysis. The position and orientation of the axis are applied at the beginning of the step and remain fixed during the step. When the drum radius is large compared to the axle displacement, as in this example, it is a reasonable approximation to define the axle in the original configuration without significantly affecting the accuracy of the results.

Results and discussion

Figure 3.1.2–1 and Figure 3.1.2–2 show the reaction force parallel to the ground (referred to as rolling resistance) and the torque, T, on the tire axle at different spinning velocities. The figures compare the solutions obtained for a tire rolling on a flat rigid surface with those for a tire in contact with a rotating drum. The figures show that straight line free rolling, $T = 0.0$, occurs at a spinning velocity of approximately 9.0 rad/s. Full braking occurs at spinning velocities smaller than 8.0 rad/s, and full traction occurs at velocities larger than 9.75 rad/s. At these spinning velocities all contact points are slipping, and the rolling resistance reaches the limiting value μN.

Figure 3.1.2–3 and Figure 3.1.2–4 show shear stress along the centerline of the tire surface in the free rolling and full traction states for the case where the tire is rolling along a flat rigid surface. The distance along the centerline is measured as an angle with respect to a plane parallel to the ground passing through the tire axle. The dashed line is the maximum or limiting shear stress, μp, that can be transmitted across the surface, where p is the contact pressure. The figures show that all contact points are slipping during full traction. During free rolling all points stick.

A better approximation to the angular velocity that corresponds to free rolling can be made by using the results generated by rollingtire_brake_trac.inp to refine the search about an angular velocity of 9.0 rad/s. The file rollingtire_trac_res.inp restarts the previous straight line rolling analysis from Step 3, Increment 8 (corresponding to an angular velocity of 8.938 rad/s) and performs a refined search up to 9.04 rad/s. Figure 3.1.2–5 shows the torque, T, on the tire axle computed in the refined search, which leads to a more precise value for the free rolling angular velocity of approximately 9.022 rad/s. This result is used for the model where the free rolling solutions at different slip angles are computed.

Figure 3.1.2–6 shows the transverse force (force along the tire axle) measured at different slip angles. The figure compares the steady-state transport analysis prediction with the result obtained from a pure Lagrangian analysis. The Lagrangian solution is obtained by performing an explicit transient analysis using Abaqus/Explicit (discussed in "Import of a steady-state rolling tire," Section 3.1.6). With this analysis technique a prescribed constant traveling velocity is applied to the tire, which is free to roll along the rigid surface. Since more than one revolution is necessary to obtain a steady-state configuration, fine meshing is required along the full circumference; hence, the Lagrangian solution is much more costly than the steady-state solutions shown in this example. The figure shows good agreement between the results obtained from the two analysis techniques.

Figure 3.1.2–7 compares the free rolling solutions with and without material history effects included. The solid lines in the diagram represent the rolling resistance (force parallel to the ground along the traveling direction); and the broken lines, the torque (normalized with respect to the free radius) on the axle. The figure shows that free rolling occurs at a lower angular velocity when history effects are included. The influence of material history effects on a steady-state rolling solution is discussed in detail

in "Steady-state spinning of a disk in contact with a foundation," Section 1.5.2 of the Abaqus Benchmarks Guide.

Figure 3.1.2–8 shows the camber thrust as a function of camber angle. The lateral force at zero camber and zero slip is referred to as ply-steer and arises due to the asymmetry in the tire caused by the separation of the belts by the interply distance. Discretization of the contact patch is responsible for the non-smooth nature of the curve, and an overall camber stiffness of 44 N/degree is reasonably close to expected levels.

Figure 3.1.2–9 shows the torque on the rim as the rotational velocity is applied with user subroutine **UMOTION**, based on the free rolling velocity predicted in user subroutine **URDFIL**. As the torque on the rim falls to within a user-specified tolerance of zero torque, the rotational velocity is held fixed and the step completed. Initially, when the free rolling rotational velocity estimates are beyond a user-specified tolerance of the current rotational velocity, only small increments of rotational velocity are applied. The message file contains information on the estimates of free rolling velocity and the incrementation as the solution progresses. The angular velocity thus found for free rolling conditions is 9.026 rad/s.

Acknowledgments

SIMULIA gratefully acknowledges Hankook Tire and Yokohama Rubber Company for their cooperation in developing the steady-state transport capability used in this example. SIMULIA thanks Dr. Koishi of Yokohama Rubber Company for supplying the geometry and material properties used in this example.

Input files

rollingtire_brake_trac.inp	Three-dimensional full model for the full braking and traction analyses.
rollingtire_trac_res.inp	Three-dimensional full model for the refined braking and traction analyses.
rollingtire_slipangles.inp	Three-dimensional full model for the slip angle analysis.
rollingtire_camber.inp	Three-dimensional full model for the camber analysis.
rollingtire_materialhistory.inp	Three-dimensional full model with material history effects.
rollingtire_drum.inp	Three-dimensional full model for the simulation of rolling on a rigid drum.
rollingtire_freeroll.inp	Three-dimensional full model for the direct approach to finding the free rolling solution.
rollingtire_freeroll.f	User subroutine file used to find the free rolling solution.

Reference

- Koishi, M., K. Kabe, and M. Shiratori, "Tire Cornering Simulation using Explicit Finite Element Analysis Code," 16th annual conference of the Tire Society at the University of Akron, 1997.

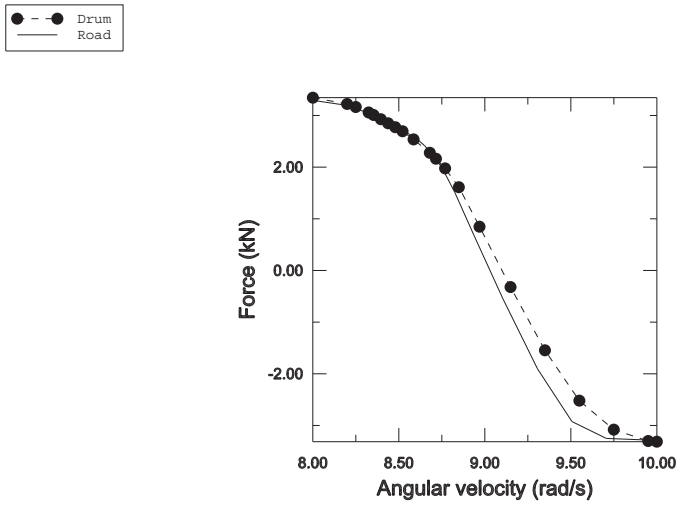

Figure 3.1.2–1 Rolling resistance at different angular velocities.

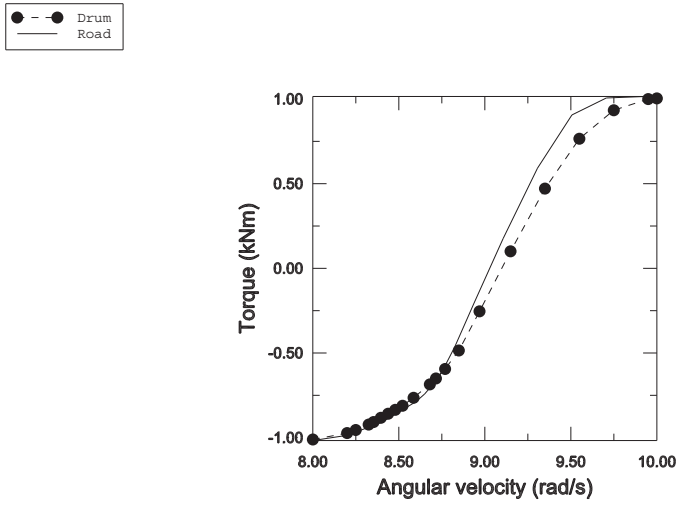

Figure 3.1.2–2 Torque at different angular velocities.

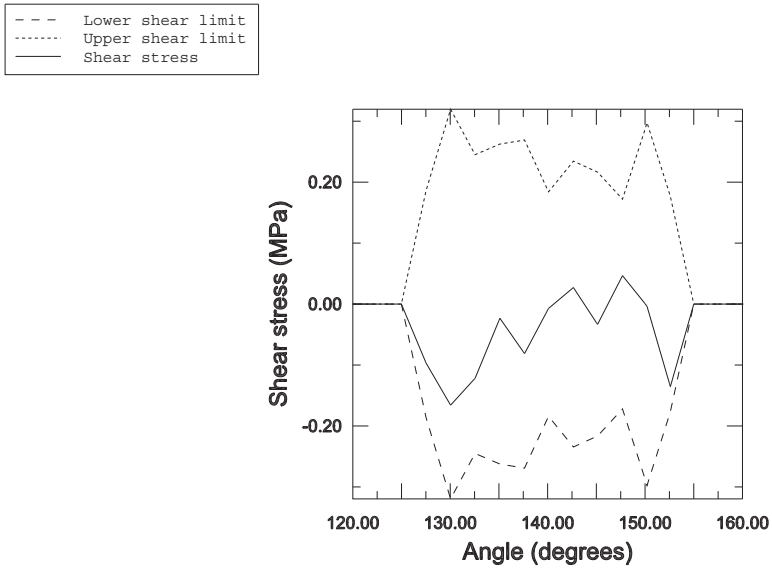

Figure 3.1.2–3 Shear stress along tire center (free rolling).

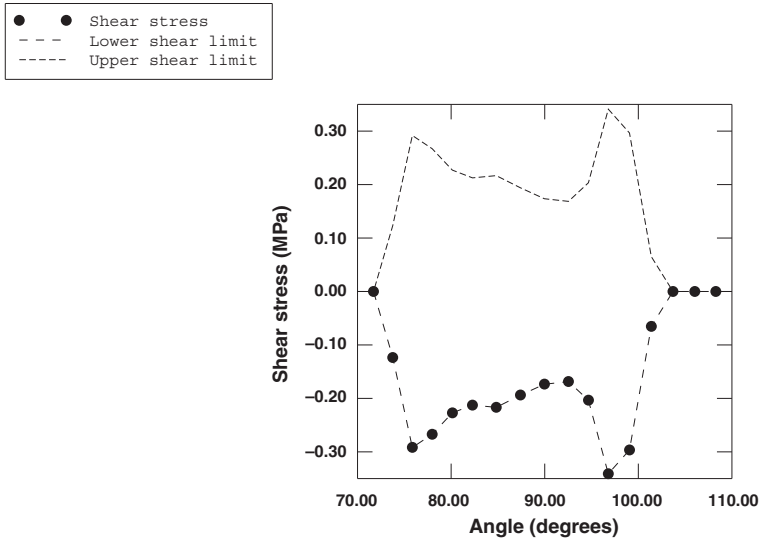

Figure 3.1.2–4 Shear stress along tire center (full traction).

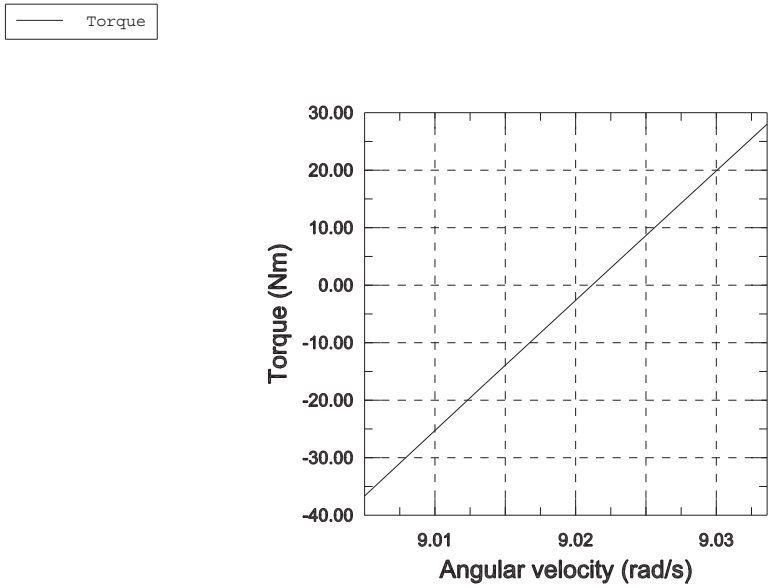

Figure 3.1.2–5 Torque at different angular velocities (refined search).

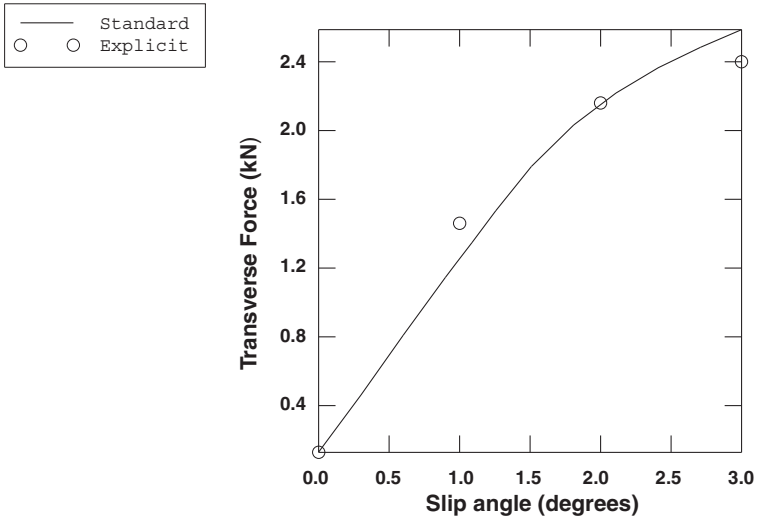

Figure 3.1.2–6 Transverse force as a function of slip angle.

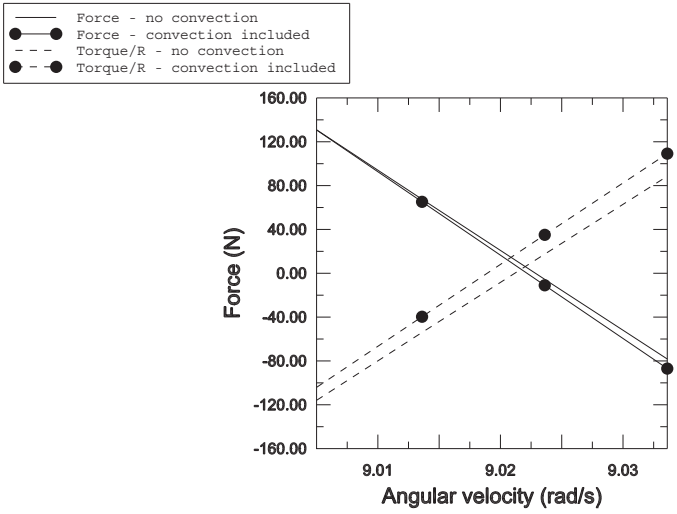

Figure 3.1.2–7 Rolling resistance and normalized torque as a function of angular velocity (R=0.3162 m).

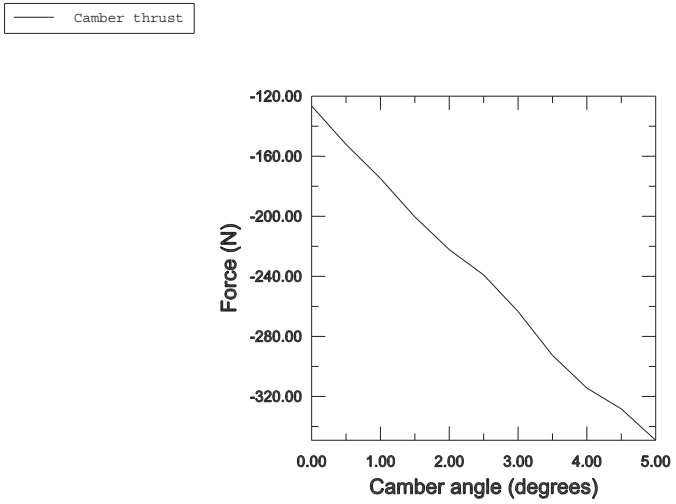

Figure 3.1.2–8 Camber thrust as a function of camber angle.

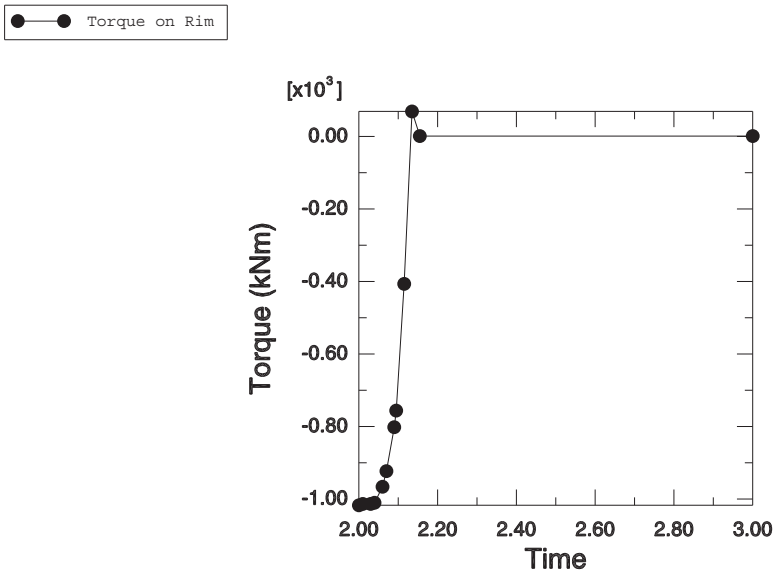

Figure 3.1.2–9 Torque on the rim for the direct approach to finding the free rolling solution.

3.1.3 SUBSPACE-BASED STEADY-STATE DYNAMIC TIRE ANALYSIS

Product: Abaqus/Standard

This example illustrates the use of subspace-based steady-state dynamic analysis to model the frequency response of a tire about a static footprint solution.

Subspace-based steady-state dynamic analysis ("Subspace-based steady-state dynamic analysis," Section 6.3.9 of the Abaqus Analysis User's Guide) is an analysis procedure that can be used to calculate the steady-state dynamic response of a system subjected to harmonic excitation. It does so by the direct solution of the steady-state dynamic equations projected onto a reduced-dimensional subspace spanned by a set of eigenmodes of the undamped system. If the dimension of the subspace is small compared to the dimension of the original problem (i.e., if a relatively small number of eigenmodes is used), the subspace method can offer a very cost-effective alternative to a direct-solution steady-state analysis.

The purpose of this analysis is to obtain the frequency response of a 175 SR14 tire subjected to a harmonic load excitation about the footprint solution discussed in "Symmetric results transfer for a static tire analysis," Section 3.1.1. Symmetric results transfer and symmetric model generation are used to generate the footprint solution, which serves as the base state in the steady-state dynamics calculations.

Problem description

A description of the tire being modeled is given in "Symmetric results transfer for a static tire analysis," Section 3.1.1. In this example we exploit the symmetry in the tire model and utilize the results transfer capability in Abaqus to compute the footprint solution for the full three-dimensional model in a manner identical to that discussed in "Symmetric results transfer for a static tire analysis," Section 3.1.1.

Once the footprint solution has been computed, several steady-state dynamic steps are performed. Both direct-solution steady-state dynamic analysis and subspace-based steady-state dynamic analysis are used. Besides being used to validate the subspace projection results, the direct steady-state procedure allows us to demonstrate the computational advantage afforded by the subspace projection capability in Abaqus.

Model definition

The model used in this analysis is essentially identical to that used in the first simulation discussed in "Symmetric results transfer for a static tire analysis," Section 3.1.1, with CGAX4H and CGAX3H elements used in the axisymmetric model and rebar in the continuum elements for the belts and carcass. In addition, instead of using a nonuniform discretization about the circumference, the uniform discretization shown in Figure 3.1.3–1 is used.

The incompressible hyperelastic material used to model the rubber includes a viscoelastic component described by a 1-term Prony series of the dimensionless shear relaxation modulus:

$$g_R(t) = 1 - \bar{g}_1^P(1 - e^{-t/\tau_1}),$$

with relaxation coefficient $\overline{g}_1^P = 0.3$ and relaxation time $\tau_1 = 0.1$. Since the material is incompressible, the volumetric behavior is time independent. This time domain description of the material must be written in the frequency domain to perform a steady-state dynamic analysis. By applying a Fourier transform, the expressions for the time-dependent shear modulus can be written in the frequency domain as follows:

$$G_s(\omega) = G_0[1 - g_1^P] + G_0 \frac{g_1^P \tau_1^2 \omega^2}{1 + \tau_1^2 \omega^2},$$

$$G_\ell(\omega) = G_0 \frac{g_1^P \tau_1 \omega}{1 + \tau_1^2 \omega^2},$$

where $G_s(\omega)$ is the storage modulus, $G_\ell(\omega)$ is the loss modulus, and ω is the angular frequency. Abaqus will perform the conversion from time domain to frequency domain automatically if the Prony series parameters are defined. See "Time domain viscoelasticity," Section 22.7.1 of the Abaqus Analysis User's Guide, for a more detailed discussion on frequency domain viscoelasticity.

Loading

The loading sequence for computing the footprint solution is identical to that discussed in "Symmetric results transfer for a static tire analysis," Section 3.1.1, with the axisymmetric model contained in tiredynamic_axi_half.inp, the partial three-dimensional model in tiredynamic_symmetric.inp, and the full three-dimensional model in tiredynamic_freqresp.inp. Since geometric nonlinearity is accounted for in the static steps used in computing the footprint solution, the steady-state dynamic analyses, which are linear perturbation procedures, are performed about the nonlinear deformed shape of the footprint solution.

The first frequency response analyses of the tire are performed using the subspace-based steady-state dynamic analysis. The excitation is due to a harmonic vertical load of 200 N, which is applied to the analytical rigid surface through its reference node. The frequency is swept from 80 Hz to 130 Hz. The rim of the tire is held fixed throughout the analysis. Prior to the subspace analysis being performed, the eigenmodes that are used for the subspace projection are computed in an eigenfrequency extraction step. In the frequency step the first 20 eigenpairs are extracted, for which the computed eigenvalues range from 50 to 185 Hz.

The accuracy of the subspace analysis can be improved by including some of the stiffness associated with frequency-dependent material properties—i.e., viscoelasticity—in the eigenmode extraction step. In general, if the material response does not vary significantly over the frequency range of interest, the frequency extraction can be set to evaluate properties at the frequency in the center of the frequency span. Otherwise, more accurate results will be obtained by running several separate frequency analyses over smaller frequency ranges. In this example a single frequency sweep is performed to evaluate properties at 105 Hz.

The main advantage that the subspace projection method offers over mode-based techniques ("Mode-based steady-state dynamic analysis," Section 6.3.8 of the Abaqus Analysis User's Guide) is that it allows frequency-dependent material properties, such as viscoelasticity, to be included directly in the analysis. However, there is a cost involved in assembling the projected equations, and this cost must

be taken into account when deciding between a subspace solution and a direct solution. Abaqus offers four methods to control how often the projected subspace equations are recomputed. These methods are computing the projected equations for every frequency in the analysis, recomputing projected equations only at the eigenfrequencies, recomputing projected equations when the stiffness and/or damping properties have changed by a user-specified percentage, and computing the projected equations only once at the center of the frequency range specified in the steady-state dynamic step. Computing the projected equations for every frequency is, in general, the most accurate option; however, the computational overhead associated with recomputing the projected equations at every frequency can significantly reduce the cost benefit of the subspace method versus a direct solution. Computing the projected equations only once at the center of the frequency range is the most inexpensive choice, but it should be chosen only when the material properties do not depend strongly on frequency. In general, the accuracy and cost associated with the four subspace projection methods are strongly problem dependent. In this example problem the results and computational expense for all four subspace projection methods are discussed.

The results from the various subspace analyses are compared to the results from a direct-solution steady-state dynamic analysis.

Results and discussion

Each of the subspace analyses utilizes all 20 modes extracted in the eigenfrequency extraction step. Figure 3.1.3–2 shows the frequency response plots of the vertical displacements of the road's reference node for the direct solution along with the four subspace solutions using each of the subspace projection methods discussed above. Similarly, Figure 3.1.3–3 shows the frequency response plots of the horizontal displacement of a node on the tire's sidewall for the same five analyses. As illustrated in Figure 3.1.3–2 and Figure 3.1.3–3, all four of the subspace projection methods yield almost identical solutions; except for small discrepancies in the vertical displacements at 92 and 120 Hz, the subspace projection solutions closely match the direct solution as well. Timing results shown in Table 3.1.3–1 show that the subspace projection method results in savings in CPU time versus the direct solution.

Input files

tiredynamic_axi_half.inp	Axisymmetric model, inflation analysis.
tiredynamic_symmetric.inp	Partial three-dimensional model, footprint analysis.
tiredynamic_freqresp.inp	Full three-dimensional model, steady-state dynamic analyses.
tiredynamic_axi_half_ml.inp	Axisymmetric model, inflation analysis with Marlow hyperelastic model.
tiredynamic_symmetric_ml.inp	Partial three-dimensional model, footprint analysis with Marlow hyperelastic model.
tiredynamic_freqresp_ml.inp	Full three-dimensional model, steady-state dynamic analyses with Marlow hyperelastic model.
tiretransfer_node.inp	Nodal coordinates for axisymmetric model.

Table 3.1.3–1 Comparison of normalized CPU times (normalized with respect to the direct-solution analysis) for the frequency sweep from 80 Hz to 130 Hz and the eigenfrequency extraction step.

Direct-solution analysis method	Normalized CPU time
Subspace (projection at all frequencies)	0.89
Subspace (projection at eigenfrequencies)	0.54
Subspace (projection when properties change)	0.49
Subspace (projection computed once)	0.36
Direct	1.0
Eigenfrequency extraction	0.073

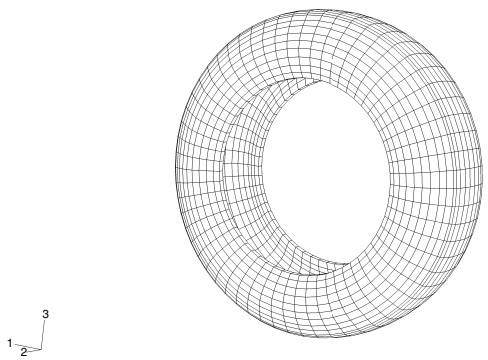

Figure 3.1.3–1 Uniform three-dimensional tire mesh.

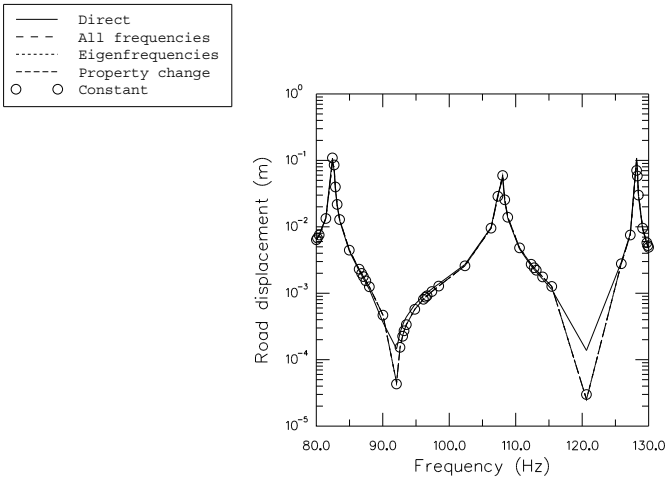

Figure 3.1.3–2 Frequency response of the vertical road displacement due to a vertical harmonic point load of 200 N applied to the reference node.

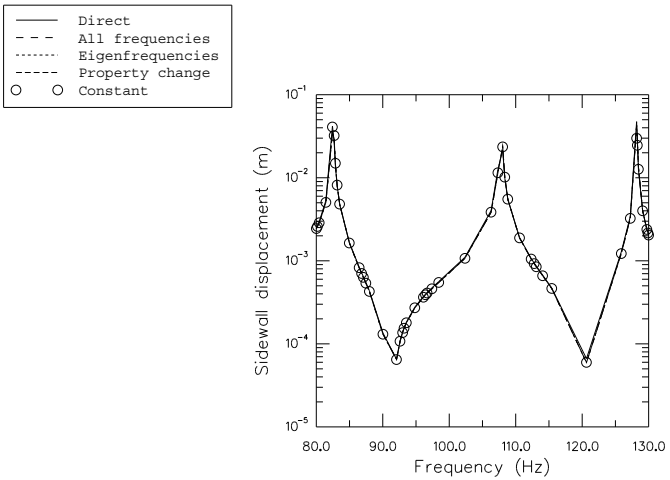

Figure 3.1.3–3 Frequency response of the horizontal sidewall displacement due to a vertical harmonic point load of 200 N applied to the reference node.

3.1.4 STEADY-STATE DYNAMIC ANALYSIS OF A TIRE SUBSTRUCTURE

Product: Abaqus/Standard

This example illustrates the use of the substructuring capability in Abaqus to create a substructure from a tire under inflation and footprint loading.

Use of tire substructures is often seen in vehicle dynamic analyses where substantial cost savings are made using substructures instead of the whole tire model. Since tires behave very nonlinearly, it is essential that the change in response due to preloads is built into the substructure. Here the substructure must be generated in a preloaded state. Some special considerations for creating substructures with preloads involving contact are also discussed.

Related topics

- "Defining substructures," Section 10.1.2 of the Abaqus Analysis User's Guide

Problem description and model definition

A description of the tire model used is given in "Symmetric results transfer for a static tire analysis," Section 3.1.1. In this problem inflation and fooptprint preloads are applied in a series of general analysis steps identical to "Symmetric results transfer for a static tire analysis," Section 3.1.1. Symmetric model generation and symmetric results transfer are used to exploit the symmetric nature of the structure and loading. Nodes in the bead area are tied to the rigid body representing the rim.

The substructure's retained nodes include the rim node and all nodes in the footprint. To enhance the dynamic response of the substructure, these interfacial degrees of freedom are augmented with generalized degrees of freedom associated with the first 20 fixed interface eigenmodes. Depending on the nature of the loading, it may be necessary to increase the number of generalized degrees of freedom to cover a sufficient range of frequencies. The extra cost incurred due to the addition of the extra frequency extraction step is offset by the enhanced dynamic response of the substructure.

Loading

An inflation load of 200 kPa is applied in the axisymmetric half-tire model contained in substructtire_axi_half.inp. This is followed by a footprint load of 1650 N applied to the three-dimensional half-tire model given in substructtire_symmetric.inp; and, subsequently, results are transferred to the full tire model with the complete footprint load of 3300 N. All of these steps are run with the NLGEOM=YES parameter, so all preload effects including stress stiffening are taken into account when the substructure is generated.

To retain degrees of freedom that are involved in contact constraints at the footprint, it is necessary to replace the contact constraints with boundary conditions. This is done once the footprint solution is obtained by fixing the retained nodes in the deformed state and removing the contact pair between the footprint patch and the road surface. Without this change, the contact constraints produce large stiffness terms in the substructure stiffness that can produce non-physical behavior at the usage level.

The mechanical response of the substructure is unchanged because the tire is held in its deformed state by a fixed boundary condition. These boundary conditions on the retained degrees of freedom are then released in the substructure generation step, in which they are replaced with concentrated loads. To carry out these steps, it is necessary to obtain the list of nodes in contact with the road. Hence, the substructure is generated in a restart analysis following the analysis with the preloads. This makes it possible to construct the list of nodes that are involved in contact with the road at the end of the preloading. It is necessary to activate element removal in the analysis prior to substructure generation to enable the removal of the contact constraints.

To enhance the dynamic response of the substructure, several restrained eigenmodes are included as generalized degrees of freedom. These restrained eigenmodes are obtained from an eigenfrequency extraction step with all the retained degrees of freedom restrained. In this example the first 20 eigenmodes, corresponding to a frequency range of 50 to 134 Hz, are computed. With 67 nodes in the footprint, one rim node with six degrees of freedom, and 20 generalized degrees of freedom, the substructure has 227 degrees of freedom.

At the usage level the nodes that form the footprint patch in the tire model are restrained to a single node. The steady-state response of the substructure to harmonic footprint loading is analyzed over a range of frequencies from 40 to 130 Hz.

Results and discussion

A steady-state dynamic analysis of the substructure is relatively inexpensive compared to running a similar analysis with the entire tire model. The results for the frequency sweep are shown in Figure 3.1.4–1, which compares the response of the substructure to the response of the entire tire model. All resonances in the tire model are captured by the substructure. This result shows that, although the static response of the tire is used to condense the stiffness and the mass for the retained degrees of freedom, relatively few generalized degrees of freedom can adequately enhance the dynamic response of the substructure. However, the associated expense of calculating the restrained eigenmodes must be taken into account when considering the total cost.

The tire model used for comparison in this example is the same as the model used in “Symmetric results transfer for a static tire analysis,” Section 3.1.1, with one difference. Friction is activated in a step prior to the steady-state dynamics step to activate constraints in the contact tangential direction on nodes in the footprint so that constraints equivalent to those applied on the footprint nodes in the substructure model are produced.

Input files

substructtire_axi_half.inp	Axisymmetric model, inflation analysis.
substructtire_symmetric.inp	Partial three-dimensional model, footprint analysis.
substructtire_full.inp	Full three-dimensional model, final equilibrium analysis.
substructtire_generate.inp	Substructure generation analysis.
substructtire_dynamic.inp	Usage level model with steady-state dynamics analysis.

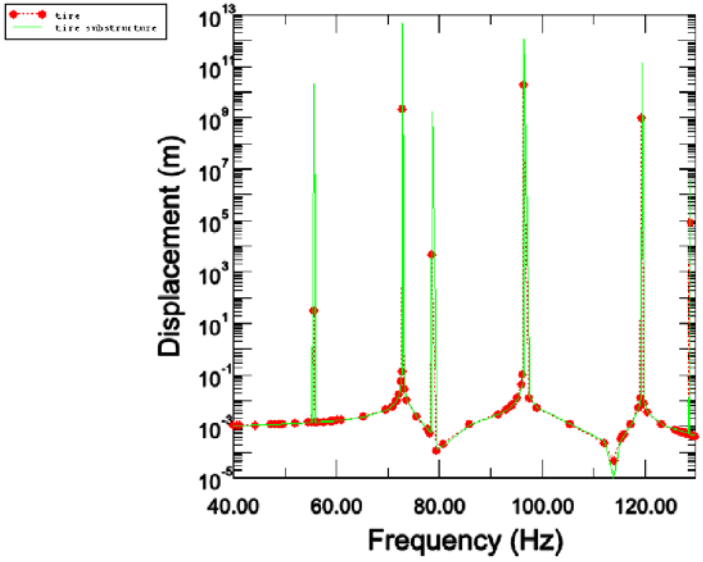

Figure 3.1.4–1 Vertical response of the road node due to unit vertical harmonic load.

3.1.5 COUPLED ACOUSTIC-STRUCTURAL ANALYSIS OF A TIRE FILLED WITH AIR

Product: Abaqus/Standard

This example studies the acoustic response of a tire and air cavity subjected to an inflation pressure and footprint load.

The air cavity resonance in a tire is often a significant contributor to the vehicle interior noise, particularly when the resonance of the tire couples with the cavity resonance. This example demonstrates how the ALE adaptive mesh domain can be used to update an acoustic mesh when structural deformation causes significant changes to the geometry of the acoustic domain. The effect of rolling motion is ignored; however, the rolling speed can have a significant influence on the coupled acoustic-structural response. This effect is investigated in detail in "Dynamic analysis of an air-filled tire with rolling transport effects," Section 3.1.9.

The acoustic elements in Abaqus model only small-strain dilatational behavior through pressure degrees of freedom and, therefore, cannot model the deformation of the fluid when the bounding structure undergoes large deformation. Abaqus solves the problem of computing the current configuration of the acoustic domain by periodically creating a new acoustic mesh. The new mesh uses the same topology (elements and connectivity) throughout the simulation, but the nodal locations are adjusted periodically so that the deformation of the structural-acoustic boundary does not lead to severe distortion of the acoustic elements. The calculation of the updated nodal locations is based on adaptive mesh smoothing.

Problem description

A detailed description of the tire model is provided in "Symmetric results transfer for a static tire analysis," Section 3.1.1. We model the rubber as an incompressible hyperelastic material and include damping in the structure by specifying a 1-term Prony series viscoelastic material model with a relaxation modulus of 0.3 and relaxation time of 0.1 s. We define the model in the frequency domain with a direct specification of the Prony series parameters since we want to include the damping effects in a steady-state dynamic simulation.

The air cavity in the model is defined as the space enclosed between the interior surface of the tire and a cylindrical surface of the same diameter as the diameter of the bead. A segment of the tire is shown in Figure 3.1.5–1. The values of the bulk modulus and the density of air are taken to be 426 kPa and 3.6 kg/m^3, respectively, and represent the properties of air at the tire inflation pressure.

The simulation assumes that both the road and rim are rigid. We further assume that the contact between the road and the tire is frictionless during the preloading analyses. However, we use a nonzero friction coefficient in the subsequent coupled acoustic-structural analyses.

Model definition

We use a tire model that is identical to that used in the simulation described in "Symmetric results transfer for a static tire analysis," Section 3.1.1. The air cavity is discretized using linear acoustic elements and is coupled to the structural mesh using a surface-based tie constraint with the slave surface defined on the acoustic domain. We model the rigid rim by applying fixed boundary conditions to the nodes on the bead

of the tire, while the interaction between the air cavity and rim is modeled by a traction-free surface; i.e., no boundary conditions are prescribed on the surface.

Symmetric model generation and symmetric results transfer, together with a static analysis procedure, are used to generate the preloading solution, which serves as the base state in the subsequent coupled acoustic-structural analyses.

In the first coupled analysis we compute the eigenvalues of the tire and air cavity system. This analysis is followed by a direct-solution and a subspace-based steady-state dynamic analysis in which we obtain the response of the tire-air system subjected to harmonic excitation of the spindle.

A coupled structural-acoustic substructure analysis is performed as well. Frequency-dependent viscoelastic material properties are evaluated at 230 Hz, which is the middle of the frequency range of the steady-state dynamic analysis. The viscoelastic material contributions to the stiffness and structural damping operator are taken into account. They are assumed to be constant with respect to frequency. A substructure is generated using mixed-interface dynamic modes (see "Defining the retained degrees of freedom" in "Defining substructures," Section 10.1.2 of the Abaqus Analysis User's Guide). A retained degree of freedom that is loaded in the steady-state dynamic analysis is not constrained during the eigenmode extraction. Usually this modeling technique provides a more accurate solution than that obtained using the traditional Craig-Bampton substructures with the fixed-interface dynamic modes.

Loading

The loading sequence for computing the footprint solution is identical to that discussed in "Symmetric results transfer for a static tire analysis," Section 3.1.1. The simulation starts with an axisymmetric model, which includes the mesh for the air cavity. Only half the cross-section is modeled. The inflation pressure is applied to the structure using a static analysis. In this example the application of pressure does not cause significant changes to the geometry of the air cavity, so it is not necessary to update the acoustic mesh. However, we perform adaptive mesh smoothing after the pressure is applied to illustrate that the updated geometry of the acoustic domain is transferred to the three-dimensional model when symmetric results transfer is used.

The axisymmetric analysis is followed by a partial three-dimensional analysis in which the footprint solution is obtained. The footprint load is established over several load increments. The deformation during each load increment causes significant changes to the geometry of the air cavity. We update the acoustic mesh by performing 5 mesh sweeps after each converged structural load increment using an ALE adaptive mesh domain. At the end of this analysis sequence we activate friction between the tire and road by changing the friction properties. This footprint solution, which includes the updated acoustic domain, is transferred to a full three-dimensional model. This model is used to perform the coupled analysis. In the first coupled analysis we extract the eigenvalues of the undamped system, followed by a direct-solution steady-state dynamic analysis in which we apply a harmonic excitation to the reference node of the rigid surface that is used to model the road. We apply two load cases: one in which the excitation is applied normal to the road surface and one in which the excitation is applied parallel to the road surface along the rolling (fore-aft) direction.

We want to compute the response of the coupled system in the frequency range in which we expect the air cavity to contribute to the overall acoustic response. We consider the response near the first eigenfrequency of the air cavity only, which has a wavelength that is equal to the circumference of the

tire. Using a value of 344 m/s for the speed of sound and an air cavity radius of 0.240 m (the average of the minimum and maximum radius of the air cavity), we estimate this frequency to be approximately 230 Hz. We extract the eigenvalues and perform the steady-state dynamic analysis in the frequency range between 200 Hz to 260 Hz. In the eigenvalue extraction analysis, stiffness contributions from the frequency-dependent viscoelasticity material model are evaluated at a frequency of 230 Hz. In the direct-solution and subspace-based steady-state dynamic analyses, frequency-dependent contributions to the stiffness and damping are evaluated at every frequency point.

The same inflation and loading steps were used for the substructure analysis. In the substructure analysis, the frequency-dependence of viscoelastic material properties cannot be taken into account. Only a vertical excitation load case is considered.

Results and discussion

Figure 3.1.5–1 shows the updated acoustic mesh near the footprint region. The geometric changes associated with the updated mesh are taken into account in the coupled acoustic-structural analyses.

The eigenvalues of the air cavity, the tire, and the coupled tire-air system are tabulated in Table 3.1.5–1. The resonant frequencies of the uncoupled air cavity are computed using the original configuration. We obtain two acoustic modes at frequencies of 228.58 Hz and 230.17 Hz. These frequencies correspond to two identical modes rotated 90° with respect to each other, as shown in Figure 3.1.5–2 and Figure 3.1.5–3; the magnitudes of the frequencies are different since we have used a nonuniform mesh along the circumferential direction. We refer to the two modes as the fore-aft mode and the vertical mode, respectively. These eigenfrequencies correspond very closely to our original estimate of 230 Hz. The table shows that these eigenfrequencies occur at almost the same magnitude in the coupled system, indicating that the coupling has a very small effect on the acoustic resonance. The difference between the two vertical modes is larger than the difference between the fore-aft modes. This can be attributed to the geometry changes associated with structural loading. The coupling has a much stronger influence on the structural modes than on the acoustic modes, but we expect the coupling to decrease as we move away from the 230 Hz range.

Figure 3.1.5–4 to Figure 3.1.5–7 show the response of the structure to the spindle excitation. Figure 3.1.5–4 and Figure 3.1.5–5 compare the response of the coupled tire-air system to the response of a tire without the air cavity. Figure 3.1.5–6 and Figure 3.1.5–7 show the acoustic pressure measured in the crown and side of the air. We draw the following conclusions from these figures. The frequencies at which resonance is predicted by the steady-state dynamic analysis correspond closely to the eigenfrequencies. However, not all the eigenmodes are excited by the spindle excitations. For example, the fore-aft mode is not excited by vertical loading. Similarly, the vertical mode is not excited by fore-aft loading. In addition, only some of the structural modes are excited by the spindle loads, while others are suppressed by material damping. These figures further show that the air cavity resonance has a very strong influence on the behavior of the coupled system and that the structural resonance of the coupled tire-air system occurs at different frequencies than the resonance of the tire without air. As expected, this coupling effect decreases as we move further away from the cavity resonance frequency.

The eigenfrequencies obtained in the substructure analysis are identical to the eigenfrequencies obtained in the equivalent analysis without substructures. The reaction force obtained at the road reference node is also compared to the reaction force at the same node in the equivalent analysis without

substructures. As shown in Figure 3.1.5–8 the results for the two steady-state dynamics steps in the substructure analysis are virtually identical, and they compare well, in general, with the reaction force obtained in the nonsubstructure analysis. The observed small differences are due to modal truncation and the fact that constant material properties are used to generate the substructure.

Input files

tire_acoustic_axi.inp	Axisymmetric model, inflation analysis.
tire_acoustic_rev.inp	Partial three-dimensional model, footprint analysis.
tire_acoustic_refl.inp	Full three-dimensional model, eigenvalue extraction and frequency response analyses.
tire_substracous_gen.inp	Substructure generation analysis.
tire_substracous_dyn.inp	Substructure usage analysis (eigenvalue extraction and frequency response analyses).
tiretransfer_node.inp	Nodal coordinates for the axisymmetric tire mesh.
tire_acoustic_air.inp	Mesh data for the axisymmetric acoustic mesh.

Table 3.1.5–1 Eigenfrequencies in the 200–260 Hz frequency range.

Mode	Air cavity	Tire	Coupled tire-air
1		202.83	199.06
2		208.95	205.73
3		212.55	210.67
4		220.53	218.64
5		221.30	219.24
6	228.58		228.24
7	230.17		232.18
8		233.42	232.24
9		236.49	234.19
10		244.63	243.12
11		254.84	252.84
12		257.56	255.51

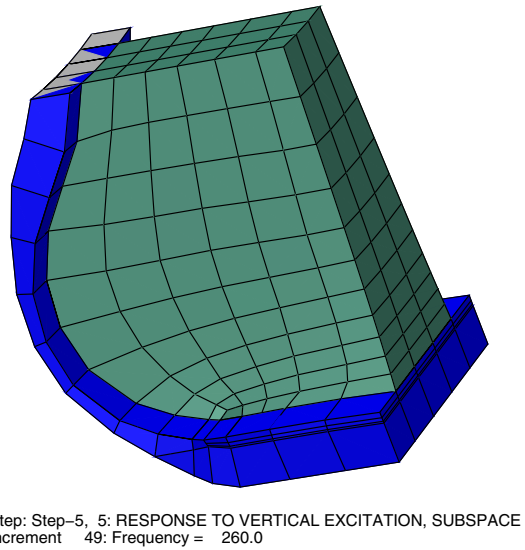

Figure 3.1.5–1 Deformation of tire and air in the footprint region.

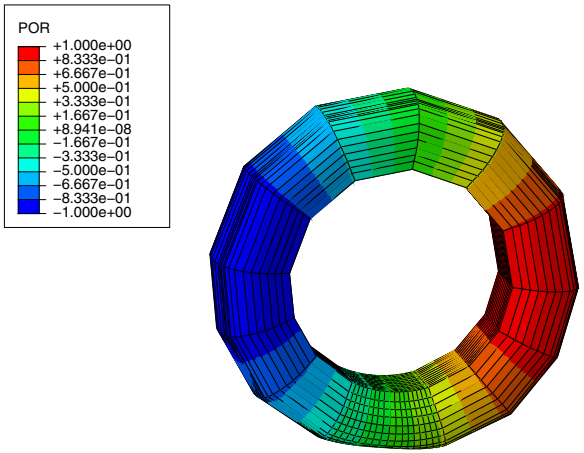

Figure 3.1.5–2 Fore-aft acoustic mode.

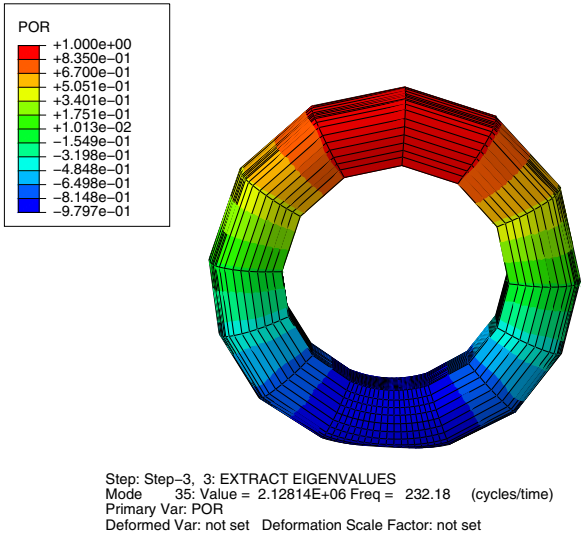

Figure 3.1.5–3 Vertical acoustic mode.

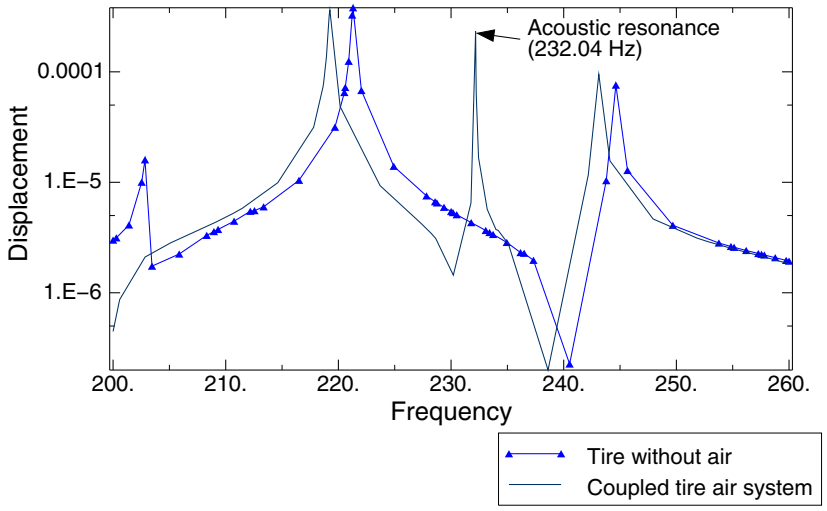

Figure 3.1.5–4 Vertical road displacement due to vertical excitation load.

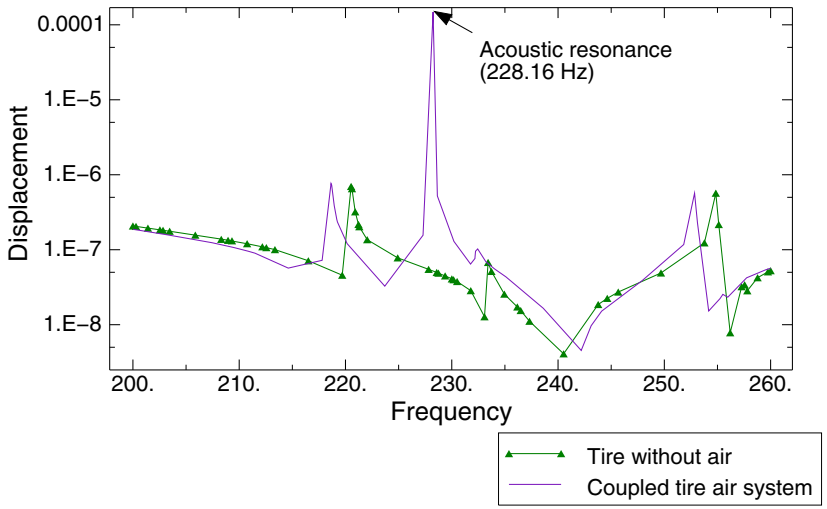

Figure 3.1.5–5 Horizontal road displacement due to horizontal excitation load.

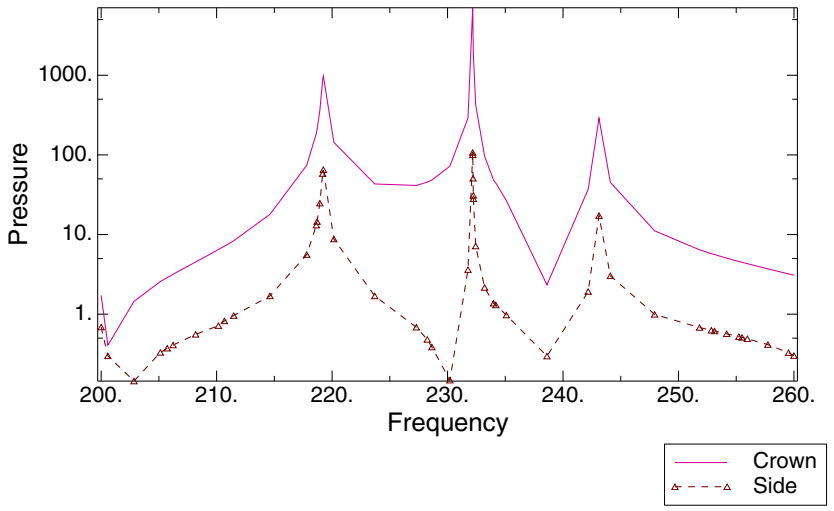

Figure 3.1.5–6 Acoustic pressure due to vertical excitation load.

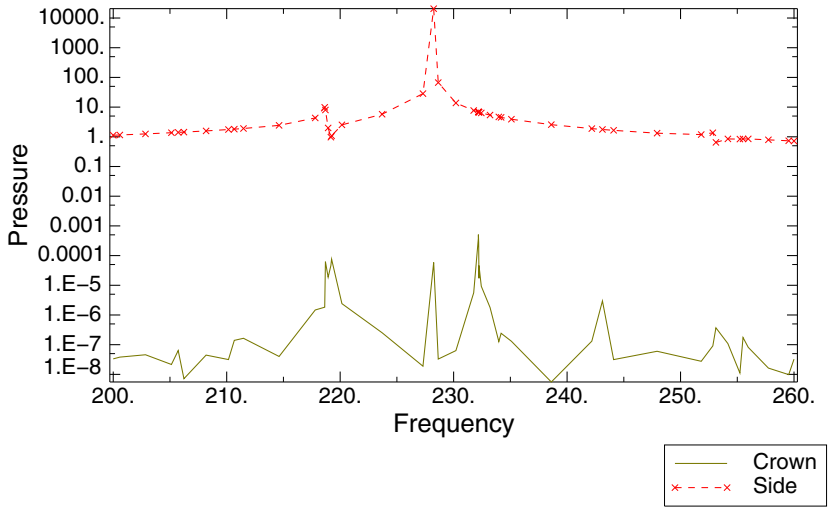

Figure 3.1.5–7 Acoustic pressure due to horizontal excitation load.

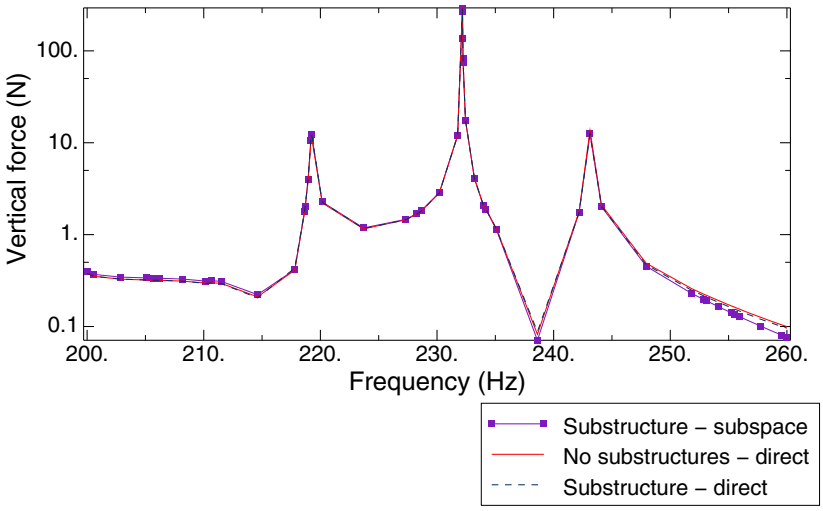

Figure 3.1.5–8 Vertical reaction force due to vertical excitation load.

3.1.6 IMPORT OF A STEADY-STATE ROLLING TIRE

Product: Abaqus/Explicit

This example illustrates the use of the results transfer capability in Abaqus to import results from an Abaqus/Standard steady-state transfer analysis to Abaqus/Explicit to simulate transient rolling.

Examples of loading during transient rolling include impact of a tire with an obstacle or vehicle acceleration. This problem analyzes the impact of a tire with a curb. Because of the small stable time increment necessary for the explicit dynamic procedure and the large time scales involved in simulating quasi-static and steady-state loading, simulating quasi-static inflation loading and steady-state rolling in Abaqus/Standard provides significant cost savings over performing these simulations in Abaqus/Explicit. Moreover, the cost to obtain a steady-state rolling simulation in Abaqus/Explicit increases with rolling speed, whereas in Abaqus/Standard the cost is independent of the magnitude of the rolling speed.

Related topics

- "Transferring results between Abaqus/Explicit and Abaqus/Standard," Section 9.2.2 of the Abaqus Analysis User's Guide

Problem description and model definition

The model used in this example differs slightly from that used in "Symmetric results transfer for a static tire analysis," Section 3.1.1. Since only elements common to both Abaqus/Standard and Abaqus/Explicit can be imported, reduced-integration solid elements are used in this example and nodes in the bead area are attached to rigid elements representing the rim. A plot of the tire before impact with the curb, a 0.025 m high step, is shown in Figure 3.1.6–1. The large rigid body rotation involved in a transient rolling analysis necessitates the use of the nondefault second-order-accurate kinematic formulation in the explicit dynamic analysis. In addition, it is recommended that the enhanced hourglass control scheme be used for both Abaqus/Standard and Abaqus/Explicit for all import analyses. Use section controls in the axisymmetric analysis to specify the enhanced hourglass control scheme.

The inflation and footprint preloads are applied in a series of general analysis steps identical to those described in "Symmetric results transfer for a static tire analysis," Section 3.1.1. Symmetric model generation and symmetric results transfer are used to exploit the symmetric nature of the structure and loading (see "Symmetric model generation," Section 10.4.1 of the Abaqus Analysis User's Guide, and "Transferring results from a symmetric mesh or a partial three-dimensional mesh to a full three-dimensional mesh," Section 10.4.2 of the Abaqus Analysis User's Guide).

The repeated dynamic impact of tire nodes as they come into contact with the road is an unavoidable source of the high frequency noise that can be seen in the reaction force at the rim. The viscoelastic property of the matrix provides sufficient damping to reduce such high frequency noise. No material damping (mass proportional or stiffness proportional) is necessary in this case. The viscoelastic stress contributions from the steady-state transport analysis are imported into the Abaqus/Explicit analysis.

Loading

An inflation load of 200 kPa is applied to the axisymmetric half-tire model in importrolling_axi_half.inp. This load is followed by a footprint load of 1650 N applied to the three-dimensional half-tire model in importrolling_symmetric.inp, and subsequently results are transferred to the full tire model with the complete footprint load of 3300 N.

The rolling analysis involves rolling the tire up to free rolling conditions. As in "Steady-state rolling analysis of a tire," Section 3.1.2, a translational velocity of 10 km/h is applied to the tire. The free rolling velocity of the tire is determined in an independent analysis similar to the one described in "Steady-state rolling analysis of a tire," Section 3.1.2. The rolling velocity corresponding to free rolling conditions is 8.9759 rad/s. Inertia loads are accounted for in this example, since the objective is to import results to a transient dynamic analysis in which inertial effects should be considered during impact with the curb. Viscoelastic effects in the rubber matrix are also included, since viscolasticity is the primary damping mechanism present in the tire.

During the transient dynamic analysis, the tire is moved forward with a prescribed velocity of 10 km/h and the vehicle load is applied to the rim reference node. The tire is allowed to rotate freely about the axle. All other degrees of freedom at the road and rim reference nodes are held fixed.

Results and discussion

Results are imported and the analysis begins at time $t = 3$ sec. A plot of the rotational velocity at the rim in Figure 3.1.6–2 shows that the oscillations at the beginning of the analysis are well within acceptable limits. Impact with the curb is initiated after about a quarter rotation of the tire subsequent to import, at approximately $t = 3.13$ sec. The vertical response of the rim reference node can be seen in Figure 3.1.6–3 and shows oscillations in the tire after impact. The contact patch and the stresses in the belts under steady-state rolling conditions in the transient dynamic solution compare well with the direct steady-state solution from Abaqus/Standard. The pressure in the footprint can be seen in Figure 3.1.6–4, and the stresses in the belts are plotted in Figure 3.1.6–5. A plot of the shear stress during impact in Figure 3.1.6–6 shows that, as expected, the maximum stress is set up in the shoulder region.

Input files

importrolling_axi_half.inp	Axisymmetric model, inflation analysis.
importrolling_symmetric.inp	Half-symmetric three-dimensional model, inflation and footprint analysis.
importrolling_full.inp	Full three-dimensional model, inflation and footprint analysis.
importrolling_roll.inp	Steady-state, free rolling solution.
importrolling_xpl.inp	Import and transient dynamic analysis.

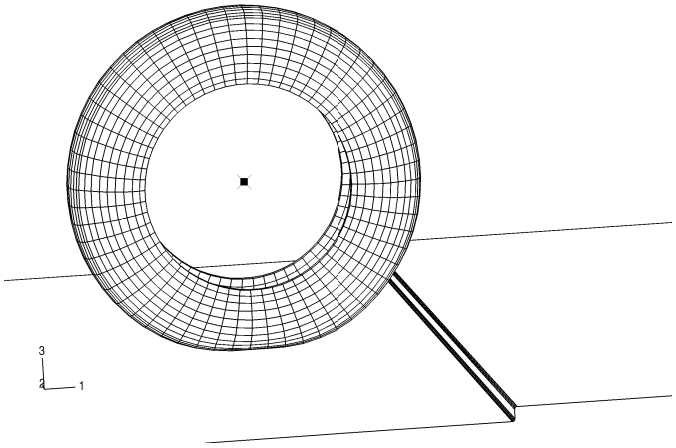

Figure 3.1.6–1 Tire before impact with the curb.

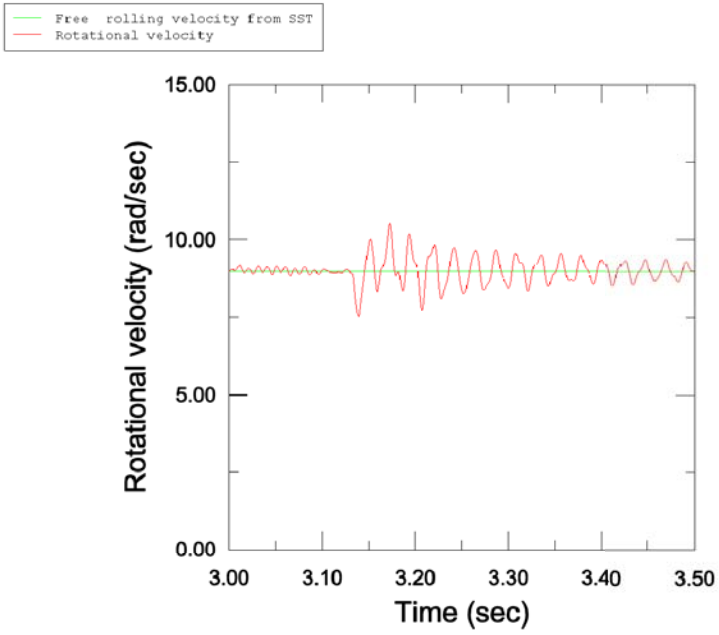

Figure 3.1.6–2 Rotational velocity at rim.

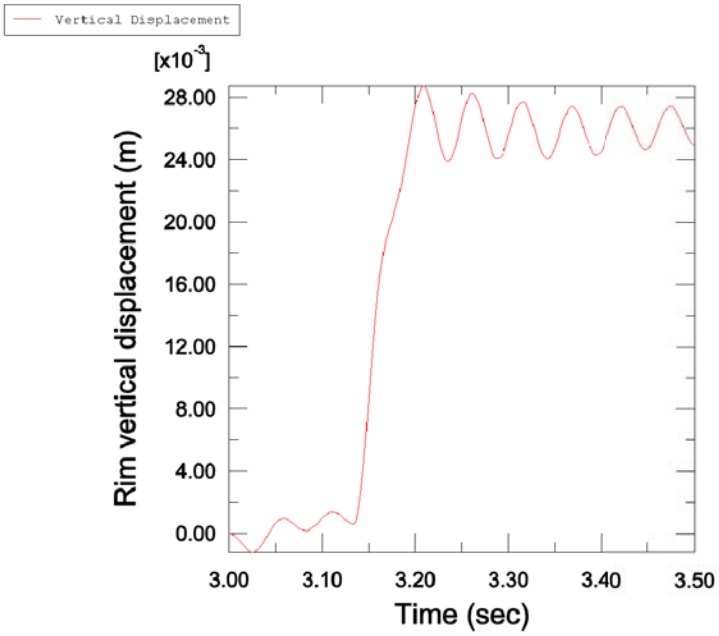

Figure 3.1.6–3 Vertical response of the rim reference node.

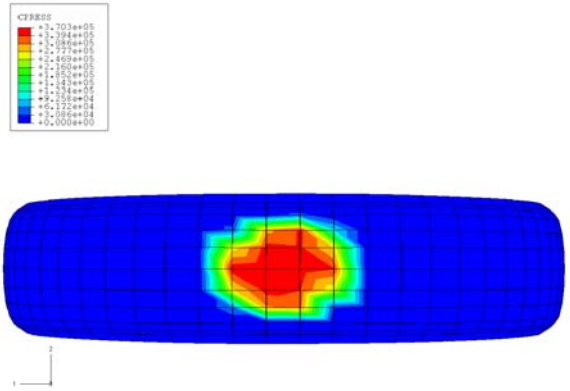

Figure 3.1.6–4 Pressure in the footprint patch.

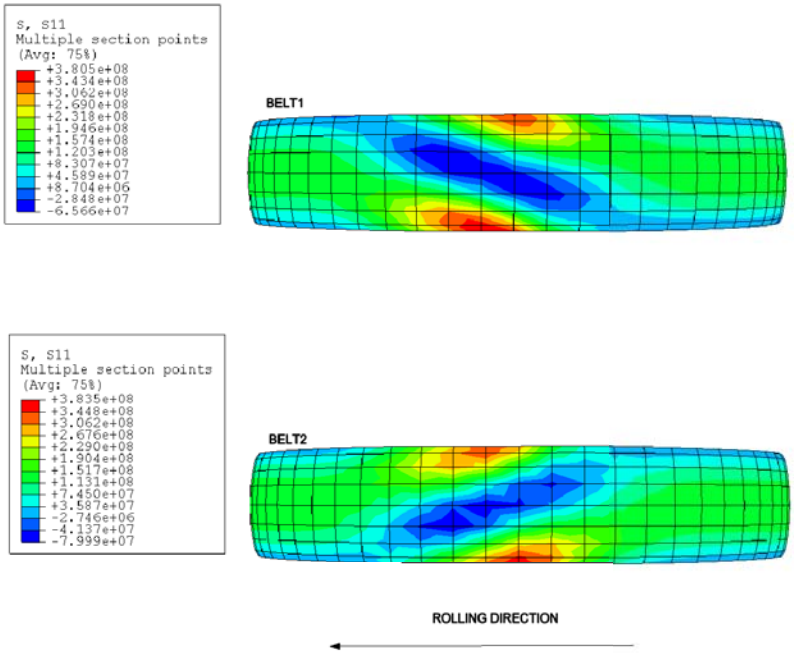

Figure 3.1.6–5 Stress in the belts.

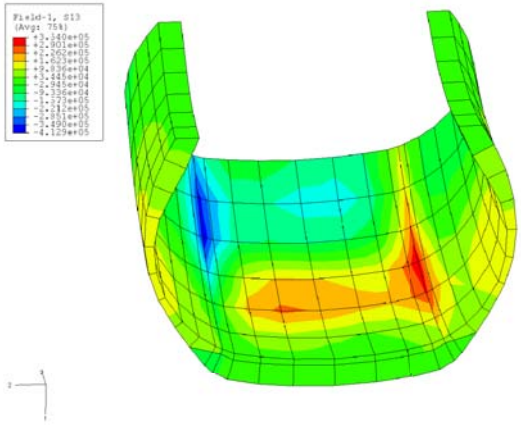

Figure 3.1.6–6 Shear stress in the shoulder region during impact with the curb.

3.1.7 ANALYSIS OF A SOLID DISC WITH MULLINS EFFECT AND PERMANENT SET

Products: Abaqus/Standard Abaqus/Explicit

This example illustrates the use of the Mullins effect to model the static and steady-state rolling interaction between a solid rubber disc and a rigid surface.

The Mullins effect is used with a hyperelastic material model to model the phenomenon of stress softening upon unloading from a certain deformation level that is observed in certain filled elastomers. A variation of this example includes modeling of permanent set as well.

Related topics

- "Mullins effect," Section 22.6.1 of the Abaqus Analysis User's Guide
- "Permanent set in rubberlike materials," Section 23.7.1 of the Abaqus Analysis User's Guide

Problem description

This example is divided into three sections. The first section involves calibration of experimental data to determine the material coefficients for the Mullins effect. The second section describes the static response of a solid disc subjected to cyclic deformation induced by contact with a flat rigid surface that represents the road. This kind of test is commonly carried out in the tire industry to investigate the effect of stress softening on the load-deflection behavior of tires. The third section is a continuation of the problem described in the second section and studies the rolling solution of the deformed disc. The rolling is modeled using both a Lagrangian approach that involves rotation of the disc mesh and the steady-state transport capability in Abaqus/Standard that obtains the steady-state solution of the rolling disc using more of an Eulerian approach. This example also illustrates the enhanced hourglass control capability and modeling of permanent set in Abaqus.

Calibration of material properties

The first step in using the Mullins effect material model is calibration of test data. Figure 3.1.7–1 shows a typical set of uniaxial tension test data for filled rubber. These data are representative of a class of rubber materials that is used in the tire industry and have been provided by Cooper Tire and Rubber Company. The bold curve labeled **`exp_mono`** represents the primary behavior of the rubber material that would be obtained from a monotonic test to a certain deformation level. These data are provided to Abaqus using a set of uniaxial test data and a customization to the hyperelastic material model specifying that material constants should be calculated from that test data. In this example the Yeoh material model is used for calibrating the primary material behavior. Reduced polynomial models, such as the Yeoh model, provide a better fit when limited test data are available, as is the case here. The unloading-reloading data, needed to calibrate the Mullins effect coefficients, are provided as stabilized loading/unloading cyclic data from three different maximum strain levels. Although the model for Mullins effect in Abaqus predicts unloading and reloading from a given maximum strain level to occur along a single curve, the real material often shows a cyclic behavior. In fact, the unloading/reloading cycles from a given maximum

strain level also show evidence of progressive damage during the first few cycles. However, after a few cycles the behavior stabilizes. The unloading-reloading data can be provided to Abaqus either in the form of data points for all loading/unloading cycles from different maximum strain levels or in the form of data points for just the stabilized cycles. In this example the stabilized cycle has been chosen because the structure considered is expected to undergo repeated cyclic loading. The curves labeled **`exp_unload1`**, **`exp_unload2`**, and **`exp_unload3`** represent the stabilized unloading/reloading cycles for maximum nominal strain levels of 0.099, 0.26, and 0.51, respectively. The above data are input using three sets of uniaxial test data (one for each maximum strain level), along with Mullins effect defined by test data.

For models that include permanent set, the data are specified using a metal plasticity material definition so that a softer response (compared to a purely hyperelastic material) is obtained in loading. These models also include the Mullins effect material model as discussed above.

During design studies the analyst may wish to calibrate the Mullins effect parameters using the loading part of the stabilized cycle, the unloading part of the stabilized cycle, or an average of the two. This can be accomplished easily by creating three data files that include the loading, unloading, and both the loading and unloading parts of the stabilized cyclic data, respectively. Subsequently any one of these files can be referenced from the input file by using an external file reference. In this example, which considers cyclic loading instead of primarily monotonic loading, both loading and unloading data have been used for calibration; hence, an average behavior is studied.

Figure 3.1.7–2 shows the calibrated response of Abaqus along with the test data. The continuous bold line represents the numerical response for cyclic loading and unloading to the three maximum strain levels for which test data have been provided (the response at the lowest maximum strain level is not visible in the scale of this figure due to a relatively small amount of damage). As the figure illustrates, the model in Abaqus approximates the stabilized cycle at each strain level with a single curve. The figure also illustrates that the model does not capture the progressive damage during the first few cycles at any strain level. Thus, while the numerical results for unloading from a given strain level begin from the primary curve, the maximum stress for the test results for the stabilized cycle may be somewhat below the measured primary material behavior.

The numerical response can be obtained by carrying out a uniaxial loading/unloading test with a single element. Alternatively, the numerical response for both the primary and the unloading-reloading behavior can be obtained by using a model definition data request and simply carrying out a **datacheck** run. In the latter case the response computed by Abaqus is printed to the data (**`.dat`**) file along with the experimental data. These tabular data can be plotted in Abaqus/CAE for comparison and evaluation purposes. The primary material behavior can also be evaluated with the automated material evaluation tools available in Abaqus/CAE.

Static response of a solid disc to cyclic deformation

A solid disc made out of the rubber material described in the earlier section is subjected to cyclic deformation. The coefficients for the Yeoh model determined during the calibration are used along with a value of $D_1 = 5.\text{E}{-}06$ to introduce a small amount of compressibility in the material. This value of D_1 is obtained based on the measured value of the initial bulk modulus of the rubber. The Mullins effect model in Abaqus assumes that the damage is associated with the deviatoric behavior only. The disc has an outer diameter of 3 inches, an inner diameter of 1.75 inches, and a thickness of 0.7 inches. The

inner surface of the disc is fully constrained. The outer surface is initially defined to be just touching a flat rigid surface. The coefficient of friction between the disc and the rigid surface is assumed to be zero. During the analysis the rigid surface is pushed up 0.15 inches, brought back to its original position, then again pushed up 0.22 inches before being pushed back to its original position. The above deformation history constitutes two displacement-controlled deformation cycles. The analysis is carried out using both Abaqus/Standard and Abaqus/Explicit. An axisymmetric model is created to define the geometry of the disc. Symmetric model generation is used to create a three-dimensional disc model using first-order reduced-integration bricks (C3D8R elements) with enhanced hourglass control. The Abaqus/Explicit model is created by importing the model definition from Abaqus/Standard. The first step in the Abaqus/Standard analysis is a do-nothing step, which is used to import the initial state into Abaqus/Explicit.

Figure 3.1.7–3 shows the force versus displacement at the rigid body reference node. The two cycles in this figure correspond to the two deformation cycles discussed earlier. During the first cycle the unloading response is softer compared to the loading response due to damage associated with the Mullins effect. During the second loading cycle the response is identical to the unloading segment of the first cycle until the displacement of 0.15 inches is reached. Beyond this point the response is a continuation of the original loading segment of the first cycle. Thus, the load-displacement behavior is consistent with the expected behavior due to the Mullins effect.

Figure 3.1.7–4 shows the time history of the energy dissipated in the whole model due to damage. The dissipation increases during the loading segment of the first cycle because the material undergoes more and more damage as it is deformed. During the unloading segment of the first cycle and the loading segment of the second cycle up to a displacement of 0.15 inches, no additional damage occurs. As a result, the total dissipation remains constant. For additional displacement beyond 0.15 inches, more damage occurs. This results in further increase of the total damage energy. During the final unloading cycle the damage energy again remains constant.

The loading in the Abaqus/Explicit analysis is carried out using displacement boundary conditions with an amplitude that uses the smooth step definition to reduce the noise in the response. Thus, the time history of the displacement is different between the Abaqus/Standard and the Abaqus/Explicit simulations, although the total amount of displacement is identical in both analyses. As a result, the time history of the damage dissipation between the two analyses shows some differences in the slope of the response. However, the total dissipation at the end of each stage is identical in the two cases.

Rolling response of a solid disc

The geometry and material of the disc are identical to those described earlier except that the inner surface of the disc is not totally constrained, as it is for the static problem. Instead, all the nodes on the inner surface are attached to a node (axle node) located at the center of the disc using kinematic coupling constraints. This facilitates the application of angular velocity or displacement to the axle node to simulate rolling in the Lagrangian approach, as well as the measurement of reaction forces and moments at the axle. The mesh is more refined for the rolling problem compared to the static problem. In particular, two elements are used through the thickness of the disc. The first step is a do-nothing step to facilitate import of the initial state from Abaqus/Standard to Abaqus/Explicit. This step is followed by a static step in which the rigid surface is pushed against the disc a distance of 0.15 inches. The next

step involves rolling of the loaded disc against the rigid surface, which is accomplished in two ways. The first is a Lagrangian analysis in which an angular velocity of 2.5 radians per second is applied to the axle node of the disc. In this example the structure reaches a steady state after one full revolution. No additional damage occurs in subsequent revolution cycles. Therefore, the total time is chosen such that the disc undergoes two revolutions. A variation of the Lagrangian analysis includes modeling of permanent set using a metal plasticity material definition. In the second analysis the rolling is simulated using the steady-state transport capability in Abaqus/Standard. Frictional and inertial effects are neglected in both cases.

The steady-state transport capability directly obtains the steady-state rolling solution of the disc on the rigid surface. Due to Mullins effect the stress state for the rolling solution can be quite different from the stress state for the static non-rolling solution. As a result, an attempt to obtain a steady-state rolling solution directly from a static non-rolling solution may lead to convergence problems in the Newton's scheme that is used to solve the overall nonlinear system of equations. Since the damage and, hence, the discontinuity in state are independent of the angular rolling speed, a time increment cutback during the steady-state transport step does not overcome the convergence difficulties. Such convergence difficulties can be resolved by introducing the damage gradually over an additional steady-state transport step preceding the actual analysis. In this example this is accomplished by following the static loading step with a steady-state transport step with a small rolling angular speed of 0.25 radians per second and with the Mullins effect ramped up over the time period of the step. This step is followed by another steady-state transport step at an angular speed of 2.5 radians per second with the MULLINS parameter set equal to STEP, which provides the solution we are interested in obtaining.

A Lagrangian simulation is also carried out in Abaqus/Explicit. The kinetic energy is monitored to ensure that the problem remains essentially quasi-static. The revolutions of the disc are carried out by applying a rotational displacement (corresponding to two full revolutions) at the axle node using an amplitude with a smooth step definition to reduce the noise in the response. The compressibility parameter, D_1, is chosen to be 5×10^{-5}, an order of magnitude higher than the actual value, to obtain relatively higher time increments and, thus, a relatively lower run time.

Figure 3.1.7–5 compares the time history of the reaction force at the axle node for the Lagrangian and the steady-state rolling analyses in Abaqus/Standard. The results for the Lagrangian problem without permanent set (curve labeled **lagr**) indicate that the reaction force increases during the loading step and decreases during the first revolution of the disc. The decrease in the reaction force is a result of lower overall stresses due to damage in the material. During the second revolution of the disc the reaction force remains constant as no additional damage occurs. The results of the Lagrangian problem including permanent set (curve labeled **fefp**) show a softer behavior compared to the former problem and clearly indicate the presence of permanent set in the footprint area as the solid disc rolls against the rigid surface. The steady-state rolling results (labeled **sst**) show a gradual transition of the reaction force during the first steady-state transport step that ramps up the Mullins effect. During the second steady-state transport step the reaction force remains constant at the value reached at the end of the prior step. This curve also illustrates that the damage associated with the Mullins effect is independent of the angular speed of rotation. The reaction force remains the same at angular speeds of both 0.25 and 2.5 radians per second. If the Mullins effect is not applied gradually over the first steady-state transport step, the discontinuity between the rolling and the static states may lead to convergence difficulties.

The same results can be observed from a different viewpoint in Figure 3.1.7–6, which shows the reaction force as a function of the number of revolutions for both Abaqus/Standard and Abaqus/Explicit. The reaction force decreases during the first revolution and remains steady (except for the noise in the Abaqus/Explicit analysis) during the second revolution.

Figure 3.1.7–7 shows a comparison of the time histories of the reaction moment at the axle node between the Lagrangian and the steady-state rolling solutions. The Lagrangian results are labeled **m-lagr**, while the steady-state rolling results are labeled **m-sst**. If the material were purely hyperelastic (without damage), the contact forces would be symmetric about a plane normal to the rigid surface and containing the axle; hence, no torque would be required to rotate the disc. However, as a result of the damage associated with Mullins effect, the contact forces are not symmetrical because material particles transition through the contact area during the very first revolution. This leads to the reaction moment during the first revolution, as shown in the results for the Lagrangian analysis. The moment reduces to zero during the second revolution. The steady-state rolling results do not include the transient solution of the first revolution; hence, they show a zero moment at all times. Figure 3.1.7–8 shows the same results from a different viewpoint. In this figure the reaction moment is plotted as a function of the number of revolutions for both Abaqus/Standard and Abaqus/Explicit.

Figure 3.1.7–9 shows a contour plot of the damage energy dissipated at material points at an instant of time that corresponds to about three-quarters of the way into the first revolution of the disc. The figure indicates damage in the material that has already passed through the contact area and no damage in the material that is yet to pass through the contact area. This corresponds to damage in about three-quarters of the disc material. The remaining quarter is still undamaged, as it has not undergone any deformation yet. The full disc will be damaged at the end of the first revolution, and the damage state remains unchanged during the second revolution.

Results and discussion

The results are discussed in the individual sections above and clearly demonstrate the different effects of damage in the material.

Input files

mullins_calibrate.inp	Unit element test to calibrate the material model.
mullins_axi_tire.inp	Axisymmetric model for the static non-rolling problem.
mullins_full_tire.inp	Full three-dimensional model for the static non-rolling problem.
mullins_full_tire_xpl.inp	Full three-dimensional model for the static non-rolling problem (quasi-static simulation using Abaqus/Explicit).
mullins_axi_tire_ref.inp	Refined axisymmetric model for the rolling problem.
mullins_full_tire_roll_lag.inp	Full three-dimensional model for the Lagrangian rolling problem.
mullins_full_tire_roll_lag_xpl.inp	Full three-dimensional model for the Lagrangian rolling problem (quasi-static simulation using Abaqus/Explicit).

mullins_full_tire_roll_sst.inp	Full three-dimensional model for the steady-state rolling problem.
mullins_calibrate_testdata.inp	Uniaxial test data for calibrating the Mullins effect coefficients.
mullins_hepl_axi_tire_ref.inp	Axisymmetric reference model for rolling problem with permanent set.
mullins_hepl_full_tire_roll_lag.inp	Full three-dimensional model for the Lagrangian rolling problem with permanent set.

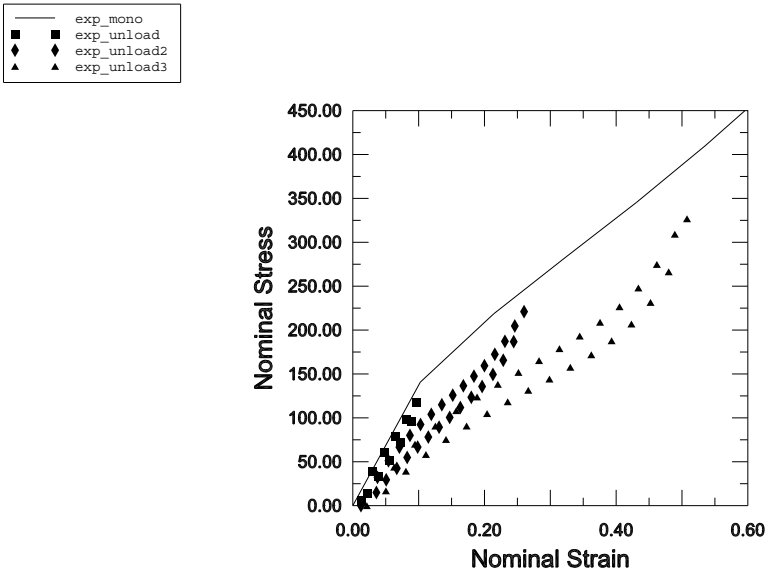

Figure 3.1.7–1 Test data for calibrating the Mullins effect.

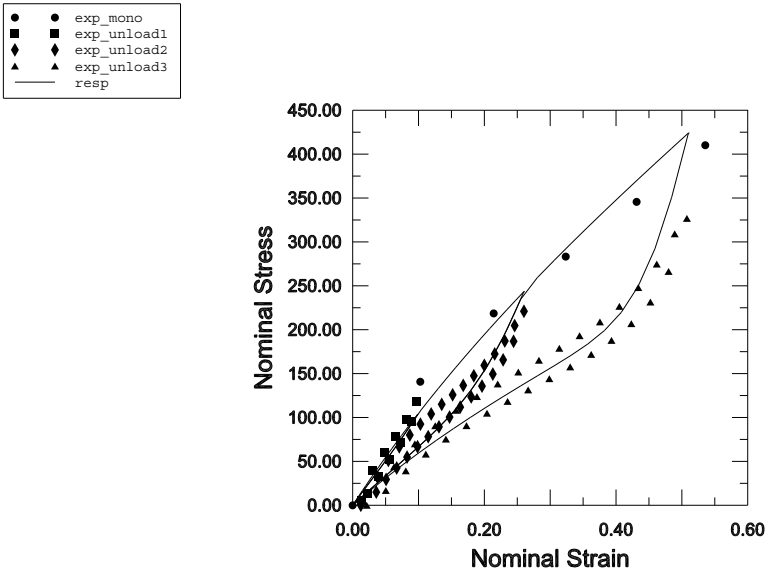

Figure 3.1.7–2 Calibration of Mullins effect.

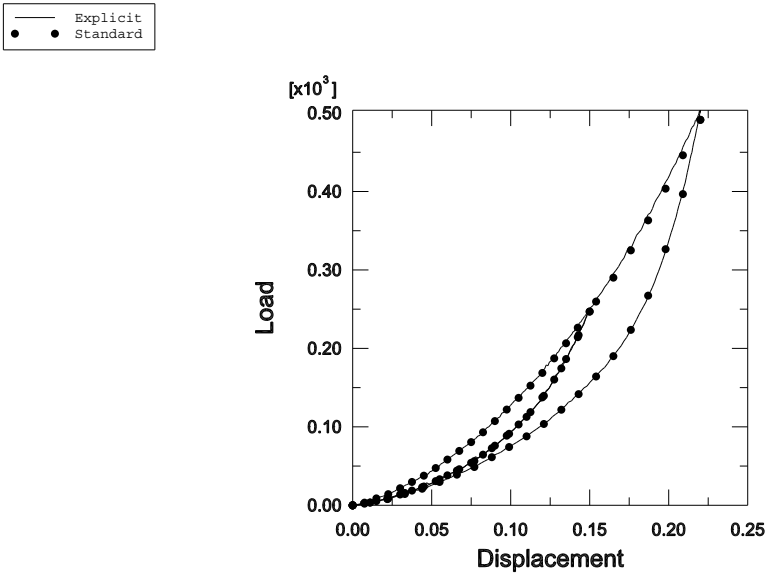

Figure 3.1.7–3 Force versus displacement for the static non-rolling solution.

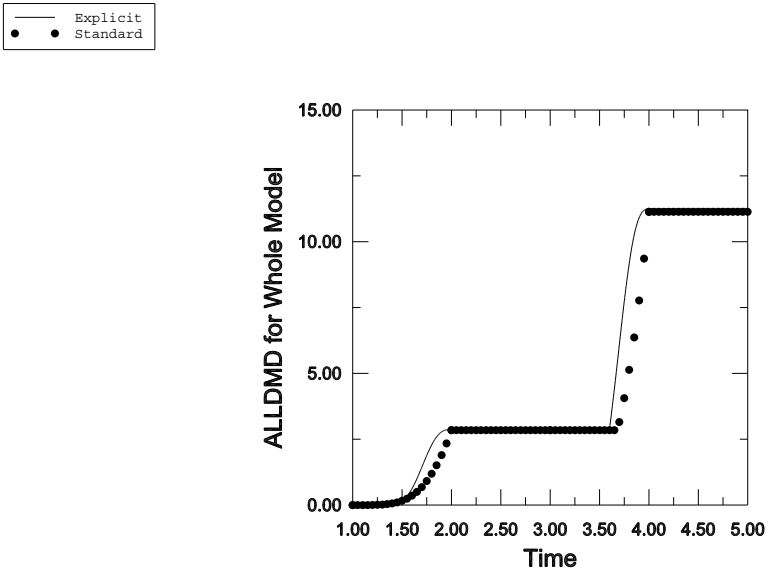

Figure 3.1.7–4 Whole model damage energy history for the static non-rolling solution.

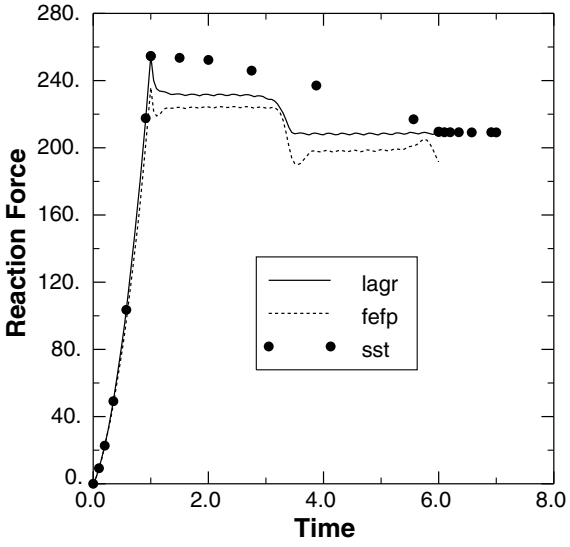

Figure 3.1.7–5 Time history of reaction force for the rolling solution.

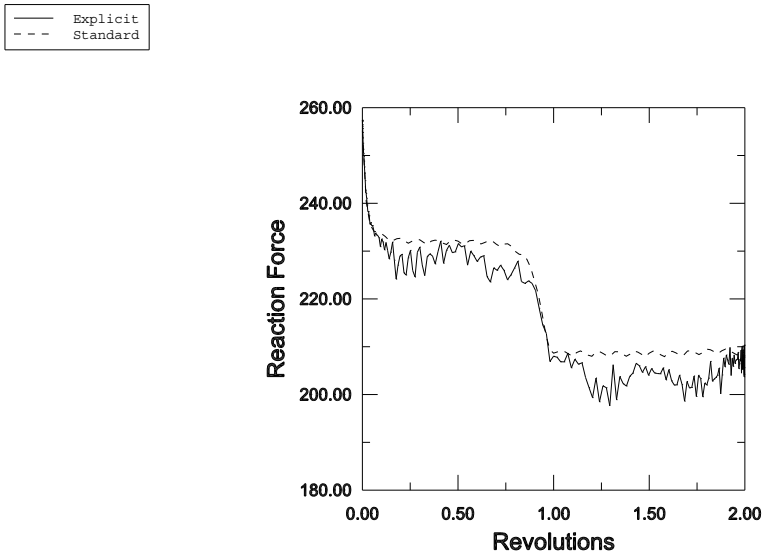

Figure 3.1.7–6 Reaction force versus number of revolutions.

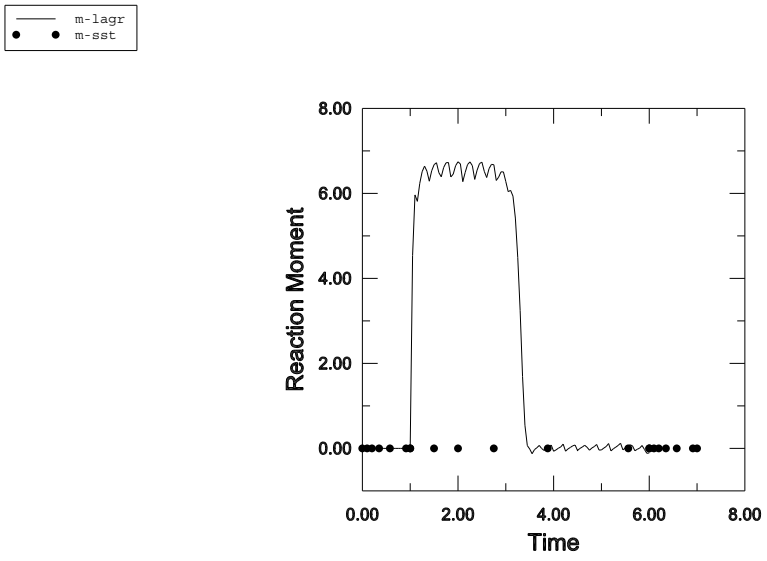

Figure 3.1.7–7 Time history of reaction moment for the rolling solution.

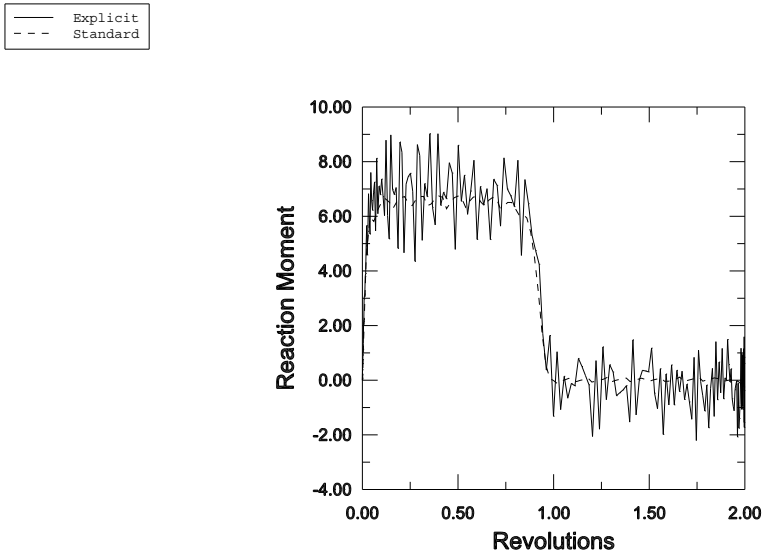

Figure 3.1.7–8 Reaction moment versus number of revolutions.

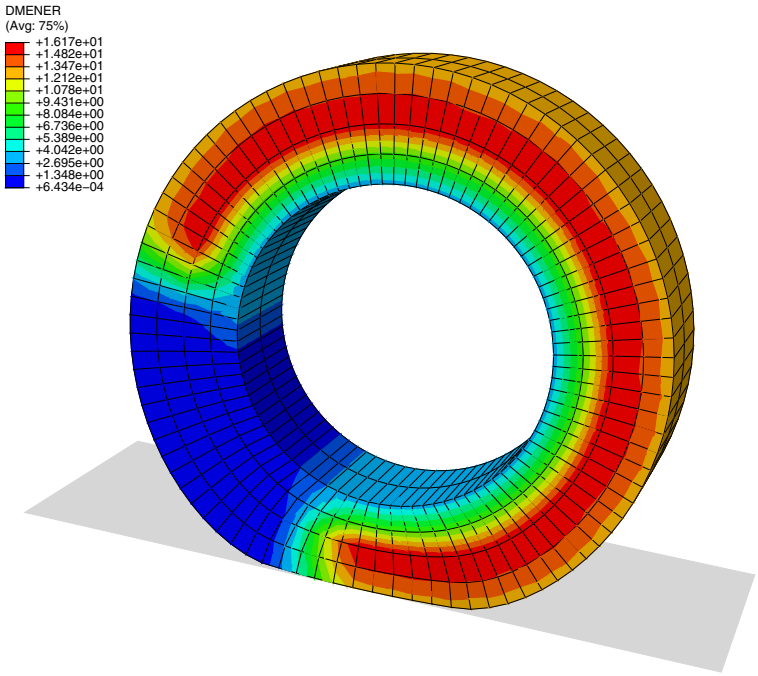

Figure 3.1.7–9 Contour plot of damage energy.

3.1.8 TREAD WEAR SIMULATION USING ADAPTIVE MESHING IN Abaqus/Standard

Product: Abaqus/Standard

This example illustrates the use of adaptive meshing in Abaqus/Standard as part of a technique to model tread wear in a steady rolling tire.

The analysis follows closely the techniques used in "Steady-state rolling analysis of a tire," Section 3.1.2, to establish first the footprint and then the state of the steady rolling tire. These steps are then followed by a steady-state transport step in which a wear rate is calculated and extrapolated over the duration of the step, providing an approximate consideration of the transient process of wear in this steady-state procedure.

Problem description and model definition

With some exceptions, noted here, the description of the tire and finite element model is the same as that given in "Import of a steady-state rolling tire," Section 3.1.6. Since the focus of this analysis is tread wear, the tread is modeled in more detail. In addition, a linear elastic material model is used in the tread region to avoid difficulties advecting the hyperelastic material state during the adaptive meshing procedure.

The axisymmetric half-model of the 175 SR14 tire is shown in Figure 3.1.8–1. The rubber matrix is modeled with CGAX4 and CGAX3 elements. The reinforcement is modeled with SFMGAX1 elements that carry rebar layers. An embedded element constraint is used to embed the reinforcement layers in the rubber matrix. The tread is modeled with an elastic material of elastic modulus 6 MPa and Poisson's ratio 0.49. The rest of the tire is modeled with the hyperelastic material model. The polynomial strain energy potential is used with coefficients $C_{10}=10^6$, $C_{01}=0.0$, and $D_1=2 \times 10^{-8}$. The rebar layers used to model the carcass fibers are oriented at 0° to the radial direction and have an elastic modulus of 9.87 GPa. The modulus in compression is set to 1/100th of the modulus in tension. The Marlow hyperelastic model is used to specify the nominal stress-nominal strain data for such a material definition. The elastic modulus in tension of the material of the belt fibers is 172.2 GPa. The modulus in compression is set to 1/100th of the modulus in tension. The fibers in the belts are oriented at +20° and −20° with respect to the hoop (circumferential) direction.

The three-dimensional model is created by first revolving the axisymmetric half-model, using symmetric model generation, by 360° to generate the partial three-dimensional model shown in Figure 3.1.8–2. A focused mesh is applied at the footprint region. The partial three-dimensional model is then reflected about a line to generate the full three-dimensional model. The results are then transferred from the end of the footprint simulation for the partial three-dimensional model (see Figure 3.1.8–2).

Adaptive meshing limitations in tire wear calculations

The use of adaptive meshing necessarily places the following restrictions on the tire model used for this example:

- Cylindrical elements are currently not supported with adaptive meshing and are not used in this model.
- Adaptive meshing generally performs poorly with hyperelastic material models, due to the inaccurate advection of deformation gradient state variables. The tread, therefore, is modeled with an elastic material definition.
- Embedded elements including rebar layers cannot be used within the adaptive mesh domain.
- Adaptive mesh smoothing on free surfaces occurs in directions determined by features of the element geometry, which may not always be consistent with or easily enable description of wear directions. As a result, as discussed below, you will generally have to do additional work to explicitly describe the direction of wear.

Loading

The analysis is conducted in five stages, beginning with an axisymmetric model and ending with a full three-dimensional model created using symmetric model generation. The first four steps follow closely those used in "Steady-state rolling analysis of a tire," Section 3.1.2.

1. Axisymmetric inflation: An inflation pressure of 200 kPa is applied to the interior of the tire, while symmetry conditions are imposed at the midplane.
2. Three-dimensional footprint analysis of the partial model: The axisymmetric half-model is revolved around the axle axis.
3. Three-dimensional footprint analysis of the whole model: The partial three-dimensional model is reflected about a line to generate the full three-dimensional model.
4. Steady-state transport: The generated full model is then subjected to a steady-state transport analysis at 30 km/h. An angular velocity of 25 rad/s is specified for the tire. These conditions correspond to a state of braking. Inertia effects and viscoelasticity are taken into account during this step.
5. Tread wear simulation: The tread wear simulation is conducted in the final step, in which the velocity of the tire is held constant and the wear is computed from the frictional energy dissipated and applied around the periphery of the tire. Inertia effects and viscoelasticity are taken into account during this simulation as well. This step is run for a duration of 3.6×10^6 s, simulating 30,000 kilometers of travel of the tire at 30 km/h.

The final step uses a wear model, which predicts a wear, or surface ablation, rate based on the steady rolling of the tire. We are interested in predicting tire configuration changes as a result of this wear rate; hence, we must introduce some modeling assumptions that enable modeling of a transient effect in a steady-state procedure.

The basic assumption made is that the steady-state transport step time can be interpreted as a real-time duration of rolling at the current angular velocity. We consider that the configuration changes due to wear have only a minor effect on the rolling tire solution at any time; hence, the results remain valid in a steady-state sense at each time through the step. With this assumption we can simultaneously consider effects at two disparate time scales: the shorter tire revolution time scale and the longer tire life time scale.

Wear model

To illustrate the wear process, a simple wear model is employed based on the assumption that the wear rate is a linear function of the local contact pressure and slip rate. Although we can calculate these quantities locally, due to the Eulerian formulation used in steady-state transport they must be applied over tread streamlines to model the wear of the entire tire perimeter.

Wear rate calculation

The wear constitutive model employed for this simulation is a form of the Archard model,

$$\dot{q} = \frac{k}{H} P A \dot{\gamma},$$

where $\dot{q}$ is the volumetric material loss, or wear, rate; k is a nondimensional wear coefficient; H is the material hardness; P is the interface normal pressure; A is the interface area; and $\dot{\gamma}$ is the interface slip rate. Here we can see that the terms $PA\dot{\gamma}$ describe a frictional energy dissipation rate. For tire rubber we assume a wear coefficient $k = 1.11 \times 10^{-4}$ and a material hardness $H = 2$ GPa.

The goal of the following development is an expression for a material recession, or ablation, rate $\dot{h}$, which can be applied to a node to simulate wear. First, consider a ribbon around the tire, where the centerline of this ribbon is defined by a sequence of nodes comprising one of the surface streamlines on the tire's tread. This centerline is then bounded on either side by the tributary region of the surface associated with each node. The combination of all such "stream ribbons" then comprises the total surface of the tire involved in tire-to-road contact interactions. We expect the wear to occur uniformly over this stream ribbon; hence, we express a wear rate for the entire ribbon,

$$\dot{q}(t) = \frac{k}{H} \int_{\text{ribbon}} P(\mathbf{x}, t) \dot{\gamma}(\mathbf{x}, t) dA,$$

where t is the time and $\mathbf{x}$ is the current configuration position. Since we are using the Eulerian steady-state transport procedure, we can now rewrite this expression in a time-independent form,

$$\dot{q} = \frac{k}{H} \int_s P(s) \dot{\gamma}(s) T(s) ds,$$

where s is a position along the streamline and $T(s)$ is the width of the stream ribbon at position s. We can also express $\dot{q}$ as a function of the local material recession rate,

$$\dot{q} = \int_s \dot{h}(s) T(s) ds.$$

Equating these two expressions in a discrete form results in the following expression, summed over a streamline:

$$\sum_{i=1}^{N} \dot{h}_i A_i = \frac{k}{H} \sum_{i=1}^{N} P_i \dot{\gamma}_i A_i,$$

where $\dot{h}_i$ is a nodal ablation velocity and A_i is the nodal contact area. This equation implies that $\dot{h}_i$ is generally not uniform along the streamline, which follows as a consequence of the stream ribbon width varying as it enters and leaves the tire footprint. Since, however, we are ablating nodes away from the footprint region solely to maintain a reasonable general shape of the worn tire configuration, we will accept the assumption of a uniform nodal ablation velocity. This enables the following expression for $\dot{h}$:

$$\dot{h} = \frac{k \sum_{i=1}^{N} P_i \dot{\gamma}_i A_i}{H \sum_{i=1}^{N} A_i}.$$

Using again the assumption that the variation in stream ribbon width can be neglected, $T_i = T$, and recognizing that the nodal contact area $A_i = T \Delta S_i$ enables a simpler expression that does not require the use of contact areas:

$$\dot{h} = \frac{k \sum_{i=1}^{N} P_i \dot{\gamma}_i \Delta S_i}{H \sum_{i=1}^{N} \Delta S_i}.$$

Wear process implementation

With this expression for wear rate in the form of a surface ablation velocity, the wear can now be applied in a steady-state transport analysis. User subroutine **UMESHMOTION** is used to specify the ablation velocity vectors at the nodes that are on the exterior surface of the tire. **UMESHMOTION** defines adaptive mesh constraint velocities and is used in conjunction with adaptive meshing, a mesh smoothing technique applied at the end of each converged increment. The ablation velocities specified through the user subroutine are applied at the tread surface nodes, and adaptive mesh smoothing adjusts nodes in the interior tread region to maintain a well-shaped mesh.

To accumulate wear quantities around each tread streamline, the nodal numbering scheme along the streamlines must be recorded in the user subroutine. This record is made in a set of common block variables. The common block records nodes that belong to node set **NADAPT** (Figure 3.1.8–4) and that lie at the reference cross-section (0°) of the full model. The common block variables also include the node numbering offsets specified for symmetric model generation, which, together with the reference cross-section definitions, completely describe the tread surface node numbering. The following variables need to be defined in the external common block:

- **nStreamlines**: The number of nodes at the reference section (full model) at which wear is applied.
- **nGenElem**: The number of sectors or element divisions along the streamline in the model.
- **nRevOffset**: The node offset specified as part of the definition of a revolved symmetric model.
- **nReflOffset**: The node offset specified as part of the definition of a reflected symmetric model. (Set this parameter equal to zero if the model is not reflected).

- **jslnodes**: The array that contains the required nodal information for all nodes potentially undergoing wear at the reference section. This is an array of size (2, **nStreamlines**). For each streamline the first component is the node number of the "root node" (node ***a*** in the following discussion), which is the node on that particular streamline at the reference section. The second component is the node that provides the wear direction (node ***b*** in the following discussion). This second component is necessary only for the tread corner nodes. Set it equal to the number of the node at the reference section that defines the wear direction. For nodes that are not located at tread corners, set the second array component equal to zero. The wear will be applied opposite to the local 3-direction for these nodes located away from tread corners.

The variables in the expression for wear are accessed from the analysis database using the utility routines **GETVRN** and **GETVRMAVGATNODE**. P is accessed from output variable CSTRESS; $\dot{\gamma}$ from variable CDISP; and the ΔS are determined from streamline nodal coordinates, accessed from variable COORD.

Wear motion directions

The wear rate, $\dot{h}$, is then applied as the components of the mesh constraint vector variable **ULOCAL**. This variable is passed into the user subroutine with default mesh smoothing motions defined in a local coordinate system **ALOCAL**, which reflects a measure of the surface normal at the current node. The 3-direction is defined as the direction of the outward normal and is based on an average of element facet normals near the node. Under most circumstances it is sufficient to describe wear as resulting in ablation, or nodal recession, opposite to this direction. At the tread corners, however, this average normal does not provide an accurate wear direction. The appropriate normal is shown in Figure 3.1.8–5 and is computed as follows: Suppose *a* is a corner node on the tread. It is possible to identify a node *b* that lies along the edge of the tread. In this case the wear direction is given by the vector *ab*. By knowing the coordinates of *a* and *b*, the wear can be calculated in the global coordinate system and rotated into the local coordinate system (**ALOCAL**) directions.

Results and discussion

The tire model is run for a duration of 3.6×10^6 s, or 1000 hours, the equivalent of 30,000 kilometers of operation at 30 km/h. Figure 3.1.8–6 shows the resulting tread profile including the effects of wear. Figure 3.1.8–7 shows the footprint distributions of the contact pressure and the contact pressure error indicator for a new tire and one in the as-worn configuration.

Input files

treadwear_axi.inp	Axisymmetric model, inflation analysis.
treadwear_rev.inp	Partial three-dimensional model, footprint analysis.
treadwear_refl.inp	Full three-dimensional model, footprint analysis.
treadwear_roll.inp	Full three-dimensional model, steady rolling analysis.
treadwear_wear_straight.inp	Full three-dimensional model, steady rolling wear analysis.

treadwear_wear_slip.inp	Full three-dimensional model, steady rolling wear analysis with slip.
treadwear.f	**UMESHMOTION** user subroutine.

Reference

- Archard, J. F., "Contact and Rubbing of Flat Surfaces," Journal of Applied Physics, vol. 24, pp. 981–988, 1953.

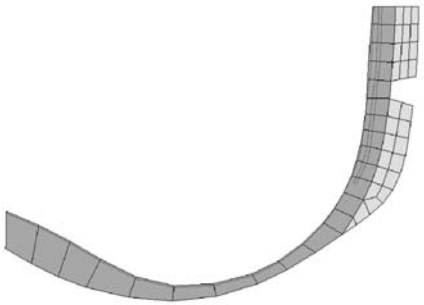

Figure 3.1.8–1 Axisymmetric cross-section of the tire.

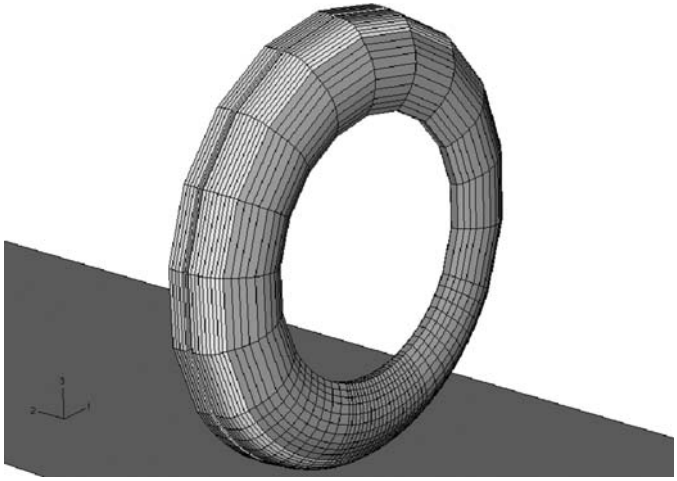

Figure 3.1.8–2 Partial three-dimensional model.

Figure 3.1.8–3 Full three-dimensional model.

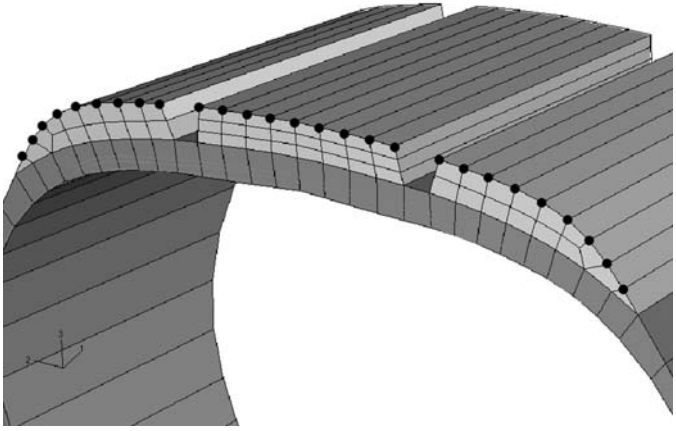

Figure 3.1.8–4 Nodes belonging to node set **NADAPT** at a particular sector (**NADAPT** includes all such nodes from all the sectors).

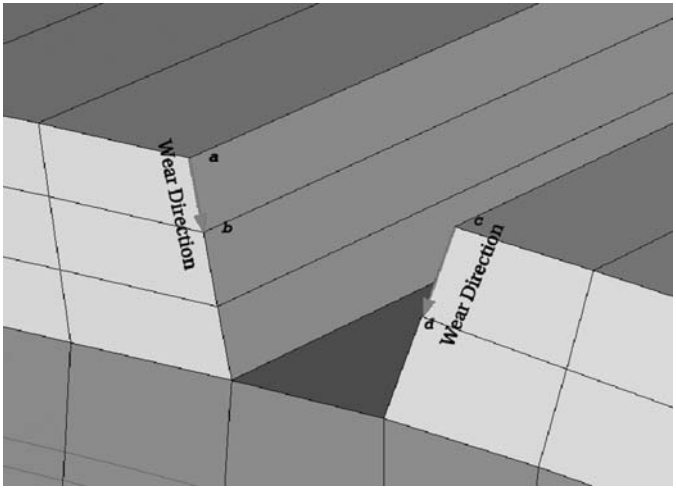

Figure 3.1.8–5 Wear directions at tread corners.

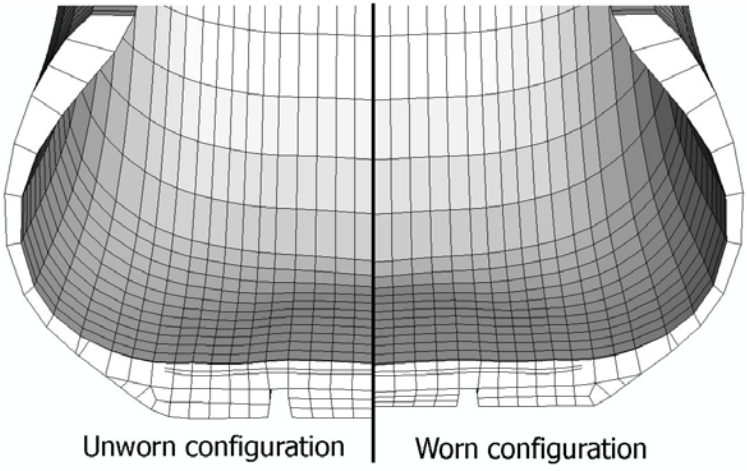

Figure 3.1.8–6 Tread profile, in the unworn and worn configurations.

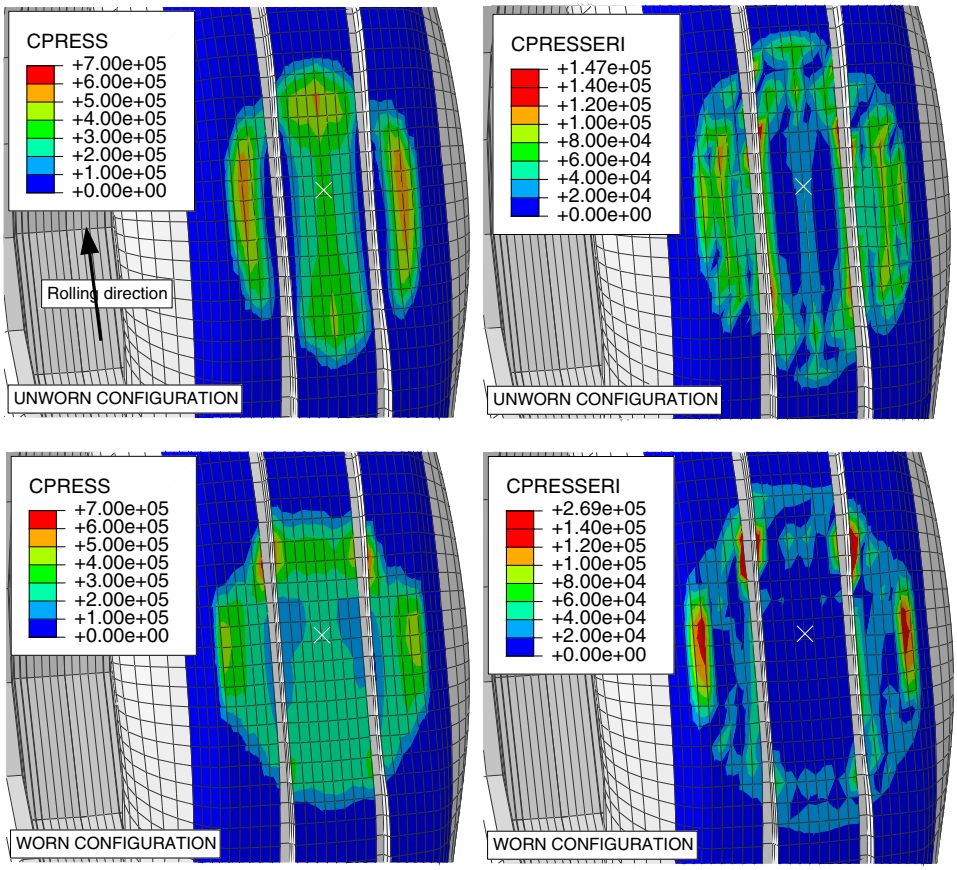

Figure 3.1.8–7 Footprint contact pressure and contact pressure error indicator, in the unworn and worn configurations.

3.1.9 DYNAMIC ANALYSIS OF AN AIR-FILLED TIRE WITH ROLLING TRANSPORT EFFECTS

Product: Abaqus/Standard

This example examines the effect of steady-state rolling transport on the acoustic response of a tire and its associated air cavity after it has been subjected to the inflation pressure and footprint load.

The air cavity resonance in a tire is often a significant contributor to the vehicle interior noise, particularly when the resonance of the tire couples with the cavity resonance. This coupled resonance phenomenon, however, is affected by the rotating motion in the fluid and the solid. This example extends the analyses of "Coupled acoustic-structural analysis of a tire filled with air," Section 3.1.5, to include rolling transport effects in the tire and air. The acoustic cavity is modeled as part of an axisymmetric model, which is inflated, revolved, reflected, and deformed to obtain a footprint in a manner consistent with the aforementioned example.

Problem description

A detailed description of the tire model is provided in "Symmetric results transfer for a static tire analysis," Section 3.1.1. We model the rubber as an incompressible hyperelastic material. Viscoelasticity in the material is ignored in this example.

The air cavity in the model is defined as the space enclosed between the interior surface of the tire and a cylindrical surface of the same diameter as the diameter of the bead. A cross-section of the tire model is shown in Figure 3.1.9–1. The values of the bulk modulus and the density of air are taken to be 426 kPa and 3.6 kg/m^3, respectively, and represent the properties of air at the tire inflation pressure.

The simulation assumes that both the road and rim are rigid. We further assume that the contact between the road and the tire is frictionless during the preloading analyses. However, we use a nonzero friction coefficient in the subsequent coupled acoustic-structural analyses.

To assess the effect of rolling motion on the dynamics of the coupled tire-air system, we first generate dynamic results for the stationary tire. In a subsequent analysis the tire and air are set into rolling motion, and corresponding dynamic results are obtained.

Model definition

We use a tire cross-section that is identical to that used in the simulation described in "Symmetric results transfer for a static tire analysis," Section 3.1.1. The air cavity is discretized using linear acoustic elements and is coupled to the structural mesh using a surface-based tie constraint with the slave surface defined on the acoustic domain. We model the rigid rim by applying fixed boundary conditions to the nodes on the bead of the tire, while the interaction between the air cavity and rim is modeled by a traction-free surface; i.e., no boundary conditions are prescribed on the surface.

We first create an axisymmetric mesh of half of the cross-section of the tire and air, then revolve it into half-symmetry. Symmetric model generation and symmetric results transfer, together with a static analysis procedure, are used to generate the preloading solution, which serves as the base state in the subsequent coupled acoustic-structural analyses.

In the first coupled analysis we reflect the revolved tire and air model into a full three-dimensional configuration. We then compute the real eigenvalues of the stationary tire and air cavity system. During frequency extraction steps, fixed boundary conditions are imposed automatically on the tire-road interface in the contact normal direction. Fixed boundary conditions are also applied in the tangential direction for points that are sticking. Points that are slipping are free to move in the tangential direction. This analysis is followed by a direct steady-state dynamic analysis in which we obtain the response of the tire-air system subjected to imposed harmonic motion of the road.

In the second coupled analysis the reflected model is restarted from the first step, after the footprint equilibrium configuration had been established. The steady-state transport procedure is used to obtain the free-rolling state of the tire at 60 km/h. The corresponding magnitude of the transport velocity is determined independently in a separate analysis. In this step the acoustic flow velocity signifies that the acoustic medium is also in rotational motion. It is assumed that the air inside the tire rotates with the same angular velocity as the tire. The direct steady-state analysis, with similar parameters to those used in the stationary case, is repeated.

Additional analyses using a substructure that was generated with the effect of acoustic flow velocity are also included.

Loading

The loading sequence for computing the footprint solution is identical to that discussed in "Symmetric results transfer for a static tire analysis," Section 3.1.1. The simulation starts with an axisymmetric model, which includes the mesh for the air cavity. Only half the cross-section is modeled. The inflation pressure is applied to the structure using a static analysis. In this example the application of pressure does not cause significant changes to the geometry of the air cavity, so it is not necessary to update the acoustic mesh. However, we perform adaptive mesh smoothing after the pressure is applied to illustrate that the updated geometry of the acoustic domain is transferred to the three-dimensional model when symmetric results transfer is used.

The axisymmetric analysis is followed by a reflection—symmetric three-dimensional analysis in which the footprint solution is obtained. The footprint load is established over several load increments. The deformation during each load increment causes significant changes to the geometry of the air cavity. We update the acoustic mesh by performing five mesh sweeps after each converged structural load increment using the adaptive mesh domain. At the end of this analysis sequence we activate friction between the tire and road using a change to friction properties. This footprint solution, which includes the updated acoustic domain, is transferred to a full three-dimensional model. This model is used to perform the coupled analysis. In the first coupled analysis we extract the eigenvalues of the undamped system, followed by a direct-solution steady-state dynamic analysis in which we apply a harmonic excitation to the reference node of the rigid surface that is used to model the road.

In the stationary and rolling analyses we compute the response of the coupled system in the same frequency range used in "Coupled acoustic-structural analysis of a tire filled with air," Section 3.1.5 (200 to 260 Hz). This band includes the natural frequencies of the fore-aft and vertical acoustic modes, at 225.67 Hz and 230.94 Hz, respectively.

The model is excited by a boundary condition specified at the road reference node in the direct-solution steady-state dynamic step. A small amount of stiffness proportional damping is applied to the rubber to avoid computing unbounded response at the eigenfrequencies.

Results and discussion

The characteristic frequencies of the coupled tire-air system are affected by the rolling motion. Generally, we expect a mode observed in the stationary coupled tire-air system to convert to a pair of modes, corresponding to forward and backward wave travel. This does not always occur in complex systems, because the stationary modes are not all affected by the rolling motion to a similar degree. However, the mode split described above can be observed for several of the structural modes and the fundamental acoustic modes of the cavity. For an observer in a nonrotating reference frame attached to the axle of the tire, similar to the reference frame used by the steady-state transport procedure, these modes appear as waves traveling clockwise and counterclockwise along the circumference of the tire. The mode corresponding to forward wave travel increases in frequency, whereas the mode corresponding to backward wave travel decreases in frequency. The modes of a stationary tire appear as static vibrations. The resonant frequencies of the stationary case are computed using the real-valued frequency extraction procedure. The complex frequency procedure will yield almost identical results for the stationary case, since the damping used in this example is relatively low. However, for the rolling analysis the complex frequency procedure must be used to obtain accurate results using all of the element contributions due to rotation. In Table 3.1.9–1 an example is shown of a pair of structural and acoustic modes splitting into a pair of corresponding modes in the rolling case. The structural mode is a radial mode of circumferential order two. If there is no footprint loading, the stationary case will predict identical frequencies for these modes; however, the split would still be observed for a rotating tire. The modes are shown in Figure 3.1.9–2, Figure 3.1.9–3, and Figure 3.1.9–4. Similar behavior is observed for radial modes of higher order.

Figure 3.1.9–5, Figure 3.1.9–6, and Figure 3.1.9–7 show the response of the structure to the imposed vertical motion at the spindle. Figure 3.1.9–5 compares the acoustic response, at the crown, of the coupled tire-air system for the stationary case and the rolling case at 60 km/h. Figure 3.1.9–6 shows the fore-aft reaction force, and Figure 3.1.9–7 shows the vertical reaction force.

These figures further show that the rolling motion of the solid has a very strong influence on the behavior of the coupled system and that the rolling motion of the air exerts a similarly strong effect in the frequency range observed here. In particular, the resonances affecting the reaction force occur at different frequencies for the stationary and rolling cases. The resonances observed in the reaction force frequency response diagram also proliferate as rolling is introduced since waves traveling against and with the direction of rolling propagate at different speeds with respect to the observer. For a stationary tire, a vertical excitation to the road produces negligible fore-aft reaction forces. However, the fore-aft reaction forces due to a vertical excitation are significant in the case of a rolling tire.

The same effect can be shown when using a substructure generated with the acoustic flow velocity. The tire model with a coarser mesh is used following the same pattern of actions: axisymmetric model followed by the revolution, reflection, and the steady-state transport analysis for a rolling tire. The substructure is used within the frequency range of 200–250 Hz using a direct steady-state dynamic

procedure. The same reaction force split resonance can also be observed for the full finite element model used in place of the substructure.

Input files

sst_acoustic_axi.inp	Axisymmetric model, inflation analysis.
sst_acoustic_rev.inp	Partial three-dimensional model, footprint analysis.
sst_acoustic_refl.inp	Full three-dimensional model, coupled structural-acoustic analyses, no transport effects.
sst_acoustic_roll100.inp	Full three-dimensional model, coupled structural-acoustic analyses, transport effects at moderate speed.
tiretransfer_node.inp	Nodal coordinates for the axisymmetric tire mesh.
tire_acoustic_air.inp	Mesh data for the axisymmetric acoustic mesh.
sst_acoustic_axi_sm.inp	Coarse axisymmetric model, inflation analysis.
sst_acoustic_rev_sm.inp	Coarse partial three-dimensional model.
sst_acoustic_refl_sm.inp	Coarse full three-dimensional model, coupled structural-acoustic analyses, no transport effects.
sst_acoustic_roll_sm.inp	Coarse full three-dimensional model, coupled structural-acoustic analyses, transport effects at moderate speed.
P_tire_acoustic_air.inp	Coarse mesh data for the axisymmetric acoustic mesh.
substracous_afv_sm_gen.inp	Frequency extraction and substructure generation, including acoustic flow velocity.
substracous_afv_sm_use.inp	Direct steady-state analysis with substructure.

Table 3.1.9–1 Example of eigenvalue splitting.

Mode description	Stationary coupled air-tire	Rolling coupled air-tire
Structural (radial, circumferential order 2)	95.467 Hz, 99.474 Hz	86.69 Hz, 103.77 Hz
Acoustic (fundamental modes of the acoustic cavity)	225.67 Hz, 230.94 Hz	218.48 Hz, 237.31 Hz

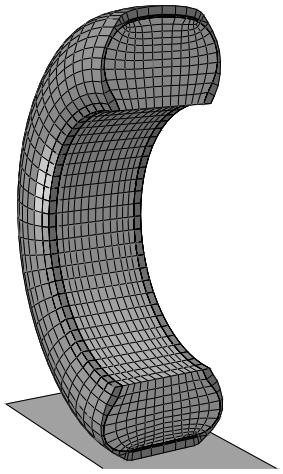

Figure 3.1.9–1 Cross-section of tire and air.

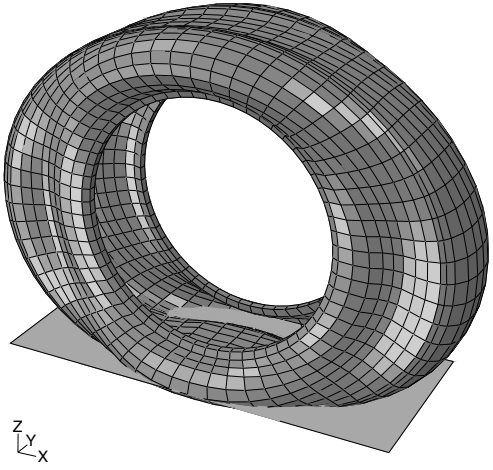

Figure 3.1.9–2 Radial mode, stationary case, at 95.46 Hz.

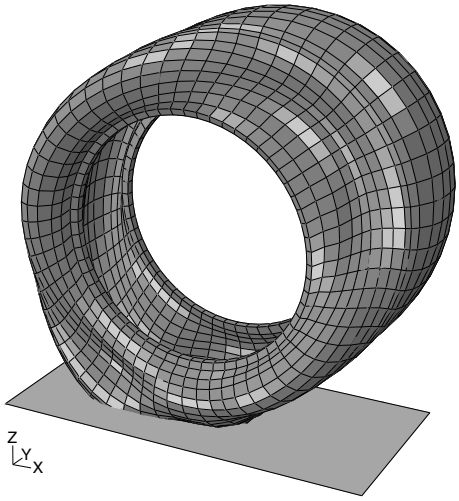

Figure 3.1.9–3 Radial mode, rolling case, backward, at 86.7 Hz (value at angle 90°).

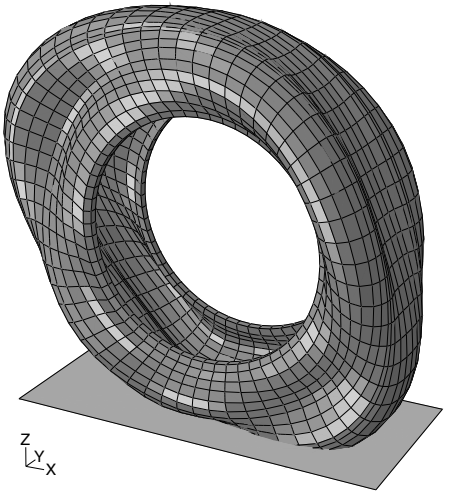

Figure 3.1.9–4 Radial mode, rolling case, forward, at 103.8 Hz (value at angle 90°).

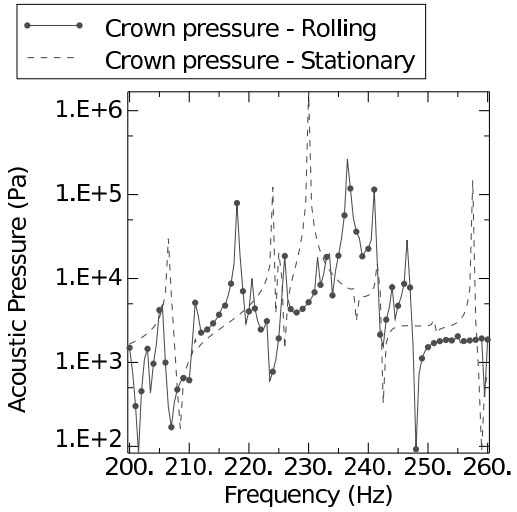

Figure 3.1.9–5 Acoustic pressure at crown due to imposed vertical motion.

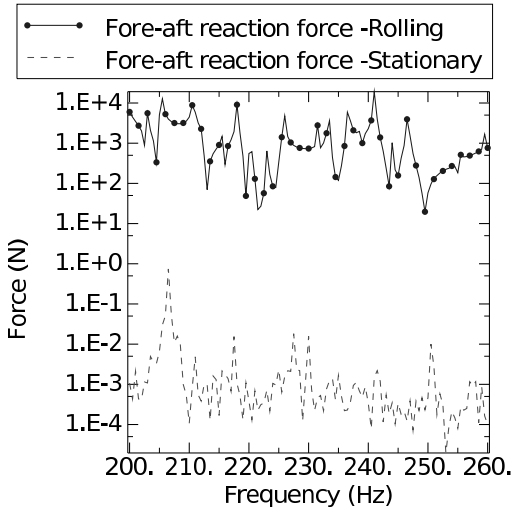

Figure 3.1.9–6 Fore-aft reaction force due to road displacement excitation.

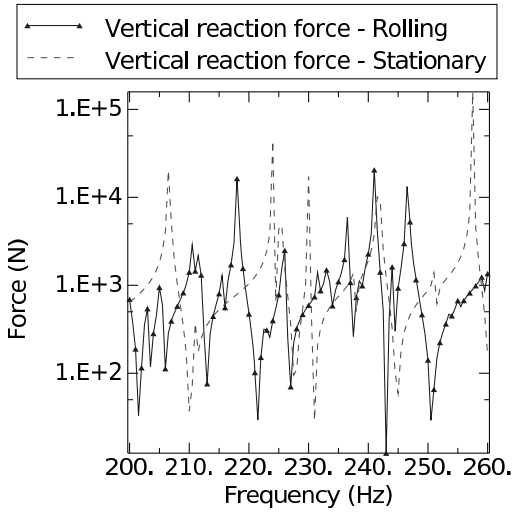

Figure 3.1.9–7 Vertical reaction force due to road displacement excitation.

3.1.10 ACOUSTICS IN A CIRCULAR DUCT WITH FLOW

Product: Abaqus/Standard

This example illustrates the use of the symmetric model generation and symmetric results transfer capabilities to create an acoustic model.

In addition, it illustrates the use of the steady-state transport capability in Abaqus to specify a rotational velocity in acoustic media and to analyze the acoustic field subject to the effects of rotational flow. A tire-shaped acoustic cavity is analyzed.

Problem description and model definition

The model is a simplified version of the acoustic cavity in a vehicle tire. The cross-section of the cavity is established using axisymmetric elements, and these elements are assigned material properties corresponding to air. A dummy step is used to establish the various files used in the subsequent three-dimensional analysis steps.

The complete toroidal cavity is created using a revolved symmetric model definition to form a circumferentially uniform mesh of 60 segments around the circle. Steady-state dynamic, eigenfrequency extraction, and complex frequency extraction procedures use the acoustic flow velocity to include the effects of the rotational flow.

The air cavity is analyzed at rest, at 28.0 radians per second (corresponding to 100 kilometers per hour), and at 320 radians per second (corresponding to Mach 0.3 at the outer edge of the cavity).

The steady-state dynamic results are computed at frequencies between 150 and 370 Hz. For the complex analyses, modes are requested between 45 and 1000 Hz.

Loading

In the time-harmonic dynamic analysis, a unit imaginary concentrated volumetric acceleration acoustic load is applied to a pair of nodes at the base of the torus. No boundary conditions are applied.

In the real and complex frequency analyses, no acoustic loads or boundary conditions are applied.

Results and discussion

Results from the steady-state dynamic analysis show the effect of the rotating flow on the acoustic pressure field. Strong effects in the field develop as speed increases.

Results from the real frequency analysis show some effect of the rotating flow on the acoustic pressure modes and the frequencies. However, real frequency analysis ignores the important convective term in the formulation, which is complex-valued. Consequently, real frequency analysis of rotating acoustic media should be regarded as a preliminary step for the complex frequency computation, and the results of the real frequency analysis should not be assigned much physical significance. Complex frequency analysis uses the entire, unsymmetric complex acoustic element formulation. The complex contributions are, however, antisymmetric; therefore, the resulting resonant frequencies computed by the complex frequency procedure are pure imaginary; that is, there is no real part of the eigenvalues

associated with gain or loss of energy. This is consistent with the physics of acoustics in rotating media. The effect of the flow on the eigenvalues is evident in the apparent splitting of the resonances as speed increases.

Input files

exa_acrotflowaxi.inp	Axisymmetric model.
exa_acrotflow3dssdd.inp	Full three-dimensional model, steady-state dynamic analysis.
exa_acrotflow3dfreq.inp	Full three-dimensional model, real and complex frequency analysis.

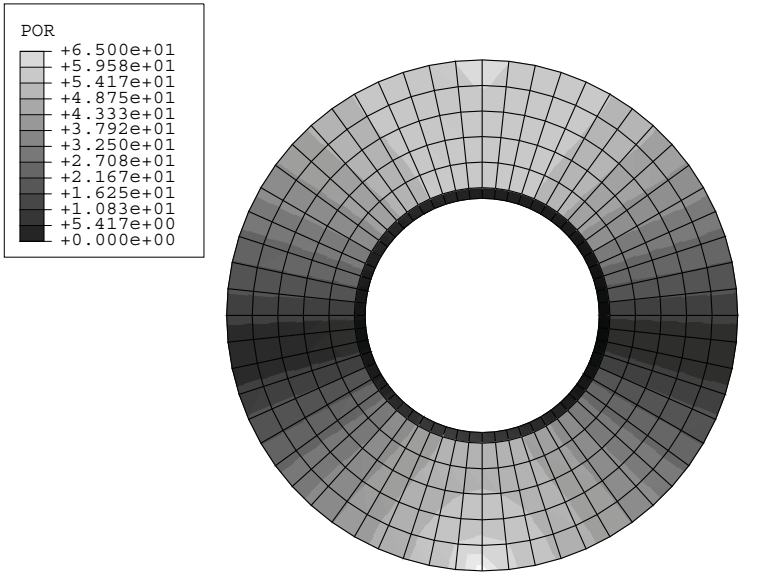

Figure 3.1.10–1 Steady-state dynamic response at 209 Hz, very low flow velocity.

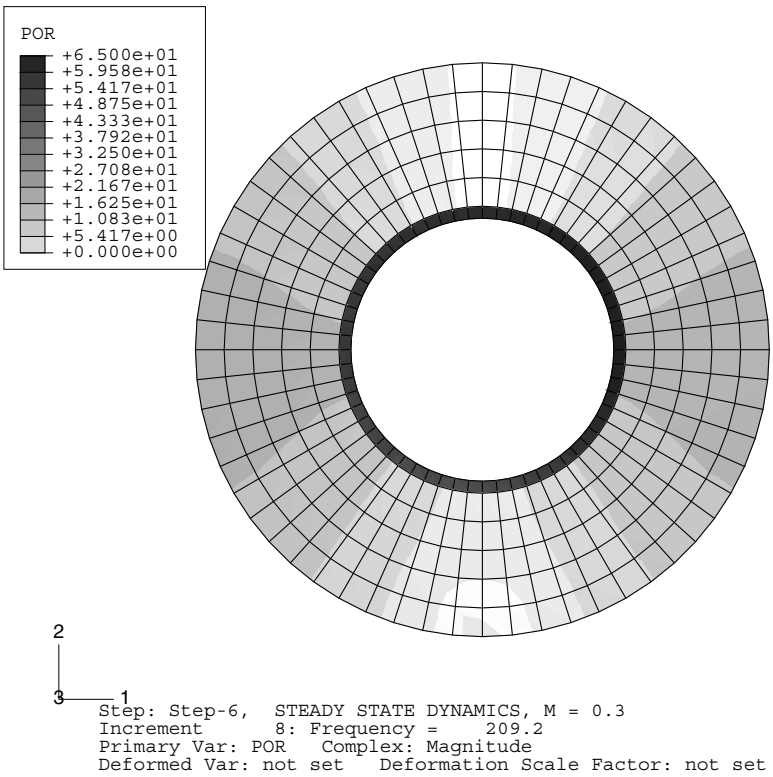

Figure 3.1.10–2 Steady-state dynamic response at 209 Hz, flow velocity of Mach 0.3.

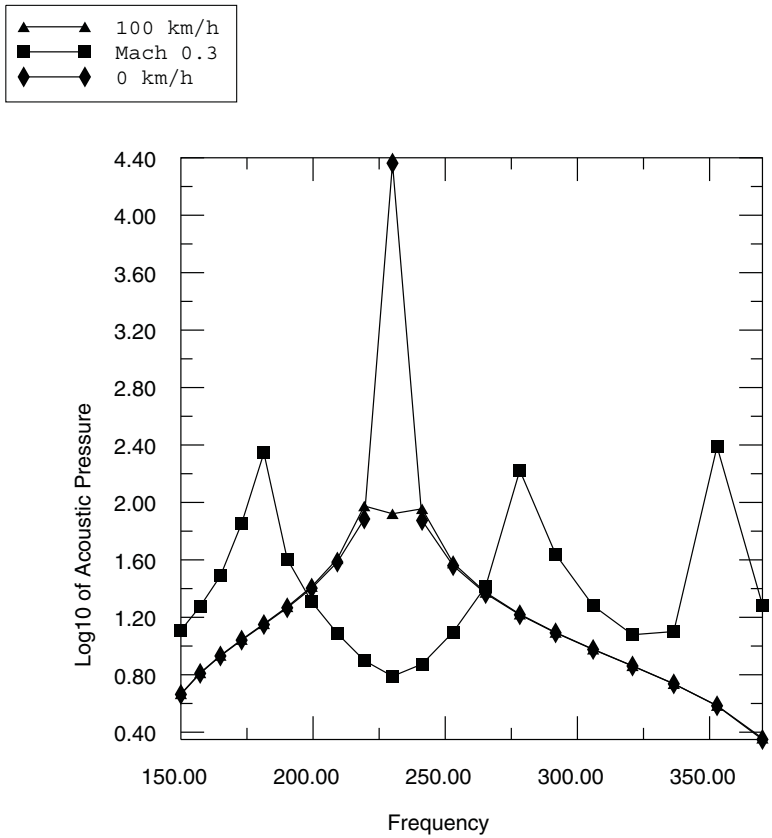

Figure 3.1.10–3 Steady-state dynamic response at node 13204, flow velocities from slow to Mach 0.3.

3.2 Vehicle analyses

- “Inertia relief in a pick-up truck,” Section 3.2.1
- “Substructure analysis of a pick-up truck model,” Section 3.2.2
- “Display body analysis of a pick-up truck model,” Section 3.2.3
- “Continuum modeling of automotive spot welds,” Section 3.2.4

3.2.1 INERTIA RELIEF IN A PICK-UP TRUCK

Product: Abaqus/Standard

This example shows how to perform inertia relief in a static analysis in Abaqus/Standard.

The example involves stopping a pick-up truck, moving with an initial velocity of 50.0 km/h (13.89 m/s), by applying braking loads. Inertia relief is used here to supply inertia forces in a static analysis that oppose the braking loads specified in the model. The solution provides the rigid body deceleration and the static stresses in the pick-up truck. For comparison purposes a dynamic analysis is performed with the same initial velocity and braking loads.

Related topics

- "Inertia relief," Section 11.1.1 of the Abaqus Analysis User's Guide

Problem description and model definition

A 1994 Chevrolet C1500 pick-up truck (see Figure 3.2.1–1) is modeled using approximately 55,000 elements. The model was obtained from the Public Finite Element Model Archive of the National Crash Analysis Center at George Washington University. The finite element model was converted into an Abaqus/Standard input file, and several missing constraints were added to carry out the analyses. The model consists of various parts—such as cabin, truck bed, doors, etc.—which are meshed with shell elements, three-dimensional beam elements, and three-dimensional solid elements. The parts are attached with connector elements, coupling elements, and multi-point constraints.

The materials used in the truck model are idealized as elastic or elastic-plastic. Suitable adjustments are made to the material properties to account for unmodeled features of various parts such as the internal details of the engine, gearbox, etc. A summary of the material properties and the parts for which they are used is given in Table 3.2.1–1 and Table 3.2.1–2.

Rigid body definitions are used for brakes and brake assemblies to take advantage of the high stiffness of these parts relative to other parts. Connector elements are used to model kinematic constraints governing relative motions between various parts (see "Substructure analysis of a pick-up truck model," Section 3.2.2, for details).

The finite element model of the truck is oriented such that the positive 1-direction goes from the rear to the front of the truck, the positive 2-direction goes from the passenger (right-hand) side to the driver (left-hand) side, and the positive 3-direction is upward. In this system the braking loads are applied at the respective wheel spindles as concentrated forces in the negative 1-direction.

To simplify the analysis, normal contact between the tires and the road surface is modeled through spring elements that have one node connected to the wheel spindle and the other node fixed against displacement in the 3-direction and kinematically constrained to the wheel spindle in the other directions. Friction between the tires and the road surface is assumed to be nonexistent. This allows the truck to translate freely in the 1- and 2-directions and rotate freely about the 3-direction; the constraints on the spring nodes prevent translation in the 3-direction and rotation about the 1- and 2-directions.

Loading

A separate static analysis is performed to obtain the correct initial configuration and stress distribution under the applied gravity load. The details of this analysis are explained in "Substructure analysis of a pick-up truck model," Section 3.2.2. This gives us the base state for the analysis of interest.

The total braking load for the truck moving at 13.89 m/s is computed by assuming the truck to be a rigid body that comes to rest over a distance of 20 m after the brakes are applied. This gives a deceleration of 4.82 m/s^2 in the 1-direction for the truck. The total mass of the truck as computed from the finite element analysis is 1.72×10^3 kg, which gives the total inertial force resisted by the brakes (or braking load) as 8.30 kN. Assuming that the front brakes provide 75% of the total resistance and the rear brakes provide the remaining 25%, the braking load for each of the front wheels is 3.11 kN and the braking load for each of the rear wheels is 1.04 kN. The four braking loads applied to the truck are balanced in a static analysis with an inertia relief load. The inertia relief load represents the dynamic effects (not modeled otherwise in a static analysis) of a constant deceleration from the truck's travel velocity to a complete stop.

Since the truck is free to translate in the 1- and 2-directions and rotate about the 3-direction, inertia relief is performed in these three directions. The other directions are constrained by boundary conditions as explained in the previous section.

For comparison purposes a transient dynamic analysis is also performed (after the initial static equilibrium under gravity load) in which the truck is accelerated from zero velocity to the final uniform velocity of 13.89 m/s. This dynamic analysis step is followed by another dynamic analysis step in which the braking loads are applied to bring the truck to a complete stop. The braking loads are ramped up smoothly from zero to the maximum value over 0.5 seconds and then kept constant for 2.88 seconds—the time required to bring the truck to rest from the initial velocity of 13.89 m/s with an average deceleration of 4.82 m/s^2. To minimize the analysis time, substructures are used in the dynamic analysis for all deformable parts except the chassis and suspension components, which are modeled as fully deformable since they are the parts that show significant stresses.

Results and discussion

The results for inertia relief in the pick-up truck model with braking loads show that the truck decelerates at 4.83 m/s^2 in the 1-direction. The truck has an angular acceleration of 0.01 rad/s^2 about the 3-direction at the center of mass due to asymmetry in the distribution of mass. The vertical displacements at the wheel spindles (the front wheel spindles dip about 0.7 mm, and the rear wheel spindles rise about 0.7 mm without loss of contact between tires and the road surface) indicate that the truck pitches forward due to the braking action. A plot of the Mises stress shown in Figure 3.2.1–2 indicates that the largest stresses occur in the suspension components and the regions where the suspension components are connected to the chassis. Plots of the active yield flag and equivalent plastic strains (not shown) indicate that there is no plastic yielding in any part of the truck.

The results for the transient dynamic analysis indicate that the average deceleration after the full braking load has been applied is around 4.94 m/s^2 in the 1-direction and the average angular acceleration about the 3-direction is 0.03 rad/s^2. The truck pitches forward with the front wheel spindles dipping

about 0.7 mm and the rear wheel spindles rising about 0.7 mm in the braking load step. The Mises stress for the dynamic analysis, shown in Figure 3.2.1–3, shows a distribution similar to that obtained for inertia relief. There is no plastic yielding in the chassis or suspension components.

Inertia relief relies on the assumption that the body undergoing loading is free to translate and rotate as a rigid body. Therefore, no external or internal constraints are allowed in the free directions (with the exception of the case where statically determinant boundary conditions are applied and all available directions are considered inertia relief directions). In a complex model like the pick-up truck, with various kinematic constraints and large geometry changes, it is necessary to ensure that the base state for the step including inertia relief is converged to a tight residual tolerance. If it is not converged to a tight tolerance, the out-of-balance forces and moments in the base state will act as internal constraints on rigid body motions. Hence, such unequilibrated forces and moments may prevent a geometrically linear or nonlinear analysis from converging. In this example the solution controls tighten the convergence tolerance in the gravity load step preceding the inertia relief step.

The comparison of results for inertia relief and dynamic analysis of the truck shows that inertia relief is an inexpensive alternative to dynamic analysis for obtaining the steady-state response of a dynamic system for certain loading situations. In this braking analysis, for example, the static analysis with inertia relief runs about 10 times faster than the general deformable transient dynamic simulation.

Input files

irltr_brake_irl.inp	Static equilibrium analysis for gravity load and initial stresses followed by inertia relief with braking loads.
irltr_brake_dyn.inp	Static equilibrium analysis for gravity load and initial stresses followed by dynamic acceleration to uniform velocity and deceleration with braking loads.

The model data are contained in multiple smaller files and referenced in the main input files. The referenced file names are given in “Substructure analysis of a pick-up truck model,” Section 3.2.2.

Table 3.2.1–1 Properties for elastic-plastic materials used in the truck model.

Elastic-Plastic Material Name	Properties				Part Name
	E (N/m^2)	ν	σ_y (N/m^2)	ρ (kg/m^3)	
Steel	2.1×10^{11}	0.3	2.7×10^{8}	7.89×10^{3}	rail (chassis), engine oil box, radiator mounting, fenders, wheel housings, cabin, bed, fan center, fuel tank, rear rim, steering support, battery tray, seat track, radiator outer
Steel	2.1×10^{11}	0.3	3.5×10^{8}	7.89×10^{3}	engine mountings, radiator mountings, radiator, fender mountings, hood, doors, cabin hinges
Plastic	2.8×10^{9}	0.3	4.5×10^{7}	1.2×10^{3}	fan cover
Glass	7.6×10^{10}	0.3	1.38×10^{8}	2.5×10^{3}	windows, windshield
Plastic	3.4×10^{9}	0.3	1.0×10^{8}	1.1×10^{3}	radiator side block
Plastic	3.4×10^{9}	0.3	1.0×10^{8}	7.1×10^{3}	dashboard interior

Table 3.2.1–2 Properties for elastic materials used in the truck model.

Elastic Material Name	Properties			Part Name
	E (N/m^2)	ν	ρ (kg/m^3)	
Steel	2.1×10^{11}	0.3	7.89×10^3	A-arm mountings, fan, door lock beams, headrest connector beams, radiator mounting beams, oil pan beams, rear axle, drive shaft, steering, A-arm-rim connectors, A-arm-rail connectors, bed-rail connector, dashboard support, steering column, rail connector, brakes, gearbox CV joint, front rim
Steel	1.2×10^{11}	0.3	3.89×10^3	engine gearbox
Steel	2.1×10^{10}	0.3	1.82×10^3	engine front
Steel	2.1×10^{11}	0.3	2.5×10^3	door lock
Rubber	2.461×10^9	0.323	8.0598×10^3	tires
Steel	2.1×10^{11}	0.3	3.5765×10^3	rear suspension
Steel	2.1×10^{11}	0.3	2.089×10^4	brake assembly
Steel	2.1×10^{11}	0.3	6.911×10^3	brake assembly
Rubber-Metal Composite	2.1×10^{11}	0.3	1.96×10^3	battery
Foam	2.0×10^9	0.3	2.527×10^2	seat bottom
Foam	2.0×10^9	0.3	7.55×10^2	seat top
Foam	2.0×10^9	0.3	1.69×10^2	seat headrest

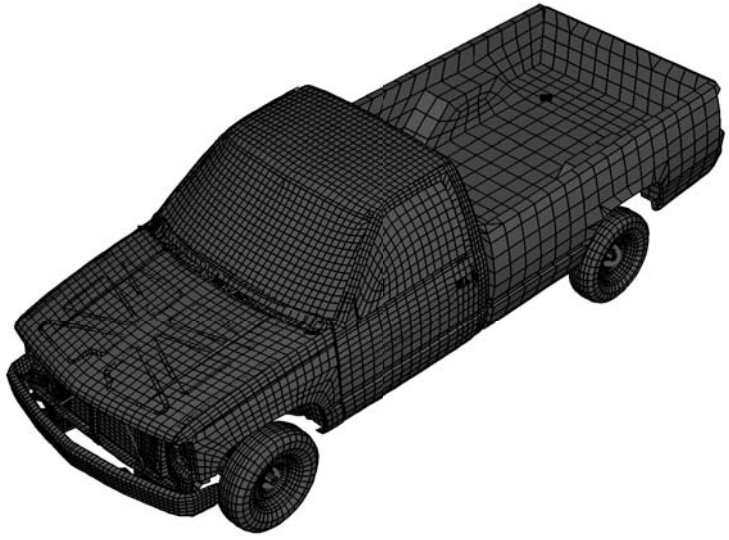

Figure 3.2.1–1 Finite element model of 1994 Chevrolet C1500 pick-up truck.

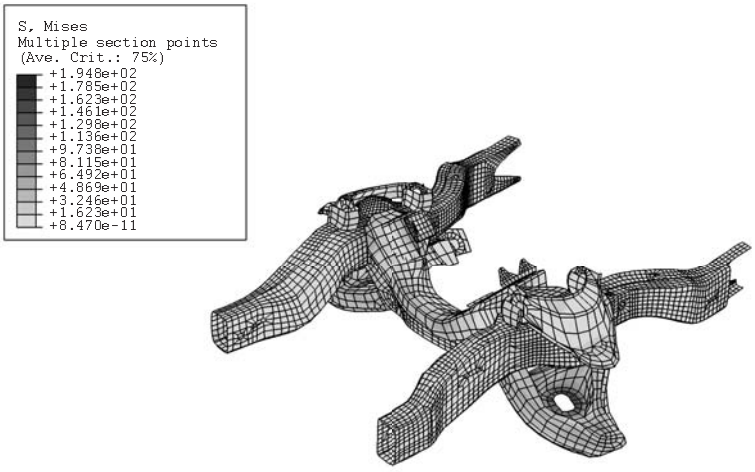

Figure 3.2.1–2 Mises stress in front chassis and A-arm components for inertia relief.

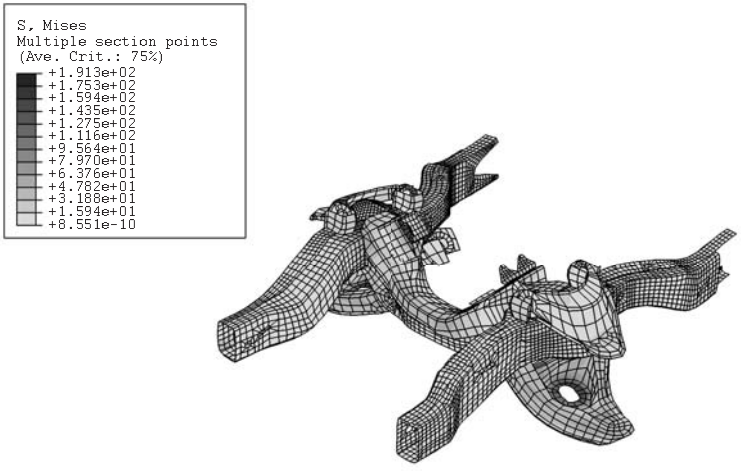

Figure 3.2.1–3 Mises stress in front chassis and A-arm components for dynamic analysis.

3.2.2 SUBSTRUCTURE ANALYSIS OF A PICK-UP TRUCK MODEL

Product: Abaqus/Standard

This example illustrates the use of the substructure capability in Abaqus to efficiently simulate the vehicle dynamics of a detailed pick-up truck model traveling over road bumps.

The pick-up truck model geometry described in "Inertia relief in a pick-up truck," Section 3.2.1, is used in this example. The model is organized as a collection of individual parts that are connected together. Twenty substructures are then created, one for each part that may undergo large motions but for which it is reasonable to assume small-strain elastic deformation (e.g., the chassis). Several parts that may deform nonlinearly (e.g., leaf springs for the rear suspension or the stabilizer bar in the front) are modeled using the usual general nonlinear modeling options. Connection points are created for each part using a coupling constraint. The parts are then attached together using appropriate connector elements. A simplified CALSPAN tire model is used (**UEL**) to model the radial forces in the tires. The vehicle is loaded statically by gravity, accelerated in a dynamic step on a flat road, and run over bumps. Without stress recovery in the substructures the substructure analysis runs an estimated 120 times faster than an equivalent analysis without substructures.

Geometry and materials

The pick-up truck model (1994 Chevrolet C1500) discussed here is depicted in Figure 3.2.2–1 riding over antisymmetric bumps. The model geometry, element connectivity, and material properties are obtained from the Public Finite Element Model Archive of the National Crash Analysis Center at George Washington University. The materials used are described in "Inertia relief in a pick-up truck," Section 3.2.1.

The model is organized as a collection of individual parts connected together. Most parts that undergo only small deformations in addition to a large rigid body motion are defined as substructures. Substructures are created for the following parts: the chassis, each of the four A-arms for the front suspension, each of the four wheels, the rear axle, the driveshaft, the engine/transmission, the cabin, each of the two doors, the hood, the seat, the front bumper, the truck bed, and the fuel tank.

The number of retained nodes for each substructure is determined primarily by its connection points with neighboring parts as illustrated in Figure 3.2.2–2 for the cabin substructure. There are twenty points associated with this substructure that are used to connect the cabin to other parts in the model. There are six retained nodes on the cabin bottom (connections to the chassis); three retained nodes for the hood connections (two hinges and the hood lock); three retained nodes for each of the two door connections (two hinges in the front and the door lock in the back); four retained nodes for the seat connections; and one node retained at the center of mass of the vehicle used for yaw, pitch, and roll measurement purposes.

Several parts deform too much to be considered substructures and are modeled using regular elements. The leaf springs in the back and the stabilizer bar in the front are both modeled with beam elements. The front brake assemblies are modeled as rigid bodies.

The connections between parts are modeled using connector elements. JOIN and REVOLUTE connectors are used to model the hinges between each of the following parts: the A-arms and chassis, the doors and cabin, the hood and cabin, the wheels and knuckles, and the leaf springs and chassis.

CARTESIAN and CARDAN connections with appropriately defined connector elasticity, connector damping, and connector friction behaviors are used to define some of the bushing connections (e.g., engine mounts). Two UNIVERSAL connectors are used to model the driveshaft connections to the transmission in the front and to the differential in the back. BEAM connectors are used to model rigid connections between parts. The available connector components of relative motion applied to an AXIAL connector are used to lock (or open) the doors and the hood. The available connector components of relative motion applied to a SLOT connector are used to specify the steering by moving the steering rack. The struts are modeled using an AXIAL connection by specifying approximate nonlinear elasticity and damping. Several of the suspension-related parts are shown in Figure 3.2.2–3.

The radial forces in the tires are modeled approximately using a simplified CALSPAN tire model (Frik, Leister, and Schwartz, 1993) implemented via user subroutine **`UEL`**. A radial stiffness of 600 N/mm is considered.

Models

For all analyses the gravity-loaded static equilibrium configuration is found first. Since the given mesh geometry corresponds to the gravity-loaded equilibrium position and data are not available for the pre-stress in the suspension springs and tires, the pre-stress forces have to be computed. To achieve this end, a separate static stress analysis with artificial properties for the suspension springs and artificial boundary conditions is first performed, as follows. The vehicle is supported with boundary conditions in the vertical direction at the four wheel spindles (where the tire **`UEL`**s will be connected) and fixed at the center of mass to prevent in-plane rigid body motion (degrees of freedom 1, 2, and 6). The stiffnesses of the suspension springs are increased artificially by a thousand times in this independent analysis to minimize deformation. The gravity load is then applied to obtain equilibrium stresses in the suspension components and reaction forces at the wheel spindles.

In the analysis of interest (with realistic properties and boundary conditions), the stresses and reaction forces obtained from the artificial static step are used as initial stresses in the suspension spring components and as pre-stress forces in the tires, respectively. A static gravity loading step is run to obtain an equilibrium configuration. This equilibrium configuration differs only slightly from the given initial geometry (the wheel spindles move laterally about two millimeters). Thus, the initial stress state in the suspension springs and tires accurately represents static equilibrium, and the vehicle is ready for dynamic loading.

The vehicle model is prescribed an initial velocity and then accelerated (0.5 g) to the desired velocity (5 m/sec or 7 m/sec) in a direct-integration implicit dynamic step. Once the “cruise” velocity is achieved, the truck model is run over symmetric or antisymmetric bumps (0.2 m high and 5.0 m long).

Results and discussion

In Figure 3.2.2–4 a snapshot of the truck moving forward with a velocity of 7 m/sec (25.2 km/h) and “jumping” over symmetric bumps is shown. The wheels loose contact with the ground and then land again on the road (not shown).

More results are presented for the case when the truck is riding over antisymmetric bumps (see Figure 3.2.2–1). Stresses are recovered for the lower left A-arm substructure and shown in Figure 3.2.2–5

when the front wheels have traveled 3.2 m over the bumps (for information on how to display results on the substructure, see "A script to visualize the element results for beams and shells within substructure in Abaqus" in the Dassault Systèmes Knowledge Base at www.3ds.com/support/knowledge-base). The radial forces on the tires are shown in Figure 3.2.2–6, beginning from the moment when the front tires are about to go over the bumps. A zero radial force indicates that the tire is out of contact. The yaw, pitch, and roll angles recorded using a CARDAN connector attached to the model at its center of mass are shown in Figure 3.2.2–7.

The advantage of using substructures instead of regular deformable elements becomes obvious when the total times needed to complete these types of analyses are compared. A full analysis using regular elements has not been performed since approximately five CPU days would be necessary to complete either of the two analyses discussed above. This total time was estimated by running a few increments, estimating the time needed per iteration, and then multiplying the time per iteration by the total number of iterations needed to complete the analysis. Using these estimates, the substructure analysis is up to 120 times faster than the regular mesh analysis, depending on the amount of recovery performed for each substructure.

The **abaqus substructurecombine** execution procedure can combine model and results data from two substructure output databases into a single output database. For more information, see "Combining output from substructures," Section 3.2.24 of the Abaqus Analysis User's Guide. To combine the substructure output databases, at least one frame of field output must be requested.

Input files

tr_entire_truck_in_phase.inp	Substructure global analysis of the truck going over in-phase bumps.
tr_entire_truck_anti_phase.inp	Substructure global analysis of the truck going over antiphase bumps.
tr_road_antiphase.inp	Definition of antiphase road profile.
tr_road_inphase.inp	Definition of in-phase road profile.
tr_all_nodes.inp	All node definitions.
tr_parameters.inp	*PARAMETER definitions.
tr_materials.inp	Material definitions.
tr_materials_plastic_irl.inp	Material definitions.
tr_initial_stress.inp	Initial stress definition for the leaf springs.
tr_lock_doors_and_hood.inp	*CONNECTOR MOTION that keeps the doors and the hood locked.
tr_substruct_recovery.inp	Output definitions for the substructures.
tr_brake_front_left.inp	*RIGID BODY definition of the front left brake assembly.
tr_brake_front_right.inp	*RIGID BODY definition of the front right brake assembly.
tr_parameters_inphase.inp	*PARAMETER definitions for the in-phase analysis.
tr_parameters_antiphase.inp	*PARAMETER definitions for the antiphase analysis.
tr_readme.inp	Description of procedure used to run the jobs.

User subroutine

exa_tr_radial_uel.f	**UEL** used to define the tire model.

Substructure generation files

tr_chassis_gen.inp	Chassis.
tr_retained_chassis.inp	Retained nodes for the chassis.
tr_susp_lower_arm_left_gen.inp	Lower left A-arm.
tr_susp_lower_arm_right_gen.inp	Lower right A-arm.
tr_susp_upper_arm_left_gen.inp	Upper left A-arm.
tr_susp_upper_arm_right_gen.inp	Upper right A-arm.
tr_rear_axle_gen.inp	Rear axle.
tr_retained_rear_axle.inp	Retained nodes for the rear axle.
tr_engine_gen.inp	Engine and transmission.
tr_driveshaft_gen.inp	Driveshaft.
tr_cabin_gen.inp	Cabin and front fenders.
tr_retained_cabin.inp	Retained nodes for the cabin.
tr_hood_gen.inp	Hood.
tr_door_left_gen.inp	Left door.
tr_door_right_gen.inp	Right door.
tr_seat_gen.inp	Seat.
tr_bed_gen.inp	Truck bed.
tr_fuel_tank_gen.inp	Fuel tank.
tr_bumper_gen.inp	Front bumper.
tr_wheel_back_left_gen.inp	Rear left wheel.
tr_wheel_back_right_gen.inp	Rear right wheel.
tr_wheel_front_left_gen.inp	Front left wheel.
tr_wheel_front_right_gen.inp	Front right wheel.

Element definitions

tr_rear_susp_leaf_springs.inp	Rear leaf spring suspension.
tr_stabilizer_elts.inp	Front stabilizer bar.
tr_steering_rods_elts.inp	Steering rods and steering rack.
tr_chassis_elts.inp	Chassis.
tr_susp_lower_arm_left_elts.inp	Lower left A-arm.
tr_susp_lower_arm_right_elts.inp	Lower right A-arm.
tr_susp_upper_arm_left_elts.inp	Upper left A-arm.
tr_susp_upper_arm_right_elts.inp	Upper right A-arm.
tr_rear_axle_elts.inp	Rear axle.
tr_engine_elts.inp	Engine and transmission.
tr_driveshaft_elts.inp	Driveshaft.
tr_cabin_elts.inp	Cabin and front fenders.
tr_hood_elts.inp	Hood.

tr_door_left_elts.inp	Left door.
tr_door_right_elts.inp	Right door.
tr_seat_elts.inp	Seat.
tr_bed_elts.inp	Truck bed.
tr_fuel_tank_elts.inp	Fuel tank.
tr_bumper_elts.inp	Front bumper.
tr_wheel_back_left_elts.inp	Rear left wheel.
tr_wheel_back_right_elts.inp	Rear right wheel.
tr_wheel_front_left_elts.inp	Front left wheel.
tr_wheel_front_right_elts.inp	Front right wheel.

Multi-point constraint definitions

tr_chassis_mpc.inp	Chassis.
tr_engine_mpc.inp	Engine and transmission.
tr_cabin_mpc.inp	Cabin and front fenders.
tr_hood_mpc.inp	Hood.
tr_door_left_mpc.inp	Left door.
tr_door_right_mpc.inp	Right door.
tr_seat_mpc.inp	Seat.
tr_fuel_tank_mpc.inp	Fuel tank.
tr_bumper_mpc.inp	Front bumper.

Coupling definitions

tr_chassis_coup.inp	Chassis.
tr_susp_lower_arm_left_coup.inp	Lower left A-arm.
tr_susp_lower_arm_right_coup.inp	Lower right A-arm.
tr_susp_upper_arm_left_coup.inp	Upper left A-arm.
tr_susp_upper_arm_right_coup.inp	Upper right A-arm.
tr_rear_axle_coup.inp	Rear axle.
tr_engine_coup.inp	Engine and transmission.
tr_driveshaft_coup.inp	Driveshaft.
tr_cabin_coup.inp	Cabin and front fenders.
tr_hood_coup.inp	Hood.
tr_door_left_coup.inp	Left door.
tr_door_right_coup.inp	Right door.
tr_seat_coup.inp	Seat.
tr_bed_coup.inp	Truck bed.
tr_fuel_tank_coup.inp	Fuel tank.
tr_bumper_coup.inp	Front bumper.
tr_wheel_back_left_coup.inp	Rear left wheel.
tr_wheel_back_right_coup.inp	Rear right wheel.
tr_wheel_front_left_coup.inp	Front left wheel.
tr_wheel_front_right_coup.inp	Front right wheel.

Connector definitions

tr_conn_aarms_left.inp	Left A-arms.
tr_conn_aarms_right.inp	Right A-arms.
tr_conn_brake_left.inp	Left front brake assembly.
tr_conn_brake_right.inp	Right front brake assembly.
tr_conn_steering_rods.inp	Steering rods.
tr_conn_stabilizer.inp	Stabilizer bar.
tr_conn_leaf_springs.inp	Leaf springs.
tr_conn_engine.inp	Engine and transmission.
tr_conn_driveshaft.inp	Driveshaft.
tr_conn_cabin_to_chassis.inp	Cabin to chassis.
tr_conn_hood.inp	Hood.
tr_conn_door_left.inp	Left door.
tr_conn_door_right.inp	Right door.
tr_conn_seat.inp	Seat.
tr_conn_bed.inp	Truck bed.
tr_conn_fuel_tank.inp	Fuel tank.
tr_conn_bumper.inp	Front bumper.
tr_conn_wheels_back.inp	Rear wheels.
tr_conn_wheels_front.inp	Front wheels.

Reference

- Frik, S., G. Leister, and W. Schwartz, “Simulation of the IAVSD Road Vehicle Benchmark Bombardier Iltis with FASIM, MEDYNA, NEWEUL, and SIMPACK,” in Multibody Computer Codes in Vehicle System Dynamics, Ed. W. Kortum and R. S. Sharp, February 1993.

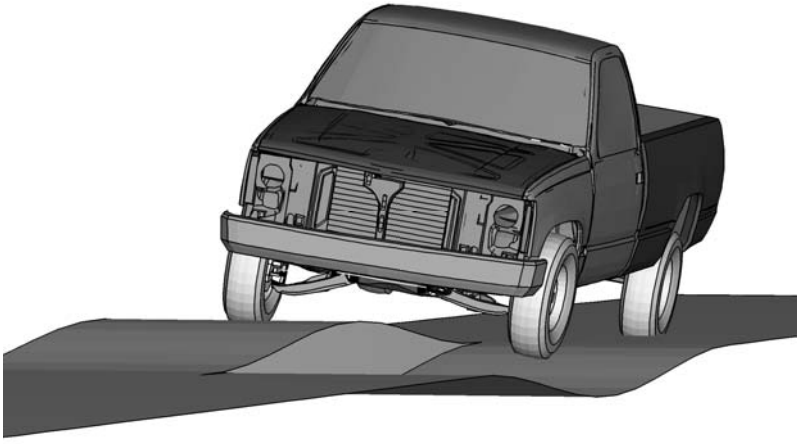

Figure 3.2.2–1 Substructure truck model going over antisymmetric (left-right) bumps.

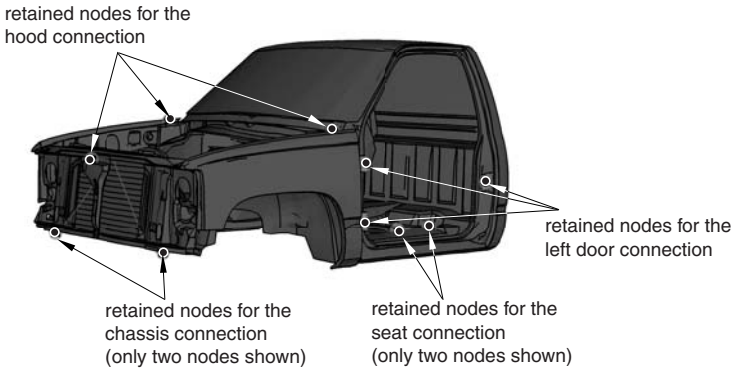

Figure 3.2.2–2 Substructure mesh for the cabin.

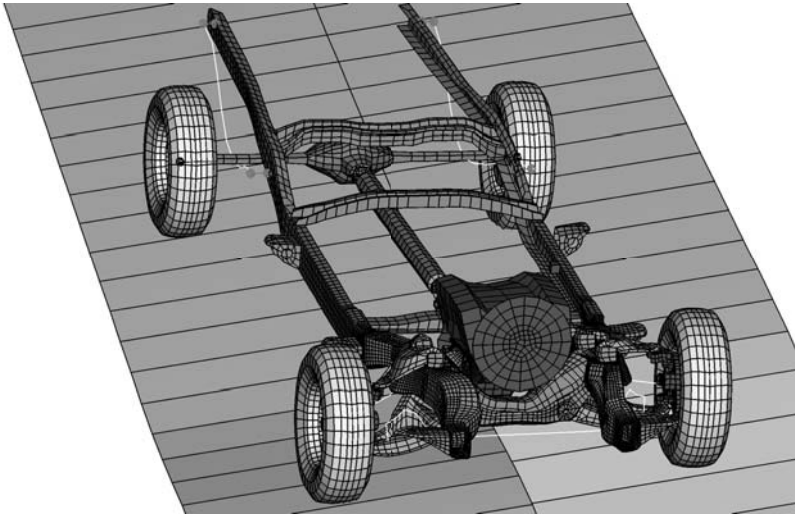

Figure 3.2.2–3 Chassis, suspension, and power-train-related parts.

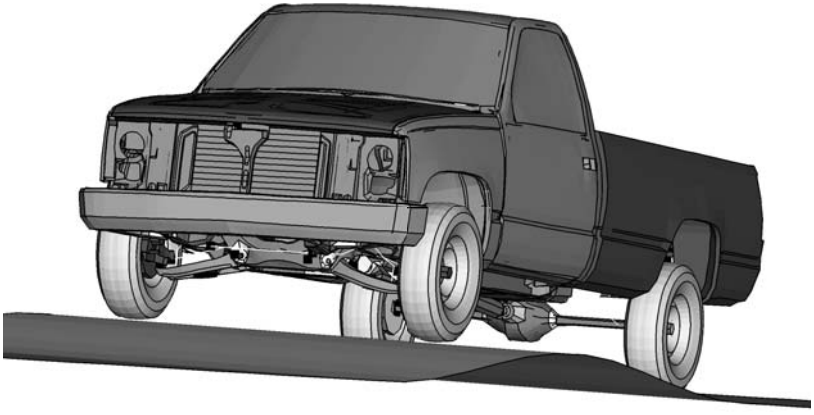

Figure 3.2.2–4 Substructure truck model going over symmetric (left-right) bumps.

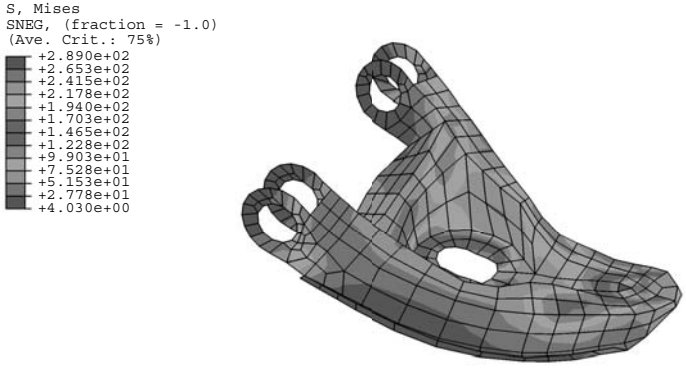

Figure 3.2.2–5 Recovered stresses in lower left A-arm.

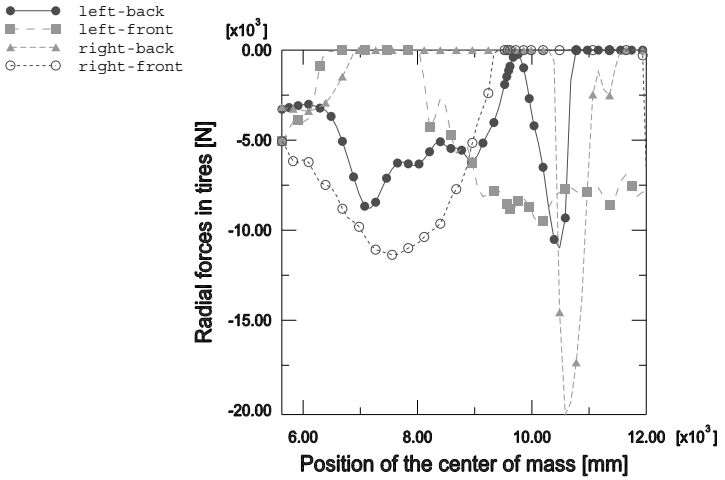

Figure 3.2.2–6 Tire radial forces for the truck going over antisymmetric bumps.

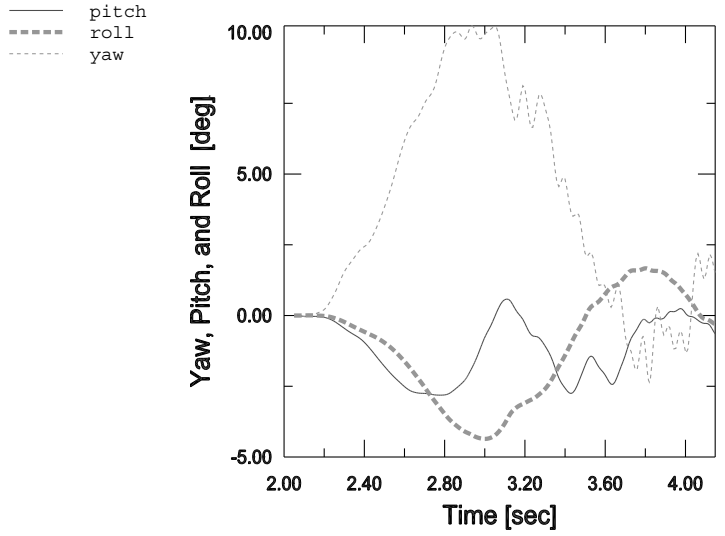

Figure 3.2.2–7 Yaw, pitch, and roll for the truck going over antisymmetric bumps.

3.2.3 DISPLAY BODY ANALYSIS OF A PICK-UP TRUCK MODEL

Product: Abaqus/Standard

This example illustrates the use of the display body capability in Abaqus to simulate efficiently the vehicle dynamics of a detailed pick-up truck model driving over a symmetric road bump.

The pick-up truck model geometry is described in "Inertia relief in a pick-up truck," Section 3.2.1. The model is organized as a collection of several parts, twenty-two of which are converted to display bodies. The display bodies are connected using connectors. Several parts that may deform nonlinearly (e.g., the leaf springs for the rear suspension and the stabilizer bar in the front) are modeled using beam elements. The mass, center of mass, and rotary inertia are computed for every part by running a datacheck analysis on separate models, each containing one part. A mass and a rotary inertia element are then created at the reference point of the display body. The reference point of each display body is connected to its attachment points using connector elements. A simplified CALSPAN tire model is used to model the radial forces in the tires via user subroutine **UEL**. The vehicle is loaded statically by gravity, accelerated in a dynamic step on a flat road, and run over bumps. The results are then compared to corresponding analyses with substructures as in "Substructure analysis of a pick-up truck model," Section 3.2.2.

Geometry and materials

The problem discussed here is a model of a pick-up truck (1994 Chevrolet C1500). The model geometry, element connectivity, and material properties are obtained from the Public Finite Element Model Archive of the National Crash Analysis Center at George Washington University. The materials used are described in "Inertia relief in a pick-up truck," Section 3.2.1.

The model is organized as a collection of individual parts connected together. Most parts that undergo only small deformations in addition to a large rigid body motion are defined as display bodies; their deformation can be neglected since only the overall motion of the vehicle is of interest. A display body is created for each of the following parts: the chassis, each of the four A-arms of the front suspension, each of the four wheels, the rear axle, the driveshaft, the engine/transmission, the cabin, each of the two doors, the hood, the seat, the front bumper, the truck bed, and the fuel tank.

The number of attachment points for each display body is determined by its connection points with neighboring parts. The display bodies of the front-wheel assembly are shown connected at attachment nodes in Figure 3.2.3–1.

Several parts deform nonlinearly and are modeled using regular elements. For example, the leaf springs in the rear and the stabilizer bar in the front are modeled with beam elements.

To create the display bodies with appropriate attachment points and realistic material properties, the following steps are taken:

1. A datacheck analysis is run on every part with deformable elements to determine its mass, rotary inertia, and center of mass.
2. An instance of this part is used to create a display body.

3. A reference node created at the center of mass for this part is also used as the reference node for the corresponding display body.
4. A mass element and a rotary inertia element are created at the reference node.
5. The reference node is then connected to the attachment points of the part using either BEAM or CARTESIAN and CARDAN connectors with stiff elastic properties.

The connections between the attachment points of two display bodies are modeled using connector elements. JOIN and REVOLUTE connectors are used to model the hinges between each of the following parts: the A-arms and chassis, the doors and cabin, the hood and cabin, the wheels and knuckles, and the leaf springs and chassis. CARTESIAN and CARDAN connections with connector elasticity, connector damping, and connector friction behaviors are used to define some of the bushing connections (e.g., the engine mounts). Two UNIVERSAL connectors are used to model the driveshaft connections to the transmission in the front and to the differential in the back. BEAM connectors are used to model rigid connections between parts. In cases where the BEAM connectors form a closed loop, the model becomes overconstrained. In such situations CARTESIAN and CARDAN connectors with elasticity are used instead of some of the BEAM connectors. A connector motion is applied to an AXIAL connector to lock (or open) the doors and the hood. For steering the vehicle, a connector motion is applied to a SLOT connector and is used to specify the steering for the steering rack. The struts are modeled using an AXIAL connection by specifying approximate nonlinear elasticity and damping.

The radial forces in the tires are modeled approximately using a simplified CALSPAN tire model (Frik, Leister, and Schwartz, 1993) implemented via user subroutine **`UEL`**. A radial stiffness of 600 N/mm is considered. Friction is not accounted for in this user subroutine.

Models

The analysis is performed using the technique described in "Substructure analysis of a pick-up truck model," Section 3.2.2.

Results and discussion

In Figure 3.2.3–2 a snapshot of the truck moving forward with a velocity of 7 m/sec (25.2 km/h) and going over a symmetric bump is shown. The wheels lose contact with the ground and then land again on the road (not shown).

The pitch and roll angles recorded using a CARDAN connector attached to the model at its center of mass are shown in Figure 3.2.3–3. The pitch angles are almost the same for the display body model and the substructure model (see "Substructure analysis of a pick-up truck model," Section 3.2.2) of a truck going over a symmetric bump with a difference of 1 degree. The difference is due to the fact that the display body model uses several CARTESIAN and CARDAN connectors with elasticity to remove overconstraints. These connectors introduce some compliance. The roll angles are almost zero for both models.

The advantage of using substructures or display bodies instead of regular deformable elements becomes obvious when the total times needed to complete these types of analyses are compared. It is estimated that a full analysis using regular elements would take approximately 5 days to complete.

It is estimated that the substructure analysis is up to 120 times faster than the regular mesh analysis, depending on the amount of recovery performed for each substructure. If the total substructure generation and analysis time for the substructure model is compared to the analysis time for the display body model, the display body model runs 5 times faster than the substructure model. If only the analysis times are compared for both models, the display body model runs 2.5 times faster than the substructure model.

Input files

tr_entire_truck_in_phase_db.inp	Display body model of the truck going over in-phase bumps.
tr_parameters_db.inp	Parameter definitions.
tr_materials_db.inp	All material definitions.
tr_initial_stress_db.inp	Initial stress definition for the leaf springs.
tr_lock_doors_and_hood_db.inp	Connector motion that keeps the doors and the hood locked.
exa_tr_radial_uel_db.f	**UEL** used to define the tire model.

Reference

- Frik, S., G. Leister, and W. Schwartz, "Simulation of the IAVSD Road Vehicle Benchmark Bombardier Iltis with FASIM, MEDYNA, NEWEUL, and SIMPACK," in Multibody Computer Codes in Vehicle System Dynamics, Ed. W. Kortum and R. S. Sharp, February 1993.

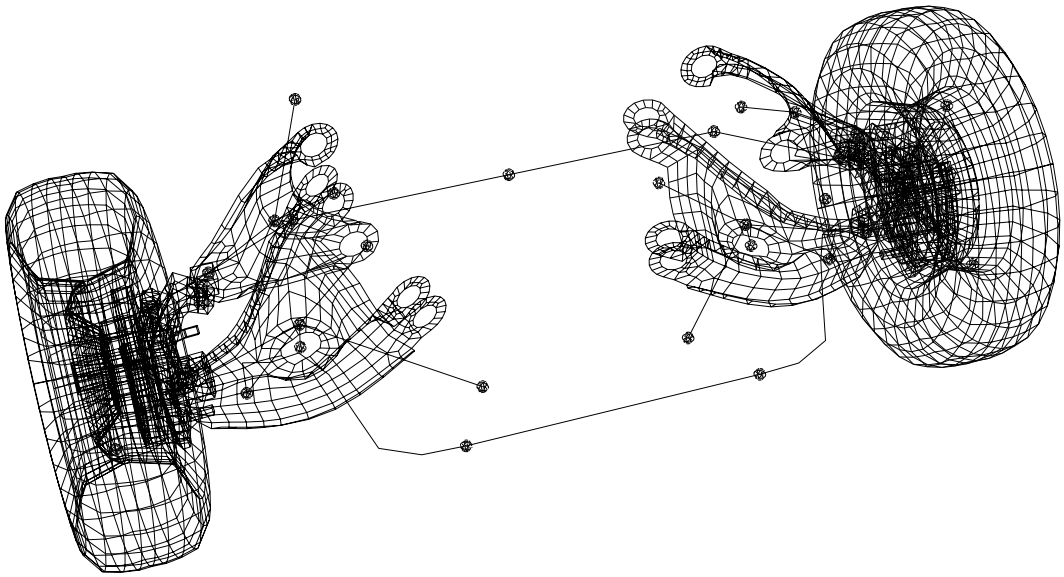

Figure 3.2.3–1 Display bodies of the front-wheel assembly connected at attachment nodes.

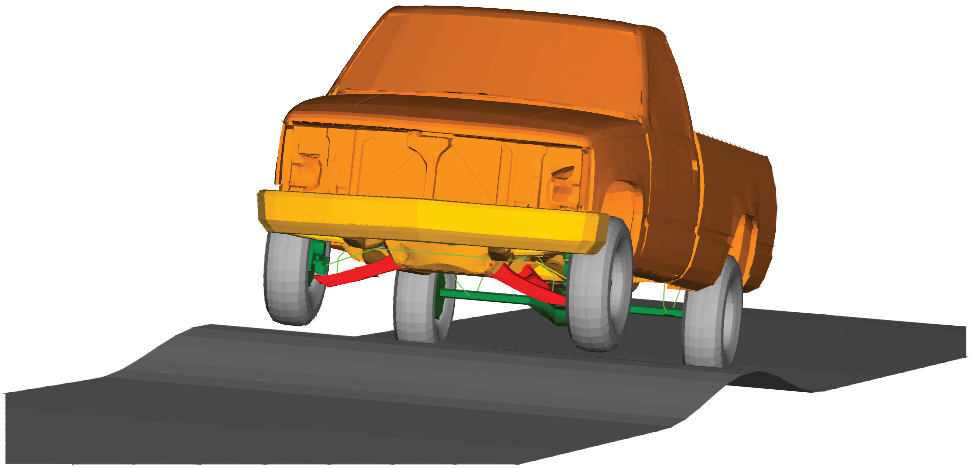

Figure 3.2.3–2 Display body truck model going over symmetric (left-right) bumps.

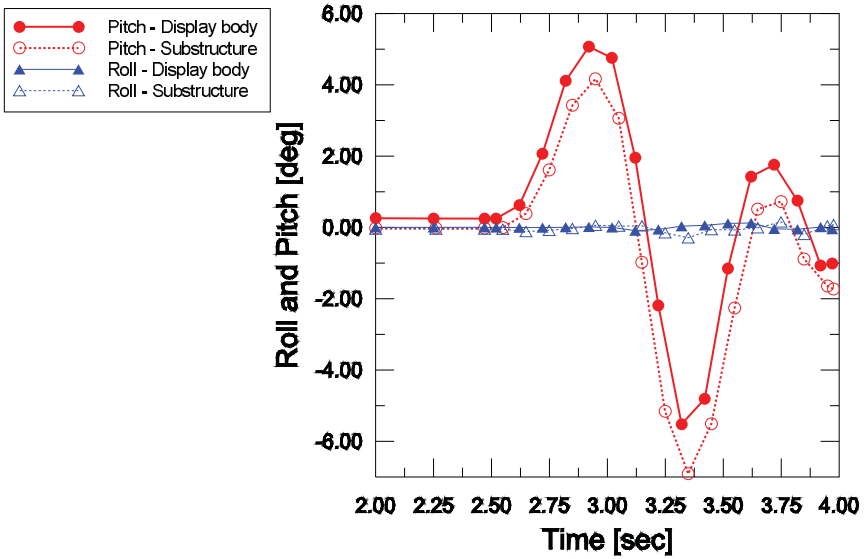

Figure 3.2.3–3 Comparison of the pitch and roll angles for the display body and substructure models of the truck going over symmetric bumps.

3.2.4 CONTINUUM MODELING OF AUTOMOTIVE SPOT WELDS

Product: Abaqus/Explicit

Objectives

This example models a range of failure mechanisms typically observed in spot welds. These virtual experiments are compared with laboratory-obtained data (courtesy of BMW).

The following Abaqus features are demonstrated:

- using three-dimensional continuum elements and intricate material models (elastic-plastic and damage constitutive behavior) to reproduce experimentally observed load-displacement curves (courtesy of BMW) of tested spot weld specimens; and
- demonstrating how virtual experiments allow for the generation of load-displacement data of structural components from readily available geometric and material data. The load-displacement curves can be used subsequently in calibrating connector behavior (not discussed in this section) for efficient use in large-scale models, such as full-vehicle analyses.

Since the material data are highly proprietary, the input files provided below contain fictitious material data. The material data used in the input files were obtained from the actual material data by subjecting it to a number of transformations that preserve the trends in the overall shape of the curves without revealing the exact material behavior. Moreover, the stiffness of the testing machine referenced in this section is fictitious. However, the results published in this example use the actual data for comparison with the physical tests. For these reasons, you will not obtain the force-deflection curves or deformed configurations published in this section when you run the associated input files.

Application description

The use of spot welds for the bonding of metal sheets is an extremely common practice in the automobile industry. The number of such bonds in a typical vehicle is on the order of several thousand. The use of Abaqus connector elements to model spot welds in full-vehicle analyses leads to efficient finite element models that are able to capture the structural response of these local features with optimal computational effort; however, load-displacement curves required for the modeling of spot welds may not be readily available. Furthermore, the number of experimental tests required for the proper calibration of a complete set of spot weld pairs in a vehicle can be prohibitive since the mechanical response of these local mechanisms is dependent on both the geometric data, such as the thickness of the metal plates and the radius of the spot weld, and the material properties of the plates being welded. Virtual testing can generate the necessary modeling parameters when experimental data are not available.

Geometry

The geometry of the patented test specimens used (Hahn et al., 1996, and Hahn and Rohde, 2004) is shown in Figure 3.2.4–1 and Figure 3.2.4–2. A single spot weld of radius 2.65 mm connects two steel plates that are 1.4 mm thick. These steel plates are 50 mm long and are bent over radii of 4.0 mm.

Materials

All specimens used in this study are made of galvanized high-strength steel H340LAD+Z100. This material behaves in an elastic-plastic manner during the initial loading stages. As the material is further loaded, it can either display a ductile damage response (caused by growth and coalescence of voids) or it can display a shear failure mechanism (caused by the formation and growth of cracks within shear bands). For confidentiality reasons, the material data published in the input files associated with this section are fictitious. The data were obtained by transforming the actual material test data to preserve the overall trends in the behavior without revealing the true material behavior.

Boundary conditions and loading

A photo of the testing machine (Hahn et al., 2000) is shown in Figure 3.2.4–3. In the physical tests the vertical sides of the specimens were longer than those shown in Figure 3.2.4–1 and Figure 3.2.4–2, and they were rigidly clamped in the clamping device (not shown) of the tensile testing machine. In the analysis these clamping conditions are modeled by fixing the bottom edges of the specimens and imposing a constant velocity of 0.15 m/s along the top edges in the vertical global 3-direction. For the physical tests and analysis, a hinge is located 400 mm from the top edges of the specimens along the vertical global 3-direction allowing the fixed edges to rotate about the horizontal axis. During the pull and peeling tests the specimens are aligned so the top edges are initially orthogonal to the vertical direction, whereas during the shear test the edges are initially parallel to the vertical direction. The combined stiffness of the loading piston and restraints used in the analysis is 50 kN/mm in pull and peeling tests and 35 kN/mm in shear tests. For confidentiality reasons both values are fictitious, but they approximate the compliance of the actual testing machine used in the physical tests.

Abaqus modeling approaches and simulation techniques

A total of 18 different simulations were performed corresponding to the three test cases (pull test, shear test, and peeling test). Each of the simulations was solved with a coarse mesh and a fine mesh using three different scaling factors for the thermal influence modeling, as discussed below.

Summary of analysis cases

Case 1 Pull test.

Case 2 Shear test.

Case 3 Peeling test.

The sections that follow discuss analysis considerations that apply to all cases, except where noted otherwise.

Mesh design

All simulations were performed with 8-node, linear brick, reduced integration elements (C3D8R). The density of the meshes increases toward the center of the plate where most of the deformation occurs.

Each test was performed with a coarse mesh using four elements through the thickness of each plate and a fine mesh using six elements through the thickness of each plate. The coarse mesh and fine mesh used for the pull and shear tests are shown in Figure 3.2.4–4 and Figure 3.2.4–5, respectively. Figure 3.2.4–6 shows the initial undeformed configuration of the coarse mesh used in the peeling test simulation, while Figure 3.2.4–7 shows the initial configuration of the fine mesh. The same meshes are used for the pull and shear tests since they are based on the same model geometry.

Material model

For confidentiality reasons, some but not all details of the Abaqus models used for constitutive behavior and progressive damage analysis are discussed below. For guidelines on obtaining the material parameters from experimental data, see "Progressive failure analysis of thin-wall aluminum extrusion under quasi-static and dynamic loads," Section 2.1.16.

Elastic-plastic behavior

Werner et al. (2004) have shown that correct modeling of the elastic-plastic deformation of spot welds is a prerequisite for realistic predictions of subsequent failure mechanisms. The authors showed that by taking into consideration material property changes in the weld nugget they could obtain different failure modes involving peeling or shearing failure of the spot weld. Furthermore, they suggested the use of hardness measurements as a possible indicator for the change in properties of the welded material. The change in hardness between the center of a spot weld and at a distance far away from the center depends on the material grades joined, as well as their thicknesses.

In this example we assume both the elastic and the plastic behavior to be isotropic with the yield surface described by a Mises yield function (see "Inelastic behavior," Section 23.1.1 of the Abaqus Analysis User's Guide). Different hardening curves are considered to encapsulate thermal effects near the spot weld. For simplicity, the specimen is partitioned into three zones corresponding to the different thermal exposures observed in the vicinity of the spot weld during the welding process. Different scaling factors for the stress-strain curves are used in the three zones as derived from hardness measurements. The geometry of each zone can be prescribed according to the welding process parameters. The scaling of the yield curve is accomplished with the use of a field variable defined as constant throughout each region, and we test three scaling magnitudes for each test. For confidentiality reasons the scaling factors given below are fictitious, but they reflect the trends of the elastic-plastic behavior near the spot weld:

- A baseline configuration, where the original material properties (no scaling) are assigned to the specimens in all three zones. While this choice is not realistic, it provides an extreme solution for comparison purposes.
- A second configuration uses a scaling of 1.2 of the yield curve in Zone 1 and a scaling of 1.1 in Zone 2.
- A third configuration uses a scaling of 1.4 of the yield curve in Zone 1 and a scaling of 1.2 in Zone 2.

These three scaling factor configurations help us to understand the effect of the thermal influence zone in capturing the correct behavior, as discussed below.

Damage initiation and evolution

The failure of aluminum-alloy sheets and thin-walled extrusions results from one or more of the following mechanisms (Hooputra et al., 2004): nucleation, growth, and coalescence of voids; shear bands; and necking. Damage due to initiation, growth, and coalescence of voids leads to ductile failure in metals; the formation of cracks within shear bands leads to shear failure. Abaqus offers phenomenological damage initiation criteria for both of these mechanisms. The ductile criterion is specified by providing the equivalent plastic strain at the onset of ductile damage as a function of stress triaxiality and strain rate. Similarly, the shear criterion is specified by providing the equivalent plastic strain at the onset of shear damage as a function of shear stress ratio and strain rate (see "Damage initiation for ductile metals," Section 24.2.2 of the Abaqus Analysis User's Guide). The actual damage initiation criterion data were provided by BMW but for confidentiality reasons, the data were transformed to preserve the overall trends without revealing the actual material behavior.

Damage evolution occurs once the damage initiation criteria are satisfied and further loading is applied. A plastic displacement–based linear damage evolution law is used for each damage initiation criterion. The value of the plastic displacement at which the damage variable reaches 1.0 (complete degradation) is taken as 0.1, based on data from independent base material testing. The default maximum degradation rule is used, and the elements are removed from the mesh once the maximum degradation has occurred (see "Maximum degradation and choice of element removal" in "Damage evolution and element removal for ductile metals," Section 24.2.3 of the Abaqus Analysis User's Guide). Damage initiation and evolution are assumed to be the same in all three thermal influence zones described above, a simplifying modeling assumption.

Initial conditions

As discussed in the material model section above, a field variable is used to scale the yield surface and capture the thermal effects of the welding process on the yield strength.

Boundary conditions

The specimens are loaded by fixing their bottom edges and imposing a constant velocity of 0.15 m/s along the top edges in the vertical global 3-direction.

Constraints

The top and bottom edges are constrained by kinematic couplings to model the rigid clamping in the testing devices. A TRANSLATOR connection is used to model the stiffness of the loading apparatus.

Interactions

General frictionless contact is defined between all surfaces, an appropriate approximation since friction forces are small when compared with the forces in the weld nugget.

Analysis steps

All simulations consist of one explicit dynamic step. All analyses consider geometric nonlinearity and utilize mass scaling to model quasi-static loading conditions (see "Mass scaling," Section 11.6.1 of the Abaqus Analysis User's Guide).

Output requests

Field output requests include the following quantities: displacement, stress, strain, element status, and damage initiation criteria variables. The history output request consists of displacement, velocity, acceleration, and reaction force at the reference points of the kinematic coupling constraints. Energy output variables are requested for the entire model.

Discussion of results and comparison of cases

The results presented in this example compare the actual material data with the physical test data. For confidentiality reasons, the actual material data are not published in the associated input files. Hence, you will not obtain the results below when you run the input files provided.

The Mises stress contour and final deformed shapes of the pull, shear, and peeling tests with the coarse mesh and baseline material (no scaling of the yield curve) are depicted in Figure 3.2.4–8, Figure 3.2.4–9, and Figure 3.2.4–10, respectively. The final deformed shape in pull and peeling tests show good qualitative agreement with experimental results provided by BMW. Shear test results predict failure of the spot weld rather than on the surrounding plate, regardless of the amount of scaling that was applied to the yield curve. This behavior was seen in some but not all experimental results, and it does not seem to influence the overall bearing capacity of the structure in shear.

The load-displacement history obtained from the simulations is compared with the experimental results in Figure 3.2.4–11 to Figure 3.2.4–16. A good match is observed for the pull and shear tests with the yield curve scaled by 1.2 in Zone 1. Results obtained with the baseline material underpredict the peak load capacity, and results obtained with the 1.4 scaling overpredict the peak load of the structures. The thermal zone scaling does not have a significant impact on the qualitative character of the loading curves. Good mesh convergence is also observed, indicating that acceptable results can be obtained even with the coarse mesh discretization.

Results obtained for the peeling test do not show such good agreement with the experimental results provided to SIMULIA by BMW; even the baseline material simulation results overpredict the peak load capacity. This overstiff behavior is shown even in the purely elastic levels of deformation (in very early deformation stages), which indicates that modeling of the loading apparatus for this loading configuration may be inexact (data not available).

In conclusion, the results from both the quasi-static spot weld connector simulations match the experimental pull and shear data very well. Changes in the material properties induced by the welding process are not essential to the capture of the peak loads during the spot weld failure.

Input files

Case 1a: Pull test, coarse mesh

spotweld_pu_cm.inp	Input file to create and analyze the model (baseline material).
spotweld_pu_cm_1p2.inp	Input file to create and analyze the model (spot weld yield surface scaled by a factor of 1.2).
spotweld_pu_cm_1p4.inp	Input file to create and analyze the model (spot weld yield surface scaled by a factor of 1.4).

Case 1b: Pull test, fine mesh

spotweld_pu_fm.inp	Input file to create and analyze the model (baseline material).
spotweld_pu_fm_1p2.inp	Input file to create and analyze the model (spot weld yield surface scaled by a factor of 1.2).
spotweld_pu_fm_1p4.inp	Input file to create and analyze the model (spot weld yield surface scaled by a factor of 1.4).

Case 2a: Shear test, coarse mesh

spotweld_sh_cm.inp	Input file to create and analyze the model (baseline material).
spotweld_sh_cm_1p2.inp	Input file to create and analyze the model (spot weld yield surface scaled by a factor of 1.2).
spotweld_sh_cm_1p4.inp	Input file to create and analyze the model (spot weld yield surface scaled by a factor of 1.4).

Case 2b: Shear test, fine mesh

spotweld_sh_fm.inp	Input file to create and analyze the model (baseline material).
spotweld_sh_fm_1p2.inp	Input file to create and analyze the model (spot weld yield surface scaled by a factor of 1.2).
spotweld_sh_fm_1p4.inp	Input file to create and analyze the model (spot weld yield surface scaled by a factor of 1.4).

Case 3a: Peeling test, coarse mesh

spotweld_pe_cm.inp	Input file to create and analyze the model (baseline material).
spotweld_pe_cm_1p2.inp	Input file to create and analyze the model (spot weld yield surface scaled by a factor of 1.2).
spotweld_pe_cm_1p4.inp	Input file to create and analyze the model (spot weld yield surface scaled by a factor of 1.4).

Case 3b: Peeling test, fine mesh

spotweld_pe_fm.inp	Input file to create and analyze the model (baseline material).
spotweld_pe_fm_1p2.inp	Input file to create and analyze the model (spot weld yield surface scaled by a factor of 1.2).
spotweld_pe_fm_1p4.inp	Input file to create and analyze the model (spot weld yield surface scaled by a factor of 1.4).

Auxiliary files

spotweld_material.inp	Input file with material model data.
spotweld_cm_part.inp	Input file with part data for Case 1a and Case 2a.
spotweld_cm_assembl.inp	Input file with assembly data for Case 1a and Case 2a.
spotweld_fm_part.inp	Input file with part data for Case 1b and Case 2b.
spotweld_fm_assembl.inp	Input file with assembly data for Case 1b and Case 2b.
spotweld_pe_cm_part.inp	Input file with part data for Case 3a.
spotweld_pe_cm_assembl.inp	Input file with assembly data for Case 3a.
spotweld_pe_fm_part.inp	Input file with part data for Case 3b.
spotweld_pe_fm_assembl.inp	Input file with assembly data for Case 3b.

References

Abaqus Analysis User's Guide

- "Mass scaling," Section 11.6.1 of the Abaqus Analysis User's Guide
- "Progressive damage and failure," Section 24.1.1 of the Abaqus Analysis User's Guide

Abaqus Keywords Reference Guide

- *DAMAGE INITIATION
- *DAMAGE EVOLUTION

Abaqus Verification Guide

- "Progressive damage and failure of ductile metals," Section 2.2.21 of the Abaqus Verification Guide

Other

- Hahn, O., J.R. Kurzok, and M. Oeter, "Test specification for KS-2 specimen," Laboratory of Materials and Joint Technology, University of Paderborn, 2000.
- Hahn, O., and A. Rohde, "Procedures to manufacture specimen and specimen clamping device," Patent Nr. 19522247 B4, April 15, 2004.
- Hahn, O., A. Rohde, and D. Gieske, "Specimen and specimen clamping device for use in tensile testing machines," Patent Nr. 19510366 C1, August 22, 1996.

- Hooputra, H., H. Gese, H. Dell, and H. Werner, "A Comprehensive Failure Model for Crashworthiness Simulation of Aluminium Extrusions," International Journal of Crashworthiness, vol. 9, pp. 449–463, 2004.
- Werner, H., H. Hooputra, H. Dell, and H. Gese, "A Phenomenological Failure Model for Sheet Metals and Extrusions," Annual Review Meeting and Workshop, Impact and Crashworthiness Laboratory, Massachusetts Institute of Technology, 2004.

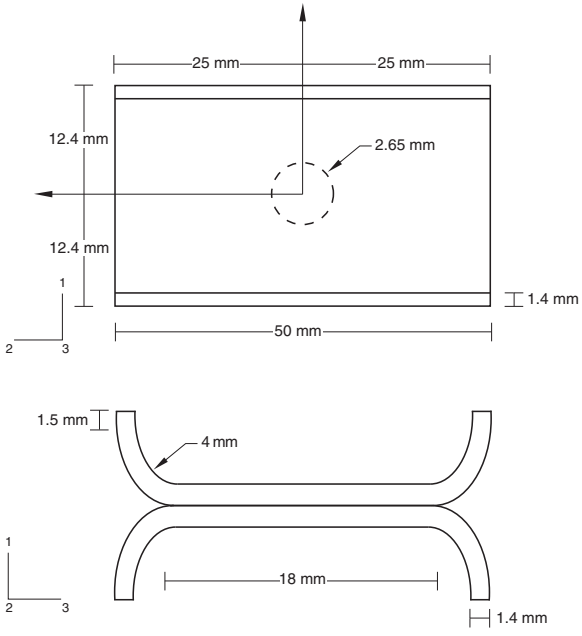

Figure 3.2.4–1 Pull and shear test specimen geometry.

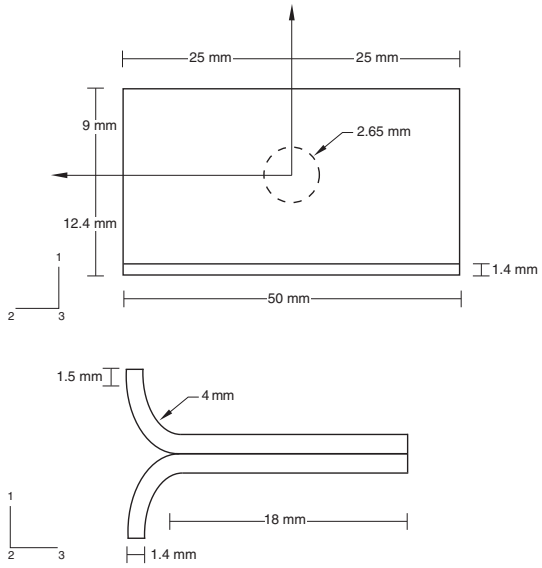

Figure 3.2.4–2 Peeling test specimen geometry.

Figure 3.2.4–3 Experimental setup.

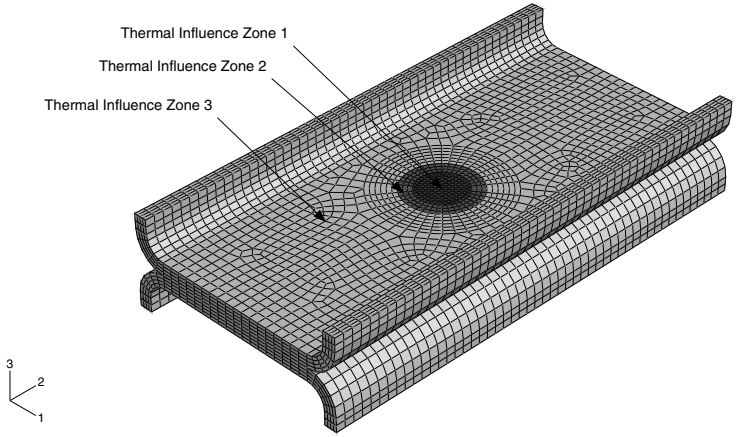

Figure 3.2.4–4 Pull and shear tests: coarse mesh and thermal influence zones.

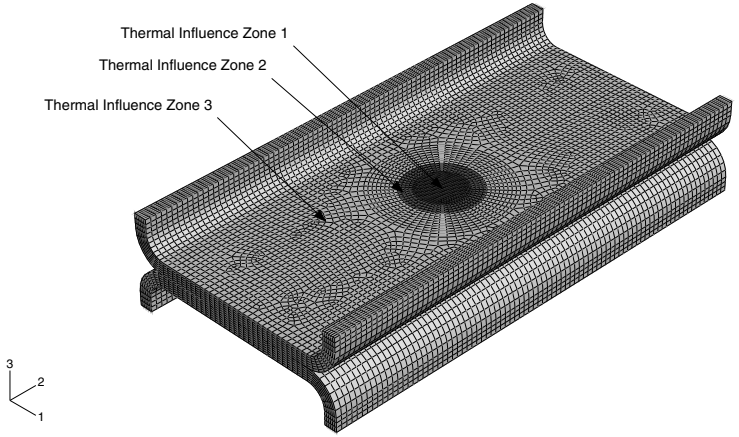

Figure 3.2.4–5 Pull and shear tests: fine mesh and thermal influence zones.

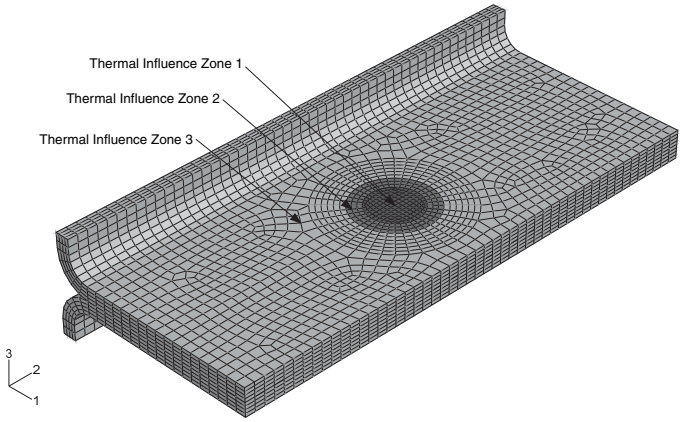

Figure 3.2.4–6 Peeling test: coarse mesh and thermal influence zones.

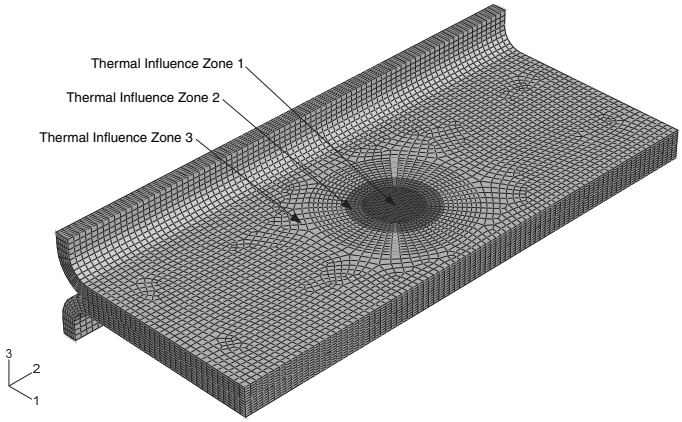

Figure 3.2.4–7 Peeling test: fine mesh and thermal influence zones.

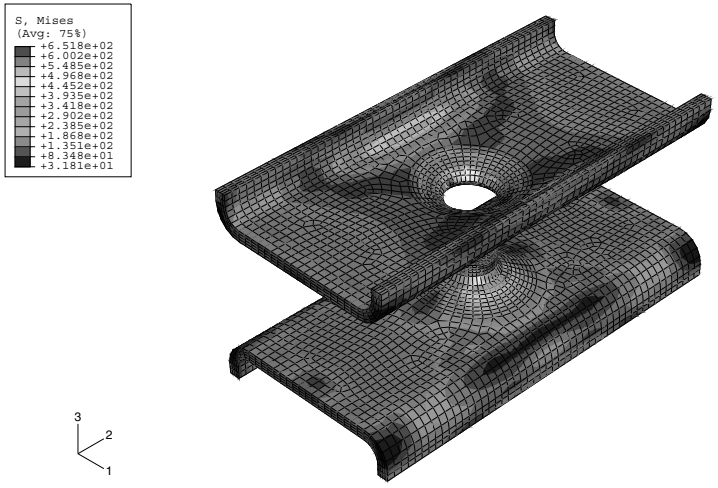

Figure 3.2.4–8 Pull test, coarse mesh, baseline material (no yield curve scaling): final deformed shape of specimen and Mises stress contours.

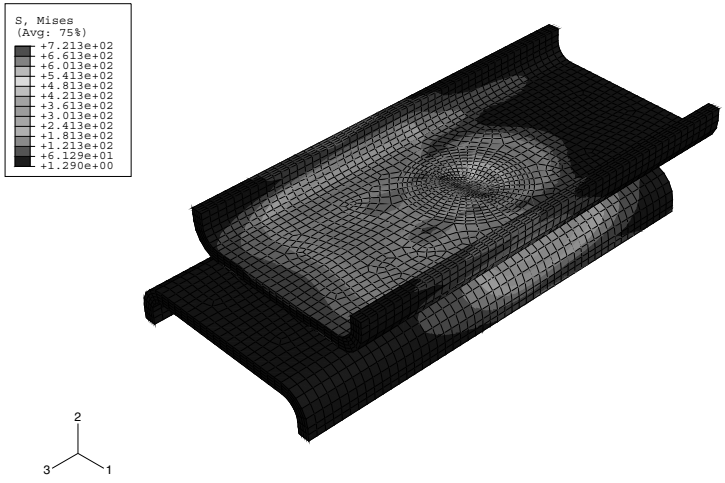

Figure 3.2.4–9 Shear test, coarse mesh, baseline material (no yield curve scaling): final deformed shape of specimen and Mises stress contours.

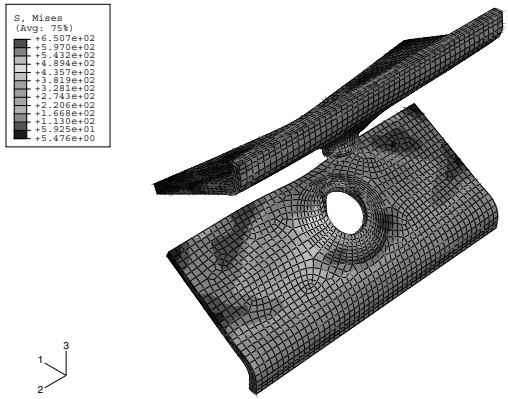

Figure 3.2.4–10 Peeling test, coarse mesh, baseline material (no yield curve scaling): final deformed shape of specimen and Mises stress contours.

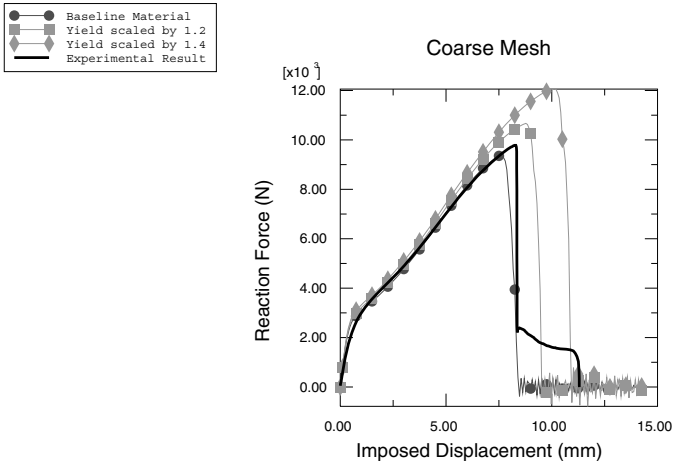

Figure 3.2.4–11 Pull test with coarse mesh: comparison of reaction force versus imposed displacement for different yield surface scaling. Experimental result courtesy of BMW.

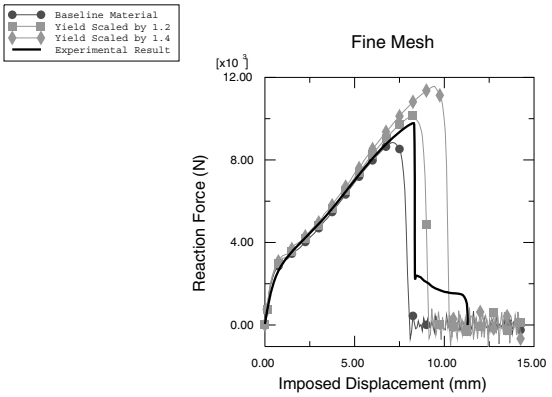

Figure 3.2.4–12 Pull test with fine mesh: comparison of reaction force versus imposed displacement for different yield surface scaling. Experimental result courtesy of BMW.

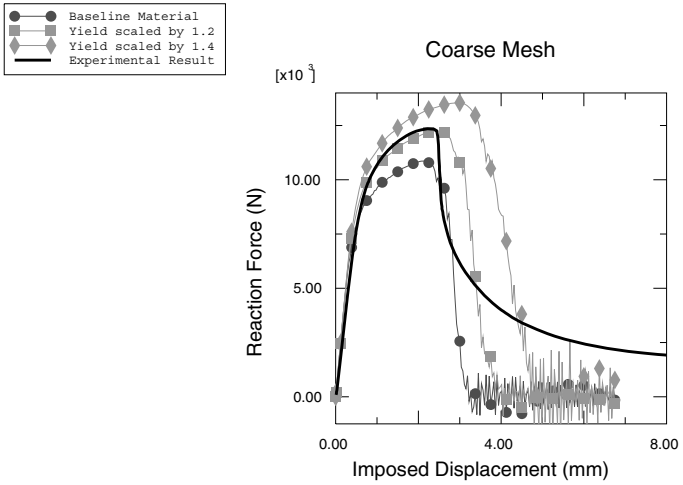

Figure 3.2.4–13 Shear test with coarse mesh: comparison of reaction force versus imposed displacement for different yield surface scaling. Experimental result courtesy of BMW.

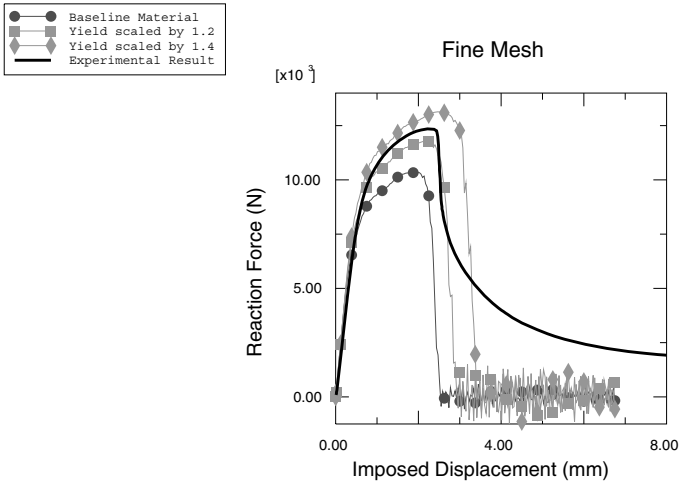

Figure 3.2.4–14 Shear test with fine mesh: comparison of reaction force versus imposed displacement for different yield surface scaling. Experimental result courtesy of BMW.

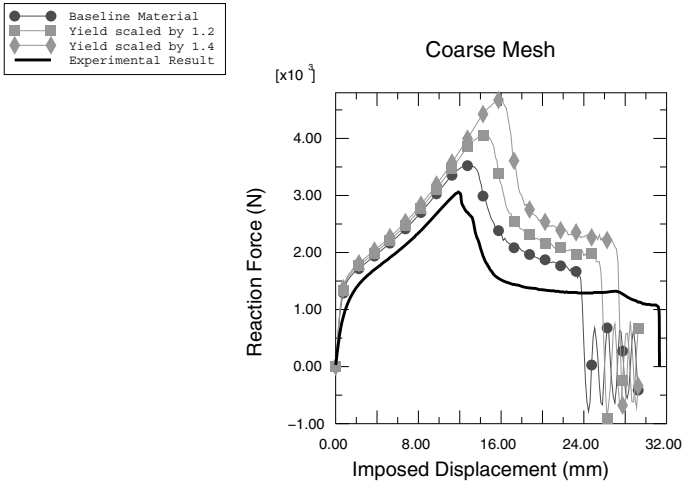

Figure 3.2.4–15 Peeling test with coarse mesh: comparison of reaction force versus imposed displacement for different yield surface scaling. Experimental result courtesy of BMW.

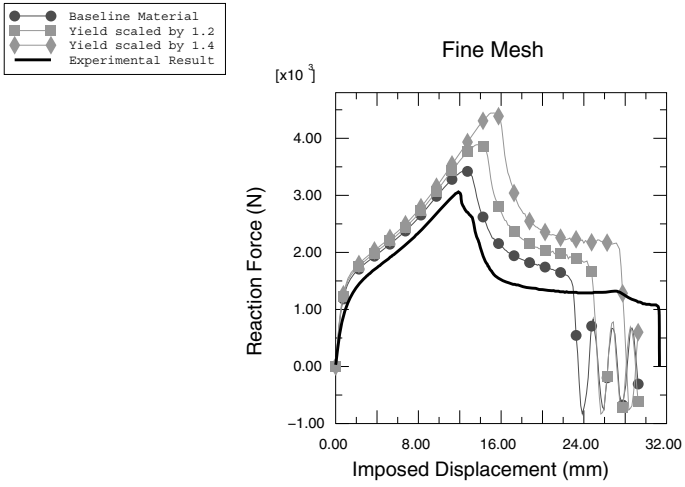

Figure 3.2.4–16 Peeling test with fine mesh: comparison of reaction force versus imposed displacement for different yield surface scaling. Experimental result courtesy of BMW.

3.3 Occupant safety analyses

- "Seat belt analysis of a simplified crash dummy," Section 3.3.1
- "Side curtain airbag impactor test," Section 3.3.2

3.3.1 SEAT BELT ANALYSIS OF A SIMPLIFIED CRASH DUMMY

Product: Abaqus/Explicit

This example shows the use of Abaqus in analyzing a simplified crash dummy restrained by a complete seat belt system as a moving vehicle comes to a sudden stop.

Automotive seat belts dramatically reduce the risk of vehicle occupant injury in the case of collision. The seat belt system includes:

- the webbing sliding through D-rings attached to the car frame;
- one retractor that models spool locking, tension preloading, and spool effects; and
- one pretensioner that tightens the seat belt.

Several SLIPRING connectors strung together are used to model the belt webbing passing through the rings. The RETRACTOR and HINGE connection types are used to model the retractor and pretensioner.

Geometry and materials

As shown in Figure 3.3.1–1, the model consists of several distinct entities: the dummy, the seat belt, the retractor, and the seat. The modeling strategy consists of applying an initial velocity for the dummy of approximately 45 miles per hour while the seat and the seat belt attachment points to the car frame are held fixed with boundary conditions, thus emulating a vehicle that comes to a sudden stop.

Dummy

A very simple dummy model is used (none of the limbs are modeled). The dummy model has two distinct parts: the lower torso and the upper torso. The lower torso is modeled with rigid surface elements. The upper torso is modeled in the same fashion except in the chest area. The human body compliance is modeled approximately by meshing a region in the chest area using deformable shell elements. In addition, four CARTESIAN and CARDAN connectors with nonlinear elastic and damping behavior are inserted between four nodes around the chest area and four nodes belonging to the rigid back of the upper torso. The upper and lower torsos overlap over a small region around the waist area, and general contact is used to model the contact interactions between them. The approximate mass of the dummy is 35 kilograms.

Seat

The seat modeling is minimal since the focus of this example is to illustrate the seat belt modeling technique. Only one solid element with crushable foam material properties is used to model the lower part of the seat. The back support is not modeled.

Seat belt webbing passing through rings

The seat belt is modeled primarily using several SLIPRING connectors strung together. To model the contact interactions between the belt and the chest and lap areas accurately, membrane elements are used

to model short portions of the belt in these regions. Figure 3.3.1–2 shows the seat belt arrangement. The node numbers associated with the connector elements are also illustrated. The seat belt is defined starting from the right side of the figure (adjacent to the B-pillar in the car) and moving to the chest area, the waist-level click-in buckle, the lap area, and finally the attachment to the car bottom floor, as follows:

- Three SLIPRING connectors are used between nodes 8300228, 8300237, 8300243, and 8300247. In this order the four nodes correspond to the exit point from the retractor at the bottom of the B-pillar, the trim exit point along the B-pillar, the shoulder-level ring at the top of the B-pillar, and the connection point with the membrane-mesh region of the belt at the top of the chest area.

  The three SLIPRING connectors model the belt as it flows and stretches through these points. As outlined in "Connector element library," Section 31.1.4 of the Abaqus Analysis User's Guide, the SLIPRING connection type activates the nodal material flow degree of freedom (10) at these four nodes. Material can flow freely between the three elements but cannot flow through the connection point with the membrane-meshed area at node 8300247. Hence, a boundary condition on this degree of freedom is specified at this node.
- The membrane-meshed area between nodes 8300247 and 8300248 models the contact with the chest area of the dummy accurately.
- Two SLIPRING connectors are used between nodes 8300248, 8300251, and 8300253. In this order the three nodes correspond to the connection point with the membrane-mesh region of the belt at the bottom of the chest area, the ring of the waist-level click-in buckle, and the connection point with the membrane-meshed region of the belt at the left side of the lap area.

  Since no material flow occurs at the connection points with the membrane-meshed regions, boundary conditions on degree of freedom 10 are specified at nodes 8300248 and 8300253.
- The membrane-meshed area between nodes 8300253 and 8300254 models the contact with the lap area of the dummy accurately.
- One SLIPRING connector is used between nodes 8300254 and 8301398. These two nodes correspond to the connection point with the membrane-mesh region of the belt at the right side of the lap area and the attachment point to the car frame.

  Boundary conditions on degree of freedom 10 are specified at both nodes.

The stretching of the belt is governed by the specified nonlinear elastic connector behavior.

Retractor

The retractor device is located at the bottom of the B-pillar. It is modeled using a RETRACTOR connector in parallel with several HINGE connectors as illustrated in Figure 3.3.1–3. The connections are as follows:

- The RETRACTOR connector is connected to the first SLIPRING connector along the B-pillar at node 8300228. It converts the material flow at this node into a rotation about a local axis oriented along the longitudinal direction of the car.
- Several HINGE connectors model the various mechanisms in the retractor device. Their axes are all parallel to each other and are oriented along the longitudinal direction of the car.

– The preload HINGE applies a small pretension elastic force typically given by a weak torsional elastic spring. Its purpose is to eliminate the slack in the belt.
– The spool lock HINGE uses a connector lock definition to lock the almost-free rotation of the spool's axle if the velocity of the belt material exiting the retractor exceeds a certain threshold.
– The spool effect HINGE is attached to the car frame and uses a connector plasticity definition to model the compression effects of the spool. This is accomplished via a tension-versus-spooled-out-material curve.

The spool effect is inactive until the spool lock connector locks; hence, the two HINGE connectors are placed in series. The preload is applied at all times and, therefore, is placed in parallel with the two other HINGE connectors.

Pretensioner

The pretensioner device is attached to the car frame in the vicinity of the waist-level click-in buckle. It is modeled using a SLIPRING connector and a RETRACTOR and a HINGE connector in parallel as illustrated in Figure 3.3.1–4. The connections are as follows:

- The pretensioner spool (HINGE) connector is attached to the car frame. It uses an amplitude-delayed connector motion definition to specify the rate at which the belt material flows into the pretensioner device.
- The RETRACTOR connector converts the specified motion in the HINGE connector into a material flow that is expelled from the following SLIPRING connector.
- The SLIPRING connector models the stiff cable to which the waist buckle is attached. Its length shortens as the pretensioner device is being triggered.
- A PIN-type MPC is used to connect the node associated with the waist-level click-in ring that slides over the seat belt (node 8300251) with the buckle it clicks into (node 8300351). By using the additional node 8300351, the material flows associated with the pretensioner SLIPRING and the SLIPRINGs of the adjacent seat belt segments are prevented from interacting with each other.

Models

Frictionless as well as frictional seat belt models are analyzed using Abaqus/Explicit.

Results and discussion

The undeformed and deformed shapes (t=0.0215 seconds) for the model are shown in Figure 3.3.1–5 and Figure 3.3.1–6, respectively. Results for belt tensions and material flow in and out of the shoulder level slipring are shown in Figure 3.3.1–7 and Figure 3.3.1–8. At this junction SLIPRING connector elements 8888803 and 8888804 share a common node 8300243. For the frictionless analysis the normalized belt tensions are shown in Figure 3.3.1–7. As expected, the two tension histories are the same. For the frictional case, the ratio of the belt tension in adjacent belt segments is shown in Figure 3.3.1–8. For the case when the belt is slipping, the ratio of the belt tension is given by $t_2/t_1 = e^{\mu\alpha}$, where t_2 and t_1 are the tensions in the adjacent SLIPRING connector elements, μ is the coefficient of friction, and α

is the angle between the two adjacent sliprings. For the seat belt model with friction where μ=0.1 and α=1.718132 radians, the ratio of the belt tension is $t_2/t_1 = 1.187$. As shown in Figure 3.3.1–8, the ratio agrees well with the analytical result. Near the end of the analysis (≈19 milliseconds) the ratio of the belt tension drops from this value. Figure 3.3.1–8 shows that the normalized accumulated slip remains constant for the remainder of the analysis; hence, we can conclude that the ratio drops because the belt starts sticking. Figure 3.3.1–9 shows that the material flows across node 8300243, which is the second node of connector element 8888803 and the first node of connector element 8888804, are identical as expected.

Input files

seatbelt_xpl.inp	Analysis of a frictionless seat belt–restrained simplified dummy using Abaqus/Explicit.
seatbelt_fric_xpl.inp	Analysis of a frictional seat belt–restrained simplified dummy using Abaqus/Explicit.

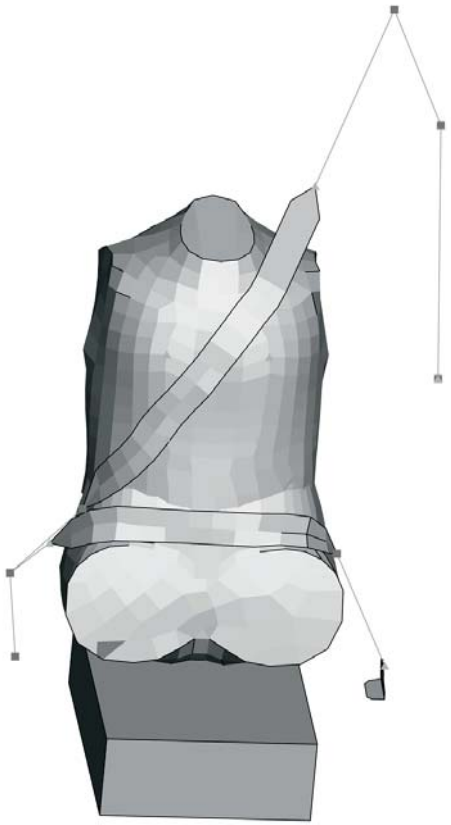

Figure 3.3.1–1 Seat belt and dummy arrangement.

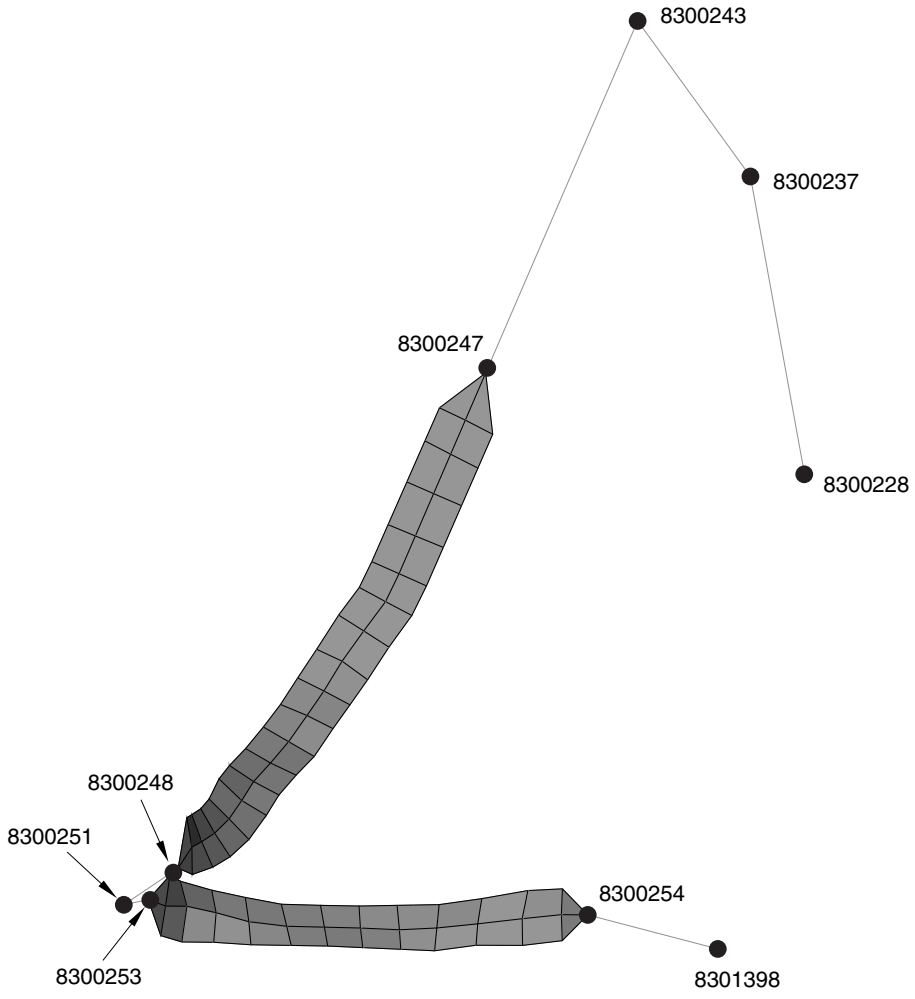

Figure 3.3.1–2 Seat belt arrangement.

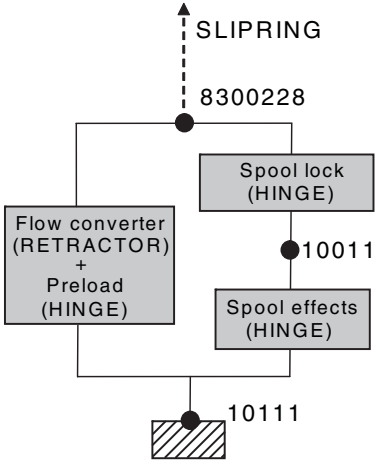

Figure 3.3.1–3 Retractor model.

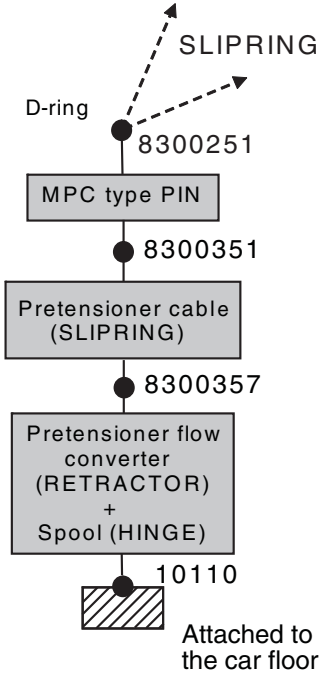

Figure 3.3.1–4 Pretensioner model.

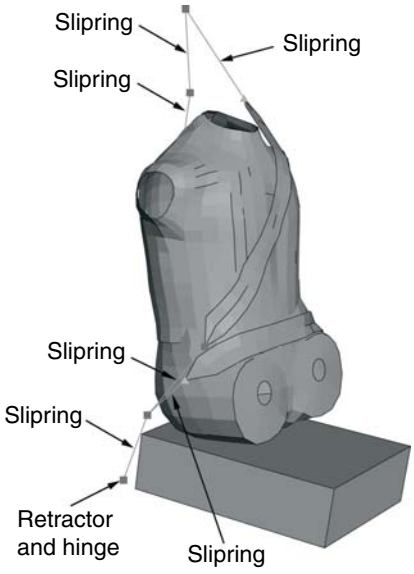

Figure 3.3.1–5 Dummy and seat belt system in the undeformed configuration.

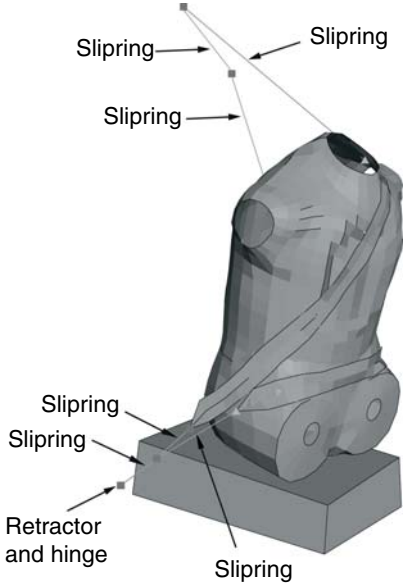

Figure 3.3.1–6 Dummy and seat belt system in the deformed configuration.

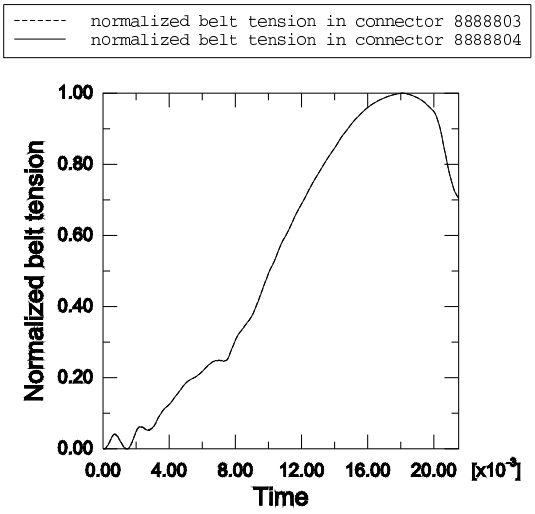

Figure 3.3.1–7 Normalized belt tension of adjacent frictionless sliprings.

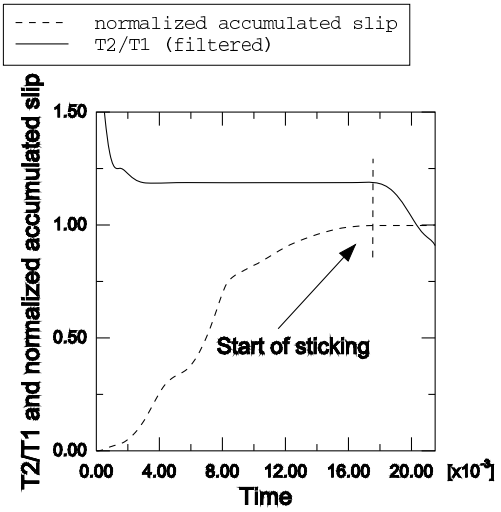

Figure 3.3.1–8 Ratio of belt tension of adjacent sliprings with friction and the normalized accumulated slip.

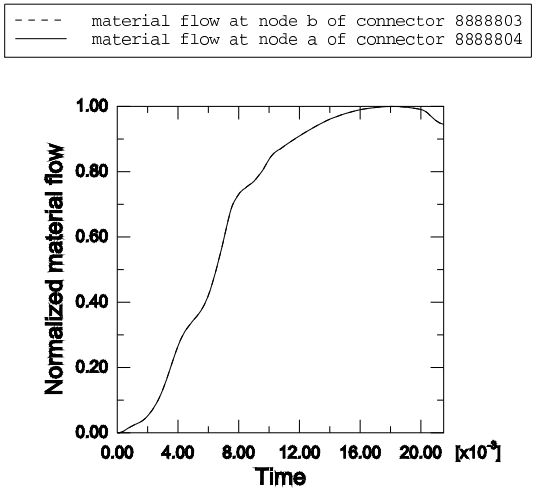

Figure 3.3.1–9 Normalized material flow across node between adjacent sliprings.

3.3.2 SIDE CURTAIN AIRBAG IMPACTOR TEST

Product: Abaqus/Explicit

This example problem illustrates the use of surface-based fluid cavities in a multi-chambered automotive airbag inflation analysis using Abaqus/Explicit.

Airbags are supplemental safety devices that minimize the chance of an occupant striking the interior of a vehicle during a crash. The proper deployment of the airbag within a fraction of a second after a collision is detected is crucial to ensure the safety of the occupant. This example describes the modeling and validation of a side curtain airbag impactor test simulation against experimental results.

Geometry and model

The side curtain airbag model described in this example was provided by Autoliv GmbH. The model setup is shown in Figure 3.3.2–1, which shows an impactor hitting the deployed side curtain airbag. The airbag is divided into 18 chambers to approximate the nonuniform distribution of the gases across the airbag and the gradients in pressure observed during the complex unfolding of the airbag. The temperature and pressure are considered to be uniform in each chamber at any point of time. Each airbag chamber is modeled as a surface-based fluid cavity. The surface-based fluid cavity capability provides a coupling between the pressure exerted by the contained gas on the chamber boundary and the deformation of the gas-filled chamber. The individual chambers are separated by fictitious partitions modeled with surface elements, which represent the area of fluid exchange between the different chambers. The airbag has three inflators located in chambers 1, 6, and 9 that are used to inflate the airbag. The inflators are activated at different times using inflation time amplitude definitions associated with the activation of fluid inflator definitions. The inflators inject a mixture of 6 gas species, with the molecular fraction, mass flow rate, and temperature of the individual species defined as functions of time. The gas species behave as ideal gases with an adiabatic temperature update. Leakage of the gases to the environment through the airbag fabric is modeled by specifying a discharge coefficient (ratio of the effective leakage area to the total airbag surface area) of 0.0003 for fluid exchange from each airbag chamber. In addition, the loss of heat energy to the environment is also considered by providing the heat energy flow rate as a function of the temperature difference across the airbag fabric.

The external skin of the airbag is represented by 3-node membrane elements (M3D3) and uses a nonlinear elastic definition of the fabric material model. The fabric material model is calibrated by specifying the uniaxial behavior of the fibers in the warp and weft directions as well as the shear behavior of the fabric. The behavior of the fibers has been defined such that they offer negligible resistance to compression until a certain compressive strain limit beyond which they begin to offer finite resistance to compression to prevent excessive deformations of the fabric elements. Bilinear shear behavior is defined reflecting an initial shear modulus of G_0=9.44 N/mm^2 and a modulus of G_1=47.2 N/mm^2 at angles greater than 60° to prevent severe shear deformation. In addition, a small amount of stiffness proportional damping is applied. A reference mesh (initial metric) is defined to specify the unfolded stress-free configuration of the airbag.

The unstressed reference configuration of the airbag is defined using the initial reference mesh for membrane elements. The initial folded configuration and the reference configuration are used to account for the wrinkles that arise from the airbag folding process. The reference mesh and the folded airbag configuration are shown in Figure 3.3.2–2 and Figure 3.3.2–3, respectively. The fabric material is defined such that any initial compressive strains along the yarn directions will cause compressive stresses in the yarn. Alternatively, the initial compressive strains along the yarn directions can be recovered stress free.

The general contact algorithm is used to consider self-contact between the airbag fabric layers as well as contact with surrounding structures during the inflation of the airbag.

The impactor is modeled as a rigid body with a total mass of 7.2 kg and is given an initial velocity of 4500 mm/s towards the deploying airbag. The mass and velocity of the impactor reflect human head mass and velocities typically observed in vehicle side impacts, respectively.

Results and discussion

The airbag at different stages of deployment is shown in Figure 3.3.2–4 (8 ms) and Figure 3.3.2–5 (16 ms). Figure 3.3.2–6, Figure 3.3.2–7, and Figure 3.3.2–8 show the time history of displacement, velocity, and acceleration of the impactor as it impacts the airbag, along with comparisons to experimental results. These plots demonstrate the close correlation between Abaqus/Explicit simulation results and physical test results.

Input files

sidecurtain_airbag_fabric.inp	Side curtain airbag impactor test.
sidecurtain_airbag_refmesh.inp	Reference mesh for the side curtain airbag.

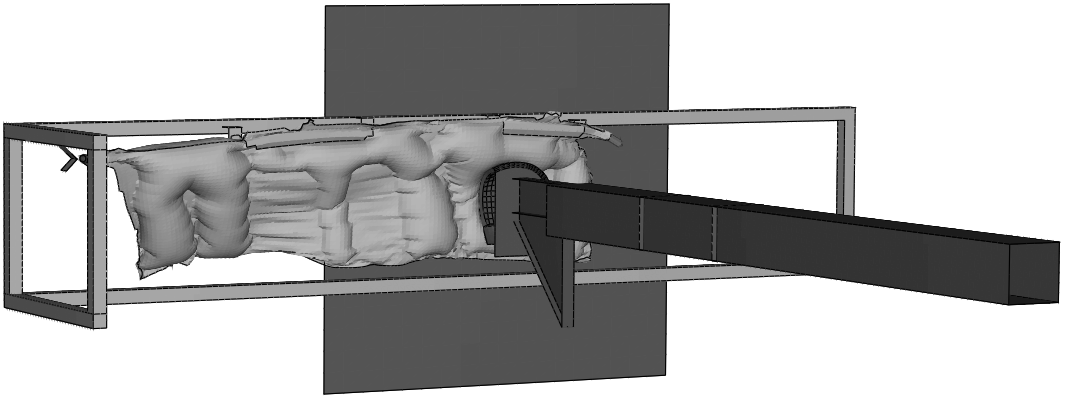

Figure 3.3.2–1 Model setup showing the fully deployed airbag (t=80 ms).

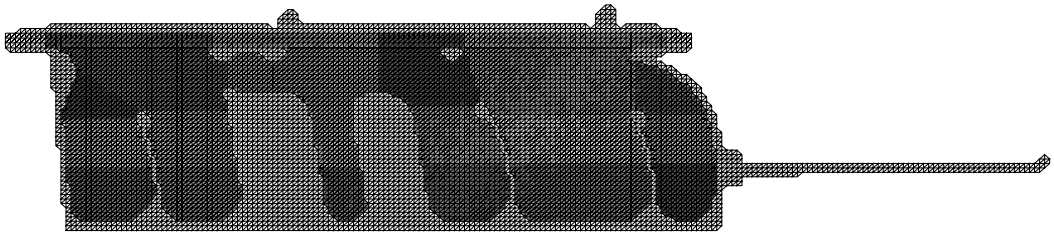

Figure 3.3.2–2 Airbag reference configuration.

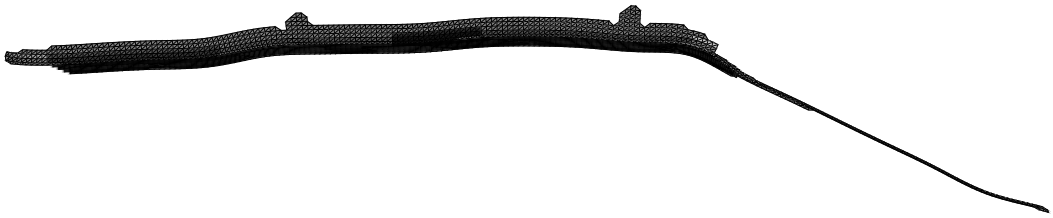

Figure 3.3.2–3 Folded airbag configuration.

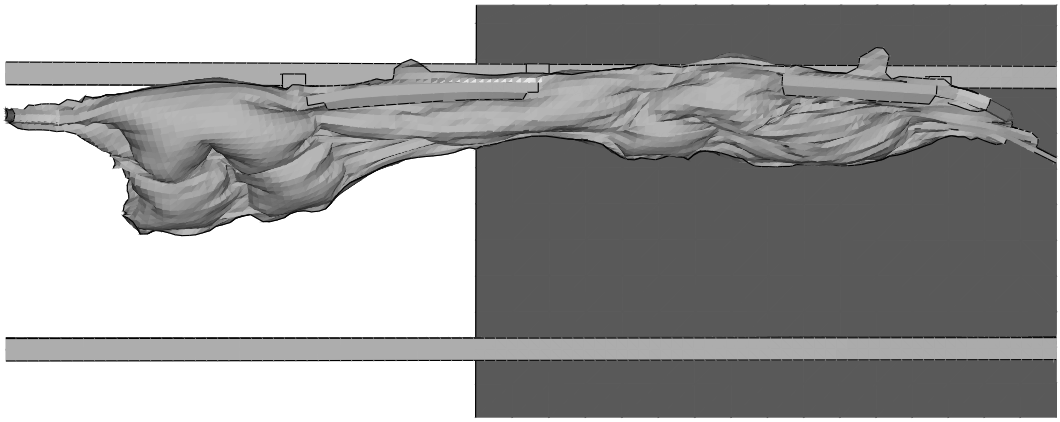

Figure 3.3.2–4 Deformed configuration at 8 ms.

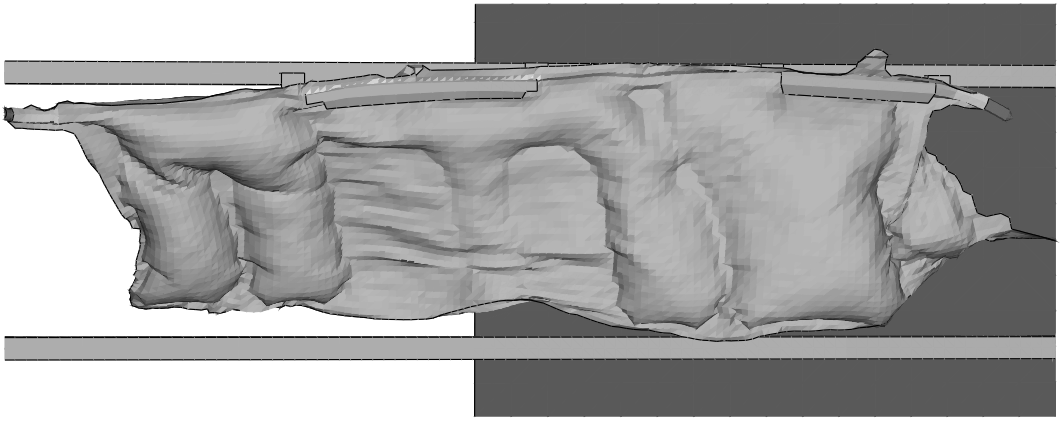

Figure 3.3.2–5 Deformed configuration at 16 ms.

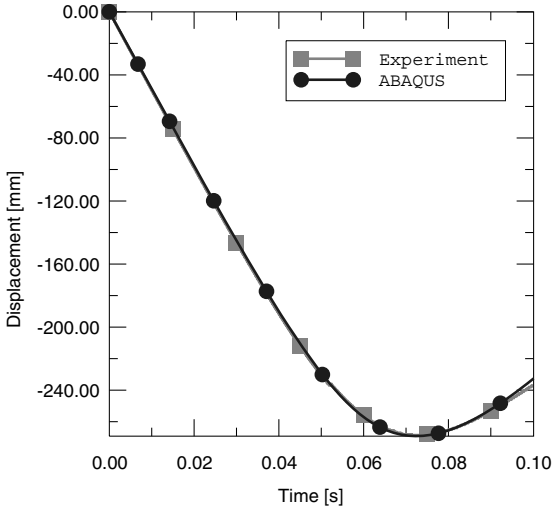

Figure 3.3.2–6 Time history of displacement of the impactor.

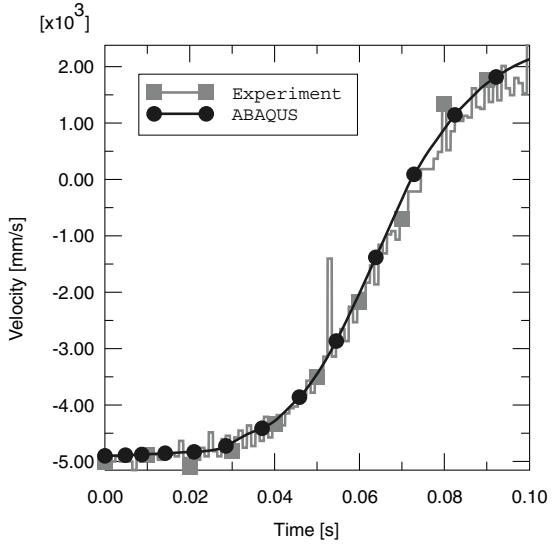

Figure 3.3.2–7 Time history of velocity of the impactor.

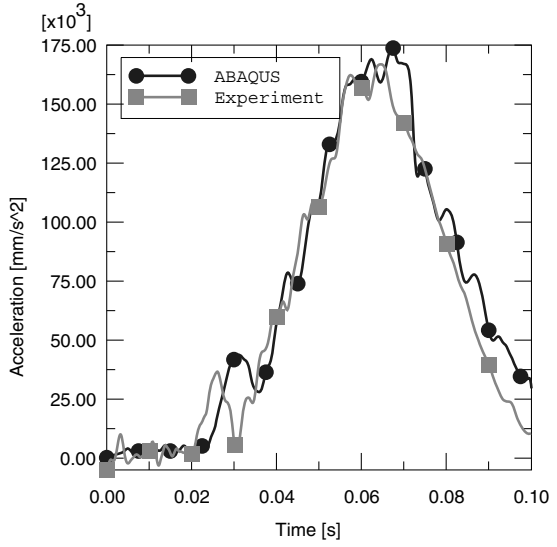

Figure 3.3.2–8 Time history of acceleration of the impactor.

4. Mechanism Analyses

- “Mechanism analyses,” Section 4.1

4.1 Mechanism analyses

- “Resolving overconstraints in a multi-body mechanism model,” Section 4.1.1
- “Crank mechanism,” Section 4.1.2
- “Snubber-arm mechanism,” Section 4.1.3
- “Flap mechanism,” Section 4.1.4
- “Tail-skid mechanism,” Section 4.1.5
- “Cylinder-cam mechanism,” Section 4.1.6
- “Driveshaft mechanism,” Section 4.1.7
- “Geneva mechanism,” Section 4.1.8
- “Trailing edge flap mechanism,” Section 4.1.9
- “Substructure analysis of a one-piston engine model,” Section 4.1.10
- “Application of bushing connectors in the analysis of a three-point linkage,” Section 4.1.11
- “Gear assemblies,” Section 4.1.12

4.1.1 RESOLVING OVERCONSTRAINTS IN A MULTI-BODY MECHANISM MODEL

Product: Abaqus/Standard

This example shows how you can resolve overconstraints in a multi-body mechanism.

An overconstraint occurs when multiple consistent or inconsistent kinematic constraints are applied to the same degree of freedom. Overconstraints may lead to inaccurate solutions or prevent convergence. A large number of overconstraint situations are detected and eventually resolved automatically either in the preprocessor or during an Abaqus/Standard analysis (see "Overconstraint checks," Section 35.6.1 of the Abaqus Analysis User's Guide). The vast majority of the overconstraints that are not resolved by the preprocessor are detected by the equation solver. The following symptoms identify such overconstrained models in Abaqus/Standard:

- Zero-pivot warning messages issued in the message (**`.msg`**) file indicating that the system of equations is rank deficient.
- Unreasonably large reaction forces.
- Very large time average forces in the message file.
- A displacement solution that violates the imposed constraints.

By default, overconstraint checks are performed continuously by the equation solver during the analysis. Abaqus/Standard does not resolve these overconstraints. Instead, detailed messages describing the modeling features that generated the overconstraint are issued to help the user resolve the problems. The message first identifies the nodes involved in either a consistent or an inconsistent overconstraint by using zero pivot information from the Gauss elimination in the solver (see "Direct linear equation solver," Section 6.1.5 of the Abaqus Analysis User's Guide). A detailed message containing constraint information is then issued.

Geometry and model

This example deals with resolving overconstraints in the multi-body mechanism model shown in Figure 4.1.1–1. The model consists of nine rigid bodies interconnected with connector elements ("Connectors: overview," Section 31.1.1 of the Abaqus Analysis User's Guide). The bodies named in the figure are connected as follows:

- **`LINK`** is connected to both **`CRANK`** and **`DISH`** using two CVJOINT (JOIN + CONSTANT VELOCITY) connector elements. Each of these rigid bodies spins about its own axis.
- **`TRANS CONNECT`** is connected to **`DISH`** using a JOIN connector element, which acts like a pin connection. **`TRANS CONNECT`** is also constrained to translate along the direction defined by **`TRANS GUIDE`** using a TRANSLATOR (SLOT + ALIGN) connector element between the two. In addition, **`TRANS CONNECT`** is attached to **`SLIDE BLOCK`** using a HINGE (JOIN + REVOLUTE) connection with the hinge axis oriented along the global *Z*-direction.
- **`SLIDE BLOCK`** in turn is constrained to slide along **`SLIDE GUIDE`** using a TRANSLATOR (SLOT + ALIGN) connector element.

- **TRANS GUIDE** and **ROD GUIDE** are connected using a CYLINDRICAL (SLOT + REVOLUTE) connector element.
- **ROD** is allowed to slide in **ROD GUIDE** using a TRANSLATOR (SLOT + ALIGN) connector element.

These connections enable the deformed configuration shown in Figure 4.1.1–2. See "Crank mechanism," Section 4.1.2, for another example using this model.

Loading and boundary conditions

Reference nodes 10009 of rigid body **ROD** and 10006 of rigid body **SLIDE GUIDE** are fixed completely. In addition, translations and rotations along the global *X*- and *Y*-directions are constrained at reference nodes 10001 of rigid body **DISH** and 10003 of rigid body **CRANK**. The mechanism is actuated using a boundary condition to prescribe a rotation of 360° about the global *Z*-direction at reference node 10001 (rigid body **DISH**) in a static step.

Understanding overconstraint messages

When Abaqus/Standard attempts to find a solution for this model, two zero pivots are identified in the first increment of the analysis suggesting that there are two overconstraints in the model. These overconstraints have to be identified and removed to render the model properly constrained. One way to identify possible overconstraints in the case of simple models is to count the number of degrees of freedom and constraints. There are nine rigid bodies in the model with a total of 54 degrees of freedom. There are 21 constraints specified using a boundary condition. The connector elements enforce additional constraints: three TRANSLATOR connection types enforce 5 constraints each, two CVJOINT connection types enforce 4 constraints each, one CYLINDRICAL connection type enforces 4 constraints, one HINGE connection type enforces 5 constraints, and one JOIN connection type enforces 3 constraints. Thus, the number of constraints enforced by connector elements is 35. Consequently, there are two (21 + 35 – 54) constraints too many in the model, corresponding to the number of zero pivots identified by the equation solver.

To help the user identify the constraints that should be removed, the following message is produced in the message file outlining the chains of constraints that generated the first overconstraint:

```
***WARNING: SOLVER PROBLEM. ZERO PIVOT WHEN PROCESSING ELEMENT 20025
INTERNAL NODE 1 D.O.F. 4

OVERCONSTRAINT CHECKS: An overconstraint was detected at one of the
Lagrange multipliers associated with element 20025. There are
multiple constraints applied directly or chained constraints that
are applied indirectly to this element. The following is a list of
nodes and chained constraints between these nodes that most likely
lead to the detected overconstraint.

LAGRANGE MULTIPLIER: 2321 <-> 863: connector element 20025 type
```

```
                     SLOT ALIGN constraining 2 translations and
                     3 rotations
..2321 -> 10007: *RIGID BODY (or *COUPLING-KINEMATIC)
....10007 -> 3159: *RIGID BODY (or *COUPLING-KINEMATIC)
......3159 -> 3031: connector element 20030 type SLOT REVOLUTE
                    constraining 2 translations and 2 rotations
........3031 -> 10008: *RIGID BODY (or *COUPLING-KINEMATIC)
..........10008 -> 3134: *RIGID BODY (or *COUPLING-KINEMATIC)
............3134 -> 2824: connector element 20035 type SLOT ALIGN
                          constraining 2 translations and
                          3 rotations
..............2824 -> 10009: *RIGID BODY (or *COUPLING-KINEMATIC)
................10009 -> *BOUNDARY in degrees of freedom
                          1  2  3  4  5  6
..863 -> 10004: *RIGID BODY (or *COUPLING-KINEMATIC)
....10004 -> 427: *RIGID BODY (or *COUPLING-KINEMATIC)
......427 -> 3157: connector element 20010 type JOIN constraining
                   3 translations
........3157 -> 10001: *RIGID BODY (or *COUPLING-KINEMATIC)
..........10001 -> 780: *RIGID BODY (or *COUPLING-KINEMATIC)
............780 -> 3156: connector element 20005 type
                         JOIN CONSTANT VELOCITY constraining
                         3 translations and 1 rotations
..............3156 -> 10002: *RIGID BODY (or *COUPLING-KINEMATIC)
................10002 -> 781: *RIGID BODY (or *COUPLING-KINEMATIC)
..................781 -> 3155: connector element 20001 type
                                JOIN CONSTANT VELOCITY constraining
                                3 translations and 1 rotations
....................3155 -> 10003: *RIGID BODY
                                      (or *COUPLING-KINEMATIC)
......................10003 -> *BOUNDARY in degrees of freedom
                                 1  2  4  5  6
..........10001 -> *BOUNDARY in degrees of freedom  1  2  4  5
....10004 -> 3158: *RIGID BODY (or *COUPLING-KINEMATIC)
......3158 -> 1539: connector element 20015 type JOIN REVOLUTE
                    constraining 3 translations and 2 rotations
........1539 -> 10005: *RIGID BODY (or *COUPLING-KINEMATIC)
..........10005 -> 1575: *RIGID BODY (or *COUPLING-KINEMATIC)
............1575 -> 2027: connector element 20020 type SLOT ALIGN
                          constraining 2 translations and
                          3 rotations
..............2027 -> 10006: *RIGID BODY (or *COUPLING-KINEMATIC)
```

```
.................10006 -> *BOUNDARY in degrees of freedom
                            1  2  3  4  5  6

Please analyze these constraint loops and remove unnecessary
constraints.
```

The zero pivot warning message identifies an internal node (Lagrange multiplier) associated with the identified zero pivot. A typical line contains information pertaining to one constraint. The following line from the output:

```
LAGRANGE MULTIPLIER: 2321 <-> 863: connector element 20025 type
                     SLOT ALIGN constraining 2 translations and
                     3 rotations
```

identifies that the Lagrange multiplier associated with the zero pivot enforces one of the five constraints (SLOT and ALIGN) associated with connector element 20025 between user-defined nodes 2321 and 863. Each of the subsequent lines conveys information related to one constraint in the chains of constraints originating at the zero pivot node or in chains adjacent to them. For example, the line

```
....10007 -> 3159: *RIGID BODY (or *COUPLING-KINEMATIC)
```

informs the user that there is a rigid body constraint between nodes 10007 and 3159, while the line

```
.................10009 -> *BOUNDARY in degrees of freedom
                            1  2  3  4  5  6
```

states that there is a boundary condition fixing degrees of freedom 1 through 6 at node 10009.

Indentation levels are used to help in identifying the links in a chain of constraints. A detailed explanation of the chains is printed at the first occurrence of an overconstraint in the message file. Using this methodology, the following chains of constraints starting from the two nodes involved in the Lagrange multiplier constraint are identified:

```
Lagrange multiplier: 2321 -> 10007 -> 3159 -> 3031 -> 10008 -> 3134
-> 2824 -> 10009 -> *BOUNDARY

Lagrange multiplier: 863 -> 10004 -> 427 -> 3157 -> 10001 -> 780
-> 3156 -> 10002 -> 781 -> 3155 -> 10003 -> *BOUNDARY

Lagrange multiplier: 863 -> 10004 -> 427 -> 3157 -> 10001
-> *BOUNDARY

Lagrange multiplier: 863 -> 10004 -> 3158 -> 1539 -> 10005 -> 1575
-> 2027 -> 10006 -> *BOUNDARY
```

If any of the chains terminates in a free end (meaning the chain does not form a closed loop or end in a constraint), the chain does not have any contribution in generating the overconstraint. In the

example above, all the identified chains terminate in a constraint and, therefore, may contribute to the overconstraint.

A second zero pivot is generated by the same Lagrange multiplier associated with internal node 1 of connector element 20025 at degree of freedom 5. The chains associated with the zero pivot caused at degree of freedom 5 are identical to the ones at degree of freedom 4 and are not repeated in the message file.

Correcting the overconstrained model

A node set containing all the nodes in the chains of constraints associated with a particular zero pivot is generated automatically and can be displayed in the Visualization module.

In most overconstrained models there are many ways to resolve the overconstraints. The most obvious solution in the example above is to eliminate the unnecessary connector constraints. Upon investigation we see that two rotation constraints associated with the **TRANS CONNECT** rigid body are enforced by the SLOT + ALIGN connector element between the **TRANS CONNECT** and **TRANS GUIDE** bodies (nodes 2321 and 863) as well as by the JOIN + REVOLUTE connector element between the **TRANS CONNECT** and **SLIDE BLOCK** bodies (nodes 3158 and 1539), which renders the model overconstrained. Without affecting the intended kinematic behavior of the system, the JOIN + REVOLUTE connector can be replaced by a JOIN connector, enforcing only three displacement constraints and removing the two extra constraints on these degrees of freedom.

It is important to analyze the chains of constraints carefully and remove constraints properly rather than relax any two arbitrary constraints. For example, removing any two boundary conditions would neither produce the desired kinematic behavior nor remove the overconstraints.

An alternative solution is to add flexibility to some of the rigid bodies or constraints, which can be achieved by either making the **TRANS CONNECT** rigid body elastic or using appropriate combinations of CARTESIAN and CARDAN (EULER or ROTATION as well) connectors together with flexible connections (specified using connector elasticity behavior) to enforce some of the kinematic constraints in an approximate manner.

Results and discussion

As mentioned earlier, an additional method of identifying overconstraints is to plot the reaction forces at the constrained degrees of freedom. These forces are unreasonably large in the overconstrained model even though the displacement solution looks acceptable. In this model a plot of connector reaction forces (CRF) for element 20025 (TRANSLATOR connector between nodes 863 and 2321 of rigid bodies **TRANS GUIDE** and **TRANS CONNECT**, respectively) shows that they are unreasonably large. Once the overconstraints are resolved and the analysis is rerun, there are no zero pivots generated in the message file and the connector reaction forces become very small (approximately 10^{-6} magnitude) as expected. Comparisons of the connector reaction forces shown in Figure 4.1.1–3 and Figure 4.1.1–4 suggest that the model is properly constrained.

One other option for resolving the overconstraints is to relax some of the constraints associated with the TRANSLATOR (SLOT + ALIGN) connector for which zero pivots were identified. A CARDAN connection type with connector elasticity behavior could be used instead of the ALIGN

connector. Alternatively, the HINGE constraint attached to the **SLIDE BLOCK** rigid body could be relaxed by using JOIN and CARDAN connection types with connector elasticity behavior for the CARDAN components.

Input files

mbmech_overconst.inp	Overconstrained multi-body mechanism model.
mbmech_overconst_crig.inp	Overconstrained multi-body mechanism model using the *CONNECTOR ELASTICITY, RIGID option.
mbmech_resolved.inp	Multi-body mechanism model with overconstraints resolved.
mbmech_resolved_crig.inp	Multi-body mechanism model with overconstraints resolved using the *CONNECTOR ELASTICITY, RIGID option.
mbmech_nodedefs.inp	Node definitions used in the overconstrained and resolved models.
mbmech_elemdefs.inp	Element definitions used in the overconstrained and resolved models.
mbmech_rigbdefs.inp	Rigid body definitions used in the overconstrained and resolved models.
mbmech_conndefs_oc.inp	Connector element definitions used in the overconstrained model.
mbmech_conndefs_res.inp	Connector element definitions used in the resolved model.
mbmech_cardan_elas.inp	Multi-body mechanism model with the HINGE connector element replaced by a JOIN + CARDAN connection and the *CONNECTOR ELASTICITY option. This model uses parts and assemblies; the connector elements are defined at the assembly level.
mbmech_cardan_elas_parts.inp	Node, element, and rigid body definitions for all parts used in mbmech_cardan_elas.inp.

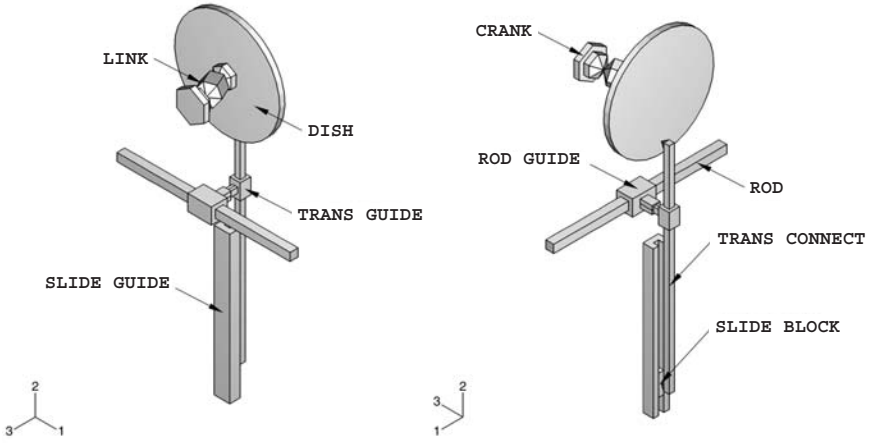

Figure 4.1.1–1 Model of the multi-body mechanism.

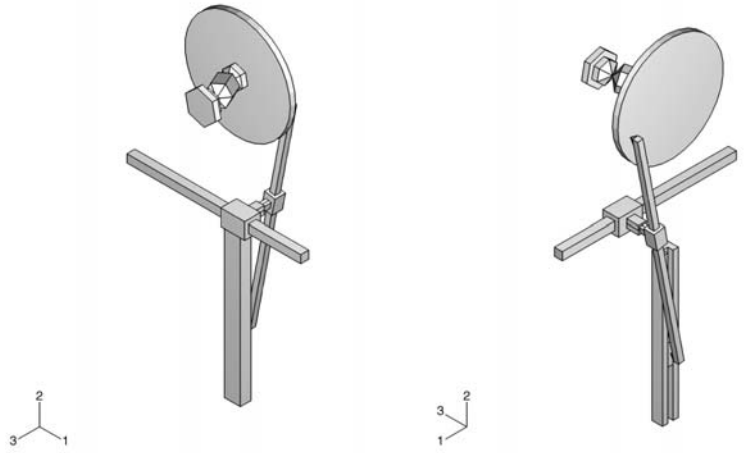

Figure 4.1.1–2 Displaced configuration of the mechanism.

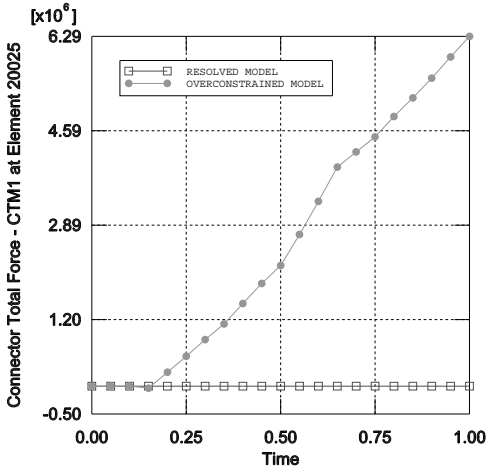

Figure 4.1.1–3 Comparison between time histories of CTM1 in element 20025 for the overconstrained and corrected models.

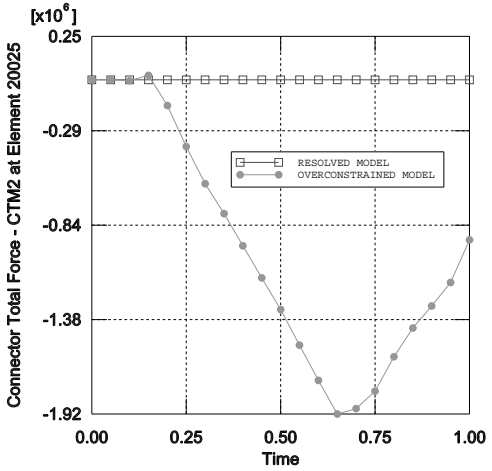

Figure 4.1.1–4 Comparison between time histories of CTM2 in element 20025 for the overconstrained and corrected models.

4.1.2 CRANK MECHANISM

Products: Abaqus/Standard Abaqus/Explicit

This example illustrates the use of connector elements to model kinematic constraints between rigid bodies in a multi-body mechanism.

Problem description

The crank mechanism considered here transmits a rotational motion through two universal joints and then converts the rotation into translational motion of two slides. The mechanism is modeled using nine rigid components attached with eight connector elements. The various kinematic constraints modeled with connector elements include TRANSLATOR, which allows relative translation along a line but no rotations; HINGE, which allows one relative rotation and fixes relative translations; CYLINDRICAL, which allows relative translation along a line and relative rotation about that line; JOIN, which fixes relative translations but leaves the rotations free; PLANAR, which keeps a point on a plane and allows only relative rotations about the normal to that plane; and UJOINT, which fixes the relative translations and enforces a universal constraint on the relative rotations. The complete model is shown in Figure 4.1.2–1.

The axes of rotation of the small and large disks are parallel but offset. A constant angular velocity of the small disk is specified about its axis with a velocity boundary condition on its rigid body reference node. All other degrees of freedom of the rigid body reference node are fixed. The rotational motion of the small disk is transmitted to the large disk through two UJOINT connections and a rigid link. A UJOINT connection, or a universal rotation constraint with shared translational degrees of freedom, between two nonaligned shafts will not transmit constant angular velocity. However, two symmetrically placed universal constraints, as here, will produce constant angular velocity coupling between the two disks. The large disk is connected to a rigid circular rod with a JOIN connection. A JOIN connection is equivalent to a ball-and-socket or a spherical joint. The circular rod connects through a sleeve to a flat block. The rod and sleeve constraint is modeled with a CYLINDRICAL connection, which allows the sleeve to translate along and rotate about the rod. The attachment of the circular rod to the flat block is a HINGE connection, which allows only a single relative rotation about the shared hinge axis. The flat block, in turn, is assumed to slide between two fixed parallel plates. This sliding constraint is modeled with a PLANAR (SLIDE-PLANE and REVOLUTE) connection. The sleeve on the circular rod is connected to a square-section sleeve on the square rod with a HINGE connection. The square rod is fixed in space. The square-section sleeve slides along the square bar without rotating. This sliding constraint is modeled with a TRANSLATOR connection.

A Python script is included that reproduces the model using the Scripting Interface in Abaqus/CAE. The script imports the parts from an ACIS file and creates the constraints and connectors that define the dynamics of the mechanism. The script creates both an Abaqus/Standard and an Abaqus/Explicit model that are ready to be submitted for analysis from the Job module.

Models with frictional interactions, plasticity, and damage in connectors are created by editing the input files without friction to introduce the friction, plasticity, or damage definitions.

A model that includes sensors and actuation via user subroutine **VUAMP** is also included to illustrate a means to model control engineering aspects in multibody analyses. Assuming that an electric motor provides the rotational input to the system, the intent is to shut off this motor (and complete the step) as the horizontal traveling head completes one full cycle. The amplitude properties can be defined in the input file or directly within the user subroutine.

Results and discussion

Figure 4.1.2–2 shows the position of the mechanism at various times. By visual inspection it can be observed that the connector elements are enforcing the correct kinematic constraints.

In this model there are nine rigid bodies with 6 degrees of freedom each, accounting for 54 rigid body degrees of freedom. The eight connector elements eliminate 33 rigid body degrees of freedom through kinematic constraints (enforced via Lagrange multipliers) as itemized in Table 4.1.2–1. Hence, the model has 21 rigid body degrees of freedom to be specified as boundary conditions or determined by the solution. In this case all remaining rigid body degrees of freedom are specified as boundary conditions, with the *z*-component of angular velocity specified for the small disk and 20 additional fixed boundary conditions used.

Files

rigmultimech_std.inp	Abaqus/Standard analysis.
rigmultimech_std_sensor.inp	Abaqus/Standard analysis with sensors and actuation via user subroutine **UAMP** in uamp_rigmultimech.f.
uamp_rigmultimech.f	Abaqus/Standard user subroutine **UAMP** to specify amplitudes.
rigmultimech_exp.inp	Abaqus/Explicit analysis.
rigmultimech_std_fric.inp	Abaqus/Standard analysis with friction.
rigmultimech_exp_fric.inp	Abaqus/Explicit analysis with friction.
rigmultimech_std_plas.inp	Abaqus/Standard analysis with plasticity.
rigmultimech_exp_plas.inp	Abaqus/Explicit analysis with plasticity.
rigmultimech_exp_dam.inp	Abaqus/Explicit analysis with damage.
rigmultimech_exp_sensor.inp	Abaqus/Explicit analysis with sensors and actuation via user subroutine **VUAMP** in vuamp_rigmultimech.f. The amplitude properties are defined in the user subroutine.
vuamp_rigmultimech.f	Abaqus/Explicit user subroutine **VUAMP** to specify amplitudes for rigmultimech_exp_sensor.inp.
rigmultimech_exp_sensor_props.inp	Abaqus/Explicit analysis with sensors and actuation via user subroutine **VUAMP** in vuamp_rigmultimech_props.f.
vuamp_rigmultimech_props.f	Abaqus/Explicit user subroutine **VUAMP** to specify amplitudes for rigmultimech_exp_sensor_props.inp. The amplitude properties are defined in the input file.
rigmultimech_bulk.inp	Node and element bulk data for the rigid bodies.

rigmultimech.py	Python script that creates both an Abaqus/Standard and an Abaqus/Explicit model using Abaqus/CAE. The script imports the parts from an ACIS file named **`rigmultimech.sat`**.
rigmultimech.sat	ACIS file containing the geometry of the model.

Table 4.1.2–1 Rigid body degrees of freedom eliminated by kinematic constraints.

Connection type	Number of kinematic constraints	Total rigid body DOFs eliminated from model
UJOINT (2)	4	8
JOIN	3	3
CYLINDRICAL	4	4
HINGE (2)	5	10
SLIDE-PLANE and REVOLUTE	3	3
TRANSLATOR	5	5
		Total eliminated: 33

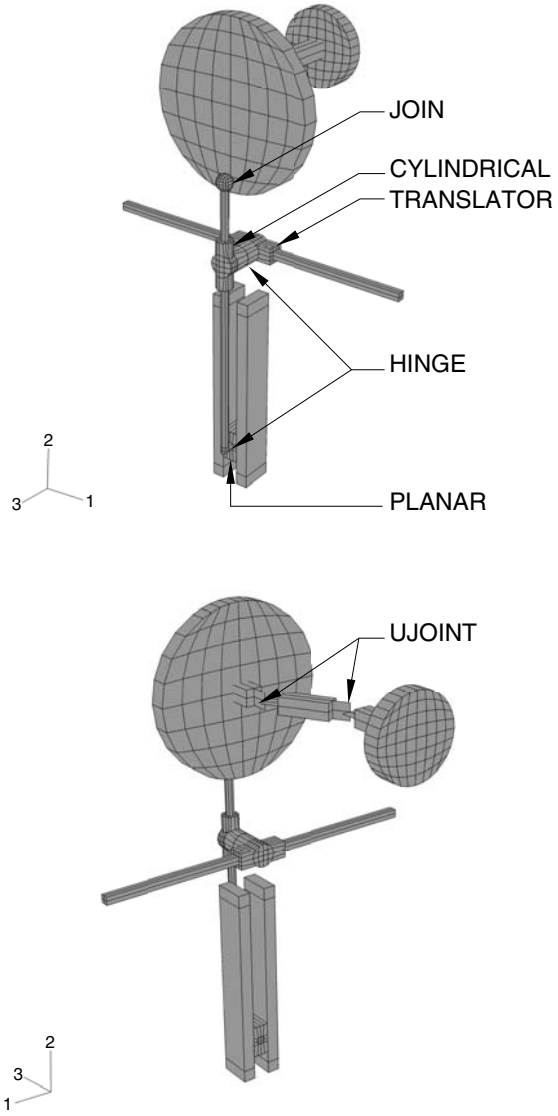

Figure 4.1.2–1 Rigid mechanism model.

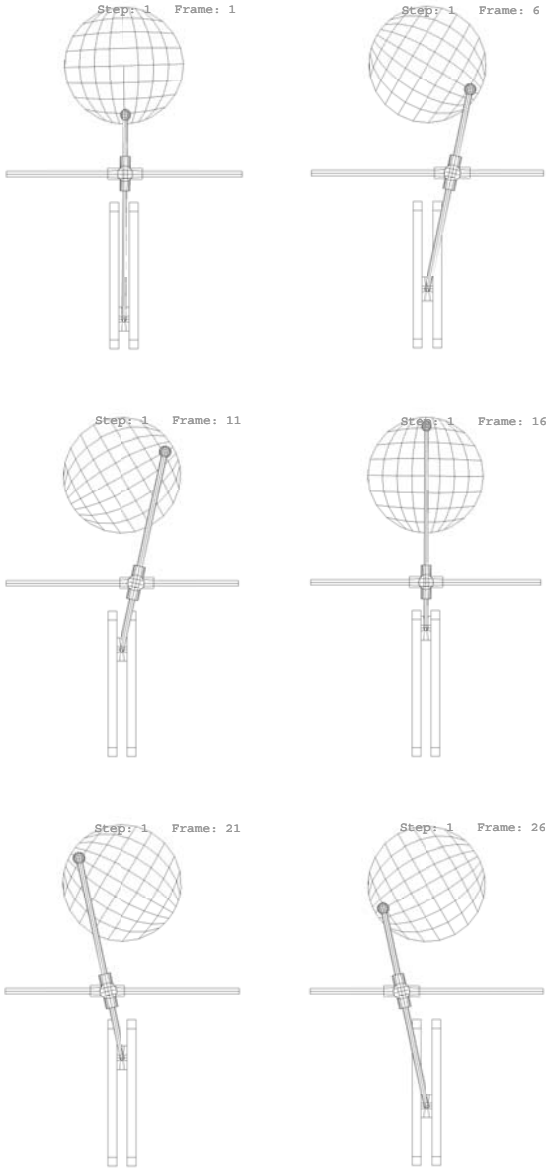

Figure 4.1.2–2 Time history of the motion of the mechanism during the first revolution.

4.1.3 SNUBBER-ARM MECHANISM

Product: Abaqus/Standard

This example illustrates the use of connector elements to model a snubbing mechanism (i.e., two solids coming into contact).

Geometry and model

A snubber is used to cushion the closing of a cowling on an aircraft. The cowling opens and closes by applying a torque about the *Z*-axis at a fixed point (the origin, Q, in Figure 4.1.3–1). The snubber-arm assembly is attached to the cowling at point C. The snubber arm is constrained at point A by a spring and is allowed to rotate relative to the cowling about point C. The other end of the spring is attached to the cowling at point E. A shoe is attached to the snubber arm at point B and contacts with a block as the cover closes, as shown in detail in Figure 4.1.3–2. The shoe is allowed to pivot about point B. The spring retains the snubber arm against a stop on the cowling with an initial force of 50 lbs when the cover is open. The shoe contacts the block as the cover closes.

A small rotational spring (10 lb/rad) keeps the shoe from rotating relative to the snubber arm while the shoe is not in contact with the block. The block is fixed to the ground. As the shoe comes into contact, the two surfaces slide relative to each other. The coefficient of friction between the block and the shoe is 0.5.

The closing speed of the cowling is slow enough so that inertia effects can be neglected. Figure 4.1.3–1 shows the position of the mechanism when the shoe and the block make initial contact. The cowling rotates five more degrees about point Q after the block and the shoe make initial contact.

Model interactions

The bodies named in Figure 4.1.3–1 and Figure 4.1.3–2 are connected as follows:

- **ARM** is connected to **COWLING** at point C using JOIN and ROTATION connector elements. The rotation is constrained using a connector stop to prevent **ARM** from rotating past the stop.
- The spring connecting **ARM** to **COWLING** is modeled using an AXIAL connector element defined between points A and E. The pre-tension in the spring is modeled using reference lengths and angles to be used in specifying connector constitutive behavior.
- **SHOE** is connected to **ARM** at point B using JOIN and ROTATION connector elements. The small rotational spring is modeled using connector elasticity behavior.

All bodies in the model are modeled using display bodies connected to the relevant connector nodes. **SHOE** (deformable elements) and **BLOCK** (rigid surface) make exception to this rule to allow contact interaction definition between these bodies. Some models include friction and plasticity effects in the connectors.

Results and discussion

Figure 4.1.3–3 shows the displaced configurations of the mechanism as the cowling is rotated. As the cowling opens, the spring pulls on the arm at point C until the arm is stopped. After contact is established, when the cowling is closing, the rotation of the arm increases the tension in the spring. During a flight this mechanism allows the absorption of vibrations between the cowling and the aircraft.

Such analyses allow one to study not only the dynamics of the snubber-arm mechanism but also the contact interaction between the block and the shoe. Figure 4.1.3–4 shows the contact pressure and frictional shear stress at a node located at the center of the shoe contact surface. Over time the coefficient of friction between the shoe and the block will decrease. Knowledge of the contact characteristics between the block and the shoe is a critical component of the design of the mechanism.

Input files

snubber_model.py	Python replay file for constructing the snubber-arm mechanism model in Abaqus/CAE.
snubber.inp	Snubber-arm mechanism model.
snubber_surf.inp	Snubber-arm mechanism model with surface-to-surface contact.
snubber_fric.inp	Snubber-arm mechanism model with friction.
snubber_plas.inp	Snubber-arm mechanism model with connector plasticity.

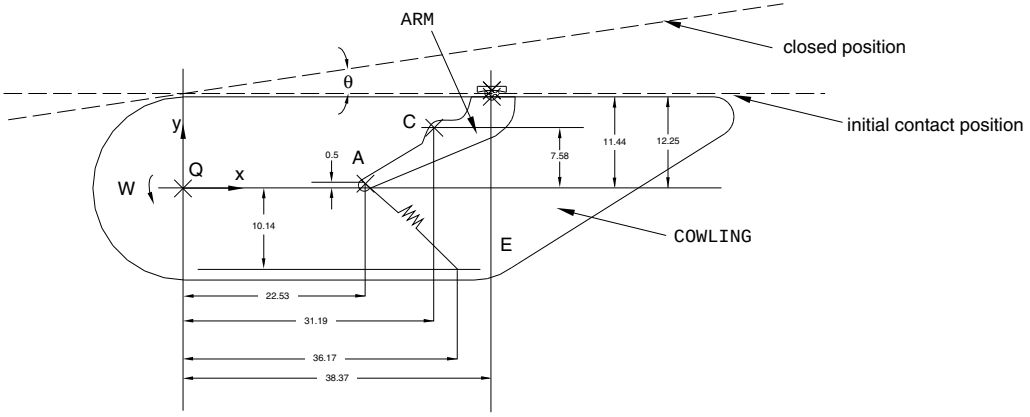

Figure 4.1.3–1 Undeformed configuration of the snubber-arm mechanism.

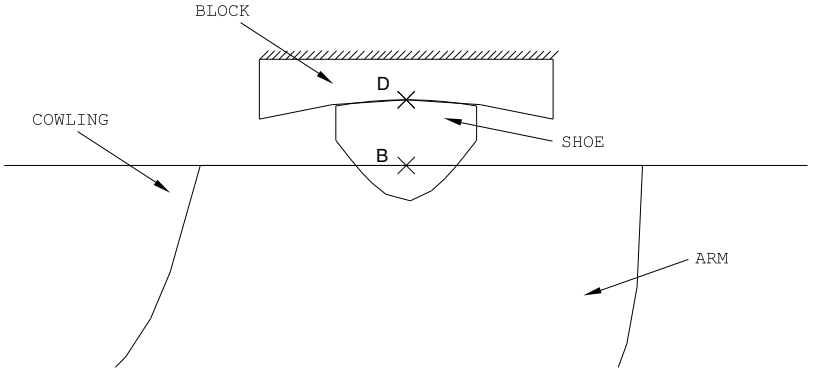

Figure 4.1.3–2 Undeformed configuration of the shoe and the block.

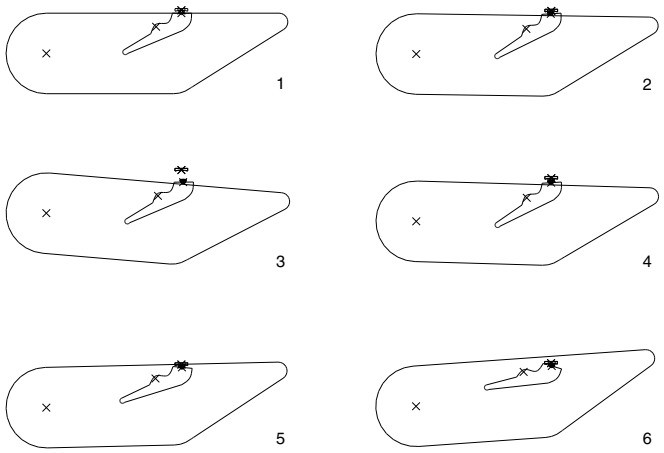

Figure 4.1.3–3 Displaced configurations of the mechanism.

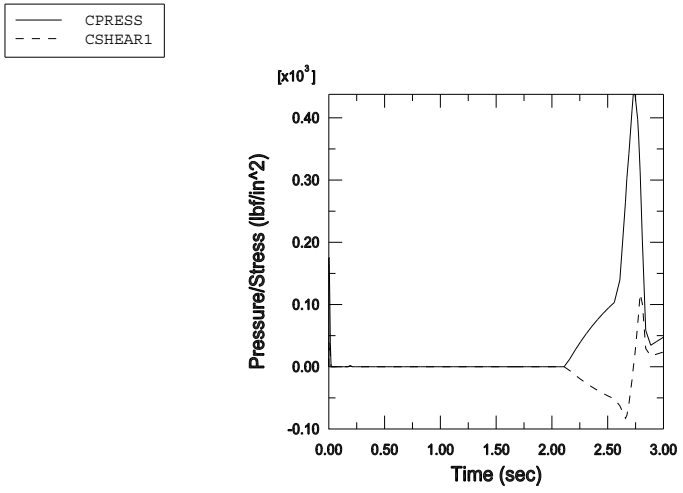

Figure 4.1.3–4 Contact pressure and frictional shear stress at the center of the shoe contact surface.

4.1.4 FLAP MECHANISM

Products: Abaqus/Standard Abaqus/Explicit

This example illustrates the use of connector elements to model a three-dimensional trailing edge mechanism.

Geometry and model

The complete model of the flap is shown in Figure 4.1.4–1. An actuator rotates a bell crank through the deployment of an actuator arm. The bell crank pushes and pulls a connecting rod that attaches to the arm of the flap.

The flap is connected to a rigid shaft on the aircraft wing structure at points E and I. An arm on the shaft is attached to the rod at point F. The other end of the rod attaches to a bell crank at point D. The bell crank is attached to the airplane so that it can rotate about point B. The axis of rotation of the bell crank passes through point B and is parallel to the global Z-axis. The rotation of the bell crank is driven by the deployment of the actuator arm. The actuator system attaches to the bell crank at point C. The other end of the actuator system is attached to the aircarft structure at point A and is allowed to compensate for the change of angle caused by the rotation of the bell crank.

A load is applied at the center of gravity of the flap so that it is colinear and oriented along the global Z-axis.

Model interactions

The bodies named in Figure 4.1.4–1 are connected as follows:

- **ACTUATOR** is connected to the ground at point A using a HINGE connector element. **ACTUATOR** and **ACTUATOR ARM** are connected using a TRANSLATOR connector element. The available component of relative motion in the translated connector element is used to modify the configuration of the actuator system as a function of time.
- **BELL CRANK** is physically attached to the ground with a hinge connection at point B. The axis of rotation of the hinge connection is parallel to the global Z-axis. However, using a HINGE connector element to attach **BELL CRANK** to the ground would overconstrain the model. Because of the connections used between point A and point C, point C is already constrained to travel in the global X–Y plane. Because the position of point B has to remain fixed in space, the rotation of **BELL CRANK** about the BD-axis is already constrained. As a result, only three translations and the rotation of **BELL CRANK** about the BC-axis need to be constrained to realize the hinge connection. **BELL CRANK** is, thus, attached to the ground using JOIN and UNIVERSAL connector elements at point B. The UNIVERSAL connection is used to constrain the relative rotation of **BELL CRANK** with respect to the ground about the BC-axis.
- **ROD** is connected to **BELL CRANK** at point D and to **ARM** at point F using JOIN connector elements. A CARDAN connector element is added at point F between **ROD** and **ARM** to introduce an elastic behavior to prevent the free rotation of **ROD** around its axis.

- **FLAP** and **ARM** are connected by a WELD connector element at point E. **FLAP** is attached to the ground using a HINGE connection at point I.

All bodies in the model are visualized using display bodies connected to the relevant connector nodes. Separate models in Abaqus/Standard and Abaqus/Explicit include friction, plasticity, and damage in the connectors.

Results and discussion

The amplitude curve used to drive the deployment of the actuator arm is shown in Figure 4.1.4–3. Figure 4.1.4–2 shows the configuration of the flap mechanism at intermediate instants as it is actuated. As the actuator system is deployed, the flap rotates around the EI-axis to modify the aerodynamics of the wing.

Input files

flap_model.py	Python replay file for constructing the flap mechanism model in Abaqus/CAE.
flap.inp	Abaqus/Standard flap mechanism model.
flap_fric.inp	Abaqus/Standard flap mechanism model with friction.
flap_exp_fric.inp	Abaqus/Explicit flap mechanism model with friction.
flap_plas.inp	Abaqus/Standard flap mechanism model with plasticity.
flap_exp_plas.inp	Abaqus/Explicit flap mechanism model with plasticity.
flap_exp_plas_dam.inp	Abaqus/Explicit flap mechanism model with plasticity and damage.

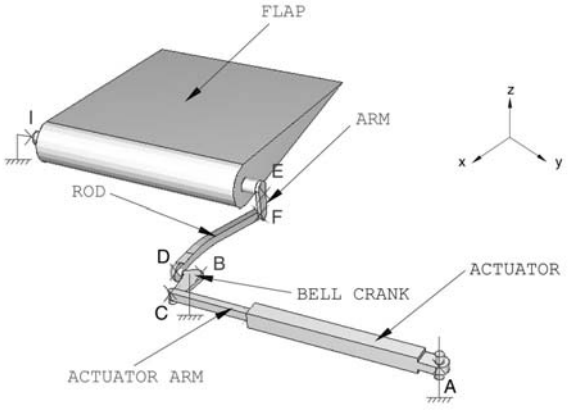

Figure 4.1.4–1 Undeformed configuration of the flap mechanism.

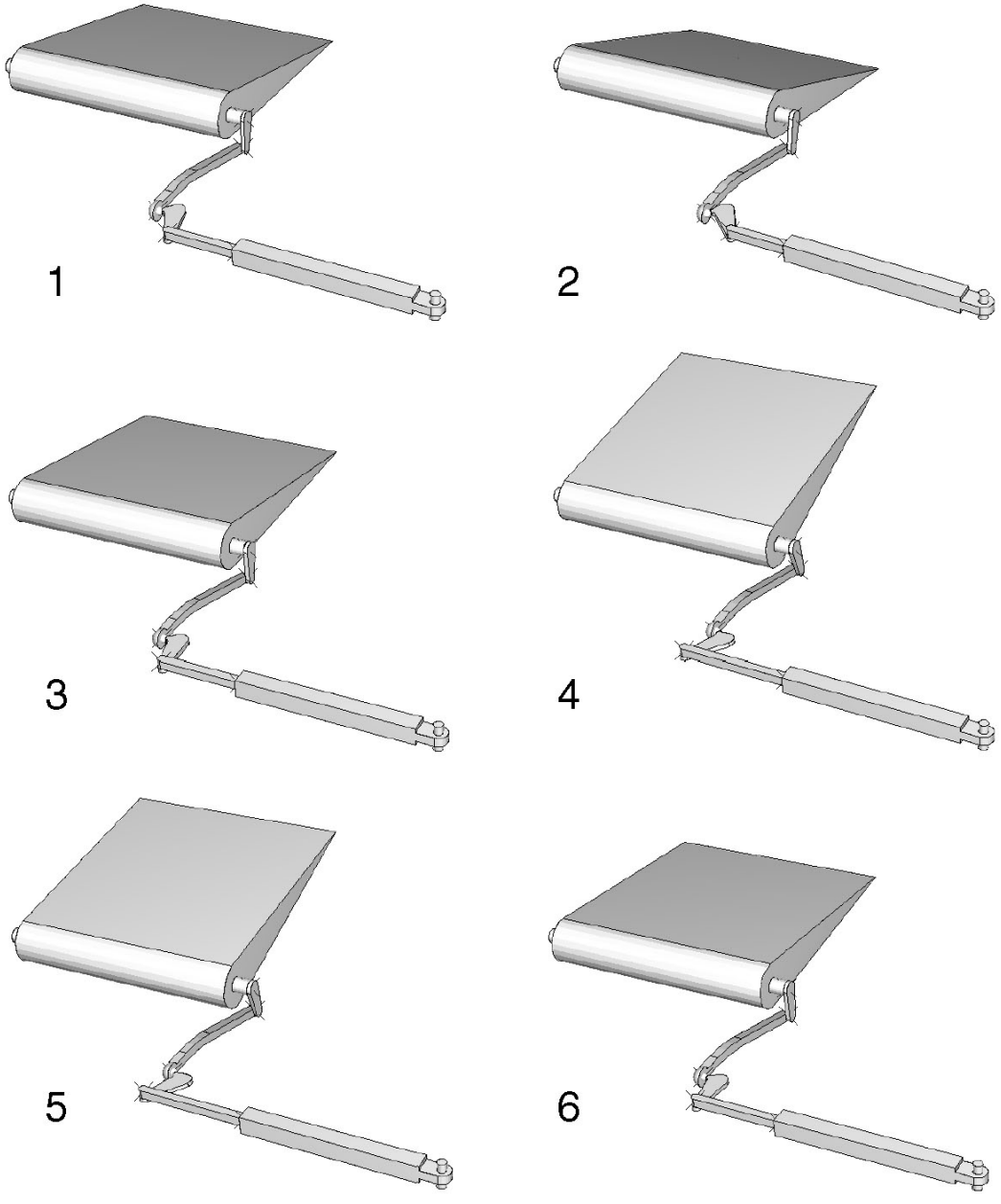

Figure 4.1.4–2 Deformed configurations of the flap mechanism.

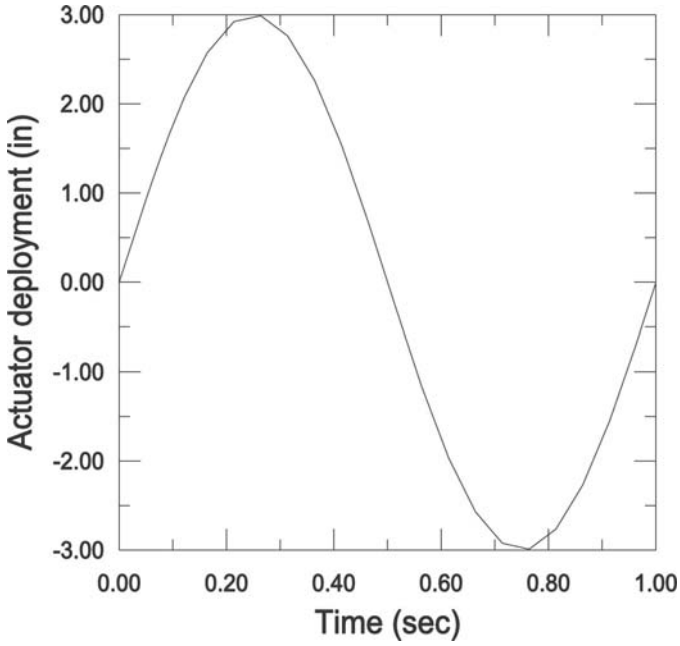

Figure 4.1.4–3 Translator connector motion.

4.1.5 TAIL-SKID MECHANISM

Products: Abaqus/Standard Abaqus/Explicit

This example illustrates the use of connector elements to model the tail-skid mechanism of an airplane.

Geometry and model

The complete model of the tail-skid mechanism is shown in Figure 4.1.5–1. It consists of a bell crank, an actuator, a tail-skid arm, and a large cylinder. The bell crank is connected to the actuator at point A and to the large cylinder at point B. The tail-skid arm is connected to the actuator at point D and to the large cylinder at point E. The large cylinder is a compressible single-use cartridge designed to absorb energy in the unlikely event of a tail strike. As such, it behaves like a compression-only linear spring with a stiffness K=875600 N/m (K=5000 lb/in) and a damping coefficient C=175100 N/m sec (C=1000 lb/in sec). The bell crank pivots about point C to move the large cylinder. The whole mechanism is attached to the aircraft frame through points C and D. All point locations are listed in Table 4.1.5–1.

Two types of analyses are of interest: the deployment and stowage kinematics analysis and the tail strike analysis. In the kinematics analysis the actuator contracts a distance of 145.8 mm (5.74 in), which will rotate the bell crank and move the mechanism from the deployed to the stowage position. The large cylinder does not compress during stowage or deployment. The tail strike analysis simulates the over-rotation of an aircraft during takeoff. In this analysis the tail-skid arm strikes the ground at a speed of 1.839 m/s (6.0 ft/s) at point F when it is at the deployed position. The strike creates a force acting at an angle of 10 degrees with respect to the 2-axis as a result of friction between the airplane and the runway. During the strike the large cylinder is compressed a maximum distance of 101.6 mm (4.0 in) to absorb energy before it bottoms out. The mass and inertia of the tail-skid components are assumed to be negligible. The body of the airplane is assumed to be rigid, has a mass of 6193 kg (270000 lb), and a mass moment of inertia of 2220 kg m^2 (1.5e8 lb in^2) relative to the 3-axis. The center of gravity of the airplane is located at –18.06 m, –1.422 m, 0.0 m (–711.0 in, –56 in, 0.0 in); it is not shown in the model because the dimension of the aircraft is much larger than the mechanism.

Model interaction

The correct behavior of the tail-skid mechanism is modeled by defining appropriate connectors between the discrete points in Figure 4.1.5–1. For visualization purposes, display bodies are attached to those points to model the bell crank, actuator, tail-skid arm, and large cylinder.

- The actuator behavior is modeled using an AXIAL connector between points A and C.
- The large cylinder behavior is modeled by the combination of an AXIAL connector and a SLIDE-PLANE connector between points E and G.
- The bell crank is connected to the large cylinder by a HINGE (REVOLUTE+JOIN) connector and to the actuator by a JOIN connector.
- The tail-skid arm is connected to the actuator and the large cylinder at points D and E, respectively, using two HINGE connectors.

The tail-skid mechanism is then connected to the aircraft frame at points C and D using two HINGE connectors. The air frame is modeled with two BEAM connectors connecting points C and D to the center of gravity of the airplane. Since both the actuator and the large cylinder consist of two display bodies, additional connectors are necessary to constrain the relative motion between them. For this purpose a SLIDE-PLANE connector element and an ALIGN connector element are defined between points A and D, and an ALIGN connector element is defined between points D and G.

In the kinematics analysis the position of the aircraft is fixed; the contraction of the actuator, which is realized through prescribed connector displacement of the AXIAL connector, moves the mechanism from the deployed to the stowage position. In the tail strike analysis the over-rotation of the airplane is modeled by allowing the airplane to be in free motion and applying an initial rotating velocity to it. During the strike the direction of the reaction of the ground to the airplane is assumed to remain fixed. As a result the reaction force is modeled by applying a fixed boundary condition at point F in a local coordinate system that will generate a reaction at an angle of 10 degrees with the 2-axis. The actuator is fixed during the strike, while the large cylinder is compressed. The large cylinder will absorb energy until it stops after being compressed 4 inches. This physical behavior of the large cylinder is modeled using the connector elasticity, connector damping, and connector stop behaviors. Separate models include friction, plasticity, and damage in the connectors.

In Abaqus/Explicit the tail strike analysis is repeated with a user-defined element in addition to the axial connector between points A and D. The element is modeled to mimic the elastic behavior of an axial connector; the damping and locking behavior are still defined through the axial connector acting in parallel with the user-defined element.

Results and discussion

A sequence of the deformed tail-skid mechanisms in the kinematics analysis is shown in Figure 4.1.5–2. By visual inspection it can be observed that the connector elements are enforcing the correct kinematic constraints. Some of the numerical results for the tail strike analysis are shown in Figure 4.1.5–3 and Figure 4.1.5–4. Figure 4.1.5–3 shows the total, elastic, and viscous force of the AXIAL connector that models the mechanical behavior of the large cylinder. Figure 4.1.5–4 shows the relative distance between points G and D. The sudden changes of the connector force and displacement shown in both figures are due to the large cylinder reaching its maximum contraction (modeled using connector stops) during tail strike.

Input files

tail_kinematics.inp	Kinematics analysis.
tail_strike.inp	Tail strike analysis.
tail_strike_fric.inp	Tail strike analysis with friction.
tail_strike_exp_fric.inp	Abaqus/Explicit tail strike analysis with friction.
tail_strike_exp_fric_plas_dam.inp	Abaqus/Explicit tail strike analysis with friction, plasticity, and damage.
tail_kinematics_model.py	Python replay file for constructing the kinematics model using Abaqus/CAE.

tail_strike_model.py	Python replay file for constructing the tail strike model using Abaqus/CAE.
vuel_tail_strike_exp_fric.inp	Abaqus/Explicit tail strike analysis with a user-defined element modeling the elastic behavior of one of the axial connectors. The element is defined in user subroutine vuel_axial_connector3d.f.
vuel_axial_connector3d.f	User subroutine **VUEL** to model the axial connector.

Table 4.1.5–1 Point locations in the deployed position.

Point	X	Y	Z
A	14.95	19.62	0.00
B	14.15	10.24	0.00
C	15.29	16.13	0.00
D	0.00	0.00	0.00
E	13.69	−3.49	0.00
F	24.72	−12.24	0.00

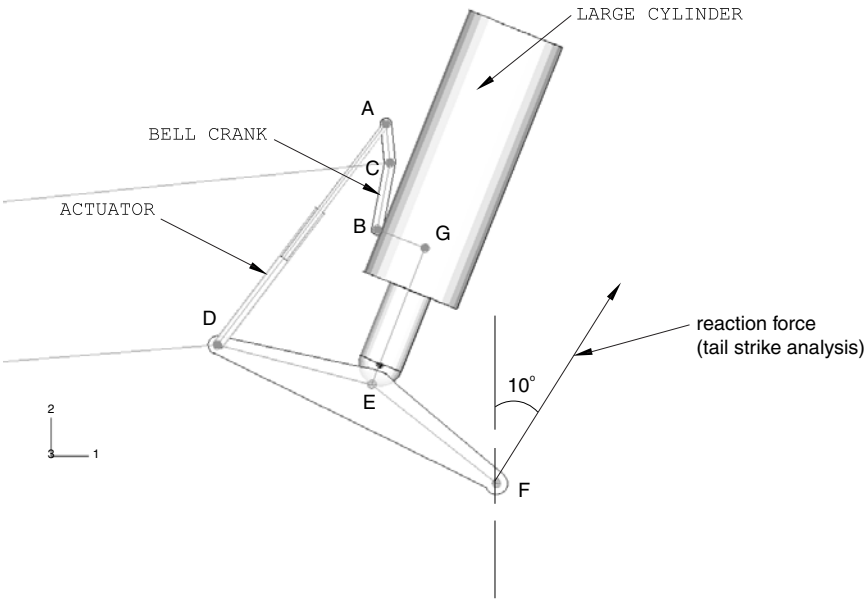

Figure 4.1.5–1 Tail-skid mechanism model (the deployed position).

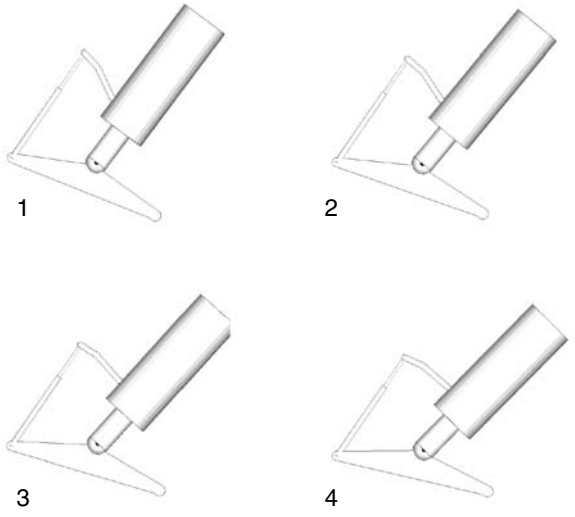

Figure 4.1.5–2 Intermediate positions of the tail-skid mechanism during tail strike.

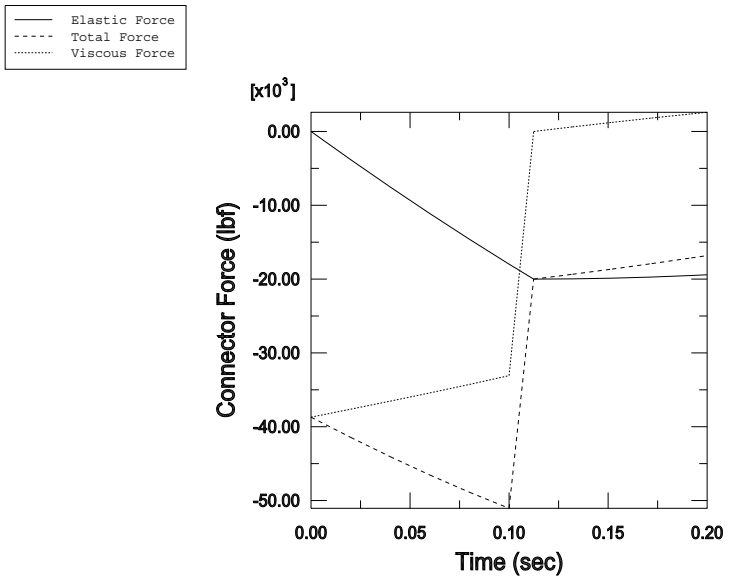

Figure 4.1.5–3 Elastic and damping forces of the connector modeling the large cylinder.

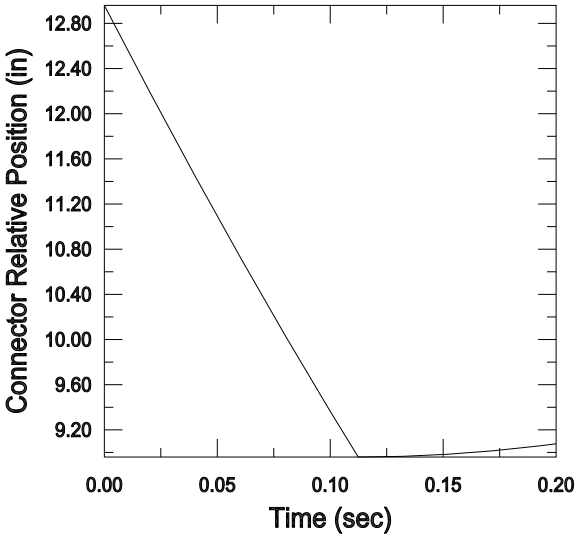

Figure 4.1.5–4 Relative displacement of the connector modeling the large cylinder.

4.1.6 CYLINDER-CAM MECHANISM

Product: Abaqus/Explicit

This example illustrates the use of connector elements to model a cylinder-cam mechanism.

Geometry and model

The cylinder-cam mechanism is shown in Figure 4.1.6–1. The solid aluminum cylinder is lying on the Z-axis and has a slot around its circumference. The centerline of the slot is defined by a plane intersecting the cylinder at 45 degrees. The slot has a radius of 7.62 mm (0.30 in) and a depth of 7.62 mm (0.30 in). A pin with a spherical end of radius 6.35 mm (0.25 in) is set into the slot. The pin is constrained to be parallel to the X-axis and remains in the X–Z plane. Because of the difference in radii, there is a 1.27 mm (0.05 in) gap between the slot and the pin head. As the cylinder rotates about the Z-axis, the pin travels in a track that is parallel to the cylinder. The pin has a weight of 13.34 N (3.0 lbf).

The cylinder rotates with a speed of 30 rpm, which drives the pin back and forth in the track. Resistance to the motion is caused by the friction between the pin and the track. The tolerance mismatch due to the pin head being smaller than the slot is considered in the model.

Model interactions

As shown in Figure 4.1.6–1, the track, the pin, and the cylinder are modeled using display bodies. The bodies in Figure 4.1.6–1 are connected as follows:

- MASS and ROTARYI elements are attached to each display body through BEAM connector elements to account for the inertia of each part in the model.
- The interaction between **PIN** and **TRACK** is modeled using ALIGN+SLOT connectors between point D and point E. The friction dissipation effects between **PIN** and **TRACK** are taken into account using connector damping behavior.
- The interaction between **PIN** and **CYLINDER** is modeled by defining a CARTESIAN connector element between point B and point C. The 1.27 mm (0.05 in) gap between the pin and the slot is modeled using a connector stop. The local coordinate system of the CARTESIAN connector element (used to measure the displacement of point C relative to point B) is attached at point B to **CYLINDER** and has its 2–3 plane lying in the plane of the slot. The connector stop is defined along component 1 of the connector element. A displacement of 1.27 mm (0.05 in) of the pin relative to the center of the slot along the Z-axis corresponds to a displacement of point C relative to point B of 0.898 mm (0.035 in) in the connector local coordinate system. The connector stop is, thus, defined at a distance of 0.898 mm (0.035 in) in the positive and negative 1-directions of the CARTESIAN connector element.

Results and discussion

Figure 4.1.6–2 shows the positions of the mechanism as the cylinder is rotated. The time histories of the displacement of point C in the global coordinate system and the displacement of point C relative to point B in the CARTESIAN connector local coordinate system are shown in Figure 4.1.6–3. In the connector local coordinate system, point C travels a maximum distance of 0.035 in relative to point B. This corresponds to the value given in the connector stop definition. When **PIN** and **CYLINDER** are in contact, the displacement of point C relative to point B in the connector local coordinate system remains constant, and the cylinder forces the pin to translate. When contact is lost, the connector relative displacement varies with time, and the motion of the pin stops as a result of damping.

Files

cylcammech.inp	Abaqus/Explicit analysis.
cylcammech.py	Python script that creates an Abaqus/Explicit model using Abaqus/CAE. The script imports the parts from an ACIS file named **cylcammech.sat**.
cylcammech.sat	ACIS file containing the geometry of the model.

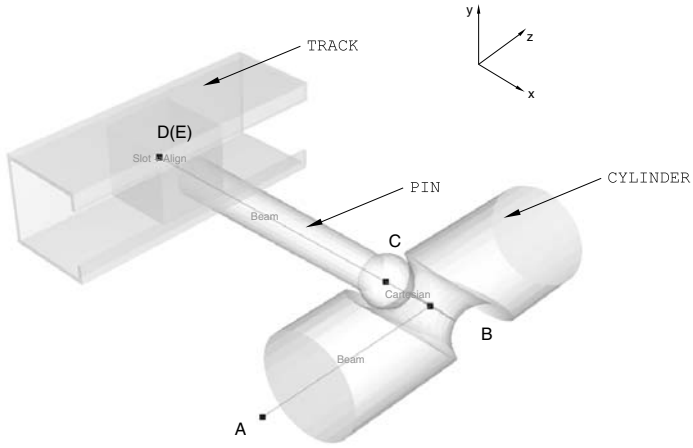

Figure 4.1.6–1 Cylinder-cam mechanism.

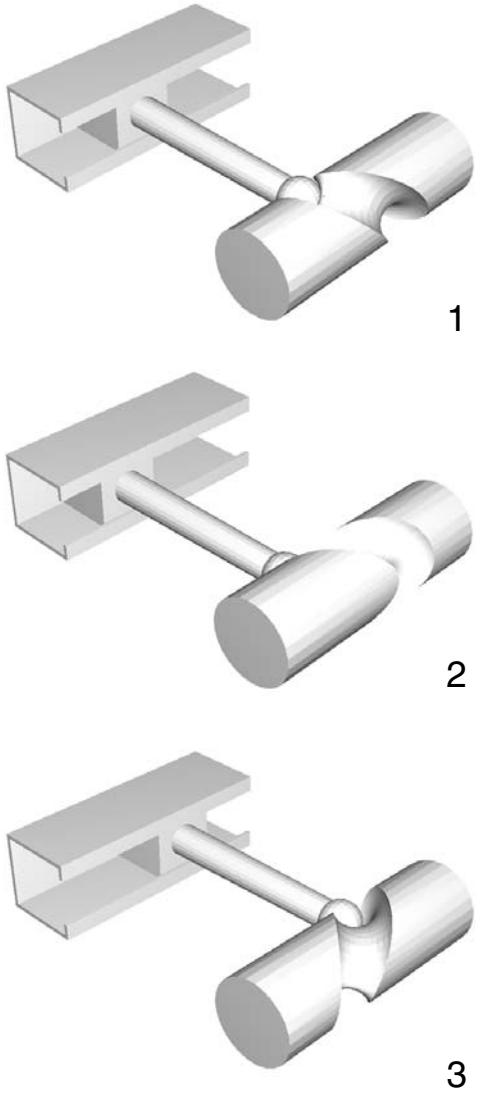

Figure 4.1.6–2 Displaced positions of the mechanism.

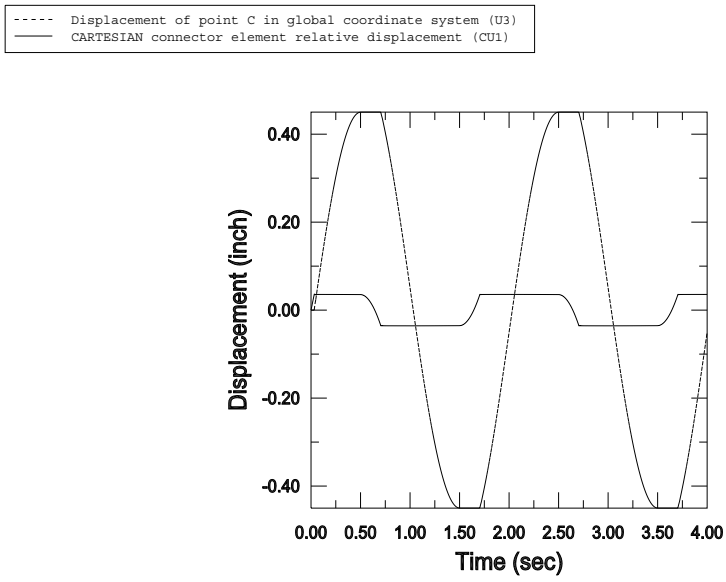

Figure 4.1.6–3 Time histories of the displacement of the pin head (Point C).

4.1.7 DRIVESHAFT MECHANISM

Products: Abaqus/Standard Abaqus/Explicit

This example illustrates the use of connectors to model a driveshaft mechanism.

Geometry and model

Driveshaft mechanisms are important components of motor vehicles. These mechanisms often contain universal joints that are used to carry motion from one shaft to another where the two shafts are not perfectly aligned. A typical universal joint assembly is shown in Figure 4.1.7–1. The joint consists of a cross that carries needle roller bearings at the four extremities. The bearing cups are attached to yokes, two on the input shaft and two on the output shaft. The universal joint is not a constant velocity joint. If the input and output shafts are not aligned, the uniform rotation of the input shaft will result in a nonuniform rotation of the output shaft. When the input shaft is rotated at constant velocity, the output shaft will accelerate and decelerate twice per revolution (a pulsation effect).

The driveshaft mechanism in this example problem consists of three shafts, **SHAFT AB** (the input shaft), **SHAFT CD** (the center shaft), and **SHAFT EF** (the output shaft). **SHAFT AB** is connected to **SHAFT CD** through a universal joint that connects B and C. **SHAFT CD** is connected to **SHAFT EF** through a universal joint that connects D and E. B31 beam elements are used to model the shafts. **SHAFT AB** and **SHAFT EF** have a length of 7 units each, and **SHAFT CD** is 10 units long. **SHAFT AB** and **SHAFT EF** are coplanar and parallel to each other. **SHAFT CD** is also coplanar to **SHAFT AB** and **SHAFT EF** but is inclined to **SHAFT AB** and **SHAFT EF** at an angle of 20 degrees. **SHAFT AB**, **SHAFT CD**, and **SHAFT EF** are circular in cross-section; and the radius of their cross-section is 0.1 units. The universal joints connecting B and C and connecting D and E are modeled using CONN3D2 elements.

The variation of angular motion between the input and output shafts can be avoided. The pulsation effect between the input shaft and the center shaft can be compensated entirely by the pulsation effect between the center shaft and the output shaft if the universal joints are oriented properly with respect to each other. A sufficient condition for the input/output velocity ratio to be constant is that the directions normal to the crosses of the universal joints be colinear. The configuration of the shafts is illustrated in Figure 4.1.7–2. In this figure we can see that the crosses lie in parallel planes. This will guarantee a constant input/output velocity ratio.

Model interactions

All the degrees of freedom except the rotational degree of freedom about the beam axis are fixed at A and F. A prescribed rotation of 360 degrees is specified at A. No other boundary conditions are specified. The bodies in Figure 4.1.7–2 are connected as follows:

- **SHAFT AB** is connected to **SHAFT CD** with a UJOINT connector element (Joint 1).
- **SHAFT CD** is connected to **SHAFT EF** with a UJOINT connector element (Joint 2).

Because the rotary motion of one shaft is to be transmitted to another shaft that is not colinear, separate coordinate orientation systems are created and used to connect the connector nodes for each UJOINT connector connecting the shafts. The coordinate systems used to define Joint 2 are the systems used to define Joint 1 rotated by 90 degrees about the global 1-axis. This ensures proper orientation of the joint crosses and a constant input/output velocity ratio. Separate models for Abaqus/Standard and Abaqus/Explicit include friction in the connectors.

Results and discussion

The rotation of **SHAFT AB** about its axis leads to a rotation of **SHAFT EF** about its axis. The rotation of the input and output shafts about their axis is plotted in Figure 4.1.7–3. We can see that the motion of these shafts is perfectly synchronized.

Input files

driveshaft_model.py	Python replay file for constructing the driveshaft mechanism model in Abaqus/CAE.
driveshaft.inp	Abaqus/Standard driveshaft mechanism model.
driveshaft_fric.inp	Abaqus/Standard driveshaft mechanism model with friction.
driveshaft_exp_fric.inp	Abaqus/Explicit driveshaft mechanism model with friction.

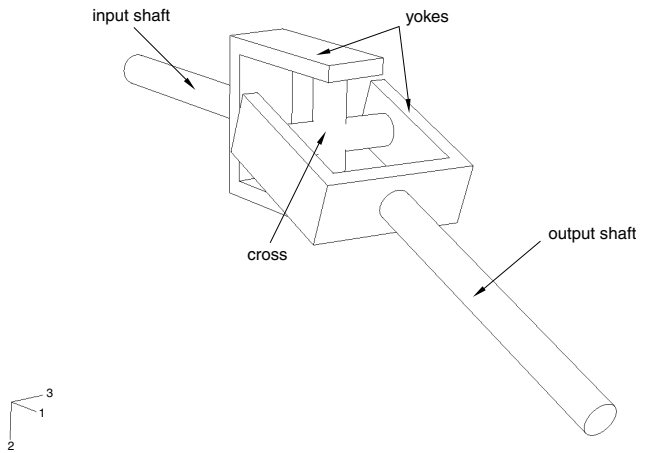

Figure 4.1.7–1 Universal joint.

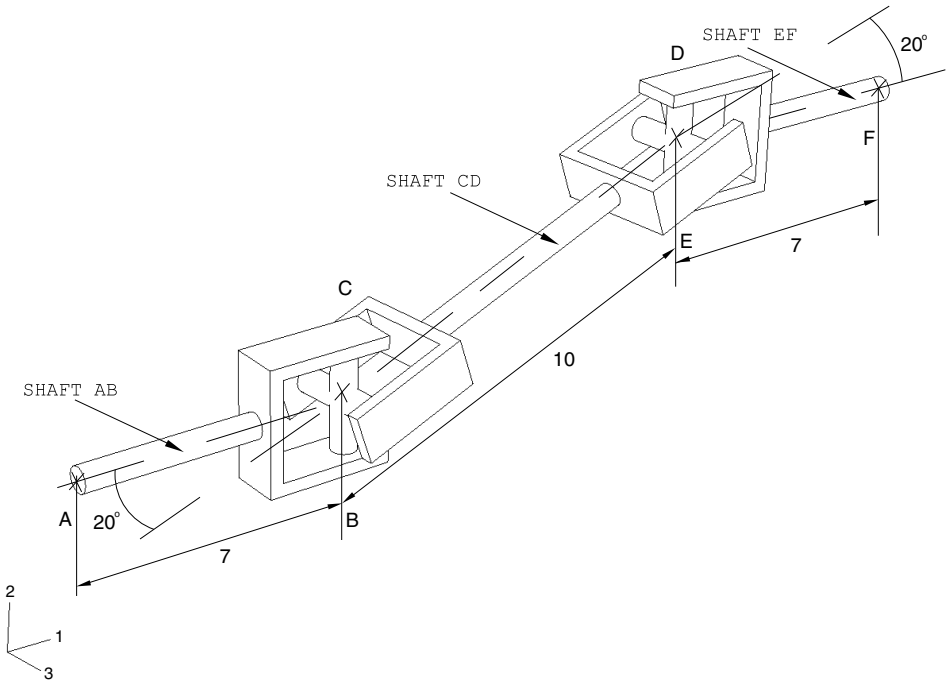

Figure 4.1.7–2 Configuration of the driveshaft mechanism.

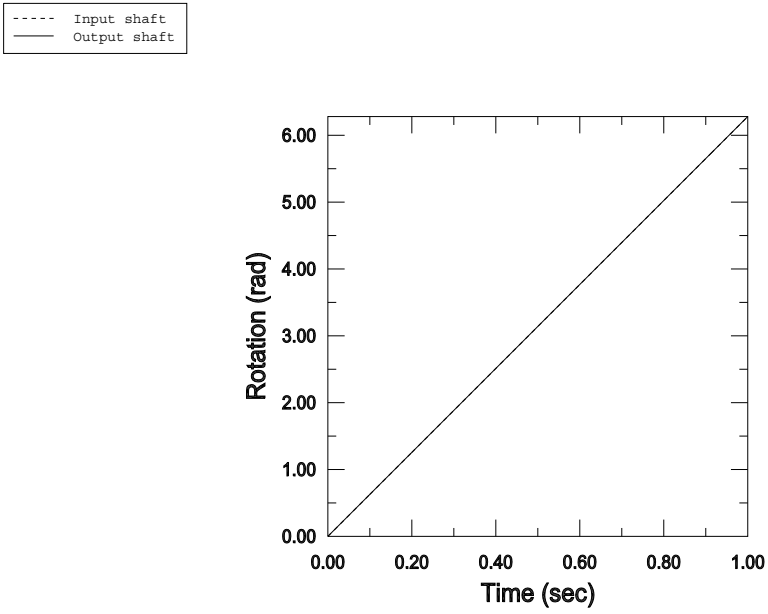

Figure 4.1.7–3 Rotation of the input and output shafts about the global 1-axis.

4.1.8 GENEVA MECHANISM

Product: Abaqus/Standard

This example illustrates the use of connector elements to model a Geneva mechanism, which converts continuous rotary motion into intermittent rotary motion.

The Geneva mechanism is essentially a timing device. It is used in counting instruments and other applications where a continuous rotary motion needs to be converted to an intermittent rotary motion. For example, it is used in clocks to limit the number of winding rotations of the clock spring and in movie film projectors to move the film frame by frame. The Geneva mechanism consists of a rotating body with a protruding pin and another rotating body with slots into which the pin slides.

Geometry and model

In this example problem the mechanism consists of three bodies named **PIN**, **SLOT1**, and **SLOT2**, as illustrated in Figure 4.1.8–1. **SLOT1** is an analytical rigid surface that overlays **SLOT2**. **SLOT2** is modeled as a display body. **SLOT1** and **SLOT2** are rigidly joined to each other at point A so as to allow them to rotate in unison about A. **SLOT2** has a radius of 3.0 units and is 1.0 units thick. The pin is constrained to be rigid. The thickness of the rigid part of **PIN** is 0.5 units. The rigid portion of **PIN** has a reference point B, and **PIN** is allowed to rotate about B. Distance AB is 4.24264 units in the model. The protruding portion of **PIN** is located at a distance of 3.0 units from reference point B, and its length is 1.0 units. The rigid portion of **PIN** has a radius of 3.0 units.

Model interactions

The contact between **PIN** and **SLOT1** takes place through a single slave node located at C, the center of the protruding portion of **PIN**. As a result, the slots in **SLOT1** (used for contact evaluation) are 0.05 units wide, whereas the slots in **SLOT2** (used for display purposes only) are 0.25 units wide. The slots have a length of about 2.0 units to allow for the pin to slide. This contact is considered to be frictionless.

All the degrees of freedom at A and B, except the rotational degrees of freedom about the 3-axis, are fixed. A rotation of 720 degrees about the 3-axis is prescribed at B over three steps.

An EULER connector is constructed connecting A, the reference point of **SLOT1**, to the ground. The connector damping and connector friction behaviors are used to introduce damping and friction in the EULER connector. Damping and friction will prevent rigid body motion of **SLOT1** and **SLOT2** after the pin has left the slot.

Results and discussion

The protruding portion of **PIN** enters the slots in **SLOT1** as **PIN** is rotated. This interaction between **PIN** and **SLOT1** results in the rotation of **SLOT1** and **SLOT2**, and they rotate 90 degrees for every complete 360 degree rotation of **PIN**. Figure 4.1.8–2 shows the configuration of the bodies of the Geneva mechanism at some intermediate instants during the analysis. Figure 4.1.8–3 shows a plot of the U3 rotation of **SLOT1** at A as a function of the U3 rotation of **PIN** at B.

Input files

geneva_model.py	Python replay file for constructing the Geneva mechanism model in Abaqus/CAE.
geneva.inp	Geneva mechanism model.

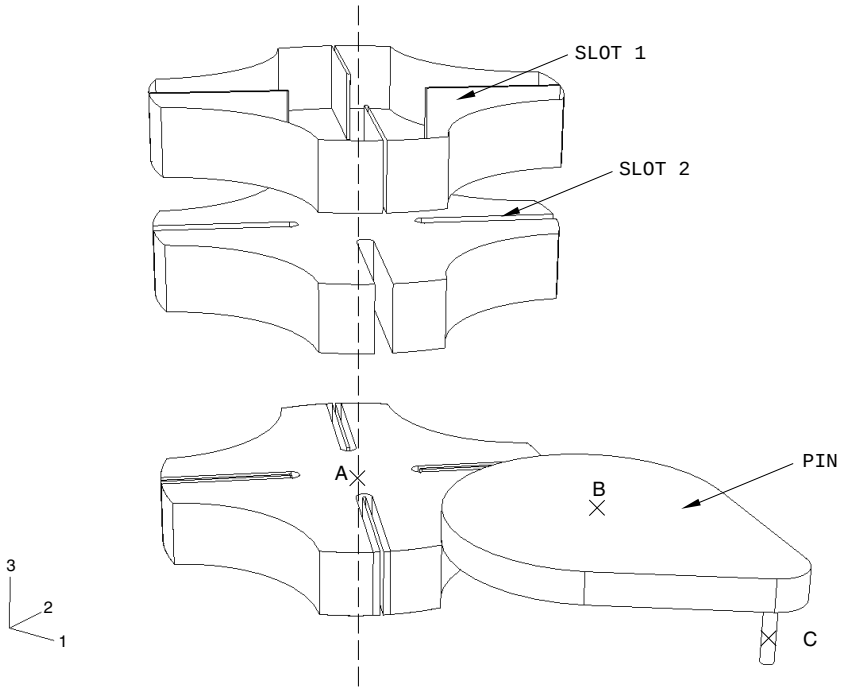

Figure 4.1.8–1 Exploded view of the Geneva mechanism.

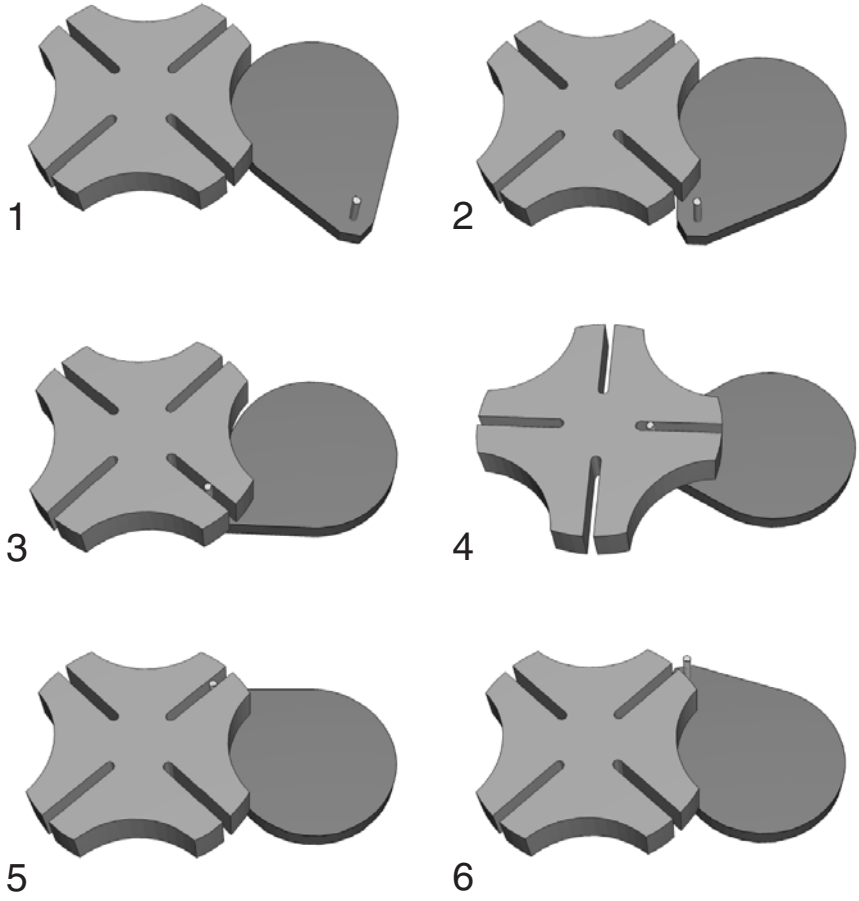

Figure 4.1.8–2 Configurations of the Geneva mechanism for increasing values of **`PIN`** rotation.

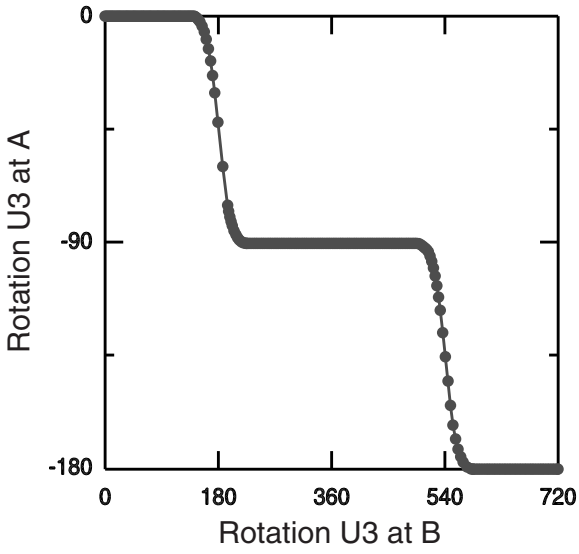

Figure 4.1.8–3 Plot of the U3 rotation of **SLOT1** at A as a function of the U3 rotation of **PIN** at B. Rotation values are in degrees.

4.1.9 TRAILING EDGE FLAP MECHANISM

Product: Abaqus/Standard

This example illustrates the use of connectors to model the deployment of a trailing edge flap mechanism in an aircraft.

Geometry and model

The trailing edge flap mechanism is a critical component of an aircraft. The shape and positioning of the trailing edge flaps are important determinants of the aircraft's lift and aerodynamic behavior.

The trailing edge flap structure in this example problem consists of three flaps, **BASE**, **MIDFLAP**, and **ENDFLAP**; and these flaps are connected to each other by arms, which are rigid links pinned to the flaps at different points. The configuration of the flaps is illustrated in Figure 4.1.9–1. There are nine arms used in the model: **ARM AB**, **ARM BF**, **ARM DEFG**, **ARM EI**, **ARM HIM**, **ARM JK**, **ARM MLJ**, **ARM NK**, and **ARM PO**. **BASE**, **MIDFLAP**, and **ENDFLAP** are modeled as display bodies; and the arms are modeled as rigid truss members. **MIDFLAP** and **ENDFLAP** are deployed by rotating **ARM AB** pinned on **BASE** at point A.

Model interactions

The bodies in Figure 4.1.9–1 are connected as follows:

- JOIN connector elements are used to connect the arms at their endpoints to **BASE**, **MIDFLAP**, and **ENDFLAP**. The endpoints of some arms are connected to other arms instead of being connected to the flaps. **ARM AB** is connected to **ARM BF** at B. **ARM BF** and **ARM EI** are connected to **ARM DEFG** at F and E, respectively. **ARM EI** and **ARM MLJ** are connected to **ARM HIM** at I and M, respectively. **ARM MLJ** is connected to **ARM JK** at J, and **ARM MLJ** is connected to **MIDFLAP** at L, which is not one of the endpoints of **ARM MLJ**.
- LINK connector elements are used to rigidly fix the positions of the pivot points on the flaps. These link connectors are called **LINK GL**, **LINK GN**, **LINK GP**, **LINK KO**, **LINK LN**, and **LINK LP**. These additional link connectors are necessary to support **BASE**, **MIDFLAP**, and **ENDFLAP** because these flaps are modeled as display bodies and not as deformable or rigid bodies. **LINK GL**, **LINK GN**, **LINK GP**, **LINK LN**, and **LINK LP** are used to position points G, L, N, and P on **MIDFLAP**; and **LINK KO** is used to position points K and O on **ENDFLAP**.

To deploy the flap, we fix **BASE** in space by fixing points A, D, and H and rotate **ARM AB** 90 degrees about point A. One analysis models plasticity effects in some of the connectors.

Results and discussion

The rotation of **ARM AB** results in the deployment of **MIDFLAP** and **ENDFLAP**. Figure 4.1.9–2 contains a series of illustrations showing the positions of the flaps at the beginning and end of the analysis and also at some intermediate instants.

Input files

edgeflap_model.py	Python replay file for constructing the trailing edge flap mechanism model in Abaqus/CAE.
edgeflap.inp	Trailing edge flap mechanism model.
edgeflap_plas.inp	Trailing edge flap mechanism model with connector plasticity.

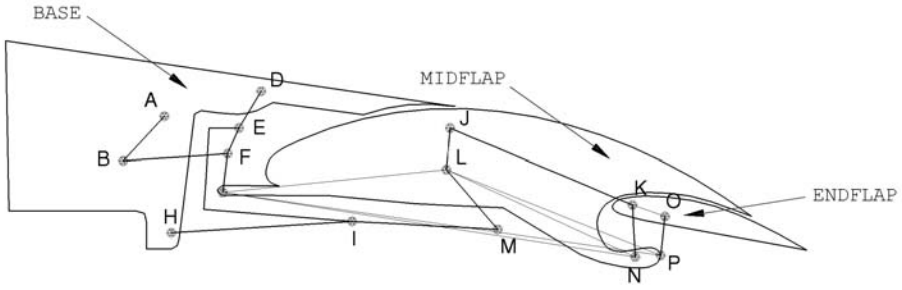

Figure 4.1.9–1 Undeformed configuration of the trailing edge flap mechanism.

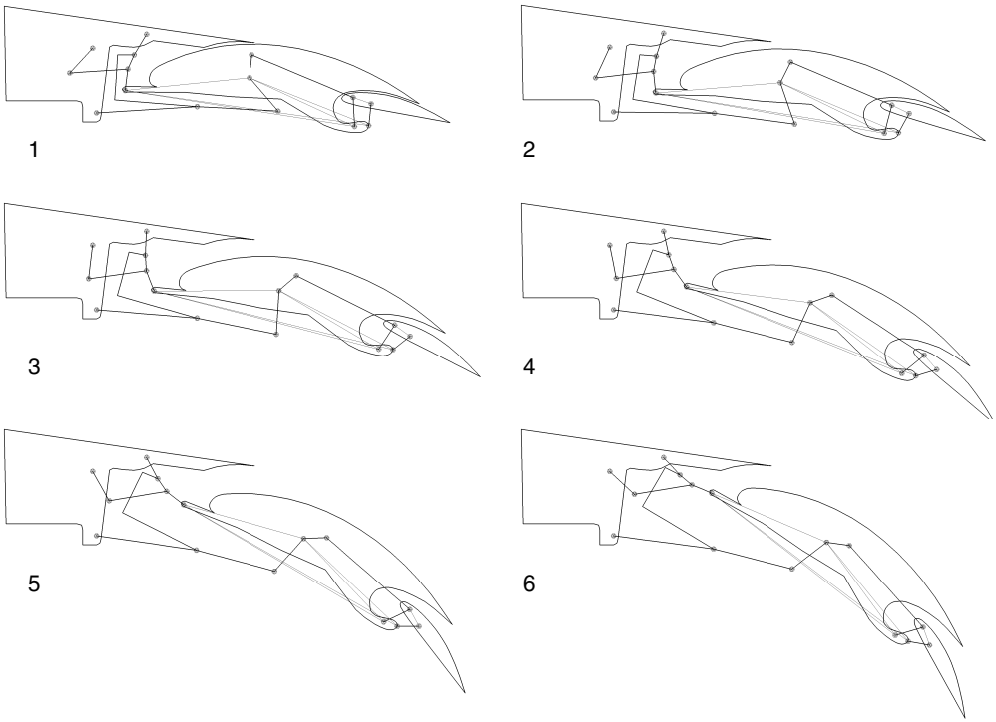

Figure 4.1.9–2 Deformed configurations of the trailing edge flap mechanism.

4.1.10 SUBSTRUCTURE ANALYSIS OF A ONE-PISTON ENGINE MODEL

Product: Abaqus/Standard

This example illustrates the use of the substructure capability in Abaqus to model efficiently multi-body systems that undergo large motions but exhibit only small linear deformations.

The example illustrates how to switch between a full-mesh representation of a part, a substructure representation, and a rigid body representation of the same part depending on the modeling needs. Both static and dynamic analyses are performed, and the results are compared between the various models.

Geometry and material

The multi-body system discussed here is the simplified one-piston engine model depicted in Figure 4.1.10–1 and in the detail shown in Figure 4.1.10–2. The model consists of several parts that are constrained together using connector elements. Each part is modeled either as a fully deformable regular mesh, a rigid body, or a substructure. The connections between parts are idealized using coupling constraints and connector elements. On each part a coupling constraint is used to constrain a few nodes near the connection points so that the connection forces get distributed to a finite area, much like in the physical model. The reference nodes in the coupling constraint are then used to define appropriate connector elements between neighboring parts that enforce the desired kinematic linkage between bodies.

The two parts of the crankshaft are rigidly connected using a BEAM connector element. The connecting rod between the crankshaft and the piston's head has HINGE connections at both ends. The gear transmission (2:1 gear ratio) between the crankshaft and the valve-cam is modeled using an equation constraint between two rotational degrees of freedom. An analytically defined rigid surface is used to model the contact surface of the cam. This surface is rigidly attached to the larger gear used to spin the cam. The contact between the cam followers and the cam is modeled using a single node on each cam follower's tip defined using a node-based surface. The connections between cam followers and push rods and between push rods and valve rockers are modeled using JOIN connectors. The valve rockers use HINGE connections about fixed points in space (the engine block is not modeled). The valve rockers are pushing against the spring loaded valves. The valve springs are precompressed and are defined using CARTESIAN connectors together with the reference lengths and angles for constitutive response and the connector elasticity behavior. The valve seats and the cylinders are not modeled. Steel material properties are used for all parts. The model is actuated by fixing the available components of relative motion to spin the right end of the crankshaft for a little more than two full revolutions. In some of the analyses the connector friction behavior is used to model frictional effects in the connector elements. Plasticity effects are specified in connectors in some of the analyses.

Models

The following three models are considered:

1. All parts are modeled using regular meshes (no substructures or rigid bodies). This is the largest model and could include the most modeling options, including nonlinear material modeling options (e.g., plasticity), if desired. A large computation time is needed to complete the analysis.
2. All parts are modeled as rigid bodies. While much less computational time is needed to complete this analysis, this model cannot compute stresses in the various parts. However, it reveals very useful information about the overall kinematics/dynamics of the model. Reaction forces at support points and connector output variables (such as connector reaction forces or elastic forces in the valve springs) are also predicted accurately.
3. Some parts (crankshaft, connection rod, piston head, cam, and cam followers) are modeled as substructures. The remainder of the parts (push rods, valve rockers, and valves) are modeled as rigid bodies. This model is very efficient in obtaining both overall kinematic/dynamic information as well as the stresses and strains in the selected parts.

The input files are organized so that one can very easily switch (just by changing a few lines) between the different models.

Before the global analysis can be run, the substructure for each part must be generated. To minimize the computational effort in the global analysis, the minimum necessary number of retained nodal degrees of freedom is chosen. The reference nodes of all coupling constraints must be retained since the parts are connected through these nodes. In addition, since the parts will undergo large rotations during the analysis, at least three nonaligned nodes must be retained at the substructure generation level to allow for the precise calculation of the rigid body motion of each part (see "Defining substructures," Section 10.1.2 of the Abaqus Analysis User's Guide). Since for most parts only two nodes in the coupling constraint are defined (most parts are connected at only two points), an additional node not aligned with the nodes in the coupling constraint is also retained for most substructures. Because of the small number of retained nodes the global analysis is very efficient. For these particular choices it runs faster than the model when all parts are modeled as rigid.

The reduced mass matrix for each substructure is generated by selecting the eigenmodes during the substructure generation. To improve the representation of the substructure's dynamic behavior in the global analysis, six dynamic modes, which are extracted using an eigenfrequency extraction preload step, are included during the substructure generation during eigenmode selection. The substructures are loaded by gravity in the vertical direction by requesting that the substructure's gravity load vectors be calculated during penetration and by specifying a distributed load at the substructure usage level.

Results and discussion

Both static and direct-integration implicit dynamic analyses are conducted. The vertical displacements of the valves and the contact forces on the cam followers are monitored.

In Figure 4.1.10–3 the vertical displacement of the valve on the left is depicted for a static analysis. The valve descends ("opens") in the beginning of the cycle and then "closes" for most of the analysis. Since the crankshaft rotates a little more than two revolutions, the valve starts opening again in the end. The normal contact force between the left cam follower and the cam is shown in Figure 4.1.10–4. A sharp peak is encountered when the valve "opens," while the contact force stays constant when the valve is "closed." Since the valve seats are not modeled, the "closed" positions for the rigid body model and for

the substructure model are slightly different due to elastic deformation of the cam followers in the latter case. The stresses in the left cam follower are depicted in Figure 4.1.10–5 for an intermediate position of the crankshaft. The stresses are recovered when output is obtained from the substructure.

Since the inertia forces of the moving parts are relatively small when compared to the compression forces in the valve springs, the contact forces and the valve displacements in the direct-integration implicit dynamic analyses are similar to those in the static analysis. However, if the valve spring stiffness is chosen to be very small (such as would happen if the spring failed), the inertial effects become very important and contact between the cam and the cam follower could be lost. In Figure 4.1.10–6 the valve displacement is depicted for such a case. Contact is established only intermittently between the two parts (corresponding to zero valve displacement). For most of the time the two parts are not contacting each other, and the valve displacement is completely different from the intended behavior.

The **abaqus substructurecombine** execution procedure combines model and results data from two substructure output databases into a single output database. For more information, see "Combining output from substructures," Section 3.2.24 of the Abaqus Analysis User's Guide.

Input files

crank_substr_sta.inp	*STATIC substructure global analysis.
crank_substr_dyn.inp	*DYNAMIC substructure global analysis.
crank_substr_sta_fric.inp	*STATIC substructure global analysis with frictional effects.
crank_substr_dyn_fric.inp	*DYNAMIC substructure global analysis with frictional effects.
crank_substr_dynimp.inp	*DYNAMIC substructure impact analysis (softer valve springs).
crank_rb_sta.inp	*STATIC analysis with rigid bodies only (no substructures).
crank_all_def_sta.inp	*STATIC regular mesh analysis.
crank_all_def_dyn.inp	*DYNAMIC regular mesh analysis.
crank_shaft_gen.inp	Substructure generation for the right half of the shaft.
crank_shaft2_gen.inp	Substructure generation for the left half of the shaft.
crank_conrod_gen.inp	Substructure generation for the connection rod.
crank_head_gen.inp	Substructure generation for the piston's head.
crank_cam_gen.inp	Substructure generation for the cam.
crank_camfollow1_gen.inp	Substructure generation for the first cam follower.
crank_camfollow2_gen.inp	Substructure generation for the second cam follower.
crank_conn_gr_ref_nodes.inp	Connector, ground, and reference node definitions.
crank_small_mass.inp	Small masses used to avoid numerical singularities in *DYNAMIC analyses.
crank_materials.inp	Material properties.
crank_shaft_nodes.inp	Node definitions for the right half of the shaft.
crank_shaft_elts.inp	Element definitions for the right half of the shaft.
crank_shaft_coupling.inp	*COUPLING definitions for the right half of the shaft.

crank_shaft2_nodes.inp	Node definitions for the left half of the shaft.
crank_shaft2_elts.inp	Element definitions for the left half of the shaft.
crank_shaft2_coupling.inp	*COUPLING definitions for the left half of the shaft.
crank_conrod_nodes.inp	Connecting rod node definitions.
crank_conrod_elts.inp	Connecting rod element definitions.
crank_conrod_coupling.inp	Connecting rod *COUPLING definitions.
crank_head_nodes.inp	Piston head node definitions.
crank_head_elts.inp	Piston head element definitions.
crank_head_coupling.inp	Piston head *COUPLING definitions.
crank_cam_nodes.inp	Cam node definitions.
crank_cam_elts.inp	Cam element definitions.
crank_cam_coupling.inp	Cam *COUPLING definitions.
crank_camfollow1_nodes.inp	Node definitions for the first cam follower.
crank_camfollow1_elts.inp	Element definitions for the first cam follower.
crank_camfollow1_coupling.inp	*COUPLING definitions for the first cam follower.
crank_camfollow2_nodes.inp	Node definitions for the second cam follower.
crank_camfollow2_elts.inp	Element definitions for the second cam follower.
crank_camfollow2_coupling.inp	*COUPLING definitions for the second cam follower.
crank_valves_nodes.inp	Node definitions for the crank valves.
crank_valves_elts.inp	Element definitions for the crank valves.
crank_valvelifters_nodes.inp	Node definitions for the crank valve lifters.
crank_valvelifters_elts.inp	Element definitions for the crank valve lifters.
crank_tierods_nodes.inp	Node definitions for the tie rods.
crank_tierods_elts.inp	Element definitions for the tie rods.

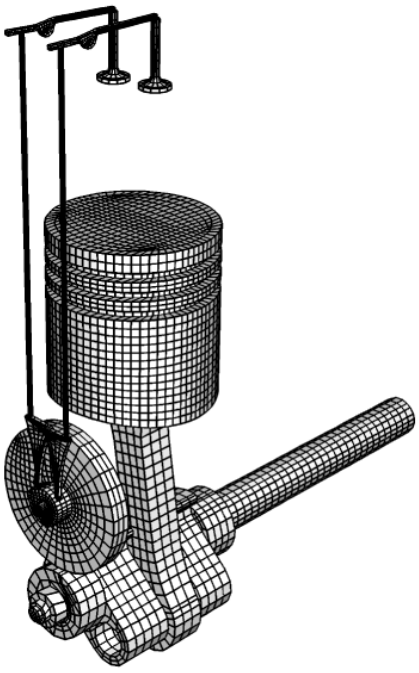

Figure 4.1.10–1 Mesh used for the complete one-piston model.

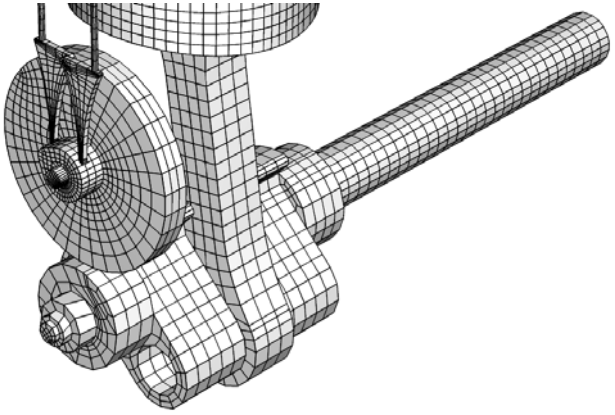

Figure 4.1.10–2 Detail of the mesh used for the one-piston model.

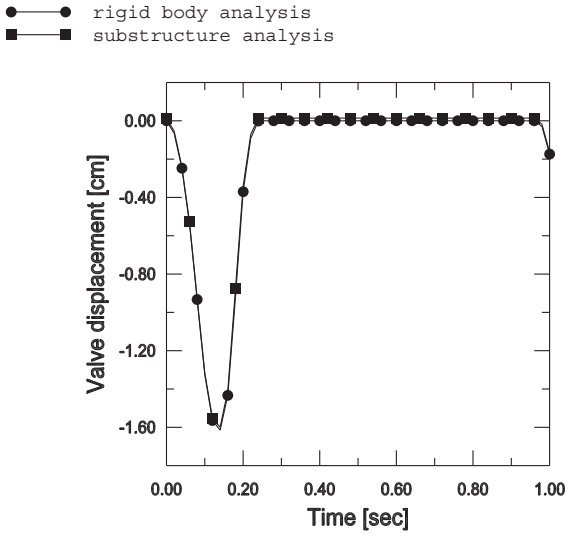

Figure 4.1.10–3 Valve displacement in static analyses.

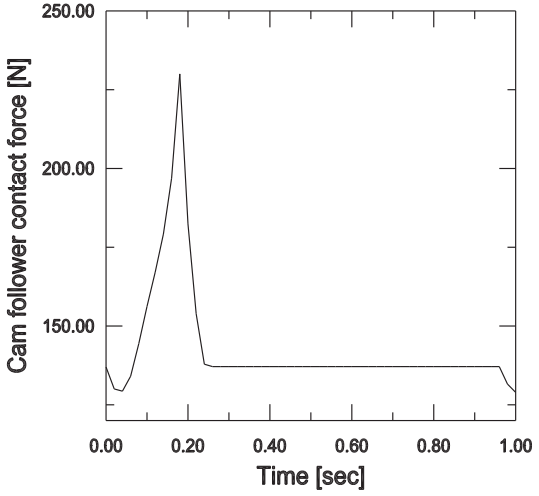

Figure 4.1.10–4 Cam follower contact force in a substructure static analysis.

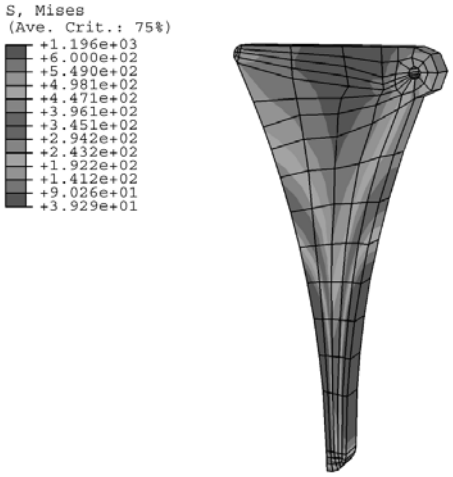

Figure 4.1.10–5 Cam follower stresses in a substructure static analysis.

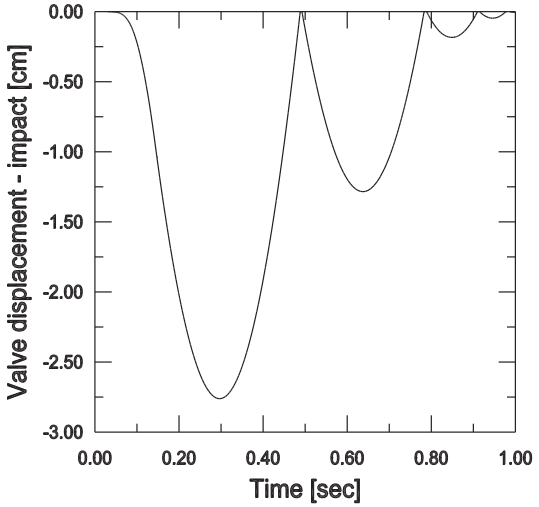

Figure 4.1.10–6 Valve displacement in a substructure direct-integration implicit dynamic analysis with very soft valve spring stiffness.

4.1.11 APPLICATION OF BUSHING CONNECTORS IN THE ANALYSIS OF A THREE-POINT LINKAGE

Products: Abaqus/Standard Abaqus/Explicit

This example illustrates the use of detailed finite element bushing models to calibrate the constitutive behavior of bushings (when experimental data for a particular bushing design are not available) so that a very inexpensive 2-node connector element representation of the bushing can be used in subsequent analyses involving the bushing.

The approach shown in this example is effective in reducing computational costs in assembly models while accurately capturing the macroscopic response of the bushing. To demonstrate this approach, a three-point linkage is simulated with connector elements used to model bushings.

Geometry and materials

The geometry of the three-point linkage (TPL) is shown in Figure 4.1.11–1. Since the main focus of this example is to illustrate modeling of the bushings, a simplified representation of the TPL is used. The TPL is connected to the subframe (assumed fixed in space) via the front and rear bushings. A ball joint connects the TPL to a wheel assembly (not shown). The TPL is a steel shell structure and is modeled as a linear elastic material with Young's modulus of 2.1×10^5 MPa, Poisson's ratio of 0.3, and a density of 7.82×10^{-9} tonnes/mm^3.

As shown in Figure 4.1.11–2, the rear bushing is a hollow cylinder with a rubber portion enclosed between two (inner and outer) thin steel tubes. The rubber portion has two symmetrically placed cutouts of different sizes, and it is rigidly bonded to the steel tubes. The steel tubes are 2 mm thick and use the same material properties as the TPL. The inner diameter of this bushing is 28 mm, the outer diameter is 72 mm, and the axial length is 20 mm. The outer steel tube is connected to the TPL using a kinematic coupling. The inner tube is connected to a fixed node that represents a subframe using a distributed coupling. The rubber is modeled as a second-order Ogden hyperelastic material ("Hyperelastic behavior of rubberlike materials," Section 22.5.1 of the Abaqus Analysis User's Guide), which may undergo nonlinear, finite deformation. The material parameters are $\mu_1 = 1.671$, $\alpha_1 = 9.0067$, $\mu_2 = 2.154\text{E}{-4}$, $\alpha_2 = -4.86970$, $D_1 = 1.0$, and $D_2 = 1.0$. The material density is 1.5×10^{-9} tonnes/mm^3.

The geometry of the front bushing is shown in Figure 4.1.11–3; it consists of three noncoaxial steel tubes with two rubber parts between them. The axial length of the bushing is 40 mm. The outer diameters of the three tubes are 40 mm, 28 mm, and 16 mm. All three tubes have a thickness of 1 mm. The outer steel tube is connected to the TPL using a kinematic coupling. The inner tube is connected to a fixed node that represents a U-shaped bracket. The front bushing uses the same rubber and steel materials as those used for the rear bushing.

Models

To characterize the nonlinear constitutive behavior of the bushings, a series of static analyses of the front bushing are performed in Abaqus/Standard and a series of quasi-static analyses of the rear bushing

are performed in Abaqus/Explicit. Self-contact occurs in the rear bushing analyses due to severe deformation. In all cases the reference node of the kinematic coupling connected to the outer steel tube is held fixed in all degrees of freedom, while the second reference node connected to the inner tube moves. For the calibration analyses, a BUSHING connector for which no constitutive behavior is defined is placed between the two reference nodes. The use of a BUSHING connector to drive the deformation in these models is desirable since this choice ensures appropriate kinematic and kinetic modeling when the connector is used in other models (such as a full-system analysis). Since the main interest is capturing the hyperelastic response of the rubber bushings, both unidirectional and coupled multidirectional tests (simultaneous deformations in up to three directions) are performed as summarized below.

To analyze several loading conditions, some connector components of relative motion can be fixed and others can be prescribed nonzero motion. The reaction forces and relative motions in the connector are saved as history output. The data from these analyses are then used in a subsequent analysis of the three-point linkage assembly to define nonlinear connector elasticity data.

Front bushing calibration tests

For the front bushing, static analyses are performed in Abaqus/Standard as follows:

Test 1_FB:

A translational motion is applied in the local 1-direction with all other relative motions fixed. The motion is applied in the positive and negative directions separately since the front bushing is not symmetric with respect to the local 1-axis. The magnitude of this motion is 5 mm. The CRF1 vs. CU1 data generated from this analysis are used to define nonlinear elasticity data for component 1.

Test 2_FB:

A translational motion is applied in the local 2-direction with all other relative motions fixed. The magnitude of this motion is 5 mm. The CRF2 vs. CU2 data generated from this analysis are used to define nonlinear elasticity data for component 2.

Test 3_FB:

A translational motion is applied in the local 3-direction with all other relative motions fixed. The magnitude of this motion is 5 mm. The CRF3 vs. CU3 data generated from this analysis are used to define nonlinear elasticity data for component 3.

Test 4_FB:

A 5° "bending" rotational motion about the local 1-direction is applied with all other relative motions fixed. The CRM1 vs. CUR1 data generated from this analysis are used to define nonlinear elasticity data for component 4.

Test 5_FB:

A 5° "bending" rotational motion about the local 2-direction is applied with all other relative motions fixed. The CRM2 vs. CUR2 data generated from this analysis are used to define nonlinear elasticity data for component 5.

Test 6_FB:

A 15° "twisting" rotational motion about the local 3-direction is applied with all other relative motions fixed. The CRM3 vs. CUR3 data generated from this analysis are used to define nonlinear elasticity data for component 6.

Test 7_FB:

A 5 mm displacement along the local 3-direction is applied about three preloaded configurations. The test attempts to capture coupling effects in the bushing after complex deformation is achieved. The preloaded configurations are:

1. A twisting of 0º about the local 3-direction.
2. A twisting of 7.5º about the local 3-direction.
3. A twisting of 15º about the local 3-direction.

This test is a collection of three two-step analyses. In each of the analyses a preload motion is applied in the first step, and the bending motion is applied in the second step. Assuming a hyperelastic-like quasi-static response in the bushing, for a given final coupled deformation, the deformation path is not relevant. Hence, the prestress and the actual loading steps can be run sequentially. The sets of CRF3 vs. CU3 data generated from the second steps of these analyses are used to define elasticity data for component 3 using independent component 6.

Test 8_FB:

A 5° bending motion about the local 2-direction is applied about three preloaded configurations. The test attempts to capture coupling effects in the bushing after complex deformation is achieved. The preloaded configurations are:

1. A twisting of 0º about the local 3-direction.
2. A twisting of 7.5º about the local 3-direction.
3. A twisting of 15º about the local 3-direction.

This test is a collection of three two-step analyses. In each of the analyses a preload motion is applied in the first step, and the bending motion is applied in the second step. Assuming a hyperelastic-like quasi-static response in the bushing, the deformation path is not relevant for a given final coupled deformation. Hence, the prestress and the actual loading steps can be run sequentially. The sets of CRM2 vs. CUR2 data generated from the second steps of these analyses are used to define elasticity data for component 5 using independent component 6.

Force vs. displacement and moment vs. rotation curves are shown in Figure 4.1.11–4 for the cases without preload (Tests 1_FB to 6_FB) and in Figure 4.1.11–5 for the cases with preload (Tests 7_FB and 8_FB).

Script files were generated to automatically create the input files and run the analyses for the uncoupled tests and each of the coupled tests. These scripts essentially build up a CROSS design parametric study for the uncoupled tests and a MESH design for the coupled tests (see "Scripting parametric studies," Section 20.1.1 of the Abaqus Analysis User's Guide).

Rear bushing calibration tests

For the rear bushing, quasi-static analyses are performed in Abaqus/Explicit as follows:

Test 1_RB:

A translational motion is applied in the local 1-direction with all other relative motions fixed. The magnitude of this motion is 10 mm. The CRF1 vs. CU1 data generated from this analysis are used to define nonlinear elasticity data for component 1.

Test 2_RB:

A translational motion is applied in the local 2-direction with all other relative motions fixed. The magnitude of this motion is 5 mm. The CRF2 vs. CU2 data generated from this analysis are used to define nonlinear elasticity data for component 2.

Test 3_RB:

A translational motion is applied in the local 3-direction with all other relative motions fixed. The magnitude of this motion is 5 mm. The CRF3 vs. CU3 data generated from this analysis are used to define nonlinear elasticity data for component 3.

Test 4_RB:

A 5° "bending" rotational motion about the local 1-direction is applied with all other relative motions fixed. The CRM1 vs. CUR1 data generated from this analysis are used to define nonlinear elasticity data for component 4.

Test 5_RB:

A 15° "bending" rotational motion about the local 2-direction is applied with all other relative motions fixed. The CRM2 vs. CUR2 data generated from this analysis are used to define nonlinear elasticity data for component 5.

Test 6_RB:

A 5° "twisting" rotational motion about the local 3-direction is applied with all other relative motions fixed. The CRM3 vs. CUR3 data generated from this analysis are used to define nonlinear elasticity data for component 6.

Test 7_RB:

A 10 mm displacement in the local 1-direction is applied about several preloaded configurations. The displacement is applied in the positive and negative directions separately since the rear bushing is not symmetric with respect to the local 1-axis. The test attempts to capture coupling effects in the bushing after complex deformation is achieved. The preloaded configurations are a combination of a displacement in the local 2-direction and a rotation about the local 2-direction for which the following design points were selected:

1. A displacement of 0.0 mm in the local 2-direction.
2. A displacement of 2.5 mm in the local 2-direction.

3. A displacement of 5.0 mm in the local 2-direction.
4. A 0° “bending” rotational motion about the local 2-direction.
5. A 7.5° “bending” rotational motion about the local 2-direction.
6. A 15° “bending” rotational motion about the local 2-direction.

This test is a collection of 18 two-step analyses. In each of the analyses two preload motions are applied in the first step, and the translational motion in the local 1-direction is applied in the second step. Assuming a hyperelastic-like quasi-static response in the bushing, the deformation path is not relevant for a given final coupled deformation. Hence, the prestress and the actual loading steps can be run sequentially. The sets of CRF1 vs. CU1 data generated from the second steps of these analyses are used to define elasticity data for component 1 using independent components 2 and 5.

Test 8_RB:

A 5 mm displacement in the local 2-direction is applied about several preloaded configurations. The test attempts to capture coupling effects in the bushing after complex deformation is achieved. The preloaded configurations are a combination of a displacement in the local 1-direction (positive and negative loadings are considered separately due to asymmetry) and a rotation about the local 2-direction, for which the following design points were selected:

1. A displacement of –10.0 mm in the local 1-direction.
2. A displacement of –5.0 mm in the local 1-direction.
3. A displacement of 0.0 mm in the local 1-direction.
4. A displacement of 5.0 mm in the local 1-direction.
5. A displacement of 10.0 mm in the local 1-direction.
6. A 0° “bending” rotational motion about the local 2-direction.
7. A 7.5° “bending” rotational motion about the local 2-direction.
8. A 15° “bending” rotational motion about the local 2-direction.

This test is a collection of 15 two-step analyses. In each of the analyses two preload motions are applied in the first step, and the translational motion in the local 2-direction is applied in the second step. Assuming a hyperelastic-like quasi-static response in the bushing, the deformation path is not relevant for a given final coupled deformation. Hence, the prestress and the actual loading steps can be run sequentially. The sets of CRF2 vs.CU2 data generated from the second steps of these analyses are used to define elasticity data for component 2 using independent components 1 and 5.

Force vs. displacement and moment vs. rotation curves are shown in Figure 4.1.11–6 for the cases without preload (Tests 1_RB to 6_RB). Figure 4.1.11–7 shows a comparison of the force vs. displacement with no preload and with the most extreme preload conditions for Tests 7_RB and 8_RB.

Script files were generated to automatically create the input files and run the analyses for the uncoupled tests and each of the coupled tests. As in the case of the front bushing, these scripts essentially build up a CROSS design parametric study for the uncoupled tests and a MESH design for the coupled tests. Furthermore, Python files were created to automatically gather the force vs. displacement data points and to create corresponding report files.

Additional comments on calibration tests

Since each bushing has several symmetry planes, the tests above (unless specified otherwise) are conducted only for positive relative motions when the responses in the opposite directions are symmetric. Therefore, nonlinear elasticity data are generated only for positive relative motions for those cases. Nonlinear elasticity is defined for negative relative motions by symmetrizing the elasticity data with respect to the origin.

The analyses chosen above are deemed appropriate to generate the necessary and complete nonlinear elasticity data to enable BUSHING connectors to represent the front and rear bushings in subsequent analyses of the TPL. The quasi-static analyses were run over sufficiently large motion ranges to cover the motion range expected in the analysis where the BUSHING connector is used. Nonlinear elasticity data are generated in all six relative uncoupled directions in the BUSHING connector. For the front bushing, elasticity data are generated (Tests 7_FB and 8_FB) for two coupled deformation modes (involving two components of local motion each) that were thought to be the dominant coupling modes in the subsequent analysis where the BUSHING connectors are used. For the rear bushing, elasticity data are generated (Tests 7_RB and 8_RB) for two coupled deformation modes (involving three components of local motion each) that were thought to be the dominant coupling modes in the subsequent analysis where the BUSHING connectors are used. In general, the number and complexity of coupled deformation tests can be increased to match any particular modeling needs.

TPL models

Three different models are created for the analysis of the three-point linkage system: a fully meshed model, a bushing connector model, and a substructure model. They all model the TPL using the front and rear bushings to connect to the subframe (not modeled) that is assumed to be fixed in space. Loads are applied to a reference point where the ball joint is attached to model loads that the wheel assembly would exert on the TPL. The constraint imposed by the fixed subframe is modeled in all three cases by constraining the motion of the inner cylinder distributed coupling reference node in all six degrees of freedom.

In the fully meshed model the linkage itself is modeled using shell elements, while the front and rear bushings are modeled using continuum elements. The front bushing is connected to the reference node of a U-bracket that is modeled as a rigid body (see Figure 4.1.11–1). The rigid body reference node of the U-bracket is held fixed in all six degrees of freedom.

In the bushing connector model the bushings in the fully meshed model are replaced with BUSHING connectors. The constitutive data for the connectors are obtained from the series of tests described above. The front bushing is connected to the reference node of a U-bracket that is modeled as a rigid body (see Figure 4.1.11–1). The rigid body reference node of the U-bracket is held fixed in all six degrees of freedom.

In the substructure model the three-point linkage is modeled with a substructure, and the bushings are modeled with connector elements as defined in the bushing connector model. For clarity, the U-bracket is not represented in the substructure model since it is considered to be rigid and fixed. The rear bushing inner cylinder is connected to the subframe via a large bolt.

Two load cases are applied in all three models:

Load case 1:

A geometrically nonlinear, single-step, static analysis is performed where a concentrated force of 250 N is applied at the ball joint reference node in the negative global 1-direction. The analysis models a horizontal load at the ball joint.

Load case 2:

A geometrically nonlinear, two-step, static analysis is performed. In the first step the TPL is lifted by 10º about the global 1-direction by applying a displacement boundary condition of 20 mm to the ball joint reference node in the negative global 3-direction. In the second step a concentrated force of 250 N is applied at the ball joint reference node in the negative global 1-direction. The analysis models a horizontal load on the ball joint as the wheel and, hence, the ball joint go over a bump.

Results and discussion

It can be seen from the results of Tests 7_FB and 8_FB (Figure 4.1.11–5) that the front bushing behavior in both the local 3-direction and about the local 2-direction is affected significantly by the amount of preload about the local 3-direction. For the rear bushing it can be seen from the results of Tests 7_RB and 8_RB (Figure 4.1.11–7) that the behavior in the local 1-direction and especially the behavior in the local 2-direction are affected significantly by the amount of the combined preload (in the local 2-direction and about the local 2-direction for Test 7_RB, and in the local 1-direction and about the local 2-direction for Test 8_RB).

The Mises stresses in the TPL calculated for each of the three modeling approaches are very similar, as shown in Figure 4.1.11–8, Figure 4.1.11–9, and Figure 4.1.11–10. In addition, displacement histories at the ball joint (where the loading was applied) show very good agreement between the three models (Figure 4.1.11–11). As expected, the bushing connector model analysis and the substructure model analysis produced identical displacements at the ball joint. When compared with the fully meshed model, the differences for the displacement histories in both directions are 4% toward the end of the curves.

The main motivation to use the BUSHING connector in this and similar applications is to reduce the complexity of the models and the computation time. In this TPL analysis the fully meshed model analysis takes approximately 50 times longer than the analysis that uses connectors to model the bushings. Furthermore, the substructure model analysis completes in about one-eighth of the time required for the analysis that uses connectors to model the bushings, approximately 400 times faster than the original fully meshed model.

In summary, this example demonstrates significant improvement in analysis efficiency when bushings are modeled with pre-calibrated BUSHING connectors or substructures without sacrificing accuracy.

Files

tpl_fb_uncoupled.inp	Front bushing model template used for generating constitutive data curves for all tests without preload.
tpl_fb_uncoupled.psf	Python script file to automatically generate input files and run analyses for all tests without preload.

tpl_fb_CRF3vsCU3.inp	Front bushing model template used for generating constitutive data curves for Test 7_FB.
tpl_fb_CRF3vsCU3.psf	Python script file to automatically generate input files and run analyses for Test 7_FB.
tpl_fb_CRM2vsCUR2.inp	Front bushing model template used for generating constitutive data curves for Test 8_FB.
tpl_fb_CRM2vsCUR2.psf	Python script file to automatically generate input files and run analyses for Test 8_FB.
tpl_rb_uncoupled.inp	Rear bushing model template used for generating constitutive data curves for all tests without preload.
tpl_rb_uncoupled.psf	Python script file to automatically generate input files and run analyses for tests without preload.
tpl_rb_CRF1vsCU1.inp	Rear bushing model template used for generating constitutive data curves for Test 7_RB.
tpl_rb_CRF1vsCU1.psf	Python script file to automatically generate input files and run analyses for Test 7_RB.
tpl_rb_CRF2vsCU2.inp	Rear bushing model template used for generating constitutive data curves for Test 8_RB.
tpl_rb_CRF2vsCU2.psf	Python script file to automatically generate input files and run analyses for Test 8_RB.
tpl_const_data_ext-rb_CRF1vsCU1.py	Python file to automatically gather force vs. displacement results for Test 7_RB.
tpl_const_data_ext-rb_CRF2vsCU2.py	Python file to automatically gather force vs. displacement results for Test 8_RB.
tpl_full_loadcase1.inp	Fully meshed model analysis for Load case 1.
tpl_full_loadcase2.inp	Fully meshed model analysis for Load case 2.
tpl_connectors_loadcase1.inp	Bushing connector model analysis for Load case 1.
tpl_connectors_loadcase2.inp	Bushing connector model analysis for Load case 2.
tpl_substructure_gen.inp	Substructure generation analysis for the three-point linkage.
tpl_substructure_loadcase1.inp	Substructure model analysis for Load case 1.
tpl_substructure_loadcase2.inp	Substructure model analysis for Load case 2.

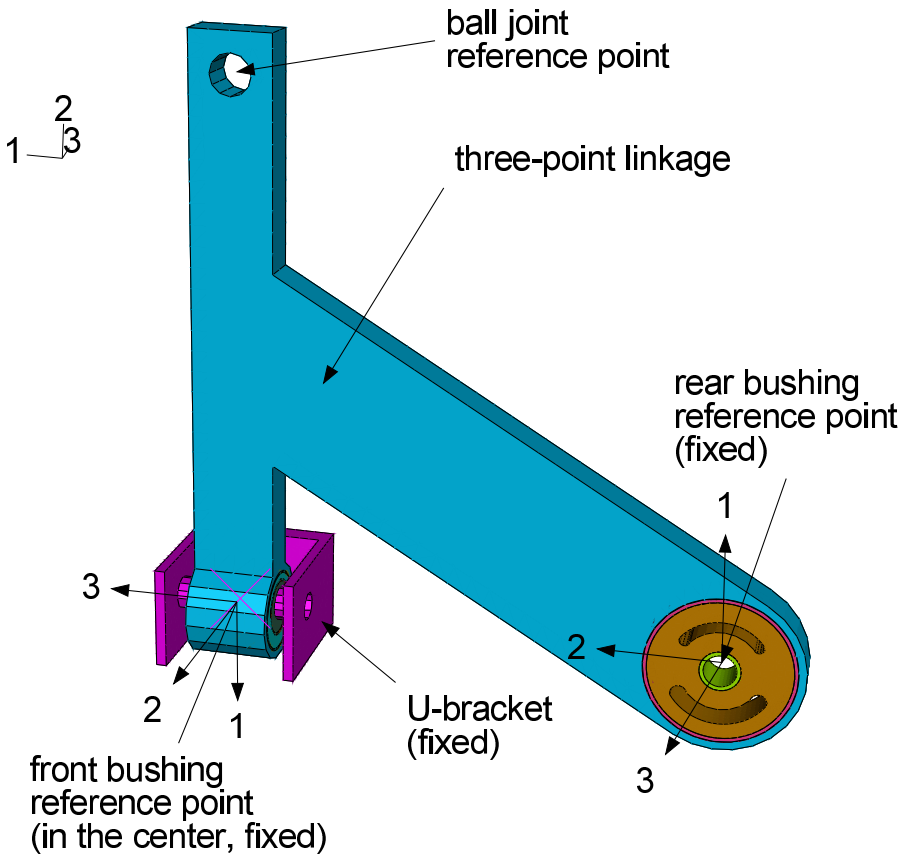

Figure 4.1.11–1 Three-point linkage (TPL) assembly.

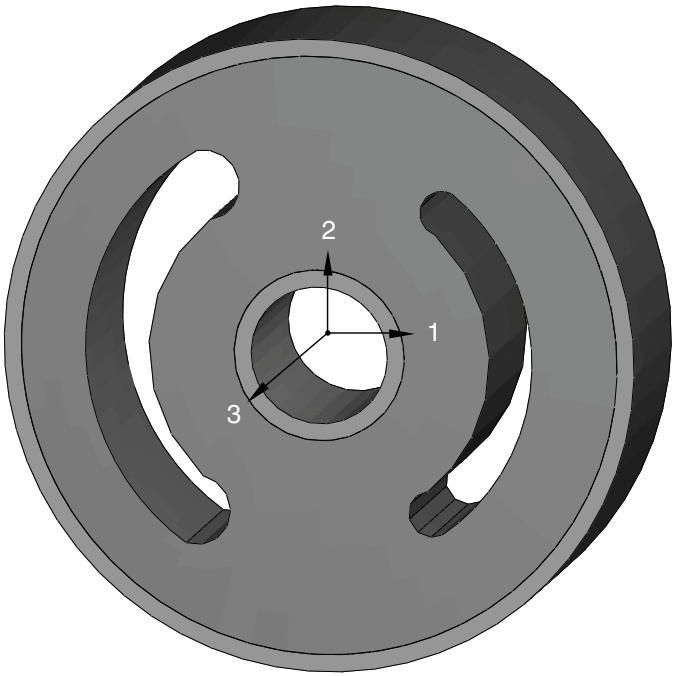

Figure 4.1.11–2 Rear bushing geometry.

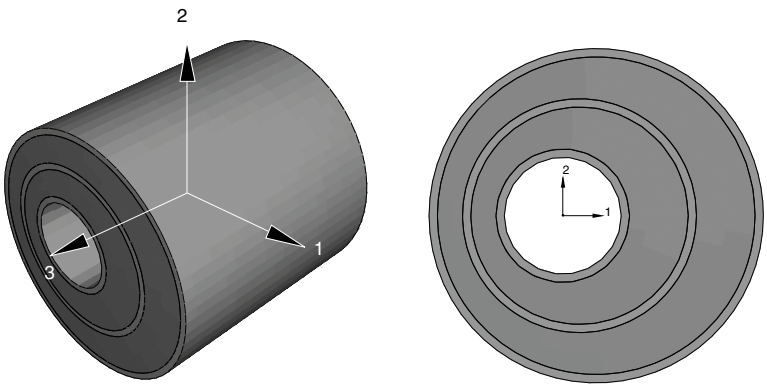

Figure 4.1.11–3 Front bushing geometry.

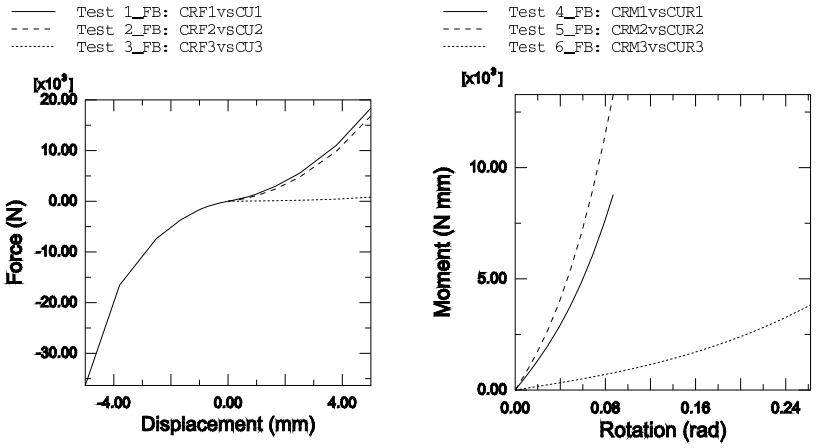

Figure 4.1.11–4 Front bushing coupled force vs. displacement and moment vs. rotation curves without preload.

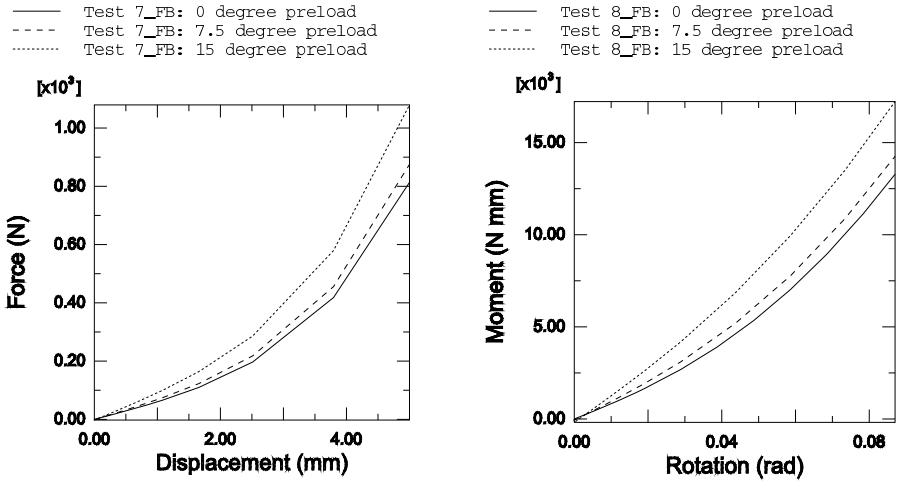

Figure 4.1.11–5 Front bushing coupled force vs. displacement and moment vs. rotation curves with preload.

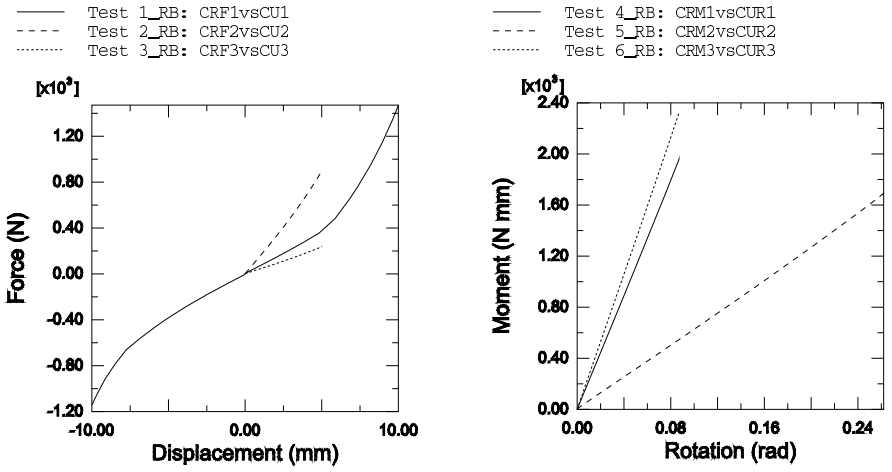

Figure 4.1.11–6 Rear bushing force vs. displacement and moment vs. rotation curves without preload.

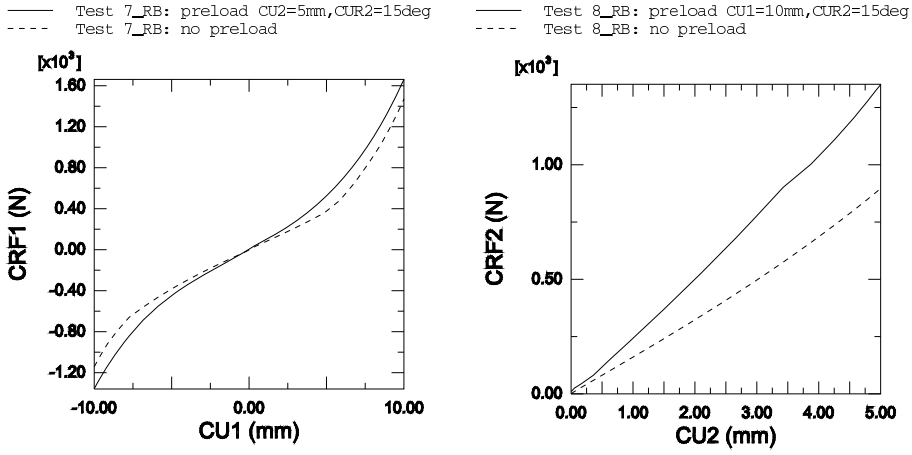

Figure 4.1.11–7 Comparison of rear bushing coupled force vs. displacement for Tests 7_RB and 8_RB.

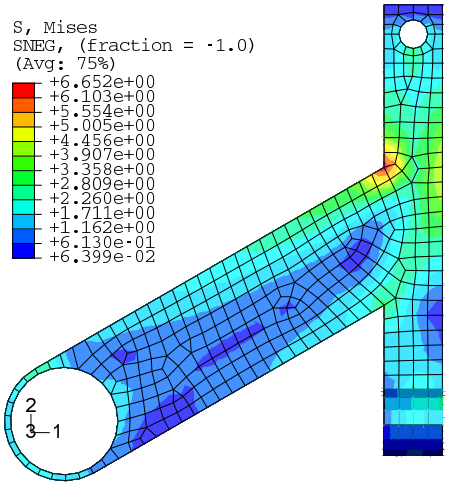

Figure 4.1.11–8 Mises stresses in the TPL for the fully meshed model (Load case 2).

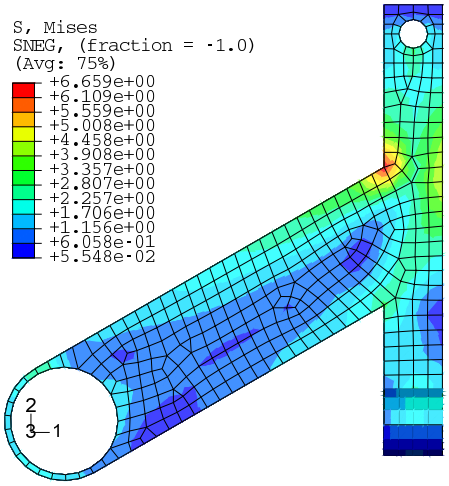

Figure 4.1.11–9 Mises stresses in the TPL for the bushing connector model (Load case 2).

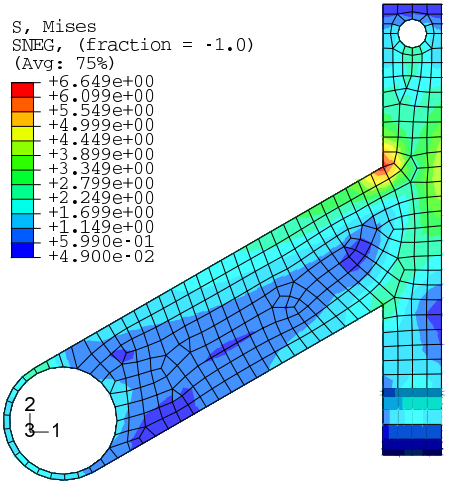

Figure 4.1.11–10 Mises stresses in the TPL for the substructure model (Load case 2).

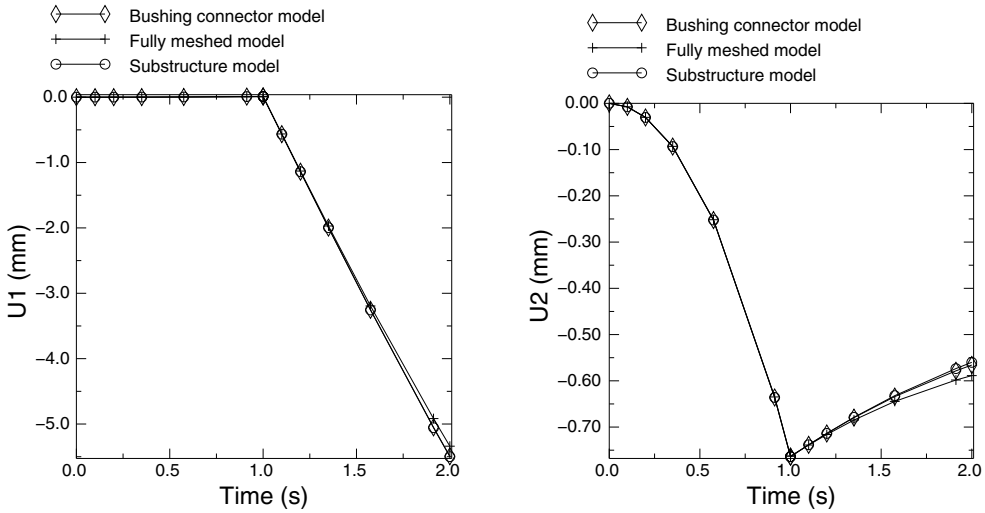

Figure 4.1.11–11 Comparison of displacements at the ball joint reference node (Load case 2).

4.1.12 GEAR ASSEMBLIES

Product: Abaqus/Explicit

Objectives

This example illustrates the use of connectors in modeling the kinematics of gear assemblies.

Application description

Gears are widely used in a variety of machinery to transfer torque (rotational motion) from one shaft to another shaft and to act as a means to change the torque (rotational speed) acting on a shaft. Three types of gear assemblies (spur gear assembly, rack and pinion mechanism, and screw gear assembly) are studied in this example with a focus on the proper transmission of torque and rotational motion between the gears. The units used are millimeters-tonnes-seconds.

Geometry

Spur gears

A spur gear assembly consists of a driving gear (labeled **`Pinion`**) with input torque acting on it and a driven gear (labeled **`Gear`**) that receives the torque from the pinion, as shown in Figure 4.1.12–1. In this example the gear ratio is chosen as 2.5; i.e., the gear has 2.5 times more teeth than the pinion and, hence, it rotates 2.5 times slower than the pinion. To measure the power transmission in the gear system, a linear torsional spring is placed on each shaft such that the ratio of their elastic constants is the square of the ratio of the gear radius on the respective shaft. The whole gear assembly is mounted on a single rigid body whose reference node is constrained to prevent rigid body motion. The pitch circle radius of the pinion and the gear is 1.04573 units and 2.61433 units, respectively, as marked by the position of node 2 in Figure 4.1.12–1. The elastic constant of the torsional spring on the pinion shaft is chosen as 1 unit while that on the gear shaft, as calculated from the gear ratio, is 6.25 units.

Rack and pinion

A rack and pinion mechanism is a special case of the spur gear assembly with one of the gears having an infinite radius. The mechanism consists of a spinning pinion pulling the rack toward itself, as shown in Figure 4.1.12–2. A groove is provided to guide the movement of the rack. The whole rack and pinion assembly is mounted on a rigid body whose reference node is constrained to prevent any rigid body motion. The pitch circle radius of the pinion is 2.5 units.

Screw gear and housing

A screw gear mechanism is similar to a rack and pinion mechanism except that the translational motion takes place along the axis of rotation of the gear, as shown in Figure 4.1.12–3. As in the case of the rack and pinion arrangement, a slot guides the direction of the motion of the screw. The screw gear and housing assembly is mounted on a rigid body whose reference node is constrained to

prevent any rigid body motion. The motion involves turning the screw one complete revolution as it runs along the grooves of the screw thread of a fixed housing. The screw has a radius of 1.5 units and a pitch of 2 units.

Abaqus modeling approaches and simulation techniques

This example illustrates the use of connectors for modeling gear assemblies in Abaqus/Explicit. The focus in this example is purely on the kinematics of gears without the consideration of gear-teeth forces.

Summary of analysis cases

Case 1: Spur gears	A rotating pinion driving a gear.
Case 2: Rack and pinion	A rotating pinion pulling a rack guided in a slot.
Case 3: Screw gear	A rotating screw moving through a groove in a housing.

Mesh design

All three cases of gear assemblies use CONN3D2 elements with the section behavior defined in detail in the following sections.

Case 1: Spur gears

This case illustrates using connectors to model the kinematics of a spur gear assembly.

Mesh design

Each spur gear is modeled using one CONN3D2 element with connection type HINGE and one CONN3D2 element with connection type FLOW-CONVERTER.

Material model

The HINGE of the pinion has a torsional stiffness of 1 unit, and the HINGE of the gear has a torsional stiffness of 6.25 units.

Boundary conditions

The first nodes of both HINGEs are fixed. The second node of the HINGE of the pinion is driven by 18.85 radians.

Interactions

As shown in Figure 4.1.12–1, the pinion and gear are each modeled with a HINGE and a FLOW-CONVERTER sharing a node (nodes 1 and 3, respectively). Nodes 1 and 3 of HINGEs **`HG1`** and **`HG2`**, respectively, are free to rotate, whereas their second nodes (node 4 and 6, respectively) form a rigid body along with node 5 (reference node). This rigid body has all of its degrees of freedom fixed to prevent overall rigid body motion of the gear system.

The second node of FLOW-CONVERTERs **FC1** and **FC2** is common (node 2) with all of its rotations fixed. Any relative rotation in HINGE **HG1** causes material flow at node 2 of FLOW-CONVERTER **FC1**. The gear mechanism formed by HINGE **HG2** and FLOW-CONVERTER **FC2** mirrors the pinion mechanism formed by FLOW-CONVERTER **FC1** and HINGE **HG1**. Thus, any material flow at common node 2 of FLOW-CONVERTER **FC2** results in a relative rotational motion between the two nodes of HINGE **HG2**.

The gear ratio of 2.5 is maintained by defining the scaling factor β (with proper sign) in FLOW-CONVERTERs **FC1** and **FC2**; for this case, the scaling factors are 1.0 and −0.4, respectively. The display bodies of the gear and pinion have reference nodes 10 and 11, respectively, that form a rigid body with the respective unconstrained nodes of HINGEs **HG1** and **HG2**.

Case 2: Rack and pinion

This case illustrates using connectors to model the kinematics of a rack and pinion mechanism.

Mesh design

The pinion is modeled using one CONN3D2 element with connection type HINGE and one CONN3D2 element with connection type FLOW-CONVERTER. The rack is modeled using one CONN3D2 element with connection type SLIPRING. The groove in which the rack moves is modeled using one CONN3D2 element with connection type TRANSLATOR.

Material model

Both the HINGE and the SLIPRING are defined as rigid elastic.

Boundary conditions

The first nodes of the HINGE and TRANSLATOR are fixed. Degree of freedom 10 of the common node of the SLIPRING and TRANSLATOR is also fixed. The second node of the HINGE of the pinion is driven by 6.28 radians.

Interactions

The rack and pinion mechanism, as shown in Figure 4.1.12–2, is modeled similarly to the spur gears described in Case 1. The pinion is modeled with HINGE **HG** (nodes 1 and 6) and FLOW-CONVERTER **FC** (nodes 1 and 2) that share a common node (node 1). The rack is modeled with a SLIPRING **SR** (nodes 2 and 3) and TRANSLATOR **TR** (nodes 4 and 3) that is used to guide the motion of SLIPRING **SR**. SLIPRING **SR** and FLOW-CONVERTER **FC** share a common node (node 2).

Nodes 2, 4, and 6 are part of a rigid body with reference node 5 that is constrained to prevent any rigid body motion of the rack and pinion system. A fixed boundary condition on degree of freedom 10 is imposed at node 3 of SLIPRING **SR** to prevent any material flow past this node. Any relative rotation between nodes 1 and 6 of HINGE **HG** results in material flow at node 2 of FLOW-CONVERTER **FC**. This material flow at node 2 results in tension in the adjoining SLIPRING **SR** that drives the rack.

The relation between the translational motion of the rack and the rotational motion of the pinion is maintained by defining the scaling factor β (with proper sign) of FLOW-CONVERTER **FC**; for this

case, the scaling factor is 0.4. As mentioned before, the motion of the rack occurs parallel to the axis of the TRANSLATOR **TR**, and it can be measured via the connector displacement of TRANSLATOR **TR**. In this example available component 4 in HINGE **HG** and available component 1 in SLIPRING **SR** are both defined as rigid elastic. The display bodies of the rack and pinion have reference nodes 10 and 11, respectively, that form a rigid body with the respective unconstrained nodes of SLIPRING **SR** and HINGE **HG**.

Case 3: Screw gear

This case illustrates using connectors to model the kinematics of a screw gear and housing assembly.

Mesh design

The screw is modeled using one CONN3D2 element with connection type HINGE, one CONN3D2 element with connection type FLOW-CONVERTER, and one CONN3D2 element with connection type SLIPRING. The groove in which the screw moves is modeled using a CONN3D2 element with connection type TRANSLATOR.

Material model

Both the HINGE and the SLIPRING are defined as rigid elastic.

Boundary conditions

The first nodes of the TRANSLATOR are fixed. Degree of freedom 10 of the common node of the SLIPRING and TRANSLATOR is also fixed. The second node of the HINGE of the screw is driven by 20 radians.

Interactions

The screw gear system, as shown in Figure 4.1.12–3, is modeled similarly to the rack and pinion system described in Case 2. The screw is modeled with HINGE **HG** (nodes 6 and 1), FLOW-CONVERTER **FC** (nodes 1 and 2), and SLIPRING **SR** (nodes 2 and 3). The housing is modeled with TRANSLATOR **TR** (nodes 4 and 3). HINGE **HG** and FLOW-CONVERTER **FC** share a common node (node 1). SLIPRING **SR** and FLOW-CONVERTER **FC** share node 2.

Nodes 2, 4, and 11 are part of a rigid body with reference node 5 that is constrained to prevent any rigid body motion of the housing. Material flow at node 3 of the SLIPRING is prevented via a fixed boundary condition on degree of freedom 10. Similar to the rack and pinion mechanism, the relative rotation between nodes 1 and 6 of HINGE **HG** results in material flow at node 2 of FLOW-CONVERTER **FC**. This material flow at node 2 causes tension in the belt of SLIPRING **SR**, resulting in a translational displacement of node 3. Nodes 3 and 6 are tied together as a rigid body and, hence, the translational motion of node 3 results in the linear motion of the screw. The rotational motion of the screw is identical to the rotational motion of node 1.

The scaling factor β of FLOW-CONVERTER **FC** is defined to scale the rotational motion of node 1 in relation to its translational motion; for this case, the scaling factor is -3.14. As in the case of the rack and pinion mechanism, TRANSLATOR **TR** guides the direction of the motion of the screw. Available

component 1 in SLIPRING **SR** is defined as rigid elastic. The display bodies of the screw and the housing have reference nodes 10 and 11, respectively, that form a rigid body with the respective unconstrained nodes of HINGE **HG** and SLIPRING **SR**.

Discussion of results and comparison of cases

Case 1: Spur gears

The pinion shaft is given an angular displacement of 18.85 radians by defining connector motion in HINGE **HG1**. The final angular displacement of the gear shaft is measured to be 7.54 radians, with the gear ratio holding at 2.5 throughout the analysis duration, as shown in Figure 4.1.12–4. The ratio of the input to output power, which is calculated by taking the product of connector moment CTM1 and connector motion CUR1 of the respective HINGEs, is also found to be constant.

Case 2: Rack and pinion

The pinion is rotated one complete revolution by defining connector motion in HINGE **HG**. The rack moves 15.7 units, measured by CU1 of TRANSLATOR **TR** in Figure 4.1.12–5. This distance is the same as the circumference of the pitch circle of the pinion.

Case 3: Screw gear

The screw is given an angular rotation of 20 radians by defining connector motion in HINGE **HG**. The screw moves 6.37 units, measured by CU1 of TRANSLATOR **TR** as shown in Figure 4.1.12–6.

Input files

spur_gear.inp	Spur gear assembly.
rack_pinion.inp	Rack and pinion assembly.
screw_gear.inp	Screw gear assembly.

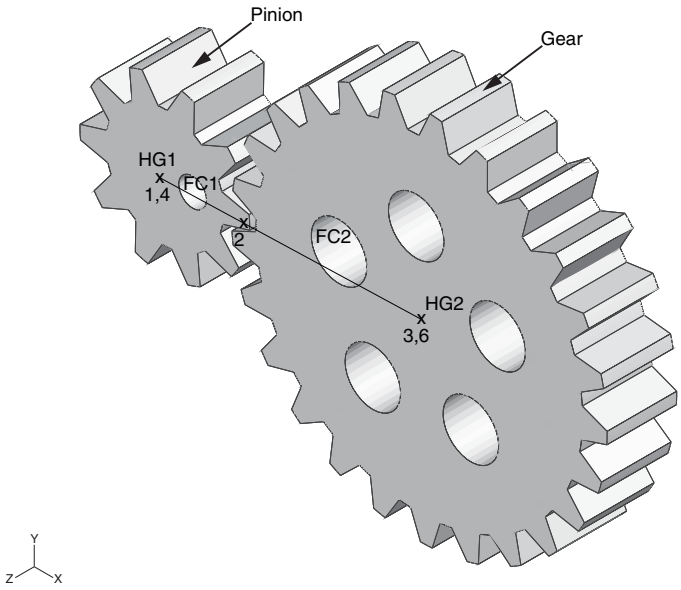

Figure 4.1.12–1 Spur gear assembly.

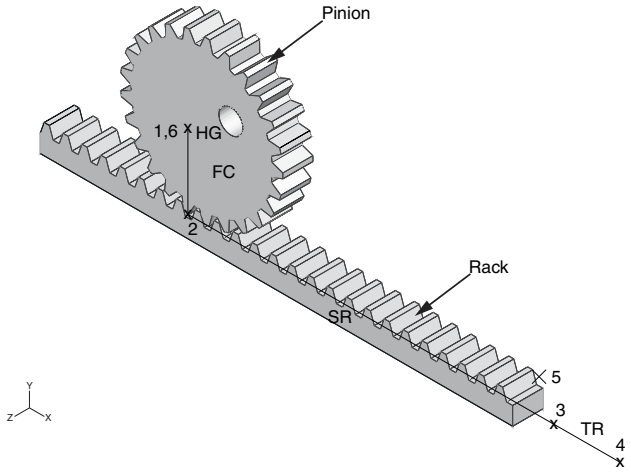

Figure 4.1.12–2 Rack and pinion assembly.

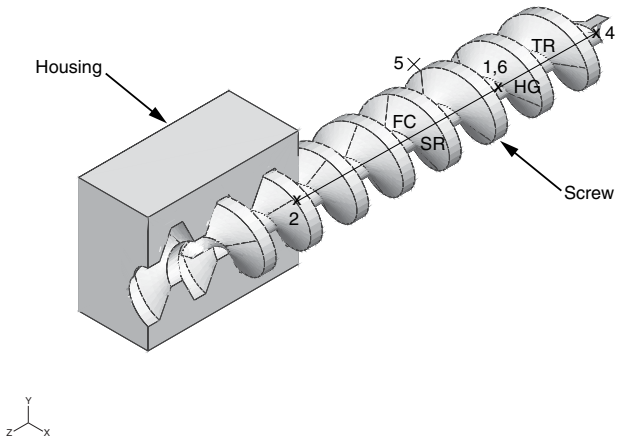

Figure 4.1.12–3 Screw gear assembly.

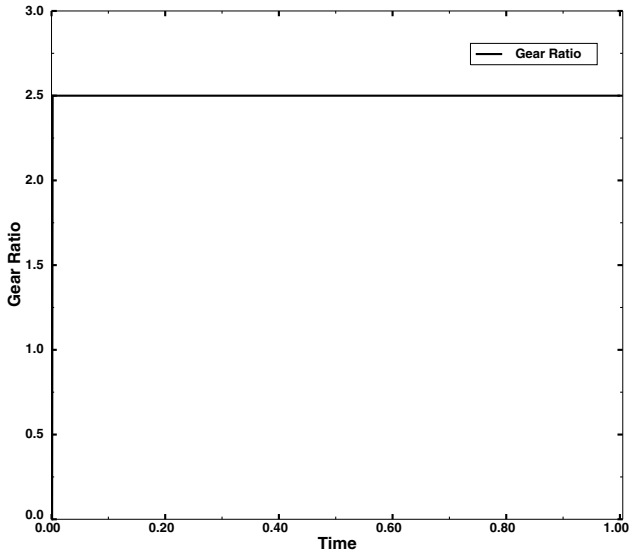

Figure 4.1.12–4 Ratio of angular displacement of the pinion (CUR1 of HINGE **`HG1`**) to that of the gear (CUR1 of HINGE **`HG2`**).

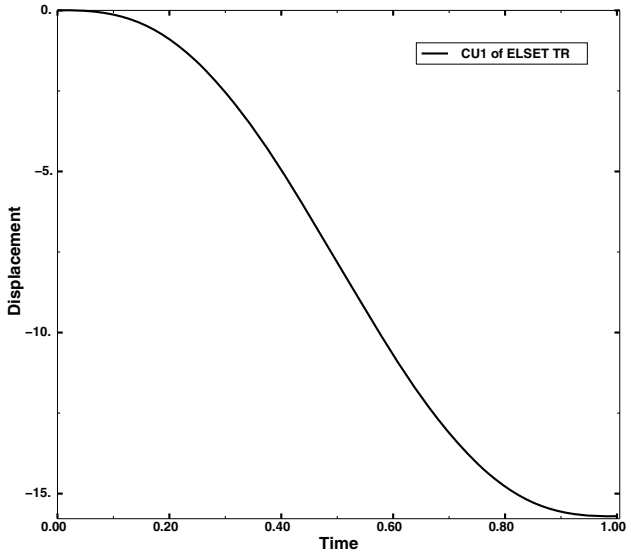

Figure 4.1.12–5 Displacement of the rack (CU1 of TRANSLATOR **TR**).

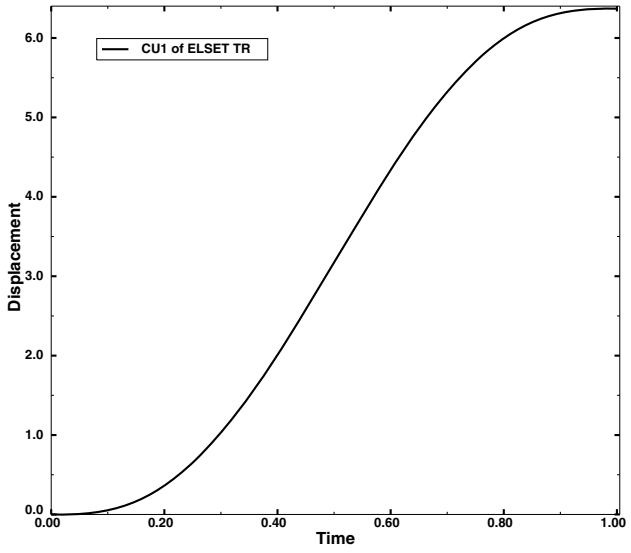

Figure 4.1.12–6 Displacement of the screw (CU1 of TRANSLATOR **TR**).

5. Heat Transfer and Thermal-Stress Analyses

- “Heat transfer and thermal-stress analyses,” Section 5.1

5.1 Heat transfer and thermal-stress analyses

- "Thermal-stress analysis of a disc brake," Section 5.1.1
- "A sequentially coupled thermomechanical analysis of a disc brake with an Eulerian approach," Section 5.1.2
- "Exhaust manifold assemblage," Section 5.1.3
- "Coolant manifold cover gasketed joint," Section 5.1.4
- "Conductive, convective, and radiative heat transfer in an exhaust manifold," Section 5.1.5
- "Thermal-stress analysis of a reactor pressure vessel bolted closure," Section 5.1.6
- "Coupled thermomechanical analysis of viscoelastic dampers," Section 5.1.7

5.1.1 THERMAL-STRESS ANALYSIS OF A DISC BRAKE

Products: Abaqus/Standard Abaqus/Explicit

This example shows the fully coupled thermal-stress analysis of a disc brake.

Disc brakes operate by pressing a set of composite material brake pads against a rotating steel disc: the frictional forces cause deceleration. The dissipation of the frictional heat generated is critical for effective braking performance. Temperature changes of the brake cause axial and radial deformation; and this change in shape, in turn, affects the contact between the pads and the disc. Thus, the system should be analyzed as a fully coupled thermomechanical system.

In this section two thermally coupled disc brake analysis examples are discussed. The first example is an axisymmetric model in which the brake pads and the frictional heat generated by braking are "smeared" out over all 360° of the model. This problem is solved using only Abaqus/Standard. The heat generation is supplied by user subroutine **FRIC**, and the analysis models a linear decrease in velocity as a result of braking.

The second example is a three-dimensional model of the entire disc with pads touching only part of the circumference. The disc is rotated so that the heat is generated by friction. This problem is solved using both Abaqus/Standard and Abaqus/Explicit.

It is also possible to perform uncoupled analysis of a brake system. The heat fluxes can be calculated and applied to a thermal model; then the resulting temperatures can be applied to a stress analysis. However, since the thermal and stress analyses are uncoupled, this approach does not account for the effect of the thermal deformation on the contact which, in turn, affects the heat generation.

Another type of geometrical model for a disc brake is used by Gonska and Kolbinger (1993). They model a "vented" disc brake (Figure 5.1.1–1) and take advantage of radial repetition by modeling a pie-slice segment (Figure 5.1.1–2). Like the axisymmetric model, this requires the effect of the pads to be smeared, but it allows the modeling of radial cooling ducts while still reducing the model size relative to a full model.

Geometry and model

Both models analyzed in this example have solid discs, which allows the models to use coarser meshes than would be required to model the detail of a typical disc brake that has complicated geometrical features such as cooling ducts and bolt holes. The first example further simplifies the model by considering the pads to be "smeared" around the entire 360° so that the system is axisymmetric. The second example is a full three-dimensional model of the entire annular disc with pads touching only part of the circumference. However, the geometry of the disc has been simplified by making it symmetrical about a plane normal to the axis. Therefore, only half of the disc and one brake pad is modeled, and symmetry boundary conditions are applied.

The dimensions of the axisymmetric model are taken from a typical car disc brake. The disc has a thicker friction ring connected to a conical section that, in turn, connects to an inner hub. The inner radius of the friction ring is 100.0 mm, the outer radius is 135.0 mm, and it is 10.0 mm thick. The conical section is 32.5 mm deep and 5.0 mm thick. The hub has an inner radius of 60.0 mm, an outer radius of 80.0 mm, and is 5.0 mm thick. The pads are 20.0 mm thick and initially cover the entire friction ring surface.

Two analyses of the axisymmetric model are performed in which the pads and disc are modeled using fully integrated and reduced-integration linear axisymmetric elements. Reduced integration is attractive because it decreases the analysis cost and, at the same time, provides more accurate stress predictions. Frictional contact between the pads and the disc is modeled by contact pairs between surfaces defined on the element faces in the contact region. Small sliding is assumed. The mesh is shown in Figure 5.1.1–3, with the pads drawn in a darker gray than the disc. There are six elements through the thickness of the friction ring and four elements through the thickness of each of the pads. The mesh is somewhat coarse but is optimized by using thinner elements near the surfaces of the disc and pads where contact occurs for better resolution of the thermal gradients in these areas.

The disc for the three-dimensional model has an outer radius of 135.0 mm, an inner radius of 90.0 mm, and a thickness of 10.0 mm (the half-model has a thickness of 5.0 mm). The ring has a thinner section out to a radius of 100.0 mm, which has a thickness of 6.0 mm (the half-model has a thickness of 3.0 mm). The pad is 10.0 mm thick and covers a little less than one-tenth the circumference. The pad does not quite reach to the edge of the thicker part of the friction ring.

The pad and disc of the three-dimensional model are modeled with C3D8T elements in Abaqus/Standard and with C3D8RT elements in Abaqus/Explicit; the contact and friction between the pad and the disc are modeled by contact pairs between surfaces defined on the element faces in the contact region. The same mesh is used in both Abaqus/Standard and Abaqus/Explicit. It is shown in Figure 5.1.1–4, with the pad drawn in a darker gray than the disc. The disc is a simple annulus with a thinner inner ring. This mesh is also rather coarse with only three elements through the thickness of the disc and three elements through the pad. The elements on the contact sides are thinner since they will be in the areas of higher thermal gradients. There are 36 elements in the circumferential direction of the disc.

Material properties

The thermomechanical properties for the axisymmetric model were taken from a paper by Day and Newcomb (1984) describing the analysis of an annular disc brake. The pad is made of a resin-bonded composite friction material, and the disc is made of steel. Although Day and Newcomb note that material changes occur in the pad material because of thermal degradation, the pad in the axisymmetric model has the properties of the unused pad material. For the axisymmetric model the modulus, density, conductivity, and coefficient of friction are divided by 18 since the pads actually cover only a 20° section of the disc, even though they are modeled as being smeared around the entire circumference.

The pad for the three-dimensional model is also a resin-bonded composite friction material whose thermomechanical properties are listed in Table 5.1.1–1 and coefficient of friction is listed in Table 5.1.1–2. The properties were taken from a paper by Day (1984). It is noted that above certain temperatures, approximately 400°C, the pad material becomes thermally degraded and μ is assumed constant from this point on.

It is assumed that all the frictional energy is dissipated as heat and distributed equally between the disc and the pad; therefore, the fraction of dissipated energy caused by friction that is converted to heat is set to 1.0, and the default distribution is used. This fractional value allows the user to specify an unequal distribution, which is particularly important if the heat conduction across the interface is poor. In this example the conductivity value specified with the gap conductance is quite high; hence, the results are

not very sensitive to changes in distribution. In Abaqus/Explicit arbitrarily high gap conductivity values may cause the stable time increment associated with the thermal part of the problem to control the time incrementation, possibly resulting in a very inefficient analysis. In this problem the gap conductivity value used in the Abaqus/Explicit simulation is 20 times smaller than the one used in the Abaqus/Standard simulation. This allows the stable time increment associated with the mechanical part of the problem to control the time incrementation, thus permitting a more efficient solution while hardly affecting the results.

Loading

The pads of the axisymmetric model are first pressed against the disc. The magnitude of the load is divided by 18 since the pads are not actually axisymmetric. The frictional forces are then applied through user subroutine **FRIC** to simulate a linear decrease in velocity of the disc relative to the pads. The braking is done over three steps; then, when the velocity is zero, a final step shows the continued heat conduction through the model.

The pad of the three-dimensional model is fixed in the nonaxial degrees of freedom and is pressed against the disc with a distributed load applied to the back of the pad. In Abaqus/Standard the disc is then rotated by 60° using an applied boundary condition to the center ring. In Abaqus/Explicit this boundary condition is prescribed using smooth step data to minimize the effects of centrifugal forces at the beginning and end of the step. Frictional forces between the surfaces generate heat in the brake.

The initial temperature of both models is 20°C.

Solution controls (Abaqus/Standard only)

Since the three-dimensional model has a small loaded area and, thus, rather localized forces and heat fluxes, the default averaged flux values for the convergence criteria produce very tight tolerances and cause more iteration than is necessary for an accurate solution. To decrease the computational time required for the analysis, the solution controls override the automatic calculation of the average forces and heat fluxes. Solution controls are first used to set parameters for the displacement field and warping degrees of freedom equilibrium equations. The convergence criterion ratio is set to 1%, and the time-average and average fluxes are set to a typical nodal force (displacement flux):

$$f_d = pA = (1.7\text{E}6)(1.77\text{E-}4) \approx 300,$$

where $\boldsymbol{p}$ is the pressure and $\boldsymbol{A}$ is the area of a typical pad element. Solution controls are next used to set parameters for the temperature field equilibrium equations. The convergence criterion ratio is set to 1%, and the time-average and average fluxes are set to the nodal heat flux (temperature flux) for a typical pad element. The heat flux density generated by an interface element due to frictional heat generation is $q_g = \eta\tau v$, where η is the gap heat generation factor, τ is the frictional stress, and $\boldsymbol{v}$ is the velocity. Therefore, the nodal heat flux is

$$f_t = q_g A = \eta(\mu p)(\omega r)A,$$

where A is the contact area of a typical pad element, μ is the friction coefficient, and p is the contact pressure. The angular velocity, ω, is obtained as the total rotation, $\pi/3$, divided by the total time, 0.015 sec. The radius, r, is set to 0.120 m, which is the distance from the axis to a point approximately in the middle of the pad surface. This yields

$$f_t = \frac{(1.0)(.37)(1.7\text{E}6)(\frac{\pi}{3})(0.12)(1.77\text{E-}4)}{0.015} \approx 900.$$

Additional solution controls can reduce the solver cost for an increment by improving the initial solution guess, solving thermal and mechanical equations separately, and reducing the wavefront of three-dimensional finite-sliding contact analysis. These features are discussed below. The impact of combining these features is also discussed.

When the default convergence controls are used, it is possible to obtain faster convergence with a parabolic extrapolation step. For the three-dimensional model the use of this feature yields a 14% enhancement in computational speed per increment.

The coupling between the thermal and mechanical fields in this problem is relatively weak. It is, therefore, possible to obtain a more efficient solution by specifying separate solutions for the thermal and mechanical equations each increment. This technique results in faster per-iteration solution times at the expense of poorer convergence when a strong interfield coupling is present. Use of this technique also permits the use of the symmetric solver and storage scheme. The resulting symmetric approximation of the mechanical equations was also found to be cost effective for this problem, when combined with a quality initial solution guess obtained by specifying parabolic extrapolation in the step. Neither of these approximations impacts solution accuracy. For the three-dimensional model the use of the separated solution scheme, parabolic extrapolation, and symmetric matrix storage yields a 50% decrease in the total solution time.

In the three-dimensional model the deformable master surface is defined from a large number of connecting elements resulting in a large wavefront. By default, Abaqus/Standard employs an automated contact patch algorithm to reduce the wavefront and solution time. For instance, in the coupled thermomechanical analysis a substantial savings in solution time (a 30% to 50% decrease) is obtained when the automatic contact patch algorithm is employed compared to an analysis that uses a fixed contact patch encompassing the entire master surface. The reduction in solution time is system dependent and depends on several factors, such as CPU type, system memory, and IO speed. This solution time savings is in addition to any of the other savings discussed in this section. The additional savings is, therefore, realized when the separated solution scheme and parabolic extrapolation are also specified.

Results and discussion

The temperature distribution of the axisymmetric model at an early time increment is shown in Figure 5.1.1–5. The temperature is greatest at the interfaces between the disc and pads, and the heat has just started to conduct into the disc. Figure 5.1.1–6 shows the temperature distribution at the end of the analysis when the velocity is zero. The heat has conducted through the friction ring of the disc. Figure 5.1.1–7 is a displaced plot of the model at the end of the analysis and shows the characteristic

conical deformation due to thermal expansion. The displacement has been magnified by a factor of 128 to show the deformation more clearly.

The temperature distribution of the disc surface of the three-dimensional model after a rotation of 60° is shown in Figure 5.1.1–8 (Abaqus/Standard) and Figure 5.1.1–9 (Abaqus/Explicit). The agreement between the two results is excellent. The hottest region is the area under the pad, while the heat in the regions that the pad has passed over has dissipated somewhat. Figure 5.1.1–10 shows the temperature distribution of the inside of the brake pad predicted by Abaqus/Standard, while Figure 5.1.1–11 shows the same result obtained with Abaqus/Explicit. Again excellent agreement between the two results is noted. Figure 5.1.1–12 shows the temperature distribution in the disc predicted by Abaqus/Standard with the thickness magnified by a factor of 20. The heat has conducted into the disc in the regions that the pad has passed over.

The stresses predicted by Abaqus/Standard do not account for the effects of centrifugal loads (fully coupled thermal-stress is a quasi-static procedure), while the stresses predicted by Abaqus/Explicit do. These effects can be significant, especially during the early transient portion of the simulation when the initially stationary disc is brought up to speed. To compare the stress results between Abaqus/Standard and Abaqus/Explicit, we gradually initiated and ended the disc rotation in the Abaqus/Explicit simulation; thus, in Abaqus/Explicit, the centrifugal stresses at the beginning and end of the step are small compared with the thermal stresses. At points in between, however, the effects of centrifugal loading are more pronounced and differences between the stress states predicted by Abaqus/Standard and Abaqus/Explicit are observed. The overall effect on the thermal response, however, is negligible.

The Abaqus/Explicit analysis did not include mass scaling because its presence would artificially scale the stresses due to the centrifugal loads. It is possible to include mass scaling to make the analysis more economical, but any results obtained with mass scaling must be interpreted carefully in this problem.

Input files

Abaqus/Standard input files

discbrake_std_cax3t.inp	Axisymmetric model with CAX3T elements.
discbrake_std_cax3t.f	User subroutine **FRIC** used in discbrake_std_cax3t.inp.
discbrake_std_cax4t.inp	Axisymmetric model with CAX4T elements.
discbrake_std_cax4t.f	User subroutine **FRIC** used in discbrake_std_cax4t.inp.
discbrake_std_cax4rt.inp	Axisymmetric model with CAX4RT elements.
discbrake_std_cax4rt_surf.inp	Axisymmetric model with CAX4RT elements using the surface-to-surface approach.
discbrake_std_cax4rt.f	User subroutine **FRIC** used in discbrake_std_cax4rt.inp.
discbrake_3d.inp	Three-dimensional model.
discbrake_postoutput.inp	∗POST OUTPUT analysis of the three-dimensional model.
discbrake_3d_extrapara.inp	Three-dimensional model with the second step run with ∗STEP, EXTRAPOLATION=PARABOLIC and with the default ∗CONTROLS option.

discbrake_3d_extrapara_300c.inp	Three-dimensional model with the second step run with *STEP, EXTRAPOLATION=PARABOLIC. It is assumed that several revolutions occurred and the initial temperature for the disc brake and pad is 300°C.
discbrake_3d_separated.inp	Three-dimensional model run using the *SOLUTION TECHNIQUE, TYPE=SEPARATED option.

Abaqus/Explicit input file

discbrake_3d_xpl.inp	Three-dimensional model.

References

- Day, A. J., "An Analysis of Speed, Temperature, and Performance Characteristics of Automotive Drum Brakes," Journal of Tribology, vol. 110, pp. 295–305, 1988.
- Day, A. J., and T. J. Newcomb, "The Dissipation of Frictional Energy from the Interface of an Annular Disc Brake," Proc. Instn. Mech. Engrs, vol. 198D, no. 11, pp. 201–209, 1984.
- Gonska, H. W., and H. J. Kolbinger, "ABAQUS Application Example: Temperature and Deformation Calculation of Passenger Car Brake Disks," ABAQUS Users' Conference Proceedings, 1993.

Table 5.1.1–1 Thermomechanical properties.

Temperature of property measurement (°C)	20	100	200	300
Young's modulus, E (N/mm^2)	2200	1300	530	320
Poisson's ratio, ν	0.25	0.25	0.25	0.25
Density, ρ (kg/m^3)	1550	1550	1550	1550
Thermal expansion coefficient (K^{-1})	10×10^{-6}	–	30×10^{-6}	–
Thermal conductivity, κ (w/mK)	0.5	0.5	0.5	0.5
Specific heat, C_p (J/kgK)	1200	1200	1200	1200

Table 5.1.1–2 Brake lining temperature characteristic.

Temperature of property measurement (°C)	100	200	300	400
Friction coefficient, μ	0.38	0.41	0.42	0.24

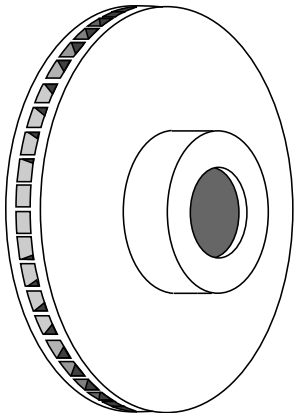

Figure 5.1.1–1 A vented brake disc design.

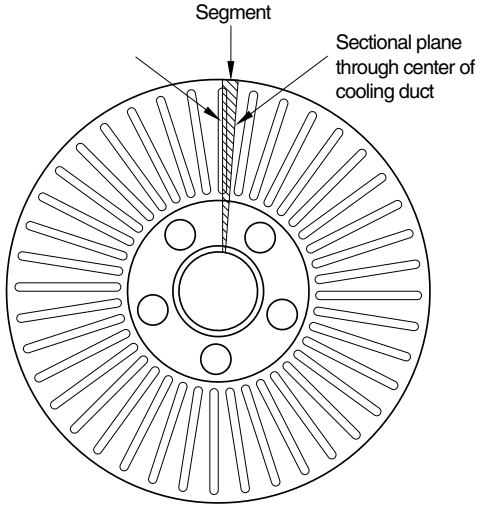

Figure 5.1.1–2 Modeling a segment of a brake disc.

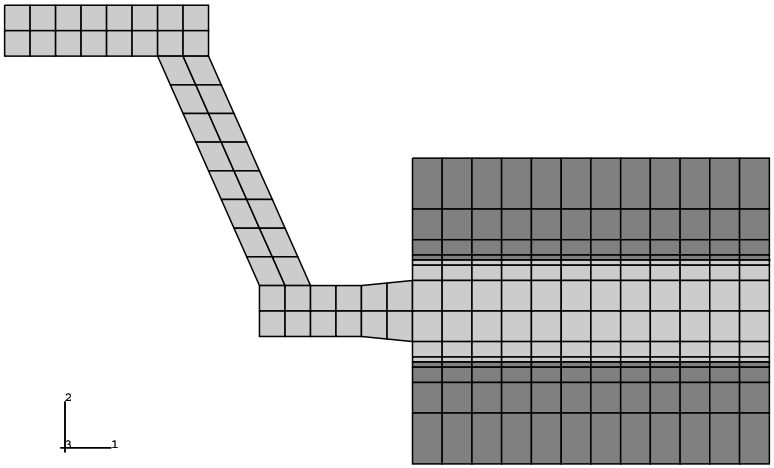

Figure 5.1.1–3 Mesh for the axisymmetric model, Abaqus/Standard.

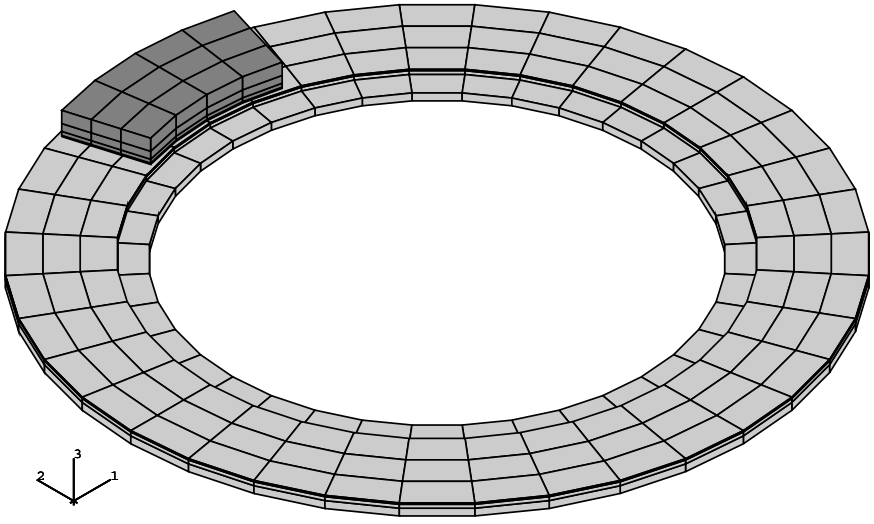

Figure 5.1.1–4 Mesh for the three-dimensional model.

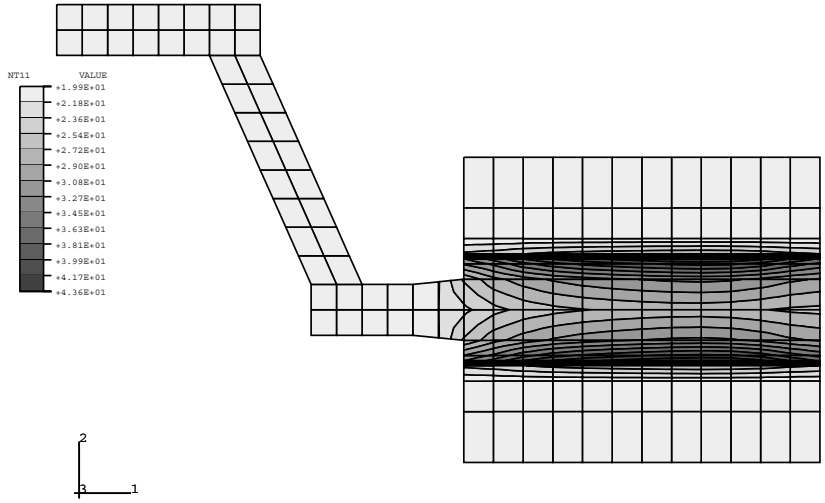

Figure 5.1.1–5 Isotherms of the axisymmetric model at $t = 0.675$, Abaqus/Standard.

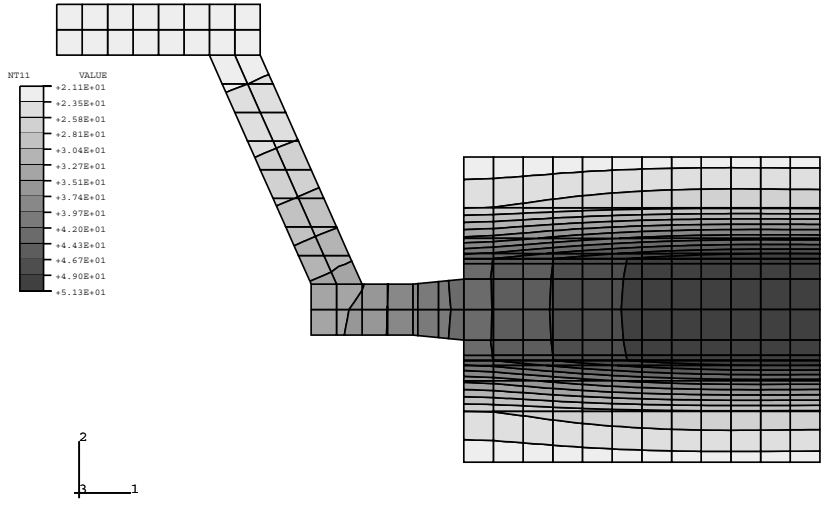

Figure 5.1.1–6 Isotherms of the axisymmetric model when braking has ended, Abaqus/Standard.

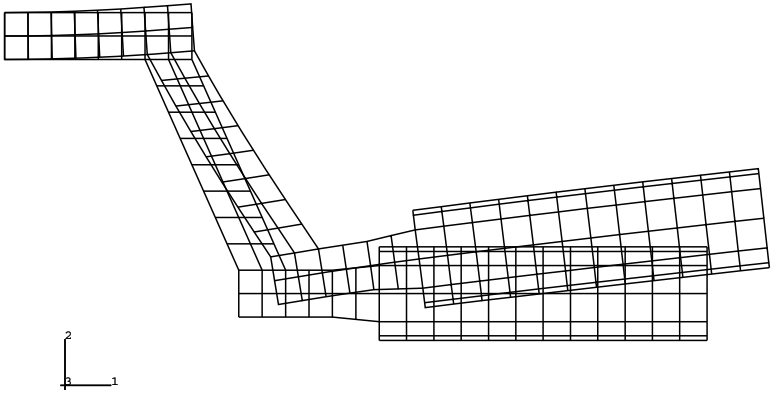

Figure 5.1.1–7 Deformation of the axisymmetric disc, displacement magnified by 128, Abaqus/Standard.

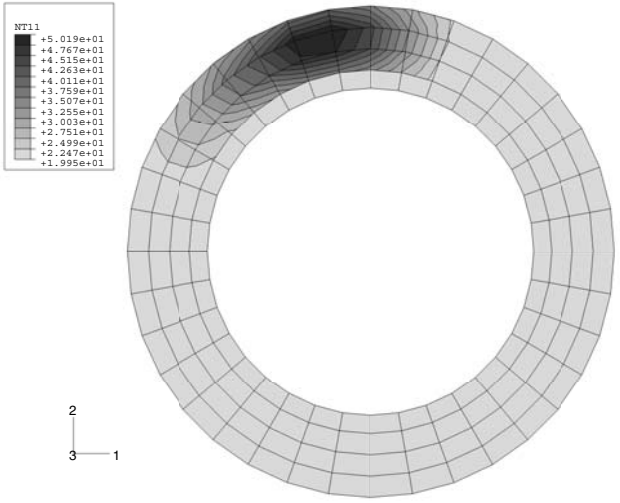

Figure 5.1.1–8 Isotherms of the disc surface, Abaqus/Standard.

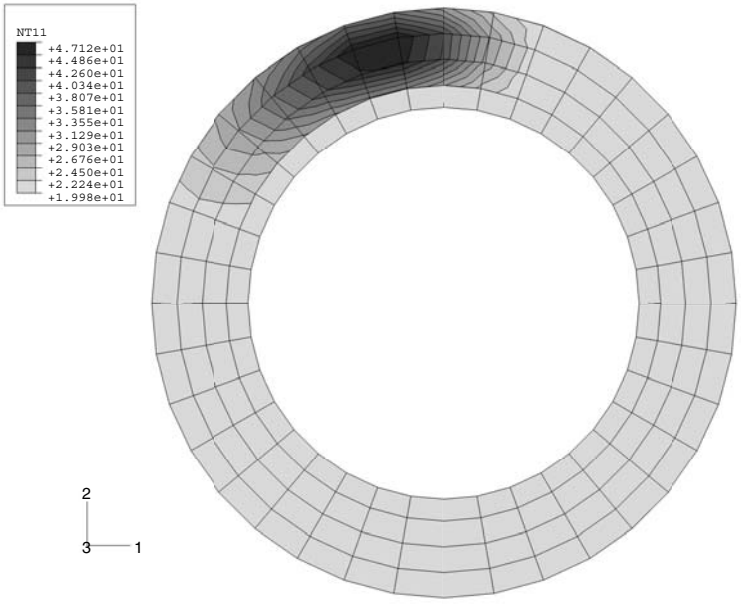

Figure 5.1.1–9 Isotherms of the disc surface, Abaqus/Explicit.

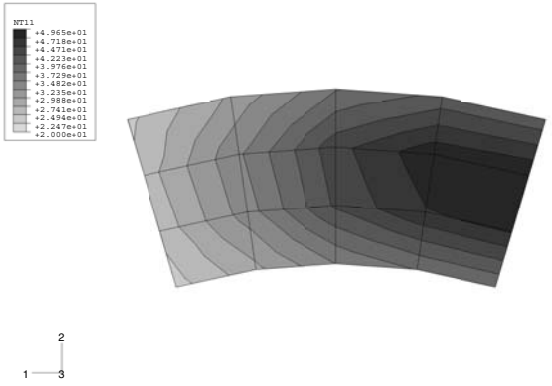

Figure 5.1.1–10 Isotherms of the inside of the brake pad, Abaqus/Standard.

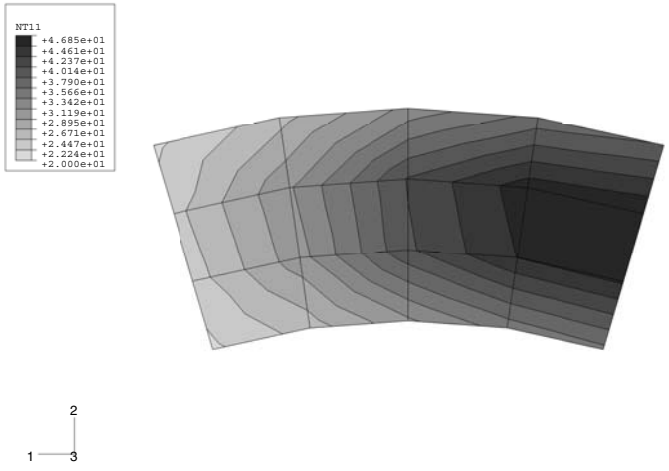

Figure 5.1.1–11 Isotherms of the inside of the brake pad, Abaqus/Explicit.

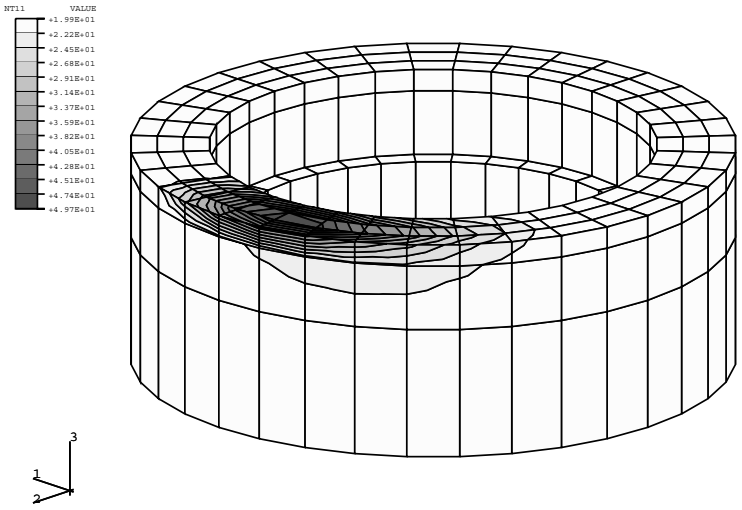

Figure 5.1.1–12 Isotherms of the disc with the thickness magnified 20 times, Abaqus/Standard.

5.1.2 A SEQUENTIALLY COUPLED THERMOMECHANICAL ANALYSIS OF A DISC BRAKE WITH AN EULERIAN APPROACH

Product: Abaqus/Standard

This example shows the sequentially coupled thermomechanical analysis of a disc brake using an Eulerian approach.

The prediction of fatigue and failure of a disc brake system is fundamental in assessing product performance. Disc brakes operate by pressing a set of brake pads against a rotating disc. The friction between the pads and the disc causes deceleration. The brake system then converts the kinetic energy of vehicle motion into heat. Severe temperature changes as well as mechanical loadings cause inelastic deformation and circumferential tensile stress in the disc, which may eventually lead to the failure of the disc.

The traditional way of analyzing this kind of problem is to use a Lagrangian approach in which the mesh used to discretized the disc rotates relative to the brake assembly. Since many revolutions are typically required to reach the state of interest to the analyst, this approach is prohibitively expensive and cumbersome. The steady-state transport analysis capability in Abaqus/Standard ("Steady-state transport analysis," Section 6.4.1 of the Abaqus Analysis User's Guide), which uses the Eulerian method in which the finite element mesh of the disc does not rotate relative to the brake assembly but the material "flows" through the mesh, provides a cost-effective alternative approach. The paths that the material points follow through the mesh are referred to as streamlines. This kinematic description converts the moving disc brake problem into a pure spatially dependent simulation. Thus, the mesh has to be refined only in a fixed region where the brake pads are in contact with the disc initially.

Geometry and model

The model analyzed in this example is a solid disc. An axisymmetric model is created to define the cross-sectional geometry of the disc, as shown in Figure 5.1.2–1. The disc has a thicker friction ring connected to a conical section that, in turn, connects to an inner hub. The inner radius of the friction ring is 86.5 mm, the outer radius is 133.0 mm, and the ring is 13.0 mm thick. The conical section is 27.2 mm deep. The inner radius of the conical section is 64.75 mm, the outer radius is 86.5 mm, and the section is 6.4 mm thick. The conical section has a thinner section out to a radius of 71.25 mm, which has a thickness of 4.5 mm. The hub has an inner radius of 33.0 mm, an outer radius of 71.25 mm, and is 6.2 mm thick. Symmetric model generation ("Symmetric model generation," Section 10.4.1 of the Abaqus Analysis User's Guide) is used to create a three-dimensional disc, as shown in Figure 5.1.2–2, by revolving the two-dimensional cross-section about the symmetry axis and to create the streamlines needed for the steady-state transport analyses in this example. There are eight elements through the thickness of the friction ring, four elements through the thickness of the hub, and four elements through the conical section. There are 40 element sectors in the circumferential direction of the disc, with a more refined mesh used in the region with higher thermal and stress gradients. The model consists of 9440 first-order forced convection/diffusion bricks (DCC3D8) in the heat transfer analysis, giving a total of about 11520 degrees of freedom; and it consists of 9440 first-order bricks (C3D8) in the subsequent steady-state transport analysis, giving a total of about 34560 degrees of freedom.

The disc pads are not modeled in the example. Instead, the thermal and mechanical interactions between the disc and the pads are represented by the application of appropriate distributed heat fluxes in the heat transfer analysis and by the application of appropriate concentrated loads in the steady-state transport analysis, respectively.

Material properties

The disc is made of metallic material, with a Young's modulus of 93.5 GPa, a yield stress of 153 MPa, a Poisson's ratio of 0.27, and a coefficient of thermal expansion of 11.7×10^{-6} per °C at room temperature. In this example the dissipation of the frictional heat-generated temperature fluctuates, ranging from a minimum value of 40°C to a maximum value of 560°C over the entire braking cycle. The temperature distribution when the disc is heated to its peak value is shown in Figure 5.1.2–3. Under such operating conditions plastic deformation, as well as creep deformation, is observed. The two-layer viscoelastic-elastoplastic model, which is best suited for modeling the response of materials with significant time-dependent behavior as well as plasticity at elevated temperatures, is used to model the disc (see "Two-layer viscoplasticity," Section 23.2.11 of the Abaqus Analysis User's Guide). This material model consists of an elastic-plastic network that is in parallel with an elastic-viscous network. The Mises metal plasticity model with kinematic hardening is used in the elastic-plastic network, and the power-law creep model with strain hardening is used in the elastic-viscous network. Because the elastic-viscoplastic response of the material varies greatly over this temperature range, temperature-dependent material properties are specified.

The thermal properties for the disc are temperature dependent with a conductivity of 51×10^{-3} W/mm per °C, a specific heat of 501 J/kg per °C, and a density of 7.15×10^{-6} kg/mm at room temperature.

Problem description and loading

A simulation of braking a solid disc rotating initially at an angular velocity of 155.7 rad/sec is performed. The braking time is approximately 5 seconds, followed by a cooling period of 600 seconds. A sequentially coupled thermomechanical analysis is performed on the solid disc using the Eulerian approach: a forced convection/diffusion heat transfer analysis is followed by a steady-state transport analysis. Heat fluxes with film condition and prescribed mass flow velocity through user subroutine **UMASFL** are applied to the thermal model, which consists of three steps. The first step, which lasts 0.2 seconds, simulates the response of the disc under constant distributed fluxes and a constant angular velocity. The second step involves 4.8 seconds during which the distributed fluxes and the angular velocity are decreased linearly to small values near zero at the end of the step. The final step, which lasts 600 seconds, simulates the continued cooling in the model. The resulting temperatures obtained during the heat transfer analysis are applied to the subsequent mechanical analysis, which involves five steady-state transport analysis steps.

The purpose of the first step in the mechanical analysis is to obtain a steady-state solution for a disc under constant concentrated loads due to the application of the brake pads to the disc. There is only one increment in this step. A constant temperature of 40°C is used, and a constant angular transport velocity of 155.7 rad/sec is specified.

The second step obtains a series of quasi-steady-state transport solutions under different temperature loading passes through the disc. The pass-by-pass steady-state transport analysis technique is used for this purpose. This step lasts 0.2 seconds with a constant angular velocity of 155.7 rad/sec throughout the entire step. Several increments are involved, with each increment corresponding to a complete temperature loading pass through the disc. The temperature values obtained during the first step of the heat transfer analysis are read into this step.

The third step also obtains a series of quasi-steady-state transport solutions under different temperature loading passes through the disc. However, this step involves 4.8 seconds over which the angular velocity is decreased linearly from 155.7 rad/sec at the beginning of the step to a small value close to zero at the end of this step. There are several increments in this step, with each increment corresponding to a complete temperature loading pass through the disc. The temperature values obtained during the second step of the heat transfer analysis are read into this step.

The fourth step obtains a steady-state solution for the disc due to the removal of the concentrated loads. There is only one increment in this step.

The last step obtains a series of quasi-steady-state transport solutions when the disc cools down. There are several increments over a step period of 600 seconds. The temperatures obtained during the last step of the heat transfer analysis are read into this step. Since the angular velocity is very small, this step essentially simulates a long-term elastic-plastic response for the disc.

Solution controls

Since the modified Newton's method is used in a steady-state transport analysis, more numerical iterations are necessarily required to obtain a converged solution. To decrease the computational time required for the analysis due to the unnecessary cutback of the increment size, the time incrementation control parameters are used to override the default values (see "Time integration accuracy in transient problems," Section 7.2.4 of the Abaqus Analysis User's Guide).

Results and discussion

One of the considerations in the design of a disc brake system is the stress distribution and deformation in the region where the brake pads are applied. Circumferential tensile stress, which may cause the fracture of the disc, will develop, making this region critical in the design. The results shown in Figure 5.1.2–6 through Figure 5.1.2–11 are measured in this region (element 7817, integration point 5; see point A in Figure 5.1.2–2). The temperature in this region (node 7820) is shown in Figure 5.1.2–4 as a function of the time over the entire braking process. Figure 5.1.2–5 shows the Mises stress distribution just before the distributed loads are removed and the cooling period starts (Step 3, increment 60).

Figure 5.1.2–6, Figure 5.1.2–7, and Figure 5.1.2–8 show the evolution of the circumferential stress, circumferential plastic strain, and circumferential viscous strain, respectively, as a function of the time throughout a complete braking cycle. A tensile stress of 54 MPa is developed after the disc is cooled down completely. Both plastic strain and viscous strain reach their saturation levels during the cooling period. The time evolution of the circumferential stress versus the circumferential plastic strain, shown in Figure 5.1.2–9, is obtained by combining Figure 5.1.2–6 with Figure 5.1.2–7. Similarly, the time evolution of the circumferential stress versus the circumferential viscous strain,

shown in Figure 5.1.2–10, is obtained by combining Figure 5.1.2–6 with Figure 5.1.2–8. The shapes of the stress-strain curves represent the plastic and viscous energies dissipated, respectively, over an entire braking cycle. These dissipated energies, which could be used to predict the fatigue life for the disc, are shown in Figure 5.1.2–11 as a function of the time.

Acknowledgments

SIMULIA gratefully acknowledges PSA Peugeot Citroën and the Laboratory of Solid Mechanics of the Ecole Polytechnique (France) for their cooperation in developing the Eulerian algorithm for steady-state transport analysis and for supplying the geometry and material properties used in this example.

Input files

discbrake_sst_heat_axi.inp	Axisymmetric model for the heat transfer analysis.
discbrake_sst_heat_symm.inp	Three-dimensional model for the heat transfer analysis.
exa_discbrake_sst_heat_symm.f	User subroutine **UMASFL** used in discbrake_sst_heat_symm.inp.
discbrake_sst_axi.inp	Axisymmetric model for the mechanical analysis.
discbrake_sst_symm_pbp.inp	Three-dimensional model for the mechanical analysis.

References

- Maitournam, M. H., “Formulation et Résolution Numérique des Problèmes Thermoviscoplastiques en Régime Permanent,” Thèse de l’Ecole des Ponts et Chaussées, 1989.
- Nguyen-Tajan, T. M.L., “Modélisation Thermomécanique des Disques de Frein par une Approche Eulérienne,” Thèse de l’Ecole Polytechnique, 2002.

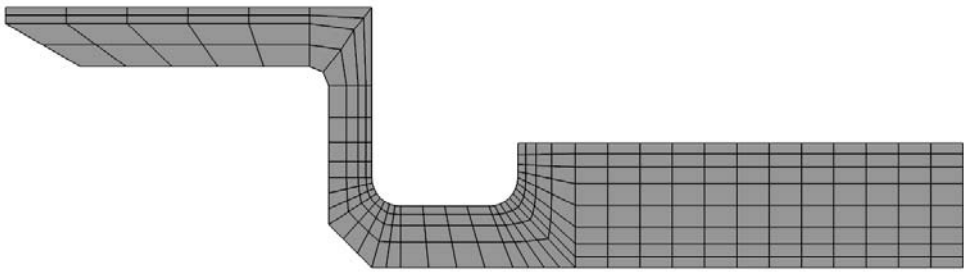

Figure 5.1.2–1 Mesh for the axisymmetric model.

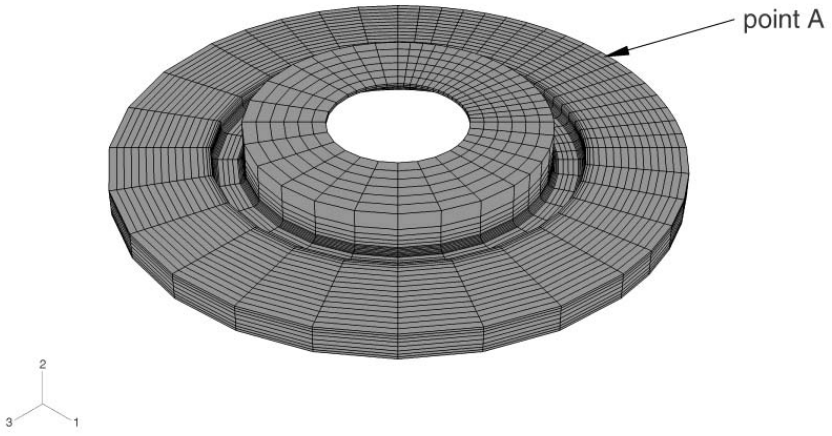

Figure 5.1.2–2 Mesh for the three-dimensional model.

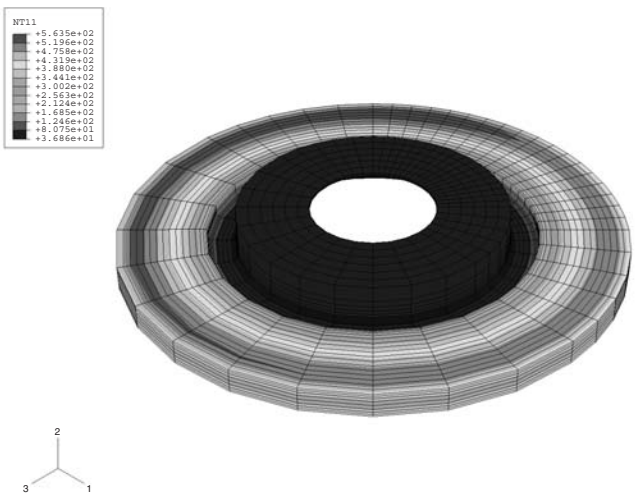

Figure 5.1.2–3 Temperature distribution when the disc is heated to its peak value.

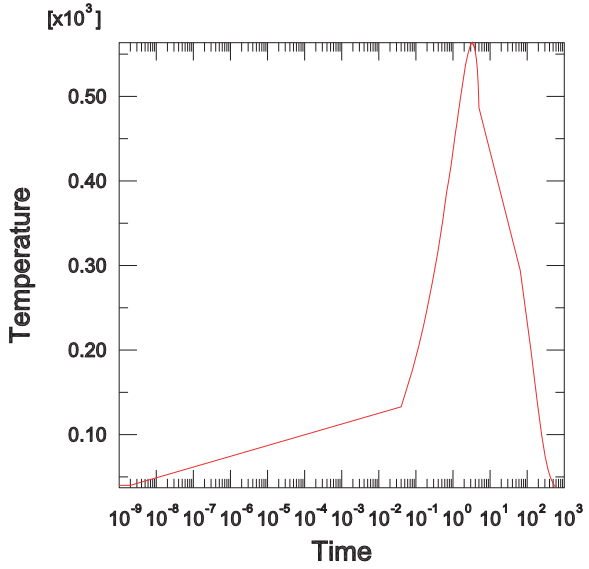

Figure 5.1.2–4 Temperature at node 7820 as a function of time during the entire braking period.

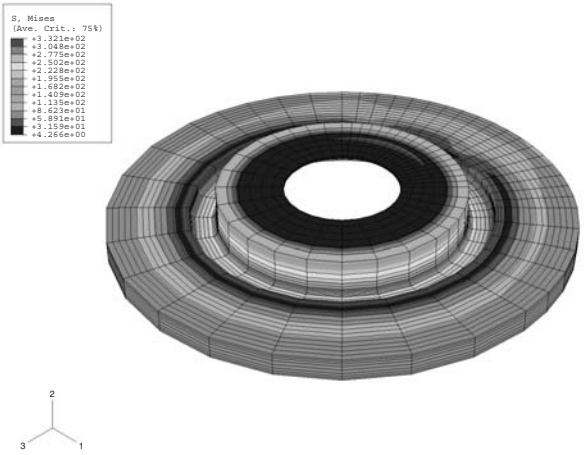

Figure 5.1.2–5 Mises stress distribution (Step 3, increment 60) just before the cooling period starts.

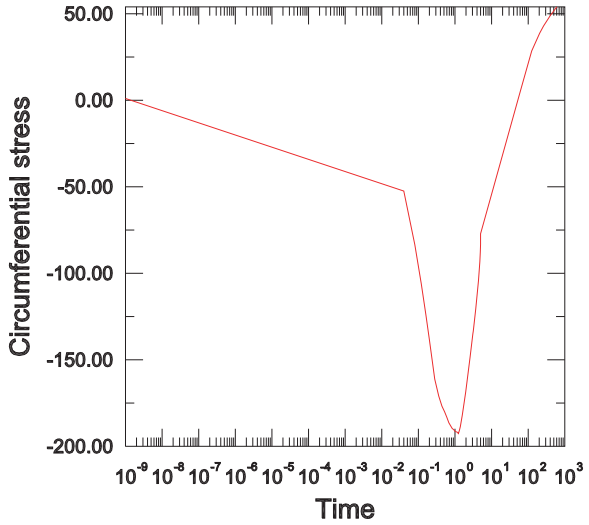

Figure 5.1.2–6 Evolution of the circumferential stress as a function of time.

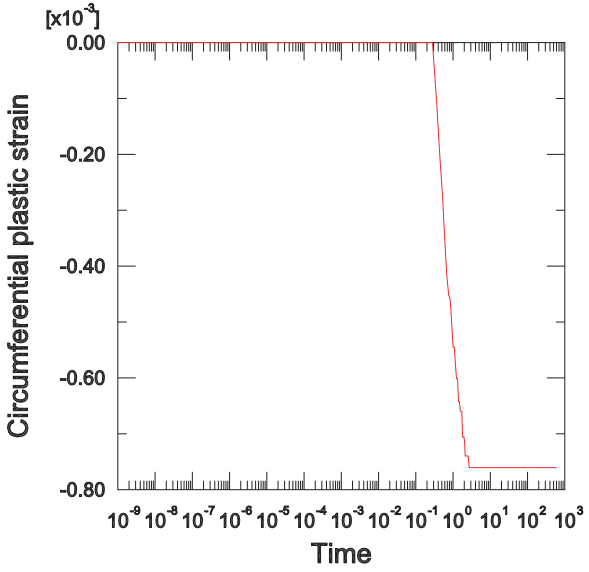

Figure 5.1.2–7 Evolution of the circumferential plastic strain as a function of time.

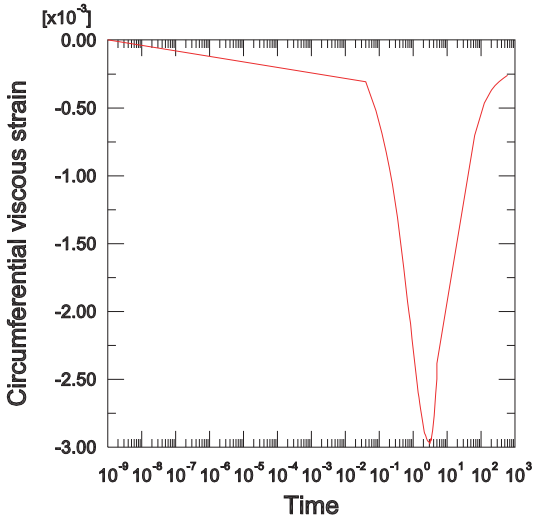

Figure 5.1.2–8 Evolution of the circumferential viscous strain as a function of time.

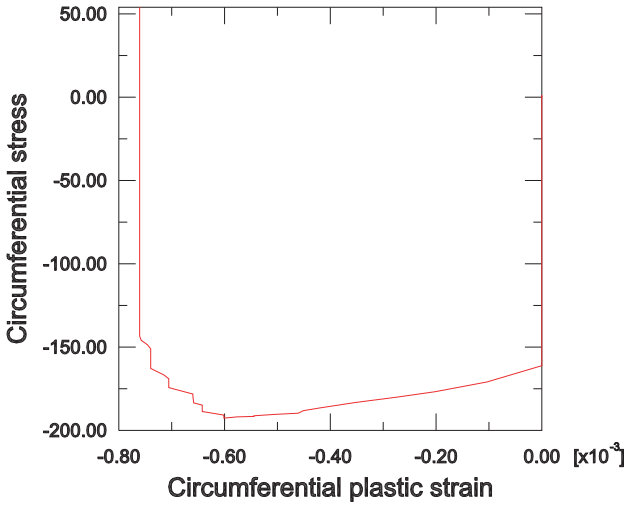

Figure 5.1.2–9 Evolution of the circumferential stress versus the circumferential plastic strain.

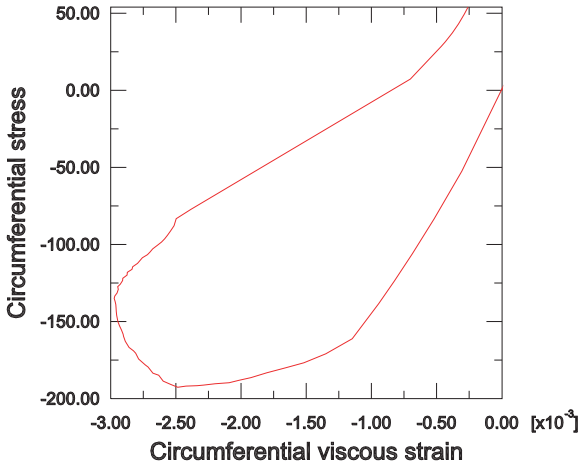

Figure 5.1.2–10 Evolution of the circumferential stress versus the circumferential viscous strain.

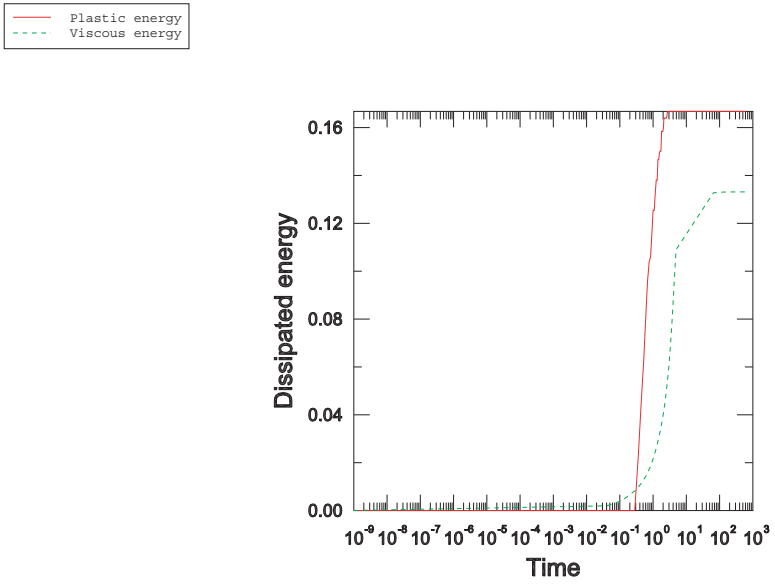

Figure 5.1.2–11 Evolution of the plastic dissipated energy and the viscous dissipated energy as a function of time.

5.1.3 EXHAUST MANIFOLD ASSEMBLAGE

Product: Abaqus/Standard

This example shows how to model varying boundary constraints with the prescribed assembly load capability of Abaqus.

Engine exhaust manifolds are commonly subject to severe thermal cycles during operation and upon shutdown. Thermal expansion and contraction of the manifold is constrained by its interaction with the engine head to which it is bolted. These constraints govern the thermomechanical fatigue life of the manifold.

The initial assembly procedure consists of bolting the flanges of the manifold to the engine head with prescribed bolt forces that produce uniform axial bolt stresses. Under subsequent operating conditions such as thermal cycling and creep, these bolt forces may increase or relax, possibly changing normal pressures and resulting in lateral slippage between the engine head and the manifold flanges. Thus, the boundary constraints on the manifold flanges are a function of the response of the entire assembly to its operating conditions. As such, these boundary constraints cannot be prescribed *a priori*. This example shows how to simulate these varying boundary constraints with the prescribed assembly load capability of Abaqus.

The problem scenario consists of three steps:

1. Apply prescribed bolt loads to fasten the exhaust manifold to the engine head.
2. Subject the assembly to the steady-state operating temperature distribution.
3. Return the assembly to ambient temperature conditions.

Geometry and model

The exhaust manifold assemblage being analyzed is depicted in Figure 5.1.3–1. It consists of a four tube exhaust manifold with three flanges, bolted with seven bolts to a small section of the engine head.

The manifold is cast from gray iron with a Young's modulus of 138 GPa, a Poisson's ratio of 0.283, and a coefficient of thermal expansion of 13.8×10^{-6} per °C. In this example the region of the manifold where the hot exhaust gases converge is subject to temperatures ranging from an initial value of 300 K to an extreme of 980 K. The elastic-plastic response of gray cast iron varies greatly over this range of temperatures, so the temperature-dependent plasticity curves shown in Figure 5.1.3–2 are used for the manifold material. Gray cast iron exhibits different behavior in tension and compression; therefore, these curves represent the average response. The Mises metal plasticity model with isotropic hardening is used. The three manifold flanges contain a total of seven bolt holes. The 9.0 mm diameter of these bolt holes is slightly greater than the 8.0 mm diameter of the bolt shanks to allow for some unobstructed lateral motion of the manifold.

For simplicity, only a portion of engine head directly beneath the manifold flanges is modeled. The head is made from aluminum, with a Young's modulus of 69 GPa, a Poisson's ratio of 0.33, and a coefficient of thermal expansion of 22.9×10^{-6} per °C. The head has four exhaust ports leading into the manifold tubes. It has seven bolt holes used to secure the manifold.

Seven bolts fasten the manifold to the head. The bolts are made from steel, with a Young's modulus of 207 GPa, a Poisson's ratio of 0.3, and a coefficient of thermal expansion of 13.8×10^{-6} per °C. The bolt shanks have a diameter of 8 mm. The bolt head diameters are 16 mm.

Three-dimensional, deformable-to-deformable, small-sliding contact conditions apply to the model. The bottoms of the bolt heads form contact bearing surfaces, with the top surfaces of the manifold flanges lying directly beneath them. In addition, the bottoms of the manifold flanges form contact bearing surfaces with the top of the engine head. Each of these surfaces is defined in Abaqus with a surface definition. Respective mating surfaces are paired together with contact pairs. Normal pressures will be transmitted through these contact pairs as a result of the bolt tightening forces in Step 1. The forces carried by the bolts will vary as they respond to the thermal cycling of the assembly in subsequent steps. These fluctuations in bolt loads will result in varying normal pressures transmitted across the contact pairs. Lateral slip of the mating components will occur if the critical frictional shear stress limit is surpassed by lateral forces developed in the system. A friction coefficient of 0.2 is used between all contacting surfaces. Contact conditions are not necessary between the bolt shanks and the holes in the manifold flanges because of the design clearance between them. Contact between the bolt shanks and the holes in the engine head is not modeled.

All three structural components (manifold, head, and bolts) are modeled with three-dimensional continuum elements. The model consists of 7450 first-order brick elements with incompatible deformation modes, C3D8I, and 282 first-order prism elements, C3D6. The C3D6 elements are used only where the complex geometry precludes the use of C3D8I elements. The C3D8I elements are selected to represent the bending of the manifold walls with only one element through the thickness of the tube walls.

Loading and boundary constraints

It is assumed that the engine head is securely fixed to a stiff and bulky engine block, so the nodes along the base of the head are secured in the direction normal to the base (the global x-direction) but are free to move in the two lateral directions to account for thermal expansion. It is also assumed that the bolts are threaded tightly into the engine head, with the bolt threads beginning directly beneath the section of engine head modeled. Therefore, the nodes at the bottom of the bolt shanks are shared with the nodes of the surrounding engine head elements and are also secured in the global x-direction. The manifold flanges are sandwiched between the top of the engine head and the base of the bolt heads using contact pairs. The line of action of the bolt forces (bolt shank axes) is along the global x degree of freedom. Soft springs acting in the global y- and z-directions are attached to the outlet end of the manifold and to the two ends of the head to suppress rigid body motions of the manifold and head, respectively. These springs have no influence on the solution.

In the first step of the analysis each of the seven bolts is tightened to a uniform bolt force of 20 kN. In subsequent steps the variation of the bolt loads is monitored as the bolts respond to the thermal loading on the assembly as a whole. The "prescribed assembly load" capability of Abaqus is used. For each bolt we define a "cut," or pre-tension section, and subject the section to a specified tensile load. As a result, the length of the bolt at the pre-tension section will change by the amount necessary to carry the prescribed load, while accounting for the compliance of the rest of the system. In the next step the prescribed bolt

loads are replaced by the condition that the length changes calculated in the previous step remain fixed. The remainder of the bolt is free to deform.

The same procedure is used for all seven bolts. First, pre-tension sections are defined as "cuts" that are perpendicular to the bolt shank axes by defining surfaces on the faces of a group of elements within each bolt shank, as shown in Figure 5.1.3–3. The line of action of the bolt force is in the direction that is normal to this surface. Next, each bolt is assigned an arbitrary, independent node that possesses one degree of freedom (DOF 1), to which the bolt force will be applied. These nodes are called the "pre-tension nodes" (all seven bolt pre-tension nodes are placed into a node set named **BOLTS**). The spatial position of a pre-tension node is irrelevant. Finally, each surface is associated with the appropriate pre-tension node using a pre-tension section.

A portion of the Abaqus model definition section defining the pre-tension section is shown below:

```
*ELSET, ELSET=BCUT1, GENERATE
19288,19307
*SURFACE, NAME=BOLT1
BCUT1,S2
*NODE, NSET=BOLTS
99991,   21.964    ,  -139.80    ,  -12.425
…
99997,   21.964    ,   137.38    ,  -12.226
*PRE-TENSION SECTION, SURFACE=BOLT1, NODE=99991
```

In Step 1 of the analysis a concentrated clamping load of 20 kN is applied to each of the pre-tension nodes in node set **BOLTS**. In Step 2 the concentrated load from Step 1 is removed and replaced by a "fixed" boundary condition that will hold the pre-tension section length changes from Step 1 fixed. Over the course of a step in which a load is replaced by a boundary condition, CF1 is ramped down, while RF1 is ramped up to replace it. Therefore, the total force across the bolt is the sum of the concentrated force (CF1) and the reaction force (RF1) on the pre-tension node. This total force is available as TF1. Additionally in this step of the analysis nodal temperatures depicting the steady-state temperature distribution in the manifold are read from an external file. The temperature distribution is shown in Figure 5.1.3–4. These nodal temperatures can be generated by an Abaqus heat transfer analysis. Each of the nodes in the model has its temperature ramped up from the initial ambient temperature of 300 K to its final steady-state temperature. These nodal temperatures are interpolated to the element integration points so that the correct temperature-dependent plasticity data can be used in the constitutive calculations. Finally, in Step 3 the nodal temperatures are ramped back down to the initial ambient temperature of 300 K.

Results and discussion

The analysis is performed as a small-displacement analysis. The nonlinearities in the problem are the result of changing contact conditions, frictional slip and stick, and temperature-dependent plasticity.

Figure 5.1.3–5 shows the lateral displacement of the bottom surface of the flange at the end of the heat-up step. As a result of frictional sticking, the ends of the two outer manifold flanges have expanded outward relative to one another by only about 0.75 mm. Plastic yielding conditions result since thermal

expansion of the remainder of the manifold is constrained by this limited lateral flange motion. A separate thermal-stress analysis of the manifold only, with no bolt constraints included, produced relative lateral expansions of about 1.1 mm and very little plasticity.

Figure 5.1.3–6 is a plot of the forces carried by each of the seven bolts throughout the load history. This plot can be obtained with the *X*–*Y* plotting capabilities in Abaqus/CAE. The curves contain the values of the total forces (TF1) for the pre-tension nodes in node set **BOLTS**. The loads carried by the bolts increase significantly during the heat-up step. The loads do not return precisely to the original bolt load specification upon cool down because of the residual stresses, plastic deformation, and frictional dissipation that developed in the manifold.

Input files

manifold.inp	Input data for the analysis.
manifold_node_elem.inp	Node and element definitions.
manifold_nodaltemp.inp	Nodal temperature data.

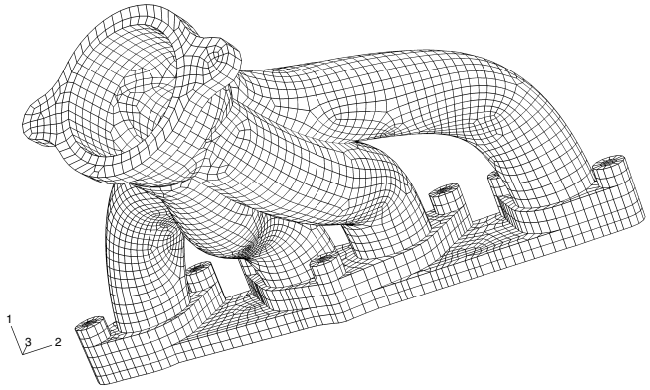

Figure 5.1.3–1 Manifold assemblage.

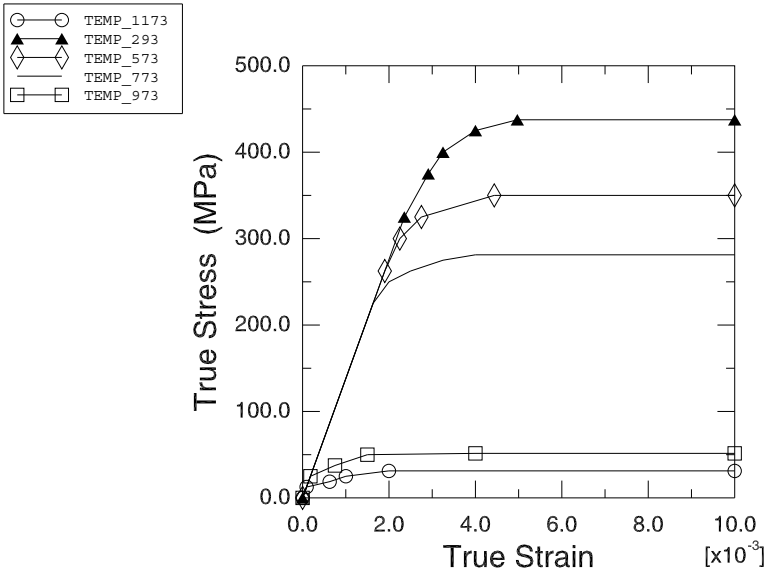

Figure 5.1.3–2 Gray cast iron temperature-dependent plasticity curves.

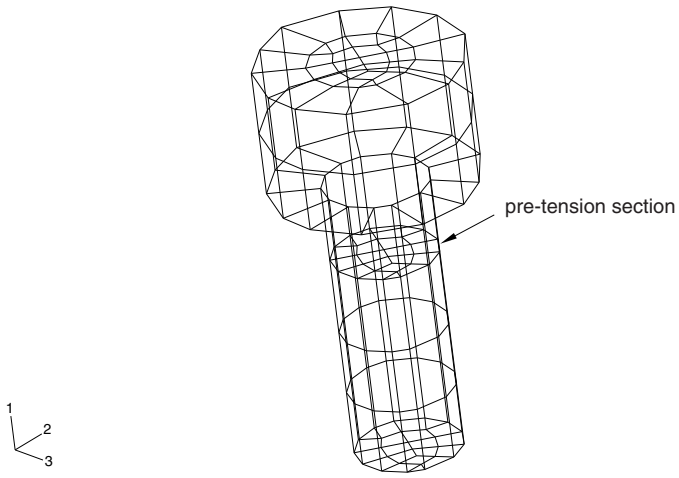

Figure 5.1.3–3 Pre-tension section.

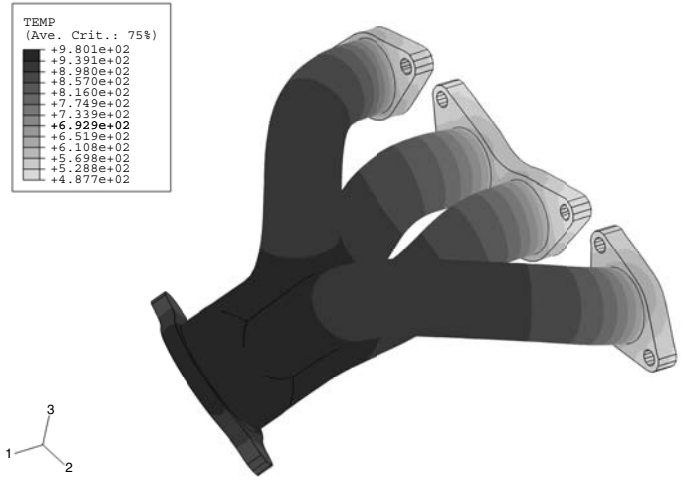

Figure 5.1.3–4 Steady-state temperature distribution.

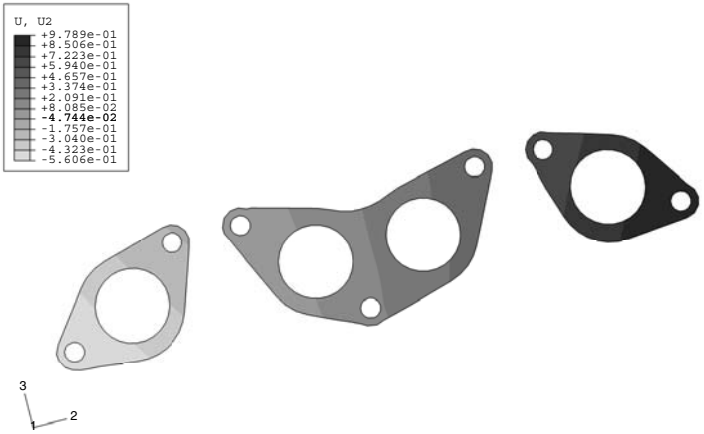

Figure 5.1.3–5 Lateral expansion of manifold footprint.

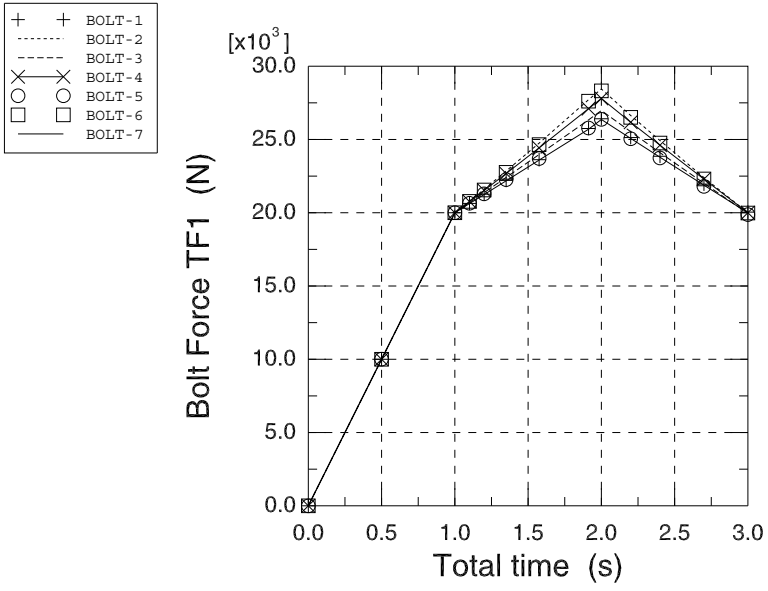

Figure 5.1.3–6 History of bolt forces.

5.1.4 COOLANT MANIFOLD COVER GASKETED JOINT

Product: Abaqus/Standard

This example shows how to use gasket elements to model a coolant manifold cover gasketed joint.

Engine gaskets are used to seal the mating surfaces of engine components to maintain the integrity of the closed system throughout a wide range of operating loads and environmental conditions. Inadequate gasket performance leads to diminished engine pressure and fluid leakage, resulting in degradation of engine performance and potential engine damage. The gasket, the engine component flanges, and the fasteners—collectively referred to as a gasketed joint—must be considered as a unit when determining the system sealing performance because most gasketed joints do not obtain a uniform contact stress distribution due to nonuniform bolt spacing and flange distortion during assembly and subsequent operational loading.

Engine gaskets are often complicated geometric constructs of various engineering materials and are subject to large compressive strains. The compressive response of the gasket is highly nonlinear. Such complexities make detailed modeling of gaskets with continuum elements difficult and impractical when analyzing complete assemblies.

Abaqus has a dedicated class of elements, referred to as gasket elements, that simplify the modeling of such components while maintaining the essential ingredients of the nonlinear response. Typical use of these gasket elements involves a tabular representation of the pressure versus closure relationship in the thickness direction of the gasket. The pressure versus closure models available in Abaqus allow the modeling of very complex gasket behaviors, including nonlinear elasticity, permanent plastic deformation, and loading/unloading along different paths. These behaviors are usually calibrated directly from test data. In this manner a complex gasket can be modeled effectively using a single gasket element in the thickness direction.

In this example a paper foam gasket with a silkscreened silicone bead is compressed between the lower engine intake manifold and the coolant manifold cover. The coolant manifold cover seals the lower intake manifold coolant passages so that the coolant can be distributed to the cylinder heads. An exploded view of the gasketed joint model is shown in Figure 5.1.4–1. It consists of two steel bolts, an aluminum coolant manifold cover, a paper foam gasket with a silicone bead, and—for simplicity—only a portion of the lower intake manifold, which is composed of steel. Symmetry conditions reduce the structure to a half model. The gasketed joint is subjected to the following mechanical and environmental load conditions:

1. Simulate the bolt loading sequence to fasten the joint.
2. Heat the assembly to the maximum operating temperature and apply interior cavity pressure.
3. Cool the assembly to the minimum operating temperature while maintaining interior cavity pressure.
4. Return the assembly to ambient conditions with the interior pressure removed.
5. Disassemble the gasketed joint.

Geometry and material

The portion of the lower intake manifold that is modeled has two passages. Coolant flows from one passage into the manifold cover and back out through the other passage. Two steel bolts secure the cover

to the manifold. The bolt shanks have a diameter of 6.0 mm, and the bolt heads have a diameter of 11.8 mm. The bolts and the lower intake manifold are assigned a Young's modulus of 2.0×10^5 MPa, a Poisson's ratio of 0.28, and a coefficient of thermal expansion of 1.6×10^{-5} per °C. The aluminum coolant manifold cover has a Young's modulus of 7.1×10^4 MPa, a Poisson's ratio of 0.33, and a coefficient of thermal expansion of 2.3×10^{-5} per °C.

The metal components (bolts, cover, and intake manifold) are modeled with three-dimensional continuum elements: 1304 first-order brick elements with incompatible deformation modes (C3D8I) and 208 first-order prism elements (C3D6). The C3D8I elements are chosen to capture the bending of the cover, using only one element through its thickness. The C3D6 elements are used only where geometric constraints preclude the use of C3D8I elements.

The gasket schematic shown in Figure 5.1.4–2 has two distinct regions. The majority of the gasket is composed of a 0.79 mm thick, flat, crushable paper foam material. To ensure proper sealing pressures for this joint, a 0.076 mm thick silicone bead has been silkscreened along the top surface of the gasket encircling the interior cavity. Placing silicone beads on gaskets results in a change in the load transmitting characteristics of the gasket, which often improves both the recovery properties of the gasket and its potential to remain sealed for the long term.

The entire gasket, including the bead, is modeled as a flat sheet with one gasket element through the thickness (see Figure 5.1.4–3). A relatively fine mesh is used for the gasket to capture the in-plane variation of the gasket sealing pressure. This creates a mismatched mesh across the contacting surfaces, but Abaqus contact definitions do not require one-to-one matching meshes across contact pairs. The gasket components (silicone bead region and paper foam region) are modeled with 973 first-order 8-node area elements (GK3D8) and 29 first-order 6-node area elements (GK3D6). The physical thickness of the entire sheet of gasket elements corresponds to the initial combined height of the paper foam and the silicone bead, 0.866 mm. The elements in the region of the gasket beneath the silicone bead are assigned different gasket properties from the rest of the elements in the gasket model. The paper foam region is initially not in contact with the cover. The initial gap is 0.076 mm. No pressure is generated in this portion of the gasket until the gap has closed. Gasket region property distinctions, such as initial gaps and different pressure versus closure relationships, are assigned to corresponding element sets by referring to different gasket behavior definitions.

Experimentally determined pressure versus closure curves for the two distinct gasket regions without the initial gap taken into account are shown in Figure 5.1.4–4. Tabular representations of these curves are specified using a gasket thickness-direction behavior that is associated with the respective gasket behavior definitions. Creep/relaxation properties of the gasket and temperature-dependent pressure versus closure properties, capturing such effects as the glassy transition temperature of the silicone bead, are not accounted for in this example. Initially, Abaqus considers the gasket behavior to be nonlinear elastic, such that loading and unloading occur along the same user-defined nonlinear path. Abaqus considers yielding to occur once the slope of the pressure versus closure curve decreases by at least 10%. In addition to the single loading curve, whose closure increases monotonically, the user can define any number of unloading curves at different levels of plastic closure. Yielding occurs at a closure of 0.1118 mm for both regions of the gasket in this example, after which the gasket stiffness decreases slightly up to a closure of 0.15 mm, the final point on the loading curve. Beyond the data of the loading curve defined by the user, Abaqus considers the gasket to behave with a fully crushed elastic response

by linearly extrapolating the last segment of the last specified unloading curve (alternatively, the user could have specified a piecewise linear form).

A single unloading curve is defined for each of the two gasket regions: the unloading curve for the silicone bead region is defined at 0.11 mm of plastic closure, and the unloading curve for the paper foam region is defined at 0.09 mm of plastic closure. Any unloading of the gasket beyond the yield point occurs along a curve interpolated between the two bounding unloading curves, which—for this example—are the initial, nonlinear elastic curve and the single unloading curve.

Gasket materials often have higher coefficients of thermal expansion than most of the metals from which the bolts and flanges are made. For situations involving wide and rapid temperature fluctuations resultant differences in relative expansion and contraction can have a significant effect on the sealing properties of the gasket. The coefficient of thermal expansion for the silicone bead region is 1.2×10^{-4} per °C, and for the paper foam region it is 3.0×10^{-5} per °C.

In this case, because of the differences in thermal expansion between the aluminum cover and the steel intake manifold, it is important to account for the membrane and transverse shear properties of the gasket and to model frictional effects between mating surfaces. For this analysis the silicone bead region of the gasket is defined to have a membrane stiffness of 75 MPa and a transverse shear stiffness of 40 MPa. The base foam material is defined with a value of 105 MPa for the membrane stiffness and a value of 55 MPa for the transverse shear stiffness. A friction coefficient of 0.2 is used between all mating surfaces.

A separate analysis is included in this example problem using the "thickness-direction only" version of the gasket elements (GK3D8N and GK3D6N). These elements respond only in the thickness direction and have no membrane or transverse shear stiffness properties. They possess only one degree of freedom per node. As a result, frictional effects cannot be included at the surfaces of these elements. They are more economical than more general gasket elements that include membrane and transverse shear responses and may, thus, be preferable in models where lateral response can be considered negligible.

Loading and boundary constraints

Symmetry boundary constraints are placed along the nodes on the symmetry plane. Furthermore, it is assumed that the intake manifold is a stiff and bulky component, so nodes along the base of the portion of the manifold modeled are secured in the normal direction (the global z-direction). Except for a soft spring constraint to eliminate rigid body motion, these manifold base nodes are free to displace laterally to allow for thermal expansion. Soft springs are also attached to the cover to eliminate rigid body motion in the x- and z-directions.

The bottoms of the bolt heads form contact bearing surfaces with the top surface of the cover flange. In addition, the top of the gasket interacts with the bottom of the cover, while the bottom of the gasket contacts the top of the manifold. Each of these surfaces is defined with a separate surface definition. Mating surfaces are paired together with contact pairs. Three-dimensional, deformable-to-deformable, small-sliding contact conditions apply to each of these contact pairs. The gasket is attached to the manifold base using the no-separation contact behavior, thus constraining it against rigid body motion in the global z-direction. The gasket membrane is allowed to stretch, contract, or shear as a result of frictional effects on both sides of the gasket. The bolts are assumed to be threaded tightly into the base.

Therefore, the nodes at the bottom of the bolt shanks are shared with the intake manifold. Contact between the bolt shanks and the bolt holes is not modeled.

The "prescribed assembly load" capability is used to define pre-tension loads in each of the bolts. For each of the two bolts we define a "cut" or pre-tension section and subject the section to a specified load. As a result, the length of the bolt at the pre-tension section changes by the amount necessary to carry the prescribed load, while accounting for the compliance of the rest of the joint. Once a bolt has been pre-tensioned, the applied concentrated bolt load is replaced with a "fixed" boundary condition, which specifies that the length change of the bolt at the "cut" remains fixed, while the remainder of the bolt is free to deform.

The sequence in which the bolts are tightened can have an impact on the distribution of the resultant contact area stress. A poorly specified bolt sequence can cause excessive distortion of the gasket and the flanges, which may lead to poor sealing performance. In the first step of the analysis the left bolt is pre-tensioned to a load of 6000 N using a pre-tension section. In the second step the right bolt is pre-tensioned to 6000 N and the prescribed load on the left bolt is replaced with a fixed boundary condition as described above. Since only half of each bolt is modeled, a total load of 12000 N is carried by each bolt.

Step 3 is the beginning of the three-step thermomechanical operational cycle. In Step 3 the entire assembly is heated uniformly to its maximum operating temperature of 150°C, while simultaneously the interior cavity is pressurized to 0.689 MPa and the prescribed load on the pre-tension section of the right bolt is replaced with a fixed boundary condition. In Step 4 the system temperature is decreased to the minimum operating temperature of −40°C while maintaining the interior pressure load of 0.689 MPa. In Step 5 the gasketed joint is returned to the ambient temperature conditions and the internal cavity pressure is removed.

The sixth and final step in the analysis simulates disassembly of the gasketed joint by removing the bolt loads. This process demonstrates the interpolated unloading response for the different regions of the permanently deformed gasket.

Results and discussion

The prime interest in this problem is the variation of bolt forces during the initial assembly and thermomechanical cycle and the resultant distribution and variation of the gasket sealing pressure.

The function of the fasteners in a gasketed joint is to apply and maintain the load required to seal the joint. The bolt pattern and tension are directly related to the sealing pressure in the clamped gasket. At the maximum service temperature the bolt loads can be expected to be at their peak as a result of thermal expansion effects. It is important to ensure that the stress values of the metal engine components remain below yield and that there is no significant bending of the flanges, which may cause improper sealing of the gasket. At the minimum operating temperature the bolt loads are expected to reach a minimum as a result of thermal contraction effects. Hence, it is necessary to assess that adequate sealing pressure is retained throughout the gasket.

Figure 5.1.4–5 shows the bolt load variation over the course of the six analysis steps. During the first step the pre-tension section node on the right bolt was prescribed a zero change of length constraint, which implies that the right bolt has just been placed in position but not torqued tightly. Hence, as the left bolt is tightened during Step 1, a small reaction load is generated in the right bolt. At the end of

the second step during which the right bolt is tightened to carry a force of 6000 N, the force in the left bolt increases to 6200 N. In Step 3 the deformation of the assembly causes the bolt forces to increase to maximum values of 6800 N in the left bolt and 6600 N in the right bolt because of thermal expansion and interior pressurization. When the assembly is cooled to the minimum operating temperature, the bolt loads reach their minimum values. Due to thermal cycling and interior cavity pressure inducing inelastic response in the gasket, the bolt forces at the end of the operational cycle reduce to 6050 N in the left bolt and 5950 N in the right bolt.

The gasket sealing pressure pattern depends on the rigidity of the flanges. Hence, it is useful to predict how the structure will deform due to the applied loading. Figure 5.1.4–6 shows the deformed shape of the coolant manifold cover at a displacement magnification factor of 50. Bowing of the cover from initial assembly and subsequent operational loads will lead to a nonuniform sealing pressure distribution in the gasket. Figure 5.1.4–7 illustrates the distribution of the contact pressure along with the contact pressure error indicator on the gasket surface after initial fastening of the joint. The error indicator field is used to assess the contact pressure accuracy and validate the existing mesh refinement. High values of the error indicator are observed in the regions near the boundary between the two materials used for modeling the gasket response. Capturing the contact pressure gradients more accurately would require increasing the mesh refinement in these regions.

Figure 5.1.4–8 shows the sealing pressure as a function of position along the perimeter of the silicone bead at the end of each of the analysis steps. The sealing pressure reaches a minimum at the point equidistant from the bolts, making this the critical point in the gasketed joint design. This figure also reflects the reduction in the sealing pressure near the bolt holes as a result of plastic deformation of the gasket body during the operational cycle. Figure 5.1.4–9 is a contour plot of the permanent deformation in the gasket after completion of the thermomechanical cycle.

Figure 5.1.4–10 follows the pressure/closure history of one point in the gasket during this analysis in relation to the user-specified loading/unloading test data. The “mechanical closure” (total closure, E11, minus thermal closure, THE11) is plotted along the abscissa of this figure. The material point traced (element 18451, integration point 1) is located along the inside periphery of the silicone bead at the symmetry plane of the assembly nearest the left bolt. Step 1 shows that this point follows the initial elastic loading curve up to the closure of 0.1118 mm. After this amount of closure, further loading causes plastic deformation. In the second step the tightening of the bolt results in a very small amount of unloading for this material point. For purposes of clarity, this deformation is not shown in the figure. Step 3 involves heating the system to the maximum operating temperature and pressurizing the interior cavity so that further yielding of the material point occurs. Step 4 results in the partial unloading of the point due to the thermal contraction associated with cooling the assembly to the minimum operating temperature. For this case the unloading path is based on a curve interpolated between the initial, nonlinear elastic curve and the single unloading curve. The return of the assembly to ambient conditions partially reloads this point along the same path as the previous unloading; however, no further yielding of this material point occurs during this step. In the final step the gasket is unloaded completely.

The analysis using the “thickness-direction only” gasket elements runs in nearly half the CPU time of the full three-dimensional gasket element model. Minimum gasket sealing pressures in Step 4 of this analysis are predicted to be about 20% lower because frictional effects are neglected.

Input files

manifoldgasket.inp	Input data for the analysis.
manifoldgasket_mesh.inp	Node, element, and surface definitions.
manifoldgasket_thick.inp	"Thickness-direction only" gasket element analysis.
manifoldgasket_thick_mesh.inp	Node, element, and surface definitions for the "thickness-direction only" gasket element analysis.

Reference

- Czernik, D. E., *Gasket Handbook,* McGraw-Hill, New York, 1996.

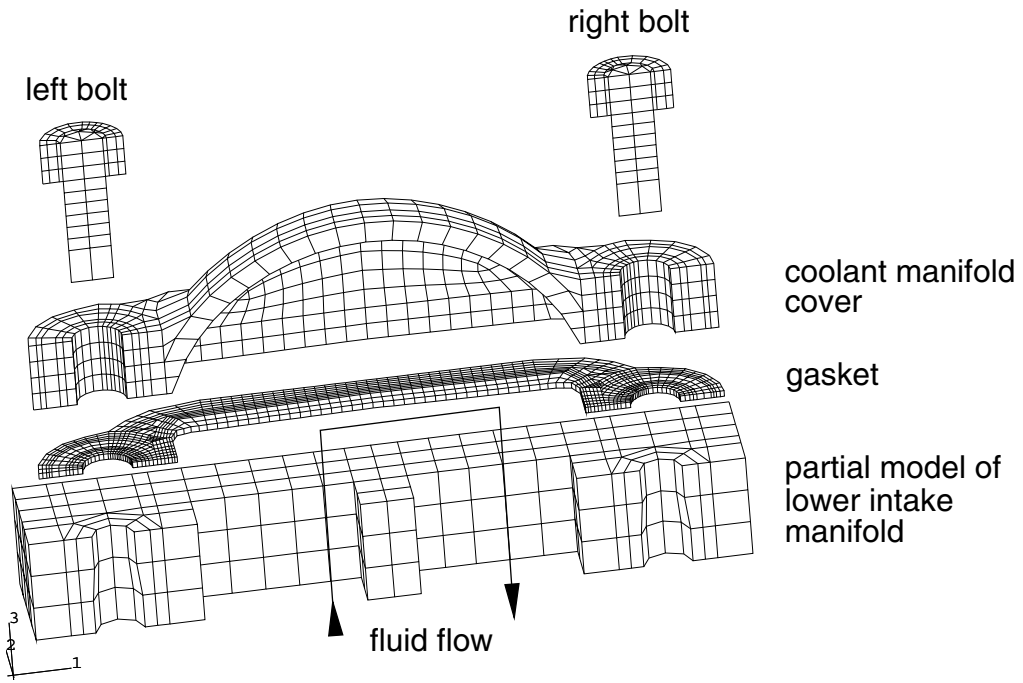

Figure 5.1.4–1 Coolant manifold assemblage.

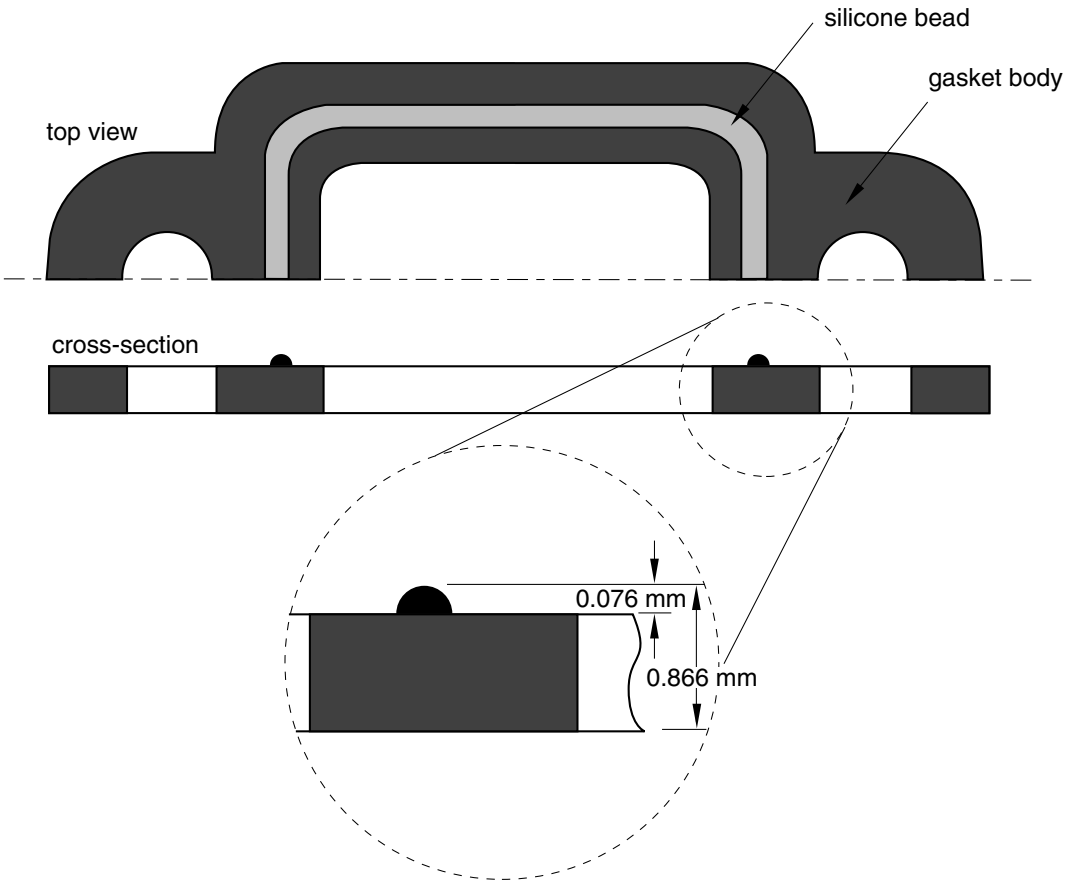

Figure 5.1.4–2 Schematic representation of a silicone bead printed on the gasket body.

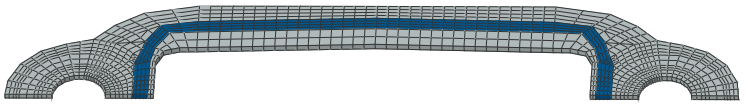

Figure 5.1.4–3 Mesh of gasket with silicone bead highlighted.

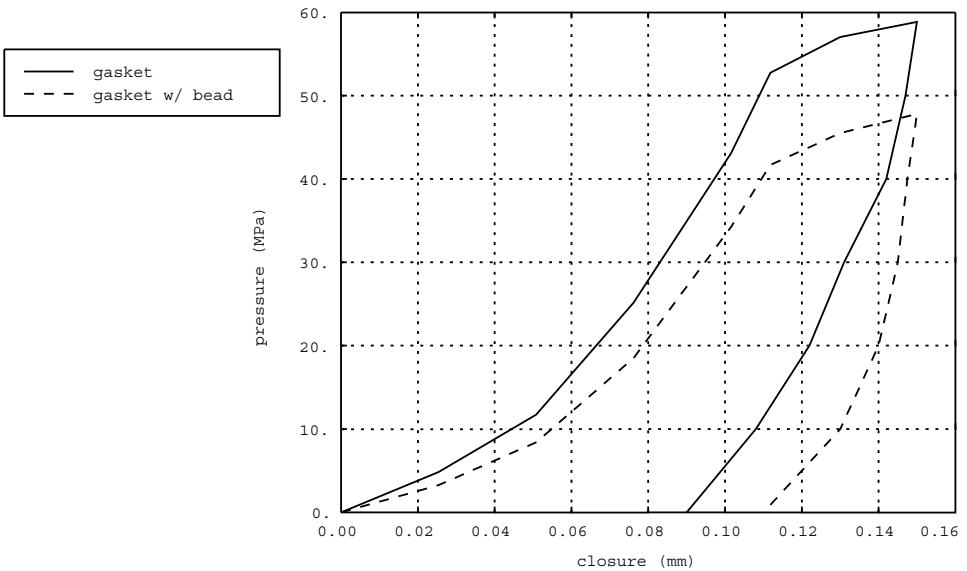

Figure 5.1.4–4 Pressure versus closure behavior for the gasket and the gasket with silicone bead.

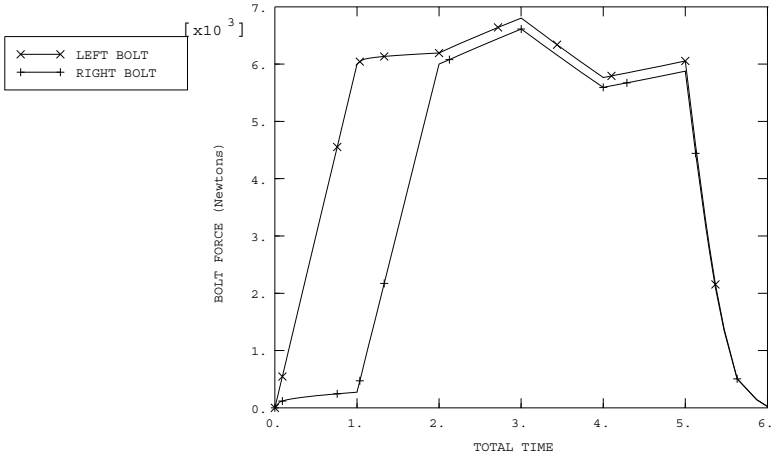

Figure 5.1.4–5 History of bolt force.

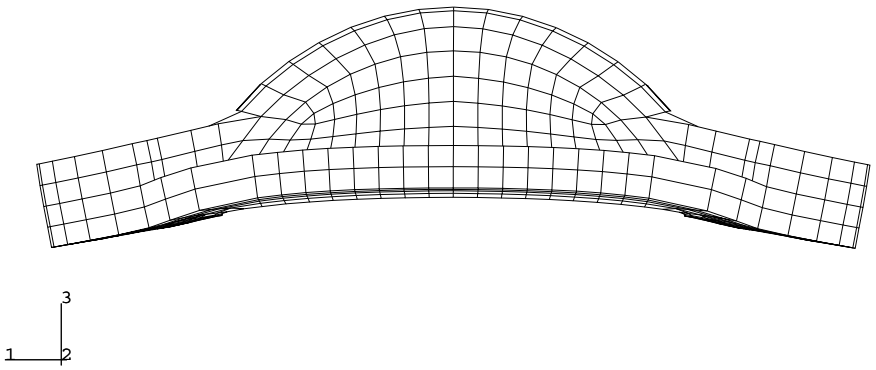

Figure 5.1.4–6 Deformed shape of coolant manifold cover at a displacement magnification factor of 50.

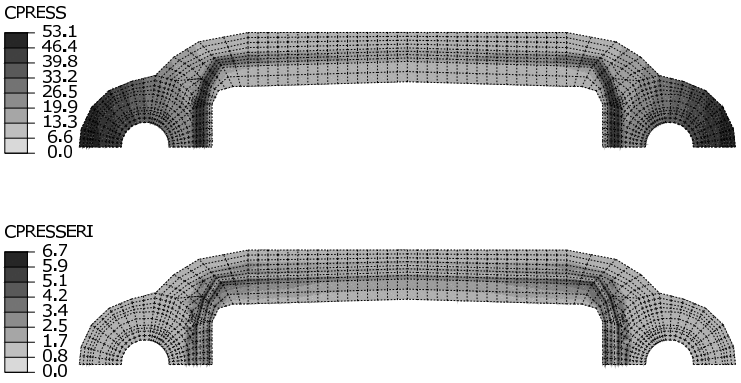

Figure 5.1.4–7 Contact pressure and contact pressure error indicator on the gasket surface after the initial fastening sequence.

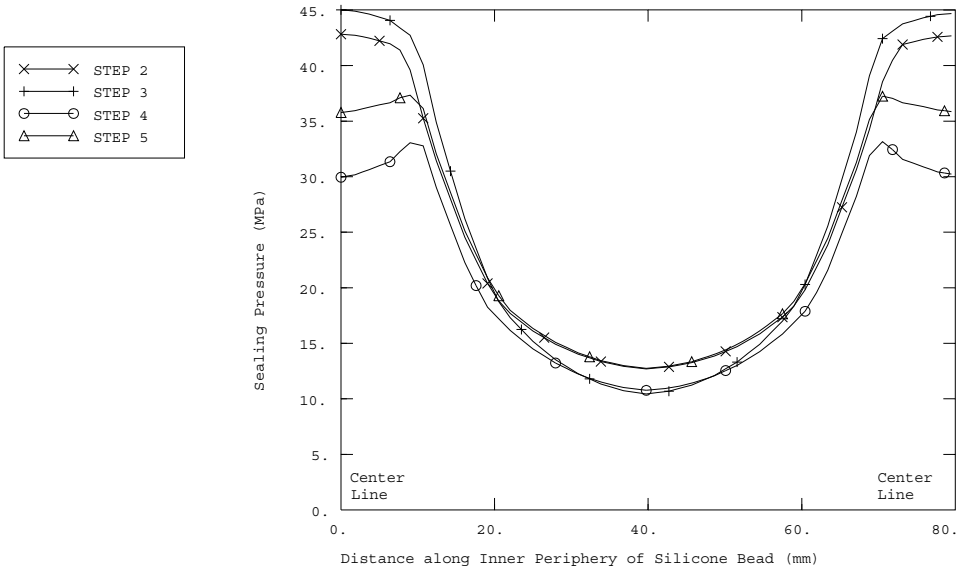

Figure 5.1.4–8 Sealing pressure along inside periphery of silicone bead region of gasket.

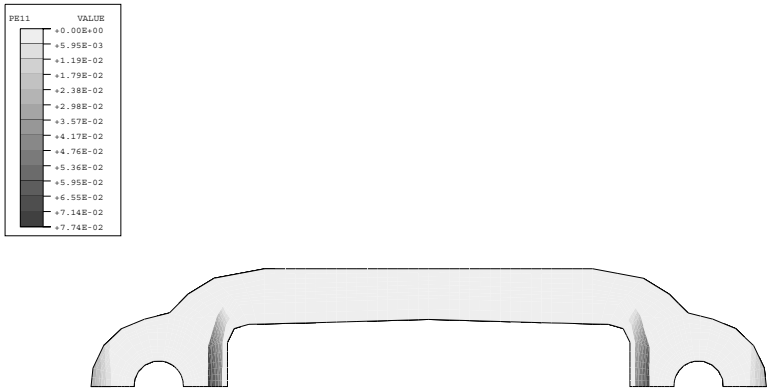

Figure 5.1.4–9 Plastic closure in gasket after operational cycle.

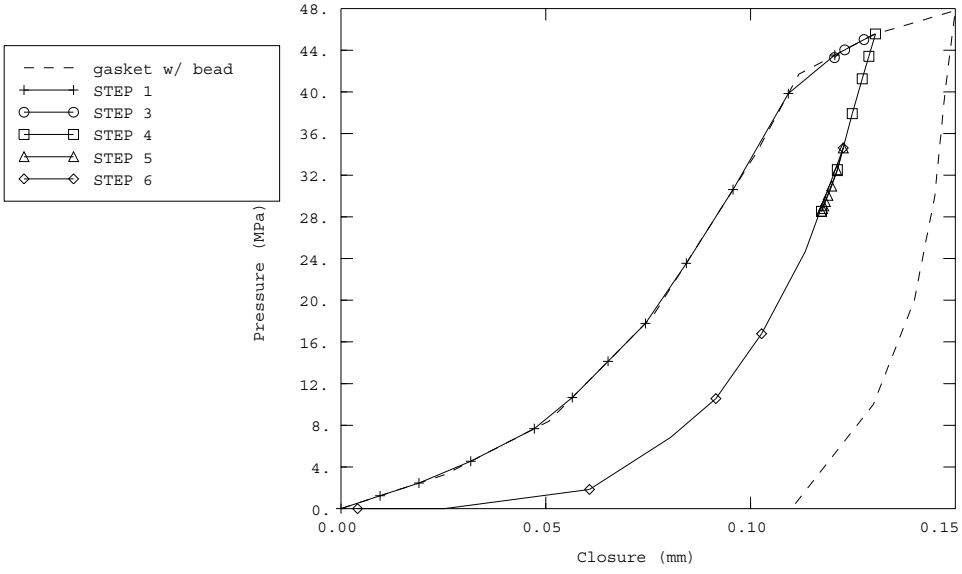

Figure 5.1.4–10 Typical pressure-closure diagram for material point in silicone bead region of gasket.

5.1.5 CONDUCTIVE, CONVECTIVE, AND RADIATIVE HEAT TRANSFER IN AN EXHAUST MANIFOLD

Product: Abaqus/Standard

Objectives

This example shows conductive, convective, and radiative heat transfer of an exhaust manifold.

The following Abaqus features are demonstrated:

- computing steady-state heat transfer in an exhaust manifold,
- comparing results for radiation heat transfer formulations using cavity radiation and average-temperature radiation conditions, and
- using film conditions to simulate the convective heat transfer from the exhaust gases.

Application description

Heat transfer in engine exhaust manifolds is governed by three effects: conduction through the metal, convection from the hot exhaust gases, and radiative exchange between different parts of the metal surface. This example illustrates the computation of the equilibrium thermal state of a manifold subject to these effects. The units of length in this example are millimeters; otherwise, standard metric units are used.

The procedure consists of a single heat transfer step in which the thermal loading conditions are ramped up from zero. The boundary constraints on the manifold flanges are a simplification of those experienced under operating conditions: the temperatures at the cylinder head and the outlet are fixed. Convection due to heat transfer from the hot exhaust is applied at the internal surfaces of the manifold tubes. Radiation is modeled between the internal surfaces of the tubes using several methods: the cavity radiation method, with and without cavity parallel decomposition enabled, and using average-temperature radiation conditions.

Geometry

The exhaust manifold part being analyzed is depicted in Figure 5.1.5–1. It consists of a four tube exhaust manifold with three flanges, as in "Exhaust manifold assemblage," Section 5.1.3.

Materials

The manifold is cast from gray iron with a thermal conductivity of 4.5×10^{-2} W/mm/°C, a density of 7800×10^{-9} kg/mm^3, and a specific heat of 460 J/kg/°C. The manifold begins the analysis with an initial temperature of 20°C. The part is dimensioned in millimeters, and the temperature is measured in °C, so the Stefan Boltzmann constant is taken as 5.669×10^{-14} W/mm^2/K^4 and absolute zero is set at 273.15°C below zero. The surface emissivity of gray iron is taken as a constant value of 0.77.

Initial conditions

The initial temperature of the manifold is set to 20°C.

Boundary conditions and loading

The hot exhaust gases create a heat flux applied to the interior tube surfaces. In this example this effect is modeled using a surface-based film condition, with a constant temperature of 816°C and a film condition of 500×10^{-6} W/mm^2/°C. A temperature boundary condition of 355°C is applied at the flange surfaces attached to the cylinder head, and a temperature boundary condition of 122°C is applied at the flange surfaces attached to the exhaust.

Abaqus modeling approaches and simulation techniques

The radiative transfer between the interior surfaces of the manifold tubes is modeled using several methods for comparison: through the cavity radiation method, with and without cavity parallel decomposition enabled, and through average-temperature radiation conditions (see "Cavity radiation," Section 41.1.1 of the Abaqus Analysis User's Guide). Using the cavity radiation methods, geometric view factors are computed in Abaqus between each facet of the mesh on the exposed interior tube surface. These view factors quantify the effect of radiative transfer between each facet and each of the other facets in the user-defined cavity. The view factors, in turn, are used to compute a fully populated interaction matrix to compute the radiation flux between each pair of facets in the model. When modeling radiation through average-temperature radiation conditions, the flux at each facet is equal to that resulting from a black enclosure, held at the average temperature in the cavity, enclosing the facet. For the cavity radiation methods, some of the facets on the interior of the manifold have a view of the exterior, which is not modeled in this example. The exterior ambient temperature is taken to be the average of the temperatures used for the cylinder head and exhaust boundary conditions. Only the temperatures on the surface are considered when using average-temperature radiation conditions, so an ambient temperature does not need to be defined. For simplicity, all methods are defined using a single surface that includes all of the interior facets of the manifold tubes.

Summary of analysis cases

Case 1 Steady-state heat transfer with film and radiation effects; radiation modeled using the cavity radiation method without parallel decomposition enabled.

Case 2 Steady-state heat transfer with film and radiation effects; radiation modeled using the cavity radiation method with parallel decomposition enabled.

Case 3 Steady-state heat transfer with film and radiation effects; radiation modeled using average-temperature radiation conditions.

The following sections discuss analysis considerations that are applicable to all cases.

Analysis types

Due to the fourth-order dependence of the radiation flux on the surface temperatures, this example problem is intrinsically nonlinear. For all cases the steady-state heat transfer procedure is used. This is a general analysis step in Abaqus, chosen because iteration is required for convergence. An initial increment is chosen as one-tenth of the final value.

Mesh design

The manifold is meshed using linear hexahedral and wedge heat transfer elements with linear interpolation.

Discussion of results and comparison of cases

Figure 5.1.5–2 shows the nodal temperature field for the manifold. On the left, results obtained using the cavity radiation method are shown (results with and without cavity parallel decomposition enabled were identical); on the right, results using the average-temperature radiation conditions are shown. In this problem we observe good agreement between all methods, although some differences can be discerned between the cavity radiation and average-temperature radiation condition results in the plots.

The peak temperature in the field is higher when using the cavity radiation method. The effect of radiation heat transfer is to smooth out the temperature field in the equilibrium solution: high-temperature zones radiate more heat, which is absorbed by the cooler areas. In the cavity radiation method, this smoothing effect is limited and affected by the geometric view factors: the distance and orientation of the surface facets affects the degree to which radiation exchange can occur. This is not the case when using average-temperature radiation conditions. Each facet absorbs or emits radiative heat flux based on its temperature and the averaged cavity temperature only; the localizing effects of view factors are ignored. Therefore, the average method results reflect the greater smoothing effect of the radiation model used, resulting in lower peak values.

Figure 5.1.5–3 shows the flux magnitude results. The flux field shows even greater agreement than the temperature field.

Solving the cavity radiation equations without parallel decomposition enabled involves the inversion of a fully populated matrix operator. Therefore, this method is significantly more computationally expensive than either the cavity radiation method with parallel decomposition enabled (even when only 1 CPU is used) or the average-temperature radiation condition method. Table 5.1.5–1 illustrates the differences and compares the computational costs between the methods. In the case of the cavity radiation method with parallel decomposition enabled, we include the performance results for 1, 2, and 4 CPUs. No significant performance enhancement was observed when using multiple CPUs with the other two methods. In this problem the cavity surface contained 4505 facets—it consists of the entire interior of the manifold. The timing results were obtained on a desktop computer using Xeon processors, but the relative comparisons between run times are more pertinent than the specific run times.

Input files

heattransfermanifold.inp	Input data for the analysis using average-temperature radiation conditions.
heattransfermanifold_cavity.inp	Input data for the analysis using the cavity radiation method without parallel decomposition enabled.
heattransfermanifold_cavity_parallel.inp	Input data for the analysis using the cavity radiation method with parallel decomposition enabled.

References

Abaqus Analysis User's Guide

- "Steady-state analysis" in "Uncoupled heat transfer analysis," Section 6.5.2 of the Abaqus Analysis User's Guide
- "Cavity radiation," Section 41.1.1 of the Abaqus Analysis User's Guide

Abaqus Keywords Reference Guide

- *CAVITY DEFINITION
- *HEAT TRANSFER
- *RADIATION VIEW FACTOR
- *SFILM
- *SRADIATE

Abaqus Theory Guide

- "Uncoupled heat transfer analysis," Section 2.11.1 of the Abaqus Theory Guide
- "Cavity radiation," Section 2.11.4 of the Abaqus Theory Guide
- "View factor calculation," Section 2.11.5 of the Abaqus Theory Guide

Table 5.1.5–1 Relative computational costs of the cavity radiation methods and average-temperature radiation conditions.

	Cavity Radiation				Average-Temperature Radiation Conditions
	Parallel Decomposition			No Parallel Decomposition	
	1 CPU	2 CPUs	4 CPUs		
Increments	6	6	6	6	6
Total iterations	14	14	14	7	10
Wall clock time (sec)	147	81	51	375	12

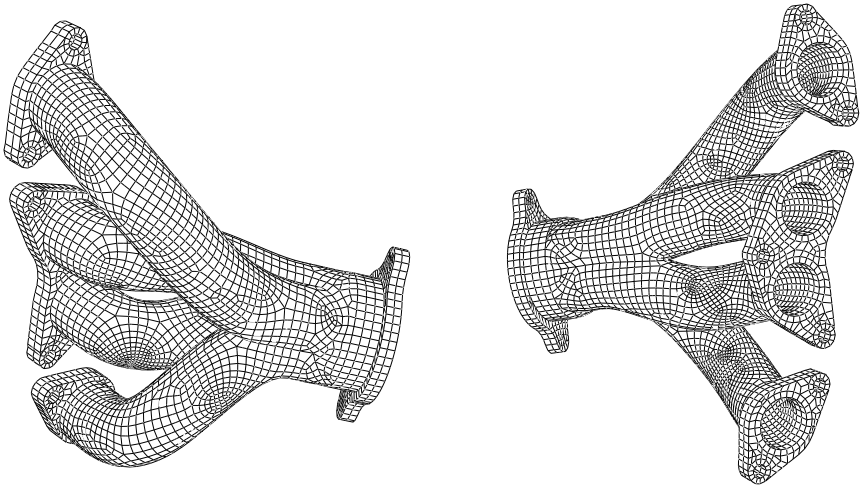

Figure 5.1.5–1 Manifold mesh.

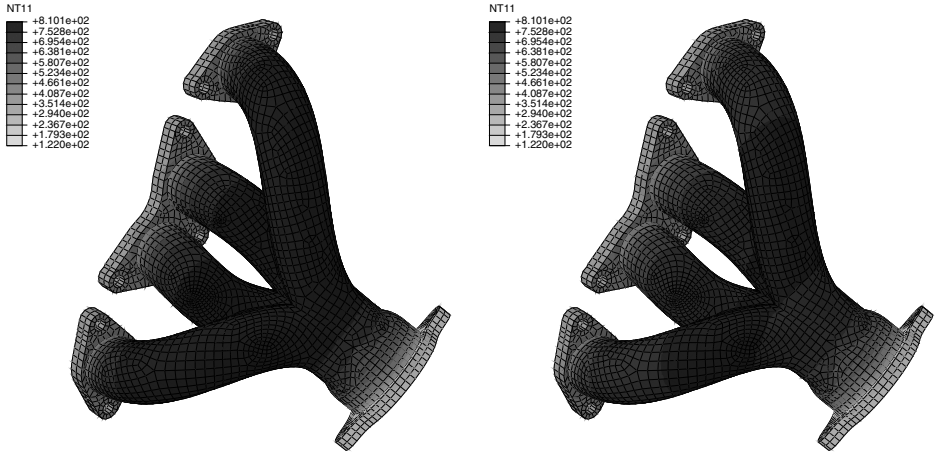

Figure 5.1.5–2 Equilibrium temperature field in the manifold using cavity radiation (left) and average-temperature radiation conditions (right).

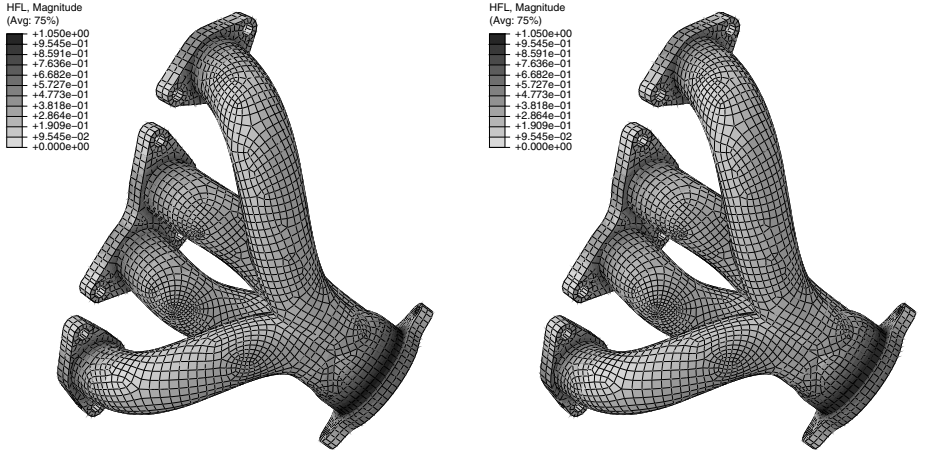

Figure 5.1.5–3 Equilibrium heat flux magnitude field in the manifold using cavity radiation (left) and average-temperature radiation conditions (right).

5.1.6 THERMAL-STRESS ANALYSIS OF A REACTOR PRESSURE VESSEL BOLTED CLOSURE

Products: Abaqus/Standard Abaqus/CAE

Objectives

This example examines the thermal and stress behavior of the bolted closure region of a nuclear reactor vessel assembly.

The following Abaqus features for heat transfer and static stress analyses are demonstrated:

- specifying adaptive remeshing rules in different regions of a model in a particular analysis step;
- using an automated process to remesh the model adaptively based on the remeshing rules specified; and
- viewing error indicator results as a means of assessing mesh quality.

Application description

The vessel assembly forms the pressure boundary surrounding the fuel core. This example considers the strength of sustaining the following loading conditions:

- pre-tension load in the stud bolts,
- constant internal pressure, and
- specified heat-up/cool-down rate.

These loading conditions cover the most basic design requirements of a reactor vessel. A short and rapid temperature change is one of the most severe loading cases and will be considered in this example. The International System of units (SI) will be used in the following sections to describe the model. The analysis itself is performed in English units. The model and analysis are derived from details of the Shippingport pressurized water reactor (1958).

Geometry

The problem domain comprises a cylindrical vessel shell, a hemispherical bottom head, a dome-shaped closure head, and the closure and seal assembly, as shown in Figure 5.1.6–1. The overall height of the vessel shell including the bottom head is 7650 mm (301 in). The bottom head has an inner radius of 1410 mm (55.5 in) and a thickness of 157 mm (6.18 in). The inner radius of the vessel shell is 1380 mm (54.5 in), and the thickness is 213 mm (8.40 in). The closure head has a height of 2330 mm (91.8 in), an inner radius of 1310 mm (51.5 in), and a thickness of 210 mm (8.25 in). The closure head is attached to the vessel shell by a seal and closure assembly. The assembly includes 40 stud bolts passing through the bolting flanges of the closure head and the vessel shell, each of which is restrained by two cap nuts. To complete the closure assembly, an omega seal is welded to the under surface of the closure head and top surface of the vessel shell. The stud bolt is 2290 mm (90 in) in length and has a diameter of 146 mm (5.75 in). The closure nuts are 304 mm (12 in) long with a thickness of 28.6 mm (1.13 in).

Boundary conditions and loading

The outside of the vessel is exposed to air that has a constant temperature of 21°C (70°F). The inside of the vessel is filled with hot water with an operating temperature of 320°C (600°F). During a cool-down process, the internal temperature is reduced by 38°C (100°F) in two hours. The water inside imposes a constant pressure of 1.38×10^7 Pa (2000 psi) on the internal surface of the vessel.

Abaqus modeling approaches and simulation techniques

The objective of this analysis is an understanding of stresses near the vessel-to-head interfaces. Although the assembly contains many features, such as inlet and outlet nozzles, the example ignores these details since they are far away from the vessel-to-head interface. The rest of the geometry is cyclically symmetric, which allows the example to model the entire 360° structure at a reduced computational expense by analyzing only a single repetitive sector of the model. Since there are 40 stud bolts along the circumference of the reactor vessel, the following analysis is performed on a 9° model with one sector as shown in Figure 5.1.6–2.

The example also takes advantage of the fact that the thermal and mechanical responses of the vessel are only weakly coupled. Based on this fact, a sequentially coupled thermal-stress analysis is performed on the reactor vessel. The distribution of the temperature field is obtained first through a heat transfer analysis, then the mechanical response of the vessel is obtained by performing a static stress analysis with the temperature field specified using the results of the thermal analysis.

Summary of analysis cases

Case 1 Steady-state and transient heat transfer analyses, with adaptive remeshing in Abaqus/CAE.

Case 2 Static stress analysis, with adaptive remeshing in Abaqus/CAE.

The following sections discuss analysis considerations that are applicable to both analyses. More detailed descriptions are provided later including discussions of results and listings of the files provided. The models for the two analyses were generated using Abaqus/CAE and imported ACIS-format files.

Analysis types

The thermal analysis includes a steady-state and a transient heat transfer step. The structural analysis is performed using multiple linear general static steps.

Mesh design

The omega seal is meshed with first-order brick elements, while the rest of the model is meshed with second-order tetrahedral elements. The geometry is partitioned to create a fine initial mesh in the area near the closure assembly, where the geometry is most complex and high stress and heat flux are expected. The purpose of this mesh design is to obtain an accurate estimate of the error indicators specified in the remeshing rules, which will result in faster convergence in the adaptivity procedure.

Adaptive remeshing rules

The patch recovery techniques that Abaqus/CAE uses to calculate the error indicator variables can have a significant impact on the analysis solution time. In particular, the element energy density is calculated after each increment and is more costly than the other error indicator variables. To reduce the computational expense, the omega seal is excluded from the region where remeshing rules are specified. The closure head and the vessel shell are also partitioned in such a way that regions relatively farther away from the stud bolt are not included in the remeshing regions. Four separate remeshing rules are defined in the closure head, the vessel shell, the cap nuts, and the stud bolt. In both the thermal and structural analyses, the remeshing rules are specified in only the last step.

Additional details of the remeshing rules used in the two analyses are discussed with each example.

Constraints

To simulate the welding constraints, the bottom surfaces of the omega seal are tied to the surfaces of the bolting flanges in both analyses.

Adaptivity process

Each adaptivity process specifies a maximum number of three remesh iterations.

Heat transfer analysis

The example starts by performing a heat transfer analysis to obtain the temperature distribution in the pressure vessel under the thermal loading.

Analysis types

The analysis consists of a steady-state heat transfer step, representing the steady operation of the reactor. This step is followed by a transient heat transfer step, representing a rapid cool-down event. The resulting temperatures obtained are applied to the subsequent mechanical analysis.

Mesh design

When performing the heat transfer analysis, first-order hexahedral diffusive heat transfer elements (DC3D8) are used in the omega seal, and the rest of the geometry is meshed with second-order tetrahedral diffusive heat transfer elements (DC3D10).

Adaptive remeshing rules

The heat flux error indicator is chosen in all remeshing rules. For each remeshing rule the sizing method is set to uniform error distribution and the error indicator target is set to automatic target reduction.

Material model

The heat transfer analysis requires specification of thermal conductivity, which is 46.7 W/m/°C (2.25 Btu/h/in/°F), and specific heat, which is 460 J/kg/°C (0.11 Btu/lb/°F). The density of the material

is also specified, which is 7850 kg/m^3 (0.284 lb/in^3). One solid, homogenous section is used to assign material properties to the elements.

Initial conditions

The initial temperature is set to 21°C (70°F) in the entire model.

Boundary conditions

No temperature boundary conditions are applied. The thermal response of the model is driven entirely by thermal loading through film coefficients.

Interactions

Conductive heat transfer is defined between adjacent/contacting surfaces, and a gap conductance coefficient is specified, which is 1220 W/m^2/°C (1.5 Btu/h/in^2/°F). Heat flux on the surfaces is applied by film conditions. The outer surfaces are exposed to air, which has a film coefficient of 28 W/m^2/°C (0.035 Btu/h/in^2/°F). The inner surfaces are in contact with water with a film coefficient of 580 W/m^2/°C (0.70 Btu/h/in^2/°F). The outer surfaces are initially associated with a sink temperature of 21°C (70°F), and the inner surfaces, 320°C (600°F). During a subsequent two-hour cooling process, the sink temperature associated with the inner surfaces is reduced by 38°C (100°F).

Analysis steps

The heat transfer analysis is performed using a steady-state step followed by a transient step. The purpose of the first step is to obtain a steady-state solution of temperature distribution in the whole model. The second step lasts for 7200 seconds (2 hours), and it simulates the response of the thermal model during a rapid cooling process.

Convergence

The convergence of the error indicator HFLERI during a three-iteration adaptivity process is presented in Table 5.1.6–1. Convergence is observed in each of the remeshing regions.

Run procedure

The model for the heat transfer analysis is generated using Abaqus/CAE to import the geometry, create the thermal loading, mesh the assembly, create the remeshing rules, and run the adaptivity process. Python scripts are provided to build the model and to submit the adaptivity process. The scripts can be run interactively or from the command line.

To create the heat transfer model, select **File→Run Script** from the Abaqus/CAE main menu and select **`adaptReactorVesselHT_model.py`**.

When you are ready to run the adaptivity process, select **File→Run Script** and select **`adaptReactorVesselHT_job.py`**. After the Abaqus Scripting Interface scripts have created the model and run the adaptivity process, you can use Abaqus/CAE to view the model and to explore variations of the example.

Results and discussion

The magnitude of the heat flux (HFL) along a particular path near the head to vessel interface is shown in Figure 5.1.6–3. This figure shows the spatial variation of the heat flux as the mesh is refined through the three remesh iterations. Figure 5.1.6–4 shows the original mesh and the final mesh resulting from the adaptive remeshing process. The refined mesh shows how Abaqus/CAE reacted to the higher temperature gradients in the bolted flange region.

Structural analysis

The temperature distribution calculated in the heat transfer case will now augment bolting and pressure loads to define the structural loading of the vessel assembly.

Analysis types

A series of static steps is performed to simulate the mechanical response of the model under both thermal and force loading.

Mesh design

The omega seal is meshed with first-order reduced-integration continuum elements (C3D8R), and the rest of the geometry is meshed with modified second-order tetrahedral elements (C3D10M).

Adaptive remeshing rules

The response of the model varies from step to step during the analysis; therefore, the time history-dependent error indicator ENDENERI is chosen to capture the extreme of the model's response to the load history. For each remeshing rule the sizing method is set to uniform error distribution and the error indicator target is set to automatic target reduction.

Material model

The linear static structural analysis requires specification of Young's modulus, which is 2.07×10^7 N/m^2 (3.0×10^7 lbf/in^2), and Poisson's ratio, which is 0.29. A thermal expansion coefficient is also defined, which is 6.3×10^{-6}. One solid, homogenous section is used to assign material properties to the elements.

Boundary conditions

Symmetry boundary constraints are placed on the two side surfaces of the sector. Since the two symmetry constraints overlap at the centerline and such definitions are not allowed by the analysis input file processor, partitions are made on the side surfaces so that the centerline and a small part of its surrounding region are excluded from the symmetry boundary constraints. The nodes on the centerline are constrained separately and are free to move only in the axial direction. The center node on the outer surface of the bottom head is fixed to prevent rigid body motion.

Loading

A pre-tension load of 2200 kN (5×10^6 lbf) is applied to the stud bolt. The inner surfaces of the head and the vessel shell are subject to a constant pressure of 1.38×10^7 Pa (2000 psi) from the water.

Predefined fields

When the bolt loading is applied in the pre-assembly step, a constant temperature of 21°C (70°F) is applied. The temperature field is specified using the thermal results from the previous steady-state heat transfer analysis when the inner pressure is applied. The results of the temperature after each increment during the transient heat transfer analysis are imported in the last step when no additional loading is applied.

Interactions

The outer surface of the stud bolt is tied to the inner surfaces of the cap nuts. Small-sliding surface-to-surface contact interactions are defined between the contact surfaces of the cap nuts and the bolting flange on the head and vessel shell. A friction coefficient of 0.2 is specified in the contact between the cap nuts and the bolting flanges. The analysis assumes that the contact between the closure head and the vessel shell is frictionless. The augmented Lagrange method is chosen to enforce the contact constraints.

Analysis steps

The structural analysis is performed by using two static steps. The bolt force and internal pressure are both applied in the first step, a predefined temperature field is also specified using the results obtained in the steady-state heat transfer step. The temperature obtained from the transient heat transfer step is specified in the last loading step, and the structure expands with the change of temperature.

Output requests

Default field output requests are specified in the first step. In the second step, field output requests are made at specified time points to match the results of the structural analysis to those of the thermal analysis at the exact step times.

Convergence

The convergence of error indicators ENDENERI and MISESERI during a three-iteration adaptivity process is presented in Table 5.1.6–2.

Run procedure

The model for the static analysis is generated using Abaqus/CAE to import the geometry, create the structural loading, mesh the assembly, create the remeshing rules, and run the adaptivity process. Python scripts are provided to build the model and to submit the adaptivity process. The scripts can be run interactively or from the command line.

To create the structural model, select **File→Run Script** from the Abaqus/CAE main menu and select **`adaptReactorVesselSTR_model.py`**.

When you are ready to run the adaptivity process, select **File→Run Script** and select **`adaptReactorVesselSTR_job.py`**. After the Abaqus Scripting Interface scripts have created the model and run the adaptivity process, you can use Abaqus/CAE to view the model and to explore variations of the example.

Results and discussion

The magnitude of the Mises stress (MISES) along a particular path near the head to vessel interface is shown in Figure 5.1.6–5. This figure shows the spatial variation of the Mises stress as the mesh is refined through the three remesh iterations. Figure 5.1.6–6 shows the original mesh and the final mesh resulting from the adaptive remeshing process. The refined mesh shows how Abaqus/CAE reacted to the higher stress gradients near the nut-to-bolted flange interfaces and the vessel-to-head interface.

Discussion of results and comparison of cases

The thermal and structural cases presented in this example are complementary; the structural case depends on the thermal case. You can compare how adaptive remeshing refines the mesh in each case. As seen, in Figure 5.1.6–4 and Table 5.1.6–1 for the heat transfer case and Figure 5.1.6–6 and Table 5.1.6–2 for the structural case, the mesh refinement is significantly different.

Files

To create the models and to run the adaptivity processes, you can use the Python scripts listed below.

Heat transfer analysis

adaptReactorVesselHT_model.py	Script to create the model.
adaptReactorVesselHT_job.py	Script to analyze the model.

Structural analysis

adaptReactorVesselSTR_model.py	Script to create the model.
adaptReactorVesselSTR_job.py	Script to analyze the model.

References

Abaqus Analysis User's Guide

- "Adaptive remeshing: overview," Section 12.3.1 of the Abaqus Analysis User's Guide

Abaqus/CAE User's Guide

- "Understanding adaptive remeshing," Section 17.13 of the Abaqus/CAE User's Guide

Other

- Naval Reactors Branch, Division of Reactor Development, United States Atomic Energy Commission, *The Shippingport Pressurized Water Reactor,* Reading, Massachusetts: Addison Wesley Publishing Company, 1958.

Table 5.1.6–1 The convergence of the thermal error indicator HFLERI during an adaptivity process with three iterations.

Remeshing Region	Error Indicator Result (%)			Element Count		
	1	2	3	1	2	3
Stud Bolt	11.7	7.0	4.1	1080	1386	2112
Closure Head	4.9	2.5	1.7	2210	4846	9226
Cap Nuts	2.8	1.5	1.4	1500	4210	5317
Vessel Shell	5.4	2.3	1.5	2443	5124	11036

Table 5.1.6–2 The convergence of the stress-based error indicator ENDENERI during an adaptivity process with three iterations.

Remeshing Region	Error Indicator Result (%)			Element Count		
	1	2	3	1	2	3
Stud Bolt	1.8	1.7	1.5	1334	1737	2211
Closure Head	8.7	4.7	3.2	2210	5120	13320
Cap Nuts	6.0	5.7	4.8	1500	3315	7534
Vessel Shell	6.7	3.6	2.7	2438	5813	15290

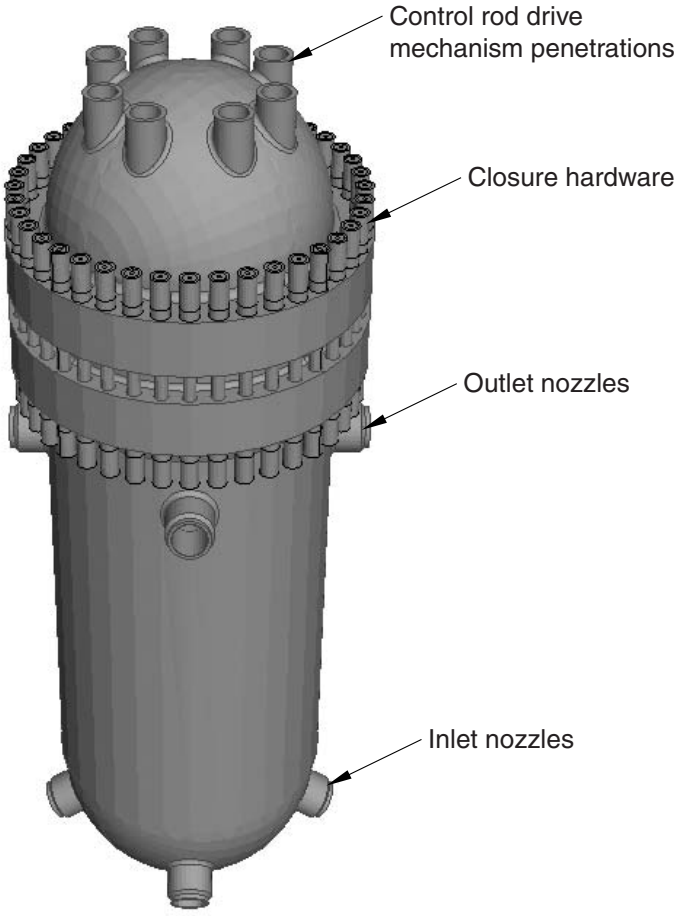

Figure 5.1.6–1 Reactor vessel assembly.

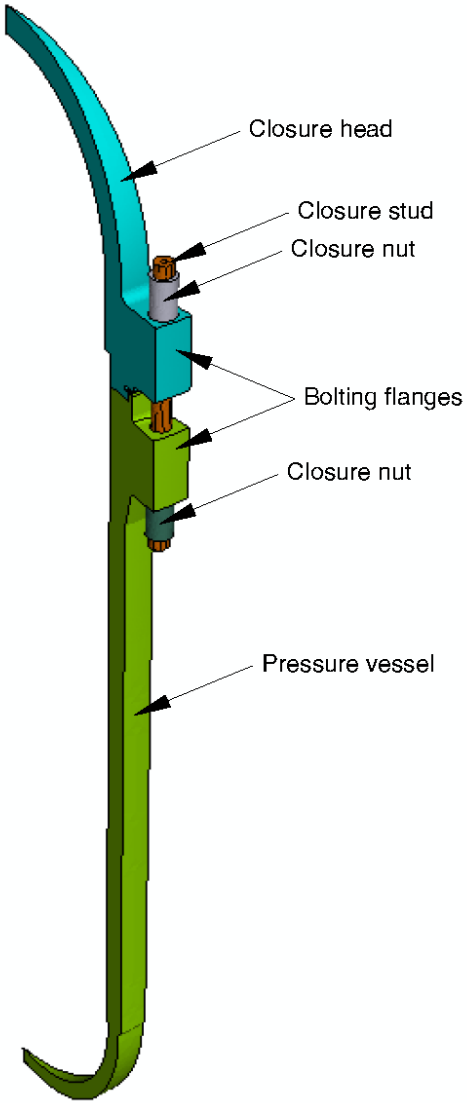

Figure 5.1.6–2 9° sector model.

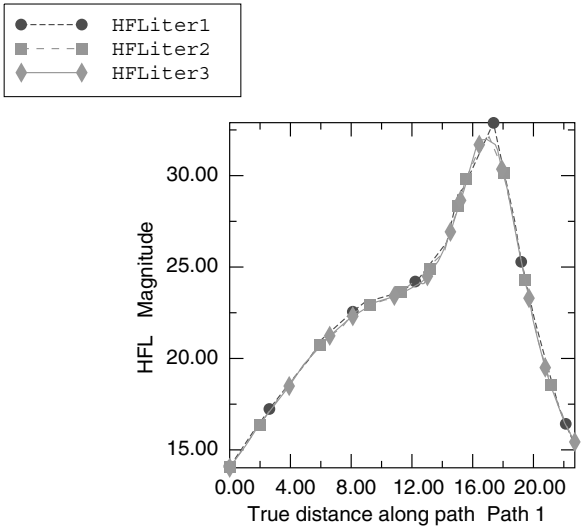

Figure 5.1.6–3 Heat flux along a path near the vessel-to-head interface.

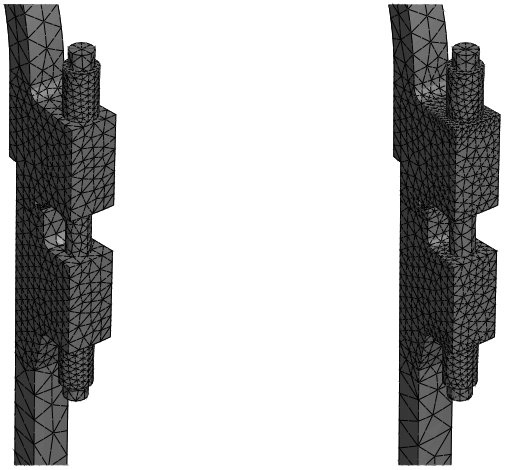

Figure 5.1.6–4 Original and refined mesh for the heat transfer analysis.

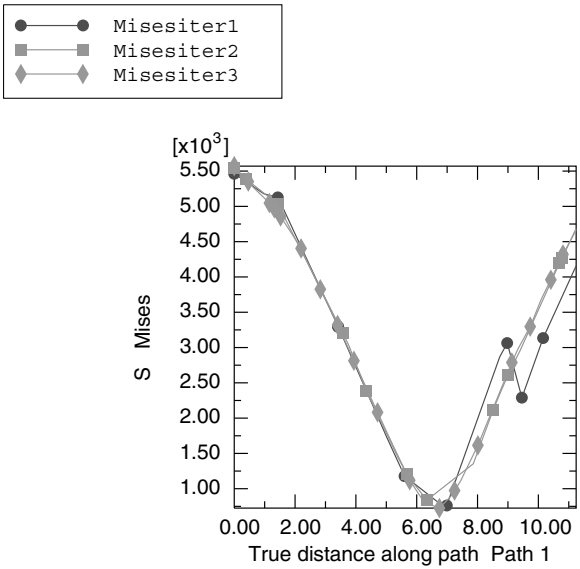

Figure 5.1.6–5 Mises stress along a path near the vessel-to-head interface.

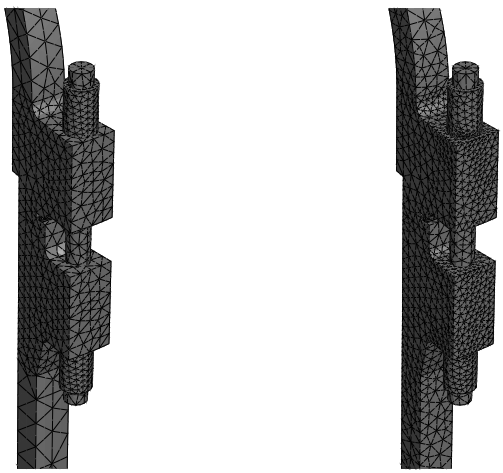

Figure 5.1.6–6 Original and refined mesh for the structural analysis.

5.1.7 COUPLED THERMOMECHANICAL ANALYSIS OF VISCOELASTIC DAMPERS

Product: Abaqus/Standard

Objectives

This example examines the response of a viscoelastic damper under cyclic loading with the damper material modeled as a linear viscoelastic material using a Prony series calibrated to capture the hysteresis response accurately.

The following Abaqus features and techniques are demonstrated:

- using Prony-series viscoelasticity to account for material hysteresis,
- using the thermorheologically simple (TRS) material model to account for temperature dependence in a viscoelastic material,
- accounting for heat generated by mechanical energy dissipation through coupled temperature-displacement analysis, and
- comparing the response of a structure experiencing large deformations using elastic or hyperelastic material models.

Application description

One tool commonly used in Abaqus to model stress relaxation in viscoelastic materials is the Prony series. However, using the Prony series to model stress relaxation in dissipating materials often leads to underprediction of the size of the hysteresis loop for the material when subjected to cyclic loading (Dalrymple et al., 2007). If both the stress relaxation and hysteretic behavior of a given material must be modeled accurately, a more complicated material model, such as the parallel rheological framework model, is required. However, in some structures the stress relaxation response may be of secondary importance to the hysteretic energy dissipation under cyclic loading. In such cases it can be reasonable to calibrate the Prony series coefficients in a manner that accurately captures the hysteresis response of the material at the expense of accurately modeling the stress relaxation response. In this example the response of a viscoelastic damper under cyclic loading is examined. The damper material is modeled as a linear viscoelastic material with a Prony series calibrated to capture the hysteresis response accurately.

One of the salient characteristics of damping materials is their ability to convert mechanical energy into other forms of energy, typically heat. However, the mechanical response of these materials is often highly sensitive to temperature. This analysis examines the importance of accounting for the interdependence of heat generation and transport with mechanical response through the use of a fully coupled thermomechanical analysis.

Geometry

The model consists of a layer of viscoelastic damping material between two steel plates, as shown in Figure 5.1.7–1. The damper dimension is 3.5 inches in the x-direction, and the viscoelastic material and steel plates are each 0.5 inches thick, for a total dimension of 1.5 inches in the y-direction.

Materials

The model contains two materials, steel and a viscoelastic damping material with a response described by Shen and Soong (1995). Details of the material response are provided in "Material model" below.

Initial conditions

The initial temperature in the structure is uniformly 21.7 °C.

Boundary conditions and loading

The damper is subjected to sinusoidal shear loading at a rate of 1 Hz for a period of 10 seconds such that the nominal engineering shear strain in the viscoelastic damping material has an amplitude of approximately 50%. This loading is imposed by specifying the displacement of the top surface.

For heat conduction, the damper's boundaries are assumed to be adiabatic (i.e., no heat is transferred to or from the environment).

Abaqus modeling approaches and simulation techniques

Four analyses are performed comparing the predicted response if heat generation from mechanical dissipation is or is not accounted for and comparing the effect of modeling the viscoelastic damping material as a linear elastic or hyperelastic material.

Summary of analysis cases

Case 1	Quasi-static stress analysis with linear elasticity for the viscoelastic damper material
Case 2	Quasi-static stress analysis with hyperelasticity for the viscoelastic damper material
Case 3	Coupled temperature-displacement analysis with linear elasticity for the viscoelastic damper material
Case 4	Coupled temperature-displacement analysis with hyperelasticity for the viscoelastic damper material

Analysis types

Two types of analyses are performed: a transient, static, stress/displacement analysis that neglects the generated heat and a coupled transient temperature-displacement analysis. Both analysis types neglect inertial effects (i.e., the model is quasi-static) and use general steps with geometric nonlinearity since the model undergoes large displacements. In the coupled analysis (see "Fully coupled thermal-stress analysis," Section 6.5.3 of the Abaqus Analysis User's Guide), transient heat transfer resulting from heat generated by dissipation of mechanical energy is modeled along with the force-displacement. The resulting temperature changes will affect the structure's response due to material temperature dependence in the viscoelastic damper and thermal expansion.

Mesh design

A single mesh refinement is examined, with 8 elements through the thickness of each layer of the damper (resulting in a total of 24 elements in the *y*-direction) and 32 elements in the *x*-direction. Plane strain is assumed. CPE4 and CPE4H elements are used for the stress analysis for the steel and viscoelastic damper materials, respectively. The coupled analysis uses CPE4T and CPE4HT elements.

Material model

This section provides the properties used for the various materials in the model.

Steel

The steel's mechanical response is modeled with linear elasticity. The Young's modulus of the steel is $E = 29.0 \times 10^6$ psi, and the Poisson's ratio is $\nu = 0.3$.

Viscoelastic damper

The mechanical response of the viscoelastic damper material is determined from experimental data provided by Shen and Soong. For temperature dependence, the material is assumed to be thermorheologically simple. Shen and Soong provide the following TRS shift function based on temperature:

$$\log A = -0.0561(\theta - \theta_0),$$

which is a simplified form of the Williams-Landell-Ferry (WLF) relationship implemented within Abaqus (see "Time domain viscoelasticity," Section 22.7.1 of the Abaqus Analysis User's Guide):

$$\log A = -\frac{C_1(\theta - \theta_0)}{C_2 + (\theta - \theta_0)}.$$

The form of the TRS shift function given by Shen and Soong can be replicated using the WLF relationship by selecting values of C_1 and C_2 such that $C_1/C_2 = 0.0561$ and $C_2 \gg \theta - \theta_0$. Therefore, the parameters of the WLF TRS definition of the material implemented within Abaqus are defined as $\theta_0 = 21.7$ °C, $C_1 = 56.1$, and $C_2 = 1000$ °C.

The storage and loss moduli along with the corresponding frequencies from Shen and Soong were shifted using the TRS shift function to a reference temperature of 21.7 °C. This choice of reference temperature, which in practice is arbitrary, was made based on the temperature at which the regression performed by Shen and Soong yields no shift. The original moduli, along with the shifted values, are given in Table 5.1.7–1. As a general practice, it is important that the time scales or frequencies of the loading in the analysis be within the scope of the time scales and frequencies of the experimental data used to characterize the material response. The loading in this analysis is 1 Hz, which is within the range of frequencies given in Table 5.1.7–1.

The Levenburg-Marquardt algorithm (Press et al., 1992), a least-squares approach, was used to obtain the Prony series parameters (see Table 5.1.7–2) for the Maxwell model using the temperature-shifted frequencies and storage and loss moduli. The initial shear modulus is 2.0845 ksi.

For the instantaneous elastic response of the material, it is assumed that the bulk modulus is constant with respect to time or frequency. The material is assumed to be nearly incompressible with an initial Poisson's ratio of 0.495. This results in a bulk modulus of $K = 2.078 \times 10^5$ ksi.

This example compares two different approaches for modeling the instantaneous elastic response of the damping material. The first is to model the response as linear. The initial Young's modulus of E = 6.232 ksi is determined from the initial shear modulus and Poisson's ratio.

The second approach utilizes a neo-Hookean hyperelastic material definition (see "Hyperelastic behavior of rubberlike materials," Section 22.5.1 of the Abaqus Analysis User's Guide). Hyperelasticity is based on finite deformation theory, which may be more appropriate for this model considering the large strains that are experienced. Another consequence of this change is that the stress-strain relationship for the material will be nonlinear. The neo-Hookean model is chosen due to the lack of comprehensive data for the instantaneous stress-strain response of the viscoelastic damping material. The strain energy potential constants ($C_{10} = 1.0423 \times 10^3$ and $D_1 = 9.6267 \times 10^{-6}$) are determined from the initial shear and bulk moduli.

Heat transfer

The properties of the materials related to heat transfer are given in Table 5.1.7–3. The inelastic heat fraction (see "Fully coupled thermal-stress analysis," Section 6.5.3 of the Abaqus Analysis User's Guide) for the viscoelastic damper material is specified as 1.071×10^{-4}. This assumes that all energy dissipated by viscoelasticity is converted into heat and accounts for the change of energy units from in-lbf in the mechanical analysis to BTUs, which are used to define the material properties related to heat transfer given in Table 5.1.7–3.

Initial conditions

The initial temperature of all nodes is 21.7 °C.

Boundary conditions

The nodes on the top surface are constrained in the *y*-direction. The nodes on the bottom surface are constrained in both the *x*- and *y*-directions. No thermal boundary conditions are specified, meaning that there is no heat transfer with the environment.

Loading

A sinusoidal time-varying *x*-direction displacement with an amplitude of 0.25 inches and a frequency of 1 Hz is applied to the nodes on the top surface.

Convergence

Adaptive time stepping is used with a creep strain error tolerance (CETOL) of 5×10^{-3}. Increments that are sufficiently small to satisfy this tolerance typically converge within 2–3 iterations.

Discussion of results and comparison of cases

Figure 5.1.7–2 shows a contour of the logarithmic shear strain in the damper at the maximum stroke of the final cycle in the coupled model using hyperelasticity, showing the large deformations present in the viscoelastic damper material. The hysteresis responses predicted using the two different material models are shown in Figure 5.1.7–3 for the coupled thermomechanical analysis and Figure 5.1.7–4 for the uncoupled stress analysis. The importance of accounting for the heat generated by dissipation of mechanical energy is immediately apparent in the way that the hysteresis loops flatten and decrease in area over time in the coupled analyses. These changes occur because the material loses stiffness as the temperature increases. No such decrease is noted in the pure stress analysis—the cyclic hysteresis response reaches a steady state after a single cycle has been completed.

Figure 5.1.7–3 and Figure 5.1.7–4 show that the forces are slightly higher when using the hyperelastic model for the damping material than when using the linear elastic model. This difference is expected due to the nonlinear nature of the stress-strain relationship obtained using hyperelasticity and the use of finite deformation theory.

Figure 5.1.7–5 shows the contour of the temperature in the damper, indicating that some regions of the damper experience a temperature increase of approximately 8 degrees over the 10-second duration of the analysis. This increase is due to the heat generated by mechanical energy dissipation. The generated heat accumulates in the viscoelastic material faster than it is conducted to the cooler steel plates, leading to a steady temperature increase. Figure 5.1.7–6 shows the time history of the temperature at the central node (node 1217) of the damper in the coupled analysis. The temperature rise is more pronounced in the model using hyperelasticity due to the higher stresses (and subsequently greater energy dissipation) experienced when using the hyperelastic material definition.

One additional aspect of interest for this material definition is how the predicted stress relaxation compares to the material's actual response. Recall that for this viscous damper, the hysteresis response is of primary interest. Therefore, the viscoelastic Prony series was calibrated to capture that aspect of the material response accurately. Shen and Soong performed relaxation experiments on a test fixture using the material in this example. The force response of that test fixture can be approximated using the model from this example by multiplying the sum of the *x*-direction reaction forces in the upper nodes of the model by 5, permitting a direct comparison between experiment and simulation.

Figure 5.1.7–7 compares the time history of the experimentally measured and simulated reaction forces resulting from loading the damping material to a nominal engineering shear strain of 20% over one second and then holding the displacements of the test fixture constant. As seen in the figure, the force in the simulation drops more quickly than it does in the experiment, and to a much lower value. This result highlights the intrinsic limitation of linear viscoelasticity described in the introduction of this example—it is generally not possible to represent both the hysteresis response and the stress relaxation response accurately using a linear viscoelastic Prony series. Therefore, while the approaches described in this example are appropriate for modeling a viscoelastic material under cyclic loading, the approach described here is not recommended for analyses in which stress relaxation is of primary importance.

Acknowledgments

SIMULIA would like to thank Professor Gary Dargush at SUNY Buffalo for providing the model used in this example, which is based on work by Rajesh Radhakrishnan (2000).

Input files

Case 1

visco_damper_uncoupled_linelastic.inp Uncoupled analysis with linear elasticity.

Case 2

visco_damper_uncoupled_hyperelastic.inp Uncoupled analysis with hyperelasticity.

Case 3

visco_damper_coupled_linelastic.inp Coupled analysis with linear elasticity.

Case 4

visco_damper_coupled_hyperelastic.inp Coupled analysis with hyperelasticity.

References

Abaqus Analysis User's Guide

- "Fully coupled thermal-stress analysis," Section 6.5.3 of the Abaqus Analysis User's Guide
- "Time domain viscoelasticity," Section 22.7.1 of the Abaqus Analysis User's Guide

Abaqus Keywords Reference Guide

- *COUPLED TEMPERATURE-DISPLACEMENT
- *INELASTIC HEAT FRACTION
- *TRS
- *VISCO
- *VISCOELASTIC

Other

- Dalrymple, T., J. Choi, and K. Miller, "Elastomer Rate-Dependence: A Testing and Material Modeling Methodology," 172nd Technical Meeting of the Rubber Division of the American Chemical Society, Cleveland, OH, pp. 1–16, 2007.
- Press, W. H., S. A. Teukolsky, W. T. Vetterling, and B. P. Flannery, *Numerical Recipes in Fortran*, 172nd Technical Cambridge University Press, Cambridge, U.K, 1992.

- Radhakrishnan, R., *Coupled Thermomechanical Analysis of Viscoelastic Dampers*, Master's Thesis, State University New York, Buffalo, NY, 2000.
- Shen, K. L., and T. T. Soong, "Modeling of Viscoelastic Dampers for Structural Applications," Journal of Engineering Mechanics, vol. 121, issue 6, pp. 694–701, 1995.

Table 5.1.7–1 Original and shifted storage and loss moduli from Shen and Soong (1995).

θ (°C)	f (Hz)	G′ (ksi)	G″ (ksi)	fr (Hz)	Gr′ (ksi)	Gr″ (ksi)
21	1	0.199	0.259	1.096	0.199	0.258
	1.5	0.265	0.326	1.644	0.264	0.325
	2	0.3	0.395	2.192	0.299	0.394
	2.5	0.365	0.463	2.74	0.364	0.462
	3	0.386	0.487	3.288	0.385	0.486
32	1	0.093	0.128	0.265	0.09	0.124
	1.5	0.1	0.158	0.398	0.097	0.153
	2	0.131	0.189	0.53	0.127	0.183
	2.5	0.147	0.213	0.663	0.142	0.206
	3	0.182	0.242	0.795	0.176	0.234
38	1	0.074	0.09	0.122	0.07	0.085
	1.5	0.068	0.102	0.183	0.064	0.097
	2	0.1	0.114	0.244	0.095	0.108
	2.5	0.106	0.125	0.305	0.1	0.119
	3	0.114	0.14	0.366	0.108	0.133

Table 5.1.7–2 Prony series parameters.

$g_1 = 0.0396$	$t_1 = 1.766$ s
$g_2 = 0.1018$	$t_2 = 0.1536$ s
$g_3 = 0.8586$	$t_3 = 0.0127$ s

Table 5.1.7–3 Thermal properties.

Quantity	Steel	Viscoelastic Damper
Density (lbf-s^2/in^4)	7.30×10^{-4}	9.93×10^{-5}
Thermal expansion (in/in-°C)	10.8×10^{-6}	9.0×10^{-5}
Thermal conductivity (BTU/s-in-°C)	7.0×10^{-4}	6.0×10^{-6}
Specific heat (BTU-in/lbf-s^2-°C)	76.3	300

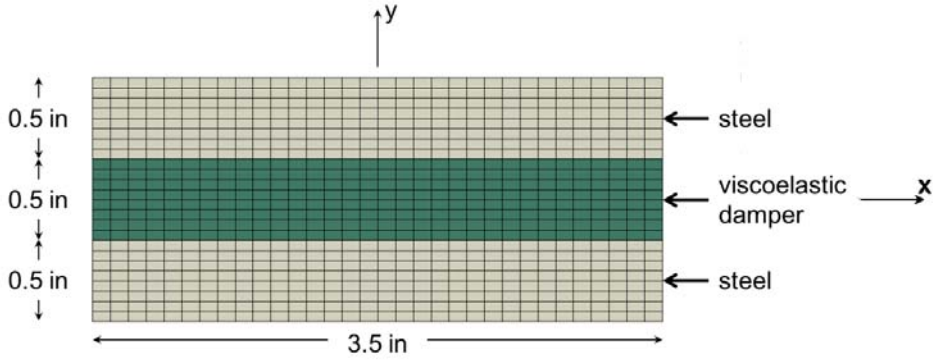

Figure 5.1.7–1 Viscoelastic damper geometry.

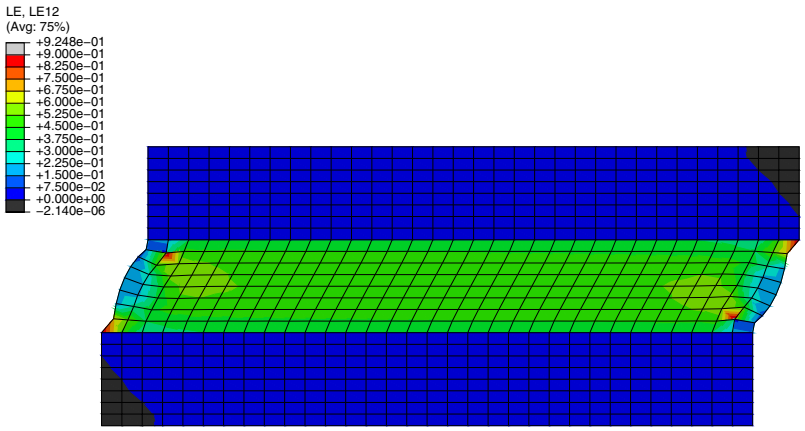

Figure 5.1.7–2 Shear component of the log strain at t=9.25 s for the coupled temperature-displacement model using hyperelastic materials.

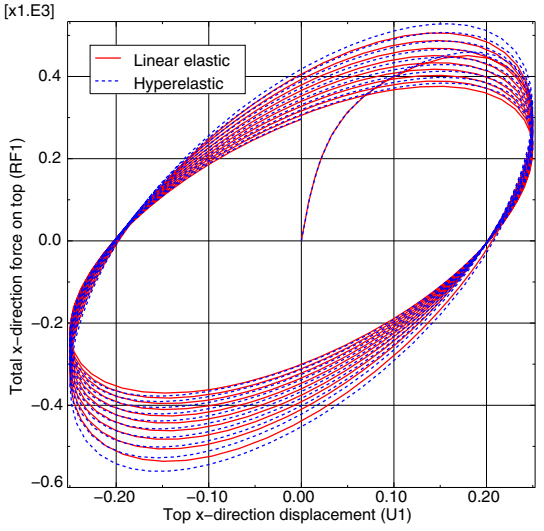

Figure 5.1.7–3 Hysteresis response for the coupled thermomechanical analysis.

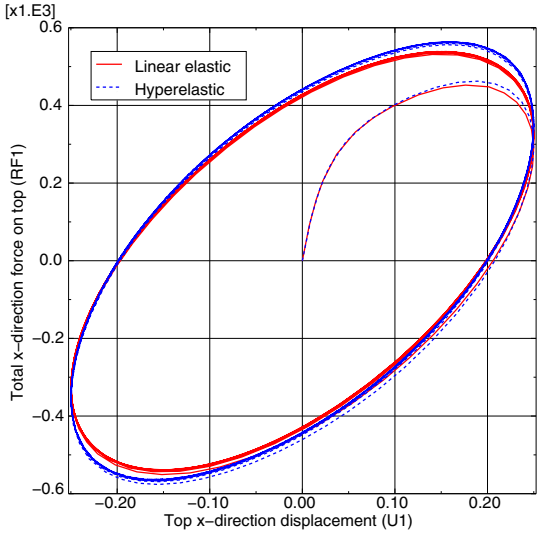

Figure 5.1.7–4 Hysteresis response for the pure stress analysis (no thermal coupling).

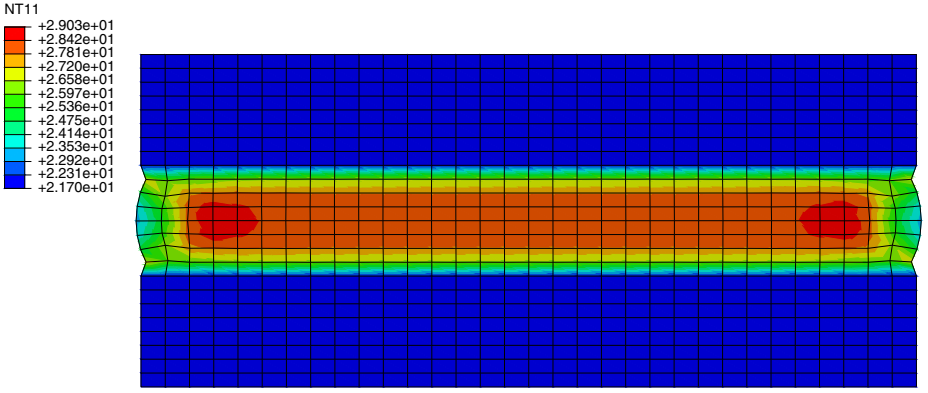

Figure 5.1.7–5 Temperature contour in fully coupled model with hyperelasticity at t=10 s.

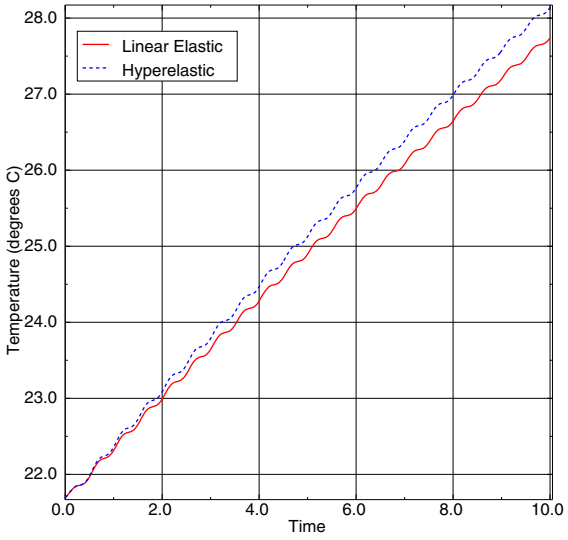

Figure 5.1.7–6 Temperature history at center of viscoelastic region for coupled analysis.

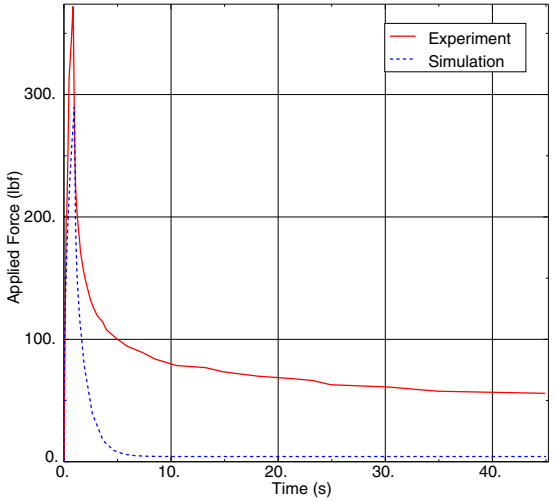

Figure 5.1.7–7 Comparison of relaxation response from experiments by Shen and Soong with prediction using material calibrated to capture hysteresis response.

6. Fluid Dynamics and Fluid-Structure Interaction

- "Fluid dynamics and fluid-structure interaction," Section 6.1

6.1 Fluid dynamics and fluid-structure interaction

- “Conjugate heat transfer analysis of a component-mounted electronic circuit board,” Section 6.1.1

6.1.1 CONJUGATE HEAT TRANSFER ANALYSIS OF A COMPONENT-MOUNTED ELECTRONIC CIRCUIT BOARD

Products: Abaqus/Standard Abaqus/Explicit Abaqus/CFD Abaqus/CAE

Objectives

This example examines the transient conjugate heat transfer between a single printed circuit board (PCB)–mounted electronic component and the ambient air.

It demonstrates Abaqus techniques to analyze a conjugate heat transfer problem using:

- Abaqus/CFD for solving both the laminar flow field and buoyancy-driven natural convection heat transfer occurring external to a structure,
- Abaqus/Standard or Abaqus/Explicit for solving the heat transfer within the structure, and
- the co-simulation technique to maintain fidelity of the solution on the interface.

Application description

The single printed circuit board (PCB)–mounted electronic component is subjected to a passive power dissipation that results in the transfer of heat both within the component and the PCB due to conduction. Furthermore, the heated surface of the component and the PCB induces a temperature-dependent density differential in the surrounding air, thereby setting up a buoyancy-driven natural convection process external to the surface. Heat is thus transferred from the component and PCB surfaces to the ambient air through this convection process. Understanding the resulting conduction-convection conjugate heat transfer phenomenon results in more accurate damage estimation and life prediction for electronic components.

The details of the model are largely derived from Eveloy and Rodgers (2005).

Geometry

Nominal component/PCB geometry dimensions are considered. The PCB dimensions are $7.8 \times 11.6 \times 0.16$ cm. The mounted electronic component consists of an encapsulant of dimension $3 \times 3 \times 0.7$ cm that encapsulates a heat slug of dimension $1.8 \times 1.8 \times 0.3$ cm mounted atop a die of dimension $0.75 \times 0.75 \times 0.2$ cm. The assembled PCB-component package is shown in Figure 6.1.1–1. The cross-section view of the assembled package is shown in Figure 6.1.1–2. The size of the computational domain that encloses the electronic package is taken to be $27.8 \times 20 \times 12.56$ cm for the Abaqus/CFD flow computations.

Materials

The PCB material has a thermal conductivity of 19.25 W/m/K, a density of 8950 kg/m^3, a specific heat of 1300 J/kg/K, and a thermal expansion of 1.6×10^{-5} /K. The heat slug material has a thermal conductivity of 398 W/m/K, a density of 8940 kg/m^3, a specific heat of 385 J/kg/K, and a thermal expansion of 3.3×10^{-6} /K. The die material has a thermal conductivity of 130.1 W/m/K, a density of 2330 kg/m^3, a specific heat of 712 J/kg/K, and a thermal expansion of 3.3×10^{-6} /K. The encapsulant material has

a thermal conductivity of 0.63 W/m/K, a density of 1820 kg/m^3, a specific heat of 882 J/kg/K, and a thermal expansion of 1.9×10^{-5} /K. For the external fluid domain, properties of air, namely a density of 1.127 kg/m^3, a thermal conductivity of 2.71×10^{-2} W/m/K, a specific heat of 1006.4 J/kg/K, a thermal expansion of 3.43×10^{-3} /K, and a viscosity of 1.983×10^{-5} kg/m/s, are assumed.

Initial conditions

The initial temperature of the assembled electronic package and the external fluid (ambient air) is set to 293 K. In addition, the fluid is initially assumed to be quiescent and, hence, its velocity is set to zero everywhere.

Boundary conditions and loading

The electronic component of the assembled package is subjected to a passive power dissipation corresponding to a specified body heat flux value of 5×10^7 W/m^3. The bottom surface of the external computational domain is assumed to be a rigid floor, and an adiabatic wall condition is assumed there. The electronic package is firmly attached to the bottom of the computational domain, as shown in Figure 6.1.1–3. The computational domain boundaries for the external flow and heat transfer calculations are positioned at sufficient distances from the assembled electronic package such that the effects of the boundaries on the results are negligible. A no-slip, no-penetration flow wall boundary condition is enforced at the bottom surface. At the top, an outlet boundary condition is specified with the fluid pressure set to zero. For all other boundaries, free-stream conditions are applied for both the velocity and temperature.

Gravity loading is applied along the negative y-axis (see Figure 6.1.1–3).

Interactions

The component-mounted circuit board is subjected to volumetric power dissipation, which generates heat within the structure. Heat transfer to the surface of the structure takes place via conduction. The heated surface then generates a buoyancy-driven natural convection in the surrounding ambient air.

Abaqus modeling approaches and simulation techniques

The co-simulation approach coupling Abaqus/CFD to either Abaqus/Standard or Abaqus/Explicit is used to solve the conjugate heat transfer problem. The Abaqus/CFD model of the co-simulation consists of the external region bounding the electronic package (see Figure 6.1.1–3); whereas, the component-mounted PCB electronic package (see Figure 6.1.1–1) is modeled either in Abaqus/Standard or Abaqus/Explicit. Co-simulation regions across which data will be exchanged during the co-simulation analysis are identified on each model at the location of the electronic package surface.

Analysis types

The Abaqus/Standard model includes a transient heat transfer step; whereas the Abaqus/Explicit model includes a dynamic coupled thermal-stress analysis step with all translational degrees of freedom fixed. The Abaqus/CFD model includes an incompressible laminar flow analysis coupled with the energy equation that governs the temperature distribution.

Mesh design

The Abaqus/Standard model is meshed with linear hexahedral (DC3D8) elements. The Abaqus/Explicit model is meshed with coupled linear hexahedral (C3D8RT) elements. The Abaqus/CFD model is meshed with linear hexahedral (FC3D8) fluid elements.

Results and discussion

The heat generated within the electronic component gets distributed to its surface and also to the surface of the PCB substrate by conduction. The heated air near the component surface becomes less dense and rises upward due to buoyancy. The Grashof number (a parameter describing the ratio of buoyancy to viscous forces) for this problem, based on the board length, was estimated to be of the order 10^6 as reported by Eveloy and Rodgers (2005). Because of incompressibility, the upward rising air entrains cold air from the surroundings, thereby setting up a natural convection flow. The upward rising hot air and entrained cold air from the sides are illustrated in Figure 6.1.1–4, where the velocity vectors (V) are plotted on the center cross-sectional slice of the domain in the y–z plane. In Figure 6.1.1–4 entrainment from the out-of-plane direction appears as small dots. The contours of temperature distribution (TEMP) on the same cross-sectional slice are shown in Figure 6.1.1–5, where the hot electronic component surface and the upward rising thermal plume can be clearly seen. The temperature distribution (NT11) along a particular path in the spanwise direction (x-axis) on the surface of the component-mounted electronic package is shown in Figure 6.1.1–6. Heat is seen to spread from the component surface (the area of near-constant heat distribution) to the surfaces of the PCB substrate on either side. The temperature distribution (NT11) along a particular path in the streamwise direction (y-axis) on the surface of the electronic package shown in Figure 6.1.1–7 illustrates the same phenomenon. These distributions are qualitatively similar to the experimentally measured temperature profiles given in Eveloy and Rodgers (2005).

Files

circuit_board_cht.py	Script to generate the model in Abaqus/CAE using the orphan meshes from cfd_mesh.inp and std_heat_transfer.inp.
cfd_mesh.inp	Orphan mesh for the Abaqus/CFD domain.
std_heat_transfer.inp	Orphan mesh for the Abaqus/Standard domain.
cht_circuitboard_cfd.inp	Abaqus/CFD model used for co-simulation with Abaqus/Explicit.
cht_circuitboard_xpl.inp	Abaqus/Explicit model used for co-simulation with Abaqus/CFD.
cht_circuitboard_config.xml	Configuration file used for the Abaqus/CFD to Abaqus/Explicit co-simulation.

References

Abaqus Analysis User's Guide

- "Incompressible fluid dynamic analysis," Section 6.6.2 of the Abaqus Analysis User's Guide
- "Fluid-to-structural and conjugate heat transfer co-simulation," Section 17.3.2 of the Abaqus Analysis User's Guide

Other

- Eveloy, V., and P. Rodgers, "Prediction of Electronic Component-Board Transient Conjugate Heat Transfer," IEEE Transactions on Components and Packaging Technologies, vol. 28, no. 4, pp. 817–829, 2005.

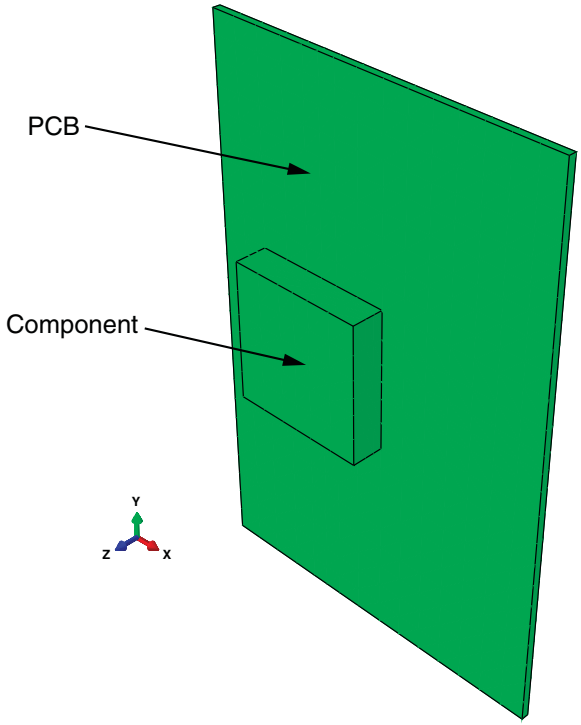

Figure 6.1.1–1 Component-mounted electronic circuit board.

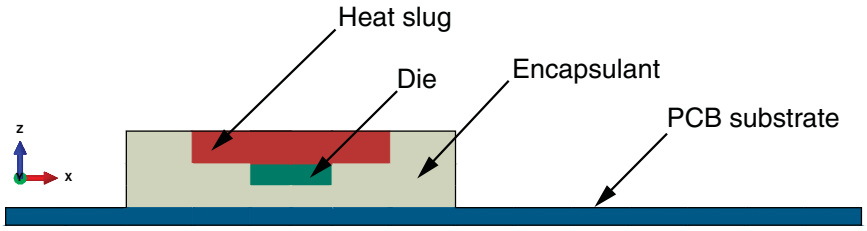

Figure 6.1.1–2 Cross-sectional view of the electronic package indicating the different materials forming the component and circuit board.

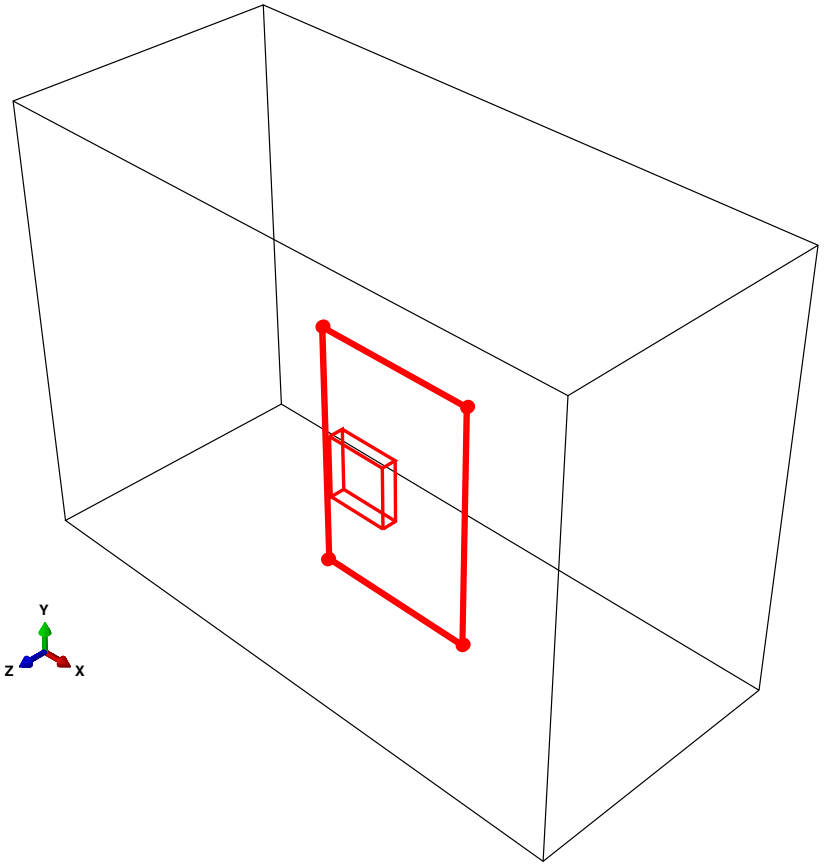

Figure 6.1.1–3 Electronic package anchored to the bottom of the computational domain (enclosing box).

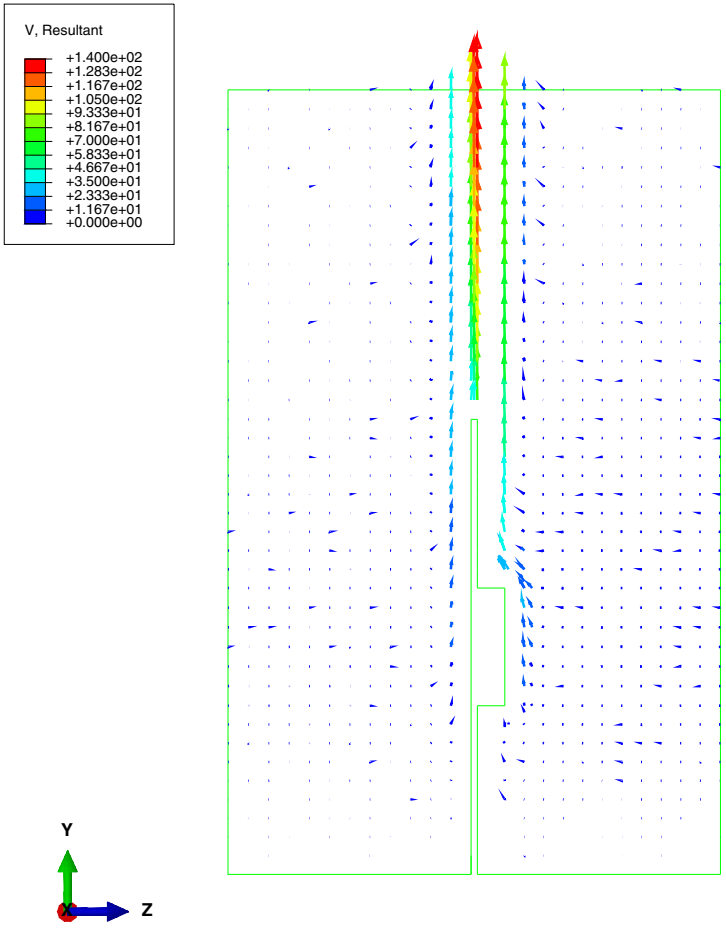

Figure 6.1.1–4 Plot of velocity vectors induced due to natural convection on a cross-sectional slice.

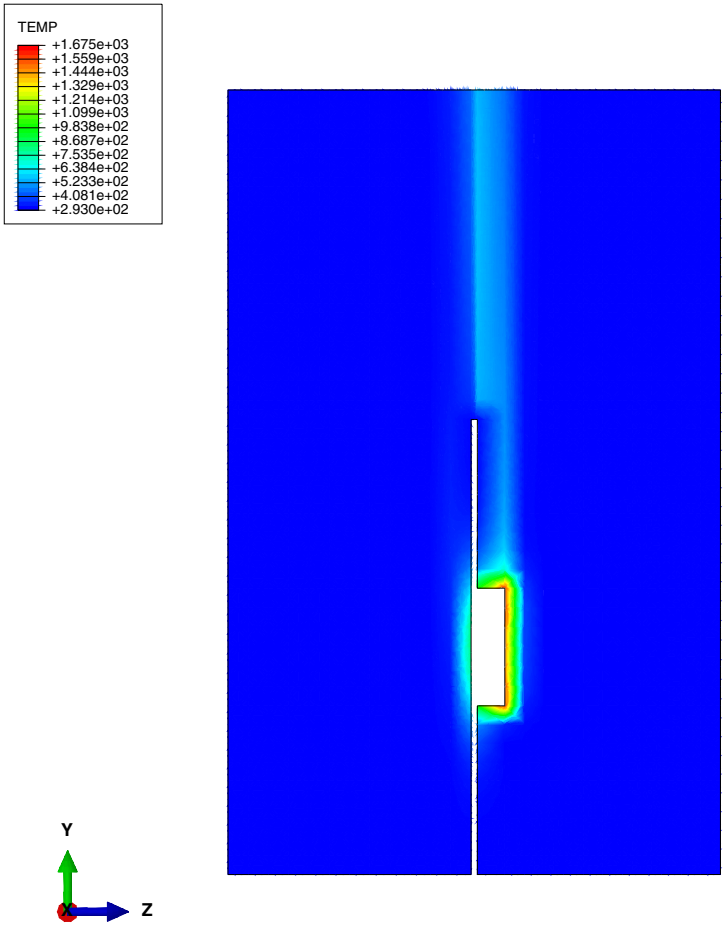

Figure 6.1.1–5 Plot of temperature contours on a cross-sectional slice.

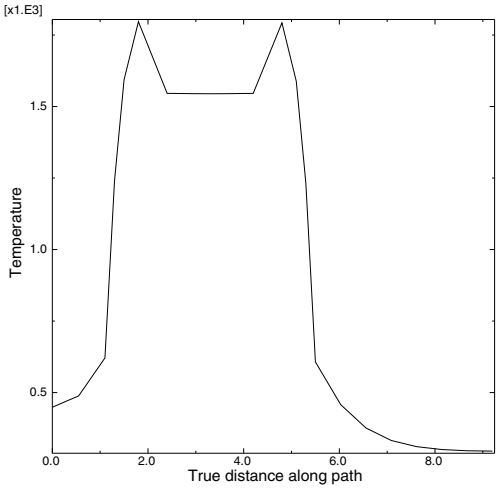

Figure 6.1.1–6 Temperature along a path in the spanwise direction (x-axis) on the surface of the electronic package.

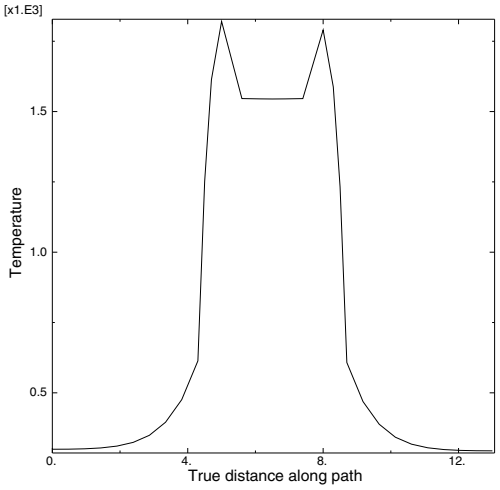

Figure 6.1.1–7 Temperature along a path in the streamwise direction (y-axis) on the surface of the electronic package.

7. Electromagnetic Analyses

- "Piezoelectric analyses," Section 7.1
- "Joule heating analyses," Section 7.2

7.1 Piezoelectric analyses

- “Eigenvalue analysis of a piezoelectric transducer,” Section 7.1.1
- “Transient dynamic nonlinear response of a piezoelectric transducer,” Section 7.1.2

7.1.1 EIGENVALUE ANALYSIS OF A PIEZOELECTRIC TRANSDUCER

Product: Abaqus/Standard

This problem performs an eigenspectrum analysis of a cylindrical transducer consisting of a piezoelectric material with brass end caps.

Various elements are used in the eigenspectrum analysis. The elements range from axisymmetric elements to three-dimensional elements, using both lower- and higher-order elements. The basis of the piezoelectric capability in Abaqus is described in "Piezoelectric analysis," Section 2.10.1 of the Abaqus Theory Guide.

Geometry and material

This problem is identical to the one discussed in a report by Mercer et al. (1987). The structure is shown in Figure 7.1.1–1 and consists of a piezoelectric material PZT4 with brass end caps. The piezoelectric material is electroded on both the inner and outer surfaces.

The properties for PZT4 in a cylindrical system are:

Elasticity Matrix:

$$\begin{bmatrix} 115.4 & 74.28 & 74.28 & 0 & 0 & 0 \\ 74.28 & 139.0 & 77.84 & 0 & 0 & 0 \\ 74.28 & 77.84 & 139.0 & 0 & 0 & 0 \\ 0 & 0 & 0 & 25.64 & 0 & 0 \\ 0 & 0 & 0 & 0 & 25.64 & 0 \\ 0 & 0 & 0 & 0 & 0 & 25.64 \end{bmatrix} \text{ GPa}$$

Piezoelectric Coupling Matrix (Stress Coefficients):

$$\begin{bmatrix} 15.08 & 0 & 0 \\ -5.207 & 0 & 0 \\ -5.207 & 0 & 0 \\ 0 & 12.710 & 0 \\ 0 & 0 & 12.710 \\ 0 & 0 & 0 \end{bmatrix} \text{ coulomb/m}^2$$

Dielectric Matrix:

$$\begin{bmatrix} 5.872 & 0 & 0 \\ 0 & 6.752 & 0 \\ 0 & 0 & 6.752 \end{bmatrix} 10^{-9} \text{ farad/m}$$

The 1-direction is radial, the 2-direction is axial, and the 3-direction is tangential. From these matrices it is seen that the poling direction is radially outwards from the axis of symmetry. (The order of the stresses in Abaqus may differ from those typically used in electrical applications. Abaqus uses the

standard mechanical convention, where the stress components are ordered as $\{\sigma_{11}\sigma_{22}\sigma_{33}\tau_{12}\tau_{13}\tau_{23}\}$. See "Piezoelectric behavior," Section 26.5.2 of the Abaqus Analysis User's Guide.)

The brass is elastic and isotropic with a Young's modulus of 104 GPa and a Poisson's ratio of 0.37.

Models

The transducer is modeled with a variety of elements. It is modeled as an axisymmetric structure utilizing both the planar, axisymmetric elements and the three-dimensional elements. For the axisymmetric elements, five meshes employing 4-node, 6-node, and 8-node elements are used in the finite element discretization. The first two meshes use 4-node elements with two levels of refinement, the third mesh uses 6-node elements, and the last two meshes use the 8-node elements with two levels of refinement. Lumped mass matrices are used for the lower-order elements. Consistent mass matrices are used in the higher-order elements. The meshes used for the 4-node and 6-node axisymmetric elements are shown in Figure 7.1.1–2. The meshes used for the 8-node axisymmetric elements are shown in Figure 7.1.1–3.

The three-dimensional model uses a slice of the structure and applies axisymmetric boundary conditions; 8-node and 20-node brick elements are used. The discretization used for each model is shown in Figure 7.1.1–3. These models use a local coordinate system to maintain the proper definitions of the material properties. Also, in order to prescribe the axisymmetric boundary conditions, the nodal degrees of freedom are transformed into a cylindrical coordinate system.

All the models are considered to be open-circuited. The potentials on the inside surface are restrained to zero. The frequencies correspond to those for antiresonance.

Results and discussion

The solutions obtained with the various Abaqus models are shown in Table 7.1.1–1. Even for these coarse models, the results are quite close to the experimental results. In addition, the results from Abaqus for the lower-order axisymmetric elements with lumped mass and the higher-order axisymmetric elements with consistent mass matrices in the computation of both the resonant and antiresonant frequencies match well with the numerical results reported in Mercer et al. The first four mode shapes for the more refined model with CAX8RE elements are shown in Figure 7.1.1–4.

Similar analyses have been performed considering the problem to be closed-circuited to obtain the resonant frequencies. For this situation, the potentials on both the inner and outer surfaces are set to zero. The results also compare well with those given in Mercer et al.

Input files

eigenpiezotrans_cax4e_coarse.inp	Coarse mesh with 4-node axisymmetric elements.
eigenpiezotrans_cax4e_fine.inp	Refined mesh with 4-node axisymmetric elements.
eigenpiezotrans_cax6e.inp	Mesh with 6-node axisymmetric elements.
eigenpiezotrans_cax8re_coarse.inp	Coarse mesh with 8-node axisymmetric elements.
eigenpiezotrans_cax8re_fine.inp	Refined mesh with 8-node axisymmetric elements.
eigenpiezotrans_c3d8e.inp	Mesh with 8-node three-dimensional elements.
eigenpiezotrans_c3d8e.f	User subroutine **`ORIENT`** used in eigenpiezotrans_c3d8e.inp.

eigenpiezotrans_c3d20e.inp	Mesh with 20-node three-dimensional elements.
eigenpiezotrans_c3d20e.f	User subroutine **ORIENT** used in eigenpiezotrans_c3d20e.f.
eigenpiezotrans_elmatrixout.inp	Data that test the use of ∗ELEMENT MATRIX OUTPUT with piezoelectric elements.
eigenpiezotrans_usr_element.inp	Data for a job that reads in the matrices output in eigenpiezotrans_elmatrixout.inp and performs an eigenvalue analysis.

Reference

- Mercer, C. D., B. D. Reddy, and R. A. Eve, "Finite Element Method for Piezoelectric Media," University of Cape Town/CSIR Applied Mechanics Research Unit Technical Report, no. 92, April 1987.

Table 7.1.1–1 Piezoelectric transducer eigenvalue estimates.

Model		Frequencies (kHz) for mode number				
Type	**# of Elements**	**1**	**2**	**3**	**4**	**5**
CAX4E	13	14.1	39.1	56.2	66.1	79.3
CAX4E	320	18.6	40.3	57.8	64.2	88.1
CAX6E	10	20.0	43.2	63.2	70.4	98.8
CAX8RE	5	19.6	42.8	61.0	66.9	96.3
CAX8RE	80	18.6	40.3	57.6	64.2	87.6
C3D8E	16	19.8	41.8	62.0	68.7	95.2
C3D20E	16	19.7	42.9	60.4	66.5	91.7
Experimental(1)		18.6	35.4	54.2	63.3	88.8
(1): Experimental results obtained from Mercer et al. (1987).						

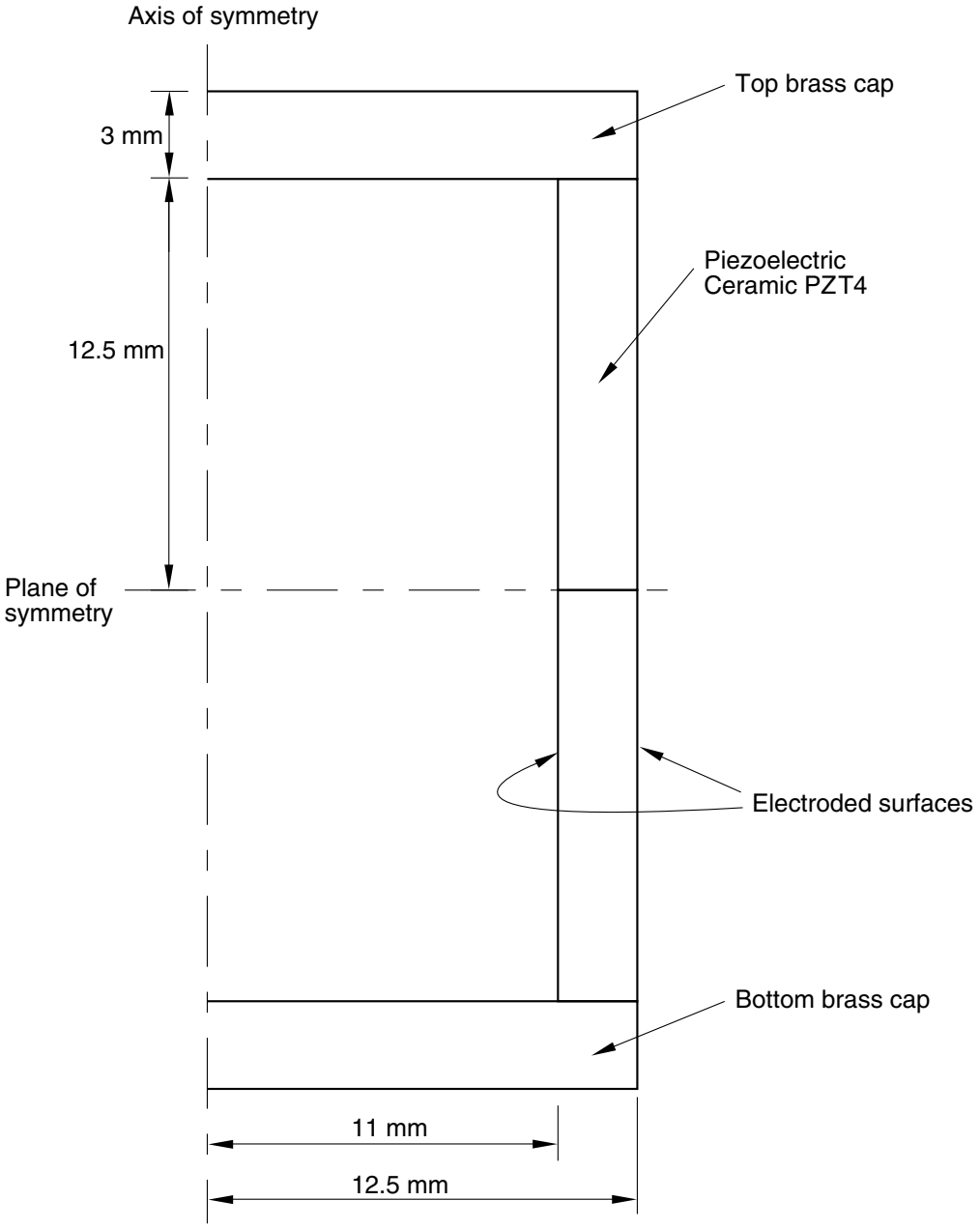

Figure 7.1.1–1 Piezoelectric transducer.

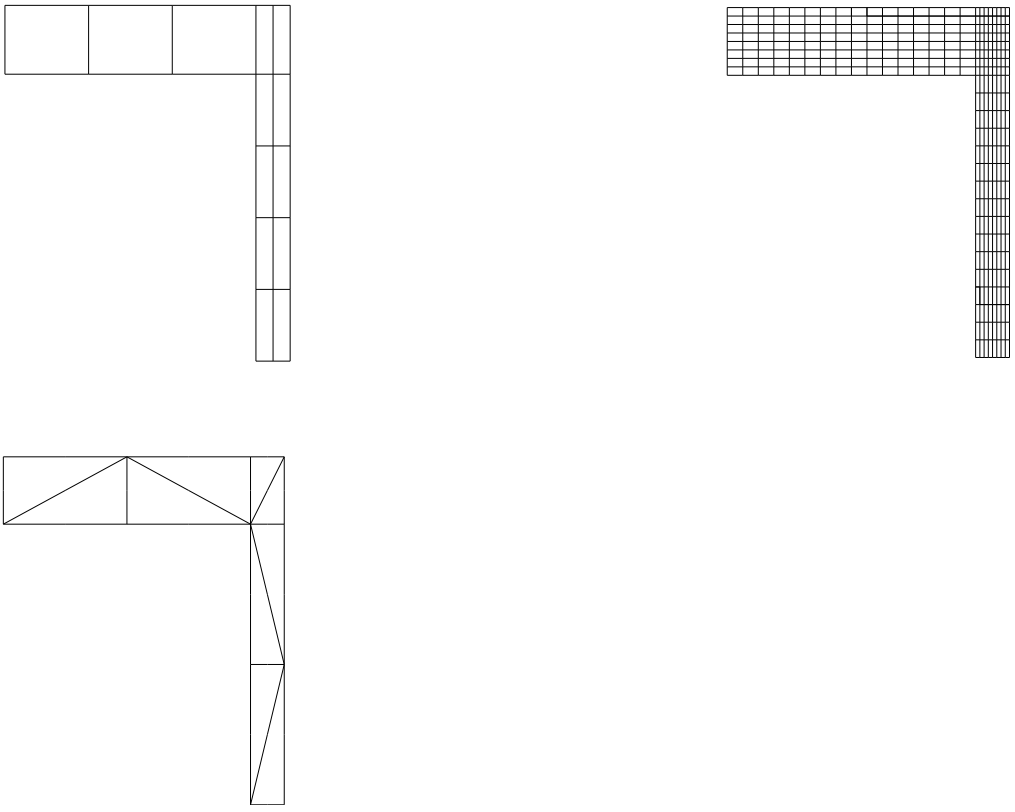

Figure 7.1.1–2 Meshes used with 4-node and 6-node axisymmetric elements.

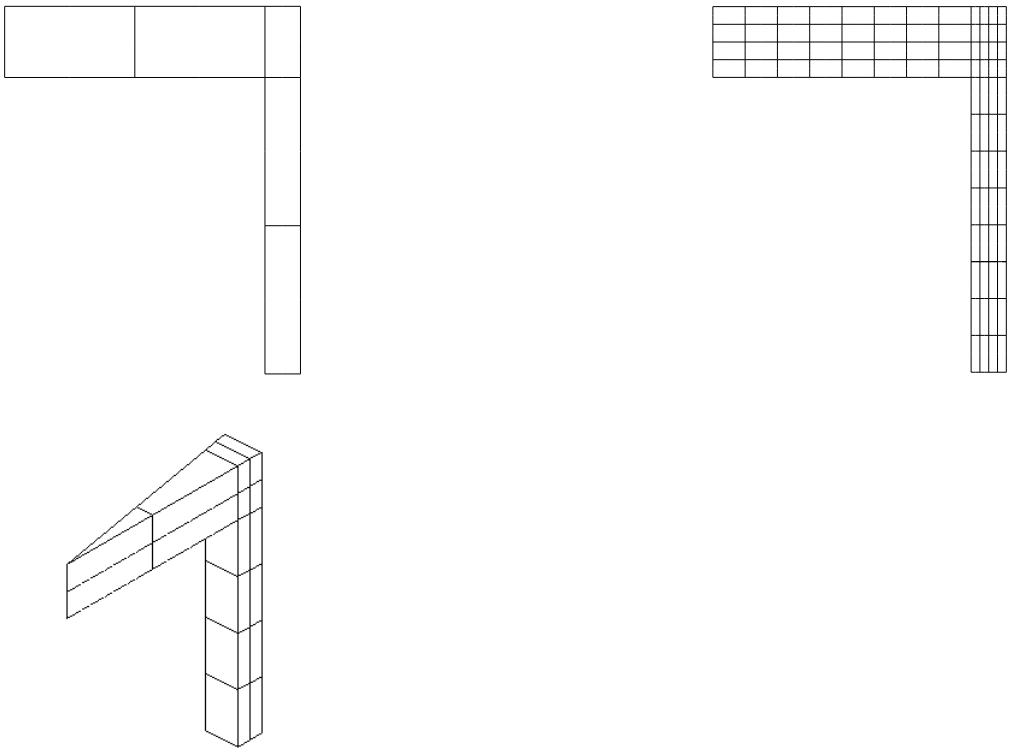

Figure 7.1.1–3 Meshes used with 8-node axisymmetric and 8-node and 20-node three-dimensional elements.

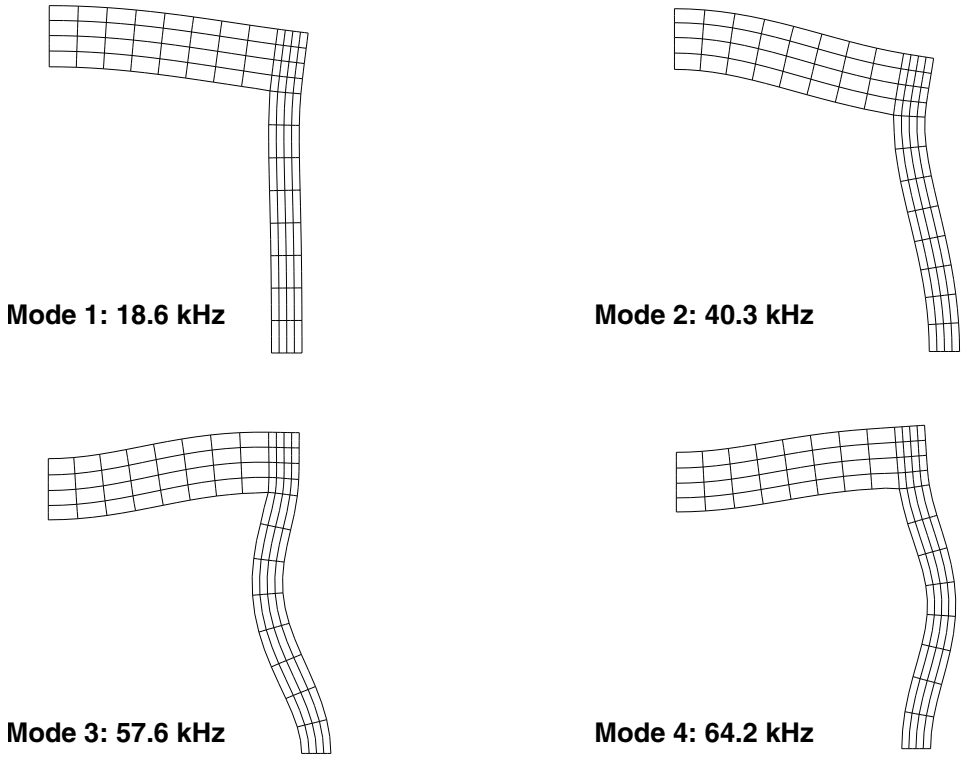

Figure 7.1.1–4 Mode shapes for 8-node axisymmetric elements.

7.1.2 TRANSIENT DYNAMIC NONLINEAR RESPONSE OF A PIEZOELECTRIC TRANSDUCER

Product: Abaqus/Standard

This example demonstrates the Abaqus capability for predicting the nonlinear transient dynamic behavior of structural systems that incorporate piezoelectric components.

The example utilizes a piezoelectric bending-type transducer that is idealized as a simple layered beam structure. The fabrication of the transducer is modeled, and the eigenfrequencies of the preloaded structure are extracted. Finally, the dynamic response due to a transient electrical potential pulse is monitored. Piezoelectric transducers are commonly used in the following application areas:

- Ultrasonic imaging systems
- Ultrasonic cleaning systems
- Ultrasonic welding/bonding systems
- Audio systems
- Acoustic transducers
- Active vibration control systems

Geometry and material

The transducer is shown in Figure 7.1.2–1. It has a composite beam that is 0.0025 m wide and 0.18 m long. The initially straight beam has a 0.0005 m thick insulating core; 0.000125 m thick PZT–5H piezoelectric strips are bonded to the top and the bottom faces of the core material. The piezoelectric strips are only 0.060 m long and are centered at the beam mid-span. The piezoelectric strips are polarized along the beams in the through-thickness direction. The properties for the PZT–5H material are as follows:

Elastic properties:

Engineering constants	
E_1	60.61 GPa
E_2	48.31 GPa
E_3	60.61 GPa
ν_{12}	0.512
ν_{13}	0.289
ν_{23}	0.408
G_{12}	23.0 GPa

Engineering constants	
G_{13}	23.5 GPa
G_{23}	23.0 GPa

Piezoelectric coupling matrix (strain coefficients):

$$\begin{bmatrix} 0 & 0 & 0 & 741 & 0 & 0 \\ -274 & 593 & -274 & 0 & 0 & 0 \\ 0 & 0 & 0 & 0 & 0 & 741 \end{bmatrix} 10^{-12} \quad \text{m/volt}$$

Dielectric matrix:

$$\begin{bmatrix} 1.505 & 0 & 0 \\ 0 & 1.301 & 0 \\ 0 & 0 & 1.505 \end{bmatrix} 10^{-8} \quad \text{farad/meter}$$

The local 1-direction is in the beam longitudinal direction, and the local 2- and 3-directions are in the beam cross-section. From these matrices it can be seen that the poling direction is in the local 2-direction of the piezoelectric strips.

The core material is elastic and isotropic with a Young's modulus of 6 GPa, a density of 1500 kg/m^3, and a Poisson's ratio of 0.35.

Model

The beam core material is modeled with 46 C3D20 elements, and the piezoelectric strips are modeled using 16 C3D20E elements each. A perfect bond between the core and the piezoelectric materials is defined with a surface-based tie constraint, for which the piezoelectric surfaces are retained as the master surfaces. The electrical potentials for the top and the bottom surfaces of each piezoelectric strip are coupled to the electrical potentials of the master nodes assigned to each surface using linear constraint equations. The electrical potentials and the reaction charges can be monitored at these master nodes. The piezoelectric surfaces bonded to the core material are assigned a zero electrical potential throughout the analysis.

The first 8 steps are used to represent the fabrication procedure and to investigate the behavior of the fabricated transducer. These include linear perturbation steps to investigate the eigenmodes of the fabricated transducer at various stages during its fabrication. Steps 9 through 11 represent a general nonlinear transient analysis of the transducer. A square wave electrical potential pulse of 200 volts is applied using a boundary condition with a step function amplitude. Immediately after the pulse, a closed circuit condition (potential gradients are prescribed) is maintained and the reaction charges are monitored. Subsequently, the circuit is opened (the potential gradient is not prescribed; the potential is an active degree of freedom that is determined as part of the solution). In the case of an open circuit condition the resulting voltage can be used to measure the transducer's open circuit free vibration. The analysis steps are as follows:

1. Static shape fabrication: deformation induced via an applied potential of 1000 volts.
2. Static shape fabrication: fix support ends, and reduce the applied potential to 0 volts.
3. Closed circuit modal analysis about the base state obtained at the end of Step 2.
4. Static shape fabrication: apply open circuit conditions.
5. Open circuit modal analysis about the base state obtained at the end of Step 4.
6. Static test at an operational load of 200 volts.
7. Closed circuit modal analysis about the base state obtained at the end of Step 6.
8. Reset to zero voltage condition.
9. Transient dynamic response: apply voltage pulse of 200 volts for 0.00265 seconds.
10. Transient dynamic response: free vibration under closed circuit condition with 0 volts.
11. Transient dynamic response: free vibration under open circuit condition.

Results and discussion

In Figure 7.1.2–2 the deformed and superimposed undeformed shapes are shown after applying 1000 volts at both piezoelectric strips. In Figure 7.1.2–3 the deformed shape is shown at the end of Step 2, where both ends are fixed and an applied potential of 0 volts is prescribed. Subsequently, the eigenfrequencies are extracted about this preloaded state. In Figure 7.1.2–4 the third eigenmode with a frequency of 150.9 cycles/sec is shown for this closed circuit condition. Figure 7.1.2–5 shows the third mode shape with a frequency of 154.4 cycles/sec under open circuit conditions. The third mode shape for the closed circuit condition with a prescribed voltage of 200 volts is again almost identical to the third mode shape shown in Figure 7.1.2–4. However, the eigenfrequency has changed to 181.7 cycles/sec.

In Steps 9 and 10 a closed circuit condition is prescribed for the piezoelectric strips, and subsequently in Step 11 the voltage boundary conditions are removed resulting in open circuit conditions. Figure 7.1.2–6 shows the time history of the potential under closed and open circuit conditions. Typically, the transducer acts as a “driver” in a closed circuit condition as the potential gradient is prescribed, thereby driving the structure. On the other hand, the transducer acts as a “receiver” in an open circuit condition as the voltage output can be used to measure the mechanical response. In Figure 7.1.2–7 the reaction charge at the top piezoelectric strip is shown under the above conditions. In a closed circuit condition the reaction charge changes in time, while in an open circuit condition the reaction charge is equal to zero. The displacement of the transducer’s center is demonstrated in Figure 7.1.2–8.

The results are presented to illustrate the general capabilities in Abaqus for predicting the transient response of piezoelectric structures. If this system represented part of an actual ultrasound system, additional output related to the design/analysis objective would be created and analyzed.

Input files

dynamictransducer.inp	Transient dynamic nonlinear response of a piezoelectric transducer.
dynamictransducer_mesh.inp	Assembly definition.

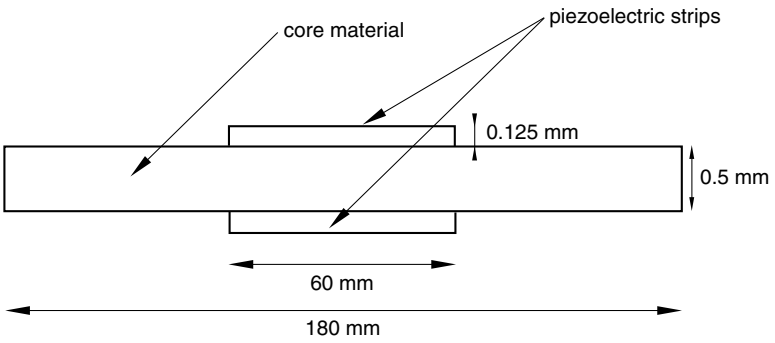

Figure 7.1.2–1 Geometry of the piezoelectric transducer.

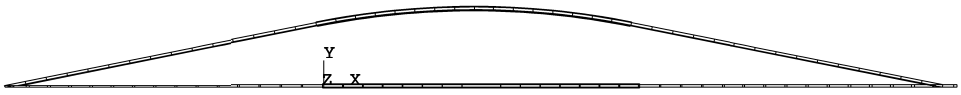

Figure 7.1.2–2 Deformed shape with superimposed undeformed shape at the end of Step 1.

Figure 7.1.2–3 Deformed shape with superimposed undeformed shape at the end of Step 2.

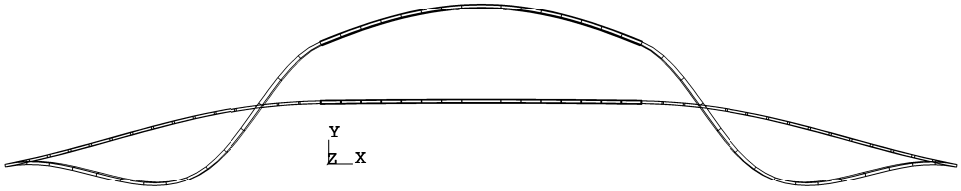

Figure 7.1.2–4 Mode shape 3 with superimposed shape of the base state after Step 2.

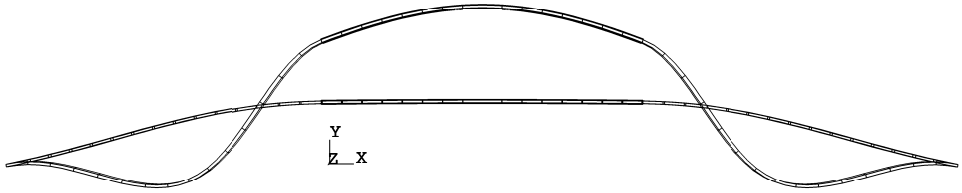

Figure 7.1.2–5 Mode shape 3 with superimposed shape of the base state after Step 4.

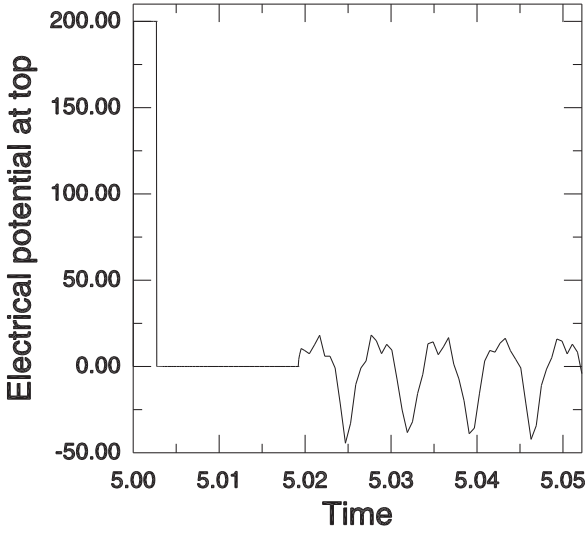

Figure 7.1.2–6 Transient response of potential at top piezoelectric strip.

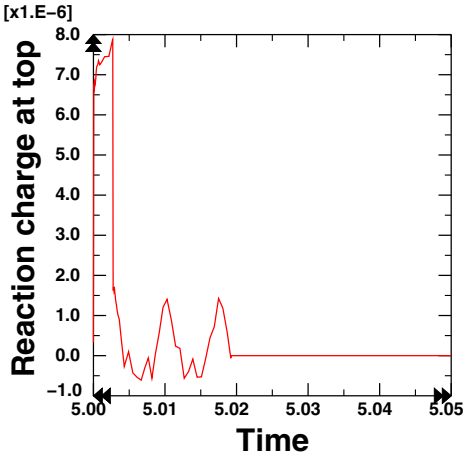

Figure 7.1.2–7 Transient dynamic response of the reaction charge at top piezoelectric strip.

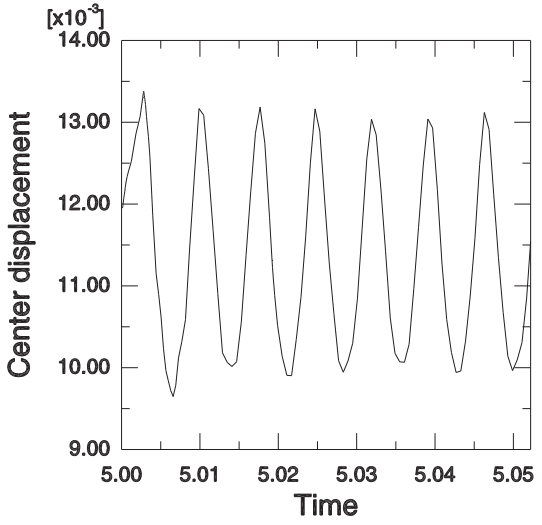

Figure 7.1.2–8 Transient response of center displacement.

7.2 Joule heating analyses

- “Thermal-electrical modeling of an automotive fuse,” Section 7.2.1

7.2.1 THERMAL-ELECTRICAL MODELING OF AN AUTOMOTIVE FUSE

Product: Abaqus/Standard

This example shows the use of the fully coupled thermal-electrical procedure to analyze an automotive fuse.

Joule heating arises when the energy dissipated by electrical current flowing through a conductor is converted into thermal energy. Abaqus provides a fully coupled thermal-electrical procedure for analyzing this type of problem.

An overview of the capability is provided in "Coupled thermal-electrical analysis," Section 6.7.3 of the Abaqus Analysis User's Guide. This example illustrates the use of the capability to model the heating of an automotive electrical fuse due to a steady 30 A electrical current. Fuses are the primary circuit protection devices in automobiles. They are available in a range of different current ratings and are designed so that when the operating current exceeds the design current for a period of time, heating due to electrical conduction causes the metal conductor to melt and—hence—the circuit to disconnect.

A description of the original problem, as well as experimental measurements, can be found in Wang and Hilali (1995). The experimental data and some of the material properties were refined subsequent to this publication. These properties are used here, and the finite element results are compared with the refined measurements (Hilali, July 1995).

Problem description

An automotive electrical fuse consists of a metal conductor, such as zinc, embedded within a transparent plastic housing. The plastic housing, which only protects and supports the thin conductor, is not represented in the finite element model. Figure 7.2.1–1 shows front and top sections of the geometry of the conductor. It consists of two 0.76 mm thick blades, with an S-shaped fuse element supported between the blades. The blades fit tightly into standard electrical terminals that are built into the circuit and provide the connection between the electrical circuit and the fuse element. The fuse element is usually much thinner than the fuse blades (in this case 0.28 mm thick) and is designed to melt when the operating current exceeds the design current for a period of time. The fuse blades are 8 mm wide and 30.4 mm long. The fuse element is approximately 3.6 mm wide.

The model is discretized (see Figure 7.2.1–1) with 8-node first-order brick elements (element type DC3D8E), using one element through the thickness. Two 6-node triangular prism elements (element type DC3D6E) are used to fill regions where the geometry precludes the use of brick elements. For comparison refined mesh input files are also included.

The electrical conductivity of zinc varies linearly between 16.75×10^3 $1/\Omega$ mm at 20°C and $12.92 \times 10^3 1/\Omega$ mm at 100°C. The thermal conductivity varies linearly between 0.1120 W/mm°C at 20°C and 0.1103 W/mm°C at 100°C. The density is 7.14×10^{-6} kg/mm^3, and the specific heat is 388.9 J/kg°C. The fraction of dissipated electrical energy released as heat is specified by the joule heat fraction. We assume that all electrical energy is converted into thermal energy.

The analysis is done in two steps. In the first step heating of the conductor due to current flow is considered. Once steady-state conditions are reached, the current is switched off and the fuse is allowed to cooldown to the ambient temperature in a second step. During the first part of the analysis, the

coupled thermal-electrical equations are solved for both temperature and electrical potential at the nodes using the coupled thermal-electrical procedure. In the subsequent cooldown period, since there is no longer any electric current in the fuse, an uncoupled heat transfer analysis ("Uncoupled heat transfer analysis," Section 6.5.2 of the Abaqus Analysis User's Guide) is performed. The coupled thermal-electrical procedure definition is general enough to request either a steady state or a transient solution; input files illustrating both analysis types are provided. The transient analysis uses an automatic time incrementation scheme that is controlled by specifying the maximum temperature change allowed in an increment to 20°C. The transient analysis is set to terminate when steady-state conditions are reached. Steady state is defined here as the point at which the temperature rate change is less than 0.1°C/s. This condition is defined as part of the definition of the coupled thermal-electrical procedure. We specify a total analysis time of 100 s, with an initial time step size of 0.1 s.

The electrical loading is a steady 30 A current. This is applied as a concentrated current on each of the nodes on the bottom edge of the left-hand-side terminal. The total current and the total heat flux across a section defined through the fuse element are output. The electrical potential (degree of freedom 9) is constrained at the bottom edge of the right-hand-side blade by using a boundary condition ("Boundary conditions in Abaqus/Standard and Abaqus/Explicit," Section 34.3.1 of the Abaqus Analysis User's Guide). This option is also used to keep the bottom edges of the fuse blades at sink temperatures (degree of freedom 11) of 29.4°C and 30.2°C, respectively.

It is assumed that the exposed metal surfaces lose heat through convection to an ambient temperature of $\theta^0 = 23.3$°C. Heat loss from the thin edges is ignored. The film coefficient varies with temperature according to the empirical relation

$$h = h^0(\theta - \theta^0)^{1/4},$$

where θ is surface temperature (°C); $\boldsymbol{h}$ is the film coefficient (W/mm^2°C); and h^0 is a constant that depends on the surface geometry—$h^0 = 4.747 \times 10^{-6}$ W/mm^2 for the blade surfaces, and $h^0 = 5.756 \times 10^{-6}$ W/mm^2 for the fuse element surfaces. This dependence is entered as a table of film property values in the film coefficient definition (see "Thermal loads," Section 34.4.4 of the Abaqus Analysis User's Guide).

Results and discussion

Figure 7.2.1–2 shows a contour plot of the magnitude of the electrical current density vector at steady-state conditions. Since the dissipated electrical energy—and, hence, the thermal energy—is a function of current density, this figure represents contours of the heat generated. The figure indicates that most of the heat is generated near the inside curves of the S-shaped fuse element and near the center hole. The dissipated energy in the fuse blades is negligible compared to that in the fuse element.

Figure 7.2.1–3 shows a contour plot of the temperature distribution at the end of the first analysis step. The maximum temperature is reached near the center of the S-shaped fuse element. This area is expected to fail first when the operating current exceeds the design current. Figure 7.2.1–4 compares the temperatures at the measuring positions (defined in Figure 7.2.1–1) with the experimental measurements (Hilali, July 1995). While the results show some discrepancies between the experiment and analysis, it is clear that the analysis is sufficiently representative to provide a useful basis for studying such

systems. Figure 7.2.1–5 shows the variation of temperature at measuring position 6 during the heating and subsequent cooldown periods.

The results discussed above are for the coarse mesh model. The refined mesh models yield slightly different results from the coarse ones. The maximum difference in the magnitude of the electrical current density vector for the steady-state analysis is approximately 11.4%.

Acknowledgments

Mr. Hilali and Dr. Wang of Delphi Packard Electric Systems supplied the geometry of the fuse, the material properties, and the experimental results. Delphi Packard assumes no responsibility for the accuracy of the analysis method or data contained in the analysis.

Input files

thermelectautofuse_steadystate.inp	Steady-state analysis.
thermelectautofuse_transient.inp	Transient analysis.
thermelectautofuse_transient_po.inp	*POST OUTPUT analysis.
thermelectautofuse_node.inp	Nodal coordinates for the model.
thermelectautofuse_element.inp	Element definitions.
thermelectautofuse_controls.inp	Identical to thermelectautofuse_steadystate.inp, except that it uses the *CONTROLS option for control of convergence criteria.
teaf-steadystate-refined.inp	Refined mesh model for the steady-state analysis.
teaf-transient-refined.inp	Refined mesh model for the transient analysis.

References

- Hilali, S. Y., Private communication, July 1995.
- Hilali, S. Y., and B. -J. Wang, “ABAQUS Thermal Modeling for Electrical Assemblies,” 1995 ABAQUS Users’ Conference, Paris, May 1995, pp. 441–457.
- Wang, B. -J., and S. Y. Hilali, “Electrical-Thermal Modeling Using ABAQUS,” 1995 ABAQUS Users’ Conference, Paris, May 1995, pp. 771–785.

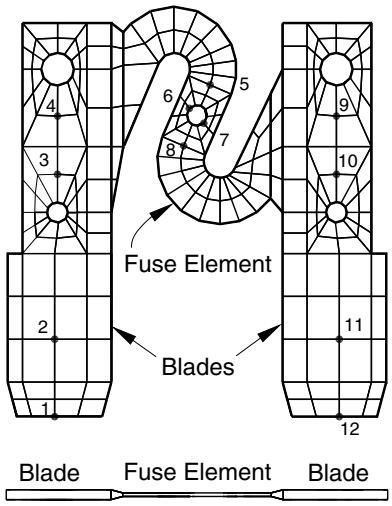

Figure 7.2.1–1 Geometry and finite element discretization.

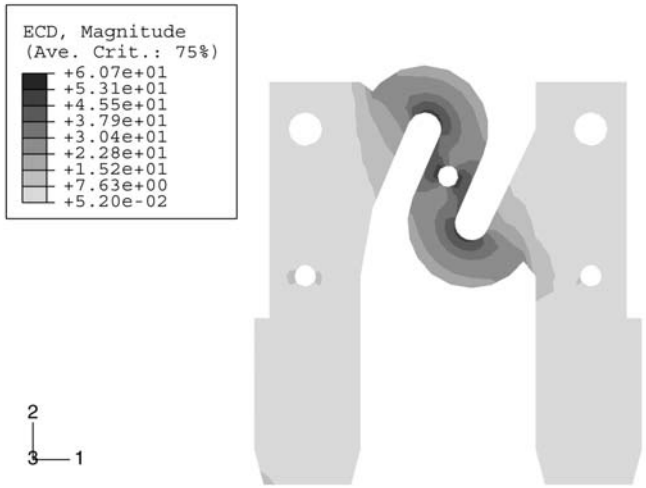

Figure 7.2.1–2 Contours of the magnitude of the current density vector (A/mm^2).

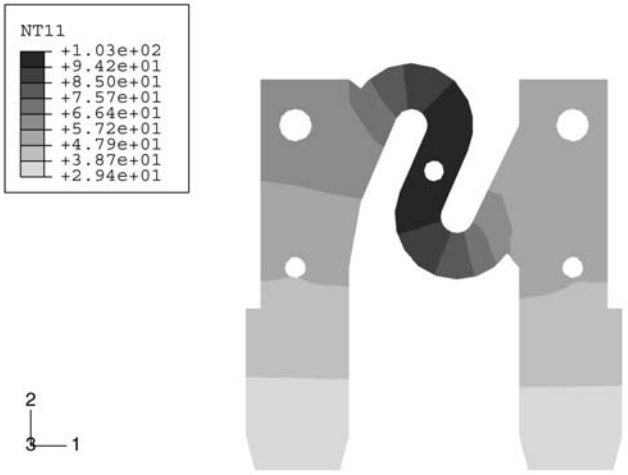

Figure 7.2.1–3 Contours of temperature field (°C).

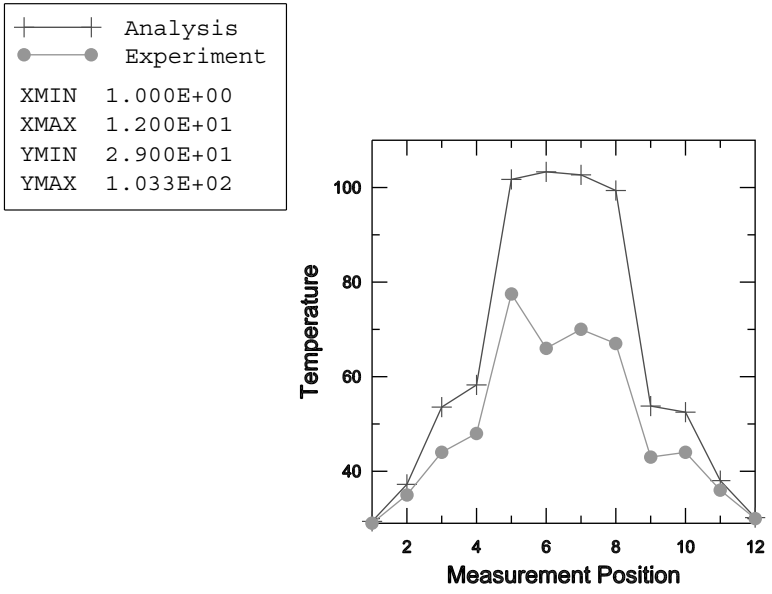

Figure 7.2.1–4 Temperature (°C) at measuring positions.

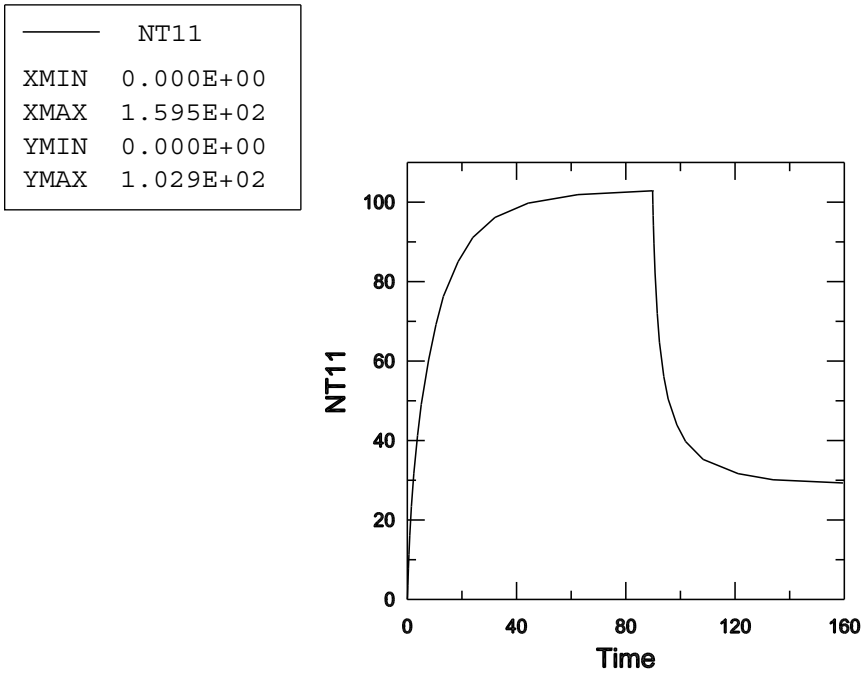

Figure 7.2.1–5 Variation of temperature (°C) at measuring position 6 with time (s).

8. Mass Diffusion Analyses

- “Mass diffusion analyses,” Section 8.1

8.1 Mass diffusion analyses

- “Hydrogen diffusion in a vessel wall section,” Section 8.1.1
- “Diffusion toward an elastic crack tip,” Section 8.1.2

8.1.1 HYDROGEN DIFFUSION IN A VESSEL WALL SECTION

Product: Abaqus/Standard

This example uses a one-dimensional problem to verify the mass diffusion capability in Abaqus.

The physical problem considered here is that of a pressure vessel shell wall fabricated from 2 1/4 Cr–1 Mo steel alloy base metal with an internal weld overlay of Type 347 stainless steel. These vessels are typically used at high temperatures and under high pressure conditions. Under such service conditions hydrogen dissolves into the alloys (Fujii et al., 1982) and during cooldown may cause disbonding of the weld overlay from the base metal and, possibly, crack initiation and growth in the base metal due to hydrogen embrittlement. In this example we are concerned with the hydrogen diffusion aspect of the problem.

Related topics

- "Mass diffusion analysis," Section 6.9.1 of the Abaqus Analysis User's Guide
- "Mass diffusion analysis," Section 2.13.1 of the Abaqus Theory Guide

Problem description

The problem is shown in Figure 8.1.1–1 and consists of a section of the vessel wall made up of a 200-mm thick base metal and a 5-mm thick weld metal. The problem is one-dimensional, the only gradient being through the thickness of the wall. The purpose of the analysis is to predict the evolution of hydrogen concentration through the wall thickness during cooling caused by a shutdown.

Geometry and model

Since the problem is one-dimensional, we use a plane mesh with only one element in the y-direction (see Figure 8.1.1–2). The mesh is graded, with more elements near the interface between the two materials because we expect very high concentration gradients in this vicinity.

The material properties of the two metals given by Fujii et al. (1982) are strongly dependent on temperature and can be written as follows.

Solubility in weld metal:

$$s_w = 1288\, e^{-1078/\tilde{\theta}} \quad \text{ppm mm N}^{-1/2}$$

Diffusivity in weld metal:

$$D_w = 9310\, e^{-6767/\tilde{\theta}} \quad \text{mm}^2/\text{h}$$

Solubility in base metal:

$$s_b = 4300\, e^{-3261/\tilde{\theta}} \quad \text{ppm mm N}^{-1/2}$$

Diffusivity in base metal:

$$D_b = \frac{274\, e^{-1157/\tilde{\theta}}}{1 + (1.05 \times 10^{-3}\, e^{3573/\tilde{\theta}})} \quad \mathrm{mm}^2/\mathrm{h},$$

where $\tilde{\theta}$ is temperature in kelvins. These temperature-dependent properties are entered in Abaqus in tabulated form, as shown in the input listings.

The wall is initially at a uniform temperature of 727.5 K (454.4°C), and during the shutdown schedule it cools down to 298.15 K (25.0°C) at a constant rate over a period of 21.5 hours.

The boundary conditions are as follows. Under the initial steady-state conditions the exterior of the weld metal has a hydrogen concentration of 35.85 ppm, which corresponds to a normalized concentration of 0.1225 $\mathrm{N}^{1/2}\mathrm{mm}^{-1}$. Normalized concentration is used as the primary solution variable (continuous over the discretized domain) and is given as the concentration divided by the solubility. The exterior of the base metal has a zero hydrogen concentration. As the cooling period begins, the hydrogen concentration at the exterior of the weld metal is assumed to drop to zero instantaneously.

Time stepping

The problem is run in two parts. The first part consists of a step in which a single increment of steady-state uncoupled mass diffusion analysis is performed with an arbitrary time step to establish the initial steady-state hydrogen concentration distribution corresponding to the initial temperature.

The hydrogen diffusion during cooling is then analyzed in four subsequent mass diffusion transient analysis steps, using automatic time stepping. This need not be done in four separate steps. We do it here because the results given by Fujii et al. (1982), with which we compare the Abaqus results, are presented at four specific times during the transient: 2.7 h (673.15 K, 400.0°C), 5.2 h (623.15 K, 350.0°C), 10.2 h (523.15 K, 250.0°C), and 21.5 h (298.15 K, 25.0°C).

The accuracy of the time integration for the mass diffusion transient analysis steps, during which cooling occurs, is controlled by the DCMAX parameter. This parameter specifies the allowable normalized concentration change per time step. Even in a linear problem such as this, DCMAX controls the accuracy of the solution because the time integration operator is not exact (the backward difference rule is used). In this case DCMAX is chosen as 0.01 $\mathrm{N}^{1/2}\mathrm{mm}^{-1}$, which is a very tight value. This is necessary to obtain an acceptably accurate integration of the concentration because the solubility of the materials decreases significantly (by more than two orders of magnitude in the base metal) as the temperature decreases and, therefore, the changes in concentration become larger for a given change in normalized concentration.

An important issue in transient diffusion problems is the choice of initial time step. As in any transient problem, the spatial element size and the time step are related to the extent that time steps smaller than a certain size may lead to spurious oscillations in the solution and, therefore, provide no useful information. This coupling of the spatial and temporal approximations is always most obvious at the start of diffusion problems, immediately after prescribed changes in the boundary values. For the mass diffusion case the suggested guideline for choosing the initial time increment (see "Mass diffusion analysis," Section 6.9.1 of the Abaqus Analysis User's Guide) is

$$\Delta t \geq \frac{1}{6D}(\Delta h)^2,$$

where Δh is a characteristic element size near the disturbance (that is, near the weld metal surface in our case), and D is the diffusivity of the material. For the weld metal in our model we choose a typical $\Delta h = 0.125$ mm and we have $D = 0.85$ mm^2/h at the initial temperature, which gives $\Delta t \geq 0.003$ h. For the base metal in our model we choose a typical $\Delta h = 1.25$ mm and we have $D = 4.88$ mm^2/h at the initial temperature, which gives $\Delta t \geq 0.053$ h. Based on these calculations an initial time step of 0.1 h is used, which gives an initial solution with no oscillations, as expected.

Results and discussion

Figure 8.1.1–3 shows hydrogen concentration distributions in the weld metal for the initial steady-state condition and four different times during the cooling period. Figure 8.1.1–4 shows corresponding hydrogen concentration distributions in the base metal. These results compare very well with those presented by Fujii et al. (1982) which are not plotted here since they would appear almost indistinguishable from the Abaqus results.

It can be observed that, although the primary solution variable (the normalized concentration) remains continuous across the material interface during the transient, the hydrogen concentration becomes increasingly discontinuous across the interface. During the cooling process the hydrogen concentration in the base metal decreases, whereas the hydrogen concentration in the weld metal increases very significantly, reaching a peak at the weld metal side of the interface.

Input files

hydrodiffvesselwall_2d.inp	Two-dimensional analysis.
hydrodiffvesselwall_3d.inp	Three-dimensional analysis.
hydrodiffvesselwall_3d_po.inp	*POST OUTPUT analysis of hydrodiffvesselwall_3d.inp.
hydrodiffvesselwall_fick.inp	Two-dimensional analysis using Fick's law.
hydrodiffvesselwall_nonlinear.inp	Nonlinear version (including concentration dependence on the material properties) of the two-dimensional analysis.
hydrodiffvesselwall_heat.inp	Heat transfer analysis that writes temperatures to a results file for use in hydrodiffvesselwall_massdiff.inp.
hydrodiffvesselwall_massdiff.inp	Two-dimensional mass diffusion analysis that reads temperatures from the results file written in hydrodiffvesselwall_heat.inp.

Reference

- Fujii, T., T. Nazama, H. Makajima, and R. Horita, "A Safety Analysis on Overlay Disbonding of Pressure Vessels for Hydrogen Service," Journal of the American Society for Metals, pp. 361–368, 1982.

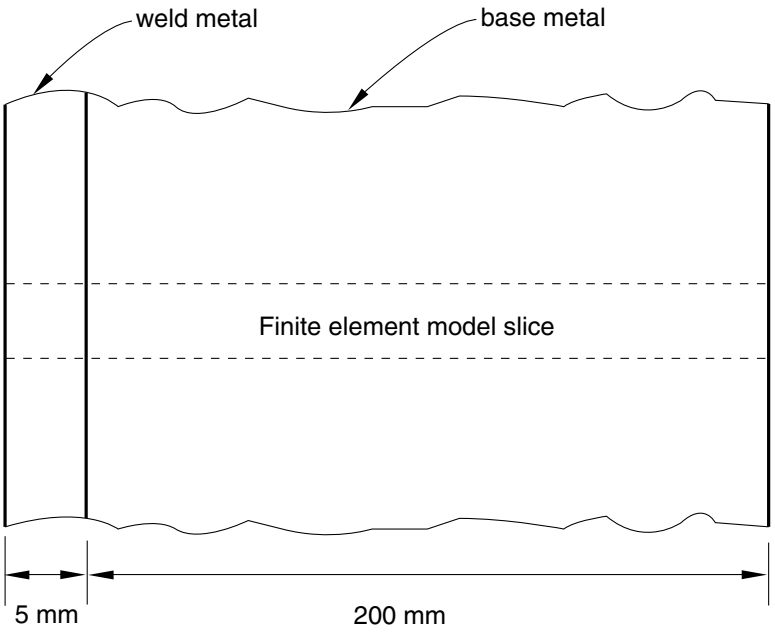

Figure 8.1.1–1 Pressure vessel shell wall section.

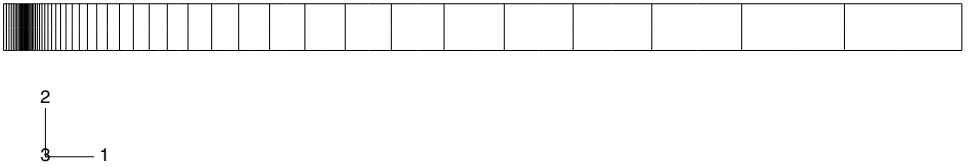

Figure 8.1.1–2 Finite element model of shell wall.

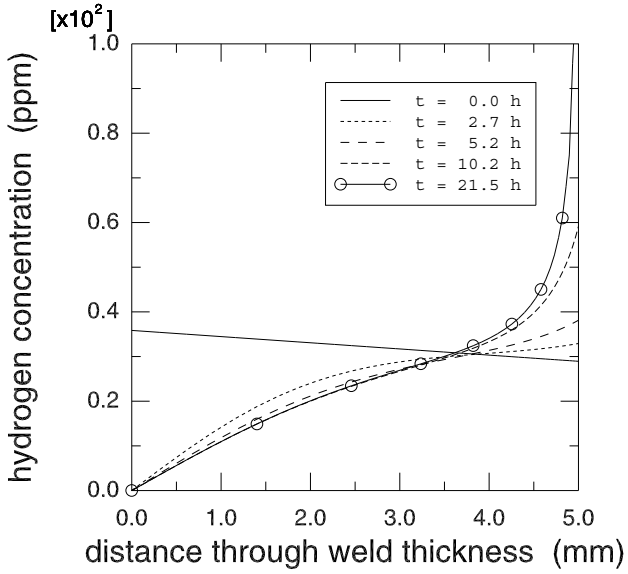

Figure 8.1.1–3 Hydrogen concentration distribution in weld metal.

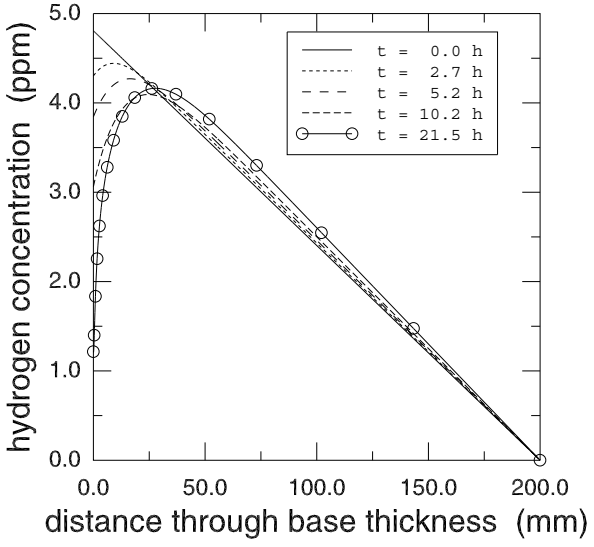

Figure 8.1.1–4 Hydrogen concentration distribution in base metal.

8.1.2 DIFFUSION TOWARD AN ELASTIC CRACK TIP

Product: Abaqus/Standard

This examples uses a two-dimensional problem to verify the sequentially coupled, stress-assisted mass diffusion capability in Abaqus.

A center-cracked plate fabricated from 2 1/4 Cr–1 Mo steel alloy is subjected to end loading in a hydrogen-rich environment. Hydrogen is drawn to the crack-tip region by high hydrostatic stresses and may assist in crack growth resulting from hydrogen embrittlement. In this example we are concerned with the hydrogen diffusion aspect of the problem.

Related topics

- "Mass diffusion analysis," Section 6.9.1 of the Abaqus Analysis User's Guide
- "Mass diffusion analysis," Section 2.13.1 of the Abaqus Theory Guide

Geometry and model

The problem geometry and boundary conditions are shown in Figure 8.1.2–1. The specimen is 10-mm thick, 20-mm wide, and 80-mm high, with a 4-mm crack at its center. The mesh near the crack is focused at the crack tip, with the element size growing as the square of the distance to the crack tip (with the first bounding node set representing the crack tip). A very fine mesh (see Figure 8.1.2–2) is used to capture accurately the gradients of concentration and stress near the crack tip. Four combinations of stress and mass diffusion analyses are presented:

- Stress analysis with quadratic elements and quarter-point spacing at the crack tip, followed by a mass diffusion analysis with linear elements.
- Stress analysis with quadratic elements and quarter-point spacing at the crack tip, followed by a mass diffusion analysis with quadratic elements and quarter-point spacing at the crack tip.
- Stress analysis with quadratic elements (no quarter-point spacing), followed by a mass diffusion analysis with quadratic elements (no quarter-point spacing).
- Stress analysis with linear elements, followed by a mass diffusion analysis with linear elements.

The quarter-point spacing technique is used in fracture mechanics analyses to enforce a $1/\sqrt{r}$ singularity at the crack tip, where r is the distance from the crack tip.

The sequentially coupled mass diffusion analysis consists of a static stress analysis, followed by a mass diffusion analysis. Equivalent pressure stresses from the static analysis are written to the results file as nodal averaged values. Subsequently, these pressures are read in during the course of the mass diffusion analysis to provide a driving force for mass diffusion.

The material properties for mass diffusion given by Fujii et al. (1982) are as follows.

Solubility:

$$s = 4300\, e^{-3261/(\theta-\theta^z)} \quad \text{ppm mm N}^{-1/2}$$

Diffusivity:

$$D = \frac{7611 \times 10^{-5}\, e^{-1157/(\theta-\theta^z)}}{1 + (1.05 \times 10^{-3}\, e^{3573/(\theta-\theta^z)})} \quad \text{mm}^2/\text{s},$$

where θ is the temperature in degrees Celsius and $\theta^z = -273$ is the absolute zero temperature.

Stress-assisted diffusion is specified by defining the pressure stress factor, κ_p, as

$$\kappa_p = \frac{\overline{V}_H \phi}{R(\theta - \theta^z)} \text{ mm N}^{-1/2},$$

where $R = 8.31432$ Jmol^{-1}K^{-1} is the universal gas constant, $\overline{V}_H = 2.0 \times 10^3$ mm^{3}mol^{-1} is the partial molar volume of hydrogen in iron-based metals, and ϕ is the normalized concentration. The concentration dependence of κ_p is entered in Abaqus in tabulated form as shown in the input listings. It is important to note that although κ_p is defined in terms of normalized concentration, ϕ, the tabular data must be entered in terms of concentration, $c = \phi s$.

The following properties are also used in the stress analysis: elastic modulus, $E = 2.0 \times 10^5$ Nmm^{-2}, and Poisson's ratio, $\nu = 0.3$.

The specimen is maintained at a constant temperature of $\theta - \theta^z = 325$ K throughout the analysis. Under the initial steady-state conditions the specimen has a uniform concentration of 50 ppm, which corresponds to a normalized concentration of 265 N$^{1/2}$mm^{-1}. Normalized concentration is used as the primary solution variable (continuous over the discretized domain) and is given as the concentration divided by the solubility. The exterior of the specimen has a constant hydrogen concentration equal to the initial concentration. A 1 MPa distributed pressure is applied to the ends of the specimen, ramped linearly over the length of the step, and the steady-state distribution of hydrogen is obtained.

Results and discussion

The analytical solution for normalized concentration, presented by Liu (1970), has the form

$$\phi = \phi_o \exp\left(-\frac{\overline{V}_H\, p}{R(\theta - \theta^z)}\right),$$

where ϕ_o is the normalized concentration obtained in the unstressed state and p is the equivalent pressure stress. This solution dictates that for a crack-tip problem, the concentration follows the singularity of the stresses.

Figure 8.1.2–3 and Figure 8.1.2–4 show the final distribution of equivalent pressure stress and concentration predicted by the Abaqus analysis in the region around the crack tip. The results shown represent the first case described above, using a quadratic, quarter-point mesh for stresses and a linear mesh for mass diffusion. The shapes of the contours show good agreement, since contours of constant pressure stress should be contours of constant concentration, as indicated by the analytical solution above.

Figure 8.1.2–5 and Figure 8.1.2–6 show the pressures (in MPa) and concentrations (in ppm) ahead of the crack tip for all four combinations of stress and mass diffusion analyses. Results are presented as functions of the ratio of the distance to the crack tip, r, over the crack length, a. For the region

immediately ahead of the crack, linear elastic fracture mechanics yields the analytical solution for equivalent pressure stress:

$$p = -\frac{\mathrm{K_I}\,(1+\nu)}{\sqrt{2\pi r}} - \frac{(1+\nu)\sigma}{3},$$

where $\mathrm{K_I} = \sigma\sqrt{\pi a}$ is the stress intensity factor for a Mode I crack of length a and σ is the externally applied distributed load.

As can be seen from the figures, the finite element results for all four combinations of element types are identical except at the first element, where the results are not expected to be valid. The results show good agreement with the analytically predicted solutions for both equivalent pressure stress and concentration as the distance to the crack tip, r, approaches zero. Farther from the crack tip, the deviation between the analytical solution and the finite element solution increases. This deviation is consistent with the fact that the linear elastic crack-tip solution is valid only as r approaches zero.

No mesh convergence studies were conducted with respect to the number of elements in the crack-tip region. For comparison with the solutions presented here, an analysis was conducted with equally spaced elements approaching the crack tip. The results (not shown here) indicate that biasing the elements toward the crack tip is necessary to capture the gradients of concentration and equivalent pressure stress adequately. In addition, the equivalent pressure stress results demonstrate that the effect of using quarter-point positioning of the nodes at the crack tip is insignificant in this problem as long as the mesh is refined sufficiently.

Differences between the finite element and analytically predicted concentrations are a direct result of the differences between the finite element and analytically predicted values of pressure stress. If the analytical values of equivalent pressure stress are used to drive the Abaqus concentration solution, the resulting curve is indistinguishable from the analytical concentration shown.

Input files

difftocrack_quarterpstress.inp	Quadratic stress analysis with quarter-point spacing at the crack tip. This analysis writes the results file used in difftocrack_linearmassdiff1.inp and difftocrack_quarterpmassdiff.inp.
difftocrack_linearmassdiff1.inp	Linear mass diffusion analysis that reads results file data from difftocrack_quarterpstress.inp.
difftocrack_stress.inp	Stress analysis with quadratic elements (no quarter-point spacing). This analysis writes the results file used in difftocrack_massdiff.inp.
difftocrack_massdiff.inp	Mass diffusion analysis with quadratic elements that reads equivalent pressure stresses from the results file written in difftocrack_stress.inp.
difftocrack_quarterpmassdiff.inp	Mass diffusion analysis with quadratic elements and quarter-point spacing. This analysis reads equivalent

	pressure stresses from the results file written in difftocrack_quarterpstress.inp.
difftocrack_linearstress.inp	Stress analysis with linear elements. This analysis writes the results file used in difftocrack_linearmassdiff2.inp.
difftocrack_linearmassdiff2.inp	Mass diffusion analysis with linear elements that reads equivalent pressure stresses from the results file written in difftocrack_linearstress.inp.
difftocrack_node.inp	Node data for all the analyses.
difftocrack_quad_elements.inp	Element data for the analyses using quadratic elements.
difftocrack_linear_elements.inp	Element data for the analyses using linear elements.

References

- Fujii, T., T. Hazama, H. Nakajima, and R. Horita, "A Safety Analysis on Overlay Disbonding of Pressure Vessels for Hydrogen Service," Journal of the American Society for Metals, pp. 361–368, 1982.
- Liu, H. W., "Stress-Corrosion Cracking and the Interaction Between Crack-Tip Stress Field and Solute Atoms," Transactions of the ASME: Journal of Basic Engineering, vol. 92, pp. 633–638, 1970.

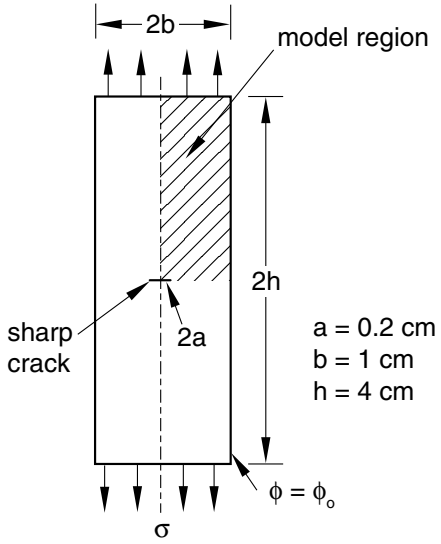

Figure 8.1.2–1 Center crack specimen geometry.

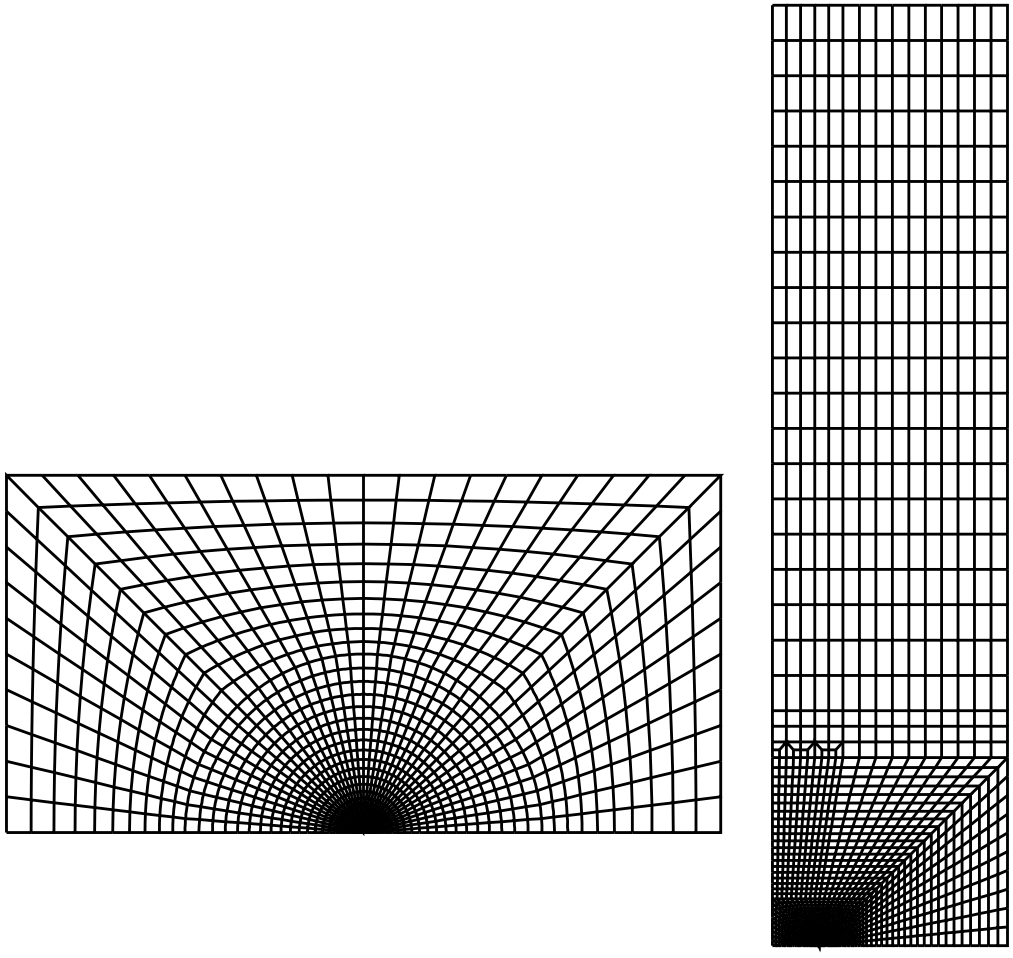

Figure 8.1.2–2 Finite element model of center crack specimen (with 1/4 symmetry) with detail of crack-tip mesh.

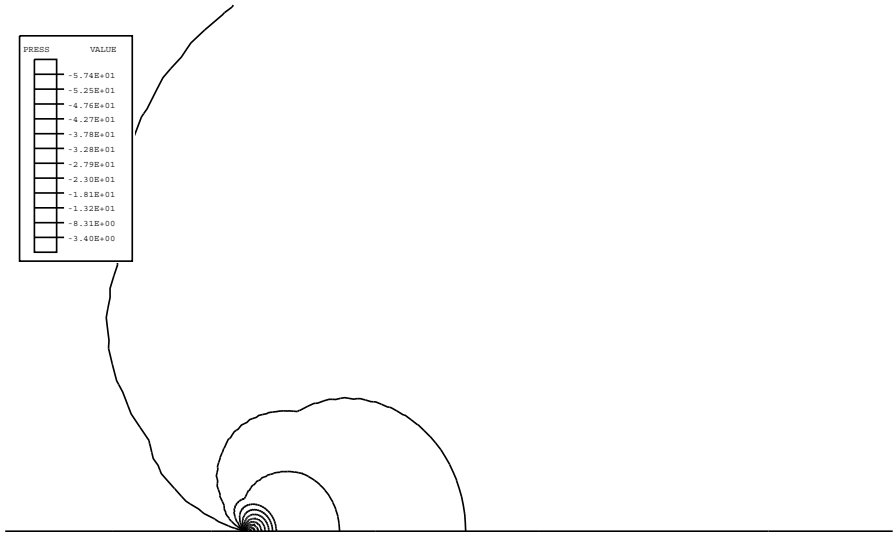

Figure 8.1.2–3 Contours of equivalent pressure stress at the crack tip.

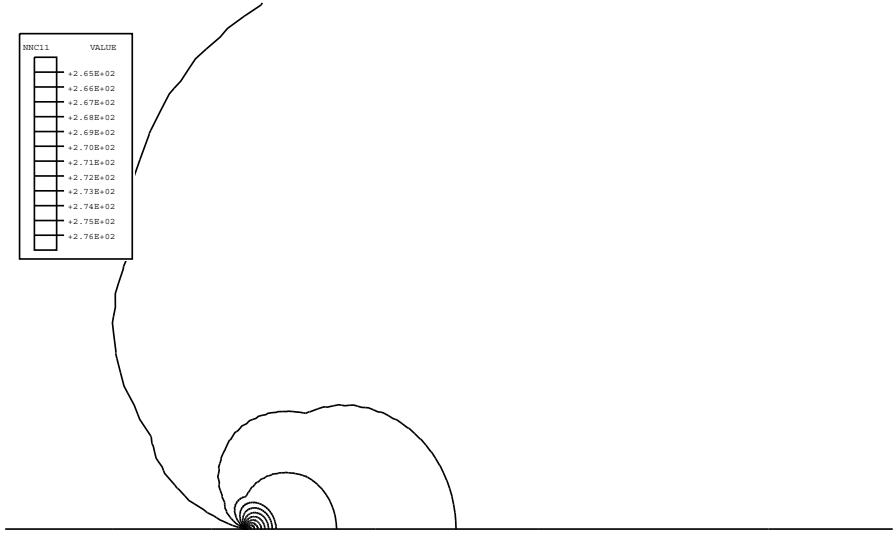

Figure 8.1.2–4 Contours of normalized hydrogen concentration at the crack tip.

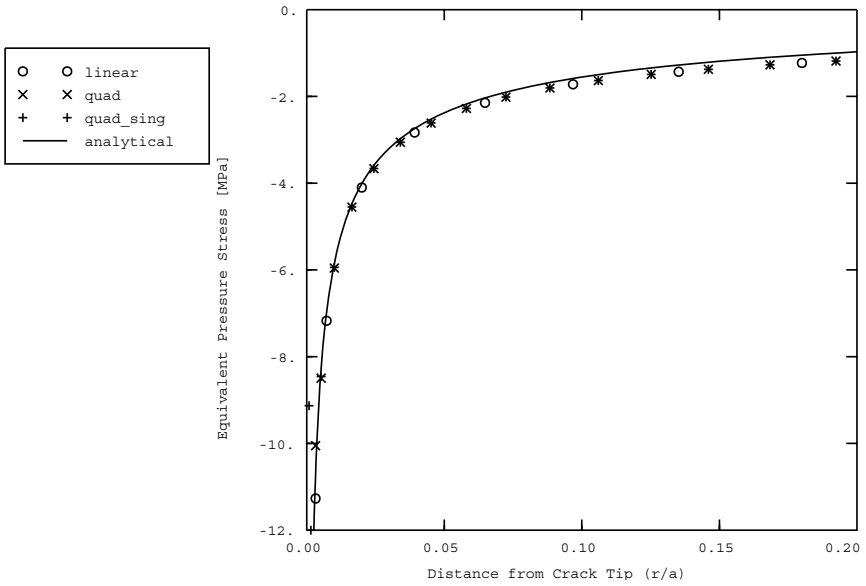

Figure 8.1.2–5 Distribution of pressure stress ahead of the crack tip.

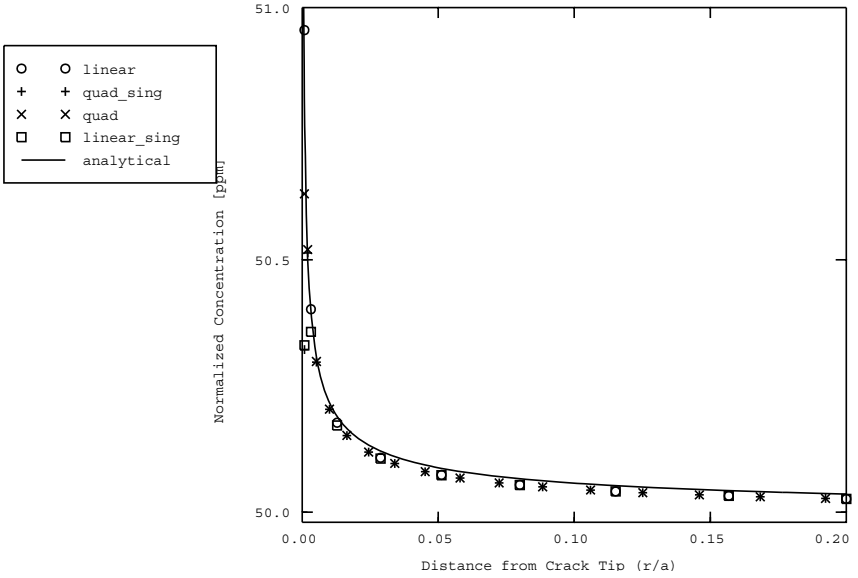

Figure 8.1.2–6 Hydrogen concentration distribution ahead of the crack tip.

9. Acoustic and Shock Analyses

- “Acoustic and shock analyses,” Section 9.1

9.1 Acoustic and shock analyses

- "Fully and sequentially coupled acoustic-structural analysis of a muffler," Section 9.1.1
- "Coupled acoustic-structural analysis of a speaker," Section 9.1.2
- "Analysis of a speaker using Abaqus-Dymola co-simulation," Section 9.1.3
- "Response of a submerged cylinder to an underwater explosion shock wave," Section 9.1.4
- "Convergence studies for shock analyses using shell elements," Section 9.1.5
- "UNDEX analysis of a detailed submarine model," Section 9.1.6
- "Coupled acoustic-structural analysis of a pick-up truck," Section 9.1.7
- "Long-duration response of a submerged cylinder to an underwater explosion," Section 9.1.8
- "Deformation of a sandwich plate under CONWEP blast loading," Section 9.1.9

9.1.1 FULLY AND SEQUENTIALLY COUPLED ACOUSTIC-STRUCTURAL ANALYSIS OF A MUFFLER

Products: Abaqus/Standard Abaqus/Explicit

This example demonstrates the solution of the acoustic field in the vicinity of a muffler in air caused by the vibrations of the muffler shell.

Steady-state and transient dynamic computations are done using both the fully coupled and sequentially coupled acoustic-solid interaction procedures in Abaqus. In the fully coupled case the solid medium of the muffler is directly coupled to the enclosed and surrounding air in a single analysis. In the sequentially coupled case the muffler vibrations are considered to be independent of the loading effects of the surrounding air, while the acoustic vibrations of the surrounding air are forced by the motion of the muffler. This allows the muffler vibration and acoustic radiation problems to be solved in sequence, using the submodeling procedure in Abaqus. The results for the sequentially coupled model are verified by comparing them to the results from the fully coupled procedure.

Related topics

- "Acoustic, shock, and coupled acoustic-structural analysis," Section 6.10.1 of the Abaqus Analysis User's Guide
- "Node-based submodeling," Section 10.2.2 of the Abaqus Analysis User's Guide

Full modeling vs. submodeling in Abaqus

The fully coupled model includes the effect of the acoustic pressure in the surrounding air loading the muffler body during vibration of the system. When modeling the acoustics of metal structures in air, such as in this case, such acoustic pressure loading is often negligible in comparison with other forces in the structure. The submodeling capability can be used in this situation. The part of the interacting system that is unaffected by the other is treated as the "global" model, while the part whose solution depends strongly on the solution of the other is treated as the "submodel." In the case of an acoustic analysis, of course, this nomenclature refers to the hierarchy of the solutions, not the geometric sizes of the models.

When sequential coupling is physically appropriate, its use offers a performance advantage over a fully coupled solution. Two problems, each smaller than the fully coupled problem, are less computationally expensive. If the applicability of the sequentially coupled solution method is uncertain, the user should make characteristic test computations in the frequency range of interest. If these computations show little difference between the fully and sequentially coupled solutions, the less expensive sequentially coupled method can be used.

Geometry and model

The system considered here consists of a cylindrical muffler and the interacting air. The muffler is a simple tube 180 mm in diameter and 1 m in length, with inlet and outlet pipes 70 mm in diameter and

100 mm in length. The muffler structure is made from stainless steel sheeting, 0.75 mm in thickness. A porous packing material, which dampens the acoustic field, surrounds the inner pipe.

Although this problem is in essence axisymmetric, a narrow three-dimensional wedge (subtending an angle of 10°) of the coupled system is modeled because Abaqus has a limitation on the use of submodeling with axisymmetric shells. Appropriate boundary conditions are applied to the three-dimensional model so that the axisymmetric solution is captured. The meshes of the surrounding air, the exterior muffler shell, and the air inside the muffler are shown in Figure 9.1.1–1, Figure 9.1.1–2, and Figure 9.1.1–3, respectively.

The air inside the muffler is meshed with AC3D10 elements (second-order tetrahedra) in Abaqus/Standard and with AC3D4 elements in Abaqus/Explicit. The innermost column of fluid elements models the undamped air. The adjacent annulus models the air in the region of the packing material. These two regions are highlighted in Figure 9.1.1–3, where the annulus is shown as the darker region. The effect of the packing material is modeled using the volumetric drag coefficient for the acoustic medium. The muffler is meshed with S4R shell elements.

The exterior fluid is shown in Figure 9.1.1–1. Its outer boundary is made up of spherical and cylindrical segments, on which spherical and cylindrical absorbing boundary conditions are imposed. The cylindrical and spherical absorbing boundary conditions can be combined in Abaqus, allowing the external mesh to conform to the geometry of the radiating object more closely. Combinations of different boundary condition types are most effective when the boundaries are continuous in slope as well as displacement. Second-order hexahedral acoustic elements (AC3D20) are used in Abaqus/Standard and reduced-integration acoustic brick elements (AC3D8R) are used in Abaqus/Explicit to fill in the volume of the exterior fluid region.

In Abaqus/Explicit the possibility of using acoustic infinite elements to model the effect of the exterior fluid is explored. The use of acoustic infinite elements removes the need of impedance-type absorbing boundary conditions on the outer boundary. Acoustic infinite elements are used in two different ways. In the first approach the mesh modeling the exterior fluid is replaced by a single row of AC3D8R elements, and acoustic infinite elements ACIN3D4 are defined on the outer boundary of this row. In the second approach ACIN3D4 elements are defined directly on the outer boundary of the muffler and tied to the muffler surface.

In the submodeling procedure performed in Abaqus/Standard the interface between the surrounding air and the muffler is meshed with 8-node acoustic interface elements (ASI8); in the Abaqus/Explicit submodeling analysis the tie constraint is used to define this coupling. The choice of mesh density (element size) is discussed in "Acoustic, shock, and coupled acoustic-structural analysis," Section 6.10.1 of the Abaqus Analysis User's Guide. In both cases the inner boundary of the exterior air mesh conforms to the muffler shell and to rigid baffles, which isolate the exterior field from the exhaust and inlet noise. These baffle pipes are the same diameter as the inlet and exhaust pipes but are modeled simply by imposing no boundary condition on the acoustic elements in this region. This is equivalent to imposing the condition that the acceleration on this boundary is zero, which is correct for a rigid baffle.

In Abaqus/Standard we are most interested in performing a frequency sweep about the first resonant frequency of the fully coupled system. For problems involving air and metal structures, the structure usually dominates the behavior of the system. Therefore, an estimate of the first important resonance of the coupled system is found by performing a frequency sweep in the vicinity of the first eigenfrequency

of the muffler shell, computed without any interaction with the interior or exterior air. This occurs at f = 172 Hz. Although the resonant frequencies of the fully coupled system do not coincide with the resonant frequencies of the muffler shell alone, they are close, especially at lower frequencies.

Using the Abaqus/Standard direct-solution steady-state dynamic procedure to search around 172 Hz, we find that the first resonant frequency for the fully coupled system occurs at approximately 180 Hz. A frequency sweep of both the fully coupled and the sequentially coupled models from 179.0 Hz to 181.0 Hz at 0.2 Hz increments is performed. A pressure wave of unit magnitude is applied to the muffler inlet at each frequency, and a plane wave absorbing boundary condition is applied at the muffler outlet.

A transient dynamic analysis is performed in Abaqus/Explicit over the period of time that corresponds to the first resonant frequency of 180 Hz found in Abaqus/Standard. The pressure boundary conditions applied at the muffler inlet have a sinusoidal variation over time to simulate the steady-state dynamic procedure performed in Abaqus/Standard. The absorbing boundary conditions are imposed in the same way as in the steady-state dynamic procedure.

The material properties for the air are a bulk modulus K_f of 0.142 MPa and a density ρ_f of 1.2 kg/m^3, yielding a characteristic sound speed of 344 m/s. The volumetric drag, γ, specified for the air in the packing material region is 1.2 N s/m. Volumetric drag values are considered "small" if they are small compared to $2\pi\rho_f f$, a condition satisfied by γ = 1.2 N s/m for the frequency range of interest. The muffler is made of stainless steel with Young's modulus E of 190 GPa, Poisson's ratio ν of 0.3, and density ρ_s of 7920 kg/m^3.

Material properties affect the mesh parameters appropriate for wave problems. The characteristic wavelength of air at $f = 180$ Hz, $\Omega = 2\pi \times 180 \approx 1131$ rad/sec, is $\lambda_a = \sqrt{\frac{K_f}{\rho_f f^2}} \approx 1.91$ m, which is long compared to the overall system geometry. The internodal spacing of roughly 40 mm used in the surrounding acoustic mesh and 30 mm in the interior acoustic mesh is adequate for this frequency. The acoustic wavelength must also be considered in selecting the overall size of the exterior domain. Accuracy of the solution requires placement of the radiating boundary at least one-quarter wavelength from the acoustic sources; in this problem a standoff distance of approximately 700 mm is selected. The characteristic flexural wavelength λ_p of the steel plating can be computed using the thickness h and the formula $\lambda_p = \frac{2\pi}{\sqrt{\Omega}}\left(\frac{Eh^2}{12\rho_s(1-\nu^2)}\right)^{1/4} \approx 203$ mm. The discretization requirements of the finite element method in wave problems require at least six nodes per wavelength; here, we use an internodal distance of approximately 30 mm for the shells.

The fully coupled model consists of all three meshes shown in Figure 9.1.1–1, Figure 9.1.1–2, and Figure 9.1.1–3, constrained at their abutting surfaces using a tie constraint.

The sequentially coupled analysis is performed in two jobs. The "global" model job consists of the meshes shown in Figure 9.1.1–2 and Figure 9.1.1–3. The shell displacements, and displacement phases in Abaqus/Standard, are saved from this analysis and drive the second "submodel" analysis through the use of a submodel boundary condition. In Abaqus/Standard the second model consists of the exterior air mesh (Figure 9.1.1–1) used in the fully coupled case, with ASI8 elements placed on the boundary that abuts the shell surface. These elements convert the displacements from the "global" analysis to the appropriate boundary conditions for acoustic elements. In this analysis the ASI8 elements conform to the acoustic submodel mesh but not to the shell mesh of the global model. The nodes of the ASI8 elements are placed in a node set, specified in the model data of the submodel. The global elements used to drive the submodel must be specified to ensure that only the displacements of the ASI8 elements are

driven by the shell elements. If this global element set is not specified, Abaqus may attempt to drive the acoustic pressure of the ASI8 elements by the interior acoustic elements, since those elements share the shell nodes in the "global" model. In Abaqus/Explicit the tie constraint is used in both the global and submodel analyses to couple the muffler structure with the surrounding acoustic medium.

Results and discussion

It is good practice to check the absorbing boundary conditions used on a particular mesh at a desired frequency by analyzing only the exterior fluid mesh with some test forcing on the boundary where acoustic excitations are expected. If the forcing is at a single point, the pressure phase angles should show a pattern of concentric circles, minimally distorted by the radiating boundary. While not a rigorous numerical test, such a result usually coincides with a properly offset radiating boundary. As shown in Figure 9.1.1–4, this criterion is met by the mesh used in this analysis.

Figure 9.1.1–5 is a plot of the radial displacement of the muffler inlet as a function of frequency for both the fully coupled and the global models. The resonant peak for the fully coupled model at 179.9 Hz is clearly illustrated. In contrast, the resonant peak for the "global" model (without the acoustic medium) occurs at approximately 180.0 Hz. The difference in the two peaks can be accounted for by the fact that the exterior air on the fully coupled model adds a small amount of damping due to radiation as well as mass to the system, which results in a lower natural frequency, as well as a slightly lower peak response. It is clear from Figure 9.1.1–5 that for the frequency range of interest the coupling between the exterior air and the muffler is most important at 179.9 Hz.

Figure 9.1.1–6 and Figure 9.1.1–7 contain contour plots of the pressure magnitude and phase for the muffler interior at 181.0 Hz for both the "global" model and the fully coupled model. In both cases the results indicate that the modeling assumptions of the sequentially coupled analysis appear to be valid for the solutions in the muffler interior.

Contour plots of the pressure magnitude and phase for the muffler exterior at 181.0 Hz are shown in Figure 9.1.1–8 and Figure 9.1.1–9. The resulting pressure magnitude in the exterior air is small in both cases. The differences in the pressure amplitudes and phase as computed by the two analyses are not considered to be significant. Two factors that account for the small differences are the different modeling methods (fully coupled vs. sequentially coupled) and the different techniques used to couple the muffler to the exterior air (tie constraints vs. acoustic interface elements).

Figure 9.1.1–10 and Figure 9.1.1–11 contain contour plots of the pressure magnitude and phase for the muffler interior at 179.9 Hz for both the "global" model and the fully coupled model. It is clear that at 181.0 Hz, the modeling assumptions of the sequentially coupled analysis are less valid than they are at 179.9 Hz for the solutions in the muffler interior. This result is anticipated by Figure 9.1.1–5. However, the solutions are still reasonably close to one another, indicating that the sequentially coupled analysis is still a reasonable approximation for this system even at a resonant peak.

Contour plots of the pressure magnitude and phase for the muffler exterior at 179.9 Hz are shown in Figure 9.1.1–12 and Figure 9.1.1–13. Again, the resulting pressure magnitude in the exterior air is small in both cases. The differences in the pressure amplitudes and phase as computed by the two analyses are less evident in the exterior than they were in the interior.

The pressure magnitudes along the muffler centerline at both 179.9 Hz and 181.0 Hz are shown in decibels in Figure 9.1.1–14. The reference pressure is chosen as one unit for convenience. The plot illustrates the variation of acoustic pressure in the muffler near resonance.

Table 9.1.1–1 shows comparative solution times and memory requirements for the fully and sequentially coupled analyses. The total computational time for the sequentially coupled case is lower, and the peak memory requirements are significantly lower. These differences will be greater for larger models. Optimal speed increases occur when global and submodels have nearly equal numbers of degrees of freedom. Here, solving the fully coupled system does not impose as much of a speed penalty as might be expected, because the sparse solver used by Abaqus exploits the extreme sparsity of the fluid-solid coupling term. When the number of system nodes involving fluid-solid coupling is a large percentage of the total number of nodes, the sparsity of the coupling term decreases, favoring the sequentially coupled procedure. Sequentially coupled analyses are even more advantageous than fully coupled analyses when many different submodels need to be analyzed, driven by a single set of global results.

Abaqus issues a series of warning messages in this example, because the narrow wedge domain results in some three-dimensional acoustic elements with bad aspect ratios. These messages can be ignored in this study, since the solutions are essentially axisymmetric and the gradient of the solution in the circumferential direction is nearly zero. Moreover, elements with scalar degrees of freedom, such as the acoustic elements used in this example, are much less sensitive to geometric distortion than elements with vector degrees of freedom, such as continuum stress/displacement elements.

The results obtained in Abaqus/Explicit agree well with the Abaqus/Standard results. For the fully coupled analysis the pressure variation in time at the muffler outlet centerline is shown in Figure 9.1.1–15 (for a clear comparison the Abaqus/Standard analysis is also performed as a transient simulation). The Abaqus/Explicit models using acoustic infinite elements give results that agree well with the results using the impedance-type absorbing boundary. In Figure 9.1.1–15 we include the results for the test using acoustic infinite elements, where the mesh modeling the exterior fluid is replaced by a single row of AC3D8R elements and acoustic infinite elements ACIN3D4 are defined on the outer boundary of this row. For the Abaqus/Explicit submodeling analysis the inside air pressure in the global model and the outside air pressure of the submodel compare well with the air pressures obtained in these regions in the fully coupled problem.

Input files

Abaqus/Standard input files

muffler_full.inp	Three-dimensional fully coupled model.
muffler_globl.inp	Muffler and internal air global model.
muffler_innerair_freq.inp	Internal air eigenanalysis model, Lanczos.
muffler_innerair_freq_ams.inp	Internal air eigenanalysis model, AMS.
muffler_submo.inp	Exterior air submodel.
muffler_shell_nodes.inp	Nodal coordinates for muffler shell mesh.
muffler_intair_nodes.inp	Nodal coordinates for interior air mesh.
muffler_extair_nodes.inp	Nodal coordinates for surrounding air mesh.

muffler_shell_elem.inp	Element definitions for muffler shell mesh.
muffler_intair_elem.inp	Element definitions for interior air mesh.
muffler_extair_elem.inp	Element definitions for surrounding air mesh.
muffler_freq.inp	Natural frequency extraction for shell mesh.
muffler_bctest.inp	Radiating boundary condition test.

Abaqus/Explicit input files

muffler_full_xpl.inp	Three-dimensional fully coupled transient analysis.
muffler_full_acoinfxpl.inp	Three-dimensional fully coupled transient analysis using acoustic infinite elements.
muffler_full_acoinftiexpl.inp	Three-dimensional fully coupled transient analysis using acoustic infinite elements tied to the muffler outer surface.
muffler_global_xpl.inp	Muffler and internal air global model, transient analysis.
muffler_submodel_xpl.inp	Muffler and exterior air submodel, transient analysis.
muffler_shell_nodes.inp	Nodal coordinates for muffler shell mesh.
muffler_shell_elem.inp	Element definitions for muffler shell mesh.
muffler_intair_nodes_xpl.inp	Nodal coordinates for interior air mesh.
muffler_intair_elem_xpl.inp	Element definitions for interior air mesh.
muffler_extair_nodes_xpl.inp	Nodal coordinates for surrounding air mesh.
muffler_extair_elem_xpl.inp	Element definitions for surrounding air mesh.
muffler_extair_elem_ainxpl.inp	Element definitions for surrounding air mesh for model using acoustic infinite elements.

Table 9.1.1–1 Comparison of relative CPU times (normalized with respect to the CPU time for the sequential analysis) and approximate problem size for the frequency sweep excluding preprocessing.

	Memory	DOF	Relative CPU Time
Global model	10 Mb	10030	0.325
Submodel	15 Mb	19030	0.675
Fully coupled model	29 Mb	29060	1.086
Sequential analysis			1.000

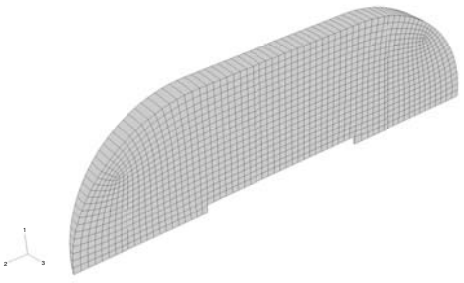

Figure 9.1.1–1 Mesh of surrounding air.

Figure 9.1.1–2 Mesh of muffler.

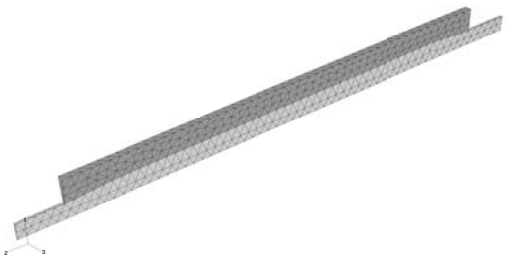

Figure 9.1.1–3 Mesh of interior air.

Figure 9.1.1–4 Radiating boundary condition test at 165 Hz.

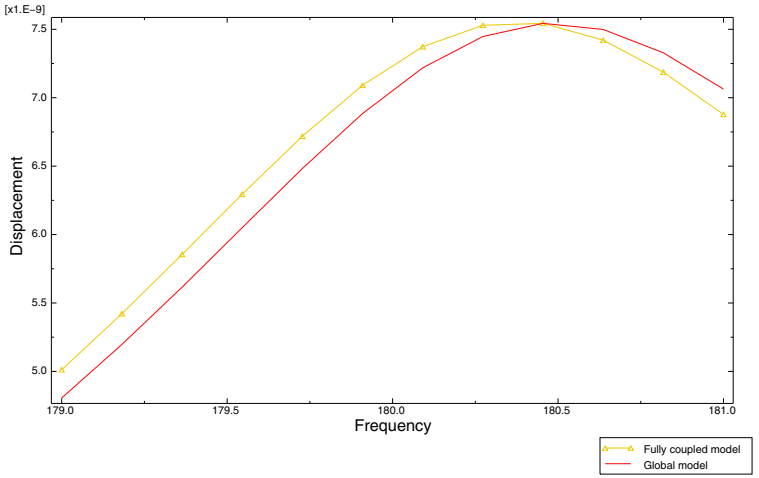

Figure 9.1.1–5 Radial displacement of the muffler inlet as a function of frequency.

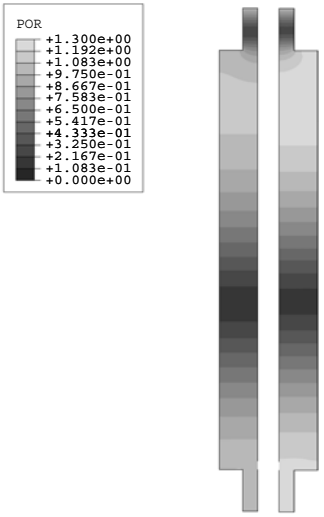

Figure 9.1.1–6 Muffler internal pressure magnitudes at 181.0 Hz, muffler inlet at top: fully coupled solution on left, "global" model (without the exterior acoustic medium) on right.

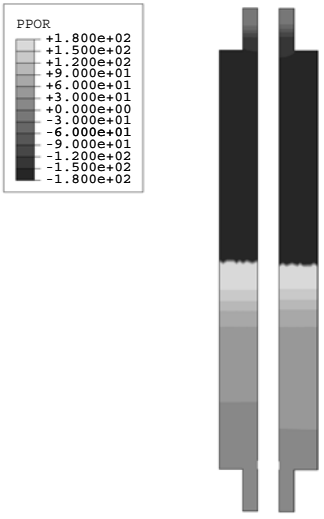

Figure 9.1.1–7 Muffler internal pressure phase at 181.0 Hz, muffler inlet at top: fully coupled solution on left, "global" model (without the exterior acoustic medium) on right.

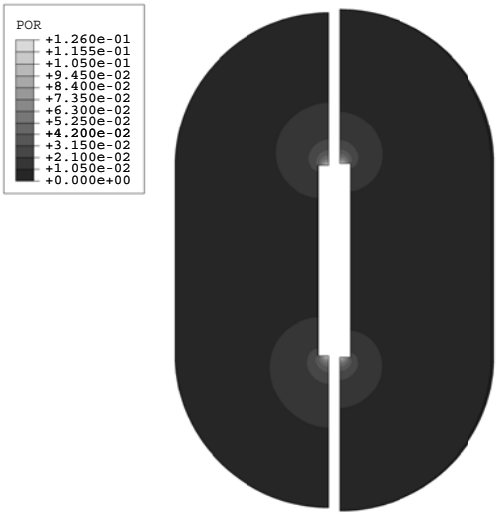

Figure 9.1.1–8 Muffler external pressure magnitudes at 181.0 Hz, muffler inlet at top: fully coupled solution on left, "submodel" on right.

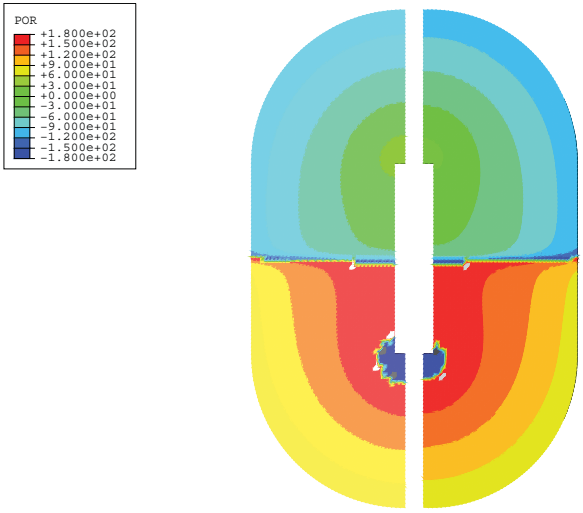

Figure 9.1.1–9 Muffler external pressure phase at 181.0 Hz, muffler inlet at top: fully coupled solution on left, "submodel" on right.

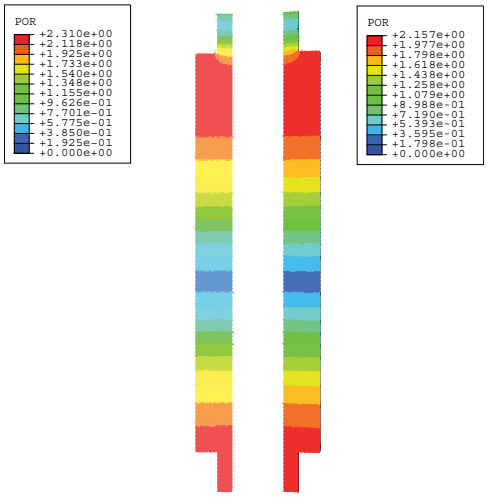

Figure 9.1.1–10 Muffler internal pressure magnitudes at 179.9 Hz, muffler inlet at top: fully coupled solution on left, "global" model (without the exterior acoustic medium) on right.

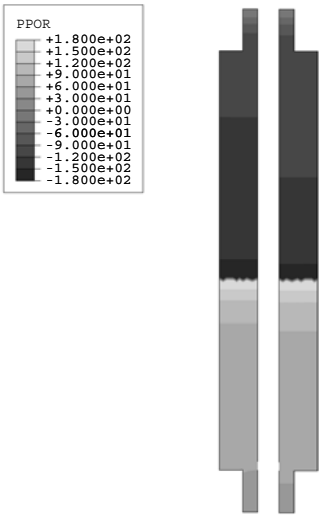

Figure 9.1.1–11 Muffler internal pressure phase at 179.9 Hz, muffler inlet at top: fully coupled solution on left, "global" model (without the exterior acoustic medium) on right.

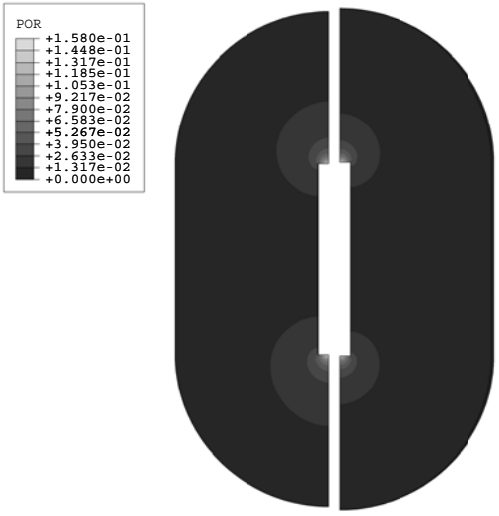

Figure 9.1.1–12 Muffler external pressure magnitudes at 179.9 Hz, muffler inlet at top: fully coupled solution on left, "submodel" on right.

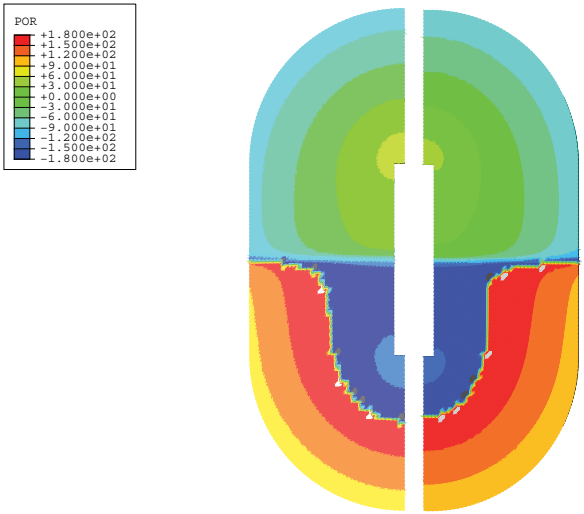

Figure 9.1.1–13 Muffler external pressure phase at 179.9 Hz, muffler inlet at top: fully coupled solution on left, "submodel" on right.

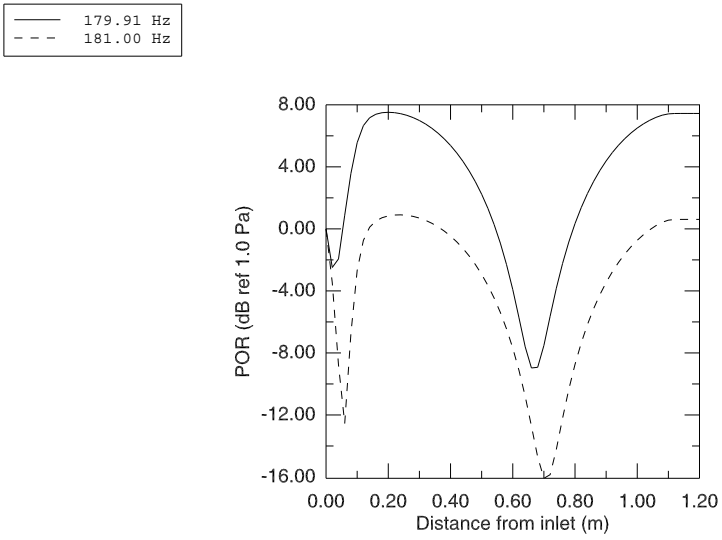

Figure 9.1.1–14 Muffler internal pressure magnitude at 179.9 and 181.0 Hz: dB along muffler centerline.

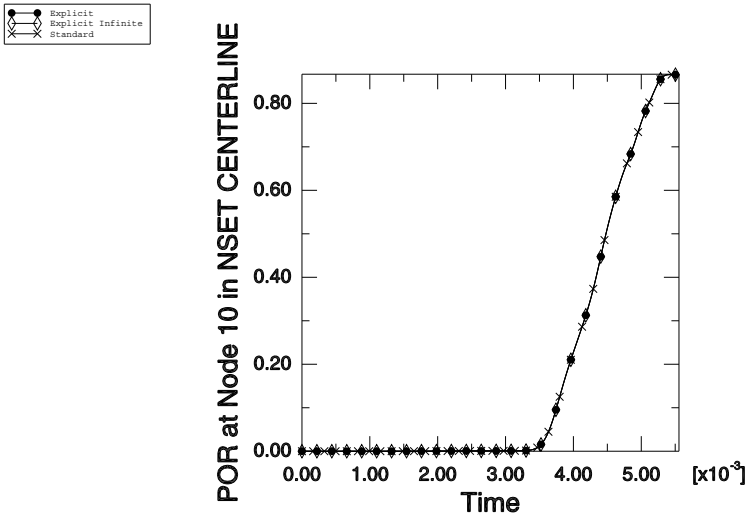

Figure 9.1.1–15 Internal pressure at the muffler outlet for the transient analysis.

9.1.2 COUPLED ACOUSTIC-STRUCTURAL ANALYSIS OF A SPEAKER

Product: Abaqus/Standard

This example illustrates the effect of coupling between a structure and an acoustic medium.

Coupling between a structure and an acoustic medium can produce problems when the solid-fluid interaction is fundamental to the overall vibrational behavior of the body or of the acoustic fluid. Typical examples of such problems include loudspeaker enclosures, fluid-filled tanks, muffler systems, and vehicle cabin enclosures.

Related topics

- "Coupled acoustic-structural medium analysis," Section 2.9.1 of the Abaqus Theory Guide

Geometry and model

The model is shown in Figure 9.1.2–1. The system considered here consists of a speaker box, a speaker cone, and the interacting interior. To simplify the problem, the effect of interacting air at the outside of the speaker box is neglected. The width, depth, and height of the speaker box are 0.5 m, 0.4 m, and 0.6 m, respectively. Its thickness is 0.005 m. The speaker box is made of wood with a Young's modulus, E, of 11.6 GPa; a Poisson's ratio, ν, of 0.3; and a density, ρ_s, of 562 kg/m^3. At the center of the front speaker box, there is a cone-shaped speaker 0.345 m in diameter, 0.04 m in height, and 0.001 m in thickness. No mass or impedance of the speaker is considered. The speaker is made of polyethylene with a Young's modulus, E, of 3.4 GPa; a Poisson's ratio, ν, of 0.3; and a density, ρ_s, of 450 kg/m^3. The air has a density, ρ_f, of 1.11 kg/m^3 and a bulk modulus, K_f, of 0.134 MPa. Volumetric drag of the air is assumed to have a negligible effect in this problem, so it is ignored in this analysis.

First-order hexahedral acoustic elements (AC3D8) and first-order acoustic triangular prism elements (AC3D6) are used to fill in the volume of the interior air region. The speaker box and speaker are meshed with S4R and S3R elements, respectively. No mesh convergence study has been done since the example is intended only as an illustration. The choice of mesh density (element size) is discussed in "Acoustic, shock, and coupled acoustic-structural analysis," Section 6.10.1 of the Abaqus Analysis User's Guide.

The surface-based tie constraint is used to couple the structure with the air inside. Surfaces are defined at the inside of the speaker box and the speaker cone and at the free surface of the air. To constrain the structure, four corner points of the bottom panel are simply supported.

A substructure analysis is performed as well. The entire speaker model is turned into a dynamic coupled structural-acoustic substructure using all the eigenmodes up to 800 Hz. A substructure load case is generated to be used in the forced response analyses.

Results and discussion

The results for each of the analyses are discussed below.

Natural frequency analyses

If the eigenvalues of the structure alone or the acoustic medium alone are not in the range of interest, it is not necessary to consider the whole system simultaneously. Thus, it is recommended that you understand the modal characteristics of each part separately before analyzing the whole system. The eigenfrequency extraction procedure takes acoustic-structural coupling effects into account by default if an acoustic medium and a structure are joined using a tie constraint. To ignore this effect, you can compute uncoupled mode sets for acoustic and structural/solid regions using the eigenfrequency extraction procedure or perform an eigenvalue extraction analysis that uses the SIM architecture.

In the SIM-based analysis, uncoupled modes are extracted and the structural-acoustic coupling is imposed in the subsequent modal steady-state dynamic procedure. To compensate for the approximation introduced by using uncoupled modes, the maximum frequency of interest for acoustic modes is increased by setting the acoustic range factor to a value greater than 1.0. In addition, residual modes are requested to reduce the modal truncation error. To request residual modes in the Lanczos eigensolver, you must first compute the static perturbation response of the load that will be applied in the subsequent mode-based analysis by specifying that load in a static perturbation step that immediately precedes the frequency extraction step. The residual modes are computed in both the coupled and uncoupled eigenvalue extraction analyses.

The results of the natural frequency analysis of the uncoupled system are summarized in Table 9.1.2–1. The natural frequencies for both the structure and the air span the same range in this example, which shows that the two parts can affect each other. Thus, the coupled approach should be adopted to understand the characteristics of the whole speaker system in this example.

Table 9.1.2–2 shows the results of the natural frequency analysis of the coupled system. Due to the coupling effect, the eigenfrequencies shift mode by mode. Each mode shape is also more complex than those in the uncoupled case, so that each mode has nonzero components on both the structural and acoustic parts. The substructure analysis based on coupled modes yields eigenfrequencies identical to those from the analysis without substructures.

Coupled forced response analyses

The response of the system is obtained by using mode-based and direct-solution steady-state dynamic analyses. The eigenvalue extraction analysis must be performed prior to the modal analysis. Two types of mode-based steady-state dynamic analyses are performed: an analysis that is based on coupled modes and a SIM-based analysis that utilizes uncoupled modes. The analyses are performed as frequency sweeps from 200 to 400 Hz. The system is excited by a concentrated force of 1.0 N at the center point of the speaker cone. The results for the coupled frequency response using each of the three methods are shown in Figure 9.1.2–2. This figure illustrates the acoustic pressure near the center point of the speaker cone, plotted as a function of frequency. The results for the mode-based steady-state dynamic analyses based on coupled and uncoupled modes show good agreement with the direct-solution steady-state dynamic results. Because the coupling between the structure of the speaker and the air inside is relatively strong, additional acoustic eigenmodes are extracted for the modal analysis based on uncoupled modes to improve accuracy. The substructure analysis produces results that are virtually identical to the results from the equivalent analysis without substructures.

Input files

speaker_direct.inp	Direct-solution steady-state dynamic analysis.
speaker_coupled.inp	Natural frequency extraction of coupled eigenmodes and mode-based steady-state dynamic analysis using coupled modes.
speaker_sim.inp	Natural frequency extraction of uncoupled eigenmodes and mode-based steady-state dynamic analysis using uncoupled modes.
speaker_gen.inp	Substructure generation for the coupled structural-acoustic model and steady-state dynamic solution without substructure.
speaker_use.inp	Direct-solution and mode-based steady-state dynamic analyses using the substructure.
speaker_ams.inp	Mode-based steady-state dynamic analysis using uncoupled eigenmodes extracted with the AMS eigensolver.
speaker_model.inp	Model definition.

Table 9.1.2–1 Uncoupled frequency analysis. Modes are arranged in order of increasing frequency starting from 201 Hz.

Mode	Frequency [Hz]	Description
1	201	Structure
2	211	Structure
3	212	Structure
4	232	Structure
5	247	Structure
6	263	Structure
7	283	Air
8	283	Structure
9	313	Structure
10	314	Structure
11	339	Air
12	352	Structure
13	361	Structure
14	382	Structure

Table 9.1.2–2 Coupled frequency analysis. Modes are arranged in order of increasing frequency starting from 204 Hz.

Mode	Frequency [Hz]	Description
1	204	Coupled mode
2	227	Coupled mode
3	228	Coupled mode
4	235	Coupled mode
5	245	Coupled mode
6	269	Coupled mode
7	292	Coupled mode
8	307	Coupled mode
9	322	Coupled mode
10	348	Coupled mode
11	352	Coupled mode
12	367	Coupled mode
13	370	Coupled mode
14	399	Coupled mode

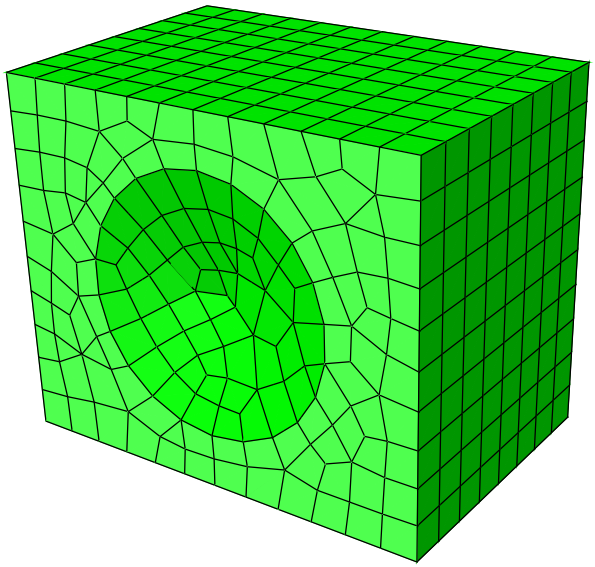

Figure 9.1.2–1 Three-dimensional model of speaker system.

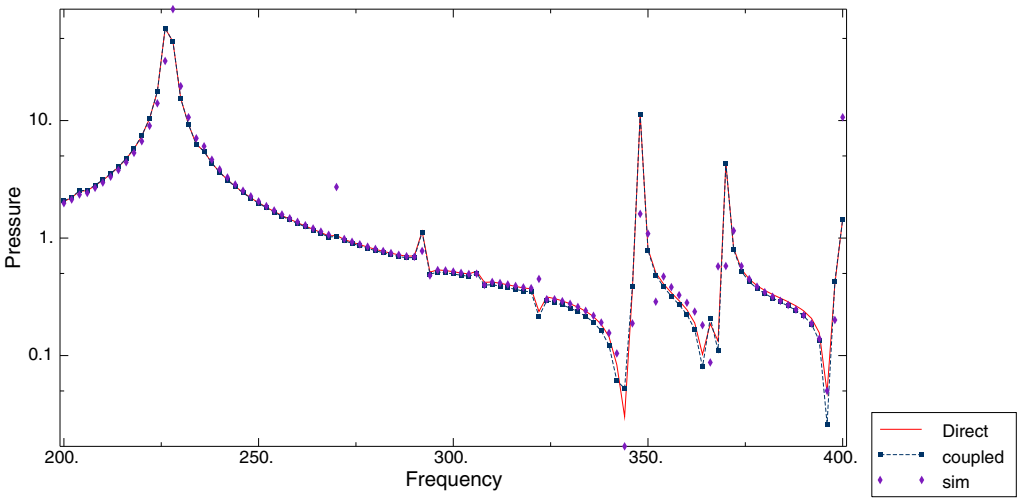

Figure 9.1.2–2 Acoustic pressure near the center of speaker cone.

9.1.3 ANALYSIS OF A SPEAKER USING Abaqus-Dymola CO-SIMULATION

Product: Abaqus/Explicit

Objectives

This example illustrates the use of the co-simulation technique to couple system-level logical models and functional-level models in Dymola with a physical model in Abaqus/Explicit.

Application description

Mobile devices like tablets and smart phones are increasingly becoming an important part of our lifestyle. One of the critical features that determines the overall quality of such a device is the audio quality of the speaker. The most commonly used speaker in mobile devices is based on the principle of moving coil transduction, as described by Jackman et al. (2009). An electromagnetic field applied on the voice coil generates a mechanical driving force (known as the Lorentz force) that generates the sound by imparting motion to the diaphragm. There are several key design challenges in the selection of the transducer and its placement. Some of the important issues to be addressed in the audio system design are discussed below.

Audio system design

The mobility and lightness of the device are major considerations, and space is at a premium. Providing many features in a mobile device requires numerous components, and packaging plays a critical role as these components compete for the limited available space. The smaller the audio speaker, the poorer its bass response. The enclosure behind the diaphragm in the speaker (referred to as the “back volume”) has a major influence on the speaker performance; it affects the audio quality by introducing cavity resonances at high frequencies and by reducing the compliance at low frequencies. In other words, the smaller the back volume, the lower the quality of the low frequency (bass) sound output. The designer must take measures to maximize the back volume, conforming to the packaging needs of the device in addition to providing an excellent bass audio quality.

The audio quality is reduced due to the inherent nonlinearities such as the total harmonic distortion. Even for microspeakers with very low diaphragm motions or excursions, the nonlinearities due to the mechanical resistance at the restraints (in addition to acoustic losses in ports) tend to be dominant. The nonlinearities are guided not so much by the displacement but by the velocity of the diaphragm excursion (Klippel and Knobloch, 2013). Hence, there is a need to model the nonlinearities that can be appropriately modeled in the time domain to reproduce the physically accurate solution. Simulating the audio response as a harmonic analysis in the frequency domain may provide inaccurate results, especially at higher levels of nonlinearity.

For transducer design it is important to have a flat frequency response while making sure that the sound output is as large as possible without distortions. The first resonant mode (along with the damping) sets the maximum for the sound output. The flat frequency response (at least in the mid-frequency range;

e.g., 1000–6000 Hz) is ensured by shifting the second resonance peak as far away as possible from the first resonance peak.

Interaction through the co-simulation technique

This example discusses a methodology that simulates the diaphragm excursion (and the subsequent acoustic response) due to electromagnetic excitation as a transient problem. The electromagnetic circuit of the speaker is assumed to have no direct contribution to the structural response of the system and, hence, is modeled independently as a reduced-order logical system in Dymola. The structural-acoustic response of the diaphragm in the speaker assembly is modeled with its full three-dimensional finite element representation in Abaqus/Explicit. The Abaqus model and the Dymola model interact with each other through the co-simulation technique in the time domain.

Abaqus model

The Abaqus model of the speaker is shown in Figure 9.1.3–1. Features such as very short edges or small faces, although important for machining and packaging of a component, have almost no bearing on the mechanics of the problem. Including such features in the numerical analysis could result in a very fine mesh density, leading to increased computation time. Such minor geometric details are excluded by combining the feature with an adjacent larger feature. Nodes and elements are created to conform to the original geometry. The diaphragm occupies the region in between the front volume and the speaker's back volumes, as shown in Figure 9.1.3–1. Symmetric notches and the racetrack-like separation between the center and the annulus region in the diaphragm (shown in Figure 9.1.3–2) are designed to achieve the flat frequency response and the first resonant peak, respectively. The other speaker components that hold the diaphragm in place are considered rigid and are not modeled. The radius of the hemispherical acoustic domain corresponds to one-third of the largest acoustic wavelength. Additional details on the modeling of the speaker are described in Jackman et al. (2009).

Dymola model

The electromagnetic component of the speaker, which functions primarily in the low frequency range, can be idealized with a lumped-parameter model in Dymola, as shown in Figure 9.1.3–3. The advantage of using a lumped-parameter model is twofold; it simplifies the modeling and improves the performance dramatically. The electromagnetic part of the model is assumed to have a linear response to the electromagnetic excitation; hence, it is modeled with a resistor and an inductor. The current sensor output from Dymola is used as an actuator in Abaqus, and the velocity output of the sensor from Abaqus is used as an actuator in calculating the back electromotive force (EMF) in the system-level functional model.

Abaqus modeling approaches and simulation techniques

Two cases are studied. The first case analyzes loading with a white noise signal to check the drop in the signal amplitude over the audible frequency range. The second case analyzes loading with a fixed frequency signal to check the fidelity of the response of the speaker.

Summary of analysis cases

Case 1 White noise analysis.

Case 2 Response fidelity analysis.

The sections that follow discuss the analysis considerations that are applicable for both cases.

Analysis techniques

Abaqus-Dymola co-simulation provides a convenient way to couple system-level logical and functional-level models in Dymola with a physical model in Abaqus. The Abaqus user subroutines **UAMP** and **VUAMP** can be used to design such system-level models interacting with physical models, but the user is required to manually code the user subroutine. Dymola provides a host of libraries that have components belonging to different engineering domains (such as fluid, thermal, and electromagnetic) as well as mathematical operators (such as controllers and Boolean operators) that can be easily dragged and dropped as icons into a user interface to build the system-level model. Co-simulation with Abaqus involves passing the state of the physical system in Abaqus as sensor data to Real Input interfaces in Dymola while reading the Real Output interfaces from Dymola into Abaqus as actuators. For more details about co-simulation, refer to "Structural-to-logical co-simulation," Section 17.4.1 of the Abaqus Analysis User's Guide.

Mesh design

The diaphragm is modeled with reduced-integration conventional shell elements (S3R and S4R), and its rim is meshed with first-order reduced-integration hexahedral continuum elements (C3D8R). Modeling the diaphragm with solid elements instead of shell elements allows the acoustic domain to be cut away more easily. The acoustic domain, both in the back volume and the volume exterior to the diaphragm, is modeled with three-dimensional continuum acoustic linear tetrahedral elements (AC3D4). The mesh of the acoustic domain is nonuniform, with the largest element size being less than one-eighth of the shortest acoustic wavelength.

Material model

The units used in the Abaqus model are mm-tonnes-sec, and SI units are used in Dymola. The diaphragm material in Abaqus is polyimide (Young's modulus=3677; density=1.4×10^{-9}; structural damping=1.5); the voice coil is made of steel (Young's modulus=110,000; Poisson's ratio=0.3; density=3.3×10^{-9}); while the air is modeled as the acoustic medium (bulk modulus= 0.142; density=1.2×10^{-12}). The electromagnetic circuit in Dymola has a resistor of 5 ohms, an inductor of 5×10^{-5} H, and a coupling factor of 3.14159 N/A.

Boundary conditions

Boundary conditions are not applied to the acoustic regions that are in contact with the surfaces of the speaker components to enforce the rigid assumption that an Abaqus acoustic domain without any

boundary condition is assumed to be a rigid termination. The surface impedance for the nonreflecting spherical boundary of the acoustic medium is defined as 550.

Constraints

The structural and acoustic media are coupled through tie constraints. The diaphragm's rim is rendered rigid with its reference point at the center of the rim.

Output requests

The component of the translational velocity of the reference node of the rigid rim of the diaphragm along the direction perpendicular to the hemispherical flat surface of the acoustic medium is declared as a sensor. This sensor output from the diaphragm is passed into Dymola as an input signal. The pressure at a certain location in the front volume acoustic medium is also stored as history output.

Run procedure

The Abaqus model can be run on any supported platform (Windows/Linux), whereas the Dymola portion of the co-simulation can be run only on Windows 64-bit platforms. For more details on how to submit an Abaqus-Dymola co-simulation job, please refer to"Structural-to-logical co-simulation," Section 17.4.1 of the Abaqus Analysis User's Guide.

Case 1: White noise analysis

This case analyzes loading with a white noise signal to check the drop in the signal amplitude over the audible frequency range.

Analysis techniques

A concentrated force with amplitude as white noise is applied on a rigidly fixed dummy node, and a sensor of this concentrated force at this node is passed from Abaqus into Dymola as an input value.

Loading

A white noise signal voltage of unit magnitude is applied through a sensor on a dummy node in Abaqus, as mentioned above.

Solution controls

This analysis is run for a duration of 0.03 s, thereby setting a threshold frequency of 33 Hz as the lower limit for the frequency range of the audio signal to obtain an accurate response from the speaker. The models's stable time increment of $\sim 10^{-8}$ determines the Nyquist frequency of 1×10^{6} Hz as the higher limit for the frequency range of the audio signal to obtain an accurate response.

Output requests

An additional sensor for a concentrated force on a dummy node along the direction of loading is defined for transferring the white noise to Dymola from Abaqus, as mentioned above.

Case 2: Response fidelity analysis

This case analyzes loading with a fixed frequency signal to check the fidelity of the response of the speaker.

Loading

A signal voltage of 2 mV with a frequency of 2000 Hz is applied. In Abaqus the reference node of the rigid rim of the diaphragm is actuated by the Lorentz force that was computed in Dymola.

Solution controls

This analysis with a signal frequency of 2000 Hz must be run for at least 0.005 s to obtain a steady response of the speaker for a few wavelengths of the signal.

Discussion of results and comparison of cases

For the white noise analysis, the Fast Fourier Transform (FFT) of the magnitude and the phase angle of the velocity of reference node on the diaphragm rim are plotted against the frequency in Figure 9.1.3–4 and Figure 9.1.3–5, respectively. The signal loss in the audible frequency range is minimal. The behavior is qualitatively similar to that obtained by Radcliffe and Gogate (1996).

For the response fidelity analysis, the acoustic signal is reciprocated in the diaphragm and in the air at almost 2000Hz, as shown in the velocity and pressure plots in Figure 9.1.3–6 and Figure 9.1.3–7, respectively.

This analysis of a speaker using the co-simulation technique between Abaqus and Dymola successfully demonstrates that the signal loss in the audible frequency range is negligible while maintaining the fidelity of original signal.

Files

Case 1: White noise analysis

speaker_white_noise.inp	Abaqus input file.
speaker_white_noise.mo	Dymola modelica file.
speaker_white_noise.sgn	File needed for co-simulation.
white_noise.inp	Include file containing white noise signal data.

Case 2: Response fidelity analysis

speaker_frequency.inp	Abaqus input file.
speaker_frequency.mo	Dymola modelica file.
speaker_frequency.sgn	File needed for co-simulation.

References

Abaqus Analysis User's Guide

- "Structural-to-logical co-simulation," Section 17.4.1 of the Abaqus Analysis User's Guide

Other

- Jackman, C., M. Zampino, D. Cadge, R. Dravida, V. Katiyar, and J. Lewis, "Estimating Acoustic Performance of a Cell Phone Speaker Using Abaqus," SIMULIA Customer Conference, 2009.
- Klippel, W., and D. Knobloch, "Nonlinear Losses in Electro-Acoustical Transducers," The Association of Loudspeaker Manufacturers & Acoustics International (ALMA), Winter Symposium, 2013.
- Radcliffe, C., and S. Gogate, "Velocity Feedback Compensation of Electromechanical Speakers for Acoustic Applications," International Federation of Automatic Control, Triennial World Congress, 1996.

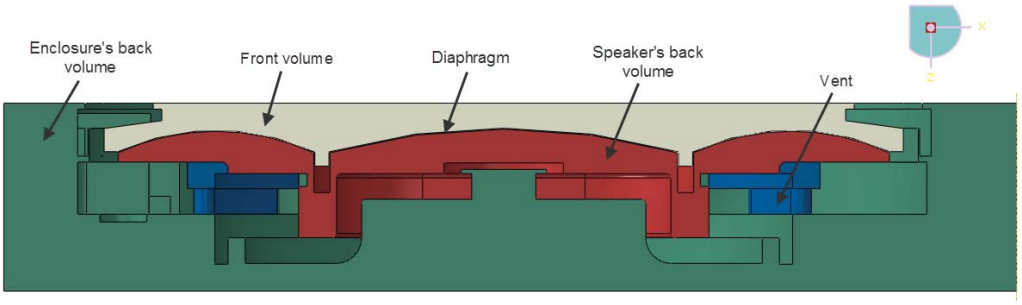

Figure 9.1.3–1 Abaqus model of the speaker.

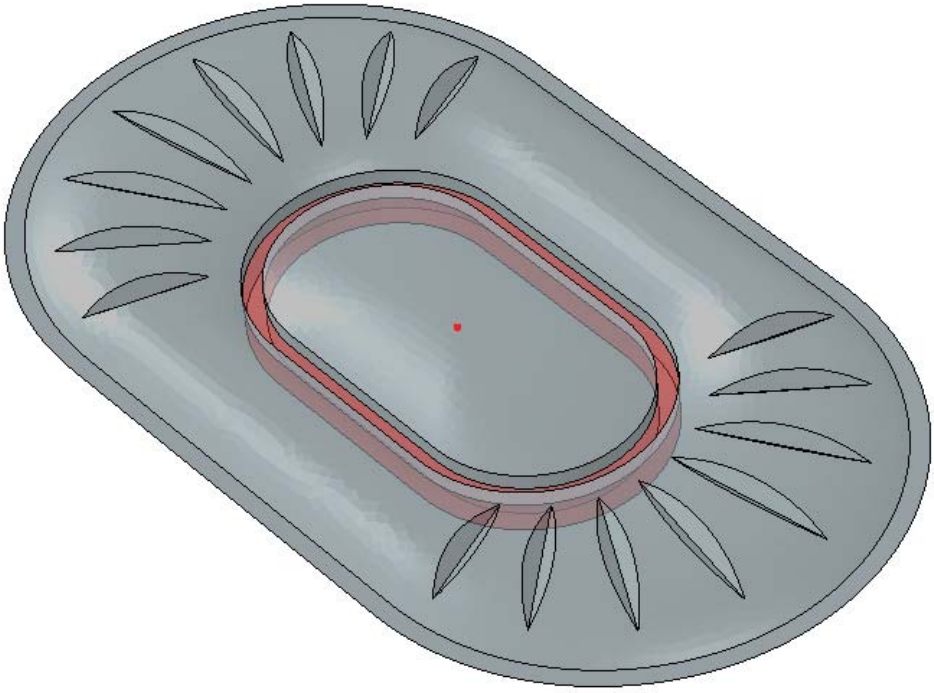

Figure 9.1.3–2 Diaphragm of the speaker in the Abaqus model. The highlighted red region is rendered rigid with its reference node at the center highlighted in red.

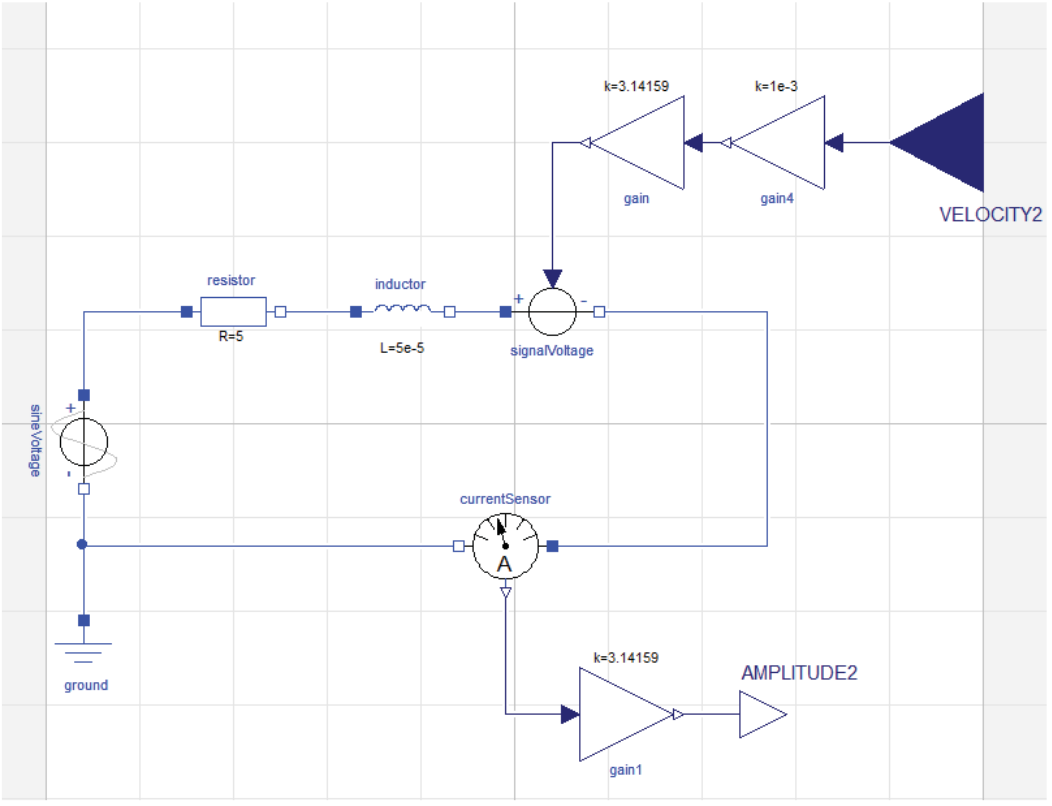

Figure 9.1.3–3 Dymola model showing the electromagnetic circuit of the speaker.

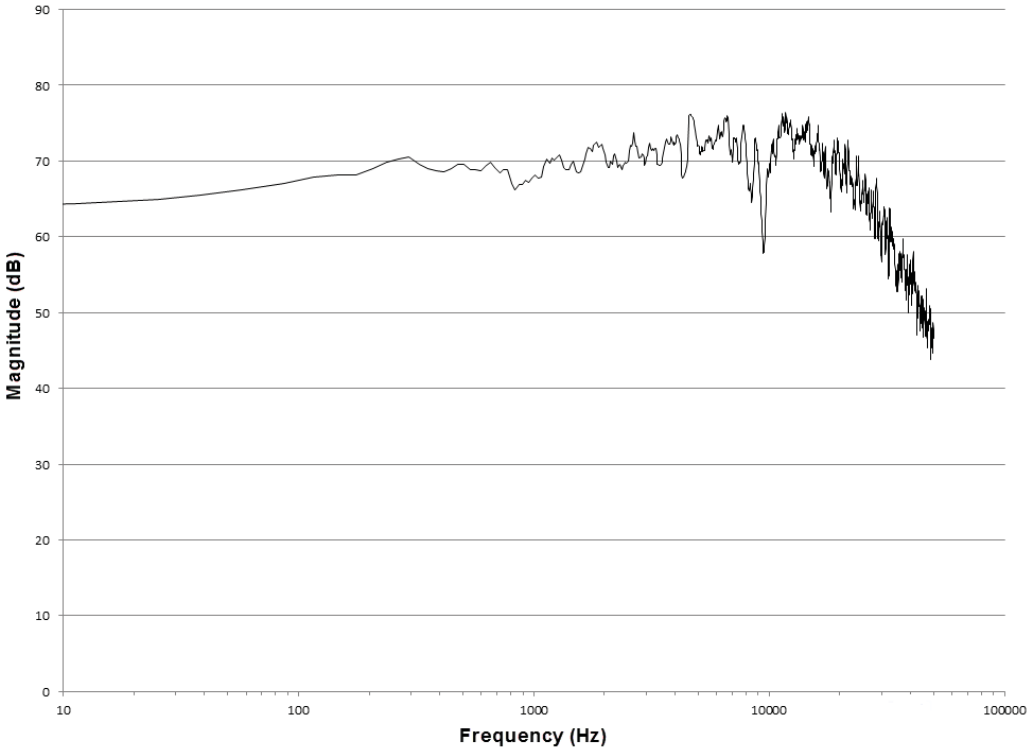

Figure 9.1.3–4 White noise analysis: magnitude of the velocity of the speaker in the frequency domain.

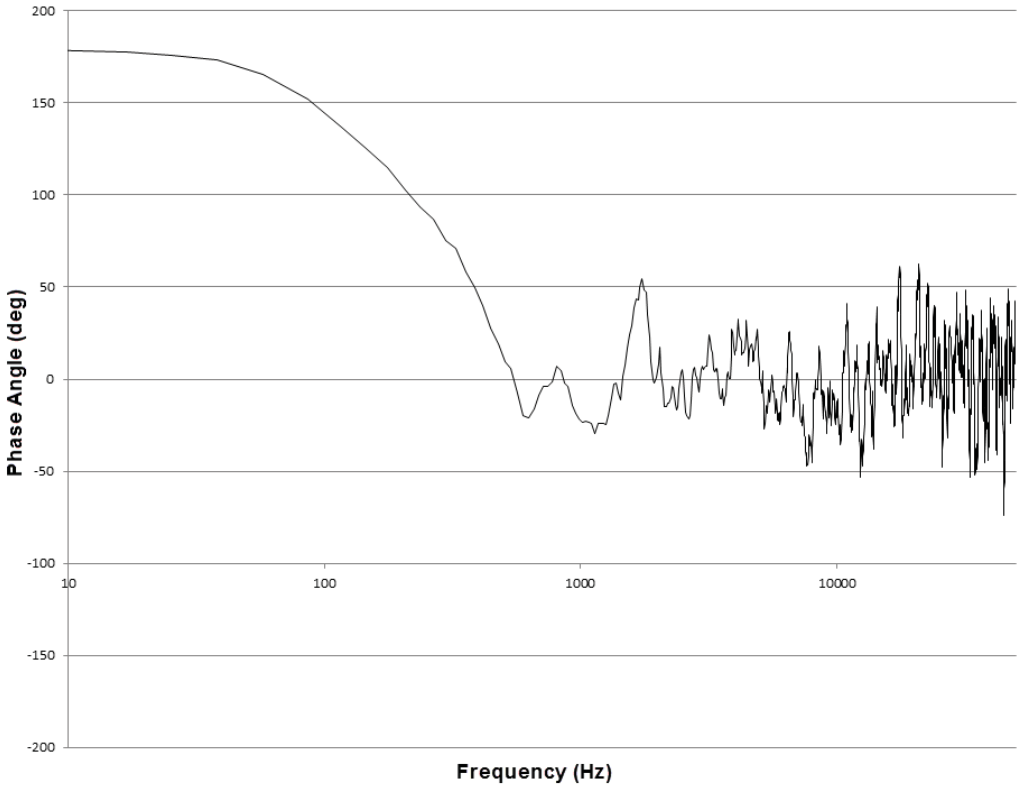

Figure 9.1.3–5 White noise analysis: phase angle of the velocity of the speaker in the frequency domain.

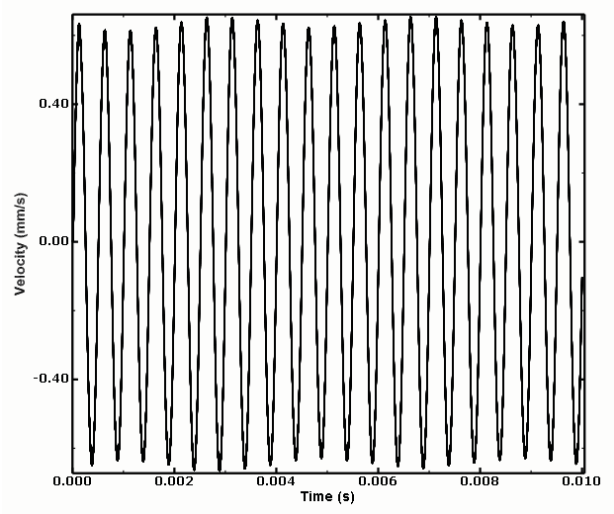

Figure 9.1.3–6 Response fidelity analysis: velocity of the reference node of the rigid part of the diaphragm.

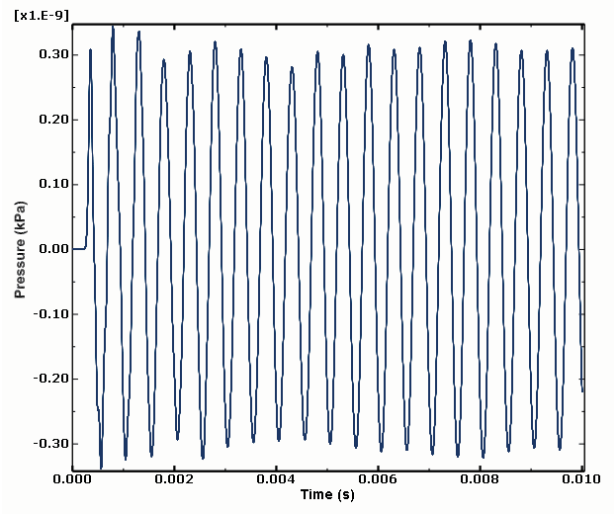

Figure 9.1.3–7 Response fidelity analysis: pressure at a point in air in front of the diaphragm.

9.1.4 RESPONSE OF A SUBMERGED CYLINDER TO AN UNDERWATER EXPLOSION SHOCK WAVE

Product: Abaqus/Explicit

This example demonstrates how Abaqus/Explicit can be used to predict the transient response of submerged structures that experience loading by an acoustic pressure shock wave resulting from an underwater explosion (UNDEX).

This class of problem is characterized by a strong coupling between the structural motions and acoustic pressures on the wetted interface between the external fluid and the structure. The structural response in a strongly coupled acoustic-structural system can be described as a combination of the following:

- Low-frequency response characterized by structural wavelengths that are significantly shorter than the associated acoustic wavelengths. The external fluid on the structure adds an effective mass to the structure on the wetted interface.
- High-frequency response characterized by structural wavelengths that are significantly longer than the associated acoustic wavelengths. The external fluid on the structure acts as a simple damping mechanism, where energy is transported away from the structure via acoustic radiation.
- Intermediate-frequency response characterized by structural wavelengths that are similar in length to the associated acoustic wavelengths. In this frequency regime the external fluid has both an added mass and a radiation damping influence on the structure.

The spherical pressure wave associated with an underwater explosion (UNDEX) shock loading is characterized by a very steep front where the maximum pressure is attained over an extremely short time duration (rise time). The pressure then drops off exponentially over a significantly longer period of time. Therefore, UNDEX shock loads can be expected to excite submerged structures over a large frequency range that will include low, high, and intermediate response frequencies. The boundaries of the external fluid must be located a sufficient distance from the structure to ensure proper low-frequency response, while the size of the acoustic elements must be small enough to accurately represent the propagation of high-frequency acoustic waves away from the submerged structure.

Problem and geometry description

This example problem is based upon an UNDEX experiment in which a submerged test cylinder is exposed to a pressure shock wave produced by a 60 lb HBX-1 explosive charge. Kwon and Fox originally described the experiment along with a set of selected experimental results. The objective of this class of analysis is to evaluate the behavior and integrity of a structure under UNDEX loading conditions.

The test cylinder is made of T6061-T6 aluminum. It has an overall length of 1.067, an outside diameter of 0.305, a wall thickness of 6.35 mm, and 24.5 mm thick welded endcaps. The cylinder is suspended horizontally in a 40 m deep fresh water test quarry. The 60 lb HBX-1 explosive charge and the cylinder are both placed at a depth of 3.66 m. The charge is centered off the side of the cylinder and located 7.62 m from the cylinder surface. The suspension depths, charge offset, and duration of the test are selected such that cavitation of the fluid is not significant and no bubble pulse occurs. Strain gauges

are placed at several locations on the outer surface of the test cylinder, as shown in Figure 9.1.4–1. The strain gauge experimental data are filtered at 2000 Hz. The experimental data presented here are obtained by digitizing the Kwon and Fox strain history curves.

When the acoustic fluid behavior is linear (i.e., no cavitation), the total acoustic pressure within the fluid consists of an incident wave and a scattered wave component. For this example the incident wave is the shock wave produced by the UNDEX charge. The scattered wave is the acoustic field generated by the interaction of the incident wave and the submerged structure. The nature of the incident wave can be determined from either empirical formulas or experimental data. Therefore, the spherical incident shock wave is applied as a transient load active on both the acoustic and structural meshes at their common surfaces (the wetted interface), and the external fluid pressure degrees of freedom represent only the unknown scattered component of the total acoustic pressure. The type of incident wave loading is either a scattered wave or a total wave formulation. The scattered wave formulation described above is the default condition for Abaqus/Explicit analyses. The total wave formulation is used for cases where nonlinear fluid response is expected or where the total acoustic pressure history is prescribed at an acoustic fluid boundary.

During the UNDEX test two pressure transducers are positioned 7.62 m from the charge, away from the cylinder but at the same depth as the cylinder. These transducers provide an experimental determination for the pressure vs. time history of the spherical incident shock wave as it travels by the point on the cylinder closest to the charge (strain gauge location B1). Figure 9.1.4–2 shows a time history curve of the incident pressure wave recorded by the transducers. The input file shock-pulse.inp contains this time history curve as an amplitude table used to define the incident wave loading.

Abaqus/Explicit model

Figure 9.1.4–3 shows the S4R finite element shell mesh used to represent the test cylinder. The mesh consists of 2402 nodes (14412 DOF) and 2400 elements with 40 circumferential divisions and 53 axial divisions. The element connectivity is such that each shell normal is directed into the external fluid. The nodes are positioned on the outside surface of the test cylinder. The S4R elements adjacent to the endcaps are dummy elements with reduced mass and stiffness used only to provide surfaces that correspond to the thickness of the endcaps. BEAM type MPCs are used to tie the endcaps to the main cylinder body. The local coordinate system is used to define the shell element material axes for postprocessing, such that the local 1-direction is aligned with the cylinder's axis for the main body and is radially directed for the endcaps. The local 2-direction is in the circumferential (hoop) direction for both the cylinder main body and the endcaps.

The external fluid is meshed with 4-node AC3D4 acoustic tetrahedral elements. The outer boundary of the external fluid is represented by a cylindrical surface with spherical ends. The characteristic radius of the outer boundary is 0.915 m. The outer boundary must be placed a sufficient distance from the cylinder so that the added mass associated with the low-frequency beam bending modes of the cylinder is represented adequately. The beam bending modes correspond to an $N = 1$ sinusoidal translation of the cylinder's cross-section through the fluid. For evaluating added mass effects when using a simple plane wave radiation impedance boundary for the external fluid, the outer boundary of the fluid can be considered rigid (nonradiating). Therefore, an analytical solution for the added mass associated with the translation of an infinite cylinder of radius R_i located within a fluid-filled infinite cylinder of radius

R_0 can be used to determine an appropriate characteristic radius for the external fluid. Results for the analytical solution presented by Blevins are listed in Table 9.1.4–1. The characteristic radius is based upon an outer boundary (R_0) to cylinder radius (R_i) ratio of 6.0, which corresponds to an added mass error of about 6% for infinite cylinders. When using enhanced surface impedance models, the outer fluid boundary location can be placed at about half of the distance required when using the plane wave radiation impedance model. However, for this example the R_0/R_i ratio was maintained at 6.0 even when using the source-based surface impedance models for the external fluid. Comparable results for the structural response can be obtained when the source-based boundaries were located half as far from the structure. For the low-frequency beam bending modes, system losses (damping) caused by hydrodynamic drag and/or fluid viscosity are not accounted for by acoustic radiation. Therefore, mass-proportional damping applied to the test cylinder mesh is used to approximate these types of losses.

Figure 9.1.4–4 shows the combined external fluid and test cylinder meshes. One quarter of the fluid mesh is omitted from this figure to allow an inspection of the acoustic element mesh inside the external fluid domain. The mesh is generated with Abaqus/CAE. The nodal seeding on the fluid outer boundary is set at 0.10 m, corresponding to 9.7 element divisions per acoustic wavelength at a response frequency of 1500 Hz. The nodal seeding on the fluid wetted interface with the test cylinder is set at 0.04 m, corresponding to 24.4 element divisions per acoustic wavelength at 1500 Hz. The radiation boundary condition is applied on the fluid outer-boundary surfaces.

Fluid-structure coupling and shock wave loading

The acoustic structural coupling between the fluid mesh acoustic pressures and the test cylinder structural displacements at their common surfaces (the wetted interface) is accomplished with a surface-based tie constraint. Figure 9.1.4–5 shows the surface mesh at the acoustic-structure wetted interface associated with the external fluid (Figure 9.1.4–3 shows the test cylinder surface). Since the acoustic mesh is coarser than the structural mesh, the surface of the external fluid at the wetted interface is designated as the master surface. This pairing creates an internal coupling of the acoustic pressure and structural displacements at the test cylinder (slave) surface nodes and ties the cylinder's acoustic pressures to the fluid mesh acoustic pressures at the wetted interface.

Figure 9.1.4–5 also illustrates the concept of a source point and a standoff point as they relate to an incident acoustic wave loading. For this example the source point represents the actual physical location of the explosive charge relative to the structure. The standoff point represents the location of the incident wave (shock front) at the start of the analysis (total time = 0.0) and is the point at which the pressure history of the incident wave is provided. For solution efficiency the standoff point should be placed at the location on the fluid-structure interface that is closest to the source point. The standoff point can be placed away from the structure closer to the source point, but this will only delay the onset of the transient response. Under no circumstances should the standoff point be located within or behind the structure being analyzed.

The incident wave can either be planar or spherical and requires the location of the standoff point and the source point. For a spherical shock wave, as in this example, the relative positions of the standoff point and source point determine how the wave's pressure will decay with distance from the source point. For a planar wave, which does not decay, the relative positions of the standoff point and source point are used to define the direction of incident wave travel. The fluid properties associated with the incident wave

includes wave speed. Defining the incident wave properties independent of the acoustic mesh allows incident wave loading to be used in the analysis of weakly coupled or uncoupled acoustic-structural systems (i.e., air blast analyses). For these cases the incident wave loading can be applied to a structure when no acoustic medium is directly modeled.

The pressure history at the standoff point is used to drive the incident wave. The amplitude definition specifies the surface name to which the incident wave loading is applied and a reference magnitude for the pressure curve. For acoustic-structural systems where the fluid and structure are both modeled and coupled, the incident wave loading must be defined to act upon both the fluid and structural surfaces at the wetted interface. Acoustic volumetric acceleration loads corresponding to the incident wave are then applied to the fluid surface, while the incident wave pressures are applied to the structural surface.

Results and discussion

The Abaqus/Explicit model for this UNDEX example has a total of 23337 active degrees of freedom and requires approximately 160 MB of memory. The transient analysis is run for 0.008 seconds with a 1.69×10^{-6} critical time increment (~4733 solution increments). Figure 9.1.4–6 shows the time history of axial displacement (U3) for the center nodes of the endcaps. These curves clearly show the periodic response associated with a dominant axially directed mode of the cylinder–endcap structure. Figure 9.1.4–7 shows the 1-direction translation (U1) of the endcap center nodes. The 1-direction is also the primary direction of shock wave propagation. The response curves clearly illustrate that there is a rigid body translation of the cylinder, and the oscillations are representative of the fundamental beam bending mode of the cylinder. Figure 9.1.4–8 shows the time history of vertical (U2) displacement for nodes located at the top and bottom midplane of the test cylinder. These curves suggest that a dominant N=2 ovalization mode of vibration occurs at about 170 Hz (based on an estimated period of 0.0059 seconds). The frequency for the first ovalization mode of the test cylinder in a vacuum is 330 Hz, based upon an Abaqus/Standard eigenvalue extraction analysis. This shift in the N=2 response mode frequency illustrates the added mass effect of the external fluid on the response of the submerged cylinder.

Figure 9.1.4–9 through Figure 9.1.4–11 contain time history plots of the test cylinder strains obtained from the Abaqus/Explicit analysis with experimental data for locations B1, C1, and A2. The experimental curves are obtained by digitizing the response plots published by Kwon and Fox. The digitized curves are shifted to the left by 0.0002 seconds on the time axis to account for an apparent time differential between the experiment and the Abaqus/Explicit solution. Figure 9.1.4–9 contains history plots of the axially directed strains at location B1. The analytical-experimental correlation at an early time (peak strain prediction) is very good, as is the prediction for the dominant response frequency of the test cylinder. The predicted strain oscillations at longer times suggest that the modeling of hydrodynamic drag damping and viscous losses by applying mass damping to the cylinder mesh could be improved. Figure 9.1.4–10 contains the history plots for the axially directed strains at location C1. The initial peak response (high frequency) contained in the Abaqus/Explicit solution is not present in the experimental data. This may be due to the sampling rate and filtering techniques used to obtain the data or to high strain gradients being averaged over the effective length of the strain gauge. Otherwise, the Abaqus/Explicit solution closely tracks the experimental data and provides a conservative estimate for the peak response. Figure 9.1.4–11 contains the history plots for the hoop-directed strains at location

A2. As in Figure 9.1.4–10, the initial peak response (high frequency) contained in the Abaqus/Explicit solution is not present in the experimental data. Otherwise, the Abaqus/Explicit solution closely tracks the experimental data. Figure 9.1.4–9 through Figure 9.1.4–11 indicate that the overall UNDEX analysis model provides a conservative estimate of the cylinder's peak response and is, therefore, appropriate for meeting the analysis objective.

Figure 9.1.4–12 shows a contour plot of accumulated equivalent plastic strain (PEEQ) on the outer surface of the test cylinder. To obtain the plot, an averaging threshold of 100% is used and the maximum contour value is specified as 9.16E−3. The plot corresponds to the end of the transient analysis, which is well after the last increment of plastic strain is detected from a plot of the cylinder's total plastic strain energy vs. solution time. The slight degree of solution nonsymmetry exhibited about the cylinder's midplane is due to the nonsymmetric nature of the free tetrahedron acoustic element mesh of the external fluid.

Input files

submerged_cyl_driver.inp	Abaqus/Explicit analysis of a submerged cylinder subjected to an UNDEX shock wave.
submerged_cyl_cylinder.inp	The finite element mesh data for the test cylinder, including element and node set definitions for output requests.
submerged_cyl_water.inp	The finite element mesh data for the external water, including element and node set definitions for surface creation and output requests.
submerged_cyl_pulse.inp	The time history of the shock wave pressure at the standoff point defined by the *AMPLITUDE option.

References

- Kwon, Y. W., and P. K. Fox, "Underwater Shock Response of a Cylinder Subjected to a Side-On Explosion," Computers and Structures, Vol. 48, No. 4, 1993.
- Blevins, R. D., *Formulas for Natural Frequencies and Mode Shapes,* Robert E. Fruger Publishing Co., 1979.

Table 9.1.4–1 Added mass for N=1 translation mode of an infinite cylinder (fluid between concentric cylinders).

Cylinder Radius Ratio (R_0/R_i)	Added Mass Ratio (External Boundary/Infinite Domain)
1.5	2.600
2.0	1.667
4.0	1.133
6.0	1.057
8.0	1.032
16.0	1.008
24.0	1.004

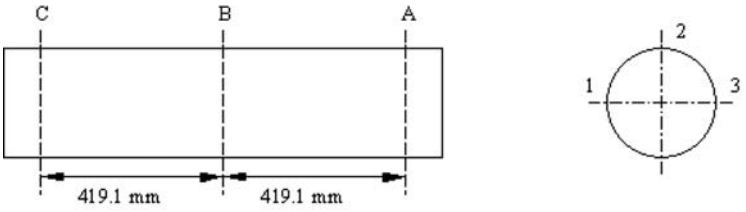

Figure 9.1.4–1 Strain gauge locations (A1, A2, B1, B2, B3, C1, C2) with B1 closest to the charge.

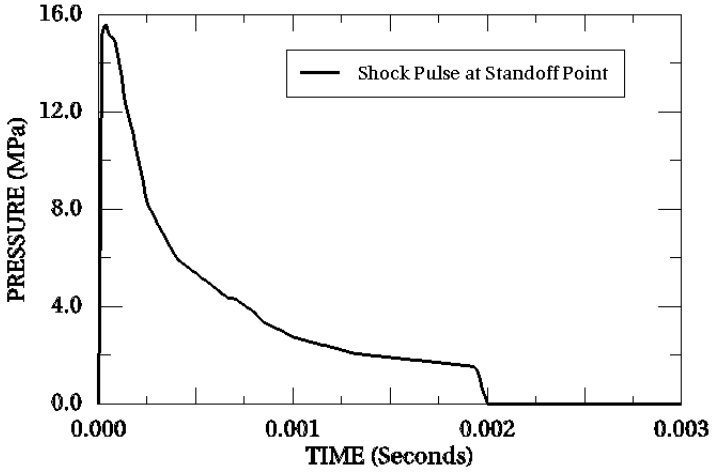

Figure 9.1.4–2 Incident pressure wave transient (shock pulse).

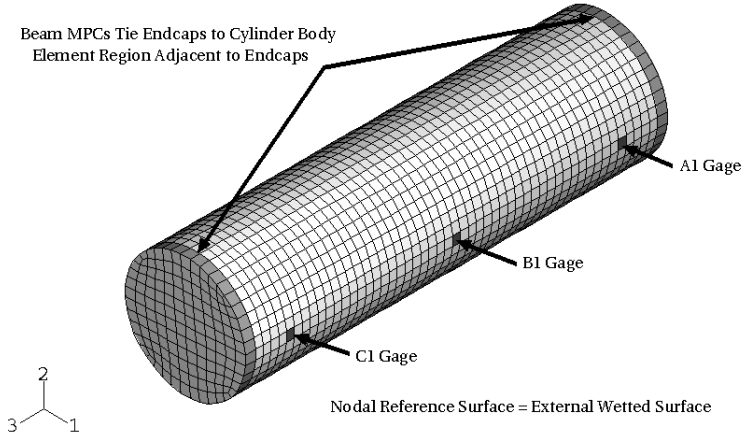

Figure 9.1.4–3 Test cylinder model.

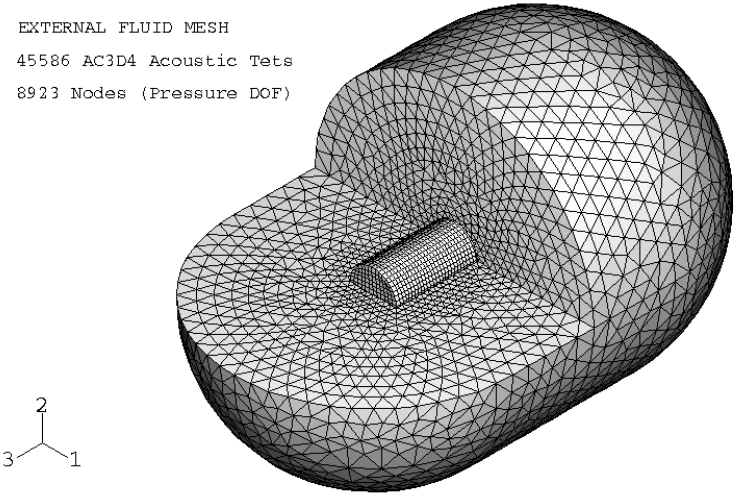

Figure 9.1.4–4 Test cylinder and external fluid acoustic mesh.

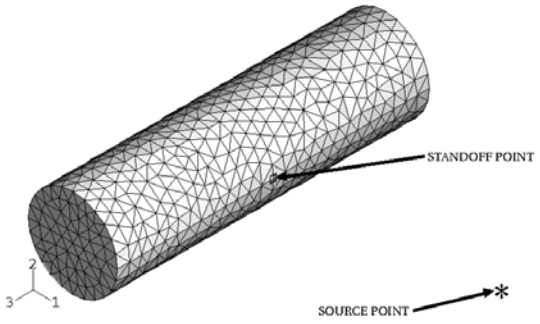

Figure 9.1.4–5 External fluid surface mesh at the acoustic-structure wetted interface.

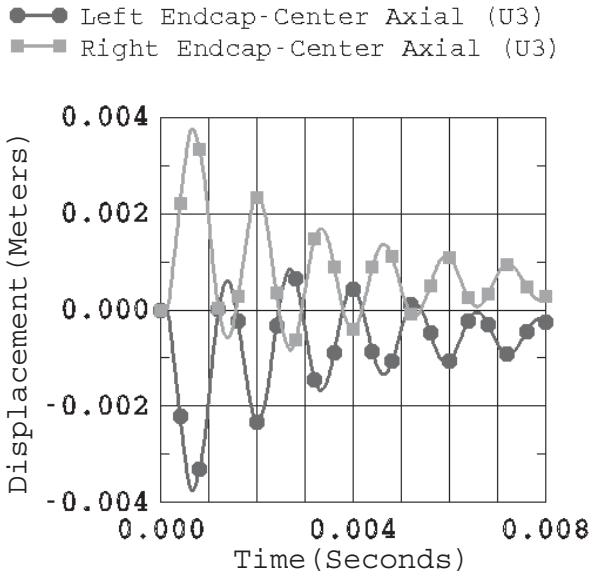

Figure 9.1.4–6 Axially directed displacements (U3) at the center of the endcaps.

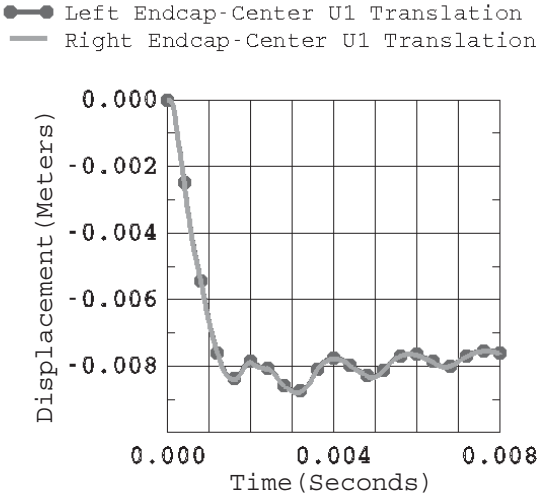

Figure 9.1.4–7 Displacements at the center of the endcaps.

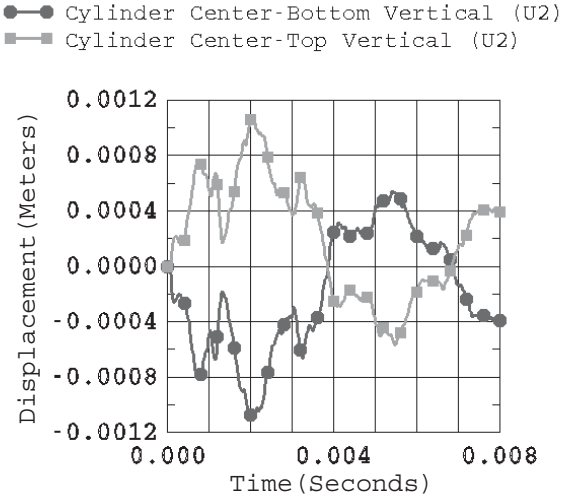

Figure 9.1.4–8 Vertical (U2) displacements at the cylinder midplane (top and bottom).

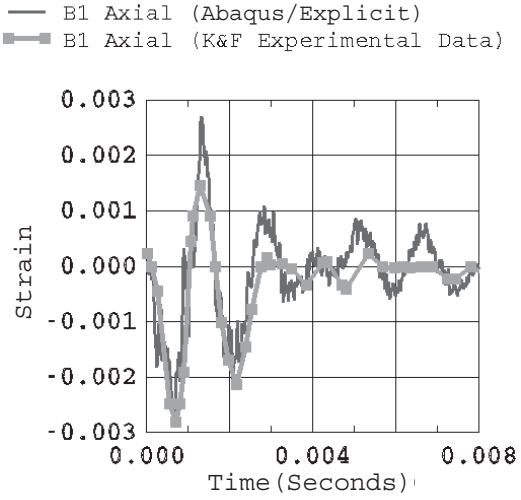

Figure 9.1.4–9 Axially directed strains at location B1.

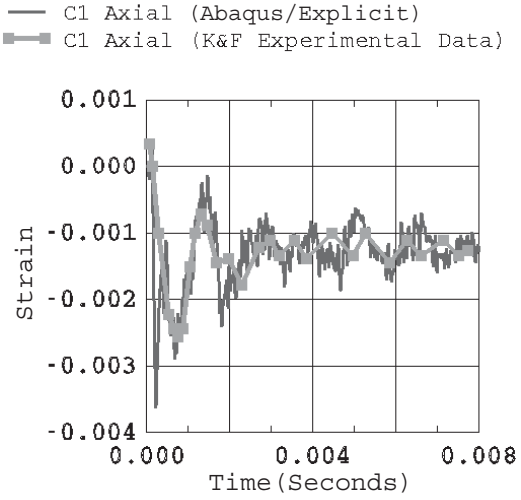

Figure 9.1.4–10 Axially directed strains at location C1.

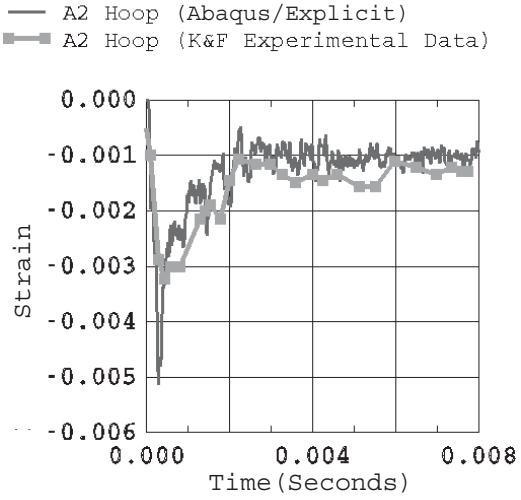

Figure 9.1.4–11 Hoop-directed strains at location A2.

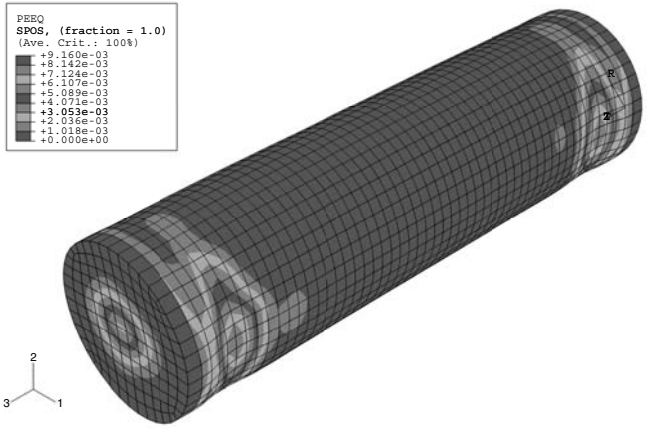

Figure 9.1.4–12 Accumulated equivalent plastic strains (PEEQ).

9.1.5 CONVERGENCE STUDIES FOR SHOCK ANALYSES USING SHELL ELEMENTS

Product: Abaqus/Explicit

This example illustrates a methodology you can use to design a computationally efficient model of a structure subjected to shock loading.

Structures subject to shock loads require careful design because of the high-frequency content of the loading signal and the low-pass filtering property of a finite element mesh. To address these issues, a simplified model is useful to estimate optimal parameters for an accurate, efficient, and realistic model.

The goal of the present study is to propose a methodology for designing a computationally efficient structural model, by answering the following questions:

- Given a load signal $f(t)$, what is the maximum element size for a given structure to obtain a reasonably accurate response?
- Given a minimum possible element size, what is the best signal $f'(t)$ to emulate the structural response to $f(t)$ with reasonable accuracy?

Model description

For the purpose of this study, consider a cylinder made of a linear elastic material with E=2.11×10^{11} N/m^2 and ν=0.3. It has an overall length of 10 m, a diameter of 3.5 m, and a wall thickness of 0.04 m. Quarter symmetry is employed by applying the appropriate boundary conditions on the corresponding geometry edges. The model is shown in Figure 9.1.5–1. Incident wave loading is applied on the outer surface of the cylinder, using the Kwon & Fox (KF) signal described in "Response of a submerged cylinder to an underwater explosion shock wave," Section 9.1.4. Abaqus/Explicit is used with a fixed time increment of 1×10^{-6} s, chosen to provide a suitable integration scheme for the load. The transient response (U, V, A) is analyzed at a standoff point over a period of 6 ms. Uniform meshes of S4R elements with various sizes are employed.

Results and discussion

First, convergence of the structural response at the standoff point is examined, applying the original KF loading signal. Errors are reported in a L^2-norm over the entire 6 ms duration of the response. The converged solution is formed by successively applying finer meshes until a desired relative accuracy is obtained. From Figure 9.1.5–2 and Table 9.1.5–1 we conclude that a mesh with h=0.025 m is a reference solution. The solution with h=0.05 m can also be considered converged; therefore, it can become the reference solution for subsequent studies (the acceleration response differs by only 1.1% with respect to the solution with h=0.025 m).

Figure 9.1.5–3 and Figure 9.1.5–4 depict the relative accuracy of the displacement and velocity responses with respect to the solution with h=0.05 m. For example, Figure 9.1.5–3 shows that if an accurate velocity response is of interest, element size restrictions can be relaxed to h=0.25 m (6.3% relative error versus the reference configuration); if the displacement response is of interest, the element size restrictions can be relaxed further to $h > 0.5$ m (Figure 9.1.5–4).

Figure 9.1.5–5 is constructed by defining a mesh characteristic frequency, Ω_h, used as x-data for the error curve. For a given number of elements, N, per excitation wavelength, the mesh characteristic frequency is

$$\Omega_h = \frac{c_s}{N \cdot h},$$

where c_s is the characteristic wave speed (here the shell flexural wave speed) and h is the element diameter. The structural wave speed is dispersive; i.e., it varies with the excitation frequency. In Figure 9.1.5–5, however, a constant reference value of c_s=1200 m/s is used. The previously defined mesh characteristic frequency also depends on the user's choice of the number of elements per wavelength, N. To preserve accuracy and to address the pollution effect (Ihlenburg and Babuska, 1995), N should increase with the excitation frequency. The choice of h, N, and the wavespeed in the medium, c_s, determines the value of the mesh characteristic frequency, Ω_h, which can be interpreted as a cutoff frequency for designing the filtered signal.

Figure 9.1.5–5 shows that by considering a mesh with h=0.05 m and N=15, the mesh characteristic frequency becomes Ω_h=1600 Hz. If the number of elements per wavelength is relaxed to N=5, Ω_h will increase to 4800 Hz. If the latter value is applied as the cutoff frequency, the filtered signal will capture the true signal more accurately; however, it is likely to produce more noise if the waves are not resolved properly.

The study presented above may lead to meshes that are impractical for realistic models, especially if the acceleration response is of primary interest. For this model of 10 m length, an element of 0.05 m provides sufficient accuracy at the standoff point. Since this may lead to prohibitive computational costs for realistic models, the next studies address ways to relax the element size restraints by modifying the shock signal applied to the structure. These following studies examine the impact of filtering and modified rise time upon the element size restrictions, in an attempt to minimize the noise at coarse meshes.

Filtered signals are applied successively to the structure, in an attempt to quantify the dependence of the optimal cutoff frequency on the element size. The sine-Butterworth second-order filter is used. Although filter performance is very important for optimal results, a comparison of various filtering techniques is beyond the purpose of this study.

The filtered signals are postprocessed via linear scaling with the parameter a such that the final and original signals are equivalent in a n-norm:

$$a_n = \left(\frac{\int_0^T (f_{KF})^n dt}{\int_0^T (f_f)^n dt} \right)^{1/n}; a_1 = \frac{\int_0^T f_{KF} dt}{\int_0^T f_f dt}; a_\infty = \frac{max_(f_{KF})}{max(f_f)}.$$

The norm can be varied to design a final signal suitable for various responses: since initially the KF is applied as a load signal, the infinity norm is suitable for obtaining a more accurate acceleration response, while the 1-norm (impulse conservation) is suitable for obtaining a more accurate velocity response.

For this study, filtered signals are designed with scaling parameters suitable for acceleration response. Sample postprocessed filtered signals are presented in Figure 9.1.5–6. By applying these as incident wave loads on the mesh with h=0.05 m, the results shown in Figure 9.1.5–7, Figure 9.1.5–8, and Figure 9.1.5–9 are obtained for the acceleration, velocity, and displacement, respectively. There is a

clear distinction between Figure 9.1.5–7, a well-captured acceleration response, and Figure 9.1.5–8 and Figure 9.1.5–9, which are poor estimates of the velocity and displacement responses, since the applied filtered load has a significantly higher impulse than the unfiltered signal.

The results presented in Figure 9.1.5–10 and Figure 9.1.5–11 are obtained by applying the same load signals to coarser meshes. A summary is presented in Table 9.1.5–1 and Figure 9.1.5–14. The expected trend is visible: as the mesh coarsens, the acceleration response when applying filtered signals is considerably less noisy than the response for unfiltered signals. As the mesh is refined, the response converges to the "wrong" solution given by the filter of choice. Thus, when computational resources are scarce, there is an obvious benefit to applying prefiltered signals, which attenuate the noise due to insufficient spatial discretization.

As an alternative to the sine-Butterworth filter, the signal can be idealized in a heuristic manner by using a linear rise, followed by an exponential decay. By keeping the decay constant, you can study the sensitivity of the structural element size to the rise time of the shock signal.

The original rise time, Δt, of the KF signal is multiplied by a rise time factor (rtf= 2, 5, 10, 15, 20) to obtain new signals, which are then applied to the structure. To account for noise contributions only, the error of the acceleration response is reported on the decay portion $[T_{max}, T]$, where T_{max} is the time stamp of the peak amplitude of the load signal.

The results using this technique are presented in Figure 9.1.5–12 and Figure 9.1.5–13 and summarized in Table 9.1.5–2 and Figure 9.1.5–15. By comparison with Figure 9.1.5–14, the smoothing strategy appears considerably more effective for the acceleration response than using a sine-Butterworth filter. For example, the case with h=0.125 m and rtf=20 (scaling the upper bound of the spectrum at ~2250 Hz) yields an error of 9%; for the same element size with h=0.125 m, the sine-Butterworth filter with a cutoff frequency of 3000 Hz yields a 32% error.

Input files

step_data.inp	Step data for all models.
cyl_h0025.inp	Model data for submerged cylinder with an element size of 0.025 m.
cyl_h005.inp	Model data for submerged cylinder with an element size of 0.05 m.
cyl_h0125.inp	Model data for submerged cylinder with an element size of 0.125 m.
cyl_h025.inp	Model data for submerged cylinder with an element size of 0.25 m.
cyl_h05.inp	Model data for submerged cylinder with an element size of 0.5 m.
sf_unfilt.inp	Amplitude data for unfiltered KF signal.
sf_300.inp	Amplitude data for KF signal filtered at 300 Hz.
sf_600.inp	Amplitude data for KF signal filtered at 600 Hz.
sf_900.inp	Amplitude data for KF signal filtered at 900 Hz.
sf_1200.inp	Amplitude data for KF signal filtered at 1200 Hz.
sf_1500.inp	Amplitude data for KF signal filtered at 1500 Hz.

sf_2000.inp	Amplitude data for KF signal filtered at 2000 Hz.
sf_3000.inp	Amplitude data for KF signal filtered at 3000 Hz.
sf_5000.inp	Amplitude data for KF signal filtered at 5000 Hz.
sr_2.inp	Amplitude data for KF signal with a rise time factor of 2.
sr_5.inp	Amplitude data for KF signal with a rise time factor of 5.
sr_10.inp	Amplitude data for KF signal with a rise time factor of 10.
sr_15.inp	Amplitude data for KF signal with a rise time factor of 15.
sr_20.inp	Amplitude data for KF signal with a rise time factor of 20.
driver_h0025.inp	Driver file for the mesh with h=0.025 m and all signals.
driver_h005.inp	Driver file for the mesh with h=0.05 m and all signals.
driver_h0125.inp	Driver file for the mesh with h=0.125 m and all signals.
driver_h025.inp	Driver file for the mesh with h=0.25 m and all signals.
driver_h05.inp	Driver file for the mesh with h=0.5 m and all signals.

References

- Ihlenburg, F., and I. Babuska, "Finite Element Solution of the Helmholtz Equation with High Wave Numbers. Part 1: The h-version of the FEM," Computers & Mathematics with Applications, no. 30(9), pp. 9–37, 1995.
- Kwon, K. W., and P. K. Fox, "Underwater Shock Response of a Cylinder Subjected to a Side-On Explosion," Computers and Structures, vol. 48, no. 4, 1993.

Table 9.1.5–1 Percent relative error in acceleration response for pre-filtered signals using sine-Butterworth filter. Reference solution is the unfiltered load signal applied to a mesh with h=0.025 m.

Cutoff (Hz)	h=0.05 m	h=0.125 m	h=0.25 m	h=0.5 m
300	142	105	105	104
600	116	102	102	102
900	91	90	95	90
1200	72	75	88	90
1500	64	64	85	101
2000	49	49	47	110
3000	33	32	43	129
5000	16	16	32	116
Unfiltered	1.2	18	91	103

Table 9.1.5–2 Percent relative error in acceleration response for smoothed rise time signals. Reference solution is the unfiltered load signal applied to a mesh with h=0.025 m. Errors are measured in L^2-norm over $[T_{max}, T]$, where T_{max} is the time stamp of the peak amplitude.

Rise time factor	h=0.05 m	h=0.125 m	h=0.25 m	h=0.5 m
2	0.7	12	67	93
5	2.1	4.0	55	93
10	4.2	4.4	20	85
15	7	7	14	70
20	9	9	20	44

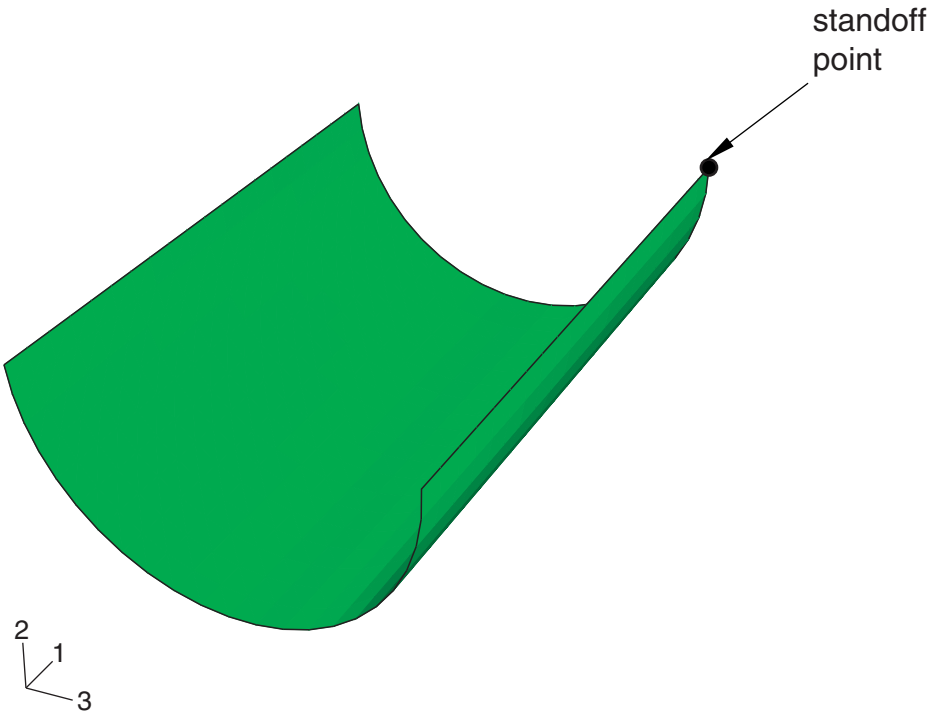

Figure 9.1.5–1 Test problem geometry.

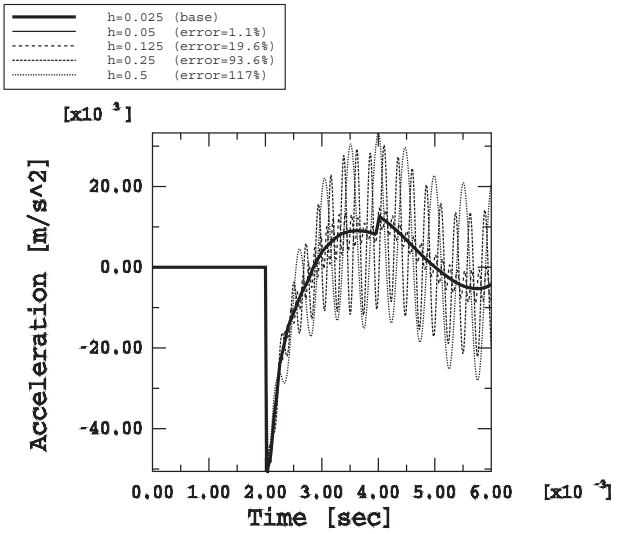

Figure 9.1.5–2 Convergence of athwartship acceleration at standoff point. Element size h [m].

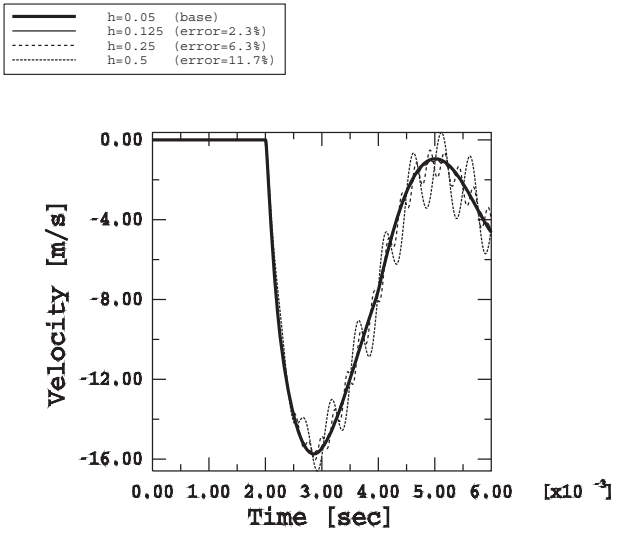

Figure 9.1.5–3 Convergence of athwartship velocity at standoff point. Element size h [m].

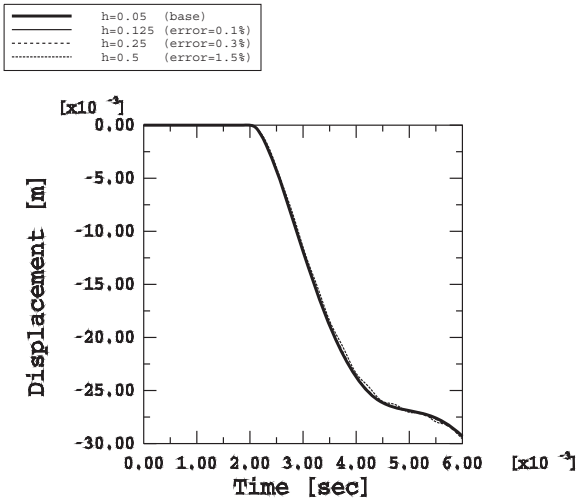

Figure 9.1.5–4 Convergence of athwartship displacement at standoff point. Element size h [m].

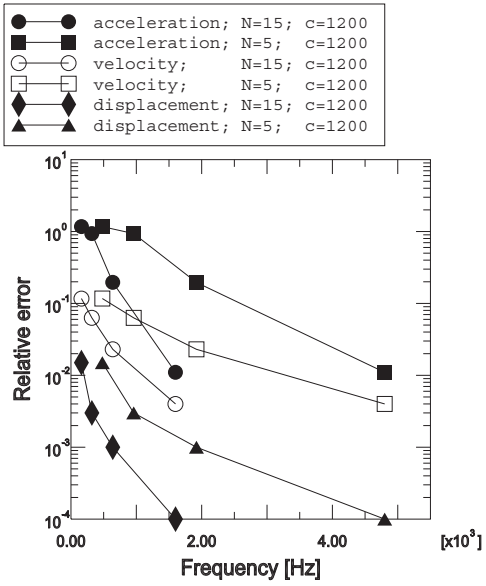

Figure 9.1.5–5 Shock cutoff frequency based on structure response. Wave speed c [m/s].

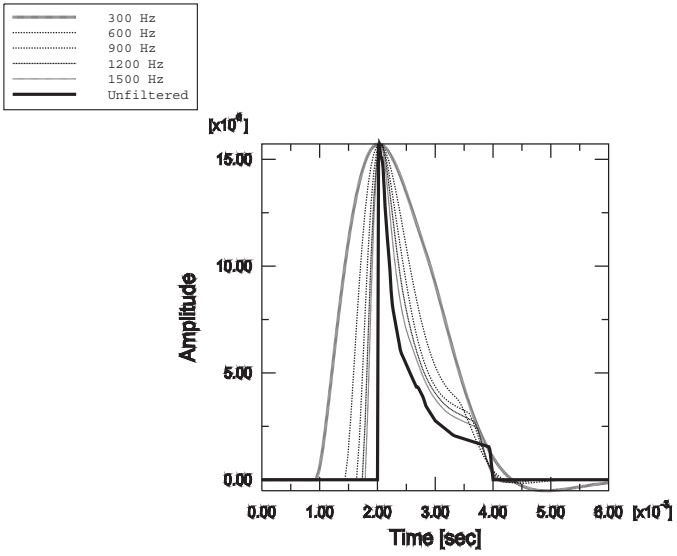

Figure 9.1.5–6 Sample signals obtained after applying sine-Butterworth filter to the original KF signal.

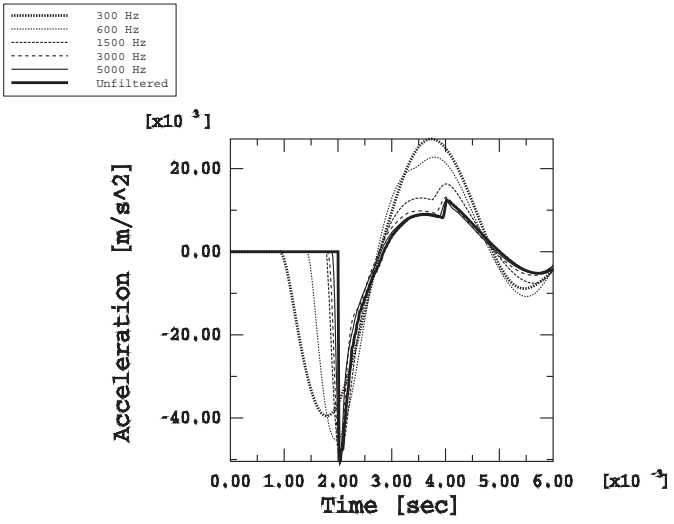

Figure 9.1.5–7 Acceleration response at standoff point for filtered load signals and mesh with h=0.05 m.

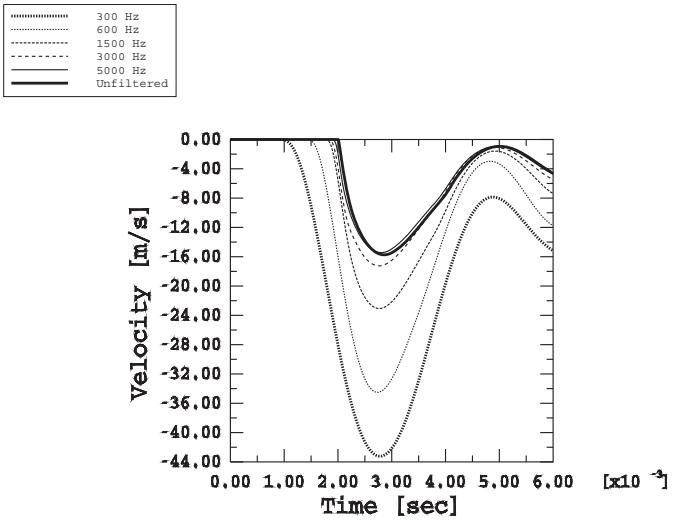

Figure 9.1.5–8 Velocity response at standoff point for filtered load signals and mesh with h=0.05 m.

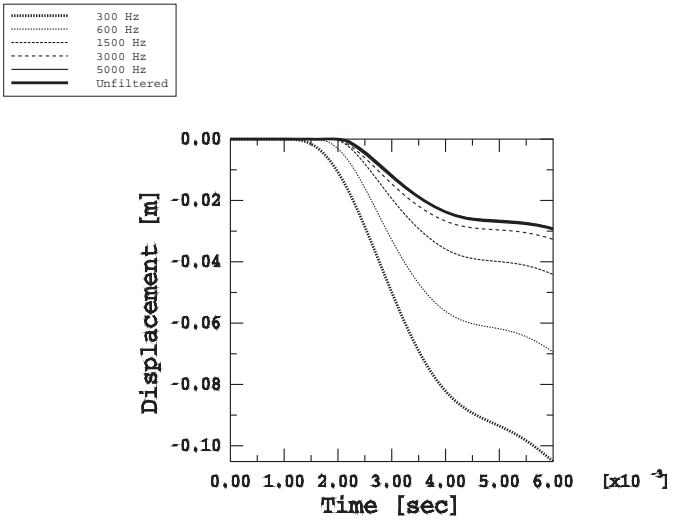

Figure 9.1.5–9 Displacement response at standoff point for filtered load signals and mesh with h=0.05 m.

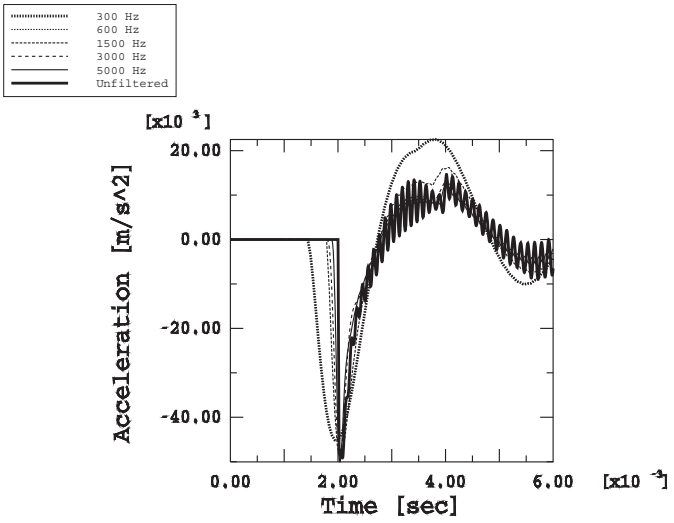

Figure 9.1.5–10 Acceleration response at standoff point for filtered load signals and mesh with h=0.125 m.

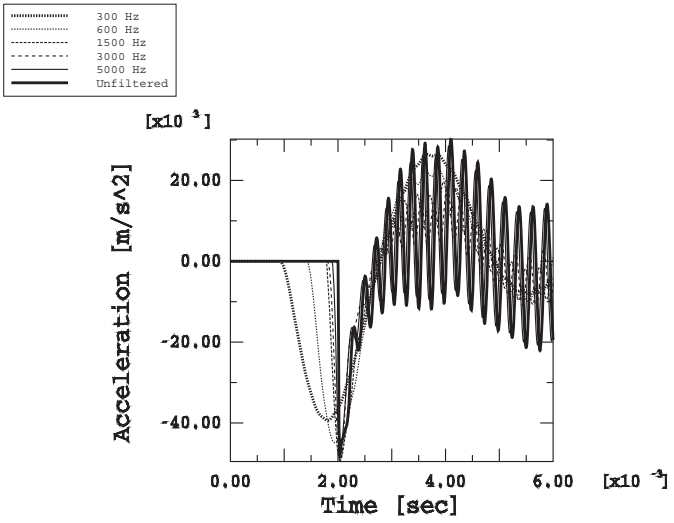

Figure 9.1.5–11 Acceleration response at standoff point for filtered load signals and mesh with h=0.25 m.

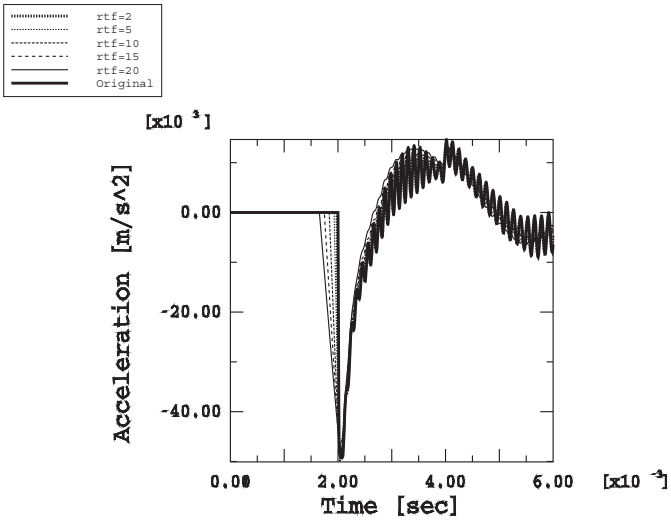

Figure 9.1.5–12 Acceleration response at standoff point for smoothed load signals and mesh with h=0.125 m.

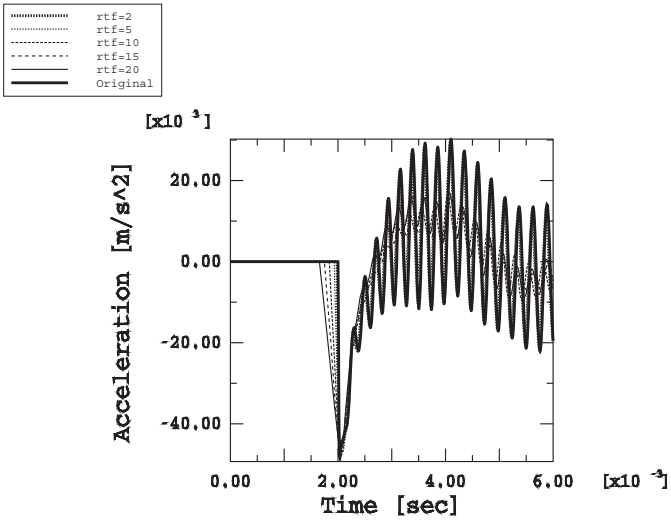

Figure 9.1.5–13 Acceleration response at standoff point for smoothed load signals and mesh with h=0.25 m.

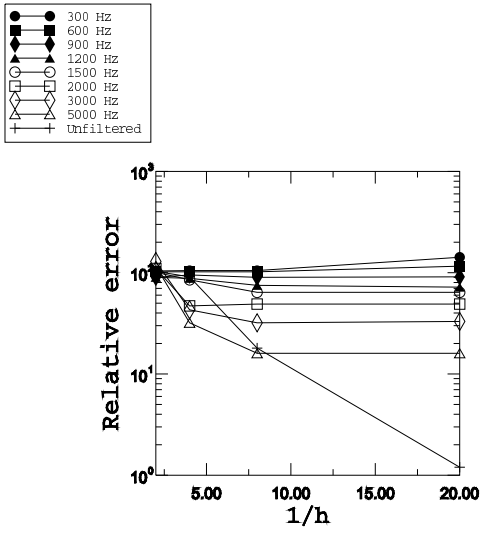

Figure 9.1.5–14 Error in acceleration response for sine-Butterworth filter with various cutoff frequencies. Element size h [m].

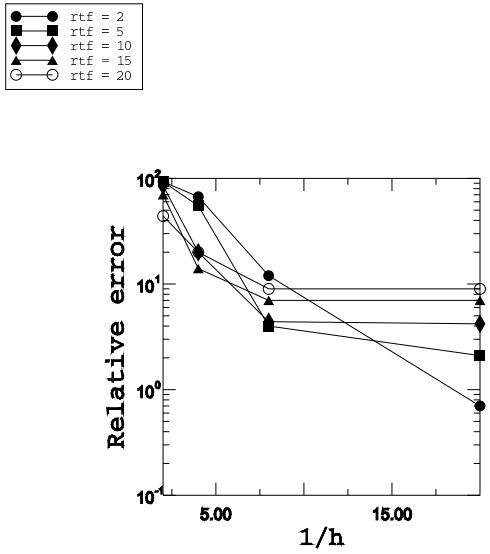

Figure 9.1.5–15 Error in acceleration response for various rise time factors. Element size h [m].

9.1.6 UNDEX ANALYSIS OF A DETAILED SUBMARINE MODEL

Product: Abaqus/Explicit

This example illustrates how Abaqus/Explicit can be used to predict the transient response of a large and complicated structure subject to a shock wave loading resulting from an underwater explosion (UNDEX).

Modeling large underwater structures subject to shock loads typically leads to computationally intensive numerical models that require considerable computing resources. A publicly available full submarine model is modified via a modeling approach that minimizes the computational costs and obtains an accurate response in a particular region of interest. Consequently, particular attention is given to structural details in the respective region of interest, while simplifications meant to reduce analysis costs are assumed elsewhere.

The structure is loaded by an incident wave with a shock profile amplitude. If structural integrity is analyzed, a reasonable assumption is that most affected regions will be around the standoff point; thus, more attention to modeling details should be paid to the front part of the submarine (Figure 9.1.6–1 and Figure 9.1.6–5).

Problem and geometry description

The model presented was created based on specifications provided by Forschungsanstalt der Bunderwehr für Wasserschall und Geophysik (FWG), Kiel, Germany (Fiedler and Schneider, 2002). This model is known as the Benchmark Target Strength Simulation (BeTSSi) model and is a reasonably sophisticated replica of a Kilo-class Soviet submarine. The complexity of the structure is considered suitable for testing target-strength simulation codes for more realistic problems (Schneider et al., 2003). In this example problem the BeTSSi model is adapted to test Abaqus/Explicit for a realistic underwater explosion (UNDEX) simulation.

Structural details include flooded bow compartments, sonar array, torpedo tubes, flooded sail compartments, sail access tubes, and an aft chamber (Figure 9.1.6–1 through Figure 9.1.6–4). The pressure hull is enveloped by an external hull only along the upper side and is in direct contact with the fluid throughout the bottom side. The intra-hull space is also flooded along the length of the submarine.

The entire structure is hit by a spherical shock wave due to the explosion of a charge located 16.5 m away from the submarine (Figure 9.1.6–1). The pressure-time signal corresponds to a 60lb HBX-1 charge, as in "Response of a submerged cylinder to an underwater explosion shock wave," Section 9.1.4, and taken from Kwon & Fox (1993).

Reduced model

Since the Kwon & Fox (KF) load signal carries a large excitation spectrum, the outside water has to extend to a large distance, corresponding to the lowest end of spectrum, and both the submarine structure and the outside water have to be discretized with a small element size, corresponding to the wavelength of the high end of the spectrum. This generates a considerably large computational model, due also to the significant difference between the length of the submarine model (62 m) and the low wavelength of the high end of the spectrum. Consequently, a modeling approach is employed in this example problem

where a "region of interest" is defined around the shock-wave standoff point. The reduced model still includes details such as flooded bow compartments, torpedo tubes, a sonar dome, and a portion of the pressure and exterior hulls, with the fluid domain defined in the intra-hull space. In addition, stiffeners are added for the detailed region of the pressure hull. The rest of the submarine model is simplified using beam elements, coupled with the region of interest using kinematic coupling constraints. The section behavior of the beams is defined using meshed cross-sections to approximate the cross-section inertia of the real structure (Figure 9.1.6–6, Figure 9.1.6–7, and Figure 9.1.6–8). The tapered region at the back of the submarine is approximated via 13 stepwise-constant circular cross-sections. Finally, the inertia effects of the outside water are included.

The exterior acoustic domain (water) envelops only the region of interest and extends to a distance of approximately 1.5 m from the submarine structure, corresponding to half the wavelength inwater at a frequency of 500 Hz. Impedance boundary conditions are applied on truncation surfaces to reduce spurious reflections.

Results and discussion

Applying the above simplifications and element sizes of $h_s = 0.05$ for the structure and $h_w = 0.1$ for both the inner and outer water domains, the aggregate model size is 1.2 million nodes and 5.1 million elements, including AC3D4, S4R, S3R, and B31 elements. The analysis is stopped after 6 ms, enough for the wavefront traveling through the acoustic medium to sweep the region of interest.

The pressure for the inner and outer acoustic domains is depicted in Figure 9.1.6–9 at the end of the 6 ms response. Observe the high-frequency content of the acoustic pressure inside the bulkheads, due to the excitation from the walls. The high-frequency content of the waves in the bulkheads' walls can be seen in Figure 9.1.6–13 and Figure 9.1.6–14.

Figure 9.1.6–10, Figure 9.1.6–11, and Figure 9.1.6–12 illustrate the history of acceleration, velocity, and displacement responses at the standoff point, respectively. A kick-off acceleration of almost 8 km/s^2 is reached due to the initial shock, followed by a rapid decay. By the end of the shock duration (4 ms), it is almost stabilized around zero. The kick-off velocity reaches a value of almost 8 m/s, while the athwartship displacement shows a maximum drift of about 10 mm.

Structural integrity is one of the major concerns of such an analysis. Almost the entire structure is assumed to be made of perfect elastic-plastic steel plates, with position-dependent thicknesses. The only exceptions are the stiffeners, defined as beams with T cross-sections. The material is the same as for the rest of the submarine model, a perfect elastic-plastic steel. High stress concentration regions are analyzed by plotting Mises stresses (Figure 9.1.6–15); permanent deformations are monitored via the equivalent plastic strain (Figure 9.1.6–16). High stress concentration regions as well as permanent deformations are observed for regions around the joints. The maximum stresses are observed on the upper panels of the sonar dome, while the largest permanent deformation is obtained around the joint between the pressure hull, the exterior hull, and the horizontal bow compartment.

Input files

undex_driver_xpl.inp	Driver input file.
undex_parts.inp	Parts definition input file.

undex_assembly.inp	Assembly input file.
undex_outwater_h01.inp	Outer water mesh data.
undex_innerwater_h01.inp	Inner water mesh data.
undex_subbody_h005.inp	Submarine structure mesh data.
undex_tapered_beam_elsets.inp	Element set definitions for the tapered region of the submarine body.
undex_tapered_beam_sections.inp	Section data for the element sets defined for the tapered region of the submarine body.
undex_ampl.inp	Amplitude data.
undex_acoustics_s.inp	Impedance and incident wave model data.
undex_materials_s.inp	Material data.
undex_ties.inp	Tie definitions.
undex_step.inp	Step data.
undex_boundary_conditions.inp	Boundary condition data.
undex_output_requests.inp	Output request data.
undex_beam_section_front.inp	Section mesh data for generating cross-section beam properties for the front region of the submarine.
undex_beam_section_sail.inp	Section mesh data for generating cross-section beam properties for the sail region of the submarine.
undex_beam_section_back1.inp	Section mesh data for generating cross-section beam properties for the 1st back region.
undex_beam_section_back2.inp	Section mesh data for generating cross-section beam properties for the 2nd back region.
undex_beam_section_back3.inp	Section mesh data for generating cross-section beam properties for the 3rd back region.
undex_beam_section_back4.inp	Section mesh data for generating cross-section beam properties for the 4th back region.
undex_beam_section_back5.inp	Section mesh data for generating cross-section beam properties for the 5th back region.
undex_beam_section_back6.inp	Section mesh data for generating cross-section beam properties for the 6th back region.
undex_beam_section_back7.inp	Section mesh data for generating cross-section beam properties for the 7th back region.
undex_beam_section_back8.inp	Section mesh data for generating cross-section beam properties for the 8th back region.
undex_beam_section_back9.inp	Section mesh data for generating cross-section beam properties for the 9th back region.
undex_beam_section_back10.inp	Section mesh data for generating cross-section beam properties for the 10th back region.
undex_beam_section_back11.inp	Section mesh data for generating cross-section beam properties for the 11th back region.

undex_beam_section_back12.inp	Section mesh data for generating cross-section beam properties for the 12th back region.
undex_beam_section_back13.inp	Section mesh data for generating cross-section beam properties for the 13th back region.

References

- Fiedler, Ch., and H. G. Schneider, "BeTSSi-Sub—Benchmark Target Strength Simulation Submarine," Technical Report, Forschungsanstalt der Bundeswehr für Wasserschall und Geophysik, Kiel, 2002.
- Kwon, K. W., and P. K. Fox, "Underwater Shock Response of a Cylinder Subjected to a Side-On Explosion," Computers and Structures, vol. 48, no. 4, 1993.
- Schneider, H. G. et al., "Acoustic Scattering by a Submarine: Results from a Benchmark Target Strength Simulation Workshop," Proceedings of Tenth International Congress on Sound and Vibration, Stockholm, Sweden, 2003.

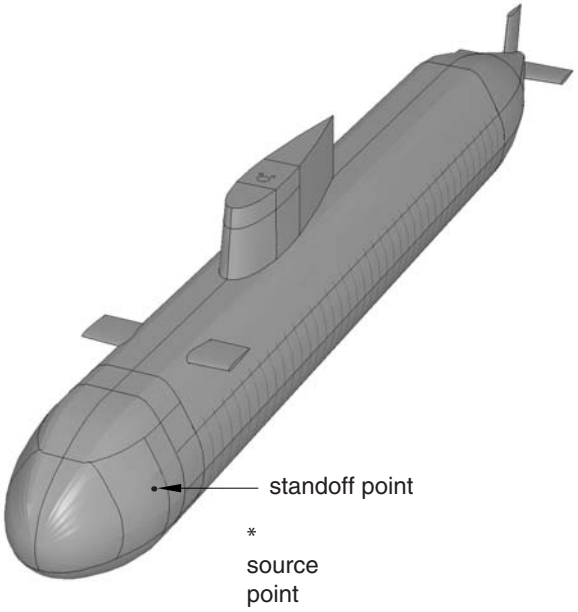

Figure 9.1.6–1 BeTSSi full submarine model.

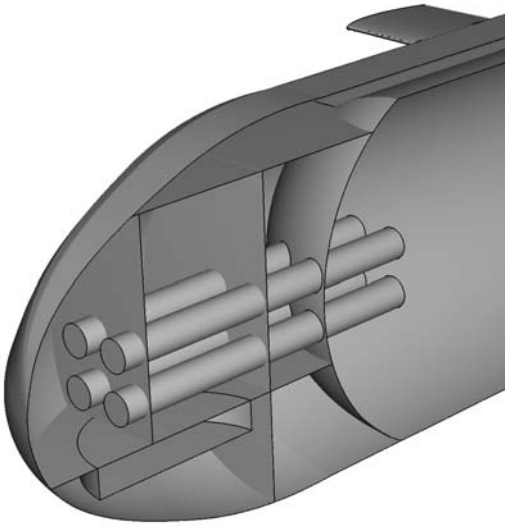

Figure 9.1.6–2 Cut view through front part of the model including details such as bulkheads, torpedo tubes, and the sonar dome.

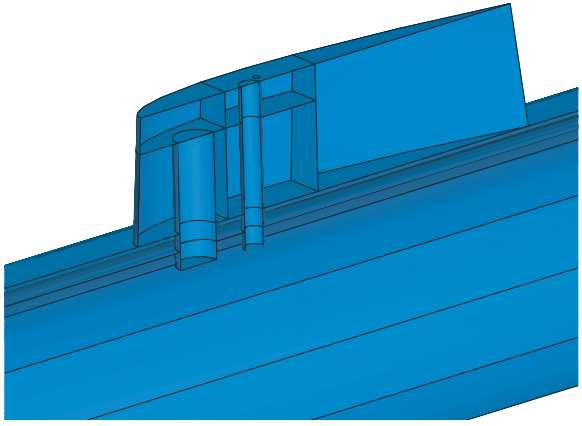

Figure 9.1.6–3 Cut view through sail; sail compartments and access tubes are visible.

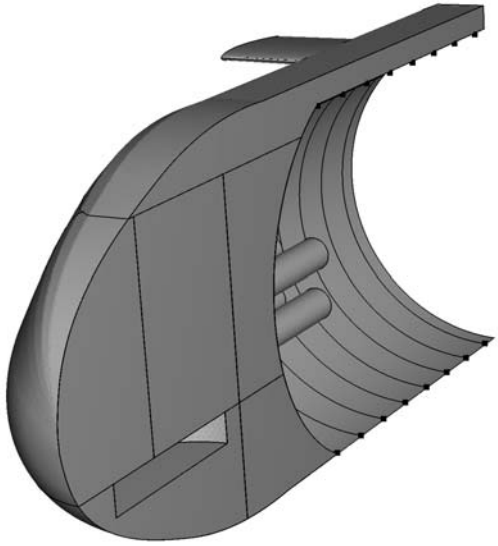

Figure 9.1.6–4 Flooded bow compartments.

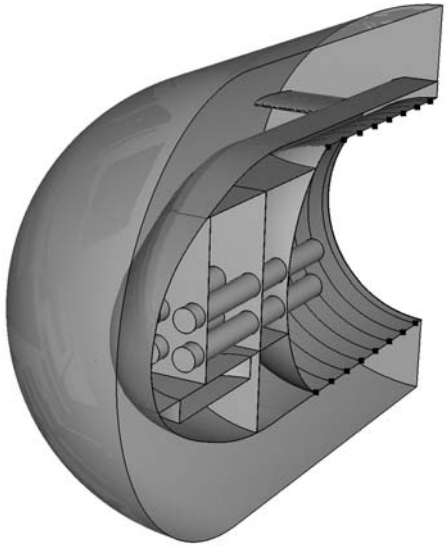

Figure 9.1.6–5 Cut view of reduced model, including exterior fluid domain.

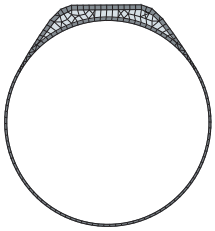

Figure 9.1.6–6 Meshed cross-section of the front beams.

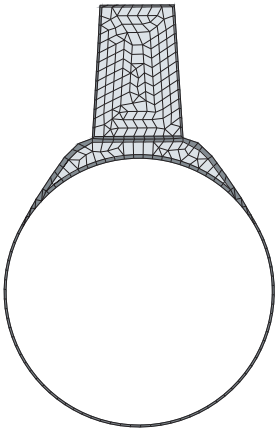

Figure 9.1.6–7 Meshed cross-section of the sail beams.

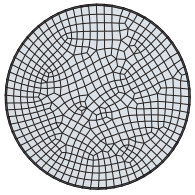

Figure 9.1.6–8 Meshed cross-section of the back beams.

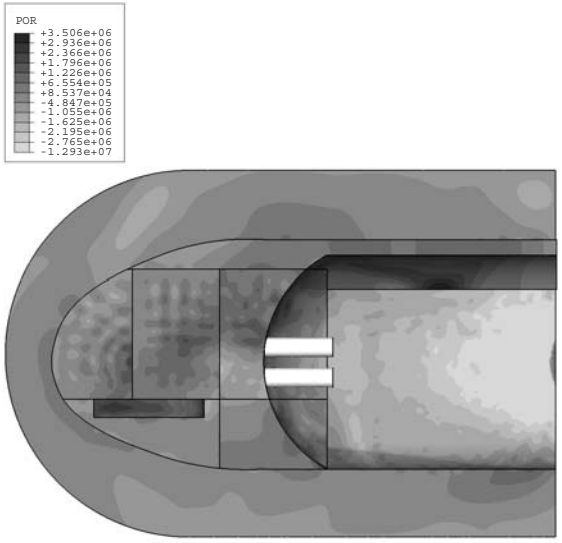

Figure 9.1.6–9 Pore pressure contours of the inner and outer water.

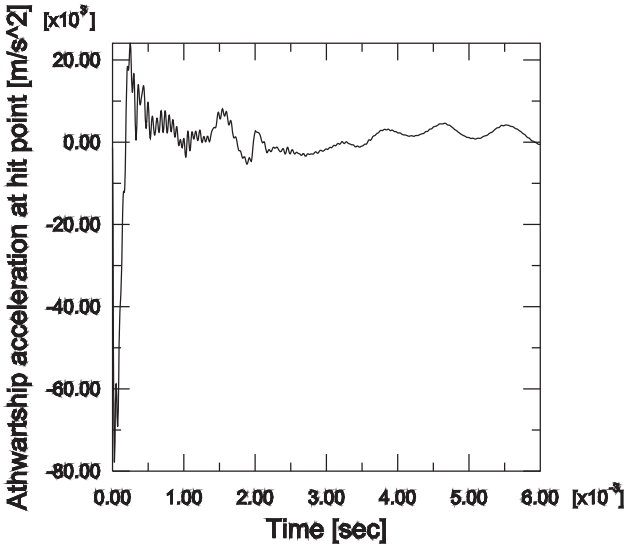

Figure 9.1.6–10 Athwartship acceleration at the standoff point.

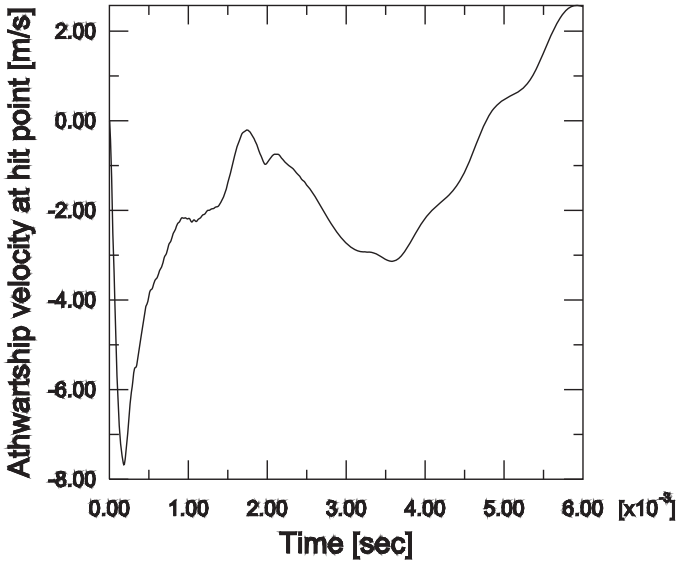

Figure 9.1.6–11 Athwartship velocity at the standoff point.

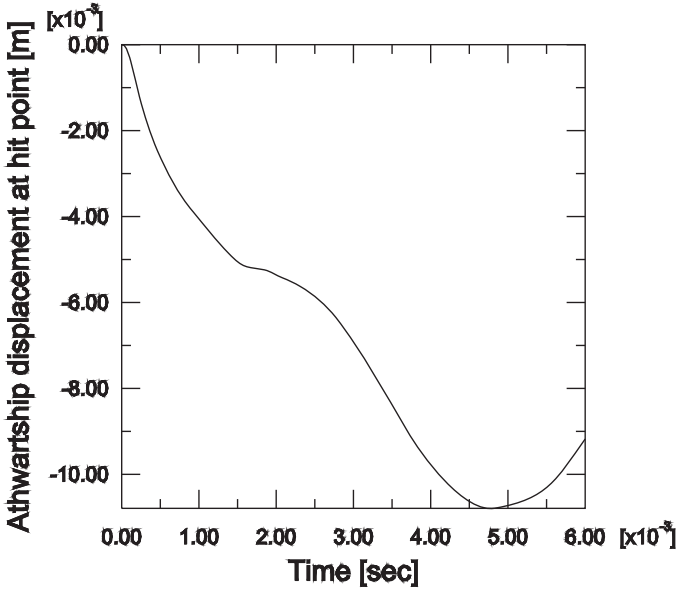

Figure 9.1.6–12 Athwartship displacement at the standoff point.

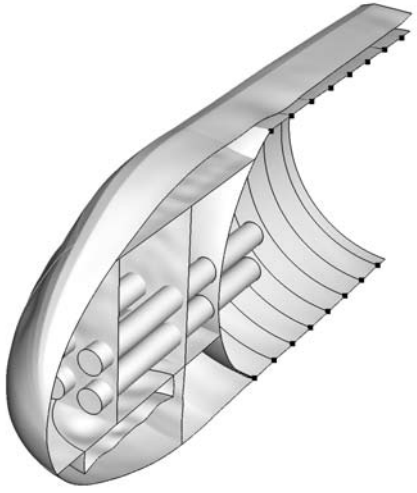

Figure 9.1.6–13 Cut view of deformed configuration.

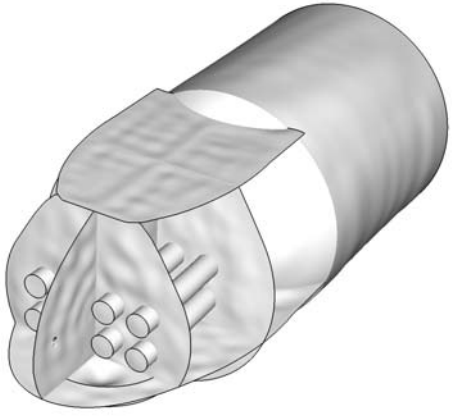

Figure 9.1.6–14 Deformed configuration of pressure hull, bulkheads, torpedo tubes, and sonar dome: whole view.

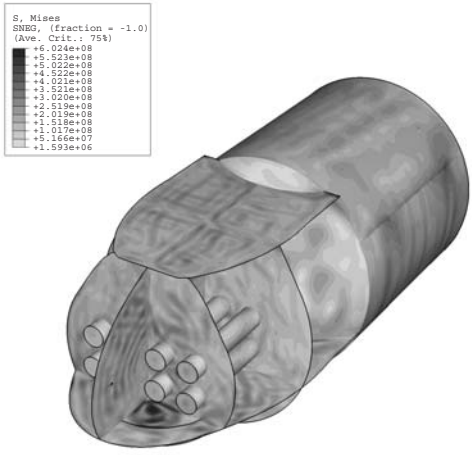

Figure 9.1.6–15 Mises stress for bow compartments, pressure hull, torpedo tubes, and sonar array.

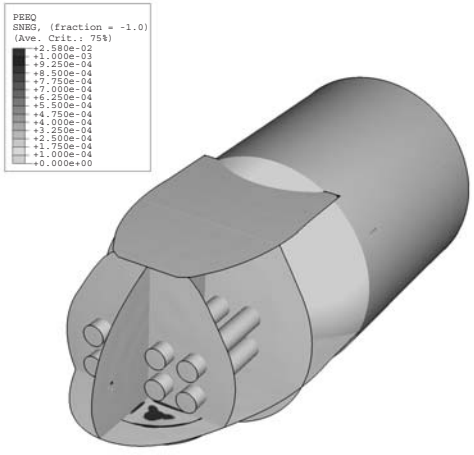

Figure 9.1.6–16 Equivalent plastic strain for bow compartments, pressure hull, torpedo tubes, and sonar array.

9.1.7 COUPLED ACOUSTIC-STRUCTURAL ANALYSIS OF A PICK-UP TRUCK

Products: Abaqus/Standard Abaqus/CAE

This example illustrates the capability in Abaqus to perform fully coupled acoustic-structural analyses of a pick-up truck model.

This type of analysis has become critically important in the automotive industry and it provides essential benefits toward designing vehicles for ride comfort and quietness. This example uses the pick-up truck model geometry described in "Inertia relief in a pick-up truck," Section 3.2.1. Only a portion of the pick-up truck is modeled, including the chassis, the cabin, and the air inside the cabin. Structural elements are used to model the cabin and the chassis, and acoustic elements are used to model the air interior. Connector elements are used to connect the various structural parts together. The coupling between the structure and acoustic medium is modeled by applying a tie constraint. Frequency domain analyses are performed for both regular models (without substructures) and for models using coupled structural-acoustic substructures.

Geometry and materials

The pick-up truck model (1994 Chevrolet C1500) discussed here is depicted in Figure 9.1.7–1 through Figure 9.1.7–3.

The air is modeled only inside the cabin, and the process of constructing the air mesh in this particular case is worth a brief discussion. Normally, if the solid geometry of the structural part (the cabin) were available, a Boolean subtraction could be performed in Abaqus/CAE to obtain the solid geometry of the included space (in this case the air inside the cabin). Unfortunately, the solid geometry of the cabin is not available since the structural model is based on a public-domain mesh, as discussed in "Inertia relief in a pick-up truck," Section 3.2.1. To overcome this issue, the following strategy is adopted. An approximate air geometry is created in Abaqus/CAE to follow roughly the contour of the cabin interior, including the dashboard, the doors, the cabin floor, the cabin top, the back wall, and the seat. The mesh created from this geometry does not conform exactly to the geometry of the cabin interior. However, on the tie constraint that connects the air mesh to the structural parts, you can adjust the nodes so that the nodes belonging to the air surface will be pushed onto the inside cabin surface or onto the seat surface to conform to the structural mesh (see Figure 9.1.7–2).

The materials used for the cabin and chassis are described in "Inertia relief in a pick-up truck," Section 3.2.1. The air properties used inside the cabin are: air density of 1.2 kg/m^3 and air bulk modulus of 1.39×10^5 Pa, which produce a sound speed of 340 m/s.

Models both with and without damping are constructed. In the models where damping is considered, two forms of damping are modeled, as follows. Rayleigh stiffness proportional damping, governed by the parameter β, is used in the structural materials in the model. For a given value of β applied to all materials in the structure (mostly steel), the damping fraction ξ_α for a mode α with natural circular frequency ω_α is given by the formula $\xi_\alpha = \beta\omega_\alpha/2$. The value of β in the model is chosen to give approximately 1% critical damping for the modes whose natural frequencies are in the middle of the range of excitation (at about 80 Hz). Surface impedance is also specified on the cabin floor to model the acoustic damping effect of a carpet by using an impedance boundary condition. The impedance properties on this surface

are chosen such that about 67% of a planar wave incident to this surface in the normal direction would be reflected.

Models

Four different models are considered.

Model 1

In the first model only the cabin and the interior air are considered. The structural part of the finite element model is shown in Figure 9.1.7–1 with the doors removed for illustration purposes. The cabin has six connection points with the chassis: two in the front and four under the seat. The outermost four of these connection points are fixed with boundary conditions, and a natural frequency extraction is performed. Several steady-state dynamic analyses (mode-based, direct-solution, and subspace-based) follow the eigenfrequency extraction step. Separate analyses with and without damping are conducted. There are 43,663 structural elements (mostly shells) and 12,171 acoustic elements in this model for a total of 207,994 degrees of freedom. The average structural element size is about 90 mm, and the average acoustic element size is approximately 325 mm. Considering that at least 5–6 elements are needed per wavelength for accurate representation of the dynamics, the highest excitation frequency for which results can be computed accurately is about 175 Hz. Two excitation cases are considered: harmonic point loading (at the two hook-up points that have not been constrained) and incident wave loading on the bulkhead below the dashboard. The latter case models engine compartment noise propagating through an air path. This airborne load is modeled both as an incident plane wave and as a diffuse field.

Model 2

In the second model the cabin-air model is reduced to a fully coupled structural-acoustic substructure. The four connection points where boundary conditions are applied in the first model are retained using the retained degrees of freedom. In addition, 200 coupled structural-acoustic eigenmodes are extracted. The eigenmodes are then retained using eigenmode selection to better represent the dynamics of the substructure in the frequency range of interest. Consequently, the substructure is represented by a total of 224 degrees of freedom to represent the 207,994 degrees of freedom in the first model. The substructure is then used in a separate, one-element natural frequency extraction analysis. The results are recovered from the substructure and compared to the results obtained from the first model.

Model 3

In the third model both the cabin and the chassis are considered on the structural side (Figure 9.1.7–3), while the air is modeled inside the cabin only. Since no air mesh is used to model the ambient air, this type of model can be used to study the structural path contributions to the noise inside the cabin. In the steady-state dynamic analyses of this model the excitation is provided by point loads applied to the engine mounts, while the chassis is supported with fixed boundary conditions at its ends. There are 53,897 structural elements in this model, while the number of acoustic elements is the same as in the first model.

Model 4

Finally, the cabin-chassis model is reduced to two substructures: a fully coupled structural acoustic cabin-air substructure and a structural-only chassis substructure. As in the previous substructure model both the retained degrees of freedom and the eigenmode selection are used to generate the two substructures. The two substructures are represented by 236 and 284 degrees of freedom, respectively. The substructures are then used in a separate, two-element natural frequency extraction analysis; and the results are compared to the results from the third model.

Results and discussion

Some of the steady-state dynamic results for the undamped cabin-air model analyses are shown in Figure 9.1.7–4 and Figure 9.1.7–5. In all analyses 200 sampling points are selected in the frequency range of interest (35–120 Hz). This frequency range corresponds to engine-induced vibrations in the range of 2100–7200 RPM. Of particular interest in these analyses is the sound pressure level at a location in the vicinity of the driver's ear. The response is shown in Figure 9.1.7–4 and is calculated from the acoustic pressure using the following equation

$$SPL = 20.0 \times log_{10}(p_{rms}/p_{ref}),$$

where $p_{rms} = p/\sqrt{2}$ and $p_{ref} = 2 \times 10^{-5}$ Pa. Figure 9.1.7–5 shows the displacement response of one of the nodes on the cabin floor where the harmonic load is applied. The results from the subspace-based and the mode-based steady-state dynamic analyses are virtually identical (as expected), and they compare quite well with the results from the direct steady-state dynamics analysis (Figure 9.1.7–4 and Figure 9.1.7–5). The sound pressure level as computed in these analyses is very high since no damping is considered (neither structural nor impedance-like at the structural-acoustic interface).

Figure 9.1.7–6 shows the noise level for the cabin-air model when damping is considered. Since the mode-based steady-state dynamics analysis would not take into account the forms of damping considered here, only results from the subspace projection and direct analyses are computed. The results compare quite well. Notably, the subspace projection analysis is approximately 20 times faster than the direct analysis. While the sound pressure level is significantly lower in this analysis when compared to the analysis with no damping, the level is still very high. This suggests that the damping considered in this model is still quite low. Impedance-type damping is considered only on the cabin floor; thus, 100% of the acoustic waves would be reflected from the cabin walls, roof, doors, and windows to produce a higher sound pressure level.

Figure 9.1.7–7 shows the real part of the acoustic pressure in the cabin volume at 120 Hz for both the plane wave (left) and diffuse field (right) excitations. The same damping is used as in the previous case—an impedance defined on the cabin floor. The same source location, a point on the radiator, and the same standoff, a point on the bulkhead, are used for both excitations. These figures illustrate the typical effect of the diffuse excitation option—it produces a more even distribution of pressure in the cabin. This occurs because the incident pressure is divided into many waves, striking the bulkhead from different directions and resulting in a degree of cancellation and averaging of the pressure load on the surface.

The results shown are obtained using the direct steady-state dynamics procedure; using the subspace projection steady-state dynamics procedure, the results appear nearly identical.

The frequency analysis performed on the cabin-air substructure generates eigenvalues identical to those from the model without substructures. Moreover, the eigenmodes obtained from the regular non-substructure model (Figure 9.1.7–8) and those recovered from the substructure model (Figure 9.1.7–9) compare very well (shown here for the air pressure for the 25th eigenmode).

The frequency response obtained for the cabin-air-chassis model is shown in Figure 9.1.7–10 and Figure 9.1.7–11. Given the size of the model, the direct steady-state dynamics analysis is computationally less efficient and, thus, is not performed. In addition to the natural frequency extraction procedure for the whole structure, a frequency analysis is performed on the equivalent cabin-air-chassis model using two substructures. While the eigenfrequencies are not identical to those obtained from the regular non-substructure model, the differences are quite small for the range of interest, as shown in Figure 9.1.7–12. Once the substructures are generated, the analysis to extract eigenfrequencies from the two-element substructure model is hundreds of times faster than the analysis to extract them from the regular non-substructure model.

The mode-based and the subspace projection steady-state dynamics procedures in Abaqus demonstrate significant improvements in computational efficiency when compared to the direct steady-state dynamics approach. When damping is small or if it can be well approximated using modal damping coefficients, the mode-based procedures are extremely efficient. When damping is more complex, the subspace projection method also demonstrates significant computational advantage in comparison with the direct-integration approach.

The use of substructures is also demonstrated to produce significant gains in computational efficiency. The reduction of the acoustic volume and of its bounding structure to a substructure has clear advantages. The low-dimensional coupled acoustic-structural substructures are very computationally efficient, and the data for the acoustic response inside the substructure can be recovered when the global analysis is completed.

Input files

tr_acous_cabin_mode.inp	Mode-based and subspace projection steady-state dynamic analysis of the cabin-air model without damping.
tr_acous_cabin_mode_ams.inp	Mode-based steady-state dynamic analysis of the cabin-air model without damping and using Abaqus/AMS.
tr_acous_cabin_direct.inp	Direct steady-state dynamic analysis of the cabin-air model without damping.
tr_acous_cabin_sp_impedance.inp	Subspace projection steady-state dynamic analysis of the cabin-air model with damping.
tr_acous_cabin_direct_impedance.inp	Direct steady-state dynamic analysis of the cabin-air model with damping.
tr_acous_cabin_subspace_bulkhead.inp	Subspace projection steady-state dynamic analysis of the cabin-air model with damping and incident wave excitation on the bulkhead.

tr_acous_cabin_direct_bulkhead.inp	Direct steady-state dynamic analysis of the cabin-air model with damping and incident wave excitation on the bulkhead.
tr_acous_cabin_gen.inp	Cabin-air coupled substructure generation for the second model.
tr_acous_cabin_sub_freq.inp	Frequency analysis of the cabin-air model using one substructure.
tr_acous_cabin_chassis_gen.inp	Cabin-air substructure generation analysis for the fourth model.
tr_acous_chassis_gen.inp	Chassis substructure generation analysis for the fourth model.
tr_acous_cabin_chassis_sub.inp	Frequency analysis of the cabin-air-chassis model using two substructures.
tr_materials_acous.inp	All material definitions.
tr_cabin_air_w.inp	Interior air model.
tr_acous_chassis_coup.inp	Coupling definitions for the chassis.
tr_cabin_elements.inp	Element definitions for the cabin.
tr_cabin_elsets.inp	Element set definitions for the cabin.
tr_cabin_nodes.inp	Node definitions for the cabin.
tr_cabin_nsets.inp	Node set definitions for the cabin.
tr_cabin_sections.inp	Section definitions for the cabin.
tr_parameters_inphase.inp	Parameter definitions.
tr_parameters.inp	Parameter definitions.
tr_all_nodes.inp	All node definitions.
tr_cabin_elts.inp	Element definitions for the cabin.
tr_cabin_coup_steer_col.inp	Coupling definitions.
tr_cabin_mpc.inp	*MPC definitions for the cabin.
tr_seat_elts.inp	Element definitions for the seat.
tr_seat_coup.inp	Coupling definitions for the seat.
tr_conn_seat.inp	Connector definitions for the seat.
tr_door_left_elts.inp	Element definitions for the left door.
tr_door_left_coup.inp	Coupling definitions for the left door.
tr_door_left_mpc.inp	*MPC definitions for the left door.
tr_conn_door_left_nobehav.inp	Connector definitions for the left door.
tr_door_right_elts.inp	Element definitions for the right door.
tr_door_right_coup.inp	Coupling definitions for the right door.
tr_door_right_mpc.inp	*MPC definitions for the right door.
tr_chassis_elts.inp	Element definitions for the chassis.

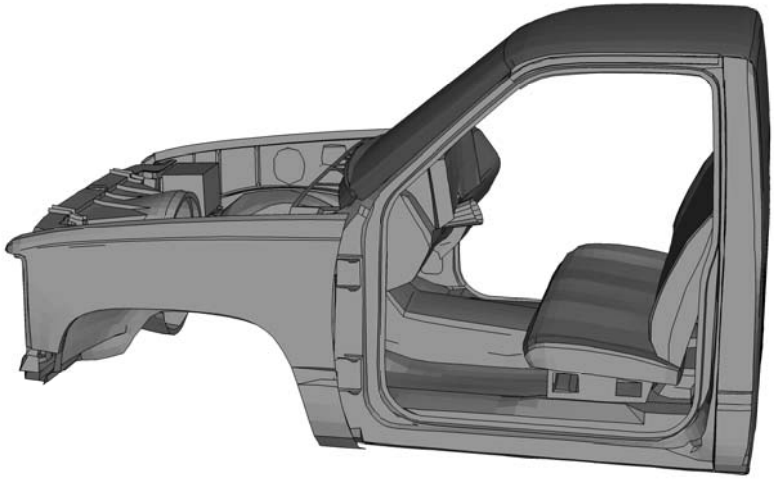

Figure 9.1.7–1 The cabin model (doors removed for clearer illustration).

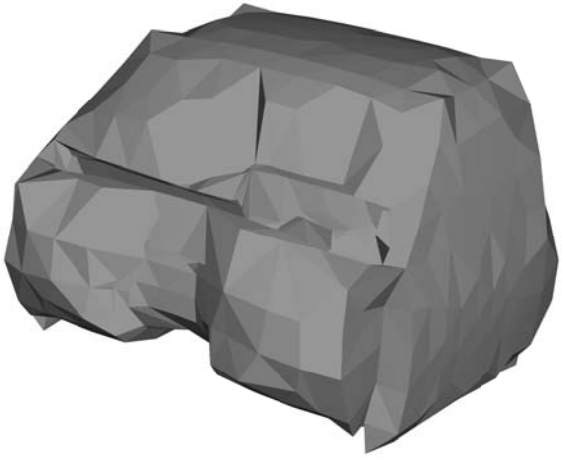

Figure 9.1.7–2 The air mesh inside the cabin.

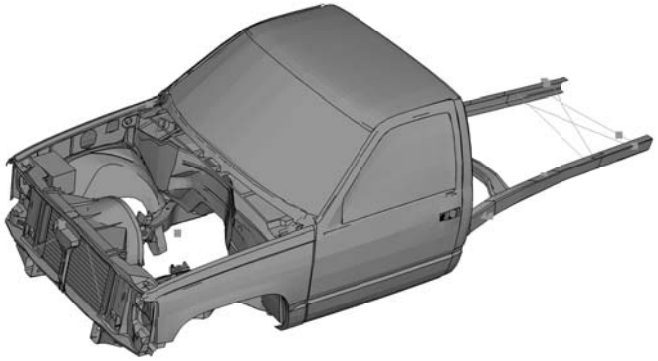

Figure 9.1.7–3 The cabin-air-chassis model.

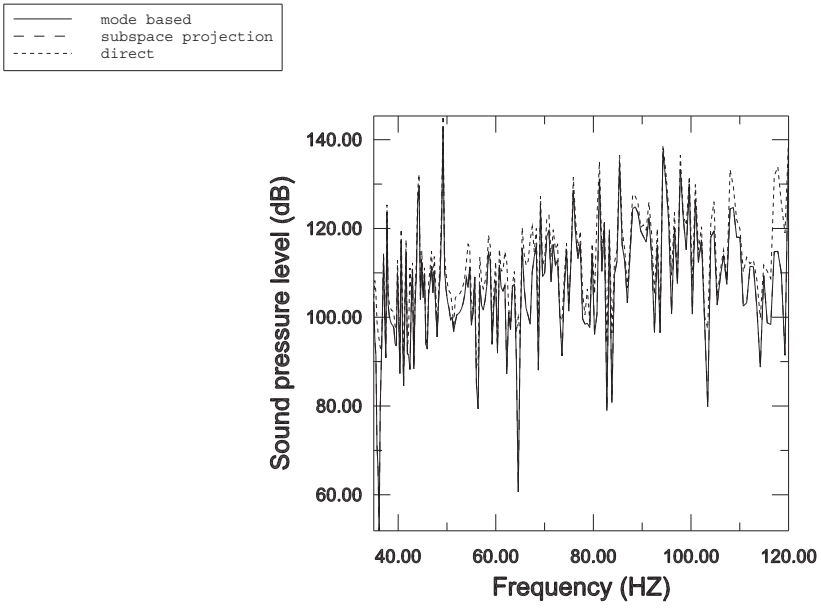

Figure 9.1.7–4 Sound pressure level at the ear position for the cabin-air model (no damping).

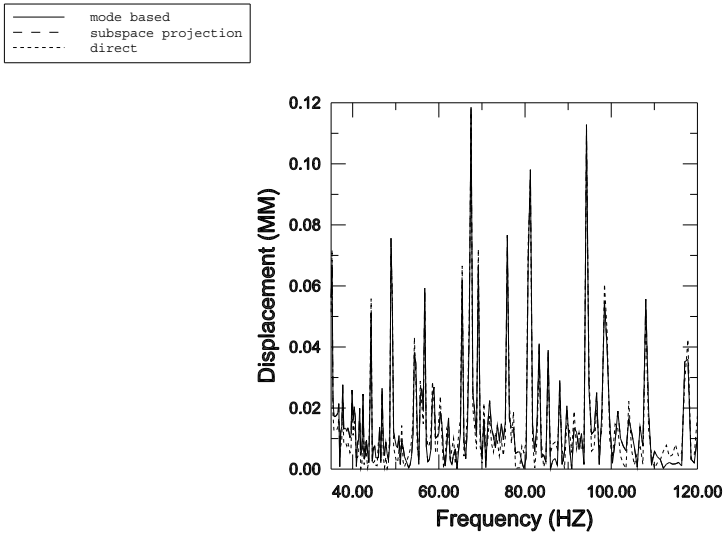

Figure 9.1.7–5 Displacement at one of the harmonically excited cabin floor points (no damping).

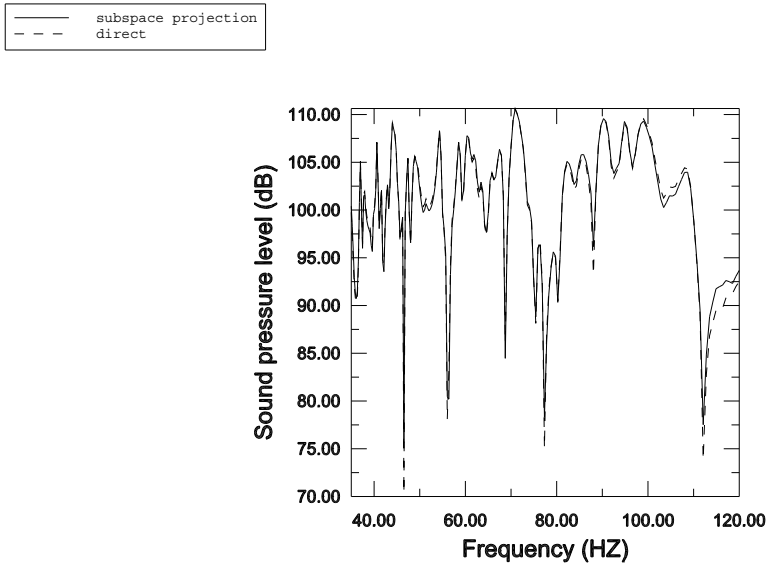

Figure 9.1.7–6 Sound pressure level at the ear position for the cabin-air model when damping is considered.

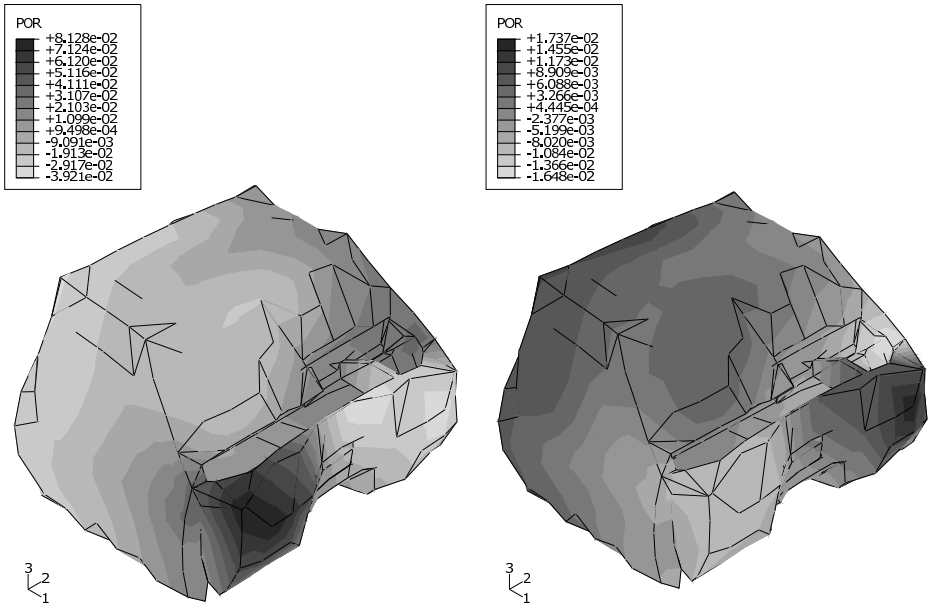

Figure 9.1.7–7 Real part of the acoustic pressure in the cabin-air model when damping is considered and when the lower bulkhead is excited with an incident pressure field (planar wave case, left; diffuse field case, right).

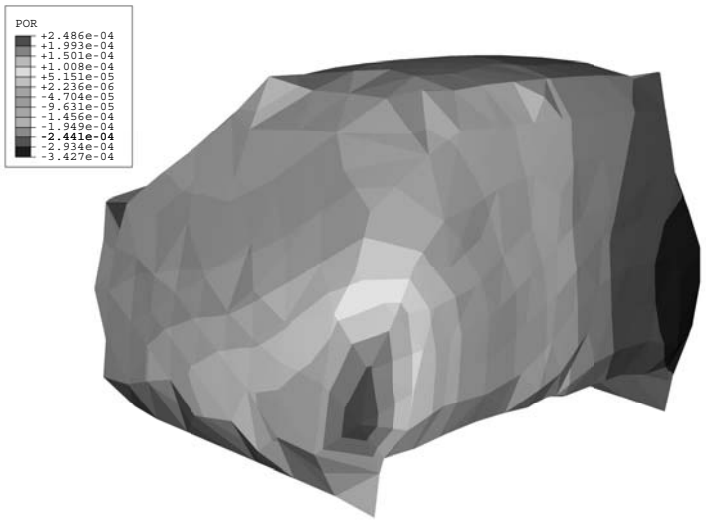

Figure 9.1.7–8 Air pressure for the 25th eigenmode (35.131 Hz) from the cabin-air model.

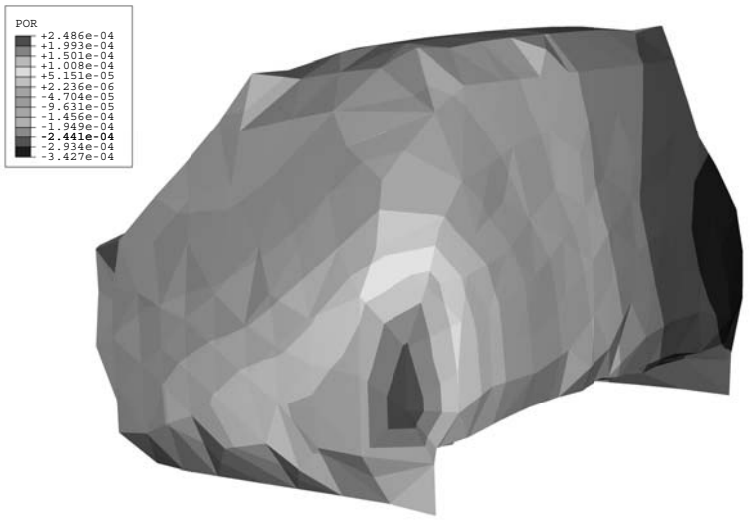

Figure 9.1.7–9 Air pressure for the 25th eigenmode (35.131 Hz) from the cabin-air substructure model.

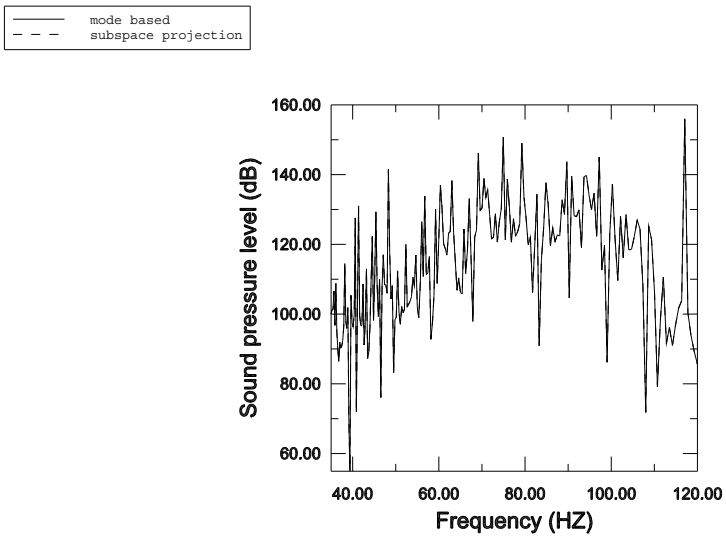

Figure 9.1.7–10 Sound pressure level at ear level from the cabin-air-chassis model (no damping).

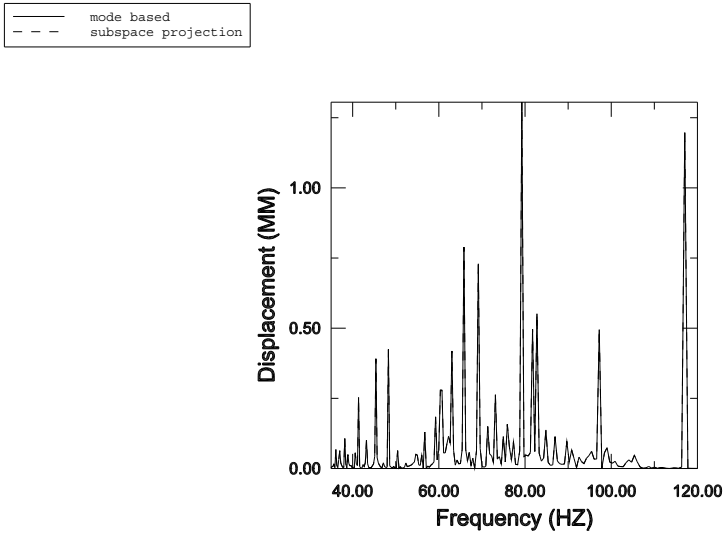

Figure 9.1.7–11 Displacement at one of the cabin floor points for the cabin-air-chassis model (no damping).

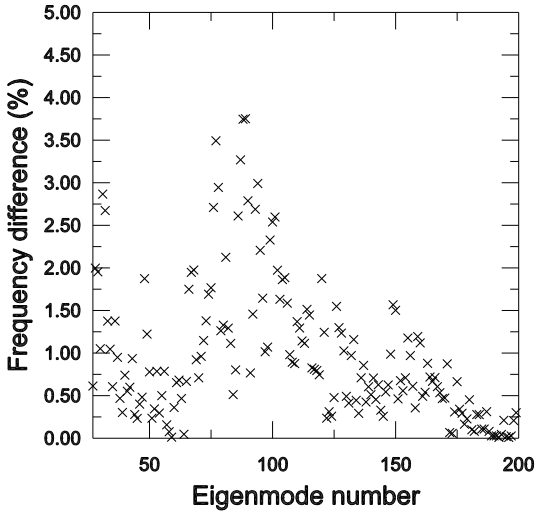

Figure 9.1.7–12 Eigenfrequency differences between the cabin-air-chassis model and the equivalent model with substructures for the range of interest (35–120 Hz).

9.1.8 LONG-DURATION RESPONSE OF A SUBMERGED CYLINDER TO AN UNDERWATER EXPLOSION

Products: Abaqus/Standard Abaqus/Explicit

This example demonstrates how Abaqus can be used to predict the long-duration response of submerged structures that experience loading by a wave resulting from an underwater explosion (UNDEX).

An emphasis on structural dynamic motions naturally leads to the use of beams to model the structure, rather than solid or shell elements. This class of problem is characterized by structural dynamic motions at speeds much slower than the acoustic wave speed in the fluid, so that the fluid can be modeled as an incompressible medium. The implication of modeling the fluid in this manner is to reduce its effect on the structure to an "added mass" on the beam.

The spherical pressure waves associated with an underwater explosion (UNDEX) event are characterized by two distinct phases. The first, very short, phase is the initial wave produced by the detonation. It involves a very steep rise to a characteristic pressure value, followed by a more gradual decay. In the second phase of the loading the gas produced by the explosive expands to a maximum volume, at which the pressure of the surrounding fluid forces it back upon itself. At some minimum volume the gas and fluid system emits another pressure pulse, and the gas bubble expands again. This process may repeat many times, causing several pressure pulses. As the gas bubble oscillates, it also acts under the effects of buoyancy, causing an unsteady motion opposite to the force of gravity.

Problem and geometry description

This problem involves a structural-dynamics model of a submerged submarine under athwartships attack from an underwater explosion. The ship is 100 m in length and 50 m below the surface; and the detonation point of the charge is centered along the ship's length, 15 m to one side and 15 m below the ship. The response of the ship to the initial direct and reflected shock waves as well as to the first few bubble pulses is of interest, so dynamic simulations are carried out to 5 seconds.

Model

The model is made of 100 B31 beam elements, arrayed along a line. Their (uniform) section properties are defined using a general beam section. The structure has an overall length of 50 m. Point mass elements of 10000 kg are defined at each node to simulate the effect of internal equipment on the beam structural dynamics. The effect of the entrained fluid is simulated using beams with additional inertia, with which a fluid mass density of 1025 kg/m^3, an outside radius of 5 m, and a fluid drag coefficient of 1.0 are specified. Structural damping is specified using a material damping definition. No additional acoustic fluid elements or absorbing boundary conditions are required.

Fluid-structure coupling and shock wave loading

The loading specification for this problem includes descriptions of the explosive charge, the fluid medium in which the wave propagates to the structure, and the geometry of the charge with respect to the structure.

In Abaqus the time histories of pressure, its derivatives, and the motion of the explosive gas bubble are defined using the Geers-Hunter model. This model is invoked using the bubble-type amplitude. Under this option material properties of the explosive, its mass, its distance from the free surface, and some other control parameters are specified. The data on this option are used to govern a separate bubble dynamics time integration operation, performed as part of the preprocessing. Parameters defined on this option do not affect the rest of the analysis. Here a charge of 100 kg is used, with model parameters set to suppress wave loss effects within the bubble simulation. An initial depth of 65 m is specified: this affects the oscillation of the gas bubble and the duration of the bubble dynamics, since the solution naturally terminates when the bubble reaches the free surface. In this analysis, however, the bubble simulation time is cut off at 0.6 seconds. The bubble migration is defined to be along the z-axis. Default values for the bubble dynamics time integration parameters are used.

The actual loads on the structure are defined using the incident wave and the associated incident wave reflection. The incident wave defines the distributed time-varying loads within an analysis step on the structural surface, due to the specified parameters. Only the surface defined for the beam elements and the reference load magnitude need to be indicated, as is the case for most distributed loads in Abaqus. The incident wave reflection defines any planes outside the computational domain for the purpose of calculating additional incident wave loads due to reflections. Here a "soft" (zero total pressure) reflecting plane is defined, located 65 m from the original position of the source and oriented normal to the z-axis. The original position of the source point is defined as (50, 15, −15), and the standoff point is defined as (50, 3.536, −3.536). The fluid properties, used for propagation of the wave across the structure, are given as mass density ρ_f = 1025 kg/m^3 and bulk modulus K_f = 2.30635 GPa.

Results and discussion

The model for this UNDEX example has a total of 606 active degrees of freedom and requires approximately 15 MB of memory and 267 KB of disk space.

Figure 9.1.8–1 shows the time history of vertical displacement (V3) for the center node of the structure using a logarithmic time axis. This curve clearly shows the initial shock-induced velocity peak, the velocity peak caused by the reflected path, and the decaying periodic response associated with a structural motion after the loading ceases at t = 0.6. The response curve clearly illustrates that there is a rigid body translation of the cylinder, due to the velocity induced by the initial shocks. The peaks due to the direct and reflected shocks are of the same sign, since the reflected wave, with a negative sign, is traveling in the opposite vertical direction from the direct wave.

Figure 9.1.8–2 shows the strain along the axis of the beam for the section points oriented along the 1-direction of the section. The 1-direction is also the y-direction in the global system. The curves suggest that a dominant mode of vibration occurs at about 2.1 Hz (based on an estimated period of 0.48 seconds). Figure 9.1.8–3 shows the axial strain for section points oriented in the section 2-direction, or the global z-direction. Again, the two peaks corresponding to the incident shocks are evident, followed by the decaying oscillation at roughly 2.1 Hz.

Input files

iw_exa_whip_std.inp	Abaqus/Standard analysis of a submerged cylinder subjected to an UNDEX shock wave.
iw_exa_whip_xpl.inp	Abaqus/Explicit analysis of a submerged cylinder subjected to an UNDEX shock wave.

Reference

- Hicks, A. N., "The Theory of Explosion Induced Hull Whipping," Naval Construction Research Establishment, Dunfermline, Fife, Scotland, Report NCRE/R579, March 1972.

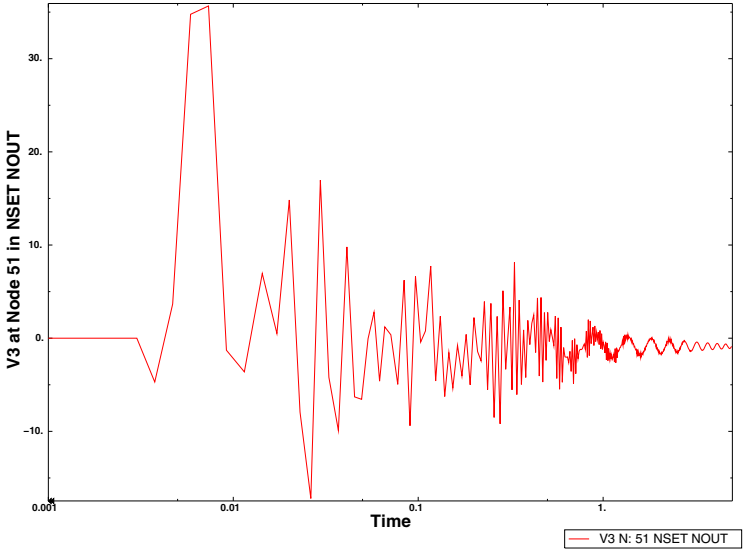

Figure 9.1.8–1 Vertical velocity at ship midpoint.

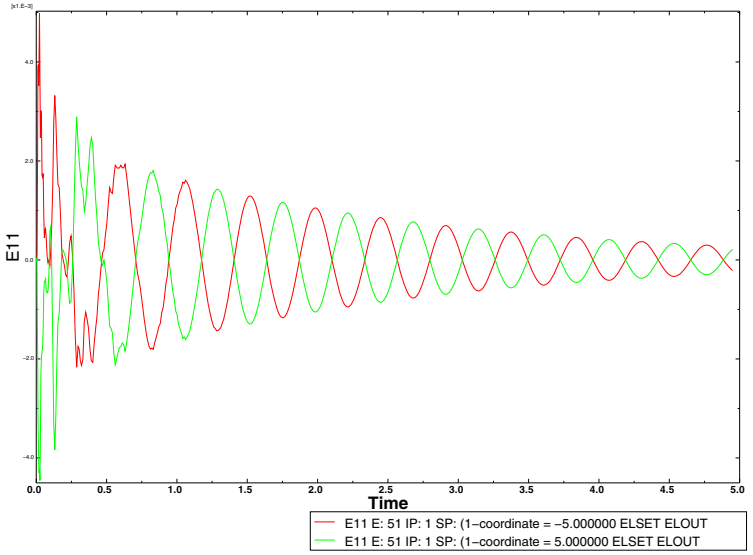

Figure 9.1.8–2 Strain at horizontal extrema at ship midpoint.

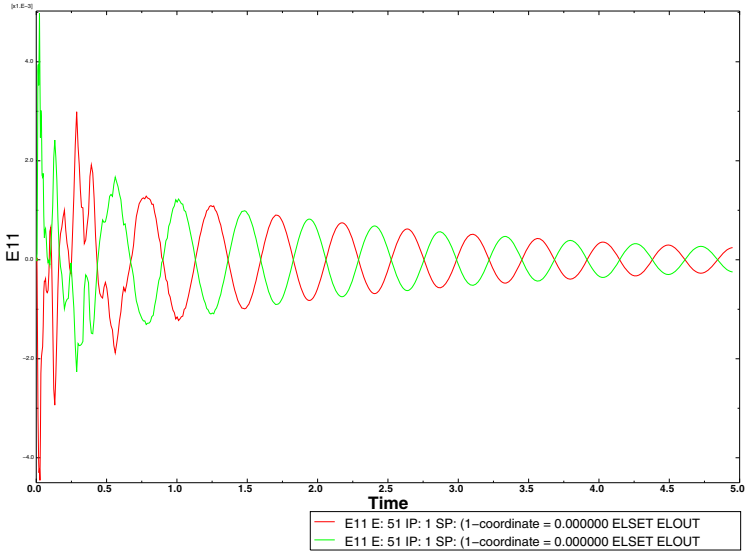

Figure 9.1.8–3 Strain at vertical extrema at ship midpoint.

9.1.9 DEFORMATION OF A SANDWICH PLATE UNDER CONWEP BLAST LOADING

Product: Abaqus/Explicit

Objectives

This example shows how to build better structures that resist blast loads by using the blast loading capability in Abaqus/Explicit.

The following Abaqus features are demonstrated:

- applying CONWEP blast loading,
- comparing computational results using Abaqus/Explicit and experimental measurements of deformation of sandwich structures under blast loads, and
- demonstrating a generic example of a nonlinear analysis of a sandwich structure.

Application description

Modern structural designs can be used to protect various systems that are vulnerable to large blast loads. Sandwich structures are a particular class of modern structures that could be explored for such applications.

Geometry

Two models are used in this example. One model is the sandwich plate structure described by Dharmasena et al. (2008) and shown in Figure 9.1.9–1. The sandwich structure consists of a square honeycomb core with vertical webs welded to top and bottom plates. The dimensions of the overall sandwich plate structure are 610 × 610 × 61 mm. The sandwich structure lies in the X–Y plane, while the blast source is 100 mm vertically above (along the z-direction) the center of the top plate of the sandwich structure. The top and bottom plates are 5 mm thick, and the square honeycomb core webs are 0.76 mm thick. The spacing between the honeycomb webs is 30.5 mm measured from the midplane.

The second model is a solid plate, which was chosen for comparison with Dharmasena et al.

Materials

The top and bottom plates and honeycomb core of the sandwich structure and the solid plate are all made of a high ductility stainless steel alloy (Al-6XN) comprised of 49% Fe, 24% Ni, 21% Cr, and 6% Mo by weight as described by Nahshon et al. (2007).

Initial conditions

All structures are initially at their undeformed state at 273 K temperature.

Boundary conditions and loading

All the edges of the sandwich structure and the solid plate are fixed. One-quarter of the full plate is modeled, assuming symmetry of the solution.

Interactions

In the sandwich structure the honeycomb web is welded to the inner surfaces of the plates.

Abaqus modeling approaches and simulation techniques

This example demonstrates the usage of CONWEP blast loading using Abaqus/Explicit. This example was chosen based on experiments reported by Dharmasena et al. (2008) that discuss the deformation of a particular sandwich structure and an equivalent solid plate subjected to CONWEP blast loads due to 1, 2, and 3 kg of TNT. The solid plate with equivalent material is presented as a simple example. The solid plate is modeled using shell elements and three-dimensional continuum elements. Finally, the main problem of interest, the sandwich structure described by Dharmasena et al., is analyzed. A tonne-millimeter-second-kelvin unit system was chosen for all simulations.

Summary of analysis cases

Case 1	Solid plate modeled with S4R shell elements under 1 kg TNT blast load.
Case 2	Solid plate modeled with S4R shell elements under 2 kg TNT blast load.
Case 3	Solid plate modeled with S4R shell elements under 3 kg TNT blast load.
Case 4	Solid plate modeled with C3D8R continuum elements under 1 kg TNT blast load.
Case 5	Solid plate modeled with C3D8R continuum elements under 2 kg TNT blast load.
Case 6	Solid plate modeled with C3D8R continuum elements under 3 kg TNT blast load.
Case 7	Sandwich structure under 1 kg TNT blast load.
Case 8	Sandwich structure under 2 kg TNT blast load.
Case 9	Sandwich structure under 3 kg TNT blast load.

Analysis types

Dynamic analysis using Abaqus/Explicit is performed for all cases. Solutions are computed up to 1.5 milliseconds, where no further permanent deformation is observed for all load values.

Material model

The mechanical properties of the steel alloy as described in Nahshon et al. (2007) are specified as follows: Young's modulus of 1.61×10^5 MPa, Poisson's ratio of 0.35, density of 7.85×10^{-9} metric tons/mm^3, and coefficient of expansion of 452×10^6 Nmm/metric tons·K.

A Johnson-Cook model is used to model the elastic-plastic behavior with the following coefficients and constants: $A = 400$ MPa, $B = 1500$ MPa, $C = 0.045$, $n = 0.4$, $m = 1.2$, and $\dot{\varepsilon_0} = 0.001$ s^{-1}. The transition temperature is 293 K, and the melting temperature is 1800 K.

Initial conditions

The temperature is initialized to 273 K for all nodes in each model.

Boundary conditions

Symmetry behavior is assumed. Only one-quarter of the structure is modeled for all cases, with the center of the plate positioned at the origin of the *X*–*Y* plane. The boundaries at $X = 305$ mm and $Y = 305$ mm are fixed for all degrees of motion (ENCASTRE). Symmetry conditions about the *x*-axis (XSYMM) are applied at the plane $X = 0$. Similarly, symmetry conditions about the *y*-axis (YSYMM) are applied at the plane $Y = 0$.

Loading

The CONWEP blast load is applied on the top surface of the plate. The source of the blast is at a standoff distance of 100 mm vertically above the center of the top surface of the plate. The property of the blast load is specified using the incident wave interaction property and the CONWEP charge property at the model level and the incident wave interaction at the step level.

Analysis steps

Each analysis consists of a single dynamic explicit step.

Output requests

Translational degrees of freedom (UT) are requested at the center of the plate.

Results and discussion

The center displacement after 1.5 milliseconds was monitored to compare each case with experimental results. Single and double precision job execution gave similar results for all cases.

The animation of the deformed plate over the entire time period of 1.5 milliseconds shows large deformations at the center. The plate stabilizes after a few oscillations. Comparison of the total work done history (ALLWK) and the total plastic dissipation history (ALLPD) indicates that most of the work done by the blast load is dissipated in plastic deformation.

Cases 1–3: Solid plate with shell elements

The solid plate model is modeled with shell elements and is subjected to CONWEP blast loading using different charge masses.

Mesh design

The plate surface is discretized using 31 × 31 S4R elements with nine integration points through the thickness of each element.

Boundary conditions

All degrees of freedom including the rotational degrees of freedom are fixed at the $X = L$ and $Y = L$ edges boundaries, where $L = 305$ mm. Symmetry boundary conditions (XSYMM) are applied at the $X = 0$ edge, and symmetry boundary conditions (YSYMM) are applied at the $Y = 0$ edge.

Loading

1, 2, and 3 kg TNT loads are used in Cases 1, 2, and 3, respectively. The blast source is kept at a standoff distance of 100 mm from the midsection of the shell elements.

Results and discussion

The artificial energy history (ALLAE) is significantly lower than the total internal energy (ALLIE), indicating that the solution is trustworthy with minimal artificial effects.

Cases 4–6: Solid plate with 3D continuum elements

The solid plate is modeled with three-dimensional continuum elements and is subjected to CONWEP blast loading using different charge masses.

Mesh design

The plate surface is discretized using 31 × 31 C3D8R elements with five layers of elements through the thickness of the plate.

Boundary conditions

All degrees of freedom including the rotational degrees of freedom are fixed at the $X = L$ and $Y = L$ face boundaries, where $L = 305$ mm. ***X***-symmetry boundary conditions are applied at the $X = 0$ face, and ***Y***-symmetry boundary conditions are applied at the $Y = 0$ face.

Loading

1, 2, and 3 kg TNT loads are used in Cases 4, 5, and 6, respectively. The blast source is kept at a standoff distance of 100 mm from the top surface of the plate.

Output requests

History output of the center deflection at the top and the bottom surfaces of the plate is requested at every increment.

Results and discussion

Similar behavior using C3D8R elements was observed as that observed using S4R elements. The top surface center deflection and the bottom surface center deflection were quite close to each other. The mean of the two values was used to compare the midsection deflection of the solid plate.

Cases 7–9: Sandwich plate structure

The sandwich plate structure is modeled using three-dimensional continuum elements for the top and bottom plates and shell elements for the square honeycomb core and is subjected to CONWEP blast loading using different charge masses.

Mesh design

The plate surface is discretized using 31×31 C3D8R elements with five layers of elements through the thickness of the plate. The honeycomb core is meshed using 30 layers of S4R shell elements along the height of the core with five integration points through their thickness.

Boundary conditions

All degrees of freedom including the rotational degrees of freedom are fixed at the $X = L$ and $Y = L$ face boundaries, where $L = 305$ mm. ***X***-symmetry boundary conditions are applied at the $X = 0$ face, and ***Y***-symmetry boundary conditions are applied at the $Y = 0$ face.

Loading

1, 2, and 3 kg TNT loads are used in Cases 7, 8, and 9, respectively. The blast source was kept at a standoff distance of 100 mm from the top surface of the plate.

Constraints

The edges of the shell elements at the top and bottom of the core are attached to the inner surfaces of the top plate and the bottom plate, respectively, using tie constraints. The shell element edges form the node-based slave surface to the master plate surfaces. The tie constraint is defined without allowing any adjustments and using the node set of the edges to identify the nodes on the slave surface that will be tied to the master surface.

Interactions

General contact is specified at the step level, including all exterior surface contact interactions.

Output requests

History output of the center deflection at the top and the bottom surfaces of the plate is requested at every increment.

Results and discussion

The analysis demonstrates significant buckling of the honeycomb webs involving self-contact near the center of the plate, as shown in Figure 9.1.9–2 for the three loading cases. Figure 9.1.9–3 shows the internal view for the 1 kg TNT blast charge case, revealing the deformation of the honeycomb core. It also confirms that tie constraints using node-based surfaces capture appropriately the weld between the webs and the inner surfaces of the plates.

Additional cases

Studies of similar structures using different parameters have been documented in the literature. Alternative material models and loading cases are mentioned here to provide examples for additional analyses. Different material models have been used to simulate the material behavior under such loads. The material model for the following atypical strain-rate hardening (Dharmasena et al., 2008) can be used for simulation of the above cases with user subroutine **VUHARD**:

$$\sigma = \begin{cases} E\varepsilon, & \varepsilon \le \frac{\sigma_Y}{E}\left(1+\left(\frac{\dot{\varepsilon_p}}{\dot{\varepsilon_0}}\right)^m\right) \\ \sigma_Y\left(1+\left(\frac{\dot{\varepsilon_p}}{\dot{\varepsilon_0}}\right)^m\right)+E_t\left(\varepsilon-\frac{\sigma_Y}{E}\left(1+\left(\frac{\dot{\varepsilon_p}}{\dot{\varepsilon_0}}\right)^m\right)\right), & \varepsilon > \frac{\sigma_Y}{E}\left(1+\left(\frac{\dot{\varepsilon_p}}{\dot{\varepsilon_0}}\right)^m\right) \end{cases}$$

The material properties used by Dharmasena et al. and Rathbun et al. (2006) are as follows: Young's modulus of $E = 2.00 \times 10^5$ MPa, Poisson's ratio of $\nu = 0.30$, density of $\rho = 7.85 \times 10^{-9}$ metric tons/mm^3, yield stress of $\sigma_Y = 300.0$ MPa, tangent modulus of $E_t = 2.00 \times 10^3$ MPa, $\dot{\varepsilon_0} = 4916$ s^{-1}, and $m = 0.154$.

In addition, the following approximate loading, which was applied on the sandwich structure described by Dharmasena et al., can be implemented with user subroutine **VDLOAD**:

$$p(t) = (p_s - p_a)\left(\frac{t_d - t}{t_d - t_a}\right) e^{-\left(\frac{t-t_a}{\theta}\right)} e^{-\left(\frac{d}{d_0}\right)^2},$$

where p_s is the shock wave pressure (360 MPa), p_a is the ambient pressure (0), t_d is the time when the shock decays to a value close to zero, t_a is the shock arrival time, d is the distance from the center of the plate (in this example, also the origin), and d_0 is a reference distance of 120 mm. All variable values are chosen based on Dharmasena et al.

Discussion of results and comparison of cases

The Abaqus/Explicit results for the solid plate using the Johnson-Cook model for the steel alloy (Cases 1–6) are shown in Table 9.1.9–1. These results compare well with the experimental results

reported by Dharmasena et al. (2008), shown in Table 9.1.9–2, for both the shell and continuum elements with CONWEP blast loading. The Abaqus/Explicit results for the sandwich structure compare within reasonable error with the experimental results. The simulation and experimental results are presented graphically in Figure 9.1.9–4. The solution differs significantly for higher loads, which Dharmasena et al. attribute to boundary conditions. At higher loads, it is likely that the edges of the sandwich panel used in the test arrangement were actually more flexible than the clamped condition used in the Abaqus model, causing differences between the numerical and experimental results. Differences in the results could also be due to debonding of the honeycomb core webs from the top and bottom plates in the experimental setup.

The sandwich structure was modeled for the same CONWEP loading with a different material model. An isotropic bilinear model with an atypical strain-rate hardening used user subroutine **VUHARD** with the material properties as described in "Additional cases" above. The displacements, shown in Table 9.1.9–3, were found to be much higher than the Johnson-Cook model and the experimental results, probably due to lower yield stress values.

In addition, the solid plate and the sandwich structure were modeled with the Johnson-Cook material model with an approximate loading, as described in "Additional cases" above, with user subroutine **VDLOAD**. The displacements, shown in Table 9.1.9–4, were found to be lower than the CONWEP blast loading and the experimental results, probably because less work was done on the model by the approximate load over the total time.

Input files

Cases 1–3 Solid plate with shell elements

exa_aco_conwep_sol_1kg.inp	Solid plate model with S4R elements and 1 kg TNT blast load.
exa_aco_conwep_sol_2kg.inp	Solid plate model with S4R elements and 2 kg TNT blast load.
exa_aco_conwep_sol_3kg.inp	Solid plate model with S4R elements and 3 kg TNT blast load.

Cases 4–6 Solid plate with continuum elements

exa_aco_conwep_spl_1kg.inp	Solid plate model with C3D8R elements and 1 kg TNT blast load.
exa_aco_conwep_spl_2kg.inp	Solid plate model with C3D8R elements and 2 kg TNT blast load.
exa_aco_conwep_spl_3kg.inp	Solid plate model with C3D8R elements and 3 kg TNT blast load.

Cases 7–9 Sandwich structure

exa_aco_conwep_snd_1kg.inp	Sandwich structure model with 1 kg TNT blast load.
exa_aco_conwep_snd_2kg.inp	Sandwich structure model with 2 kg TNT blast load.
exa_aco_conwep_snd_3kg.inp	Sandwich structure model with 3 kg TNT blast load.

Additional cases

exa_aco_conwep_snd_vuhard_1kg.inp	Sandwich structure model with user-defined material model and 1 kg TNT blast load.
exa_blast_vuhard.f	User subroutine **VUHARD** with user-defined strain-rate hardening model.
exa_aco_conwep_sol_vdload_1kg.inp	Solid plate model with user-defined approximate loading equivalent to 1 kg TNT blast.
exa_aco_conwep_snd_vdload_1kg.inp	Sandwich structure model with user-defined approximate loading equivalent to 1 kg TNT blast.
exa_blast_vdload.f	User subroutine **VDLOAD** with the approximate loading equivalent to 1 kg TNT CONWEP blast load.

References

Abaqus Analysis User's Guide

- "Acoustic, shock, and coupled acoustic-structural analysis," Section 6.10.1 of the Abaqus Analysis User's Guide
- "Acoustic and shock loads," Section 34.4.6 of the Abaqus Analysis User's Guide

Abaqus Keywords Reference Guide

- *CONWEP CHARGE PROPERTY
- *INCIDENT WAVE INTERACTION
- *INCIDENT WAVE INTERACTION PROPERTY

Abaqus Verification Guide

- "CONWEP blast loading pressures," Section 3.8.6 of the Abaqus Verification Guide
- "Blast loading of a circular plate using the CONWEP model," Section 3.8.7 of the Abaqus Verification Guide

Other

- Dharmasena, K. P., H. N. G. Wadley, Z. Xue, and J. W. Hutchinson, "Mechanical Response of Metallic Honeycomb Sandwich Panel Structures to High-Intensity Dynamic Loading," Journal of Impact Engineering, vol. 35, pp. 1063–1074, 2008.
- Nahshon, K., M. G. Pontin, A. G. Evans, J. W. Hutchinson, and F. W. Zok, "Dynamic Shear Rupture of Steel Plates," Journal of Mechanics of Materials and Structures, vol. 2–10, pp. 2049–2066, December 2007.
- Rathbun, H. J., D. D. Radford, Z. Xue, M. Y. Hu, J. Yang, V. Deshpande, N. A. Fleck, J. W. Hutchinson, F. W. Zok, and A. G. Evans, "Dynamic Shear Rupture of Steel Plates," International Journal of Solids and Structures, vol. 43, pp. 1746–1763, 2006.

Table 9.1.9–1 Center deflection computed by Abaqus/Explicit for Cases 1–9.

Model	Charge mass	Center deflection (mm)		
		Top surface	Midsection	Bottom surface
Solid plate (S4R)	1 kg TNT	–	48.54	–
	2 kg TNT	–	88.38	–
	3 kg TNT	–	109.75	–
Solid plate (C3D8R)	1 kg TNT	–	47.09	–
	2 kg TNT	–	85.72	–
	3 kg TNT	–	108.38	–
Sandwich structure	1 kg TNT	69.15	–	26.15
	2 kg TNT	110.68	–	66.14
	3 kg TNT	141.37	–	96.63

Table 9.1.9–2 Center deflection measurements from experiments.

Model	Charge mass	Center deflection (mm)		
		Top surface	Midsection	Bottom surface
Solid plate	1 kg TNT	–	37.65	–
	2 kg TNT	–	71.37	–
	3 kg TNT	–	132.94	–
Sandwich structure	1 kg TNT	47.06	–	15.29
	2 kg TNT	98.82	–	53.73
	3 kg TNT	158.04	–	127.45

Table 9.1.9–3 Center deflection computed by Abaqus/Explicit with user subroutine **VUHARD**.

Model	Charge mass	Center deflection of top surface (mm)	Center deflection of bottom surface (mm)
Sandwich structure with **VUHARD**	1 kg TNT	96.18	50.74
	2 kg TNT	156.76	114.79
	3 kg TNT	200.03	155.08

Table 9.1.9–4 Center deflection computed by Abaqus/Explicit with user subroutine **VDLOAD**.

Model	Charge mass	Center deflection (mm)		
		Top surface	Midsection	Bottom surface
Solid plate (S4R) with **VDLOAD**	1 kg TNT	–	32.10	–
Sandwich structure with **VDLOAD**	1 kg TNT	36.31	–	18.89

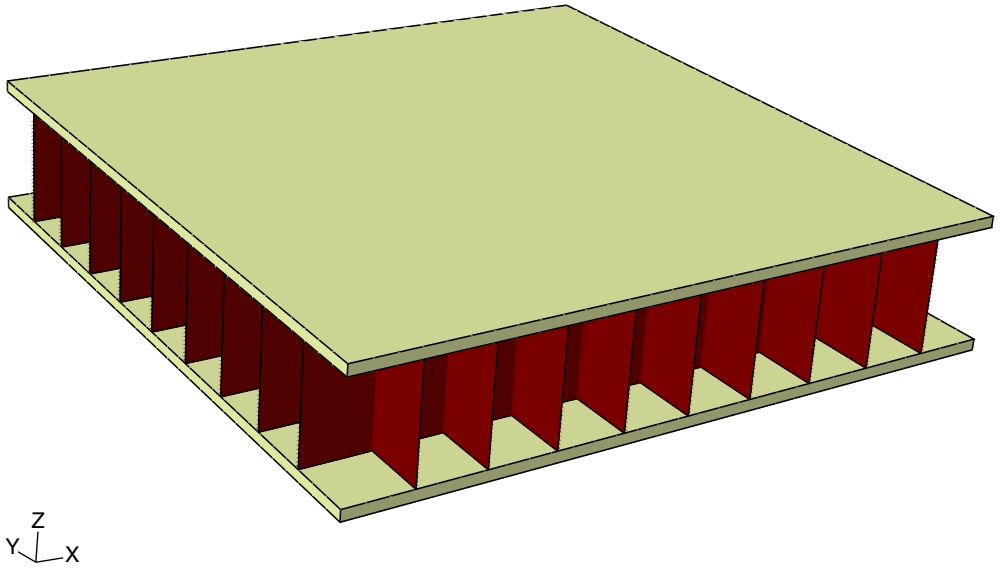

Figure 9.1.9–1 The sandwich structure model.

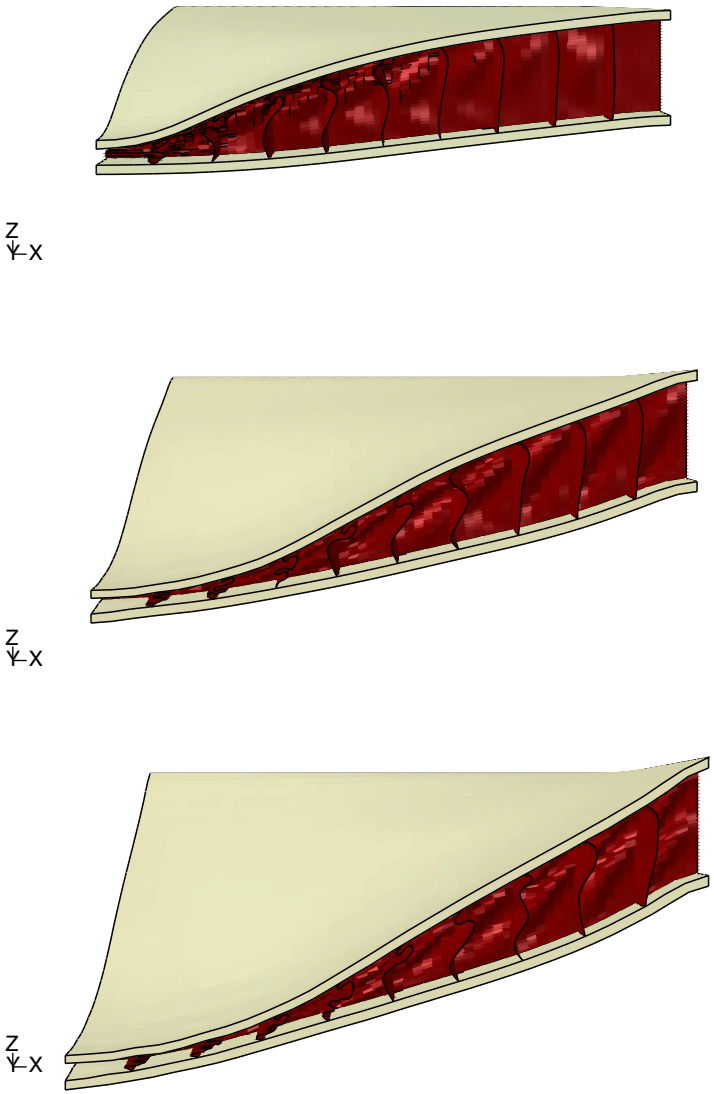

Figure 9.1.9–2 Deformed sandwich structure under CONWEP blast loads due to (from top to bottom) 1, 2, and 3 kg TNT.

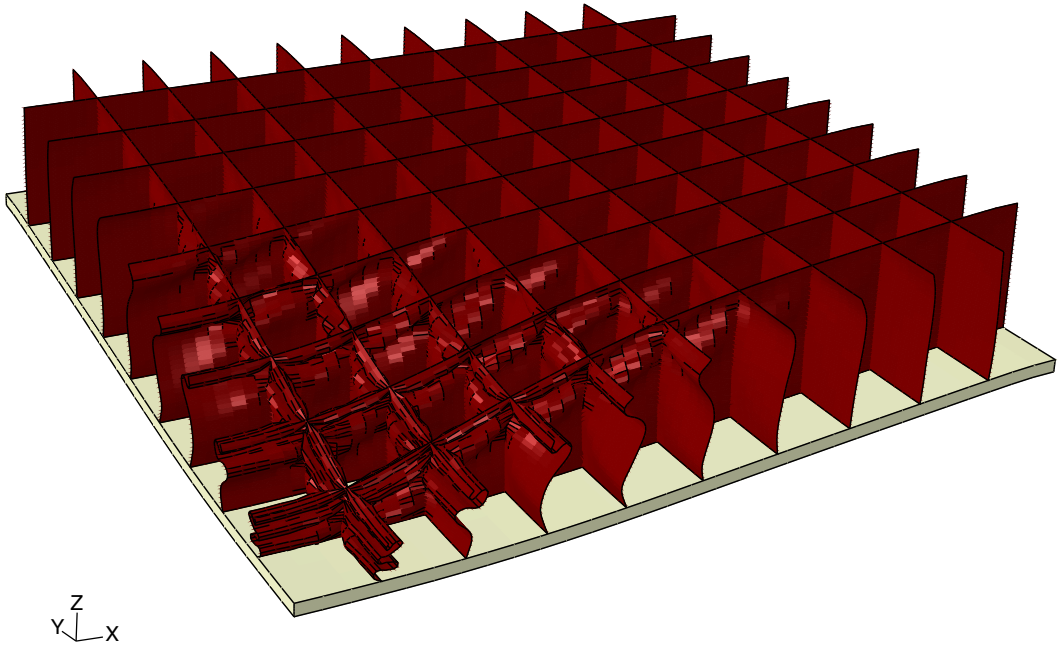

Figure 9.1.9–3 Deformation of the honeycomb core for a CONWEP charge of 1 kg TNT.

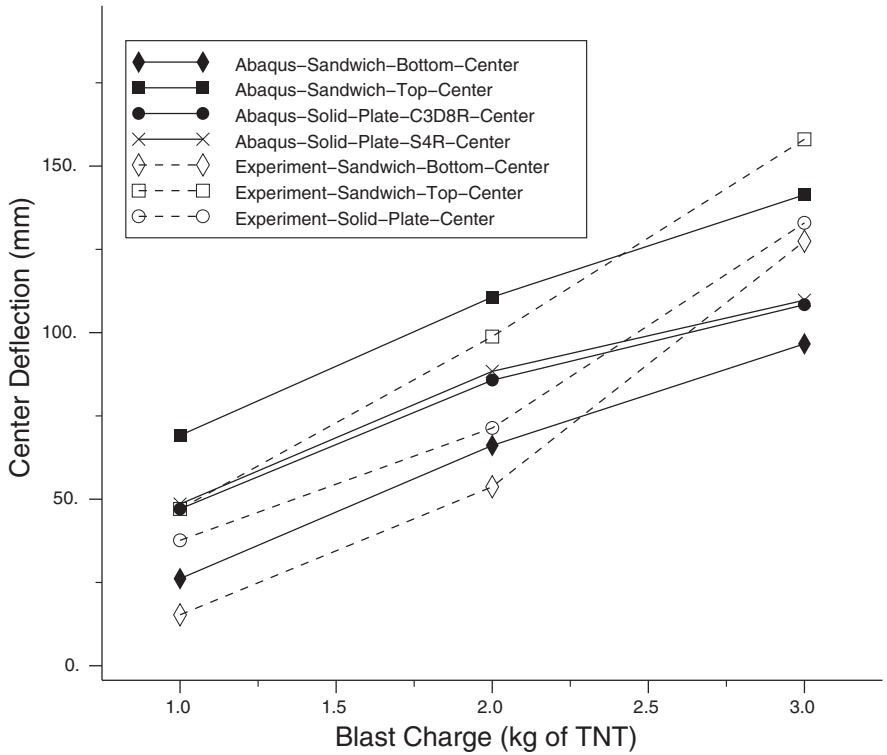

Figure 9.1.9–4 Comparison of center deflection between Abaqus/Explicit and experimental results for different blast charges.

10. Soils Analyses

- “Soils analyses,” Section 10.1

10.1 Soils analyses

- “Plane strain consolidation,” Section 10.1.1
- “Calculation of phreatic surface in an earth dam,” Section 10.1.2
- “Axisymmetric simulation of an oil well,” Section 10.1.3
- “Analysis of a pipeline buried in soil,” Section 10.1.4
- “Hydraulically induced fracture in a wellbore,” Section 10.1.5
- “Permafrost thawing–pipeline interaction,” Section 10.1.6

10.1.1 PLANE STRAIN CONSOLIDATION

Product: Abaqus/Standard

This problem examines a linear, two-dimensional consolidation case: the settlement history of a partially loaded strip of soil.

Most consolidation problems of practical interest are two- or three-dimensional, so that the one-dimensional solutions provided by Terzaghi consolidation theory are useful only as indicators of settlement magnitudes and rates. This particular case is chosen to illustrate two-dimensional consolidation because an exact solution is available (Gibson et al., 1970), thus providing verification of this capability in Abaqus.

Related topics

- "The Terzaghi consolidation problem," Section 1.15.1 of the Abaqus Benchmarks Guide

Geometry and model

The discretization of the semi-infinite, partially loaded strip of soil is shown in Figure 10.1.1–1. The loaded region is half as wide as the depth of the sample. The reduced-integration plane strain element with pore pressure, CPE8RP, is used in this analysis. Reduced integration is almost always recommended when second-order elements are used because it usually gives more accurate results and is less expensive than full integration. No mesh convergence studies have been done, although the reasonable agreement between the numerical results provided by this model and the solution of Gibson et al. (1970) suggests that the model used is adequate—at least for the overall displacement response examined. In an effort to reduce analysis cost while at the same time preserve accuracy, the mesh is graded from six elements through the height, under the load, to one element through the height at the outer boundary of the model, where a single infinite element (type CINPE5R) is used to model the infinite domain. This requires the use of two kinematic constraint features provided by Abaqus. Consider first the displacement degrees of freedom along line AC in Figure 10.1.1–1. The 8-node isoparametric elements used for the analysis allow quadratic variation of displacement along their sides, so the displacements of nodes a and b in elements x and y may be incompatible with the displacement variation along side AC of element z. To avoid this, nodes a and b must be constrained to lie on the parabola defined by the displacements of nodes A, B, and C. The QUADRATIC MPC ("multi-point constraint") is used to enforce this kinematic constraint: it must be used at each node where this constraint is required (see planestrainconsolidation.inp). Pore pressure values are obtained by linear interpolation of values at the corner nodes of an element. When mesh gradation is used, as along line AC in this example, an incompatibility in pore pressure values may result for the same reason given for the displacement incompatibility discussed above. To avoid this, the pore pressure at node B must be constrained to be interpolated linearly from the pore pressure values at A and C. This is done by using the P LINEAR MPC.

The material properties assumed for this analysis are as follows: the Young's modulus is chosen as 690 GPa (10^8 lb/in^2); the Poisson's ratio is 0; the material's permeability is 5.08×10^{-7} m/day (2.0×10^{-5} in/day); and the specific weight of pore fluid is chosen as 272.9 kN/m^3 (1.0 lb/in^3).

The applied load has a magnitude of 3.45 MPa (500 lb/in^2). The strip of soil is assumed to lie on a smooth, impervious base, so the vertical component of displacement is prescribed to be zero on that surface. The left-hand side of the mesh is a symmetry line (no horizontal displacement). The infinite element models the other boundary.

Time stepping

As in the one-dimensional Terzaghi consolidation solution (see "The Terzaghi consolidation problem," Section 1.15.1 of the Abaqus Benchmarks Guide), the problem is run in two steps. In the first transient soils consolidation step, the load is applied and no drainage is allowed across the top surface of the mesh. This one increment step establishes the initial distribution of pore pressures which will be dissipated during the second transient soils consolidation step.

During the second step drainage is allowed to occur through the entire surface of the strip. This is specified by prescribing the pore pressure (degree of freedom 8) at all nodes on this surface (node set **TOP**) to be zero. By default, in a transient soils consolidation step such boundary conditions are applied immediately at the start of the step and then held fixed. Thus, the pore pressures at the surface change suddenly at the start of the second step from their values with no drainage (defined by the first step) to 0.0.

Consolidation is a typical diffusion process: initially the solution variables change rapidly with time, while at the later times more gradual changes in stress and pore pressure are seen. Therefore, an automatic time stepping scheme is needed for any practical analysis, since the total time of interest in consolidation is typically orders of magnitude larger than the time increments that must be used to obtain reasonable solutions during the early part of the transient. Abaqus uses a tolerance on the maximum change in pore pressure allowed in an increment to control the time stepping. When the maximum change of pore pressure in the soil is consistently less than this tolerance, the time increment is allowed to increase. If the pore pressure changes exceed this tolerance, the time increment is reduced and the increment is repeated. In this way the early part of the consolidation can be captured accurately and the later stages are analyzed with much larger time steps, thereby permitting efficient solution of the problem. For this case the tolerance is chosen as 0.344 MPa (50 lb/in^2), which is 10% of the applied load. This is a fairly coarse tolerance but results in an economical and reasonable solution.

The choice of initial time step is important in consolidation analysis. As discussed in "The Terzaghi consolidation problem," Section 1.15.1 of the Abaqus Benchmarks Guide, the initial solution (immediately following a change in boundary conditions) is a local, "skin effect" solution. Due to the coupling of spatial and temporal scales, it follows that no useful information is provided by solutions generated with time steps smaller than the mesh and material-dependent characteristic time. Time steps very much smaller than this characteristic time provide spurious oscillatory results (see Figure 3.1.5–2). This issue is discussed by Vermeer and Verruijt (1981), who propose the criterion

$$\Delta t \geq \frac{\gamma_\omega}{6Ek}(\Delta h)^2,$$

where Δh is the distance between nodes of the finite element mesh near the boundary condition change, $\boldsymbol{E}$ is the elastic modulus of the soil skeleton, $\boldsymbol{k}$ is the soil permeability, and γ_ω is the specific weight of the pore fluid. In this problem Δh is 8.5 mm (0.33 in). Using the material properties shown in Figure 10.1.1–1,

$$\Delta t_{\text{initial}} = 1 \times 10^{-5} \quad \text{days.}$$

We actually use an initial time step of 2×10^{-5} days, since the immediate transient just after drainage begins is not considered important in the solution.

Results and discussion

The prediction of the time history of the vertical deflection of the central point under the load (point $\boldsymbol{P}$ in Figure 10.1.1–1) is plotted in Figure 10.1.1–2, where it is compared with the exact solution of Gibson et al. (1970). There is generally good agreement between the theoretical and finite element solutions, even though the mesh used in this analysis is rather coarse.

Figure 10.1.1–2 also shows the time increments selected by the automatic scheme, based on the tolerance discussed above. The figure shows the effectiveness of the scheme: the time increment changes by two orders of magnitude over the analysis.

Input file

planestrainconsolidation.inp	Input data for this example.

References

- Gibson, R. E., R. L. Schiffman, and S. L. Pu, "Plane Strain and Axially Symmetric Consolidation of a Clay Layer on a Smooth Impervious Base," Quarterly Journal of Mechanics and Applied Mathematics, vol. 23, pt. 4, pp. 505–520, 1970.
- Vermeer, P. A., and A. Verruijt, "An Accuracy Condition for Consolidation by Finite Elements," International Journal for Numerical and Analytical Methods in Geomechanics, vol. 5, pp. 1–14, 1981.

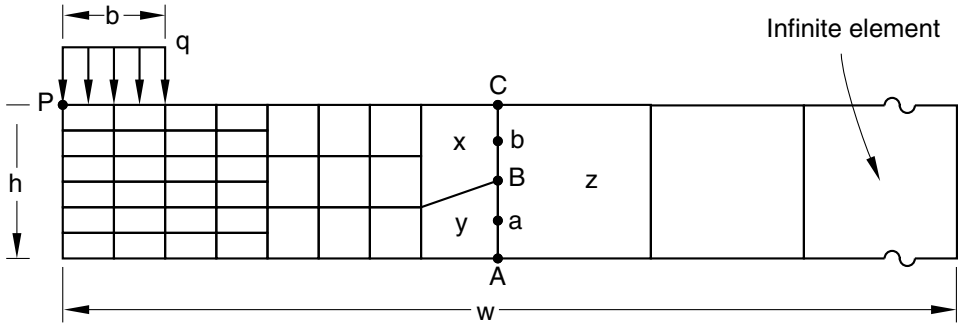

Geometry:

h = 50.8 mm (2.0 in)
b = 25.4 mm (1.0 in)
w = 533.4 mm (21.0 in)

Material:

E = 690 GPa (1.0 x 10^8 lb/in^2)
υ = 0.0
k = 5.08 x 10^{-7} m/day (2.0 x 10^{-5} in/day)
γ_w = 2.729 x 10^5 N/m^3 (1.0 lb/in^3)
e_o = 1.5

Loading:

q = 3.45 MPa (500.0 lb/in^2)

Figure 10.1.1–1 Plane strain consolidation example: geometry and properties.

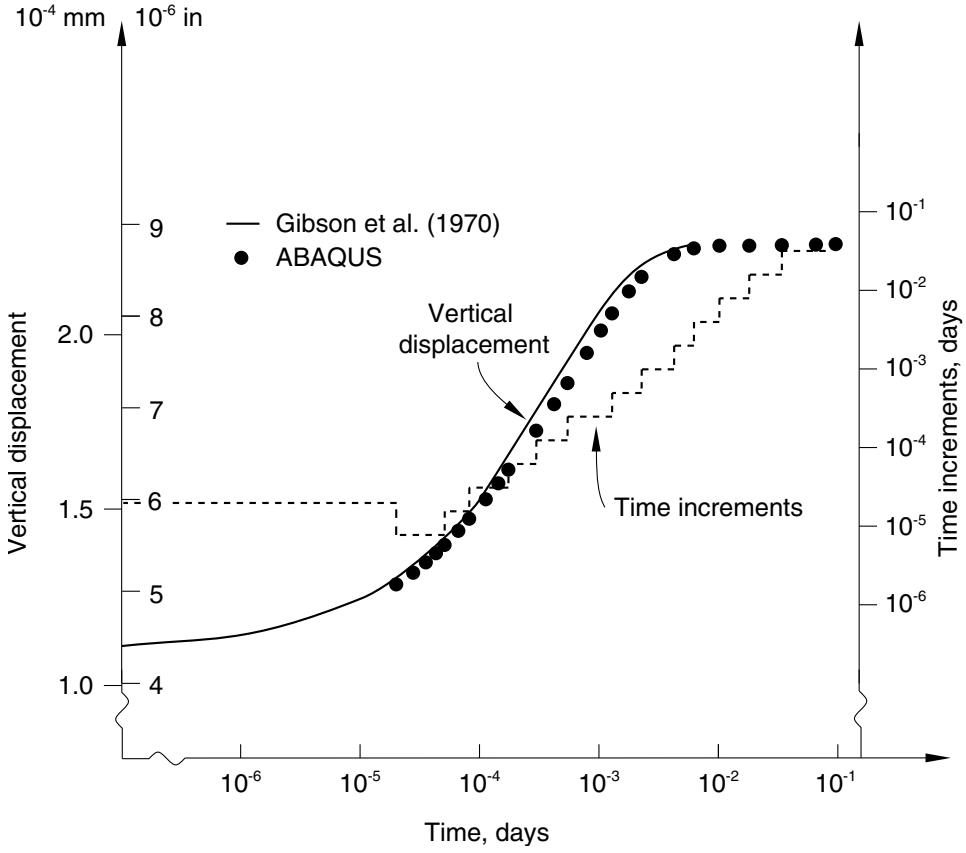

Figure 10.1.1–2 Consolidation history and time step variation history.

10.1.2 CALCULATION OF PHREATIC SURFACE IN AN EARTH DAM

Product: Abaqus/Standard

This example illustrates the use of Abaqus to solve for the flow through a porous medium in which fluid flow is occurring in a gravity field and only part of the region is fully saturated, so the location of the phreatic surface is a part of the solution.

Such problems are common in hydrology (an example is the well draw-down problem, where the phreatic surface of an aquifer must be located based on pumping rates at particular well locations) and in some problems of dam design, as in this example. The basic approach takes advantage of the Abaqus capability to perform partially and fully saturated analysis: the phreatic surface is located at the boundary of the fully saturated part of the model. This approach has the advantage that the capillary zone, just above the phreatic surface, is also identified.

Boundary conditions

A typical dam is shown in Figure 10.1.2–1. We consider fluid flow only: deformation of the dam is ignored. Thus, although we use the fully coupled pore fluid flow-deformation elements, all displacement degrees of freedom are prescribed to be zero. A more general analysis would include stress and deformation of the dam.

The upstream face of the dam (surface S_1 in Figure 10.1.2–1) is exposed to water in the reservoir behind the dam. Since Abaqus uses a total pore pressure formulation, the pore pressure on this face must be prescribed to be $u_w = (H_1 - z)g\rho_w$, where H_1 is the elevation of the water surface, z is elevation, g is the gravitational acceleration, and ρ_w is the mass density of the water. ($g\rho_w$, the weight density of the water, must be given as the value of the specific weight of the wetting fluid as part of the definition of material permeability.) Likewise, on the downstream face of the dam (surface S_2 in Figure 10.1.2–1), $u_w = (H_2 - z)g\rho_w$.

The bottom of the dam (surface S_3) is assumed to rest on an impermeable foundation. Since the natural boundary condition in the pore fluid flow formulation provides no flow of fluid across a surface of the model, no further specification is needed on this surface.

The phreatic surface in the dam, S_4, is found as the locus of points at which the pore fluid pressure, u_w, is zero. Above this surface the pore fluid pressure is negative, representing capillary tension causing the fluid to rise against the gravitational force and creating a capillary zone. The saturation associated with particular values of capillary pressure for absorption and exsorption of fluid from the porous medium is a physical property of the material and is defined in the absorption/exsorption behavior under partially saturated flow conditions.

A special boundary condition is needed if the phreatic surface reaches an open, freely draining surface, as indicated on surface S_5 in Figure 10.1.2–1. In such a case the pore fluid can drain freely down the face of the dam, so $u_w = 0$ at all points on this surface below its intersection with the phreatic surface. Above this point $u_w < 0$, with its particular value depending on the solution. This example is specifically chosen to include this effect to illustrate the use of the Abaqus drainage-only flow boundary condition.

This drainage-only flow condition consists of prescribing the flow velocity on the freely draining surface in a way that approximately satisfies the requirement of zero pore pressure on the completely saturated portion of this surface (Pagano, 1997). The flow velocity is defined as a function of pore pressure, as shown in Figure 10.1.2–2. For negative pore pressures (those above the phreatic surface) the flow velocity is zero—the proper natural boundary condition. For positive pore pressures (those below the phreatic surface) the flow velocity is proportional to the pore pressure value. When this proportionality coefficient, k_s, is large compared to $k/\gamma_w c$—where k is the permeability of the medium, γ_w is the specific weight of the fluid, and c is a characteristic length scale—the requirement of zero pore pressure on the free-drainage surface below the phreatic surface will be satisfied approximately. The drainage-only seepage coefficient in this model is specified as $k_s = 10^{-1}$ m^3/Nsec. This value is roughly 10^5 times larger than the characteristic value, $k/\gamma_w c$, based on the material properties listed below and an element length scale $\approx 10^{-1}$ m. This condition is prescribed using a pore fluid flow definition with the drainage-only flow type label (QnD) as shown in phreaticsurf_cpe8rp.inp.

Geometry and model

The geometry of the particular earth dam considered is shown in Figure 10.1.2–3. This case is chosen because an analytical solution is available for comparison (Harr, 1962). The dam is filled to two-thirds of its height. Only a part of its base is impermeable. Since the dam is assumed to be long, we use CPE8RP coupled pore pressure/displacement plane strain elements (the mesh is shown in Figure 10.1.2–4). In addition, input files containing element types CPE4P and CPE6MP are included for verification purposes. Additional input files are included to demonstrate the use of contact pairs, tie constraints, and solution transfer capabilities in coupled pore pressure-displacement analyses.

Material

The permeability of the fully saturated earth of which the dam is made is 0.2117×10^{-3} m/sec. The default assumption is used for the partially saturated permeability: that it varies as a cubic function of saturation, decreasing from the fully saturated value to a value of zero at zero saturation. The specific weight of the water is 10 kN/m^3. The capillary action in the dam is defined by a single absorption/exsorption curve that varies linearly between a negative pore pressure of 10 kN/m^2 at a saturation of 0.05 and zero pore pressure at fully saturated conditions. This is not a very realistic model of physical absorption/exsorption behavior, but this will not affect the results of the steady-state analysis significantly insofar as the location of the phreatic surface is concerned. Accurate definition of this behavior would be required if definition of the capillary zone created by filling and emptying the dam at given rates were needed.

The initial void ratio of the earth material is 1.0. The initial conditions for pore pressure and saturation are assumed to be those corresponding to the dam being fully saturated to the upstream water level: the initial saturation is, therefore, 1.0; and the initial pore pressures vary between zero at the water level and a maximum value of 12.19 kN/m^2 at the base of the dam.

Loading and controls

The weight of the water is applied by GRAV loading, and the upstream and downstream pore pressures are prescribed as discussed above. A steady-state, coupled pore fluid diffusion/stress analysis is performed in five increments to allow Abaqus to resolve the high degree of nonlinearity in the problem.

Results and discussion

The steady-state contours of pore pressure are shown in Figure 10.1.2–5. The upper-right part of the dam shows negative pore pressures, indicating that it is partly saturated or dry. The phreatic surface is best shown in Figure 10.1.2–6, where we have chosen to draw the contours in the vicinity of zero pore pressure. This phreatic surface compares well with the analytical phreatic surface calculated by Harr (1962), shown in Figure 10.1.2–2. Figure 10.1.2–7 shows contours of saturation that indicate a region of fully saturated material under the phreatic zone and decreasing saturation in and above the phreatic zone.

Input files

phreaticsurf_cpe8rp.inp	Phreatic surface calculation (element type CPE8RP).
phreaticsurf_cpe4p.inp	Element type CPE4P.
phreaticsurf_cpe6mp.inp	Element type CPE6MP.
phreaticsurf_cpe4p_contactpair.inp	Element type CPE4P using the ∗CONTACT PAIR option.
phreaticsurf_cpe4p_mapsolution.inp	∗MAP SOLUTION continuation of the phreaticsurf_cpe4p_contactpair.inp analysis.
phreaticsurf_cpe4p_tie.inp	Element type CPE4P using the ∗TIE option.

References

- Harr, M. E., *Groundwater and Seepage,* McGraw-Hill, New York, 1962.
- Pagano, L., “Steady State and Transient Unconfined Seepage Analyses for Earthfill Dams,” ABAQUS Users’ Conference, Milan, pp. 557–585, 1997.

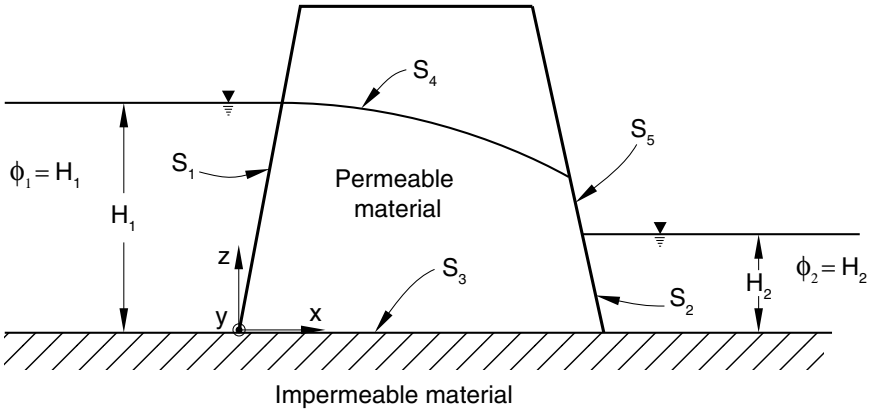

Figure 10.1.2–1 Phreatic surface problem.

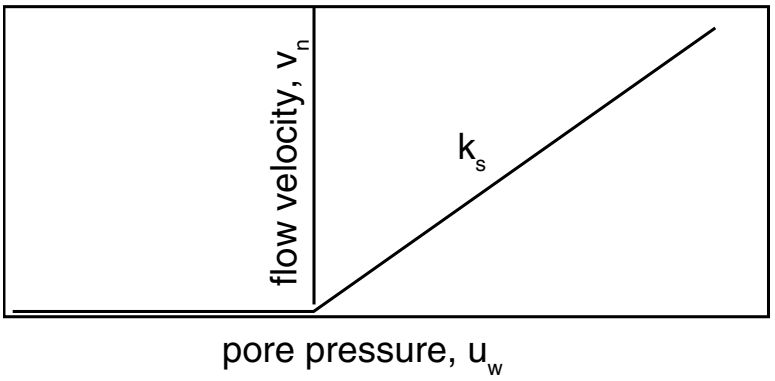

Figure 10.1.2–2 Pore pressure–flow velocity relationship defined on the drainage-only surface.

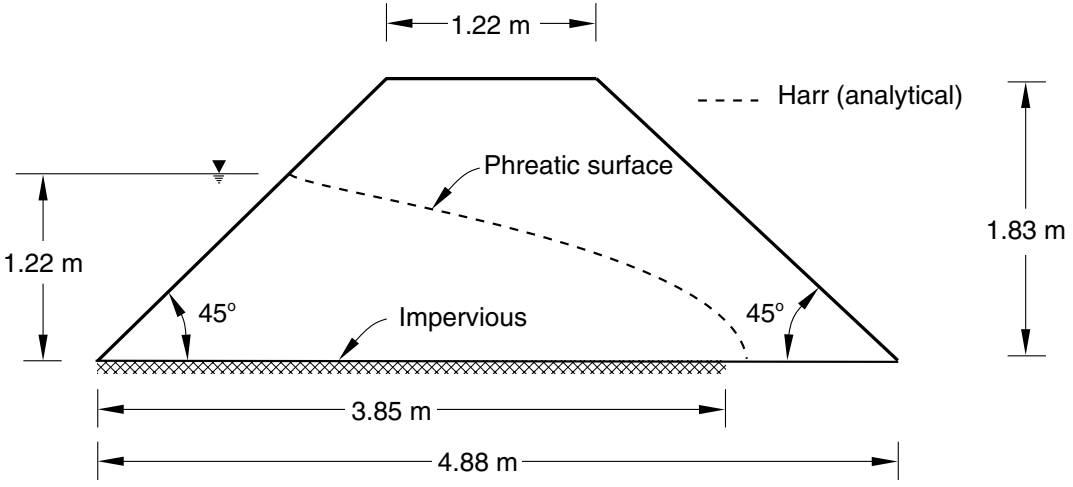

Figure 10.1.2–3 Configuration of earth dam and analytical phreatic surface.

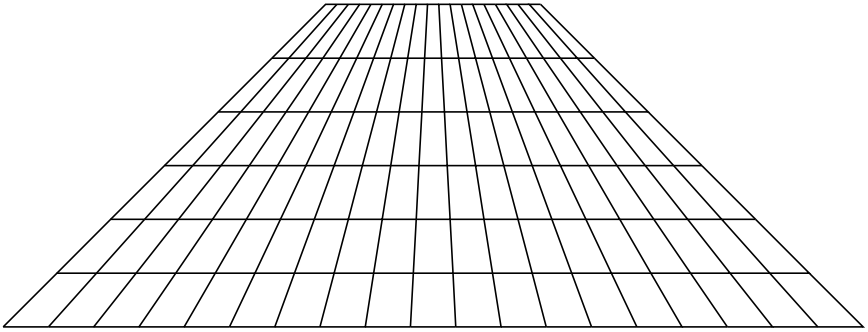

Figure 10.1.2–4 Finite element mesh.

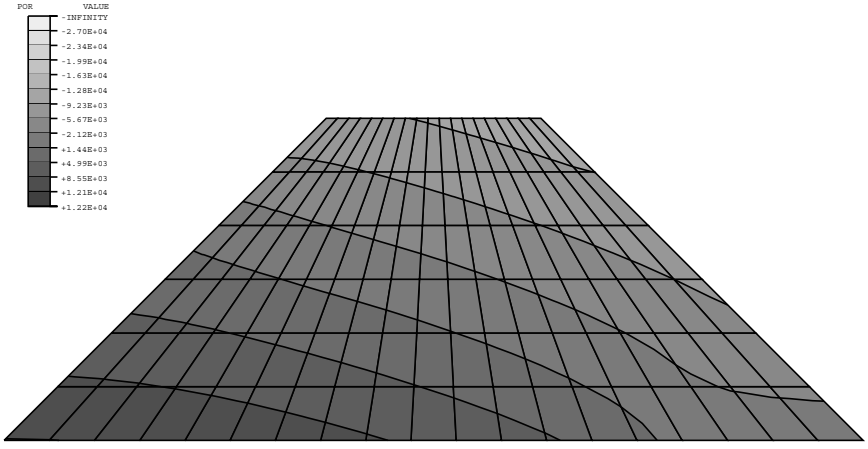

Figure 10.1.2–5 Pore pressure contours at steady state.

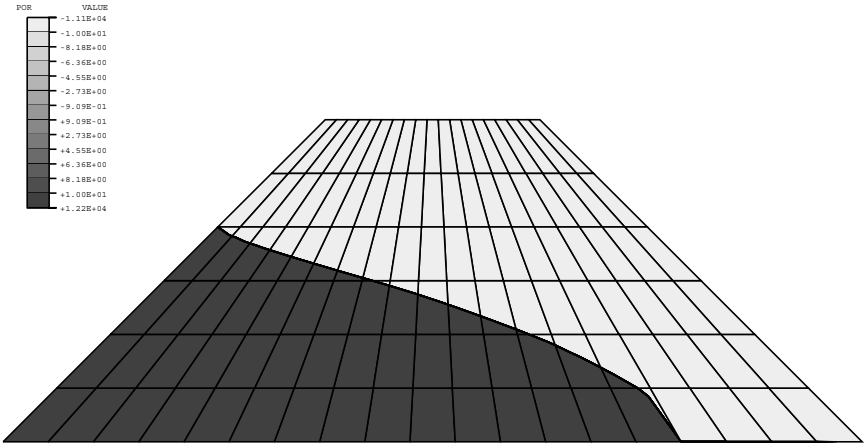

Figure 10.1.2–6 Pore pressure contours showing phreatic surface.

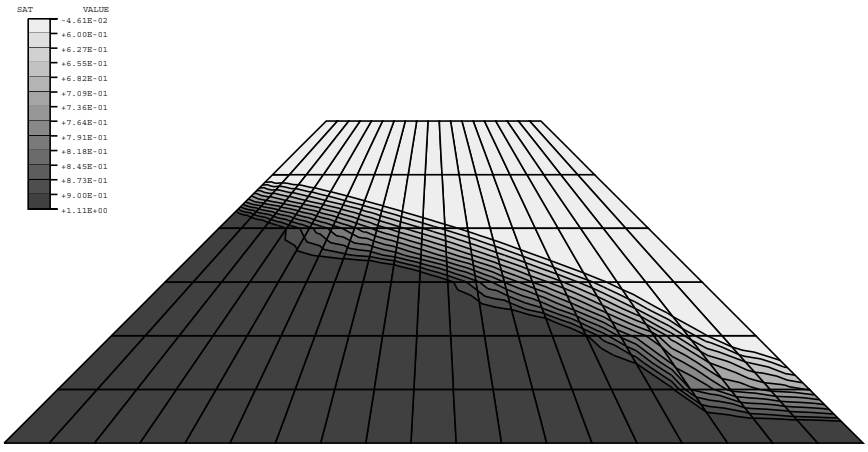

Figure 10.1.2–7 Saturation contours at steady state.

10.1.3 AXISYMMETRIC SIMULATION OF AN OIL WELL

Product: Abaqus/Standard

This example simulates the settlement of soil near an oil well.

It is assumed that the oil in question is too thick for normal pumping. Therefore, steam is injected in the soil in the vicinity of the well to increase the temperature and decrease the oil's viscosity. As a result creep becomes an important component of the soil inelastic deformation and in the prediction of the effects of the oil pumping. Five years of oil pumping are simulated. This coupled displacement/diffusion analysis illustrates the use of Abaqus to solve problems involving fluid flow through a saturated porous medium, inelastic material properties with time-dependent creep behavior, and thermal loading. No experimental data exist to compare with the numerical results of this example.

Geometry and model

The example considers an axisymmetric model of an oil well and the surrounding soil, as shown in Figure 10.1.3–1. The radius of the well is 81 m (265 ft), and the well extends from a depth of 335 m (1100 ft) to 732 m (2500 ft). A depth of 1463 m (4800 ft) is modeled with 11 different soil layers. Reduced-integration axisymmetric elements with pore pressure, CAX8RP, are used to model the soil in the vicinity of the well. The far-field region is modeled with axisymmetric infinite elements, CINAX5R, to provide lateral stiffness. Reduced integration is almost always recommended when second-order elements are used, because it usually gives more accurate results and is less expensive than full integration. A coarse mesh is selected for the illustrative purpose of this example. No mesh convergence study has been performed.

Soil layers designated by S1, T1, U1, and L1 are modeled using the Drucker-Prager plasticity model. Both the elastic and inelastic material properties are tabulated in Table 10.1.3–1. The linear form of the Drucker-Prager model with no intermediate principal stress effect ($K = 1.0$) is used. The model assumes nonassociated flow; consequently, the material stiffness matrix is not symmetric. The use of unsymmetric matrix storage and an unsymmetric solution improves the convergence of the nonlinear solution significantly. The hardening/softening behavior is specified as an extension of the Drucker-Prager plasticity material definition, and the data are listed in Table 10.1.3–1. No creep data are provided for these layers since these are far removed from the loading. These layers are assumed to be saturated with water. A high permeability is assumed for the two top soil layers S1 and T1, while a low permeability is assigned to layers U1 and L1.

Layers D1 through D7 are modeled with the modified Drucker-Prager Cap plasticity model. The material property data are tabulated in Table 10.1.3–2. As required by the creep model, no intermediate principal stress effect is included (i.e., $K = 1.0$), and no transition region on the yield surface is defined (i.e., $\alpha = 0.0$). The material's volumetric strain-driven hardening/softening behavior is specified with a cap hardening curve definition, and the data are listed in Table 10.1.3–2. The initial cap yield surface position, $\varepsilon_{vol}^{in}(0)$, is set to 0.02. Abaqus automatically adjusts the position of the cap yield surface if the stress lies outside the cap surface. Consolidation creep is modeled with a Singh-Mitchell type creep

model. The creep material data are specified using the cap creep model and are dependent on temperature. The following creep data are specified:

A=2.2E−7 1/day, α=3.05 1/MPa (0.021 1/psi), t_1=1.0 day, n=1.0 at 10°C (50°F)

A=3.5E−4 1/day, α=3.05 1/MPa (0.021 1/psi), t_1=1.0 day, n=1.0, at 100°C (212°F)

These layers consist of rich organic matter and are saturated with oil. The permeability data are specified as temperature dependent.

A uniform thermal expansion coefficient of 5.76E−6 1/°C (3.2E−6 1/°F) and a constant weight density 1.0 metric ton/m^3 (64.6 lbs/ft^3) are assumed for all layers.

For a coupled diffusion/displacement analysis care must be taken when choosing the units of the problem. The coupled equations may be numerically ill-conditioned if the choice of the units is such that the numbers generated by the equations of the two different fields differ by many orders of magnitude. The units chosen for this example are inches, pounds, and days.

Initial conditions

An initial geostatic stress field is defined for the analysis and is based on the soil weight density integrated over the depth. A coefficient of lateral stress of 0.85 is assumed. An initial void ratio of 1.5 is used throughout all soil layers with an initial uniform temperature field of 10°C (50°F).

Loading

The problem is run in five steps. The first step of the analysis is a geostatic step to equilibrate geostatic loading of the finite element model. This step also establishes the initial distribution of pore pressure. Since gravity loading is defined with distributed load type BZ and not with gravity load type GRAV, the pore fluid pressure reported by Abaqus is defined as the pore pressure in excess of the hydrostatic pressure required to support the weight of pore fluid above the elevation of the material point.

The second step is a transient soils consolidation analysis step to equilibrate any creep effects induced from the initial geostatic loading step. The choice of the initial time step is important in a consolidation analysis. Because of the coupling of spatial and temporal scales, no useful information is provided by solutions generated with time steps that are smaller than the mesh and material-dependent characteristic time. Time steps that are very much smaller than this characteristic time provide spurious oscillatory results. For further discussion on calculating the minimum time step, refer to "Coupled pore fluid diffusion and stress analysis," Section 6.8.1 of the Abaqus Analysis User's Guide. For this example a minimum initial time step of one day was selected.

The third step of the analysis models the injection of steam into the well region between a depth of 366 m to 732 m (1200 ft to 2400 ft). The region is indicated by the shaded area in Figure 10.1.3–1. The nodes in this region are heated to 100°C (212°F) during a transient soils consolidation analysis. Creep effects are not considered. The injection of the steam increases the permeability of the oil and increases the soil creep behavior.

The fourth step simulates the pumping of oil by prescribing an excess pore pressure of −1.2 MPa (−170 psi) at nodes located at the depth of 427 m to 550 m (1400 ft to 1800 ft) below the surface. The

pressure produces a pumping rate of approximately 172.5 thousand barrels per day at the end of the fifth year.

The final step consists of a consolidation analysis performed over a five-year period to investigate the settlement that results from pumping and creep effects in the vicinity of the well.

Results and discussion

The two initial steps show negligible deformations, indicating that the model is in geostatic equilibrium. Figure 10.1.3–2 shows a contour plot of the soil settlement resulting from consolidation after the five-year period. A settlement of 0.13 m (0.4 ft) is expected at the surface. A maximum soil dislocation of 0.24 m (0.78 ft) occurs above the pump intake. Figure 10.1.3–3 shows a contour plot of the excess pore pressure. The negative pore pressure represents the suction of the pump. During the five-year period, a total of 313.5 million barrels of oil are pumped (as determined from nodal output variable RVT). Figure 10.1.3–4 through Figure 10.1.3–6 show contour plots of the vertical stress components, plastic strains, and creep strains, respectively. Plastification occurs in soil layers D3 through D5. Significant creep occurs in the area in which steam is injected.

Input files

axisymoilwell.inp	Finite element analysis.
axisymoilwell_thermalexp.inp	Same as axisymoilwell.inp except that the thermal expansion of the pore fluid is also included.

Table 10.1.3–1 Soil data using Drucker-Prager model.

Soil layer	Elastic properties	Inelastic properties	Hardening behavior
S1	$E = 124$ MPa $\nu = 0.3$	$\beta = 42.0°$ K = 1.0 $\varphi = 0.0°$	0.075 MPa, 0.0 0.083 MPa, 0.058 0.075 MPa, 0.116
T1	$E = 2068$ MPa $\nu = 0.25$	$\beta = 36.0°$ K = 1.0 $\varphi = 0.0°$	0.48 MPa, 0.0 0.62 MPa, 0.058 0.48 MPa., 0.116
U1	$E = 468.8$ MPa $\nu = 0.22$	$\beta = 38.0°$ K = 1.0 $\varphi = 0.0°$	1.97 MPa, 0.0 3.17 MPa, 0.0037 2.47 MPa, 0.04
L1	$E = 2482$ MPa $\nu = 0.29$	$\beta = 38.0°$ K = 1.0 $\varphi = 0.0°$	1.97 MPa, 0.0 3.17 MPa, 0.0037 2.47 MPa, 0.04

Table 10.1.3–2 Soil data using modified Drucker-Prager cap model.

Soil layer	Elastic properties	Inelastic properties		Hardening behavior
D1	$E = 328$ MPa $\nu = 0.17$	d = 1.38 MPa $\beta = 36.9°$ R = 0.33	$\alpha = 0.0$ K = 1.0 $\varepsilon_{vol}^{in}(0) = 0.02$	2.75 MPa, 0.0 4.14 MPa, 0.02 5.51 MPa, 0.05 6.20 MPa, 0.09
D2	$E = 434$ MPa $\nu = 0.17$	d = 1.38 MPa $\beta = 39.4°$ R = 0.33	$\alpha = 0.0$ K = 1.0 $\varepsilon_{vol}^{in}(0) = 0.02$	1.38 MPa, 0.0 4.14 MPa, 0.02 6.89 MPa, 0.04 55.1 MPa, 0.1
D3	$E = 546$ MPa $\nu = 0.19$	d = 1.38 MPa $\beta = 42.0°$ R = 0.34	$\alpha = 0.0$ K = 1.0 $\varepsilon_{vol}^{in}(0) = 0.02$	1.38 MPa, 0.0 3.45 MPa, 0.02 13.8 MPa, 0.04 62.0 MPa, 0.06
D4	$E = 411$ MPa $\nu = 0.2$	d = 1.2 MPa $\beta = 40.1°$ R = 0.3	$\alpha = 0.0$ K = 1.0 $\varepsilon_{vol}^{in}(0) = 0.02$	1.38 MPa, 0.0 5.03 MPa, 0.02 6.90 MPa, 0.10 62.0 MPa, 0.3
D5	$E = 494$ MPa $\nu = 0.17$	d = 1.38 MPa $\beta = 40.4°$ R = 0.3	$\alpha = 0.0$ K = 1.0 $\varepsilon_{vol}^{in}(0) = 0.02$	2.75 MPa, 0.0 4.83 MPa, 0.02 5.15 MPa, 0.04 62.0 MPa, 0.08
D6	$E = 775$ MPa $\nu = 0.17$	d = 17 MPa $\beta = 50.2°$ R = 0.23	$\alpha = 0.0$ K = 1.0 $\varepsilon_{vol}^{in}(0) = 0.02$	2.76 MPa, 0.0 4.14 MPa, 0.005 7.58 MPa, 0.02 62.0 MPa, 0.05
D7	$E = 1{,}121$ MPa $\nu = 0.17$	d = 1.7 MPa $\beta = 58.5°$ R = 0.23	$\alpha = 0.0$ K = 1.0 $\varepsilon_{vol}^{in}(0) = 0.02$	3.44 MPa, 0.0 4.14 MPa, 0.006 7.58 MPa, 0.012 67.6 MPa, 0.03

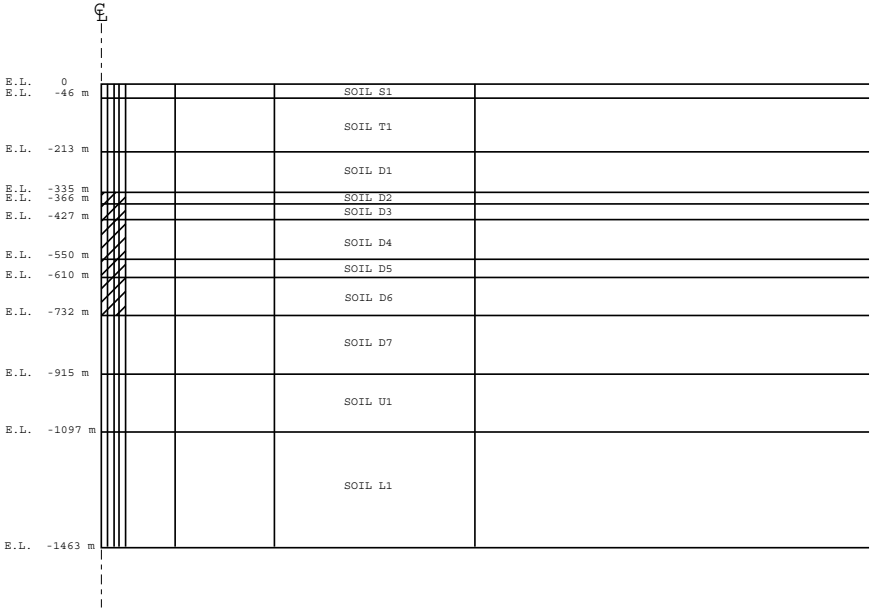

Figure 10.1.3–1 Axisymmetric model of oil well and surrounding soil.

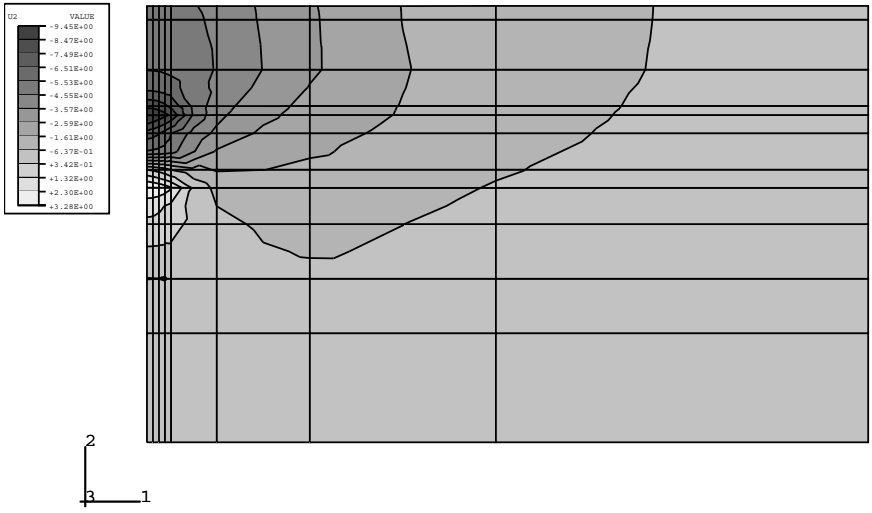

Figure 10.1.3–2 Soil settlement after five-year period.

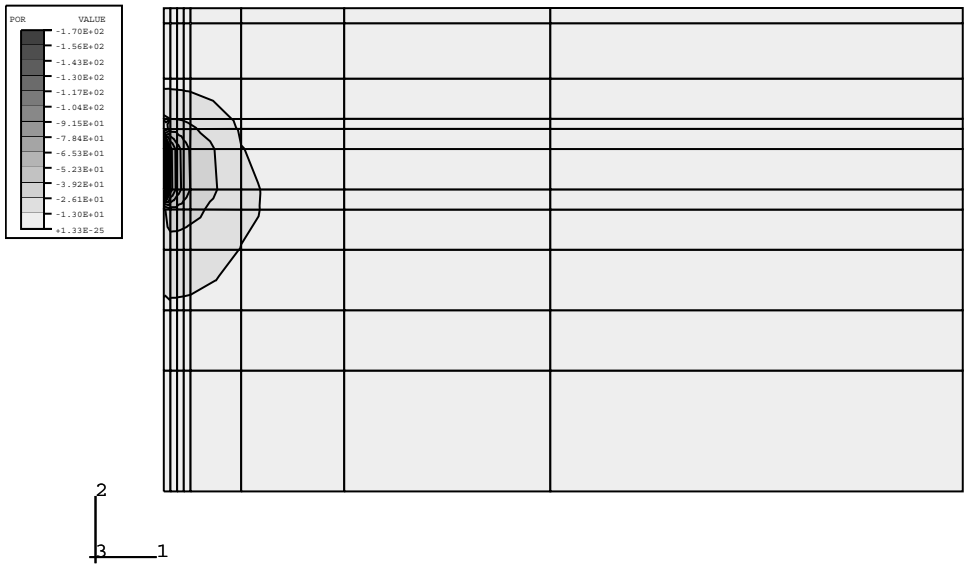

Figure 10.1.3–3 Contour plot of the pore pressure.

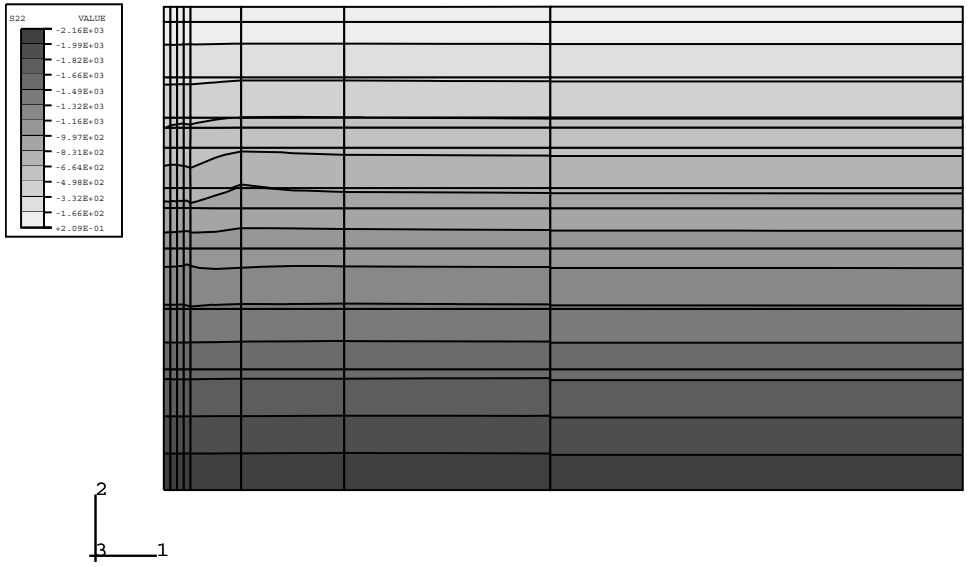

Figure 10.1.3–4 Contour plot of the vertical stress components.

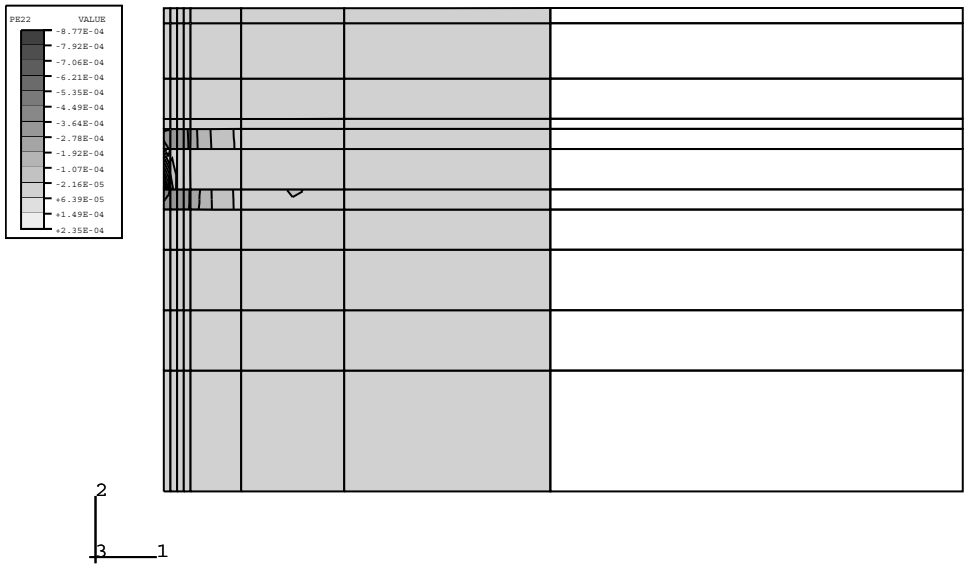

Figure 10.1.3–5 Contour plot of the vertical plastic strain components.

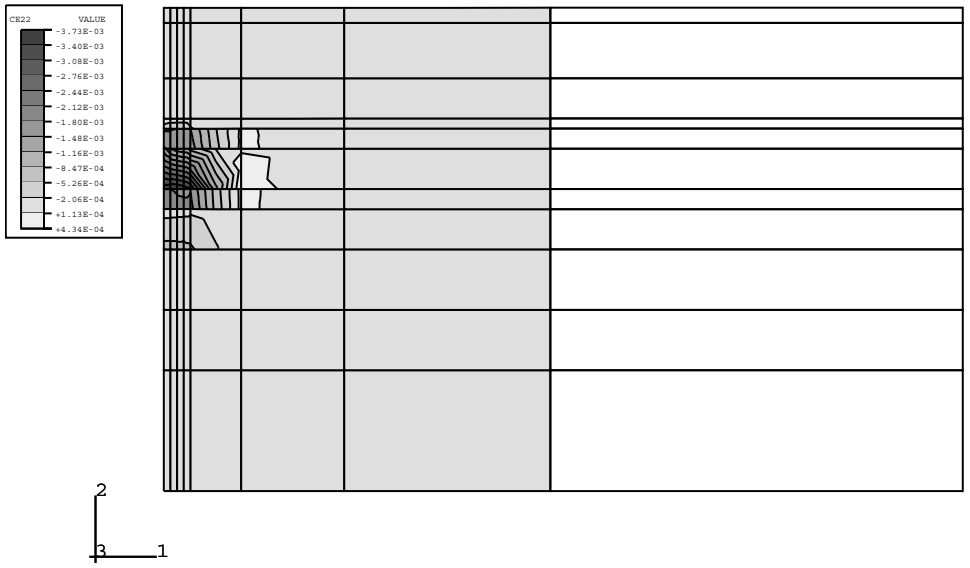

Figure 10.1.3–6 Contour plot of the vertical creep strain components.

10.1.4 ANALYSIS OF A PIPELINE BURIED IN SOIL

Product: Abaqus/Standard

This example verifies the use of pipe-soil interaction elements to model a buried pipeline subjected to large ground movement.

Oil and gas pipelines are usually buried in the ground to provide protection and support. Buried pipelines may experience significant loading as a result of relative displacements of the ground along their length. Such large ground movement can be caused by faulting, landslides, slope failures, and seismic activity.

Abaqus provides a library of pipe-soil interaction (PSI) elements to model the interaction between a buried pipeline and the surrounding soil. The pipeline itself is modeled with any of the beam, pipe, or elbow elements in the Abaqus/Standard element library. The ground behavior and soil-pipe interaction are modeled with the pipe-soil interaction elements. These elements have only displacement degrees of freedom at their nodes. One side or edge of the element shares nodes with the underlying beam, pipe, or elbow element that models the pipeline. The nodes on the other edge represent a far-field surface, such as the ground surface, and are used to prescribe the far-field ground motion. The elements are described in detail in "Pipe-soil interaction elements," Section 32.12.1 of the Abaqus Analysis User's Guide.

The purpose of this example is to determine the stress state along the length of a infinitely long buried pipeline subjected to large fault movement of 1.52 m (5.0 ft), as shown in Figure 10.1.4–1. The pipeline intersects the fault at 90.0°. The results are compared with results from an independent analysis, as described below.

Problem description

The problem consists of an infinitely long pipeline buried at a depth of 6.1 m (20.0 ft.) below the ground surface. Only a 610.0 m (2000.0 ft.) long section of the pipeline is modeled. The outside radius of the pipe is 0.61 m (24.0 in), and the wall thickness is 0.0254 m (1.0 in). The pipeline is modeled with 50 first-order PIPE21 elements. A nonuniform mesh, with smaller elements focused near the fault, is used.

The pipe-soil interaction behavior is model with PSI24 elements. The PSI elements are defined so that one edge of the element shares nodes with the underlying pipe element, and the nodes on the other edge represent a far-field surface where ground motion is prescribed. The far-field side and the side that shares nodes with the pipeline are defined by the element connectivity.

A three-dimensional model that uses PIPE31 and PSI34 elements is also included for verification purposes.

Material

The pipeline is made of an elastic–perfectly plastic metal, with a Young's modulus of 206.8 GPa (30×10^6 lb/in^2), a Poisson's ratio of 0.3, and a yield stress of 413.7 MPa (60000 lb/in^2).

The pipe-soil interaction behavior is elastic–perfectly plastic. The nonlinear constitutive model is used to define the interaction model. The behavior in the vertical direction is assumed to be different from the behavior along the axial direction. It is further assumed that the pipeline is buried deep below the

ground surface so that the response is symmetric about the origin. Abaqus also allows a nonsymmetric behavior to be defined in any of the directions (this is usually the case in the vertical direction when the pipeline is not buried too deeply). The ultimate force per unit length in the axial direction is 730.0 N/m (50.0 lb/ft), and in the vertical direction it is 1460.0 N/m (100.0 lb/ft). The ultimate force is reached at 0.0304 m (0.1 ft) in both the horizontal and vertical directions.

The loading occurs in a plane (axial-vertical), so the properties for the pipe-soil interaction behavior in the transverse horizontal direction are not important.

Loading

The loading on the pipeline is caused by a relative vertical displacement 1.52 m (5.0 ft) along the fault line. It is assumed that the effect of the vertical ground motion decreases linearly over a distance of 91.4 m (300.0 ft.) from the origin of fault, as shown in Figure 10.1.4–1.

This linear distribution of ground motion is prescribed as follows. Rigid (R2D2) elements are connected to the far-field edges of the PSI to create two rigid surfaces, one on each side of the fault line. These surfaces extend a distance of 91.4 m (300.0 ft.) from the origin of the fault. The rigid body reference nodes are also placed a distance of 91.4 m (300.0 ft.) from the fault on the ground surface. The fault movement is modeled by prescribing a rotation to each of the rigid body reference nodes so that a positive vertical displacement of 0.76 m (2.5 ft) is obtained on one side of the fault and a negative vertical displacement of 0.76 m (2.5 ft) is obtained on the other side of the fault, as shown in Figure 10.1.4–2. All degrees of freedom on the remaining far-field nodes are fully fixed. In addition, the two end points of pipeline are fully fixed. Figure 10.1.4–2 does not show the PSI elements or any of the remaining nodes on the ground surface.

Reference solution

The reference solution is obtained by using JOINTC elements between the pipeline and ground nodes to model the pipe-soil interaction. These elements provide an internal stiffness, which is modeled with linear or nonlinear springs; nonlinear springs are used in this example. The behavior of the nonlinear spring is elastic in the sense that reversed loading does not result in permanent deformation. This behavior is different from the behavior provided by the nonlinear PSI elements. However, this is not a limitation in this example since the loading is monotonic.

Another distinct difference between JOINTC elements and PSI elements is that the spring behavior associated with JOINTC elements is defined in terms of total force, whereas the constitutive behavior for PSI elements is defined as a force/unit length. This difference requires us to define a separate stiffness for each JOINTC element or to use a uniform mesh with JOINTC elements spaced at unit length intervals along the pipeline. A unit length mesh is used in this example.

Results and discussion

Figure 10.1.4–3 and Figure 10.1.4–4 show the axial and vertical forces per unit length applied to the pipeline due to relative ground motion. The figures show that permanent deformation occurs in the pipe-soil interaction model near the fault along the axial and horizontal directions, with purely elastic behavior further from the fault.

Figure 10.1.4–5 compares the axial stress in the bottom wall of the pipeline with the reference solution. The figure shows that the pipeline behavior is purely elastic. The figure also shows close agreement with the reference solution. The small differences between the solutions can be accounted for by the different mesh densities. The reaction forces at the pipeline edges and the maximum pipeline displacements are also in close agreement with the reference solution.

Input files

buriedpipeline_2d.inp	Two-dimensional model using PSI24 elements.
buriedpipeline_3d.inp	Three-dimensional model using PSI34 elements.
buriedpipeline_ref.inp	Reference solution using JOINTC elements.

Reference

- Audibert, J. M. E., D. J. Nyman, and T. D. O'Rourke, "Differential Ground Movement Effects on Buried Pipelines," Guidelines for the Seismic Design of Oil and Gas Pipeline Systems, ASCE publication, pp. 151–180, 1984.

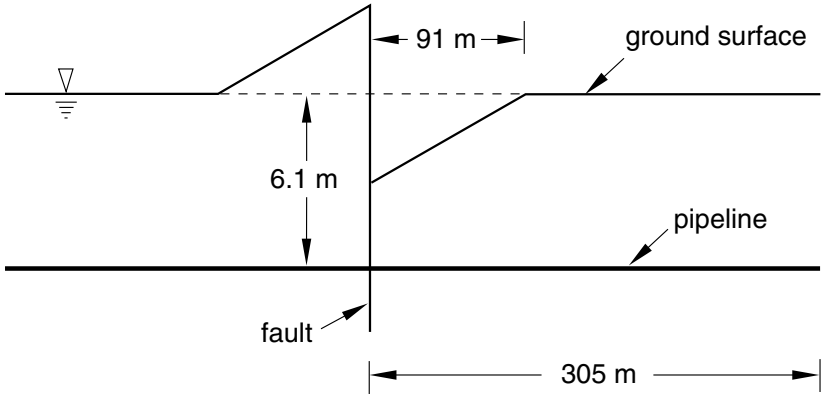

Figure 10.1.4–1 Pipe with fault motion.

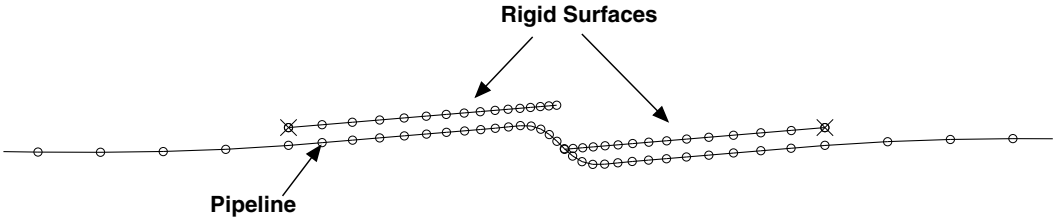

Figure 10.1.4–2 Displaced shape (magnification factor=10.0).

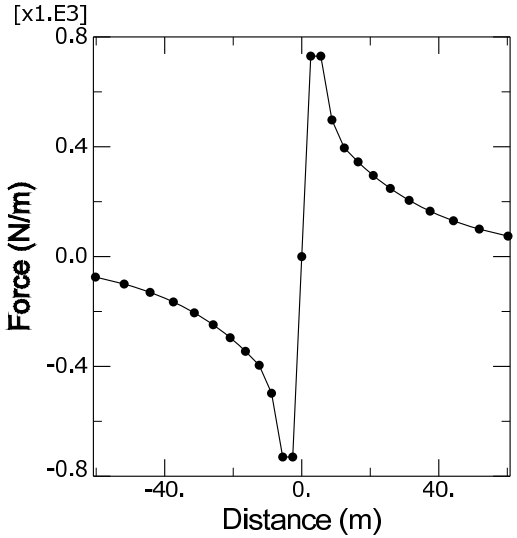

Figure 10.1.4–3 Axial force/unit length applied along the pipeline.

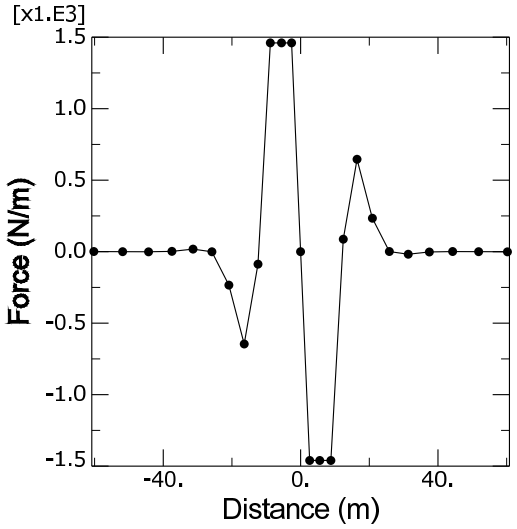

Figure 10.1.4–4 Vertical force/unit length applied along the pipeline.

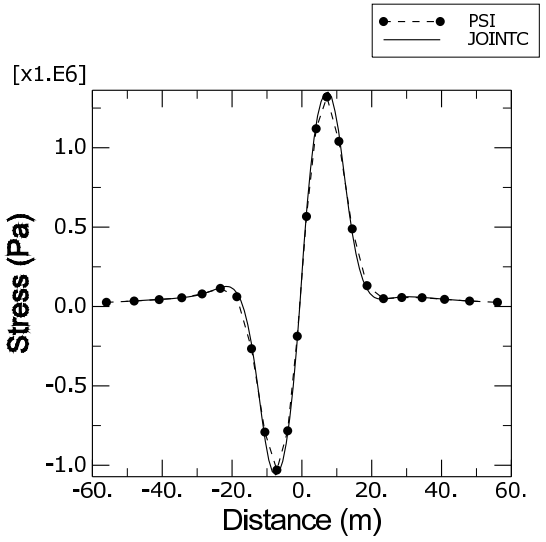

Figure 10.1.4–5 Axial stress along the bottom of the pipeline.

10.1.5 HYDRAULICALLY INDUCED FRACTURE IN A WELLBORE

Product: Abaqus/Standard

This example demonstrates the use of pore pressure cohesive elements and fluid pipe elements to model the initiation and opening of hydraulically induced cracks near an oil well borehole.

With the technique illustrated in this section you can assess the quantitative impact of the hydraulic fracture process on wellbore productivity.

Problem description

The hydraulic fracture process is commonly used in the production of oil and natural gas reservoirs as a means of increasing well productivity and extending the production lifetime of the reservoir. The objectives of a hydraulic fracture treatment are

1. to create more surface area that is exposed to the hydrocarbon bearing rocks, and
2. to provide a highly conductive pathway that allows the hydrocarbons to flow easily to the wellbore.

The productivity of a hydraulically fractured oil or gas well is directly related to the extent of the fracture and to how well the wellbore is connected to the fracture. Some rock formations contain natural fracture systems that can further increase a well's productivity, provided that the generated hydraulic fracture can grow such that it intersects these natural fractures.

A hydraulic fracture job consists of pumping fluids into a well at very high pressures so that the tractions created on the well-bore face reduce the in-situ (compressive) stress in the rock so much that the rock fractures. Once a fracture initiates in the rock formation it is possible, given enough hydraulic fluid, to propagate the fracture for a considerable distance, sometimes as far as a hundred meters or more.

Pumping stages

The initial stage often involves pumping a rather small amount of polymer laden fluid, typically 1–20 barrels (.15 to 3.2 cubic meters) so that data can be gathered on the pressure needed to fracture the formation and the rate at which the fluid will "leakoff" from the fracture into the pore space of the rock. The data gathered are used to plan subsequent stages of the job. The main stage of the job might consist of anywhere from one hundred to several thousands of barrels of hydraulic fluid. The size of this stage is determined by the target fracture size, the leakoff rate, and the capacity (rate) of the pumps.

During the next stage of the fracture job, solid material, known as proppant, is added to the injected fluid and is carried into the fracture volume. Chemicals, typically polymers, are added to the fluid in each stage of a fracture job to produce the necessary properties in the fluid (viscosity, leakoff, density). In the last stage of the job, chemicals are pumped into the fracture that help breakdown the polymers used in the previous stages and make it easier to flow fluid back through the fracture without disrupting the proppant material.

Geometry and model

The domain of the problem considered in this example is a 50 m (1969 in) thick slice of oil-bearing rock with the well borehole modeled. The domain has a diameter of 400 m (15,748 in). Three sections of rock are considered: a region where production oil recovery is targeted, and two surrounding regions of shale, as shown in Figure 10.1.5–1.

Due to symmetry only a half of the domain is modeled. Figure 10.1.5–2 shows the finite element model. The rock is modeled with C3D8RP elements, and the borehole casing is modeled with M3D4 elements.

The unopened fracture is modeled along the entire height of the model domain. Cohesive elements (COH3D8P) are used to model a vertical fracture surface.

The flowing fluid in the wellbore is modeled using fluid pipe and fluid pipe connector elements. The fluid pipe elements are tied to the formation to induce hydraulic fracture in a more realistic fashion. The valve behavior is activated on the connector element with user subroutine **UFLUIDCONNECTORVALVE** to turn off flow to the formation after the pumping stage is completed.

Rock constitutive model

A linear Drucker-Prager model with hardening is chosen for the rock, while the casing is linear elastic.

Fracture constitutive model

The fracture model consists of the mechanical behavior of the fracture itself and the behavior of the fluid that enters and leaks through the fracture surfaces.

Fracture mechanical behavior

The elastic properties of the bonded interface are defined using a traction-separation description, with stiffness values of K_{nn}=K_{ss}=K_{tt}= 8.5 × 10^4 MPa. The quadratic traction-interaction failure criterion is chosen for damage initiation in the cohesive elements; and a mixed-mode, energy-based damage evolution law is used for damage propagation. The relevant material data are as follows: N_0 = S_0 = 0.32 KPa, G_{1C}= G_{2C}=G_{3C}= 28 N/mm, and η= 2.284.

Fluid model

Tangential and normal flow are both modeled in the fracture zone cohesive elements. The following parameters are specified:

- Gap flow is specified as Newtonian with a viscosity of 1 × 10^{-6} kPaS (1 centepoise), roughly the viscosity of water.
- Fluid leakoff is specified as 5.879 × 10^{-10} m/(kPa s) for the early stages. In the final stage, when the polymer is dissolved, the fluid leakoff coefficient is increased to 1 × 10^{-3} m/(kPa s). This step-dependent fluid leakoff coefficient is set in user subroutine **UFLUIDLEAKOFF**.

Initial conditions

An initial geostatic stress field is defined using the user subroutines **SIGINI** and **UPOREP**. A depth varying initial void ratio is specified using user subroutine **VOIDRI**. Gravity loading is specified; and an orthotropic overburden stress state is imposed, with the maximum principle stress in the formation aligned orthogonal to the cohesive element fracture plane.

Loading and boundary conditions

The analysis consists of four steps:

1. A geostatic step is performed where equilibrium is achieved after applying the initial pore pressure to the formation and the initial in-situ stresses. The bottom hole shut-in pressure is applied as a traction to the well-bore face.
2. The next step represents the hydraulic fracture stage where the main volume of fluid is being injected into the well. Flow at a rate of 2.4 m^3 (15 barrels) per minute is injected along a targeted 8 m extent in the target formation in the model, and the cohesive elements adjacent to the wellbore along this length are defined as initially open to permit entry of fluid. The duration of this stage is 20 minutes.
3. Following the hydraulic fracture, another transient soils consolidation analysis is conducted. The injection into the well is terminated, and the built-up pore pressure in the fracture is allowed to bleed off into the formation. An additional boundary condition is applied at this stage, fixing the fracture surface open to simulate the behavior of the proppant material that was injected into the fracture.
4. In the final step a drawdown pressure of 20 kPa is applied to the well-bore nodes of the fracture cohesive elements. This step ends after 100 days of production or when steady-state conditions prevail, defined as pore pressure transients below 0.05 kPa/sec in the model.

When the fluid pipe elements are used to simulate fluid flow in the wellbore, the loading conditions in the analysis are modified to specify the flow as an inlet condition at the top of the wellbore. The bottom of the wellbore is tied to the formation to enable automatic injection of the fluid. User subroutine **UFLUIDCONNECTORVALVE** is used to shut off flow to the formation during and after the third step of the analysis as described above.

Results and discussion

The flow injected during Step 2, the pumping stage, initiated and grew a crack extending outward from the wellbore. Figure 10.1.5–3 shows the resulting geometry of the fracture at the end of the 20 minute pumping period. These results show that a fracture initiated within the target formation zone tends to avoid the lower shale region, where the compressive stresses are higher, but does infiltrate the upper shale region, where it can decrease well yields.

Figure 10.1.5–4 shows the fracture opening profile at various times during the pumping stage; the final profile, shown at 1200 s, is then fixed in the subsequent steps, holding the fracture open with the proppant material. Figure 10.1.5–5 shows a similar history of the pore pressure across the fracture face and indicates that the pore flow has stabilized.

Figure 10.1.5–6 shows the resulting well-bore yield following the hydraulic fracture process. This is compared to an equivalent model where the hydraulic fracturing did not occur. In this simple example the hydraulically fractured wellbore shows a marked improvement, with a flow rate more than 100 times the unfractured configuration.

Input files

exa_hydfracture.inp	Hydraulic fracture analysis.
exa_hydfracture.f	User subroutines **DISP**, **DLOAD**, **SIGINI**, **UPOREP**, **UFLUIDLEAKOFF**, and **VOIDRI**.
exa_hydfracture-flpipe.inp	Hydraulic fracture analysis with flow in the wellbore modeled with fluid pipe elements.
exa_hydfracture-pipe.f	User subroutines **DISP**, **DLOAD**, **SIGINI**, **UPOREP**, **UFLUIDLEAKOFF**, **VOIDRI**, and **UFLUIDCONNECTORVALVE**.

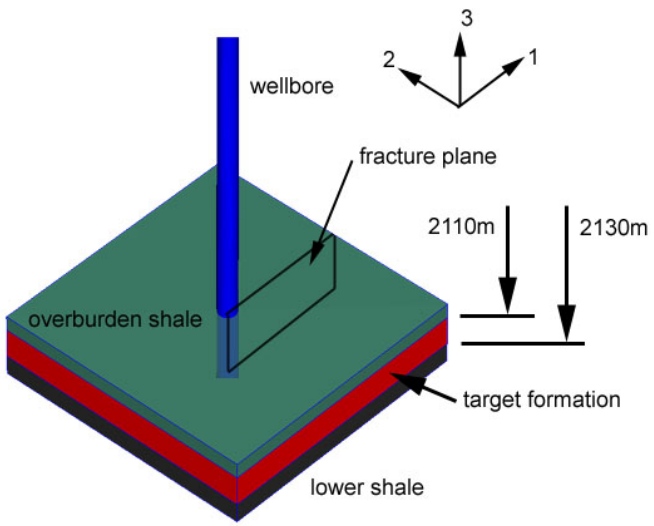

Figure 10.1.5–1 Position of the target formation and surrounding shale.

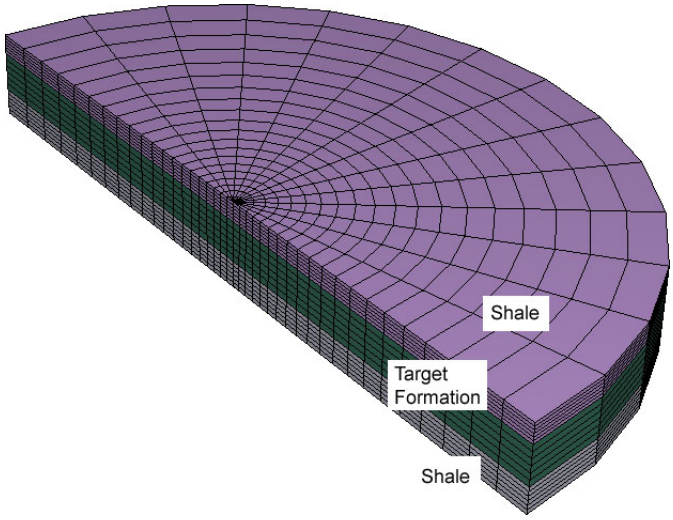

Figure 10.1.5–2 Near well-bore mesh.

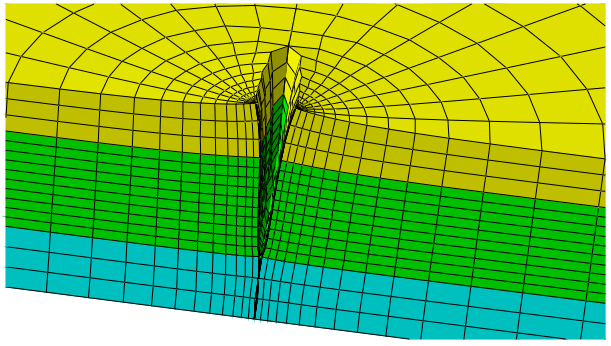

Figure 10.1.5–3 Fracture geometry following the injection stage, with the deformation magnified 50 times.

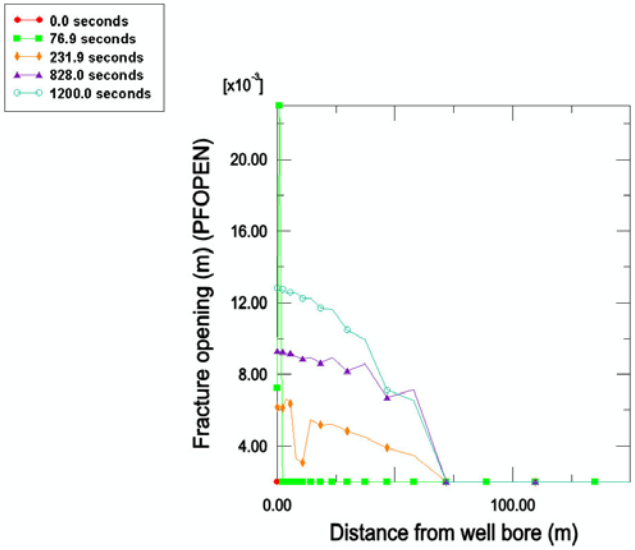

Figure 10.1.5–4 History of the fracture opening profile.

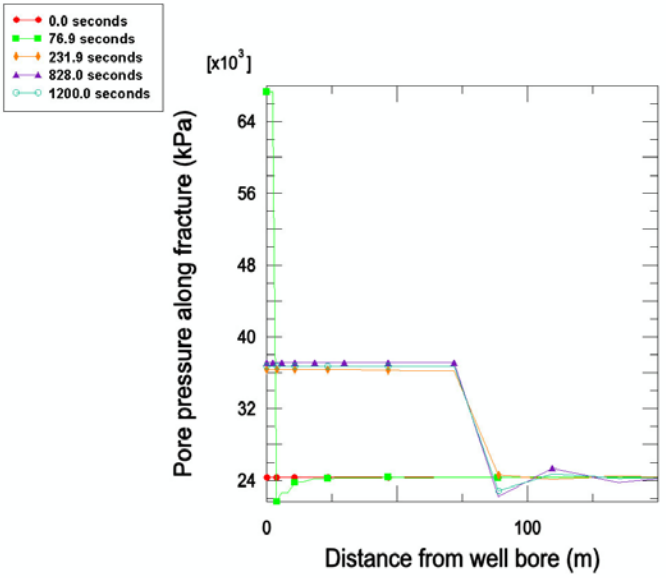

Figure 10.1.5–5 History of the fracture pore pressure profile.

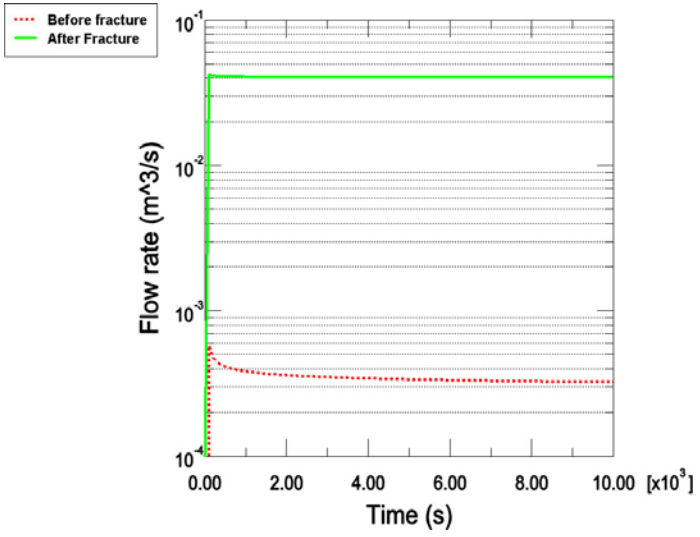

Figure 10.1.5–6 Well yield before and after the hydraulic fracture process.

10.1.6 PERMAFROST THAWING–PIPELINE INTERACTION

Product: Abaqus/Standard

Objectives

This example illustrates the use of the coupled temperature–pore pressure displacement modeling capability in Abaqus/Standard to model the effects of thaw settlement that commonly occurs in relatively warm pipelines buried in permafrost.

Application description

Thaw settlement generally occurs in shallow waters and at shore crossings where soil ice-bonded permafrost underlies the pipeline (Xu et al., 2009). Due to the heat released from the relatively warm pipeline, the surrounding permafrost may gradually thaw over years of operation and create a permafrost thaw bulb. The load carrying capacity of the soil is generally believed to be reduced as a result of the thaw formation, which could in turn (as a result of the weight of the soil above it) lead to excessive deformation and stress in the pipeline leading to its eventual damage.

Two primary mechanisms control the behavior of the problem: heat transfer from the warm pipeline to the surrounding permafrost leading to thawing of the permafrost and diffusion of the pore fluid and associated consolidation of the thawed soil mass surrounding the pipeline. The analysis is carried out utilizing two approaches. The first approach is a sequential one, in which the permafrost melting process is modeled as a pure heat transfer analysis in Abaqus, and the resulting temperature is used to drive a soils consolidation analysis. The second approach is fully coupled, in which the heat transfer and soils consolidation problems are solved in a fully coupled manner in a single analysis. This approach uses the coupled temperature–pore pressure elements that solve for the temperature field as a nodal degree of freedom in addition to the displacement and the pore pressure fields. The results obtained using these two approaches are compared, and the advantages of using a fully coupled approach are discussed. The model presented here has been adapted from Xu et al. (2009), where the first approach alone was used to investigate this problem.

Geometry

Figure 10.1.6–1 shows the geometry of the model consisting of two outer sections of sand separated by an inner section of clay, which approximates the nonuniform soil properties that are often encountered in practice along a pipeline. The geometry assumes symmetry about the right vertical plane in the figure, and the dimensions of the soil mass are as shown. The pipe diameter and thickness are assumed to be 0.4 m (15.76 in) and 0.096 m (3.8 in), respectively, and it is assumed to be buried 2.5 m below the soil surface.

Materials

The material properties assumed for this analysis are shown in Table 10.1.6–1, Table 10.1.6–2, Table 10.1.6–3, and Table 10.1.6–4 for clay, sand, steel, and water (pore fluid), respectively. The symbols E, ν, K, ρ, c, L, α, k, and e represent the Young's modulus, Poison's ratio, thermal conductivity, density, specific heat, latent heat, thermal expansion coefficient, permeability, and void ratio, respectively. The elastic and the pore fluid flow properties of the soil are assumed to depend on whether the soil is frozen (more precisely, whether the water in the soil is frozen) or thawed. The soil is assumed to be significantly stiff and impermeable when frozen compared to the corresponding properties when thawed. The properties in the frozen state and the thawed state are distinguished from each other using the symbols F and T, respectively, next to a property symbol. This approach approximately captures the effects of phase change of the pore fluid on the mechanical properties of the soil and can be improved upon with a more detailed modeling of the physics of the phase change process. In the heat transfer part of the sequential approach, the thermal properties are assumed to be weighted averages of the properties of the individual constituents (clay or sand, and water). The latent heat of fusion from ice to water is utilized to define the phase change of the soil. The pipe is assumed to be made out of steel, with the mechanical behavior defined using a linear elastic model along with thermal expansion. Inelastic response of the pipe material, such as plasticity and creep, can be easily included in the model if needed. Both the soil and the pore fluid are also assumed to undergo thermal expansion associated with the temperature variation. Thermal expansion is an important part of the overall physics of the problem, with the differential expansion of the pore fluid relative to pores in the soil often determining the initial rise in the pore pressure.

Initial conditions

The initial temperature is assumed to be −5°C everywhere in the model. The initial void ratio, pore pressure, and saturation are assumed to be 1.8, 0.0, and 1.0, respectively, everywhere in the model. Thus, the pore fluid flow is assumed to occur under fully saturated conditions. Initial effective geostatic stress in the vertical direction is defined as a function of the depth below the soil surface. The stress in the horizontal direction is assumed to be a fraction of the stress in the vertical direction.

Boundary conditions and loading

All the outer surfaces of the model (except the top surface) are assumed to be restrained from moving in a perpendicular direction. Following Xu et al. (2009), the model assumes the flow of heat and fluid across all the outer surfaces (except the top surface) to be zero. The top surface allows free drainage (zero pore pressure). The axial displacement at both ends of the pipe is restrained.

Abaqus modeling approaches and simulation techniques

In the consolidation part of the analysis in the sequential approach, the soil is modeled using pore pressure elements with displacement and pore pressure degrees of freedom, while the pipe is modeled using solid continuum elements using displacement degrees of freedom only. In the coupled analysis, the soil is modeled using the coupled elements with displacement, pore pressure, and temperature degrees of

freedom, while the pipe is modeled using coupled elements with displacement and temperature degrees of freedom only. The soil and the pipe share nodes at the interface. An alternate approach would model this interface utilizing contact constraints; however, this approach has not been used because contact is not supported with the coupled temperature–pore pressure elements.

Analysis types

The sequential approach utilizes a heat-transfer analysis first to determine the temperature profile. This temperature profile is subsequently used to drive the mechanical part of the simulation that does not model heat transfer. The latter consists of two steps: a geostatic analysis, followed by a soils consolidation analysis. On the other hand, the coupled approach solves the thermal and mechanical problem in a fully coupled manner and consists of two steps: a geostatic analysis, followed by a soils consolidation analysis.

Mesh design

The heat transfer part of the sequential approach uses first-order brick (DC3D8) elements, while the consolidation part of the sequential approach uses first-order reduced-integration (C3D8RP and C3D8R) elements for the soil and pipe regions, respectively. The coupled analysis uses first-order reduced-integration fully coupled (C3D8RPT and C3D8RT) elements for the soil and pipe regions, respectively.

Loading

Inside the pipe the fluid is assumed to be flowing at 20°C. A constant convection coefficient on the inner pipe wall is assumed. The top surface of the soil is subjected to a sinusoidal temperature variation ranging between −5°C and 5°C. The above boundary condition approximately represents the season variation of temperature at the soil surface. The weight of the pipe is considered as a load and is modeled as a body force in the vertical direction.

While the physics of this problem will likely span two or more decades, the present analysis is carried out for a period of one year in order to present the basic framework for an analysis of this type.

Solution controls

The simulations use solution controls to specify a nondefault initial value of the time average pore fluid flux. The default choice may not be appropriate in situations such as those encountered in the present problem where the fluid velocities are, in relative terms, lower compared to typical flux values encountered for other fields (such as displacements or rotations). Without the above specification, the increments would be treated as linear from the viewpoint of the continuity equation. In other words, without using solution controls to specify a nondefault initial value of the time average pore fluid flux, the pore fluid part of the incrementation will be treated as linear. Consequently, the continuity equation would be assumed to have been satisfied at the first iteration itself, without performing any further iterations to compute corrections to pore pressure.

Results and discussion

Figure 10.1.6–2 shows a contour of the temperature field around the buried pipe after a period of one year. The temperature profile can be used to determine the thaw bulb around the pipe. The results are

obtained from the heat transfer part of the sequential approach; the coupled analysis produces similar results. The thaw bulb represents the region where the permafrost has thawed and the temperature is above freezing. Figure 10.1.6–2 shows the mesh for the whole model along with the contour plot of the fluid velocities. The zero pore pressure boundary condition on the top surface allows the seepage of pore fluid across this surface. Clay is significantly less permeable compared to sand; and the effect can be observed in Figure 10.1.6–3, the flow across the top surface in the clay section is less compared to the flow in the sand section.

Figure 10.1.6–4 shows the temperature history at a point (node number 1591) in the soil in the vicinity of the pipe. The two curves were obtained from the uncoupled (sequential) and coupled analysis. The temperature results are, in relative terms, close to each other before thawing. However, upon thawing the results from the coupled analysis predict a higher temperature. The latter may be explained by recalling that unlike the coupled analysis, the heat transfer part of the uncoupled (sequential) analysis does not account for heat transfer associated with pore fluid flow. The results from both the sequential and coupled analyses predict that the temperature does not increase significantly for a certain period of time after it reaches 0°C. This behavior is due to phase change of the pore fluid as a result of thawing; all the available heat is used up as the latent heat of fusion.

Figure 10.1.6–5 shows the normalized (by the maximum vertical displacement from the uncoupled analysis) vertical displacement as a function of length along the span of the pipe for both the uncoupled (sequential) and coupled analyses. The uncoupled analysis predicts a higher peak displacement compared to the coupled analysis. This can be attributed to the difference in temperatures at points in the vicinity of the pipe as predicted by the two analyses and the associated effects on the elastic stiffness of the surrounding soil mass. It is particularly interesting to note that a fully coupled analysis can be used as a basis for a less conservative design as the predicted displacements and associated stresses are lower.

Input files

buried_pipe_permafrost_ht.inp	Heat transfer part of the sequential analysis.
buried_pipe_permafrost_consol.inp	Consolidation part of the sequential analysis.
buried_pipe_permafrost_ctup.inp	Fully coupled analysis.

References

Abaqus Analysis User's Guide

- "Coupled pore fluid diffusion and stress analysis," Section 6.8.1 of the Abaqus Analysis User's Guide
- "Geostatic stress state," Section 6.8.2 of the Abaqus Analysis User's Guide

Abaqus Keywords Reference Guide

- *GEOSTATIC
- *SOILS

Other

- Xu, J., B. Abdalla, A. Eltaher, and P. Jukes, "Permafrost Thawing-Pipeline Interaction Advanced Finite Element Model," Proceedings of the ASME 2009 28th International Conference on Ocean, Offshore, and Arctic Engineering, OMAE2009–79554, 2009.

Table 10.1.6–1 Properties for clay (F-frozen state, T-thawed state).

Property	Value
E (F)	1.03421×10^{11} Pa
E (T)	6.89476×10^{5} Pa
ν	0.30
K	2.0 J/sec m°C
ρ	1602.0 kg/m^3
c	1381.0 J/kg °C
α	9.67×10^{-6} /°C
k (F)	1.0×10^{-14} m/sec
k at $e = 1.0$ (T)	1.0×10^{-8} m/sec
k at $e = 1.8$ (T)	2.0×10^{-8} m/sec

Table 10.1.6–2 Properties for sand (F-frozen state, T-thawed state).

Property	Value
E (F)	1.03421×10^{11} Pa
E (T)	1.03421×10^{7} Pa
ν	0.30
K	2.0 J/sec m°C
ρ	1602.0 kg/m^3
c	1381.0 J/kg °C
α	5.60×10^{-6} /°C
k (F)	1.0×10^{-13} m/sec

Property	Value
k at $e = 1.0$ (T)	1.0×10^{-7} m/sec
k at $e = 1.8$ (T)	2.0×10^{-7} m/sec

Table 10.1.6–3 Properties for steel.

Property	Value
E	2.0×10^{11} Pa
ν	0.30
K	52.0 J/sec m°C
ρ	7832.0 kg/m^3
c	434.0 J/kg °C
α	12.0×10^{-6} /°C

Table 10.1.6–4 Properties for water (pore fluid).

Property	Value
K	0.58 J/sec m°C
ρ	1000.0 kg/m^3
c	4186.0 J/kg °C
α (at −5°C)	51.0×10^{-6} /°C
α (at 0°C)	51.0×10^{-6} /°C
α (at 1°C)	-16.67×10^{-6} /°C
α (at 4°C)	0.0
α (at 10°C)	29.33×10^{-6} /°C

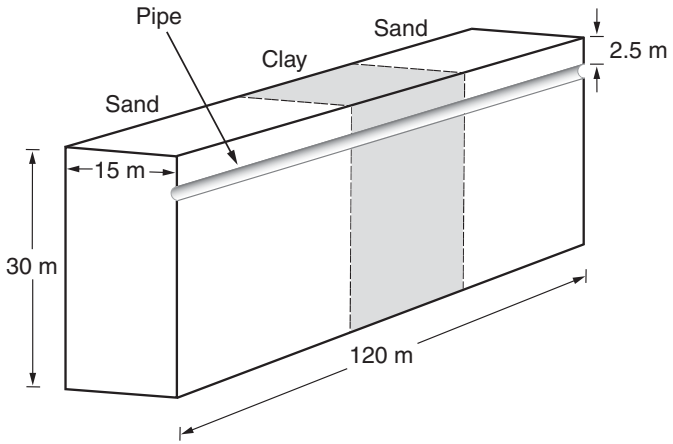

Figure 10.1.6–1 Pipeline buried in permafrost (half-symmetry model).

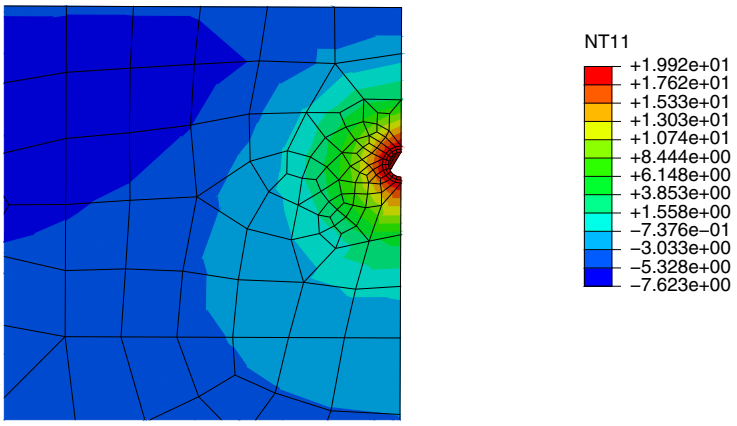

Figure 10.1.6–2 Thaw bulb around the relatively warm pipe after one year.

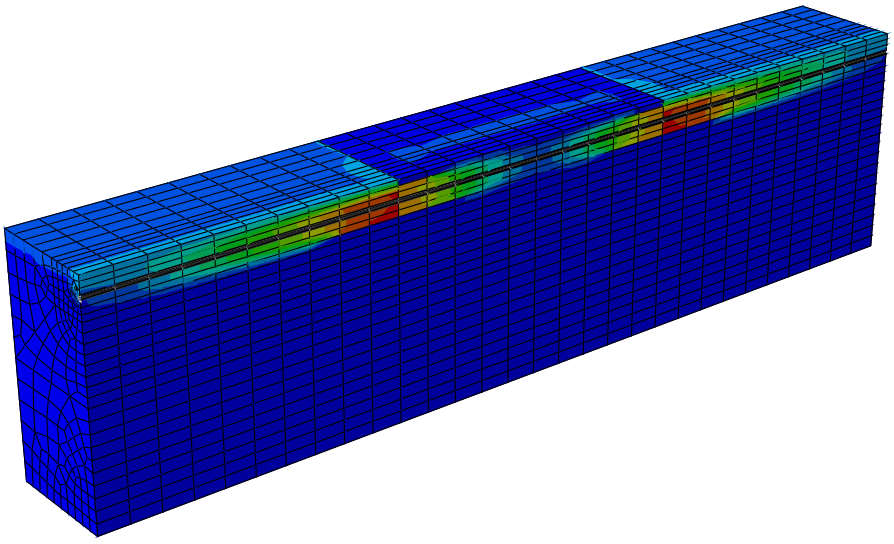

Figure 10.1.6–3 The meshed buried pipeline model showing the contour of fluid velocities. The relatively impermeable clay region exhibits low fluid velocities (blue-colored contour in top center section).

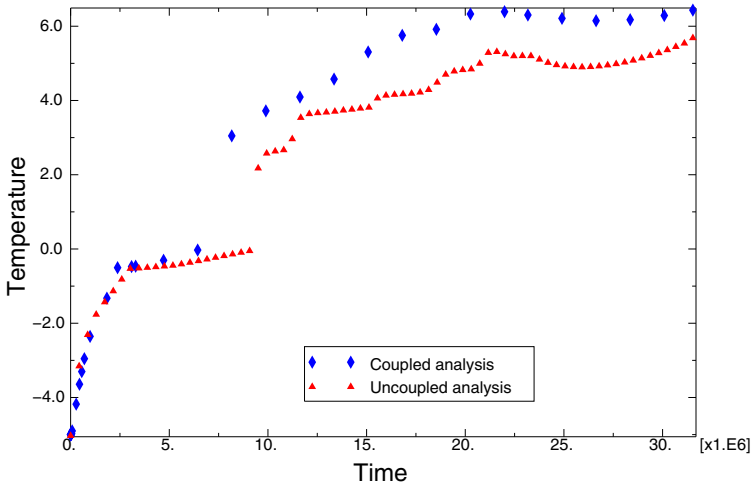

Figure 10.1.6–4 Temperature history in the soil near the pipe.

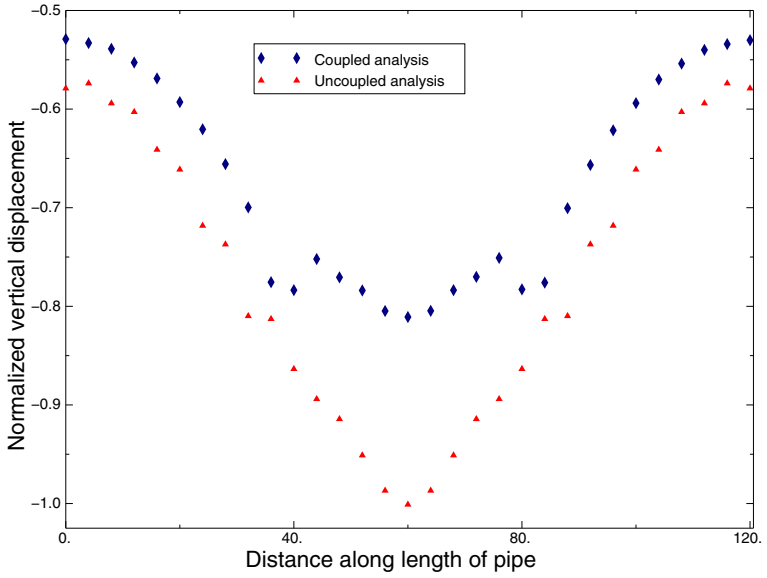

Figure 10.1.6–5 Normalized vertical displacement along the length of the pipe.

11. Structural Optimization Analyses

- “Topology optimization analyses,” Section 11.1
- “Shape optimization analyses,” Section 11.2
- “Sizing optimization analyses,” Section 11.3
- “Bead optimization analyses,” Section 11.4

11.1 Topology optimization analyses

- “Topology optimization of an automotive control arm,” Section 11.1.1

11.1.1 TOPOLOGY OPTIMIZATION OF AN AUTOMOTIVE CONTROL ARM

Products: Abaqus/Standard Abaqus/CAE

Objectives

This example uses the Optimization module to optimize the design of an automotive control arm by reducing the volume of the control arm while maximizing its stiffness.

Application description

This example illustrates topology optimization of an automotive control arm. During a topology optimization, the material properties of the elements in the design area are modified (effectively removing elements from or adding elements to the Abaqus analysis) until the optimal solution is achieved. For more information, see "Topology optimization" in "Structural optimization: overview," Section 13.1.1 of the Abaqus Analysis User's Guide.

Geometry

The control arm model is a single orphan mesh part that was meshed with quadratic tetrahedral (C3D10) elements. The control arm is symmetric about the *X*–*Y* plane, and only one half of the model is studied.

Materials

The control arm is made of an elastic material with a Young's modulus of 210 GPa and a Poisson's ratio of 0.3.

Boundary conditions and loading

The center of the model is constrained to be symmetric about the *Y*–*Z* plane. The upper left and upper right ends of the control arm are outside the design area and are fixed in all three translation degrees of freedom. The lower bearing center is also outside the design area, and its translation is constrained along the *z*-direction.

The center node of the lower bearing is loaded with a concentrated force of 70000 N in the *x*-direction and −70000 N in the *y*-direction.

Optimization features

The topology optimization is configured as described in the following sections.

Optimization task

This example creates a topology optimization task that is governed by the condition-based optimization algorithm.

Design area

The design area of the model is the region that will be modified during the optimization, as shown in Figure 11.1.1–1. Some regions are excluded from the design area because they are required for fixtures and for applying loads. The material properties of the elements excluded from the design area remain unchanged.

Design responses

A design response is created that calculates the sum of the strain energy over all the elements in the design area. A second design response calculates the volume of the design area.

Objective function

Objective functions define the objective of the optimization. In this example a single objective function attempts to minimize the sum of the strain energy of the design area. Since compliance is defined as the sum of the strain energy, and stiffness is the reciprocal of compliance, the objective function is equivalent to maximizing the stiffness of the design area.

Constraint

Optimization constraints constrain the optimization process from making changes to the topology of the model. Constraints must allow the optimization to arrive at a solution that is both feasible and acceptable. In this example a single constraint is created that specifies that the optimized model should contain 57% of the initial volume of the original control arm.

Geometry restrictions

You can apply geometric restrictions to further constrain the topology optimization process to consider only designs that can be manufactured using standard techniques, such as casting or forging. The control arm is manufactured by forging. The demold control geometric restriction shown in Figure 11.1.1–1 ensures that the structure formed by the topology optimization can be removed from the forging die and does not contain undercuts. This example also introduces a frozen area geometric restriction to limit the material that is removed from the upper arm of the structure, as shown in Figure 11.1.1–2.

Abaqus modeling approaches and simulation techniques

This example imports the model in the form of an orphan mesh from an input file. The input file contains the element sets that define the regions of the model that are used by the optimization, such as the design area and the frozen area. The example creates an optimization process with a global stop criterion of 17 design cycles.

Analysis types

A static stress analysis is performed.

Constraints

The center node is connected to the bearing surface through a kinematic coupling.

Run procedure

A Python script is included that reproduces the model using the Abaqus Scripting Interface in Abaqus/CAE. The Python script (control_arm_topology_optimization.py) imports the input file (control_arm.inp) and builds the optimization model. The Python script can be run interactively or from the command line. Both the script and the input file must be available from your working directory.

When the script completes, you can use the Optimization module to review the topology optimization model that was created in Abaqus/CAE. To run the optimization, you can submit the optimization process from the **Optimization Process Manager** in the Job module. You can use the **Optimization Process Manager** to monitor the progression of the optimization and to view the results of the topology optimization in the Visualization module.

Results and discussion

The results are available in the output database file created by the optimization process. The step contains 17 optimization iterations that correspond with the 17 design cycles of the optimization process. Figure 11.1.1–3 shows a history output plot of the strain energy and volume design responses over the 17 design cycles. The control arm is optimized such that the maximum stiffness is achieved while satisfying the specified target volume. Although the strain energy design response increases (the overall stiffness decreases) as the volume of the control arm is reduced, the optimized design achieves a topology with only 57% of the initial volume. Figure 11.1.1–4 shows how the topology optimization progressively removes material from the control arm while it seeks an optimized solution.

Files

control_arm_topology_optimization.py	Python script to import the orphan mesh from the input file and create the topology optimization.
control_arm.inp	Input file to create the orphan mesh control arm and the element sets that are used by the optimization.

References

Abaqus Analysis User's Guide

- Chapter 13, "Optimization Techniques," of the Abaqus Analysis User's Guide
- "Topology optimization" in "Structural optimization: overview," Section 13.1.1 of the Abaqus Analysis User's Guide

Abaqus/CAE User's Guide

- Chapter 18, "The Optimization module," of the Abaqus/CAE User's Guide
- "Understanding optimization processes," Section 19.5 of the Abaqus/CAE User's Guide

Other

- Bendsøe, M. P., E. Lund, N. Ohloff, and O. Sigmund, "Topology Optimization - Broadening the Areas of Application," Control and Cybernetics, vol. 34, pp. 7–35, 2005.

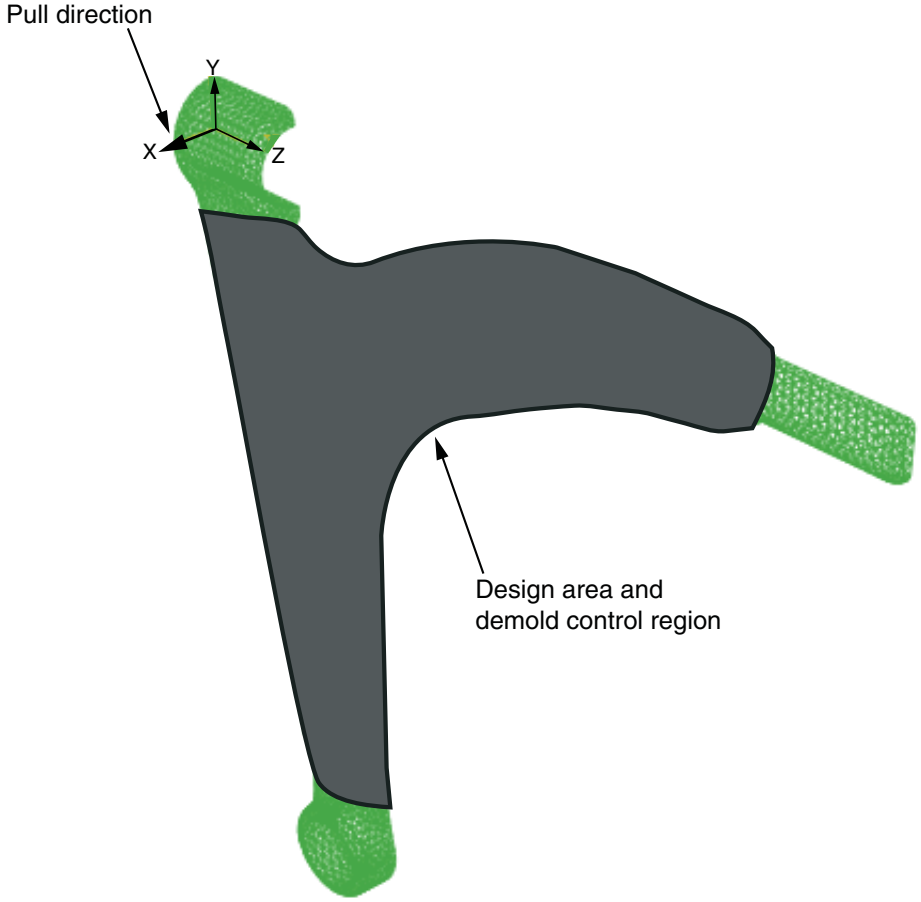

Figure 11.1.1–1 Design area and demold control region.

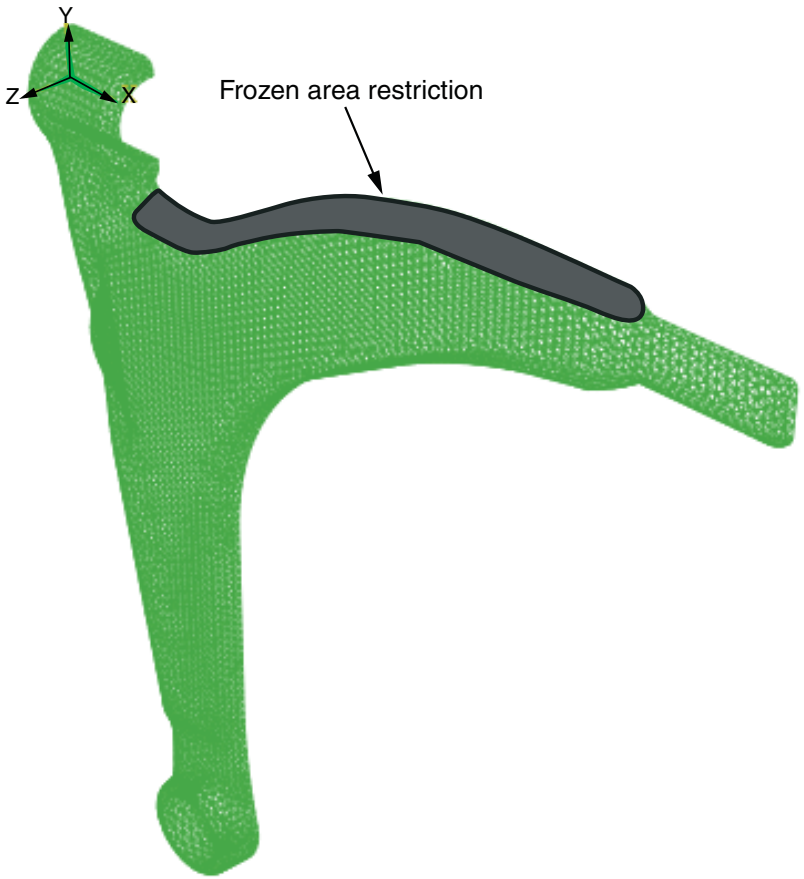

Figure 11.1.1–2 Frozen area geometric restriction.

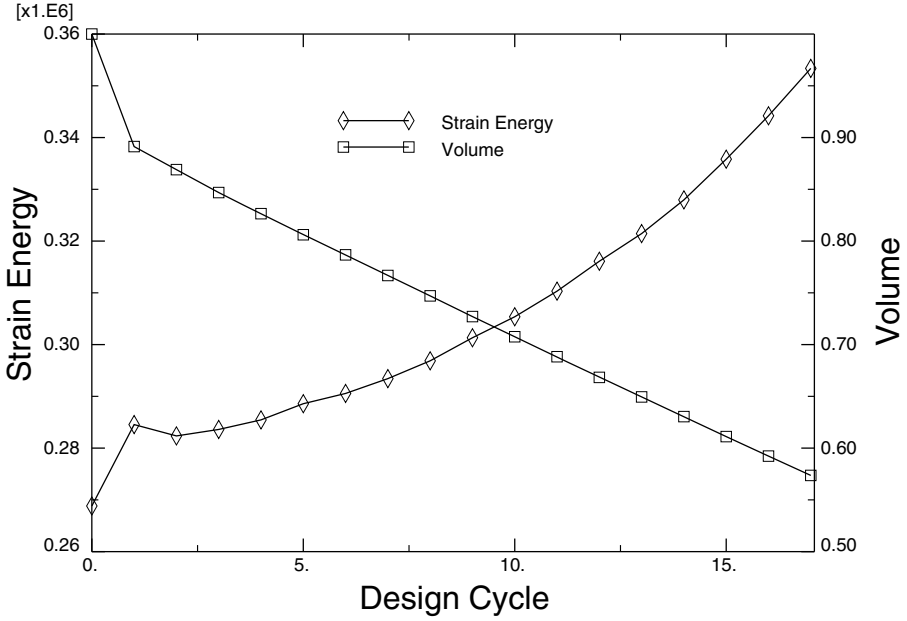

Figure 11.1.1–3 Design responses (strain energy and volume).

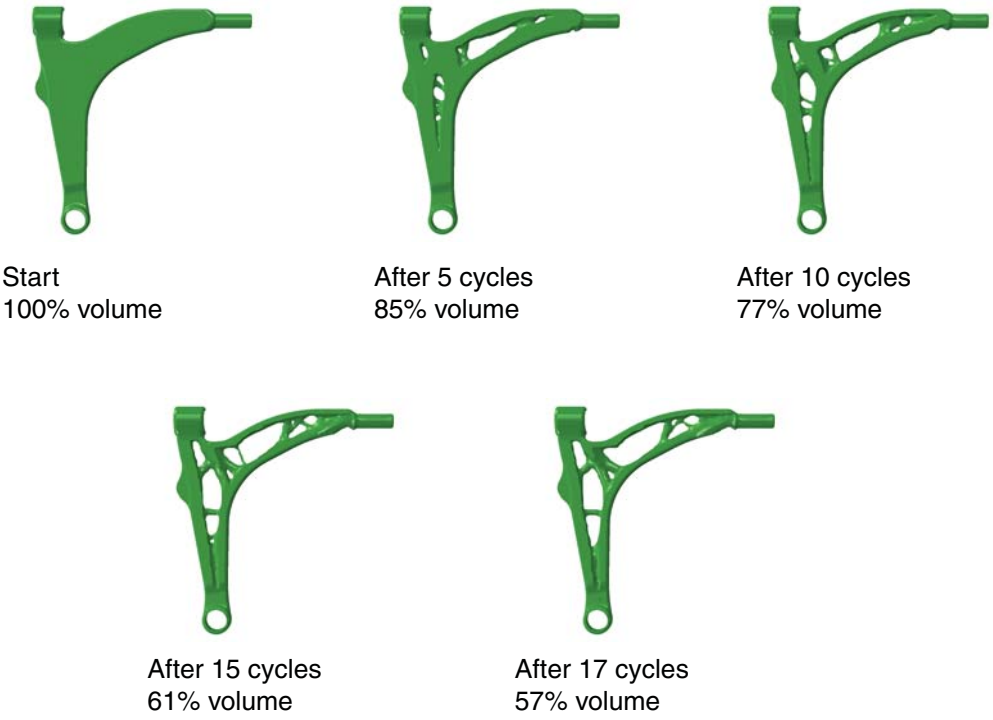

Figure 11.1.1–4 Progression of the topology optimization.

11.2 Shape optimization analyses

- “Shape optimization of a connecting rod,” Section 11.2.1

11.2.1 SHAPE OPTIMIZATION OF A CONNECTING ROD

Products: Abaqus/Standard Abaqus/CAE

Objectives

This example uses the Optimization module to minimize the stress concentrations in a connecting rod without changing the volume of the connecting rod.

Application description

This example illustrates shape optimization of a connecting rod. Shape optimization makes slight modifications to the position of the surface nodes in the design area to achieve the optimized solution. Shape optimization is typically applied at the end of the design process when the general outline of a component is fixed and only minor changes are allowed. For more information, see "Shape optimization" in "Structural optimization: overview," Section 13.1.1 of the Abaqus Analysis User's Guide.

Geometry

The connecting rod model is a single orphan mesh part that was meshed with linear tetrahedral (C3D4) elements. The connecting rod is symmetric about the *X*–*Z* plane.

Materials

The connecting rod is made of an elastic material with a Young's modulus of 210 GPa, a Poisson's ratio of 0.3, and a density of 7800 kg/m^3.

Boundary conditions and loading

The displacement of the center node of the small end is constrained in the *x*- and *y*-directions, and the rotation of the center node is constrained in the *y*- and *z*-directions. For the center node of the big end, the displacement in the *x*- and *z*-directions and the rotation in the *y*- and *z*-directions are constrained.

During the first step a 25000 N load is applied to the center node of the small end of the connecting rod in the *z*-direction.

During the second step a −2000 N load is applied to the center node of the small end of the connecting rod in the *z*-direction and a 1750 N load is applied to the center node of the big end of the connecting rod in the *y*-direction. In addition, a rotation of 0.004 radians about the *x*-axis is applied to the center node of the big end.

Optimization features

The shape optimization is configured as described in the following sections.

Optimization task

This example creates a shape optimization task. To ensure good quality elements in the final design, mesh smoothing is applied to the elements in the design area.

Design area

The design area of the model is the region that will be modified during the optimization, as shown in Figure 11.2.1–1. Regions are excluded from the design area because they are required for fixtures and for applying loads.

Design responses

A design response is created for each step that determines the maximum von Mises stress in the design area. A third design response calculates the volume of the design area.

Objective function

The objective function determines which of the two design responses results in the largest von Mises stress in the design nodes. The objective function then tries to minimize the maximum von Mises stress for that design response.

Constraint

The volume design response is configured as the single optimization constraint such that the total volume of the design area remains unchanged during the optimization process.

Geometry restrictions

The example introduces a casting restriction by defining demold control geometry restrictions that are applied to the nodes in each half of the design area in the positive x- and negative x-directions. Figure 11.2.1–2 illustrates the demold control geometry restriction that is applied to one half of the design area in the positive x-direction.

Abaqus modeling approaches and simulation techniques

This example imports the model in the form of an orphan mesh from an input file. The input file contains the element sets that are used to define the regions of the model that are used by the optimization, such as the design area and the demold control region. The example creates an optimization process with a global stop criterion of 15 design cycles. To maintain the quality of the surface elements, mesh smoothing is applied to the design area, which adjusts the position of the inner nodes in relation to the movement of the surface nodes. For more information, see “Applying mesh smoothing to a shape optimization” in “Structural optimization: overview,” Section 13.1.1 of the Abaqus Analysis User’s Guide.

Analysis types

The analysis includes two static, general steps.

Constraints

The center nodes at both the ends of the connecting rod are connected to the bearing surfaces of the connecting rod with kinematic couplings.

Run procedure

A Python script is included that reproduces the model using the Abaqus Scripting Interface in Abaqus/CAE. The Python script (conrod_shape_optimization.py) imports the input file (connecting_rod.inp) and builds the optimization model. The script can be run interactively or from the command line. Both the Python script and the input file must be available from your working directory.

When the script completes, you can use the Optimization module to review the shape optimization model that was created in Abaqus/CAE. To run the optimization, you can submit the optimization process from the **Optimization Process Manager** in the Job module. You can use the **Optimization Process Manager** to monitor the progression of the optimization and to view the results of the shape optimization in the Visualization module.

Results and discussion

The results are available in the output database file created by the optimization process. The step contains 15 optimization iterations that correspond with the 15 design cycles of the optimization process. Figure 11.2.1–3 shows a history output plot of the von Mises stress design response for each of the two load cases over the 15 design cycles. The history output plot also shows the volume design response, which is kept constant throughout the optimization.

The position of the surface nodes in the design area is optimized such that for the specified volume constraint and geometry restrictions the von Mises stress is minimized during the load case that results in the maximum stress. In this example the 25000 N load that is applied to the small end in the first step results in the highest von Mises stress in the connecting rod. Therefore, the objective function adjusts the surface nodes to reduce the maximum von Mises stress during the first step, although the resulting optimized shape allows the von Mises stress to increase slightly under the loading conditions in the second step.

Figure 11.2.1–4 shows the initial von Mises stress distribution during the first load case and the change in the stress distribution after 15 design cycles. Figure 11.2.1–5 shows similar von Mises stress distribution plots before and after optimization during the second load case.

Files

conrod_shape_optimization.py	Script to create the model and the optimization attributes using connecting_rod.inp.
connecting_rod.inp	Input file to create the orphan mesh connecting rod and the element sets that are used by the optimization.

References

Abaqus Analysis User's Guide

- Chapter 13, "Optimization Techniques," of the Abaqus Analysis User's Guide
- "Shape optimization" in "Structural optimization: overview," Section 13.1.1 of the Abaqus Analysis User's Guide

Abaqus/CAE User's Guide

- Chapter 18, "The Optimization module," of the Abaqus/CAE User's Guide
- "Understanding optimization processes," Section 19.5 of the Abaqus/CAE User's Guide

Other

- Bakhtiary, N., and P. Allinger, "A New Approach for Size, Shape and Topology Optimization," SAE International Congress and Exposition, Detroit, Michigan, USA, February 26–29, 1996.

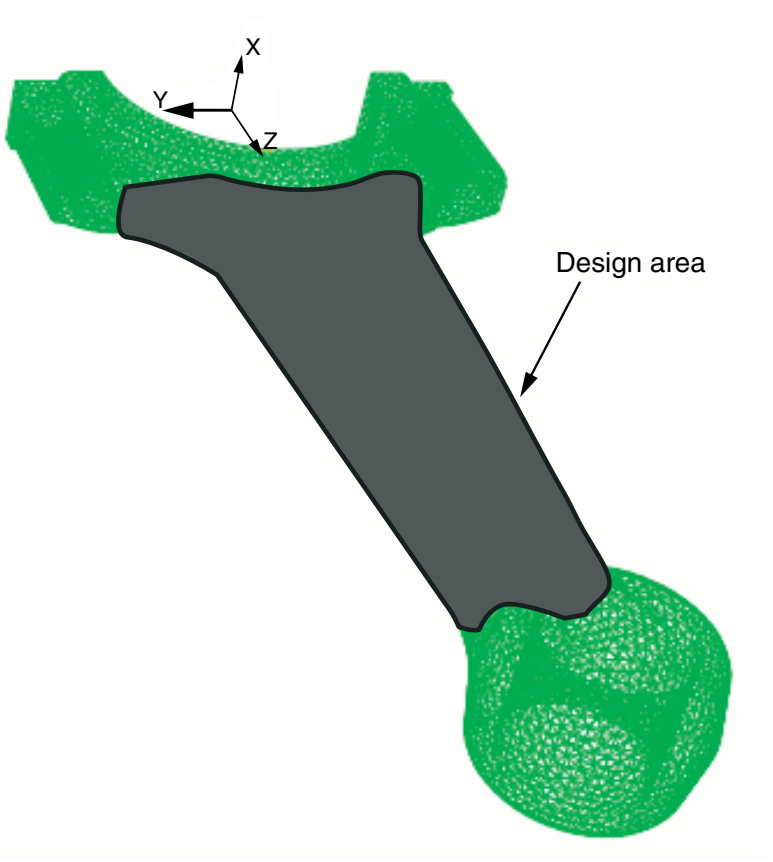

Figure 11.2.1–1 Design area.

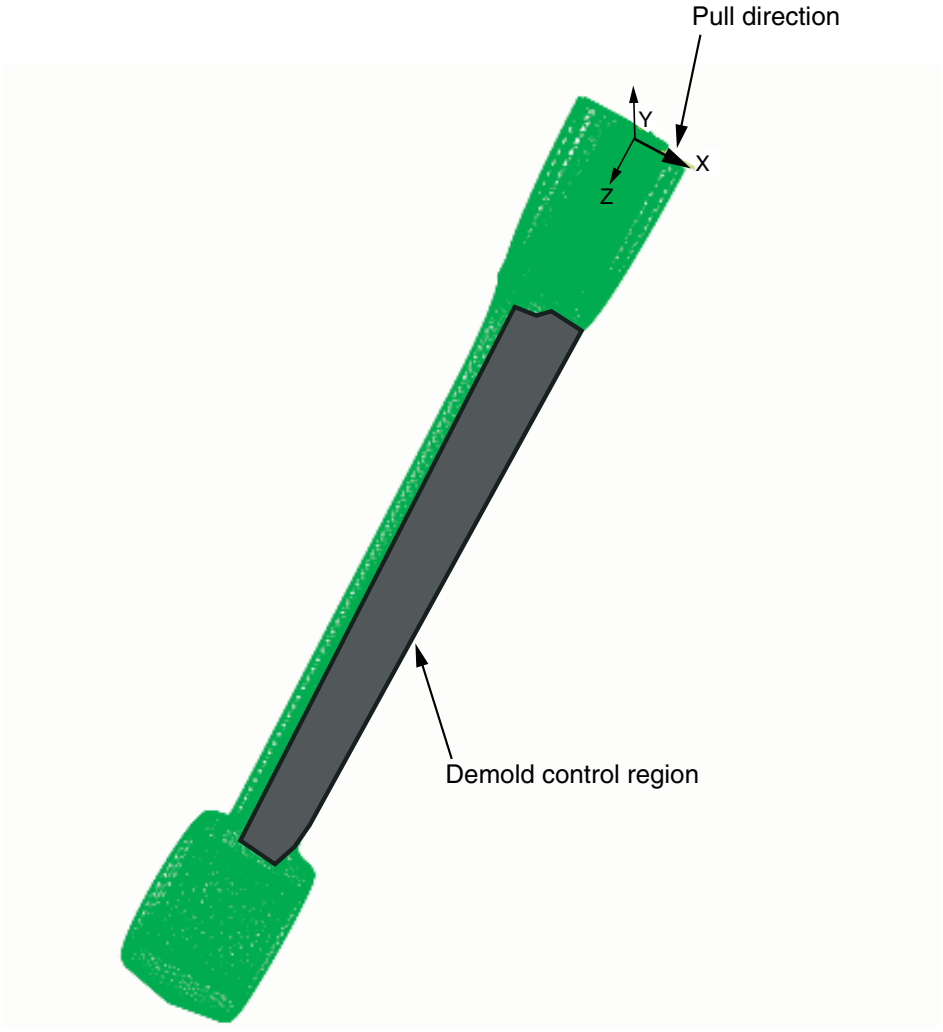

Figure 11.2.1–2 Demold control geometric restriction.

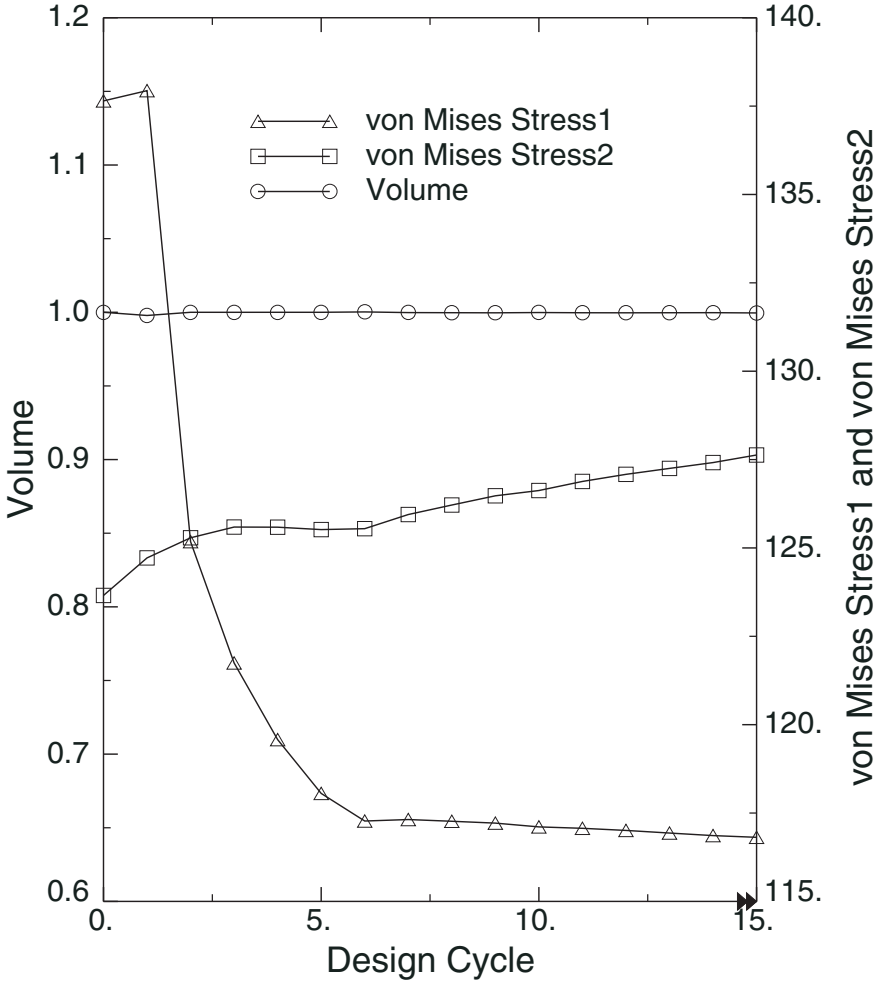

Figure 11.2.1–3 Design responses (von Mises stress and volume).

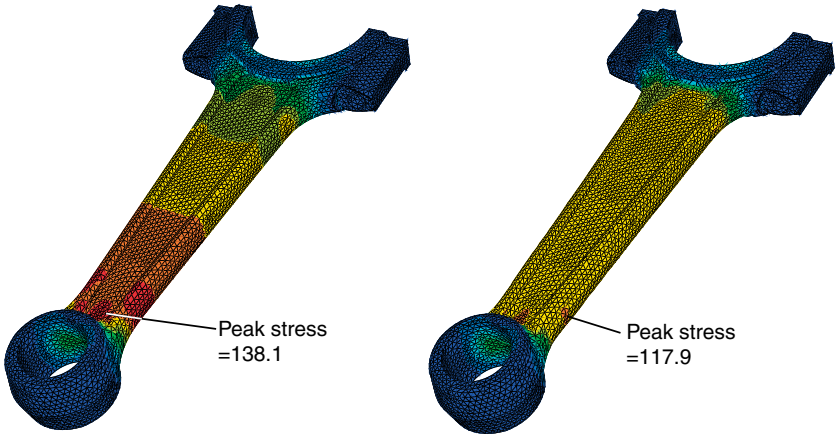

Figure 11.2.1–4 Distribution of von Mises stress before (left) and after optimization (right) during first load case.

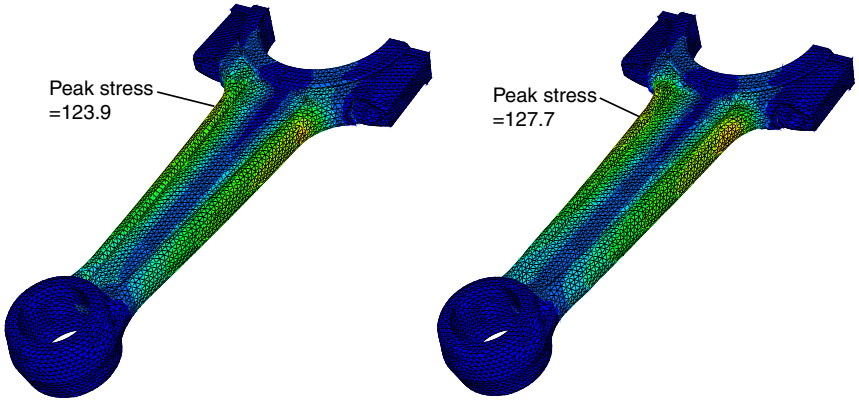

Figure 11.2.1–5 Distribution of von Mises stress before (left) and after optimization (right) during second load case.

11.3 Sizing optimization analyses

- "Sizing optimization of a gear shift control holder," Section 11.3.1
- "Sizing optimization of a car door," Section 11.3.2

11.3.1 SIZING OPTIMIZATION OF A GEAR SHIFT CONTROL HOLDER

Products: Abaqus/Standard Abaqus/CAE

Objectives

This example uses the Optimization module to minimize the sum of the strain energy (maximize the stiffness) in a pressed sheet metal holder by changing the shell thickness while maintaining the original weight.

Application description

This example illustrates sizing optimization of a pressed sheet metal holder that is used in an automotive gearbox linkage. Sizing optimization modifies the thickness of the shell elements in the design area to achieve the optimized solution. The example illustrates "free"optimization of the shell thickness, with no regard for the thickness of adjacent elements, and "clustered" optimization of the shell thickness, that forces elements in selected regions to have the same shell thickness. For more information, see "Sizing optimization" in "Structural optimization: overview," Section 13.1.1 of the Abaqus Analysis User's Guide.

Geometry

The pressed sheet metal holder is a single orphan mesh part. The part is meshed with general-purpose conventional shell (predominately S4) elements. The initial shell thickness is 1.0 mm.

Materials

The holder is made of an elastic material with a Young's modulus of 206 GPa, a Poisson's ratio of 0.3, and a density of 7840 kg/m^3.

Boundary conditions and loading

The boundary conditions and loads are shown in Figure 11.3.1–1. The four mounting holes are constrained in all directions in the initial step. During the first linear perturbation step a −2500 N load is applied to the hole in the *x*-direction. During the second linear perturbation step a torsional moment of 80,000 Nmm about the *x*-axis is applied to the hole.

Optimization features

The sizing optimization is configured as described in the following sections.

Optimization task

This example creates a sizing optimization task.

Design area

The design area of the model is the region that will be modified during the optimization, as shown in Figure 11.3.1–1.

Design responses

A design response is created for each step that determines the compliance or strain energy in the design area. A second design response calculates the volume of the entire model.

Objective function

The objective function tries to minimize the maximum compliance from the two linear perturbation steps. Compliance is the reciprocal of stiffness, and minimizing the compliance is equivalent to maximizing the global stiffness.

Constraint

The shell thickness is constrained between absolute values of 0.1 and 3.0. In addition, the volume is constrained such that the total volume of the holder is less than or equal to the original volume.

Geometry restrictions

The example introduces clustered rings of shell elements of the same thickness in the design area. In effect, clusters generate strengthening ribs or rings in the sheet metal structure you are optimizing; clustered regions can be reproduced in manufacturing by layering sheets of constant thickness.

Abaqus modeling approaches and simulation techniques

This example imports the model in the form of an orphan mesh from an input file. The input file contains the element sets that are used to define the regions of the model that are used by the optimization, such as the design area. The example creates an optimization process that you can submit for analysis.

Analysis types

The analysis includes two static, perturbation steps.

Constraints

Kinematic couplings connect the node at the center of the holes with the nodes at the edges of the hole.

Run procedure

A Python script is included that reproduces the model using the Abaqus Scripting Interface in Abaqus/CAE. The Python script (holder_sizing_optimization.py) imports the input file (holder.inp) and builds the optimization model. A second Python script (holder_sizing_optimization_w_clustering.py) performs the same optimization but introduces shell thickness clustering in the design area. The scripts

can be run interactively or from the command line. The Python scripts and the input file must be available from your working directory.

To run the optimization, you can submit the optimization process from the **Optimization Process Manager** in the Job module. You can use the **Optimization Process Manager** to monitor the progression of the optimization. In addition, when the optimization process is complete, you can use the **Optimization Process Manager** to combine the output from the optimization into a single output database file that can be viewed in the Visualization module.

Results and discussion

The optimization process is run over 15 design cycles for the free optimization and over 13 design cycles for the optimization with clustering. During each design cycle, the optimization results are saved in optimization files. In addition, the Abaqus analysis results are saved in output database files during the initial design cycle and during the last design cycle. To view the results of the optimization in the Visualization module, the optimization data in the optimization files and the analysis results in the output database files must be combined. The output database file created during the initial design cycle is selected as the base results output database file. During the combine operation, the optimization data from each design cycle and the analysis results from the last design cycle are appended to the base results output database file. Each frame of the combined output database file corresponds to a design cycle of the optimization. For more information about the files generated by an optimization process and how they are combined, see "Understanding the files generated by an optimization process," Section 19.5.2 of the Abaqus/CAE User's Guide, and "Postprocessing an optimization," Section 19.5.3 of the Abaqus/CAE User's Guide.

Figure 11.3.1–2 shows the initial displacement magnitude at the end of the second step prior to any optimization. Figure 11.3.1–3 and Figure 11.3.1–4 show the value of the shell thickness and the displacement magnitude, respectively, after free sizing optimization. Figure 11.3.1–5 and Figure 11.3.1–6 show the value of the shell thickness and the displacement magnitude, respectively, after sizing optimization with clustering in the design area.

After the optimization, the shell thickness is increased at the end of the design area where the load and moment are applied. The shell thickness is also increased close to the mounting holes. To maintain the volume of the arm, the shell thickness is reduced in the rest of the design area. As expected, the free sizing optimization produces the best results with a 45% reduction of the maximum displacement. The optimization with circular clustering in the design area, which could be manufactured by welding sheets of metal together, still leads to a 30% reduction of the maximum displacement.

Python scripts

holder_sizing_optimization.py	Script to create the model and the optimization attributes using holder.inp.
holder_sizing_optimization_w_clustering.py	Script to create the model and the optimization attributes, including shell thickness clustering, using holder.inp.

Input file

holder.inp	Orphan mesh gear shift control holder and the node and element sets that are used by the optimization.

References

Abaqus Analysis User's Guide

- Chapter 13, "Optimization Techniques," of the Abaqus Analysis User's Guide
- "Sizing optimization" in "Structural optimization: overview," Section 13.1.1 of the Abaqus Analysis User's Guide

Abaqus/CAE User's Guide

- Chapter 18, "The Optimization module," of the Abaqus/CAE User's Guide
- "Understanding optimization processes," Section 19.5 of the Abaqus/CAE User's Guide

Other

- Svanberg, K., The Method of Moving Asymptotes—A New Method for Structural Optimization International Journal for Numerical Methods in Engineering, vol. 24, pp. 359–373, 1987.

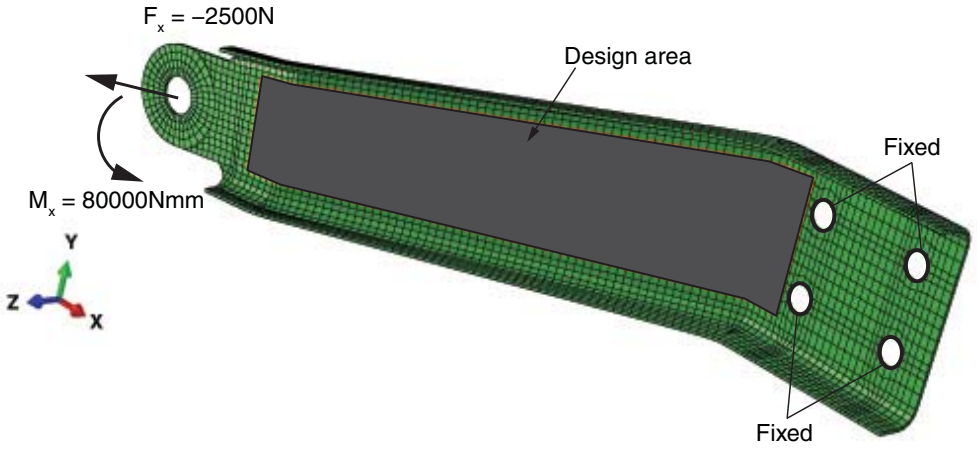

Figure 11.3.1–1 Design area, loads, and boundary conditions.

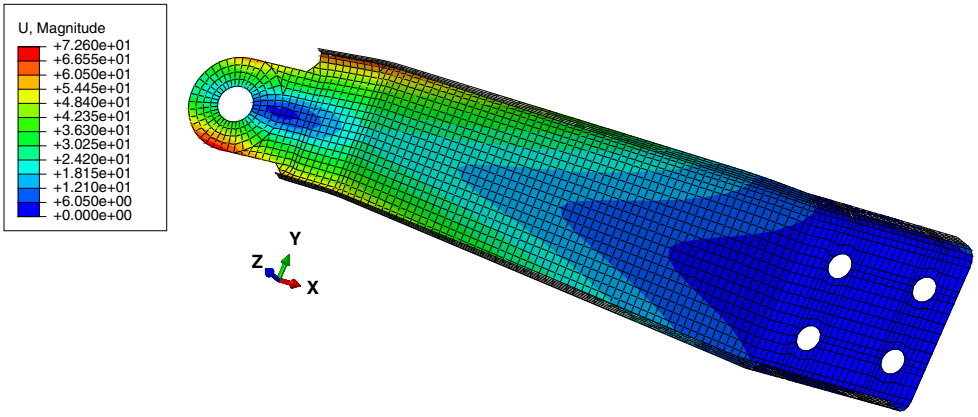

Figure 11.3.1–2 Displacement magnitude prior to the optimization.

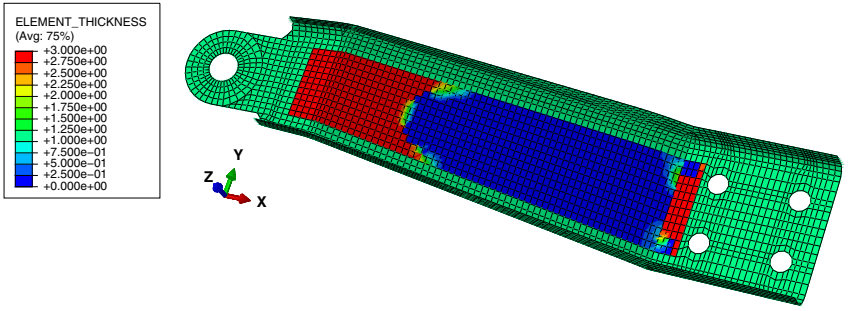

Figure 11.3.1–3 Absolute value of shell thickness after free optimization.

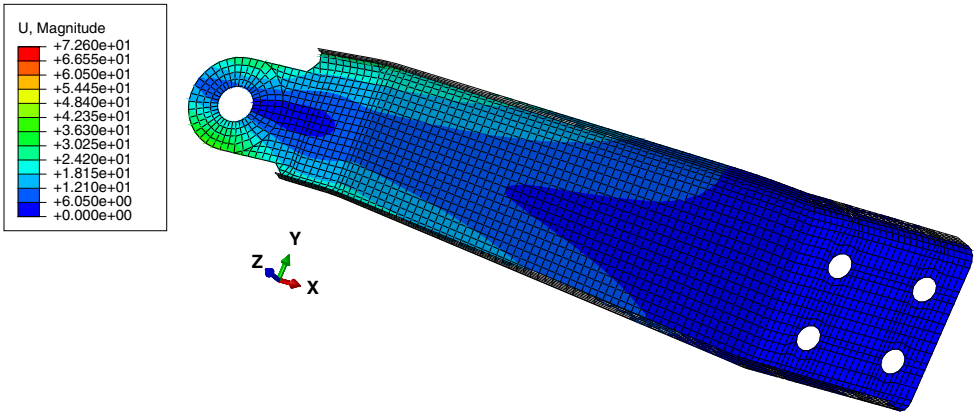

Figure 11.3.1–4 Displacement magnitude after free optimization.

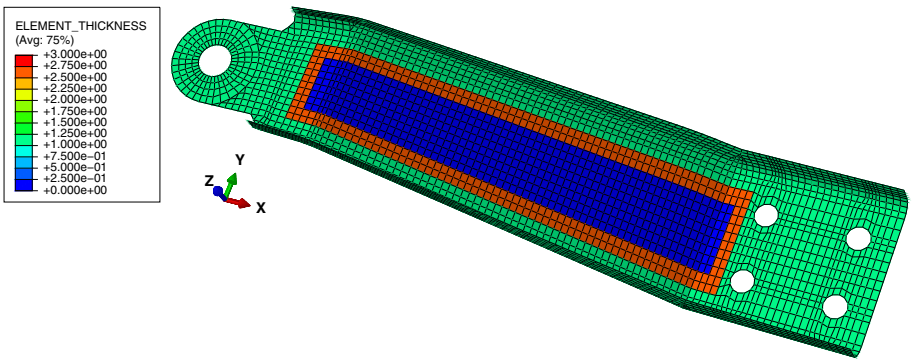

Figure 11.3.1–5 Absolute value of shell thickness after optimization with clustering.

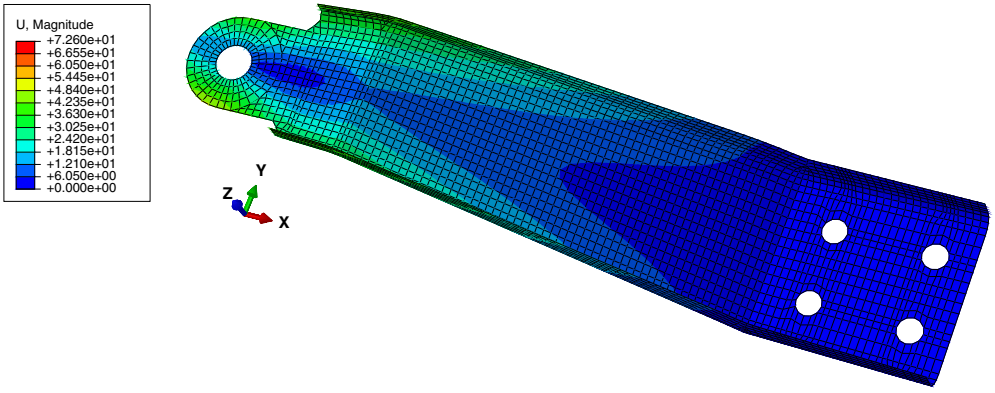

Figure 11.3.1–6 Displacement magnitude after optimization with clustering.

11.3.2 SIZING OPTIMIZATION OF A CAR DOOR

Products: Abaqus/Standard Abaqus/CAE

Objectives

This example uses the Optimization module to minimize the weight of a car door by changing the thickness of the sheet metal components while limiting the vertical displacement (sag) of the door relative to its encastered hinges.

The example also constrains the first frequency mode of the door to be higher than a specified value to avoid resonance triggered by engine vibration while maintaining its strength against the vertical load. The optimization takes into account geometric restrictions imposed by constraints in the manufacturing process and by constraints in design aesthetics. This model has been developed by The National Crash Analysis Center (NCAC) of The George Washington University under a contract with the Federal Highway Administration (FHWA) and the National Highway Traffic Safety Administration (NHTSA) of the United States Department of Transportation (US DOT).

Application description

This example illustrates sizing optimization of the sheet metal components that form a car door. Sizing optimization modifies the thickness of the shell elements in the design area to achieve the optimized solution. Clustering is applied during the sizing optimization, which forces elements in selected regions to have the same shell thickness and reproduces the real-world assembly of sheet metal components by layering parts of uniform thickness. A "free" sizing optimization of the same model generates a door that weighs less than the result of the clustered sizing optimization; however, the resulting element-by-element distribution of shell thickness would be impossible to reproduce on the production line. For more information, see "Sizing optimization" in "Structural optimization: overview," Section 13.1.1 of the Abaqus Analysis User's Guide.

Geometry

The door assembly is composed of the single orphan mesh part derived from the data supplied by the NCAC. The connections, contact definitions, and step definitions were converted to follow best practices in Abaqus. For example, regions (element sets) within the model are joined by spot welds (mesh-independent fasteners). The two hinges are modeled with hinge connectors and kinematic couplings. The door lock is modeled with a kinematic coupling.

Materials

Three materials are used to form the door—glass, plastic, and steel. The glass material properties are assigned to the element set representing the window. The plastic material properties are assigned to the element sets representing the inserts in the door trim, such as the liner. The steel material properties are assigned to the element sets representing the sheet metal door and its hinges and brackets. The material

properties assumed for this analysis are shown in Table 11.3.2–1, Table 11.3.2–2, and Table 11.3.2–3. The symbols E, ν, and ρ, represent the Young's modulus, Poisson's ratio, and density, respectively.

Elastic material properties are sufficient because the small load that is applied to model vertical door sag is insufficient to cause plastic or permanent deformation.

Boundary conditions and loading

Two load cases are applied to the model:

- a Lanczos solver frequency step that determines the first five eigenvalues, and
- a static load step that determines how much the door sags in response to a vertical load on the door lock.

During the frequency step, the hinges and the lock are restrained in all six degrees of freedom. During the static load step, a load of 500 N along the z-axis is applied to the door lock. In addition, the hinges continue to be restrained in all six degrees of freedom. To prevent the door from opening, a displacement boundary condition restrains motion of the lock in the y-direction.

Optimization features

The sizing optimization is configured as described in the following sections.

Optimization task

This example creates a sizing optimization task.

Design area

The entire car door, except for the plastic trim, is selected as the design area of the model.

Design responses

The example includes three design responses:

- a weight design response that is applied to the entire assembly,
- an eigenfrequency design response that uses the default modal analysis formulation (Lanczos), and
- a displacement design response that is applied only to the door lock.

Objective function

The objective functions tries to minimize the weight design response.

Constraint

A constraint in the frequency step restricts the first eigenfrequency from falling below a value that would trigger resonance with engine vibration at idle speed (35 Hz). A constraint in the static load step restricts the absolute displacement of the door lock in the z-direction to be less than or equal to a reasonable value (1.42 mm).

Geometric restrictions

The thickness of the element sets representing the sheet metal parts is restricted to a reasonable range ($0.5 < thickness < 2.5$). Frozen area geometric restrictions force the element sets representing the window and the hinges and their brackets to remain unchanged during the optimization. In addition, the design of the exterior-facing door panel has been finalized by the styling department, and a frozen area geometric restriction prevents changes in thickness to the elements that form the outside of the door.

Clustering restrictions

Clustering is defined for each of the element sets representing the sheet metal parts, forcing each region to be of uniform thickness.

Abaqus modeling approaches and simulation techniques

This example imports the model in the form of an orphan mesh from an input file. The input file contains the element sets that are used to define the regions of the model that are used by the optimization, such as the window and the hinges and their brackets. The example creates an optimization process that you can submit for analysis.

Analysis types

The analysis includes a frequency step and a static load step.

Mesh design

Most of the door is meshed with quadrilateral regions that are assigned S4R three-dimensional shell elements, and the small number of triangular regions are assigned S3R elements. In addition, the three-dimensional solid region that represents the arm rest is assigned C3D4, C3D6, and C3D8R three-dimensional solid elements. The sizing optimization operates only on shell elements.

Run procedure

An input file (door.inp) defines the nodes and elements that define the door along with the element sets that represent the regions of the door. The input file also defines the kinematic couplings, multi-point constraints, and spot weld connections. A Python script (door_sizing_optimization_w_clustering.py) is included that imports the input file and builds the optimization model. The scripts can be run interactively or from the command line. The Python script and the input file must be available from your working directory.

To run the optimization, you can submit the optimization process from the **Optimization Process Manager** in the Job module. You can use the **Optimization Process Manager** to monitor the progression of the optimization. In addition, when the optimization process is complete, you can use the **Optimization Process Manager** to combine the output from the optimization into a single output database file that can be viewed in the Visualization module.

Results and discussion

A maximum number of 15 design cycles is specified; however, the optimization process converges over nine design cycles. The convergence criterion for a sizing optimization is based on a combination of the change of the element thickness and the change in the value of the objective function. Minimizing the weight is the objective function, and the total weight is reduced by 14% (from 30.6 kg to 26.3 kg) while satisfying the eigenfrequency and door sag constraints.

Figure 11.3.2–1 shows the initial element thickness at the end of the second step prior to any optimization. Figure 11.3.2–2 and Figure 11.3.2–3 show the results of the sizing optimization—the value of the absolute shell thickness and the change in shell thickness. Regions of the model that take no part in the optimization, such as the plastic liner, have been removed from the figures to make the output easier to understand.

Python script

door_sizing_optimization_w_clustering.py	Script to import the input file (door.inp) and to build the optimization model.

Input file

door.inp	Orphan mesh representation of the car door assembly; and the node and element set, material, load, boundary condition, and connector definitions that are used by the optimization.

References

Abaqus Analysis User's Guide

- Chapter 13, "Optimization Techniques," of the Abaqus Analysis User's Guide
- "Sizing optimization" in "Structural optimization: overview," Section 13.1.1 of the Abaqus Analysis User's Guide

Abaqus/CAE User's Guide

- Chapter 18, "The Optimization module," of the Abaqus/CAE User's Guide
- "Understanding optimization processes," Section 19.5 of the Abaqus/CAE User's Guide

Other

- Svanberg, K., The Method of Moving Asymptotes—A New Method for Structural Optimization International Journal for Numerical Methods in Engineering, Vol. 24, pp. 359–373, 1987.

- This model has been developed by The National Crash Analysis Center (NCAC) of The George Washington University under a contract with the Federal Highway Administration (FHWA) and

the National Highway Traffic Safety Administration (NHTSA) of the United States Department of Transportation (US DOT).

Table 11.3.2–1 Properties for the glass window.

Property	Value
E	76.0×10^9 Pa
ν	0.30
ρ	2.5×10^{-9} t/mm^3

Table 11.3.2–2 Properties for the plastic components.

Property	Value
E	2.8×10^9 Pa
ν	0.30
ρ	1.20×10^{-9} t/mm^3

Table 11.3.2–3 Properties for the steel components.

Property	Value
E	210×10^9 Pa
ν	0.30
ρ	7.89×10^{-9} t/mm^3

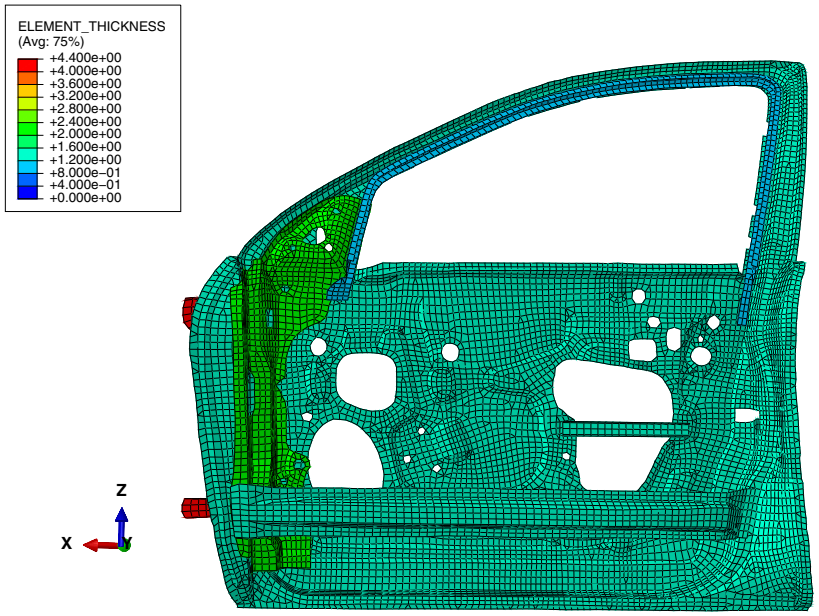

Figure 11.3.2–1 Element thickness prior to optimization.

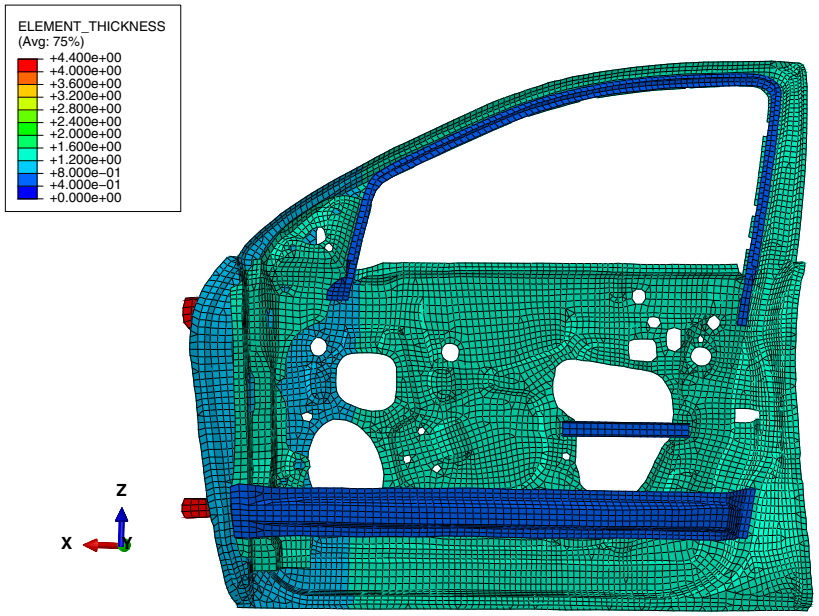

Figure 11.3.2–2 Element thickness after optimization.

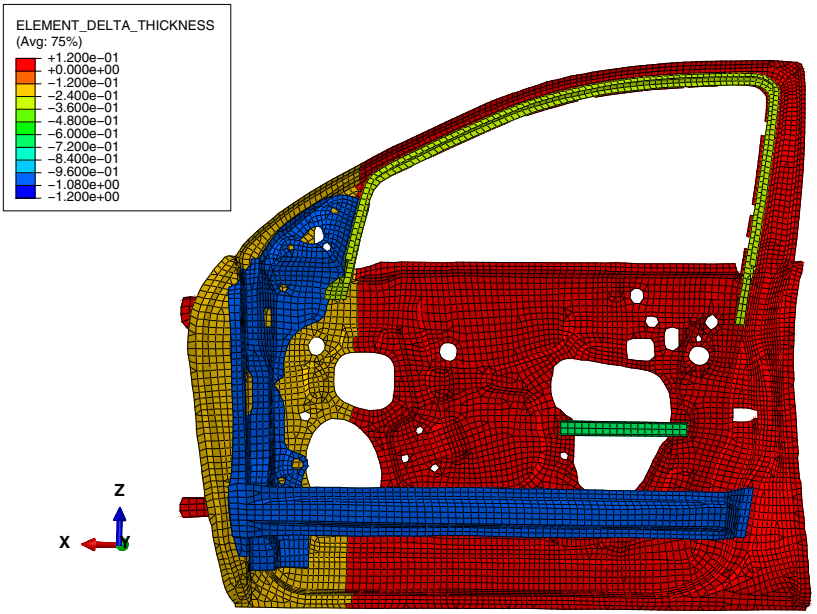

Figure 11.3.2–3 Change in element thickness during optimization.

11.4 Bead optimization analyses

- “Bead optimization of a plate,” Section 11.4.1

11.4.1 BEAD OPTIMIZATION OF A PLATE

Products: Abaqus/Standard Abaqus/CAE

Objectives

This example uses the Optimization module to optimize the stiffness of a simple plate by introducing stiffening beads.

Application description

This example illustrates condition-based bead optimization of a simply supported plate. During a bead optimization, the nodes of the shell elements are moved in the direction of the shell normal to increase the moment of inertia, which leads to a greater stiffness or higher eigenfrequencies. The resulting beads are easy to reproduce in a sheet metal stamping process without increasing the mass or cost of the finished product. For more information, see "Bead optimization" in "Structural optimization: overview," Section 13.1.1 of the Abaqus Analysis User's Guide.

Geometry

The plate is a 600 mm × 600 mm three-dimensional shell part. A shell section is assigned to the part with a thickness of 1.5 mm. The shell section uses the default Simpson integral rule with five integration points through the shell section.

Materials

The plate is made of an elastic material with a Young's modulus of 210 GPa and a Poisson's ratio of 0.3.

Boundary conditions and loading

The edges of the plate are fixed in all three translation degrees of freedom. A pressure of 1.0 is applied to a partitioned region at the center of the plate, as shown in Figure 11.4.1–1.

Optimization features

The bead optimization is configured as described in the following sections.

Optimization task

This example creates a bead optimization task that is governed by the condition-based optimization algorithm. The bead width is specified as 60 mm.

Design area

The entire plate is selected as the design area. By default, the Optimization module freezes the position of the nodes around the edge of the plate that were included in the boundary condition.

Design responses

A design response is created that calculates the maximum of the strain energy over all the elements in the design area. A second design response calculates the bead height.

Objective function

A single objective function attempts to minimize the maximum of the strain energy of the design area. Since compliance is defined as the sum of the strain energy, and stiffness is the reciprocal of compliance, the objective function is equivalent to maximizing the stiffness of the plate.

Constraint

A single constraint sets the bead height to 20 mm.

Abaqus modeling approaches and simulation techniques

The example creates an optimization process with the default maximum of three design cycles.

Analysis types

A static stress analysis is performed.

Run procedure

A Python script is included that reproduces the model using the Abaqus Scripting Interface in Abaqus/CAE. The Python script (plate_bead_optimization.py) builds the optimization model and executes the optimization job. To view the results of the optimization, you can use the Optimization Process Manager to combine the output database files that are generated and open the resulting output database file (**`Beadprocess\TOSCA_POST\BeadJob_post.odb`**). You can use the Visualization module to display a contour plot of the optimized nodal displacement (DISP_NORMAL_VAL) that shows the generated stiffening beads. You can return to the Optimization module to review the bead optimization model that was created in Abaqus/CAE.

The Python script can be run interactively or from the command line, and the script must be available from your working directory.

Results and discussion

The results are available in the combined output database file created from the Optimization Process Manager. The step contains three optimization iterations that correspond to the three design cycles of the optimization process. Figure 11.4.1–2 shows how the bead optimization moves nodes to create stiffening beads along the bending trajectories. Figure 11.4.1–3 and Figure 11.4.1–4 compare the plate stresses prior to the optimization and after the introduction of the stiffening beads.

Files

plate_bead_optimization.py	Python script to create the model and the bead optimization.

References

Abaqus Analysis User's Guide

- Chapter 13, "Optimization Techniques," of the Abaqus Analysis User's Guide
- "Bead optimization" in "Structural optimization: overview," Section 13.1.1 of the Abaqus Analysis User's Guide

Abaqus/CAE User's Guide

- Chapter 18, "The Optimization module," of the Abaqus/CAE User's Guide
- "Understanding optimization processes," Section 19.5 of the Abaqus/CAE User's Guide

Other

- Emmrich, D., "Entwicklung einer FEM-basierten Methode zur Gesaltung von Sicken für biegebeanspruchte Leitstützstrukturen im Konstruktionsprozess. " Forschungsberichte des Instituts für Produktentwicklung, 13. Karlsruhe, 2004.

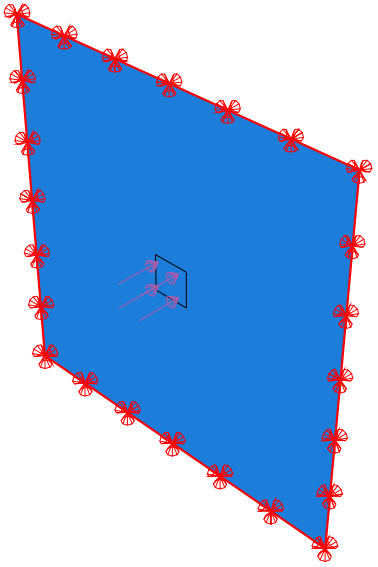

Figure 11.4.1–1 Pressure load and boundary conditions.

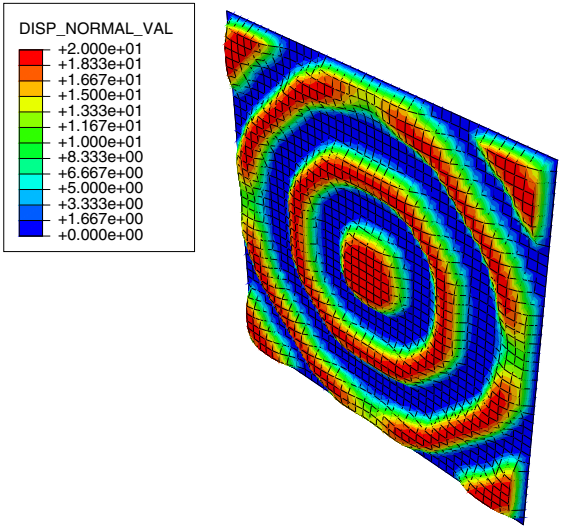

Figure 11.4.1–2 The optimized plate showing the displacement of the nodes.

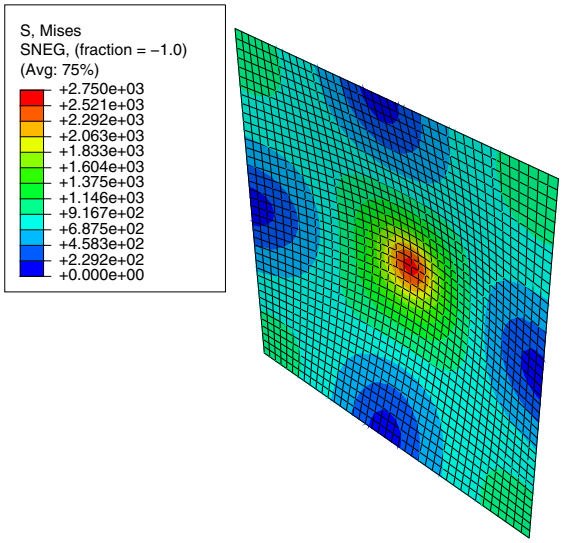

Figure 11.4.1–3 Stresses in the plate prior to optimization.

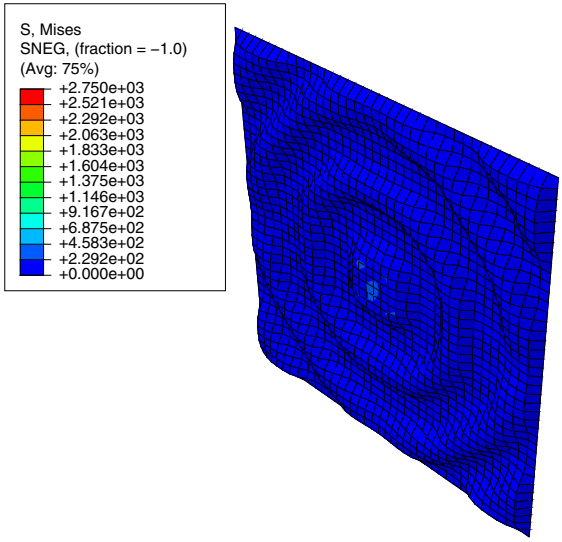

Figure 11.4.1–4 Stresses in the plate after optimization.

12. Abaqus/Aqua Analyses

- “Abaqus/Aqua analyses,” Section 12.1

12.1 Abaqus/Aqua analyses

- “Jack-up foundation analyses,” Section 12.1.1
- “Riser dynamics,” Section 12.1.2

12.1.1 JACK-UP FOUNDATION ANALYSES

Products: Abaqus/Standard Abaqus/Aqua

This example simulates a jack-up rig on a sand foundation subjected to alternating wind loading.

Geometry and model

The model—a simplified planar model for the analysis of a multiple leg, portal frame-type structure—is intended for the analysis of 3-leg jack-up rigs with shallow foundation supports. Figure 12.1.1–1 is a schematic of a 3-leg jack-up, as represented by the model. The jack-up hull is assumed to be rigid and triangular, and the connection between the hull and the legs is also taken to be rigid. The jack-up has two windward legs and one leeward leg; the model is projected onto the vertical symmetry plane that passes through the leeward leg and between the windward legs. Elastic beam columns are used to model both the upper and lower segment of each leg. The soil model is chosen to be macro-yield sand. Three degrees of freedom—vertical, horizontal, and rotational—are assumed at each spud can at the base of each leg. Mass is assumed to be concentrated at the center of the hull. The horizontal degree of freedom at the center is assumed to represent the motion of the rig for analysis purposes. Wind loading on the rig is applied as a horizontal force above the center of gravity of the hull.

The leg segments are modeled using B21 elements, and the general beam section is used to define the structural properties of the beam. The interaction between the spud can and the soil is modeled through JOINT2D elements and the joint elasticity and joint plasticity definitions. Rigid beam elements, RB2D2, are used to model the rigid hull.

The dimensions of the rig and the material properties of the sand and the spud can are as follows (force units are in kN, and length units are in meters):

Leg length upper segment	49.4
Leg length lower segment	13.5
Leg EI upper segment	2.7×10^8
Leg EI lower segment	2.7×10^9
Leg AE upper segment	2.2×10^8
Leg AE lower segment	2.2×10^9
Leg GA upper segment	8.1×10^7
Leg GA lower segment	8.1×10^8
Horizontal distance from platform center of gravity to leeward leg	23.4
Horizontal distance from platform center of gravity to windward leg	11.7
Spud can diameter	10.9

Spud can cone angle	180°
Foundation preload per spud can	50600
Foundation tensile capacity	0
Operational vertical load (weight)	62700
Vertical distance from center of gravity to load application point	7.1
Soil submerged unit weight	10.0
Soil friction angle	33°
Soil Poisson's ratio	0.2
Foundation elastic shear moduli, $G_{\nu\nu}$	5.14×10^4
G_{hh}	3.87×10^3
G_{rr}	2.04×10^3
Constant coefficient, Λ_1	1.0
Constant coefficient, Λ_2	0.5

Boundary conditions and loading

The base nodes of the JOINT2D elements are always fixed. The required preload is applied to each spud can using an initial condition. In the first step the weight loading is applied at the center of gravity of the hull. The rig is then subjected to an alternating horizontal wind loading applied at the specified location above the center of gravity of the hull.

The rig is loaded from zero to 5370 kN, unloaded to zero and then to 6440 kN in the opposite direction, reloaded to 9130 kN in the initial direction, unloaded and reloaded to 9770 kN in the opposite direction, and unloaded to zero again. Each of these loadings is done in a separate step and is ramped from zero to the specified magnitude at the end of the step.

Results and discussion

The estimated load path for the leeward spud can foundation is plotted in a graph of equivalent horizontal load, $R = \sqrt{(M/D)^2 + \Lambda_1 H^2}$, versus V/V_c. The plot is shown in Figure 12.1.1–2 and is in good agreement with the load path predicted by an independent analysis, as detailed in the reference below. The moment-horizontal load response (i.e., M/D versus H) for the leeward spud can foundation, shown in Figure 12.1.1–3, compares well with the independent analysis.

Input file

jackup.inp	Input data for this example.

Reference

- Wong, P. C. and J. D. Murff, "Dynamic Analysis of Jack-Up Rigs Using Advanced Foundation Models," Proceedings, 13th International Conference on Offshore Mechanics and Arctic Engineering (OMAE), vol. 2 - Safety and Reliability, Houston, pp. 93–109, February 1994.

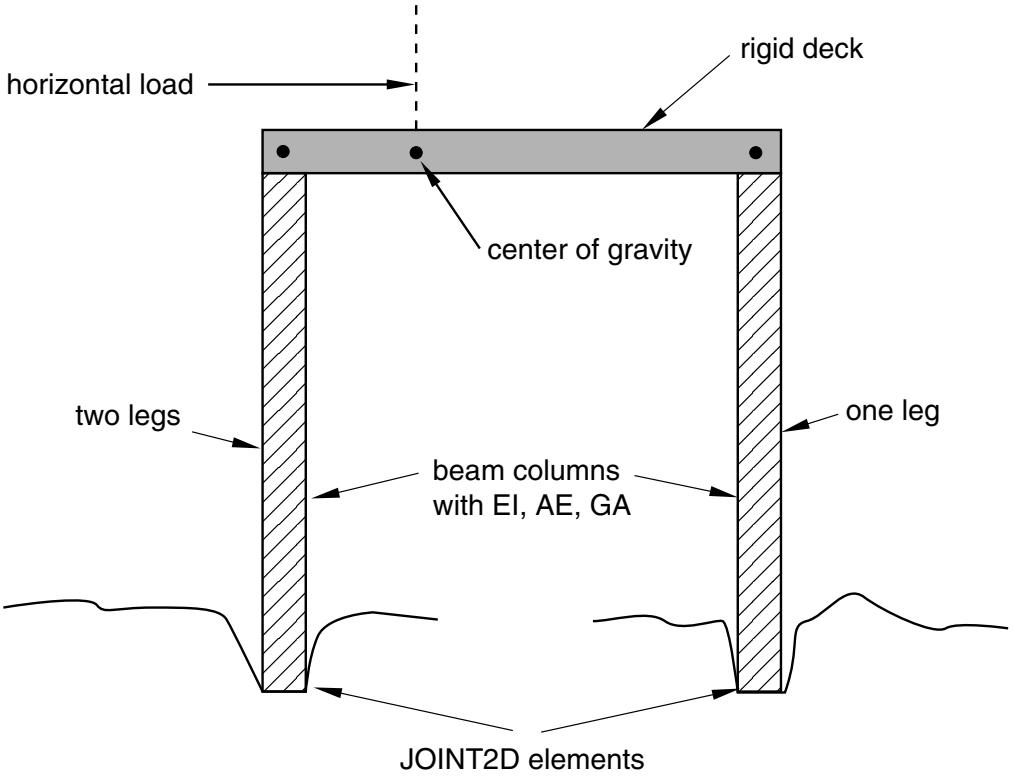

Figure 12.1.1–1 Schematic representation of jack-up rig.

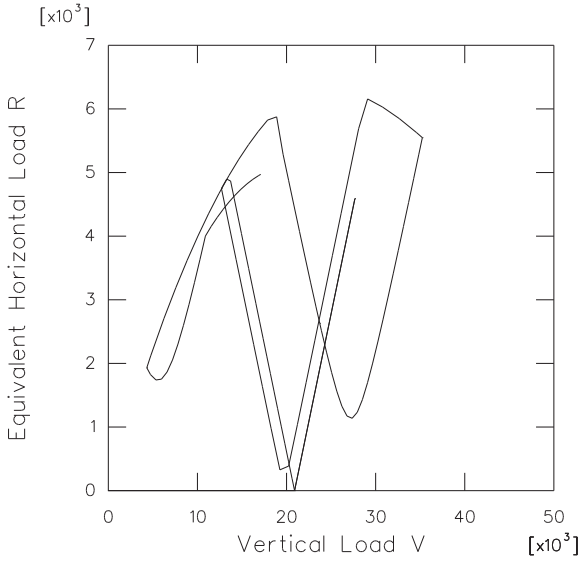

Figure 12.1.1–2 Load path for leeward spud can.

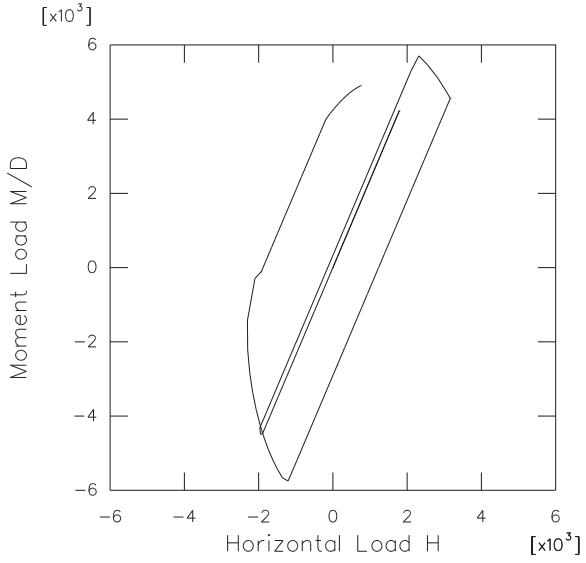

Figure 12.1.1–3 Moment versus horizontal load for leeward spud can.

12.1.2 RISER DYNAMICS

Products: Abaqus/Standard Abaqus/Aqua

This example verifies the response of a riser under different types of load conditions.

Pipelines extending from the sea floor to the ocean surface (risers) are subject to many types of load: self-weight, buoyancy, internal and external pressure, tensile forces arising from surface moorings, current drag, and oscillatory loads resulting from wave motion. The response of a riser to these loads is complex, and the difficulty of such analysis is heightened by the relative length of such pipelines (deep water risers). In this example a riser is analyzed under conditions specified by the American Petroleum Institute for comparison of drilling riser analyses (API BULLETIN 2J, 1977), and the results are compared with the results shown in that publication.

Geometry and model

The riser is shown in Figure 12.1.2–1. Its length is 463.3 m (1520 ft), and it stands in 448.1 m (1470 ft) of water. The outer diameter of the riser is 405 mm (1.33 ft), and it has a wall thickness of 15.88 mm (0.0521 ft). The pipeline is made of steel, with a Young's modulus of 206.8 GPa (4.32×10^9 lb/ft^2) and a density of 11508.685 kg/m^3 (22.332 lb-s^2/ft^4). The riser is modeled with 10 beam elements of type B21. No mesh convergence studies have been performed; hence, more elements may be required for accurate prediction of the stress in the riser.

Loading

The riser has a weight of 2575 N/m (176.36 lb/ft) and is loaded by a top tension of 2.224 MN (5×10^5 lb). Drag loading is applied by a steady current flowing by the riser with a velocity distribution varying linearly from 0.257 m/s (0.844 ft/s) at the mean water level to zero at the base of the riser. The coefficients in Morison's equation are transverse drag coefficient (C_D) 0.7, tangential drag coefficient (C_T) 0.0, and transverse inertia coefficient (C_M) 1.5.

The effective outer diameter for the drag calculations is 0.66 m (2.167 ft). Waves of peak to trough height 6.1 m (20 ft) travel across the water surface with a period of 9 seconds; these are modeled with the Airy wave theory provided in Abaqus/Aqua ("Abaqus/Aqua analysis," Section 6.11.1 of the Abaqus Analysis User's Guide). The density of the fluid is taken to be 1021 kg/m^3 (1.982 lb–s^2/ft^4). In Abaqus/Aqua, user subroutine **UWAVE** can be used to specify user-defined wave kinematics. We illustrate this capability by repeating this analysis with a user-specified Airy wave theory that is identical to the built-in Airy wave option in Abaqus/Aqua.

Boundary conditions

The base of the riser is "gimballed," supporting no moments. The top of the riser has two motions prescribed: an initial offset of 13.716 m (45 ft) from the vertical position of the riser and a sinusoidal motion about this static configuration, representing the surge of a vessel attached to the riser, with peak-to-peak amplitude of 1.22 m (4 ft) and a period of 9 seconds. The vessel surge angle is 15° out of phase

with the surface waves. The phase angle, ϕ_N, for the Airy wave definition provides an arbitrary choice of origin in time for the vertical displacement of a fluid particle. Based on the initial offset and vessel surge angle, this angle is set to −54.026°, where the negative sign indicates that the wave lags behind the vessel surge.

Analysis

The analysis is done in two steps. The first is the static step, in which the top tension is applied and the riser is moved from the vertical to its offset position by specifying the necessary horizontal displacement at the top of the pipeline. The top tension is 2.224 MN (5×10^5 lb).

In the second step, which is a dynamic step, the time increment is chosen as a fixed value of 0.125 second. The prescribed displacement at the top of the riser has a 9-second period, so this time step should provide reasonably accurate time integration once the higher modes are damped out by the fluid drag. The "half-increment residual" values calculated by Abaqus provide a measure of accuracy of the solution, and these values are typically of order 4.4 kN (1000 lb). Since these values are smaller than typical actual forces, they suggest that the time integration is reasonably accurate.

Results and discussion

The initial static step, which moves the riser to its offset position and applies the static loads, is completed in four increments. The first increment requires more iterations than subsequent increments, which is typical of this class of problem: the riser is initially unstressed and, therefore, is highly flexible. After some loading is applied, the axial tension stabilizes the system, and convergence is more rapid.

At the end of the static step the top of the riser makes an angle of 1.17° with the vertical. This value agrees well with the value of 1.20° presented in API BULLETIN 2J (1977). The angle predicted at the base of the riser is 2.48°, which compares to 2.55° reported in the API bulletin. The slight discrepancies are attributed to the relative coarseness of the model.

The dynamic solution is carried out for 18 seconds of response. Typically one equilibrium iteration is required in each of the time increments. Half-increment residual values for the first few increments are of order 178 MN (4.0×10^7 lb), and at the end of the run they are of order 4.4 kN (1000 lb). This result is typical: initially there is much high frequency content in the solution, which is reflected in the larger half-increment residual values. As the analysis proceeds, the fluid drag dissipates this "noise," the solution becomes smoother, and the half-increment residual values drop accordingly.

The envelope of pipeline excursions during the second cycle of the dynamic excitation is plotted in Figure 12.1.2–2, and the envelope of bending stress is shown in Figure 12.1.2–3. These results are in basic agreement with those given in the API bulletin.

As expected, the results obtained by the model with the Airy wave theory implemented in user subroutine **UWAVE** are identical to those due to the built-in Airy wave option.

Input files

riserdynamics_airy_disp.inp — Analysis with the Airy wave theory. User subroutine **DISP** is used to prescribe the sinusoidal surge motion. This motion could be prescribed instead through the use

	of the *AMPLITUDE option. User subroutine **DISP** is used to illustrate the use of this routine to prescribe a nonzero boundary condition value.
riserdynamics_airy_disp.f	User subroutine **DISP** used in riserdynamics_airy_disp.inp.
riserdynamics_wavedata.inp	Wave data for use in riserdynamics_airy_disp.inp.
riserdynamics_stokes_disp.inp	Analysis with the Stokes wave theory.
riserdynamics_stokes_disp.f	User subroutine **DISP** used in riserdynamics_stokes_disp.inp.
riserdynamics_airy_disp_uwave.inp	Analysis with the Airy wave theory implemented in user subroutine **UWAVE**.
riserdynamics_airy_disp_uwave.f	User subroutines **UWAVE** and **DISP** used in riserdynamics_airy_disp_uwave.inp.
exa_riserdynamics_stokes_disp_uwave.inp	Analysis with the Stokes wave theory implemented in user subroutine **UWAVE**.
exa_riserdynamics_stokes_disp_uwave.f	User subroutines **UWAVE** and **DISP** used in exa_riserdynamics_stokes_disp_uwave.inp.

Reference

- American Petroleum Institute, “Comparison of Marine Drilling Riser Analyses,” API Bulletin 2J, Washington, DC, January 1977.

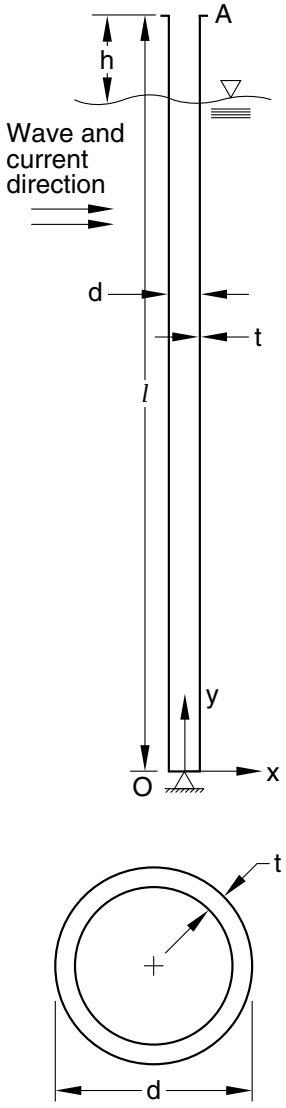

Geometry:
l = 463.3 m (1520.0 ft)
h = 15.2 m (50.0 ft)
d = 405 mm (1.33 ft)
t = 15.8 mm (0.0521 ft)

Material:
Young's modulus = 206.8 GPa
(4.32×10^9 lb/ft^2)
density = 11508.68 kg/m^3 (22.332 lb-s^2/ft^4)

Boundary conditions:
at O => $u_x = u_y = 0$
at A => static: $u_x = a$
dynamic: $u_x = a + b \sin(\frac{2\pi}{9} t)$
a = 13.716 m (45.0 ft)
b = 610 mm (2.0 ft)

Loading:
self weight 2575.0 N/m (176.36 lb/ft)
top tension = 2.224 MN (5.0×10^5 lb)

Morison coefficients:
transverse drag coefficient = 0.7
tangential drag coefficient = 0.0
transverse inertia coefficient = 1.5
effective outer diameter = 0.66 m (2.167 ft)

Airy wave definition:
wave height (peak to trough) = 6.1 m (20.0 ft)
wave period = 9.0 s

Fluid velocity:
v_x = 0.257 m/s (0.844 ft/s) at mean water level
v_x = 0.0 at base of riser
v_y = 0.0

Fluid density:
ρ_w = 1021.0 kg/m^3 (1.982 lb-s^2/ft^4)

Figure 12.1.2–1 Riser problem definition.

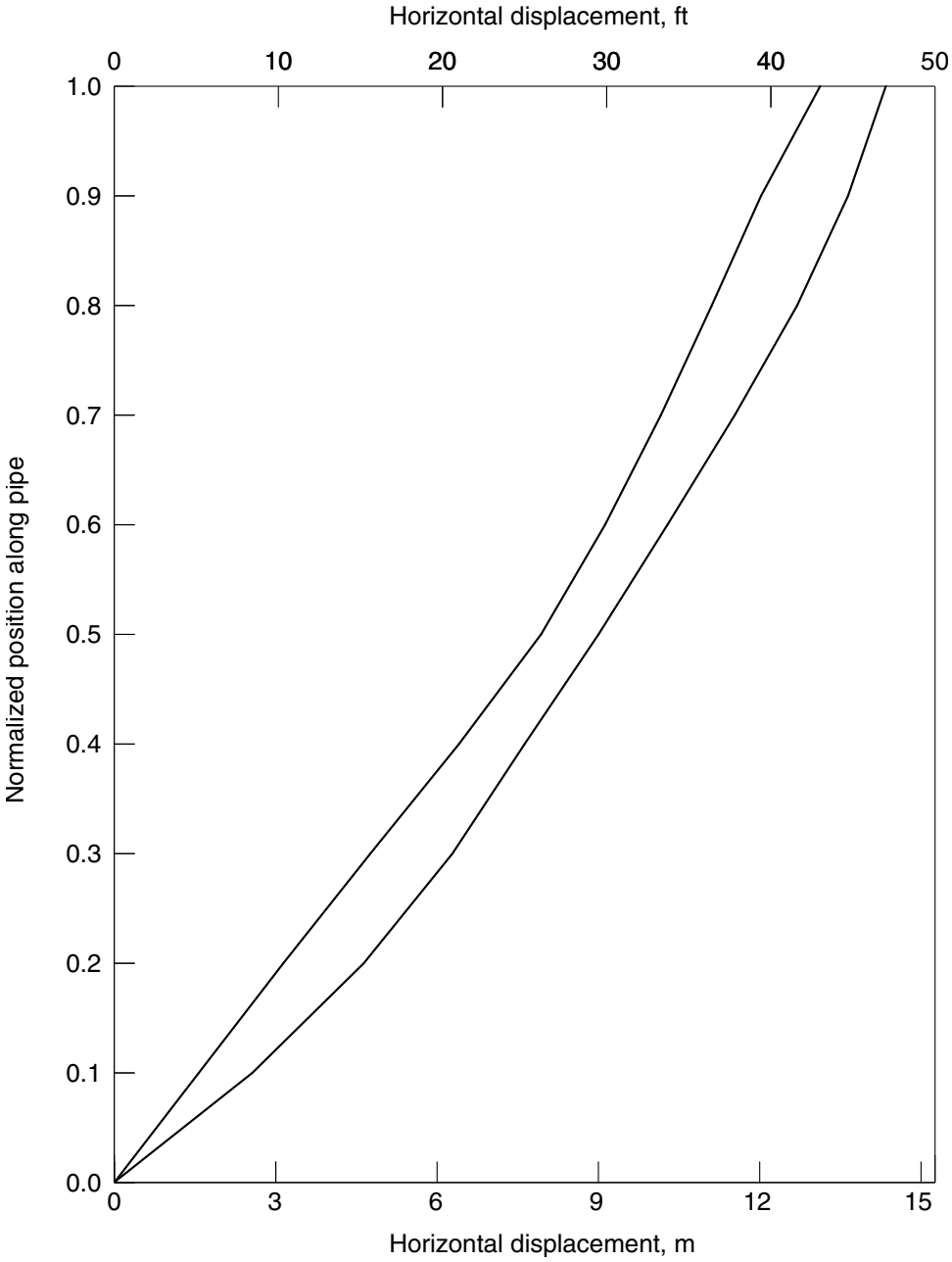

Figure 12.1.2–2 Horizontal displacement envelope during the second cycle of the dynamic excitation.

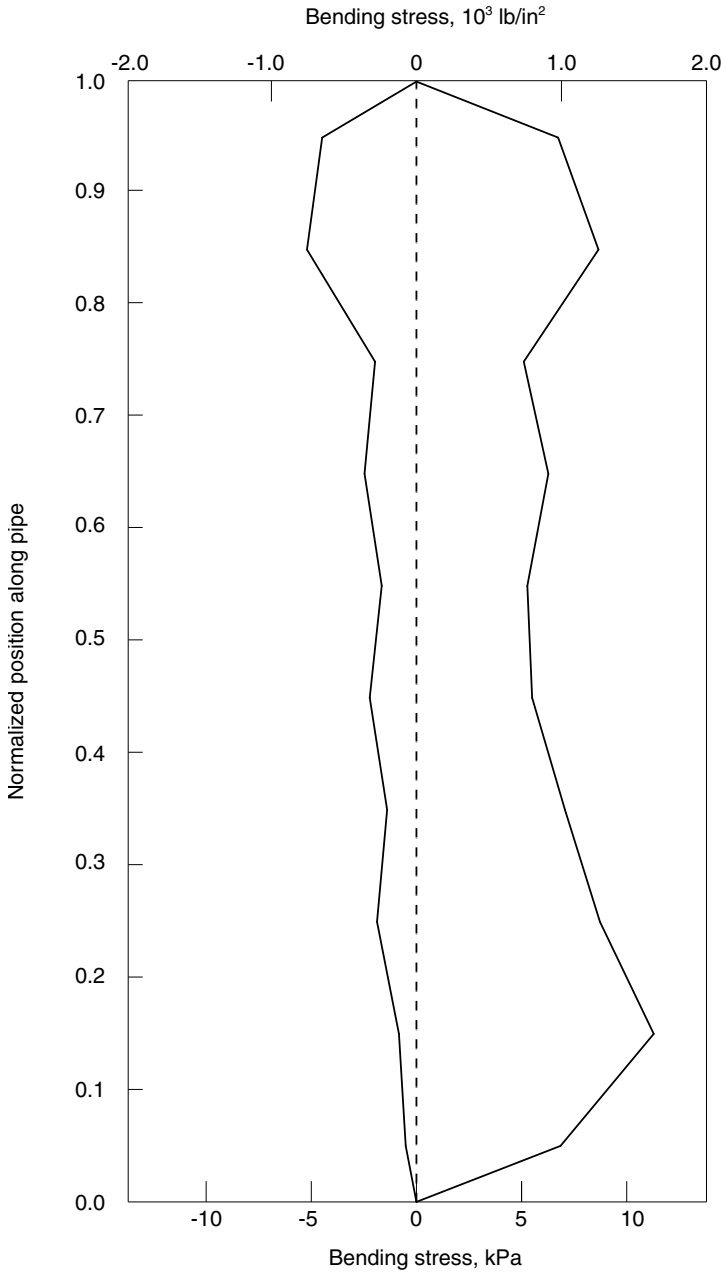

Figure 12.1.2–3 Bending stress envelope during the second cycle of the dynamic excitation.

13. Particle Methods Analyses

- “Discrete element method analyses,” Section 13.1

13.1 Discrete element method analyses

- "Mixing of granular media in a drum mixer," Section 13.1.1

13.1.1 MIXING OF GRANULAR MEDIA IN A DRUM MIXER

Product: Abaqus/Explicit

Objectives

This example demonstrates using the discrete element method (DEM) in Abaqus to analyze mixing of different particulate media in a tumbling mill.

Application description

Rotating drum mixers and tumbling mills are used for grinding, mixing, and drying of ore and granular materials. Such applications can be found in a wide range of industrial sectors such as mining. Several factors (including shape, size, density, and contact stiffness of particles; friction; adhesion between particles, speed of rotation; and tilt of the drum axis) influence the level of mixing that will be achieved in a given amount of time. These factors also influence the amount of energy required to operate the mixer. The discrete element method (DEM) is a useful tool in understanding the effects of these factors on the mixing process. This example demonstrates the use of DEM to analyze mixing of granular media with nonadhesive as well as adhesive contact behavior.

Geometry

Figure 13.1.1–1 shows the drum geometry. The drum length, L, is 760 mm; the drum outer diameter, D_o, is 620 mm; and the drum mouth diameter, D_m, is 315 mm. The interior of the drum has five equally spaced baffles to aid the mixing process. The baffles taper from the rear to the front of the drum. The wall of the drum is hollow; and the drum inner radius, R, is 300 mm. The axis of the drum is inclined at an angle of 30°. Although this laboratory size drum mixer is not of the scale of an industrial mixer, it is sufficiently large to demonstrate the mixing process.

To analyze nonadhesive contact between particles, the granular media consist of two batches of spherical limestone pellets. The first batch has a mass of 16.3 kg, and each pellet has a radius of 5 mm. The second batch has a mass of 19.3 kg, and each pellet has a radius of 6 mm. To analyze adhesive contact between particles, the granular media consist of two batches of spherical polyethylene pellets. The first batch has a mass of 9.8 kg, and each pellet has a radius of 5 mm. The second batch has a mass of 11.2 kg, and each pellet has a radius of 6 mm.

Materials

The drum is made of steel with a Young's modulus of 2.08×10^5 N/mm^2, density of 7850×10^{-9} kg/mm^3, and Poisson's ratio of 0.3.

Boundary conditions and loading

Mixing of particles in a rotating drum is influenced by the drum radius, the speed of rotation, and the degree of filling of the drum. At slow rotating speeds, particles tend to slip and slump along the walls

of the drum; while at very high speeds, centrifuging occurs, pushing the particles up along the drum wall. Rolling and cascading of particles in a rotating drum results in good mixing. The Froude number specifies the tendency of the particles to roll and cascade during mixing in a rotating drum. The Froude number is defined as $\omega^2 R/g$, where ω is the angular speed of the drum, R is the drum radius, and g is the acceleration due to gravity. A Froude number in the range of 0.001–0.1 is recommended for mixing operations. In this example the reference node of the drum is given a rotating speed of slightly less than 0.25 revolutions per second, which results in a Froude number of 0.068. The two batches of pellets together occupy less than half of the interior volume of the drum (i.e., the degree of filling is less than 0.5). The entire model in this example is subjected to gravity loading.

Interactions

Two different contact conditions between particles are considered: nonadhesive contact between limestone pellets, and adhesive contact between polyethylene pellets. Contact between particles and the drum is nonadhesive. The friction coefficient for contact between particles is 0.35. For contact between particles and the drum wall, the friction coefficient is 0.3.

Abaqus modeling approaches and simulation techniques

For this analysis the drum is assumed to be a rigid body. It is meshed with shell elements and made rigid by assigning it to a rigid body. A CARDAN connection type connector element that is aligned with the drum axis is attached to the reference node of the drum. The connector element is used to apply the torque to rotate the drum. The limestone and polyethylene pellets are modeled using PD3D elements. The particles are spherical in shape. The model used in this example has 8556 PD3D elements with a 6 mm radius and 12478 PD3D elements with a 5 mm radius.

Summary of analysis cases

Case 1	Nonadhesive contact between limestone pellets.
Case 2	Adhesive contact between polyethylene pellets.

Mesh design

It is very difficult to start such a simulation with the particles positioned precisely in an equilibrated configuration. A common DEM modeling technique is used for this analysis in which arrays of particles are initially positioned in the model and allowed to settle under gravity during the first analysis step with no other loading. The desired loading response is studied in subsequent steps.

In this case, layers of nonoverlapping particles of both sizes are introduced inside the drum. The two batches of particles are initially positioned next to each other and at a certain initial height from the interior wall of the drum. Next, these two batches of particles are dropped inside the drum and allowed to settle under gravity. This is done via a dummy step of 0.5 seconds duration in which only the gravity load is active. The drum is held fixed in its initial position during this step. At the end of the gravity settling step, we have the two batches of particles in a compacted stable configuration at the lower part of the drum. The cost of gravity settling is an additional overhead incurred in most DEM analyses.

Boundary conditions

An encastre boundary condition is applied to the free end of the connector, and all translational degrees of freedom of the reference point of the rigid body are held fixed for the duration of the analysis.

Loading

A gravity load is applied to the model. An acceleration of -9800 mm/s^2 is applied in the z-direction. Velocity type connector motion with an amplitude is applied about the connector component aligned with the drum axis. The other two connector components are held fixed. Mass proportional damping is used in the analysis to reduce the analysis noise. The total time period for the analysis, which includes gravity settling and mixing, is 5.5 seconds.

Case 1 Nonadhesive contact between limestone pellets

Two batches of spherical limestone pellets are used to analyze nonadhesive contact between particles.

Material model

Limestone has a Young's modulus of 2.0×10^4 N/mm^2, density of 2500×10^{-9} kg/mm^3, and Poisson's ratio of 0.25.

Interactions

As discussed in "Discrete element method," Section 15.1.1 of the Abaqus Analysis User's Guide, PD3D elements are rigid and the contact stiffness for interactions between DEM particles can be tuned to reflect the Hertz contact solution for contact between two elastic spheres (see Timoshenko and Goodier, 1951; and "The Hertz contact problem," Section 1.1.11 of the Abaqus Benchmarks Guide). The Hertz solution relating the contact force, $\boldsymbol{F}$, to the approach distance, δ, between remote points on two contacting spheres is

$$\mathrm{F} = \frac{4}{3}\mathrm{E}^*\sqrt{\mathrm{R}}\sqrt{\delta^3},$$

where

$$\mathrm{R} = \frac{\mathrm{R}_1\mathrm{R}_2}{\mathrm{R}_1 + \mathrm{R}_2},$$

and

$$\frac{1}{\mathrm{E}^*} = \frac{1-{\nu_1}^2}{\mathrm{E}_1} + \frac{1-{\nu_2}^2}{\mathrm{E}_2}.$$

E_1, ν_1 and E_2, ν_2 are the Young's modulus and Poisson's ratio of the two particles, respectively. R_1 and R_2 are the radii of the two particles, respectively.

The equation relating $\boldsymbol{F}$ and δ was used to generate tabular force versus overclosure relationships for contact between DEM particles. Different relationships are used for different combinations of particle

radii. In Abaqus force-overclosure tables are specified under tabular type pressure-overclosure contact surface behavior since the particle contact area is unity.

A simpler alternative is to specify an approximate linear contact stiffness over the range of δ of interest. The Hertz contact stiffness is not linear because $\boldsymbol{F}$ is not linearly dependent on δ. The normal contact stiffness (or slope of the $\boldsymbol{F}$ vs. δ curve) for a given value of indentation between particles is

$$\mathrm{K} = \frac{d\mathrm{F}}{d\delta} = 2\mathrm{E}^{*}\sqrt{\mathrm{R}}\sqrt{\delta}.$$

In Abaqus the contact stiffness can be specified using a linear type pressure-overclosure contact surface behavior. The maximum indentation δ_{max} can be assumed to be a certain percentage of the particle radius (between 0.05 and 1.0 percent). Substituting a value such as $\delta = 0.002$ into the expression for $\boldsymbol{K}$ may provide a linear contact stiffness that is adequately representative. For a given particle mass, a larger contact stiffness would require a smaller time increment. For a slow mixing process (i.e., the Froude number is at the low end of the mixing operation range), it may be possible to get reasonably accurate results with a lower contact stiffness and using larger time increments.

Case 2 Adhesive contact between polyethylene pellets

Two batches of spherical polyethylene pellets are used to analyze adhesive contact between particles.

Material model

Polyethylene has a Young's modulus of 1.0×10^3 N/mm^2, density of 1400×10^{-9} kg/mm^3, and Poisson's ratio of 0.3.

Interactions

The Johnson-Kendall-Roberts (JKR) adhesive contact model discussed in "Discrete element method," Section 15.1.1 of the Abaqus Analysis User's Guide, is used for modeling adhesive contact between PD3D elements. The surface energy per unit area, Γ, is used to specify adhesion between contacting particles; in this case, Γ = 50 J/m^2. Increasing the value of Γ leads to stronger adhesive forces between particles. The JKR model reduces to nonadhesive Hertz contact for $\Gamma = 0$. Nonadhesive contact between polyethylene pellets is modeled (Γ = 0 J/m^2) for comparison with adhesive contact results.

Discussion of results and comparison of cases

Figure 13.1.1–2 shows a series of deformed plots obtained at different times during the mixing analysis of limestone pellets. The initially generated mesh can be seen in the plot at 0.0 seconds. The configuration at the end of the gravity settling step can be seen in the plot at 0.5 seconds. The remaining four plots show the progress of the mixing process and the rolling and cascading of the particulate media. Figure 13.1.1–3 shows the total energy input to the mixing process as a function of time.

Figure 13.1.1–4 shows a comparison of the mixing process between the nonadhesive and adhesive mixing of polyethylene pellets. A series of deformed plots obtained at different times during the mixing analysis for the two conditions are juxtaposed in the figure. The steel drum has been removed from the plots for clarity. The left column of plots in Figure 13.1.1–4 corresponds to nonadhesive contact, and

the right column of deformed plots corresponds to adhesive contact. The configuration at the end of the gravity settling step can be seen in the plot at 0.5 seconds. The remaining five plots show the progress of the mixing process. As can be seen from the figure, adhesion reduces the level of mixing. Also, the rolling and cascading of the particulate media that is observed in the modeling of nonadhesive contact for the polyethylene pellets is absent for adhesive contact.

Input files

Case 1

rotating_drum_mixer.inp	DEM nonadhesive drum mixing analysis using limestone pellets.

Case 2

rotating_drum_mixer_jkr.inp	DEM adhesive drum mixing analysis using polyethylene pellets.

References

Abaqus Analysis User's Guide

- "Discrete element method," Section 15.1.1 of the Abaqus Analysis User's Guide
- "Discrete particle elements," Section 33.1.1 of the Abaqus Analysis User's Guide

Other

- Timoshenko, S., and J. N. Goodier, *Theory of Elasticity,* Second edition, McGraw-Hill, New York, 1951.

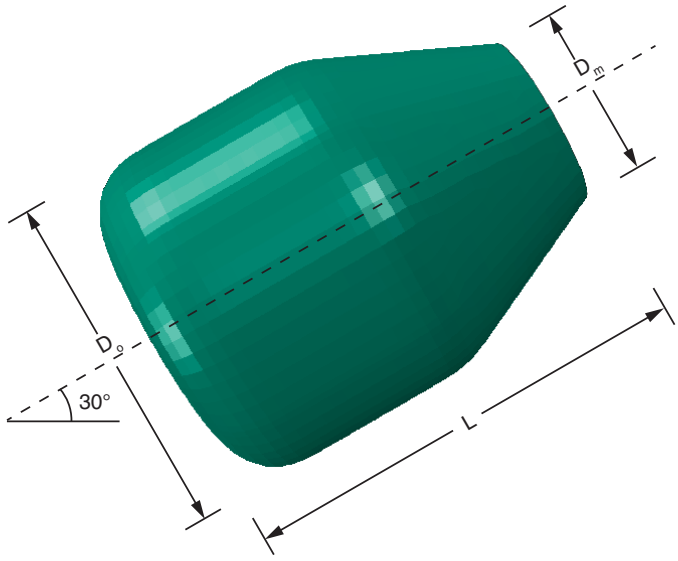

Figure 13.1.1–1 Mixer dimensions.

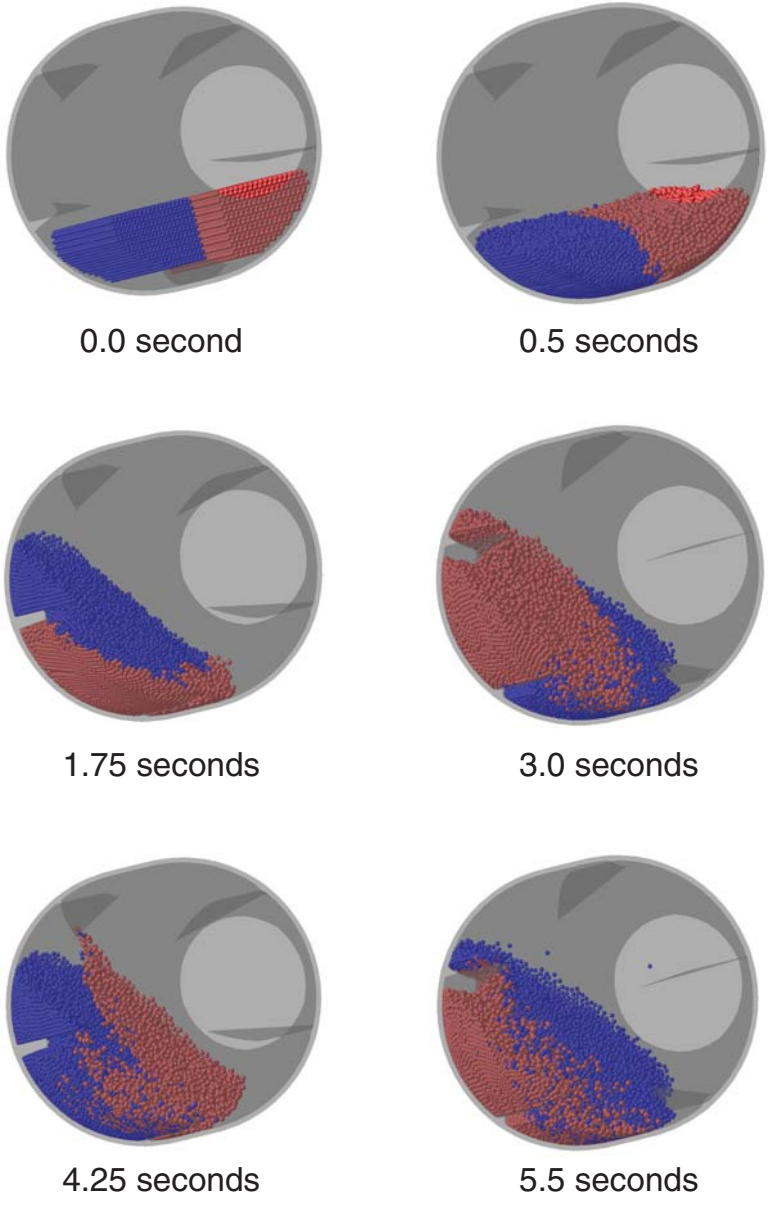

Figure 13.1.1–2 Case 1: Snapshots of the mixing process for limestone pellets.

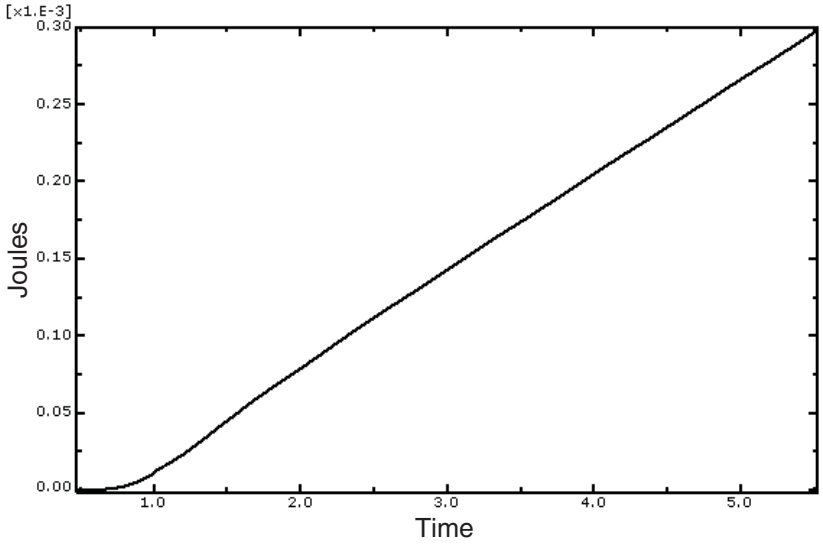

Figure 13.1.1–3 Case 1: Energy input to the drum mixer.

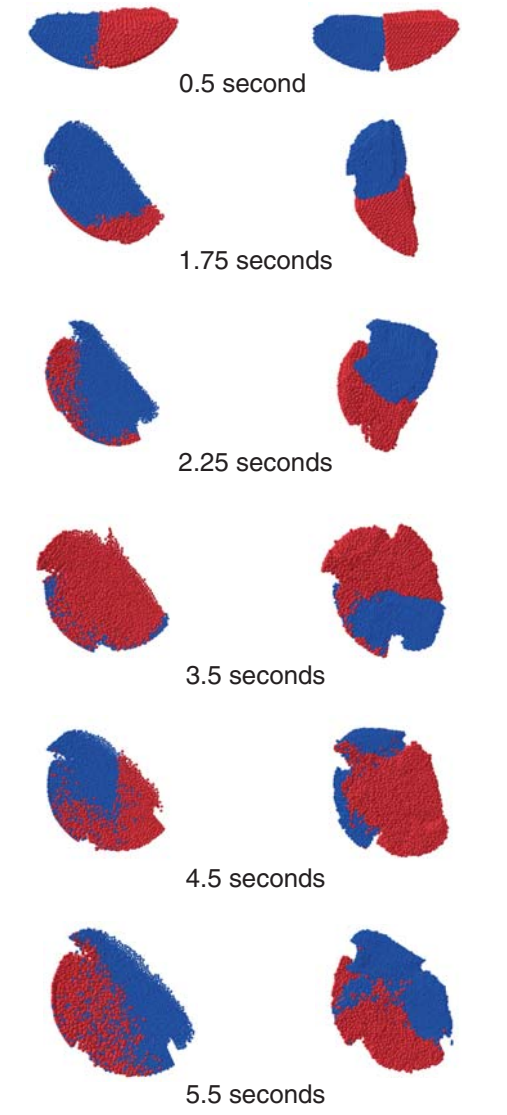

Figure 13.1.1–4 Case 2: Comparison of the mixing process for nonadhesive and adhesive contact between particles.

14. Design Sensitivity Analyses

- "Overview," Section 14.1
- "Examples," Section 14.2

14.1 Overview

- “Design sensitivity analysis: overview,” Section 14.1.1

14.1.1 DESIGN SENSITIVITY ANALYSIS: OVERVIEW

This chapter contains example problems specifically created to demonstrate the design sensitivity analysis (DSA) capability in Abaqus/Design.

In addition, "Indentation of an elastomeric foam specimen with a hemispherical punch," Section 1.1.4, includes design sensitivity analysis.

Some of these examples employ a scripting command in Abaqus/CAE to aid in creating the shape variations. The usage of this command is described below.

Using Abaqus/CAE to compute shape variations

A transitional capability for computing shape variations is provided by the internal Abaqus Scripting Interface command **`_computeShapeVariations()`**. Using the command requires some familiarity with the Abaqus Scripting Interface; specifically, the user must understand the Abaqus object model (see "The Abaqus object model," Section 6.1 of the Abaqus Scripting User's Guide) and know how to access the rootAssembly and partInstance objects.

The command procedure necessary to define a shape variation requires the following sequence of actions:

1. Create and mesh the model in Abaqus/CAE. Output the corresponding input file by selecting **Job→Create** and **Job→Write Input** from the main menu bar in the Job module.

   (In the discussion that follows it is assumed that the model is named **`Model-1`**, the part is named **`Part-1`**, and the part instance is named **`Part-1-1`**).

2. Select **Model→Copy Model** from the main menu bar to copy **`Model-1`** to **`Model-2`**, for example. Select **`Model-2`** from the **Model** list located in the context bar. This model will be used in subsequent steps to compute the shape variation.

3. In the Part module select the part for which a shape variation must be calculated from the **Part** list located under the context bar. Select **Feature→Edit** from the main menu bar to edit the associated sketch. Select **Add→Dimension** and **Edit→Dimension** to change the design parameter. End the edit of the sketch, and indicate that the geometry should be regenerated automatically.

   Editing the sketch will cause the mesh of **`Model-2`** to be deleted.

4. Use the Abaqus/CAE command line or select **File→Run Script** to execute the commands listed below. The **`_computeShapeVariations()`** command is accessed from the rootAssembly of either model and requires as input the original part instance, the modified part instance, and the name of the file to which the data lines of the shape variation option will be written. The **`.inp`** extension will be appended automatically to the specified file name.

   The following sequence of commands is appropriate for the creation of a shape variable associated with a parameter h:

```
ra1 = mdb.models['Model-1'].rootAssembly
ra2 = mdb.models['Model-2'].rootAssembly
i1 = ra1.instances['Part-1-1']
i2 = ra2.instances['Part-1-1']
ra1._computeShapeVariations(originalInstance=i1,
                            modifiedInstance=i2,
                            fileName='shape_h')
```

5. To compute the shape variation, the mesh of **Model-1** is mapped to the changed geometry of **Model-2** and then smoothed. Examine the mapped mesh of **Model-2** to verify that the mesh was mapped as expected. (In general, any changes to the geometry should be small—around 1%—so as to avoid difficulties with the mapping of the mesh).

   The shape variation is calculated simply by subtracting the initial node positions from the node positions calculated after mapping and smoothing the mesh to the changed geometry.

6. To use the shape variation data, copy to the input file for your analysis the data written by the **_computeShapeVariations()** command to the **shape_h.inp** file.

7. Verify the correctness of the data by running your analysis and using the Visualization module in Abaqus/CAE to view the shape variation.

14.2 Examples

- “Design sensitivity analysis of a composite centrifuge,” Section 14.2.1
- “Design sensitivities for tire inflation, footprint, and natural frequency analysis,” Section 14.2.2
- “Design sensitivity analysis of a windshield wiper,” Section 14.2.3
- “Design sensitivity analysis of a rubber bushing,” Section 14.2.4

14.2.1 DESIGN SENSITIVITY ANALYSIS OF A COMPOSITE CENTRIFUGE

Products: Abaqus/Standard Abaqus/Design

This example uses the design sensitivity analysis capability in Abaqus/Design to examine how the key structural responses depend on design parameters such as the thicknesses of composite laminae, the layup angles, the density of the centrifuge end plates, and geometric imperfections.

Many industries use centrifuges to separate out contaminants during purification processes. Efficiency of the purification process is directly related to the speed of rotation. Consequently, the centrifuge chamber is designed to be stiff to maintain its shape and lightweight to reduce self-stressing due to centrifugal loads.

Geometry and model

The centrifuge depicted in Figure 14.2.1–1 consists of a composite centrifuge chamber and aluminum end plates. The centrifuge chamber is a cylinder 970 mm long and 175 mm in diameter. It spins about its axis at 10000 rpm. The cylinder is a filament-wound composite (hybrid) laminate with a balanced layup. The laminate layup is $(0° / \pm\theta / 0° / \pm\theta / 0°)$, where 0° represents the layup of the fibers along the length of the cylinder and $\theta = 45°$ is the angle of the helical layers. The axial (0°) and helical layers have a thickness of 0.15 mm and 0.5 mm, respectively. Aluminum alloy end plates are bonded at both ends of the cylinder. The lower plate provides an attachment point for a magnetic bearing, while the top plate supports the magnet of the inductance drive. In the region where the cylinder meets the end plates an additional circumferential (90°) outer layer of 1 mm thickness is added to the laminate. The centrifuge is modeled using reduced-integration, 4-node shell (S4R) elements. The mesh is shown in Figure 14.2.1–2. All the displacements on the perimeter of the end plate lip are constrained at one end of the cylinder, and only the radial displacements are constrained at the other end; thus, the centrifuge is allowed to change length freely in the axial direction under loading. A static analysis with centrifugal loading is performed.

Materials

A T800 carbon fiber material is used in the 0° and 90° layers, and a HM400 material is used in the helical layers. The density of both materials is 1600 kg/m^3. The material properties for the composites are given in Table 14.2.1–1. The aluminum alloy has a Young's modulus of E = 70 GPa, a Poisson's ratio of $\nu = 0.33$, and a density of $\rho = 2800$ kg/m^3.

Design parameters and normalization

The design parameters are thickness of the helical layer (THM400), thickness of the axial layer (TT800), and angle of the helical layer (THETA). Because of the high speed of rotation of the centrifuge, geometric imperfections can have a significant effect on the displacements and stresses. To study this effect, an imperfection in the form of the first bending mode of the centrifuge is used; the magnitude of the imperfection, ALPHA, is chosen as a shape design parameter. An imperfection in the form of a bending mode is chosen because the maximum attainable rotation speed is known to be well-predicted by the natural frequency of the first bending mode of the centrifuge. The gradients of the nodal

coordinates with respect to ALPHA required to carry out the sensitivity analysis are obtained from an eigenfrequency extraction analysis. Figure 14.2.1–3 shows the first bending mode of the centrifuge. Though bending predominates in this mode, there is also a small twisting component.

All plotted sensitivity results are normalized to enable comparison between the parameters. The normalization is carried out by multiplying the response sensitivity by the value of the parameter and dividing by the maximum value of the response. For example, the sensitivity of the stress component S11 with respect to the design parameter THM400 is normalized by first multiplying the sensitivity by the value of the THM400 parameter and then dividing by the maximum S11 value found in the model. For the shape design parameter ALPHA an estimated imperfection of 0.1% of the total length of the cylinder (ALPHA = 1 mm) is used while computing the normalized sensitivities.

Results and discussion

Figure 14.2.1–4 shows the deformed shape of the centrifuge at 10000 rpm. The centrifuge contracts in the axial direction and bulges outward radially. Because of the lap joint where the composite cylinder meets the end plate, some bending is seen at both ends.

The normalized sensitivity of the radial displacement along the length of the composite cylinder (between the two end plates) is plotted in Figure 14.2.1–5 for all the design parameters except the shape design parameter. The plot shows that the radial displacement has negative sensitivity to THETA and TT800. An increase in the layup angle of the helical layer or an increase in the thickness of the axial layers will stiffen the cylinder and reduce the radial displacement. The positive sensitivity of the radial displacement to THM400 indicates that the added self-induced centrifugal load due to the increase in the mass of the helical layers will more than negate any advantage gained in the stiffness.

Figure 14.2.1–6 plots the sensitivity of the radial displacement to the shape design parameter ALPHA. Since the sensitivity is not axisymmetric for this design parameter, it is plotted for every meridian in 45° increments counterclockwise around the circumference beginning at the 1–2 plane. The radial displacement sensitivities are obtained from the global Cartesian displacement sensitivities output by Abaqus via a two-dimensional vector transformation at each meridional position. The largest sensitivities in Figure 14.2.1–6 are almost two orders of magnitude higher than those observed in Figure 14.2.1–5. This means that the geometric imperfections have a relatively large effect on the radial displacement and that the centrifuge manufacturing process must have a tight tolerance on axial shape imperfections.

The dominant section force in the structure is in the hoop direction of the cylinder. Figure 14.2.1–7 shows the contour plot of section force in the hoop direction, and Figure 14.2.1–8 shows the normalized sensitivities of section force in the hoop direction plotted as a function of the position along the length of the cylinder. As expected, only the design parameters that affect the mass (TT800 and THM400) have nonzero sensitivities with THM400 being more sensitive because of its larger thickness. As the centrifuge is allowed to contract freely in the axial direction, the net section force in the axial direction is zero. However, the stresses in the axial direction are not zero. Figure 14.2.1–9 shows the contour plot of the sensitivity of the fiber stress (S11) in the helical layer with respect to the shape design parameter. To understand in detail how the stresses in the laminate are affected by the design parameters, normalized sensitivities of the fiber stress (S11) through the thickness of the cylinder wall at a point midway along the length of the cylinder are plotted in Figure 14.2.1–10. S11 through the thickness of the wall is also

plotted after dividing it by the maximum value of S11 in the model. The plot shows that the axial layers are under compression and the helical layers are under tension. S11 has positive sensitivity to TT800: increasing the thickness of the axial layers will reduce the compressive stress in the axial layers and increase the tensile stress in the helical layers. S11 has negative sensitivity to THM400: increasing the thickness of the helical layers will reduce the stress in the helical layers and increase the stress in the axial layers. Increasing the angle of the helical layers will reduce the stress in the axial layers since S11 in the axial layers has a small positive sensitivity to THETA. The sensitivity of S11 to ALPHA is analogous to the sensitivity of the radial displacement to ALPHA around the circumference of the cylinder.

The sensitivities can be used to compute the change that would be required in the design parameters to achieve a particular change in response or to assess the change in the response that would result from a change in the design parameters. Consider, for example, the following objectives: (a) to reduce the compressive stress in the axial layer by 10% and (b) to determine the maximum compressive stress in the axial layer caused by a specified magnitude of the shape imperfection (ΔALPHA = 0.6).

a. The compressive fiber stress in the axial layer is 26.38 MPa. Figure 14.2.1–10 indicates that the most effective way to achieve the desired reduction is to increase the thickness of the axial layer. The required increase is given by

$$\Delta \mathrm{TT800} = \frac{\Delta \mathrm{S11}}{\frac{\mathrm{dS11}}{\mathrm{dTT800}}} = \frac{2.638}{69.69} = 0.0378\,\mathrm{mm}$$

An analysis of the centrifuge with TT800 = 0.15 + 0.0378 = 0.1878 mm shows the compressive stress in the axial layer to be 24.05 MPa, which is close to the desired value of 23.74 MPa.

b. The maximum compressive stress in the axial layer caused by the specified shape imperfection can be obtained from

$$\mathrm{S11} = \mathrm{S11} + \Delta\mathrm{ALPHA}\frac{\mathrm{dS11}}{\mathrm{dALPHA}} = 26.38 + 0.6 \times 13.08 = 34.2\,\mathrm{MPa}$$

An analysis using the imperfect geometry shows the maximum compressive stress in the axial layer to be 34.3 MPa, which is close to the predicted value of 34.2 MPa.

Input files

dsacentrifuge_freq.inp	Frequency analysis of the centrifuge.
dsacentrifuge.inp	Sensitivity analysis of the centrifuge subjected to centrifugal loads.
dsacentrifuge_node_elem.inp	Node and element definition.

Table 14.2.1–1 Composite material properties.

Material	E_1 (MPa)	E_2 (MPa)	ν_{12}	G_{13} (MPa)	G_{12} (MPa)	G_{32} (MPa)
T800	177000.	14920.	.21	5700.	5700.	5630.
HM400	233967.	14778.	.032	5777.	10191.	5634.

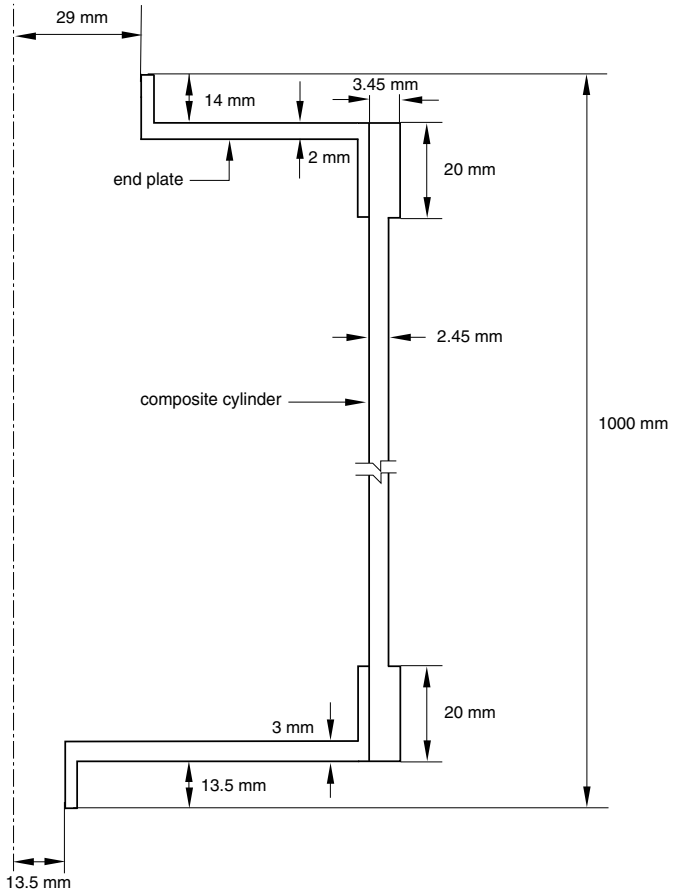

Centrifuge Chamber

Figure 14.2.1–1 Centrifuge chamber.

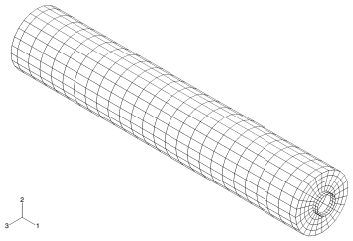

Figure 14.2.1–2 Centrifuge model using S4R elements.

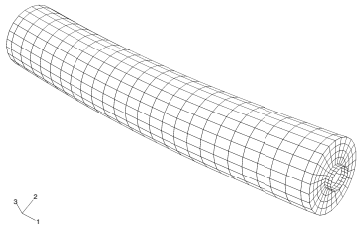

Figure 14.2.1–3 First bending-dominated mode of the centrifuge.

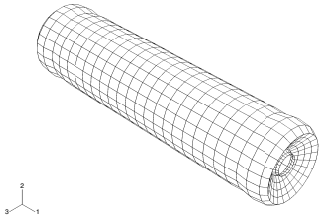

Figure 14.2.1–4 Deformed shape of the centrifuge; deformation scaled 400 times.

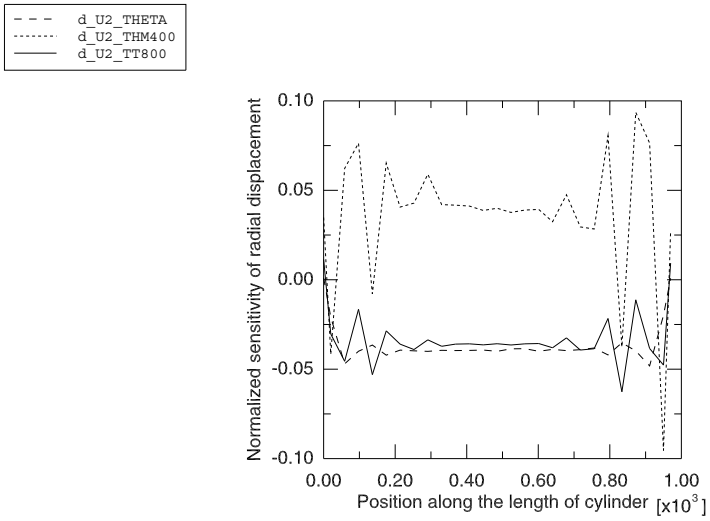

Figure 14.2.1–5 Normalized sensitivity of the radial displacement along the length of the cylinder.

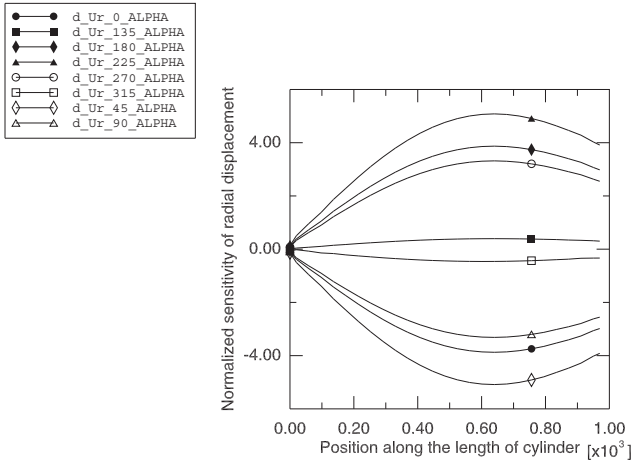

Figure 14.2.1–6 Normalized sensitivity of the radial displacement to the shape design parameter ALPHA. Sensitivities are plotted around the circumference in 45° increments.

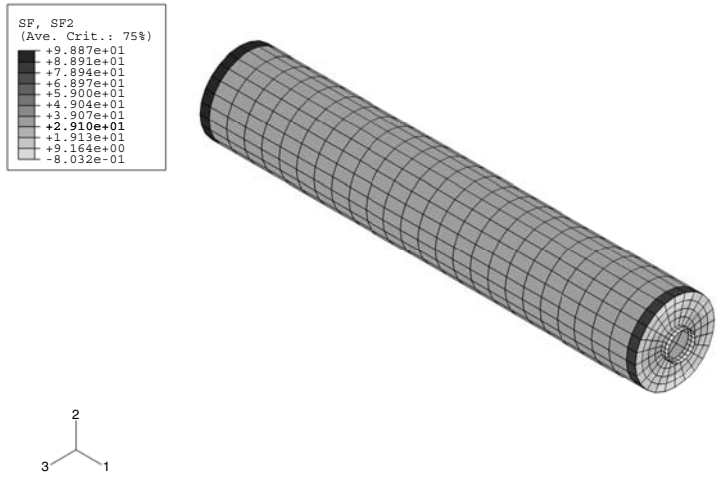

Figure 14.2.1–7 Section force in the hoop direction.

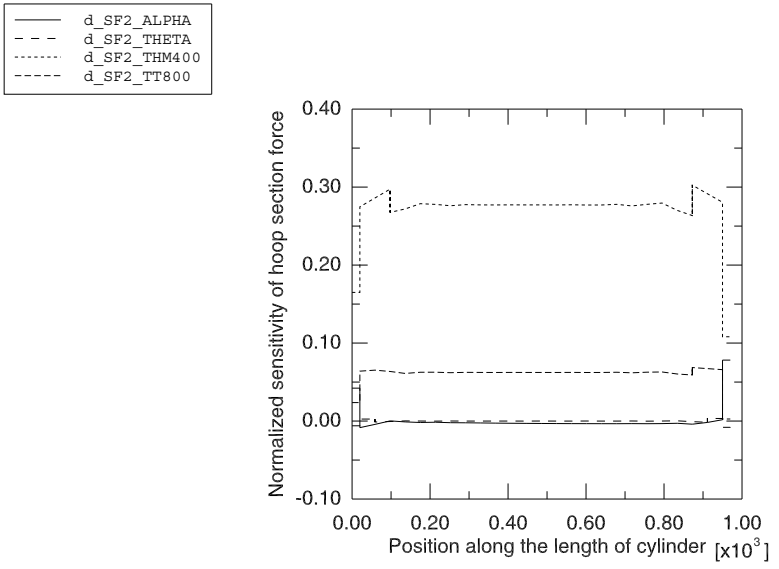

Figure 14.2.1–8 Normalized sensitivity of the section force in the hoop direction.

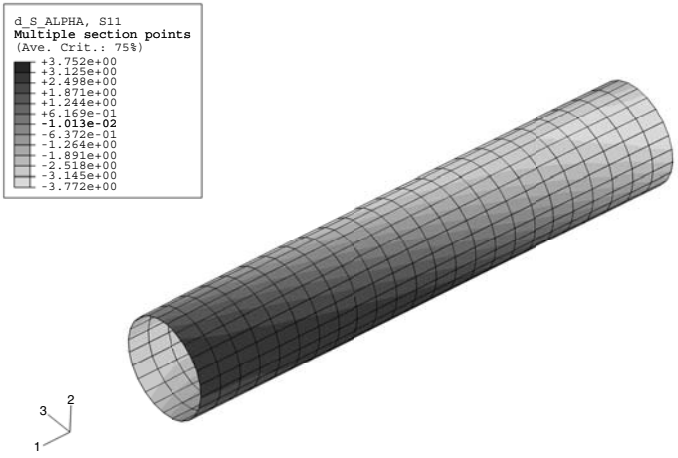

Figure 14.2.1–9 Sensitivity of the fiber stress, S11, in the helical layer to the shape design parameter ALPHA.

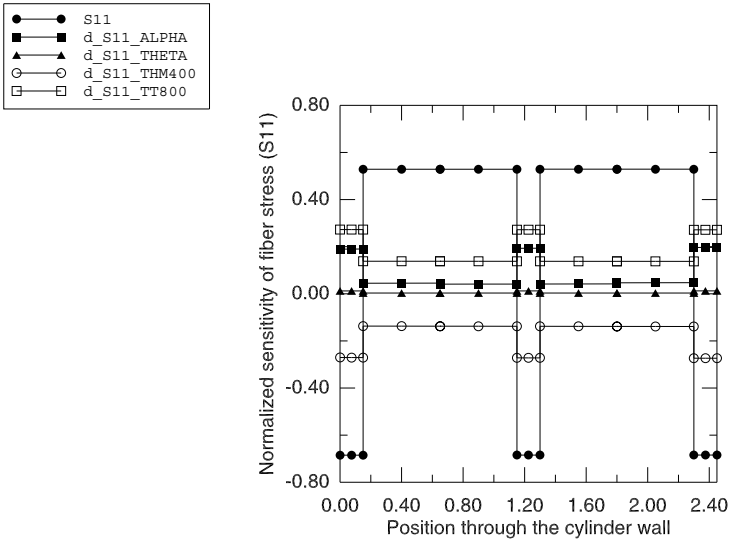

Figure 14.2.1–10 Normalized sensitivity of the fiber stress plotted through the thickness of the cylinder wall for element 590.

14.2.2 DESIGN SENSITIVITIES FOR TIRE INFLATION, FOOTPRINT, AND NATURAL FREQUENCY ANALYSIS

Products: Abaqus/Standard Abaqus/Design

This example demonstrates the application of design sensitivity analysis (DSA) to tire problems.

The base tire model and analysis is the same as that described in "Symmetric results transfer for a static tire analysis," Section 3.1.1. The design sensitivity analysis shows the effects on responses such as contact pressure and natural frequencies of three important design parameters: the thickness of the side wall, the elastic modulus of the belt rebar material, and the elastic modulus of the carcass rebar material. This example demonstrates that the DSA technique in Abaqus/Design can be used effectively for highly nonlinear analyses including features such as viscoelasticity, contact, and rebar.

Geometry and model

The geometry and model information for this example is identical to that for "Symmetric results transfer for a static tire analysis," Section 3.1.1. However, because symmetric model generation and symmetric results transfer are not available in a design sensitivity analysis, the full three-dimensional model is constructed and analyzed in one model. In addition, the convergence tolerance on the residual is tightened to improve the accuracy of the tangent stiffness, thereby providing more accurate sensitivities (see "Design sensitivity analysis," Section 19.1.1 of the Abaqus Analysis User's Guide). In addition to the inflation step and the two footprint analysis steps (displacement control and load control), a frequency extraction is appended as the last step. A sensitivity analysis is performed in each step with contact pressure as the design response in the static steps and frequency as the design response in the final frequency extraction step.

Three primary design parameters are chosen for this problem. The first is the "nominal" thickness, t_0, of the tire in the region of the sidewall. The specific region affected by t_0 is shown in the symmetric portion of the tire cross-sectional view in Figure 14.2.2–1. This region consists of one layer of elements, and the thickness t_i in the discretized model is taken as the distance between an outer node and the corresponding inner node. The thickness between each of the pairs of nodes in this region is related to the nominal thickness by $t_i = f\, t_0$, where f is defined as the ratio t_i/t_0. Thus, a change in the design parameter t_0 causes the thicknesses t_i to change proportionally (the actual value of t_0 is not important; however, for the purposes of normalization of the results, as discussed below, a value of 1 is used). A constraint on the change in the nodal coordinates due to a change in the design parameter is specified such that the outer nodes stay fixed and the inner nodes move inward along the original vectors connecting the outer nodes to the inner nodes. Figure 14.2.2–1 depicts the shape of the tire cross-section that would result from a 50% change in nominal thickness. The other two design parameters chosen are the elastic modulus of the belt rebar material, E_{belt}, and the elastic modulus of the carcass rebar material, E_{carc}. The density of the rubber material, ρ_{rubber}, is also included as a design parameter for demonstration and verification purposes.

Perturbation sizes for the finite differencing operations

As documented in "Design sensitivity analysis," Section 19.1.1 of the Abaqus Analysis User's Guide, Abaqus uses the semi-analytic approach to compute sensitivities, and this approach involves finite differencing computations at the element level. By default, Abaqus automatically determines for each element the perturbation sizes of the design parameters to be used in the finite differencing computations through a heuristic perturbation sizing algorithm. The perturbation sizes for the elements with the most contribution to the sensitivities are written to the message file. Since this algorithm can be expensive, DSA controls are provided to allow the user to directly supply perturbation sizes. If appropriate perturbation sizes are not known in advance, a smaller problem can be run with the default perturbation sizing algorithm, and the perturbation sizes determined by Abaqus can then be inserted into the larger problem.

This technique for obtaining perturbation sizes is adopted in this example. A smaller axisymmetric problem (dsatire_axi_half.inp) with one inflation (static) step and one frequency step is run. The perturbation sizes reported in the message file for each step of the smaller problem are subsequently specified in the full model (dsatire.inp) using the DSA controls.

Normalization of sensitivity results

In the subsequent plots of results, the sensitivities are normalized so that they can be compared side-by-side. Except as noted, the contour plots of contact pressures (CPRESS) and corresponding sensitivities are normalized by dividing by the maximum contact pressure at the end of the last static step, $C_{\max}$. In addition, the sensitivities of CPRESS are multiplied by the value of the design parameter. For example, the sensitivity of CPRESS with respect to t_0, d_CPRESS_tNominal, is normalized as $t_0 \times$ d_CPRESS_tNominal/$C_{\max}$. The eigenfrequency (EIGFREQ) sensitivities are divided by the first eigenfrequency value and, as for CPRESS, multiplied by the value of the appropriate design parameter.

Results and discussion

The contact pressure on the tire footprint can be considered an important factor in tire handling and wear properties. As such, the results of the sensitivity analysis are discussed in terms of the contact pressure distribution on the tire footprint. Figure 14.2.2–2 shows the actual values of the contact pressure on the full tire model looking from below at the end of the static footprint analysis. Figure 14.2.2–3 shows the normalized contact pressure distribution on a blown-up region of the full tire. As can be seen from these plots, the contact pressure is less in the center of the footprint than in the surrounding region. The maximum contact pressure occurs at node 2645, and the center of the footprint is at node 3055. These nodes are indicated on the plots, and Figure 14.2.2–4 shows the time history of CPRESS for these nodes.

The objective is to use the sensitivity results to determine how the design parameters can be modified to distribute the contact pressure more evenly so that the center of the tire picks up more of the load. Figure 14.2.2–5 to Figure 14.2.2–7 show the distributions of the normalized contact pressure sensitivity for each of the design parameters. Large variations in the sensitivities away from the center of the footprint are observed in the sensitivity contour plots. These variations can be attributed to the high gradients in contact pressure in the region surrounding the center of the footprint (see Figure 14.2.2–3),

because even small changes in the footprint size (due to small changes in the design parameters) can lead to relatively large changes in the contact pressure. These sensitivity plots show that to increase the contact pressure at node 3055 (footprint center), the value of E_{carc} should be increased, the value of E_{belt} should be increased, and the value of t_0 should be decreased. However, based on the magnitudes of the normalized sensitivities, E_{belt} has the most influence on the contact pressure at the center node. Accordingly, a new design is investigated in which the design parameter E_{belt} is increased by 5%. Figure 14.2.2–8 shows the distribution of contact pressure for the new design, and Figure 14.2.2–9 shows the time history of CPRESS at nodes 2645 and 3055 for the new design. These figures indicate that the contact pressure has increased in the center of the tire without appreciably affecting the surrounding contact pressure distribution; the actual increase is 3.20%. The predicted increase based on the (first-order) sensitivities is 2.32%, which is reasonably close to the actual increase considering the high degree of nonlinearity in this problem.

Figure 14.2.2–10 to Figure 14.2.2–14 show the first five modes of the tire. The study of the frequency sensitivities provides insight into the dynamic behavior of the design. For example, we can conclude from Figure 14.2.2–15 and Figure 14.2.2–17 that the frequency of mode 2 is most sensitive to the sidewall shape, t_0, and less sensitive to the Young's modulus of the sidewall reinforcement, E_{belt}. In retrospect, this makes good physical sense because mode 2 is primarily shear of the sidewall (see Figure 14.2.2–15), but this conclusion may have been much more difficult to formulate without the sensitivity information.. Figure 14.2.2–16, Figure 14.2.2–17, and Table 14.2.2–1 show the values of the eigenfrequency and corresponding normalized sensitivities for the first five modes of the tire. The eigenfrequencies for the new design (5% change in E_{belt} as discussed above) are the same (to five significant figures) as for the original model. This behavior is accurately predicted in Figure 14.2.2–17, where it can be seen that the eigenfrequencies are essentially independent of this design parameter.

Given the highly nonlinear nature of this problem, the user is cautioned against using the sensitivities beyond their useful limit. The sensitivities are first-order derivatives; therefore, using them to predict large changes in the design parameters is not valid, since higher-order terms are not considered. In addition, using sensitivity results to predict the outcome of simultaneous changes to the design parameters assumes that superposition is valid, which again is true only for small changes in the design parameters. For example, if the design parameters E_{carc} and E_{belt} are increased by 5% and t_0 is decreased by 5%, the contact pressure at the center of the footprint increases by 4.35%, which is nearly twice the predicted change of 2.42%. This implies that a simultaneous change of 5% is too large for predicting the net effect on the contact pressure based on the sensitivities.

Input files

dsatire_axi_half.inp	Axisymmetric model with inflation and frequency analysis for obtaining perturbation sizes.
dsatire_axi_half_node.inp	Nodal coordinates for axisymmetric model.
dsatire_axi_half_psv.inp	Parameter shape variation data for axisymmetric model.
dsatire.inp	Full model including inflation, footprint, and frequency analysis.
dsatire_model.inp	Model data for full model.
dsatire_psv.inp	Parameter shape variation data for full model.

Table 14.2.2–1 Eigenfrequency sensitivities for the first five modes.

Mode	Eigenfrequency	Normalized eigenfrequency sensitivity with respect to:			
		t_0	ρ_{rubber}	E_{belt}	E_{carc}
1	51.6	1.56E−1	−5.00E−1	−1.84E−3	1.39E−2
2	52.9	2.18E−1	−5.13E−1	−1.81E−5	4.97E−3
3	58.7	1.45E−1	−5.69E−1	2.27E−3	1.53E−2
4	60.6	1.34E−1	−5.88E−1	1.75E−3	1.54E−2
5	84.1	1.69E−1	−8.15E−1	3.48E−3	1.86E−2

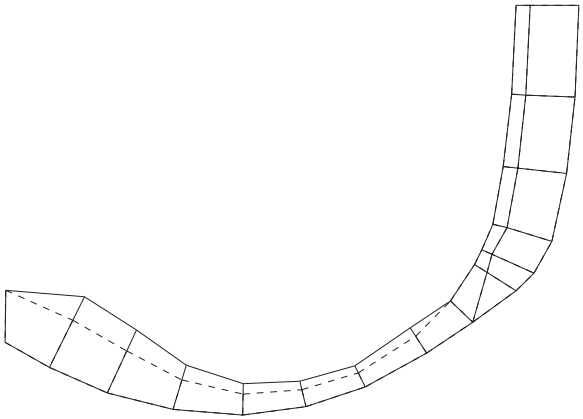

Figure 14.2.2–1 Effect of 50% change in design parameter t_0 on tire cross-section geometry (dashed line represents original geometry).

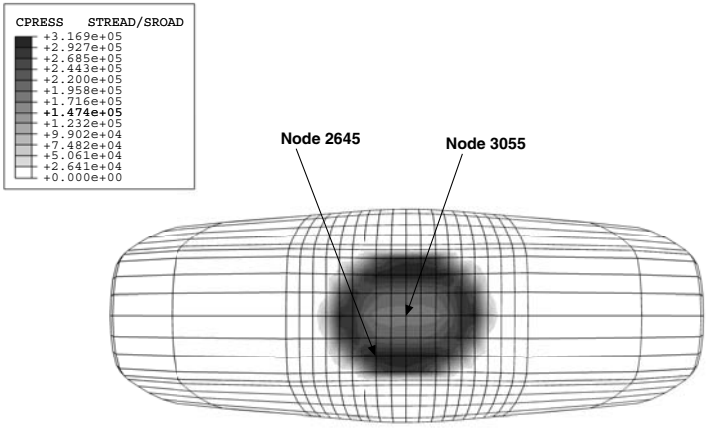

Figure 14.2.2–2 Contact pressure distribution on full tire at end of footprint (static) analysis.

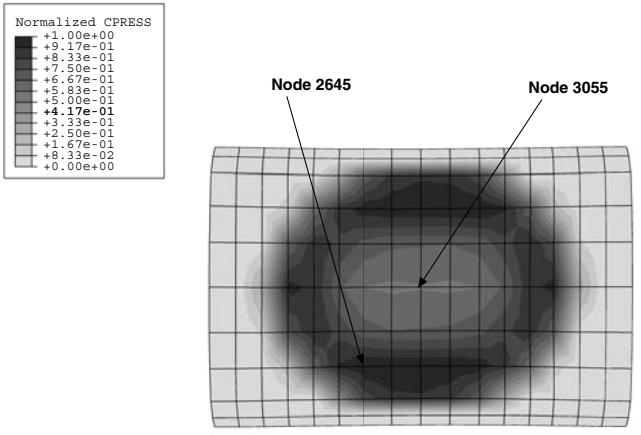

Figure 14.2.2–3 Normalized contact pressure distribution on blown-up view of tire footprint at end of footprint analysis.

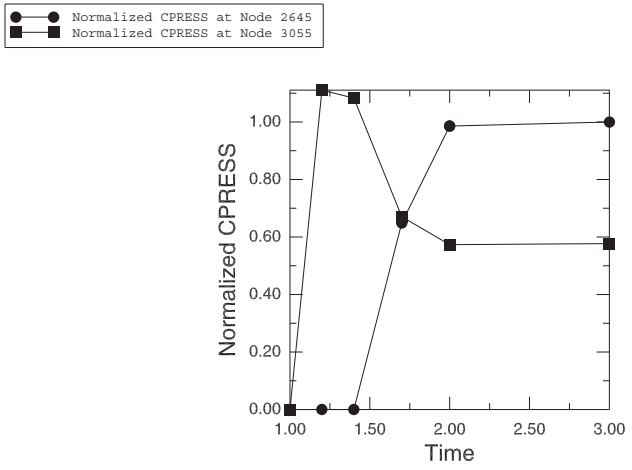

Figure 14.2.2–4 Normalized contact pressure history for center node (3055) and node with maximum contact pressure at end of footprint analysis (2645).

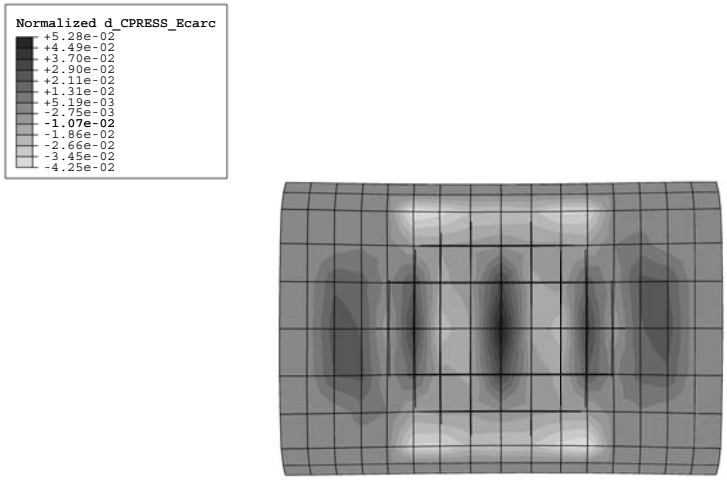

Figure 14.2.2–5 Distribution of normalized contact pressure sensitivity with respect to E_{carc} at end of footprint analysis.

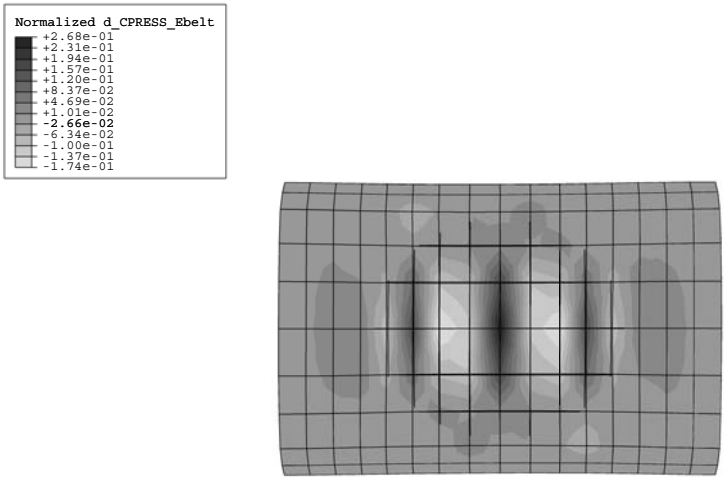

Figure 14.2.2–6 Distribution of normalized contact pressure sensitivity with respect to E_{belt} at end of footprint analysis.

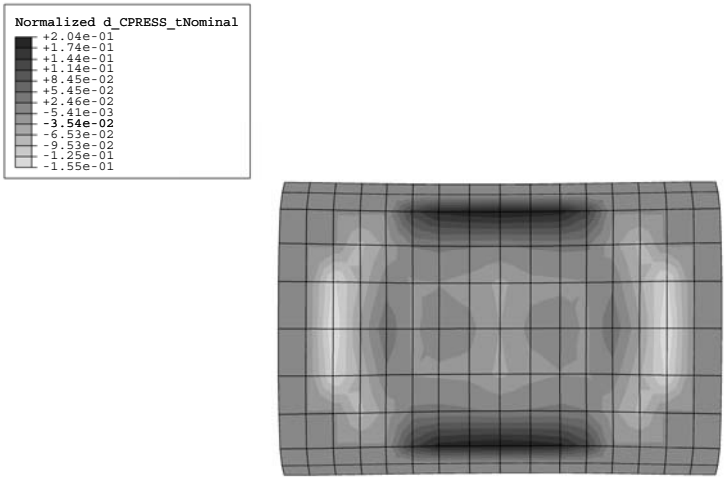

Figure 14.2.2–7 Distribution of normalized contact pressure sensitivity with respect to t_0 at end of footprint analysis.

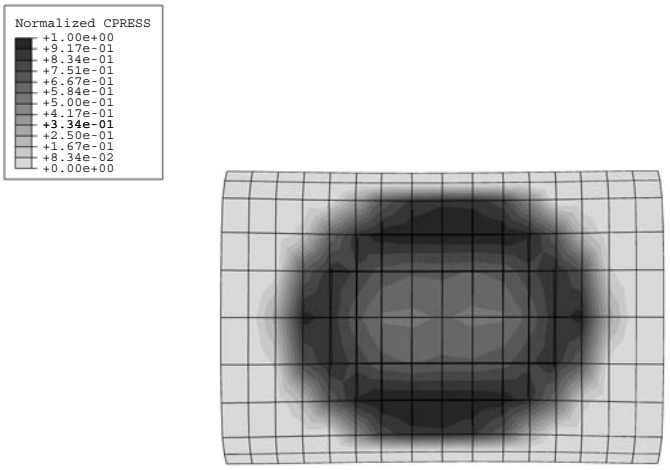

Figure 14.2.2–8 Normalized contact pressure distribution for new design (5% increase in E_{belt}).

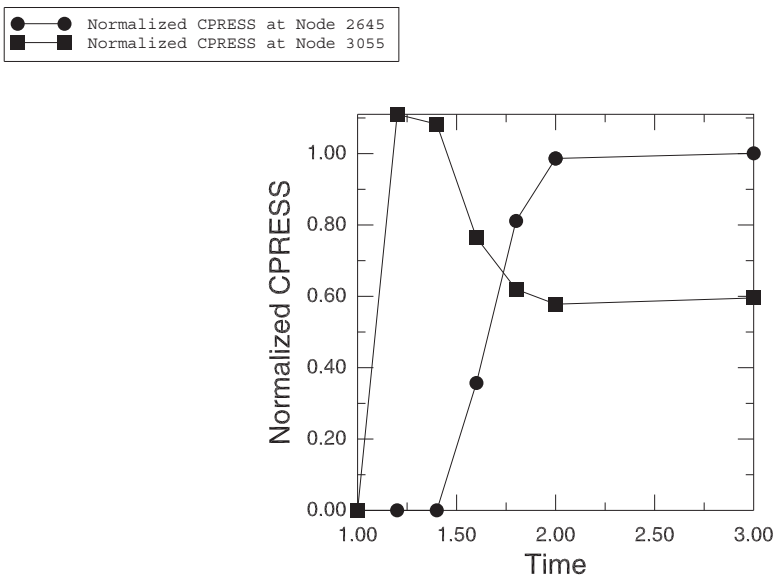

Figure 14.2.2–9 Normalized contact pressure history at nodes 3055 and 2645 for new design.

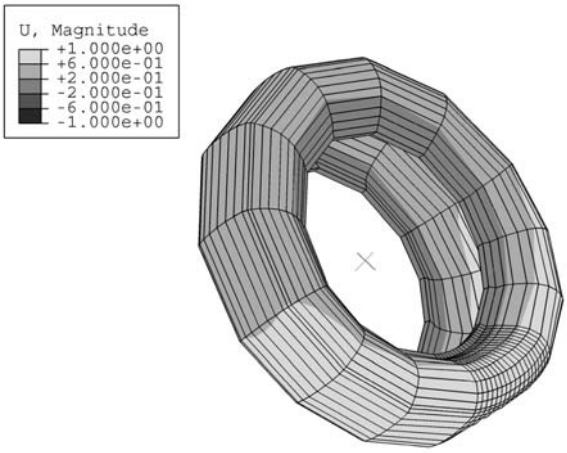

Figure 14.2.2–10 Mode 1.

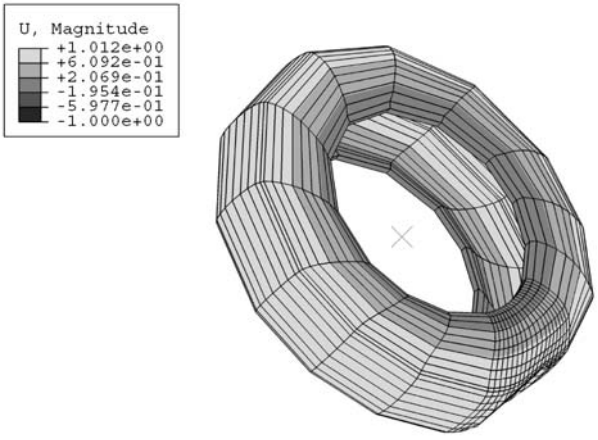

Figure 14.2.2–11 Mode 2.

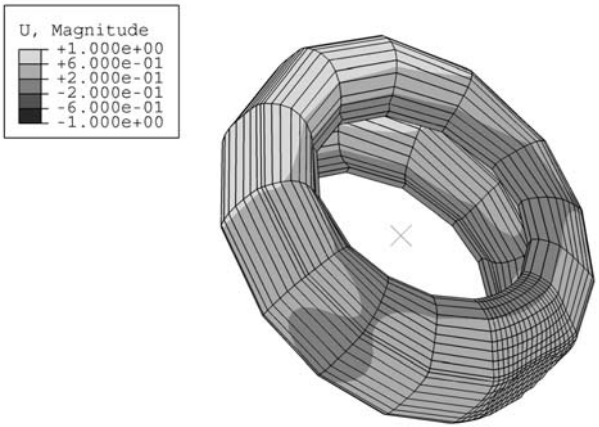

Figure 14.2.2–12 Mode 3.

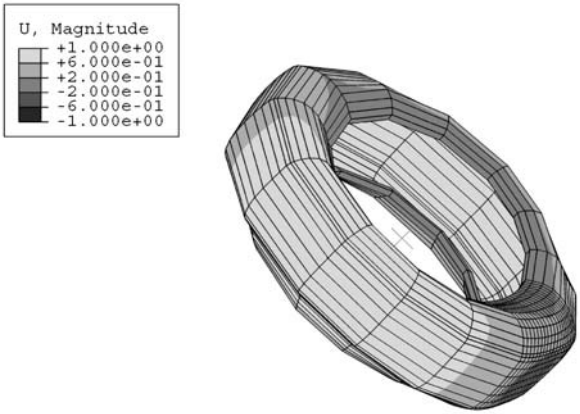

Figure 14.2.2–13 Mode 4.

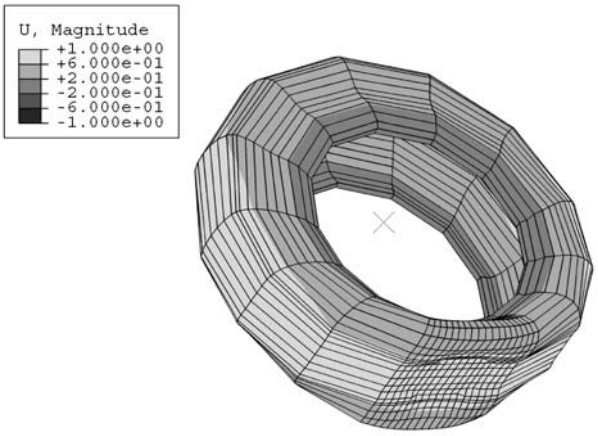

Figure 14.2.2–14 Mode 5.

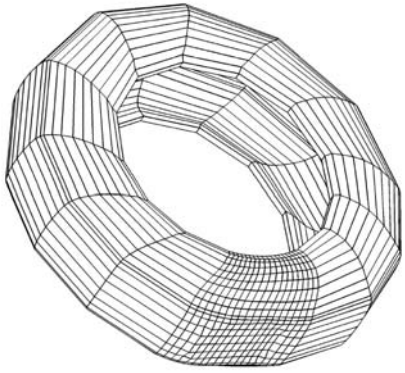

Figure 14.2.2–15 Mode 2 (wire frame).

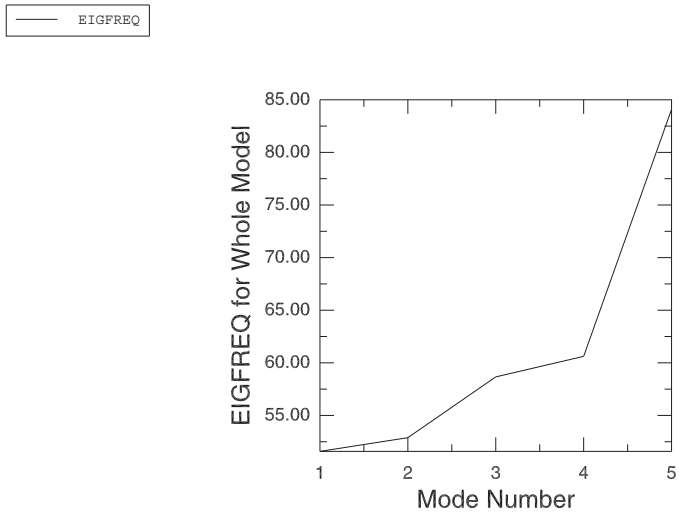

Figure 14.2.2–16 Eigenfrequencies for first five modes.

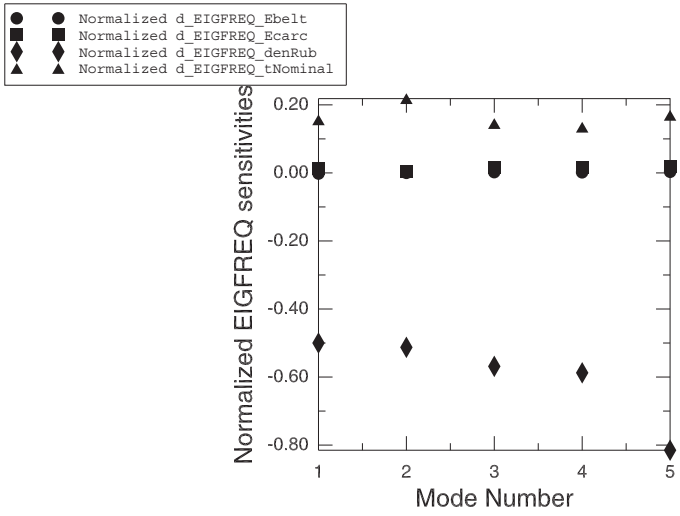

Figure 14.2.2–17 Normalized eigenfrequency sensitivities for first five modes.

14.2.3 DESIGN SENSITIVITY ANALYSIS OF A WINDSHIELD WIPER

Products: Abaqus/Standard Abaqus/Design

This example shows the design analysis of a statically loaded windshield wiper blade.

The conventional wiper system is composed of three major subsystems: the blade-arm assembly, a linkage mechanism, and the electric motor. We restrict our design and analysis to the blade-arm subsystem. Wiping performance is determined by the dynamic performance of the wiper system, while safety regulations require that the blade wipe a specific area on the windshield surface. It is a major challenge to achieve systems that optimize wiping performance and satisfy the area conditions. The interaction between the force/deflection response of the blade (rubber) element and the friction at the blade-glass interface is a critical element in design. A design sensitivity analysis of the rubber-glass interaction gives insight that can be used to improve the design before undertaking the more complex dynamic stick-slip analysis. The sensitivity analysis also identifies the design parameters that are most effective in reducing the stress in highly stressed areas. Self-contact between the flanges of the rubber element is not considered in this example.

Geometry, model properties, and design parameters

The geometry of the rubber blade is shown in Figure 14.2.3–1. The arm is assumed to be stiff relative to the rubber blade and is modeled by prescribing fixed boundary conditions. The rubber blade is modeled as a plane strain model with 231 first-order hybrid elements. An incompressible hyperelastic material with a polynomial strain energy function is used to simulate the rubber material behavior. The windshield is assumed to be rigid and is modeled as an analytical rigid surface. Surface interaction between the blade and the windshield is modeled using finite-sliding contact with an isotropic Coulomb friction coefficient of 0.2. Three shape parameters and the coefficient of friction, μ, are chosen as design parameters for the design study. We choose μ as a design parameter to study the effect of the friction coefficient on the blade-glass interface forces. The shape parameters that can be modified without requiring geometry changes to other parts of the assembly are chosen as design parameters. These shape parameters will help us to study the effect of aspects of wiper geometry on wiper stiffness. The shape parameters are the thickness, $t2$, of the neck between the bottom two flanges; the thickness, $t3$, of the wiper tip; and the width, $h2$, of the lower flange. The corresponding shape gradients (the derivatives of the nodal coordinates with respect to the shape design parameters) required as input to the sensitivity analysis are shown as symbol plots in Figure 14.2.3–2, Figure 14.2.3–3, and Figure 14.2.3–4. These gradients are input using parameter shape variation and calculated using a custom Python script derived from the Abaqus/CAE replay file. This approach requires familiarity with the Abaqus Scripting Interface. Shape variation data can be generated more easily using Abaqus/CAE; details are given in "Design sensitivity analysis: overview," Section 14.1.1.

Loading, boundary conditions, and design responses

An interference fit of 2.0 units between the blade and the windshield is used to simulate the static vertical load between them. The windshield is held fixed in the vertical direction, and the surface nodes of

the upper flange are constrained in both directions. The wiping motion is simulated by prescribing a horizontal displacement of 9.0 units to the reference node of the windshield.

It is desirable to reduce the stress concentration in the rubber element since high stresses will degrade the lifecycle of the blade and affect performance. Consequently, the sensitivity of the Mises stress is taken as the primary design response in this model. Any design change should take into account the behavior of the contact pressure between the wiper and the windshield. To this end the sensitivities of CSTRESS are also selected as design responses. Including friction makes the stiffness matrix unsymmetric; hence, the analysis is run using the unsymmetric solver. Since we are interested in the history of the contact pressure at the tip, the incremental DSA formulation is chosen. To quantify the effect of neglecting the unsymmetric terms and of using total DSA, we also compare the maximum sensitivities for various combinations of DSA formulation and stiffness matrix symmetrization.

Results and discussion

A contour plot of the Mises stress distribution on the deformed configuration of the rubber blade is shown in Figure 14.2.3–5. It is evident that the two necks between the flanges are the areas of interest. In a magnified contour plot of the Mises stress distribution in the necks (Figure 14.2.3–6) we can see that the stress concentration in the lower neck is higher than in the upper one. The normalized sensitivities of the maximum Mises stresses in the lower neck are listed in Table 14.2.3–1. Sensitivities are normalized by dividing them by the maximum Mises value (67857.7 units in element 131 of the wiper blade) and then scaling the result by the initial value of the design parameter. We notice that the shape parameters have a direct effect (increasing the parameter increases stress and vice versa) and the friction coefficient has an inverse effect on the Mises stress. Reducing the thickness of the neck makes the wiper more flexible and reduces stress concentration. Increasing the friction coefficient increases the shear force at the tip. This increased shear force increases bending of the upper neck and decreases bending in the lower neck, thus reducing the stress concentration in the lower neck. We infer from the table that the Mises stress is more sensitive to $t2$ and $t3$ than to the flange width and friction coefficient. To reduce stress concentration, a design with changes in $t2$ and $t3$ is considered. A 20% reduction in $t2$ and a 10% reduction in $t3$ is selected. The predicted percentage reduction in the Mises stress is 6.76 ($0.2832 \times 0.2 + 0.1094 \times 0.1$).

The proposed design changes will affect the contact pressure at the wiper-windshield interface, and the sensitivity results are used to quantify this effect. The time history of the normalized sensitivities of contact pressure at a point at the tip is shown in Figure 14.2.3–7. Contact pressure at this point is most sensitive to $t2$. This result is somewhat unexpected since this design parameter does not affect the interface explicitly. $t2$ has a directly proportional effect, while $t3$ has an inversely proportional effect on the contact pressures. Thus, decreasing $t2$ will decrease the contact pressure while decreasing $t3$ will increase the contact pressure. The contact pressure histories for the proposed design and the current design are shown in Figure 14.2.3–8. The plots indicate that the reduced stress concentration in the proposed design comes at the cost of decreased wiper performance. (The proposed design has a lower contact pressure, which could be suboptimal.) If desired, the contact pressure can be positively influenced by considering a positive change in $t3$.

All results discussed above are obtained in an incremental DSA analysis using the unsymmetric solver. If the user is interested only in the results at particular increments (typically, the last increment), total DSA will be advantageous computationally. Similarly, neglecting the unsymmetric terms will

improve computational efficiency. To quantify the error in such approximations, we compare the results for various combinations to the overall finite difference method (OFD). Table 14.2.3–2 lists the relative error in the maximum Mises and contact pressure sensitivities compared to the results obtained using the OFD method. For the dominant shape parameter, $t2$, the sensitivity results of the maximum Mises stress are in good agreement with the OFD method for all the combinations. However, neglecting the unsymmetric terms in total DSA gives inaccurate results for the contact pressure sensitivities. The relative error is large for the less dominant shape parameters, with total DSA giving poor results for both the Mises and contact pressure sensitivities. Total DSA gives inaccurate results for sensitivities with respect to the friction coefficient. Although the sensitivity results are problem dependent, we can infer that total DSA may give poor results if we neglect unsymmetric terms. Further sensitivities of interaction pressures are more sensitive to approximations than the sensitivities of maximum stresses in the structures. Less significant sensitivities are affected more by approximations than the dominant sensitivities.

The proposed design changes are made and the analysis is rerun. A 9% reduction in the stress concentration is observed. Predicted and actual contact pressure histories are shown in Figure 14.2.3–9. The difference between the predicted and the actual results is due to the nonlinear dependence of the design response on the design parameter. However, the rerun confirms the prediction that the proposed design is more robust, with a possibly suboptimal wiping pressure.

Input files

dsawiper.inp	Primary wiper blade design sensitivity analysis.
dsawiper_pred.inp	Wiper blade analysis incorporating design changes.
dsawiper_node.inp	Node description.
dsawiper_elem.inp	Element description.
dsawiper_t2.inp	Parameter shape variation data for thickness $t2$.
dsawiper_t3.inp	Parameter shape variation data for thickness $t3$.
dsawiper_h2.inp	Parameter shape variation data for width $h2$.

Table 14.2.3–1 Normalized sensitivities of maximum stress values.

Design Parameter	Normalized Sensitivity
$t2$	0.2832
$t3$	0.1094
$h2$	0.0154
μ	−0.0026

Table 14.2.3–2 Percentage error in maximum stress and contact pressure sensitivities.

Design Parameter	Incremental DSA; Unsymmetric Solver		Incremental DSA; Symmetric Solver		Total DSA; Unsymmetric Solver		Total DSA; Symmetric Solver	
	% Error MISES	% Error CPRESS	% Error MISES	% Error CPRESS	% Error MISES	% Error CPRESS	% Error MISES	% Error CPRESS
$t2$	0.02	0.00	0.06	0.24	0.02	0.11	2.4	22.15
$t3$	0.01	0.01	0.02	0.12	1.81	61.56	1.70	53.20
$h2$	0.37	0.00	12.35	0.13	1.12	94.41	12.36	93.01
μ	1.51	0.88	1.97	0.43	51.6	0.88	28.90	21.21

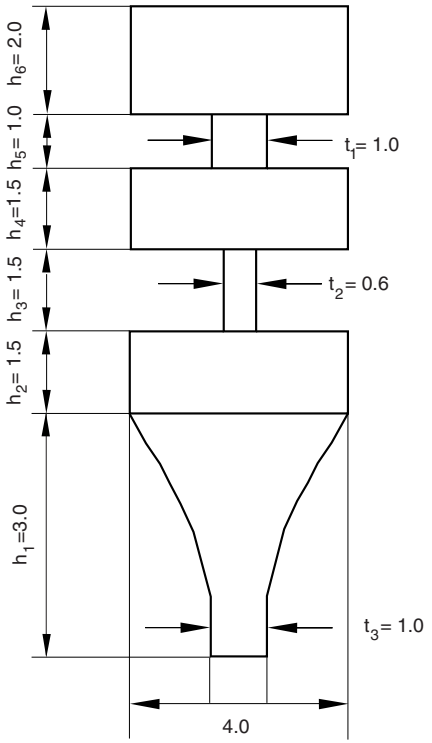

Figure 14.2.3–1 Model of the rubber windshield wiper.

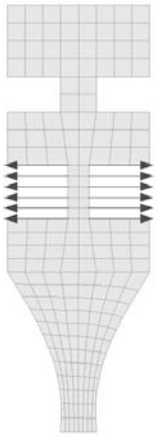

Figure 14.2.3–2 Symbol plot of the shape variation with respect to $t2$.

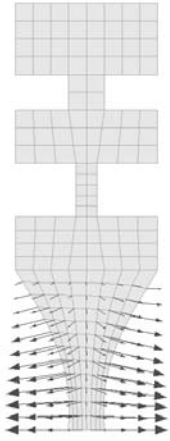

Figure 14.2.3–3 Symbol plot of the shape variation with respect to $t3$.

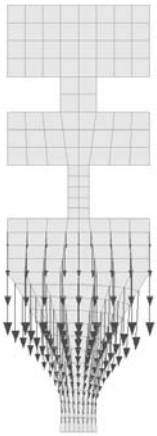

Figure 14.2.3–4 Symbol plot of the shape variation with respect to $h2$.

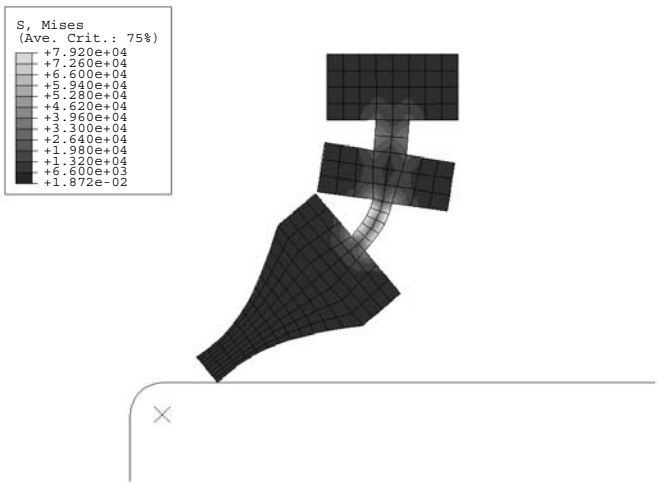

Figure 14.2.3–5 Contour plot of Mises stress.

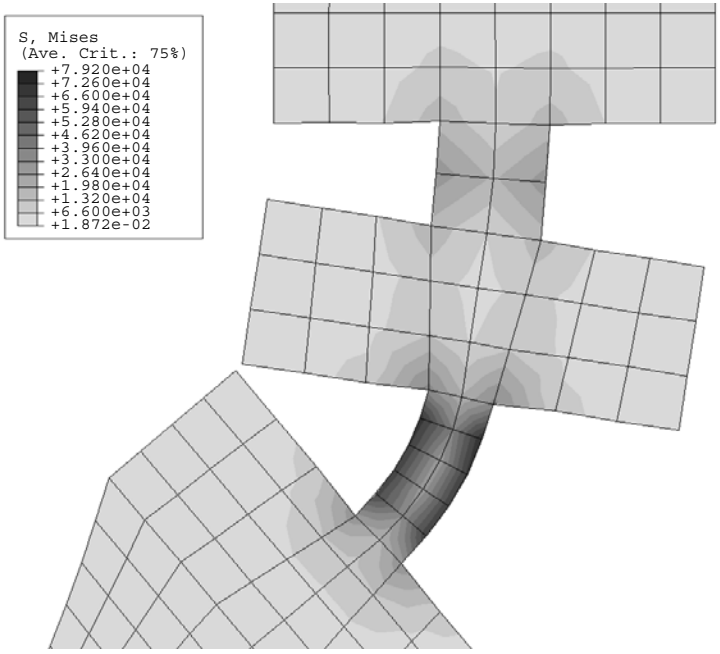

Figure 14.2.3–6 Magnified contour plot of Mises stress.

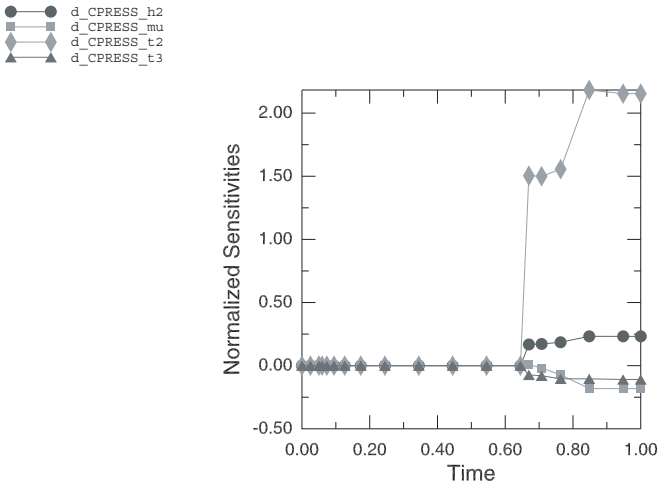

Figure 14.2.3–7 Time history of the normalized sensitivity of contact pressure at the wiper tip.

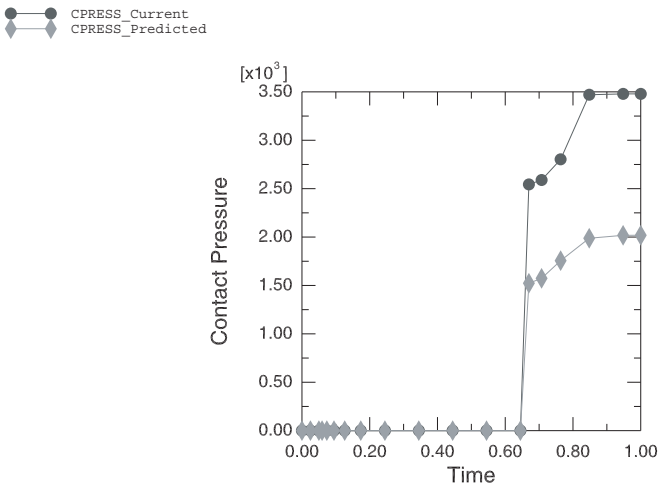

Figure 14.2.3–8 Current and predicted contact pressure history.

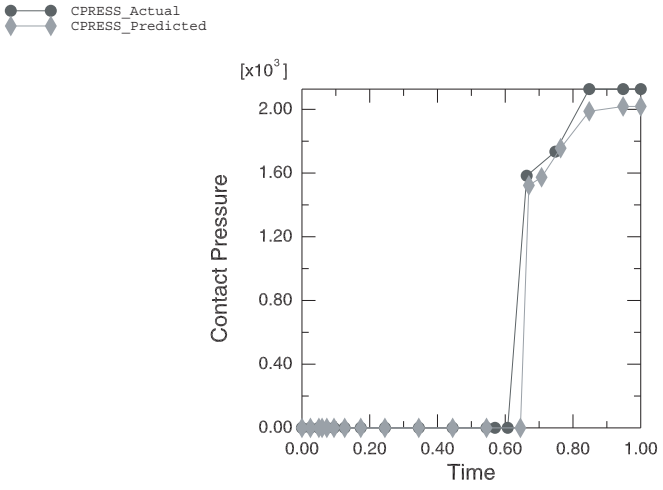

Figure 14.2.3–9 Actual and predicted contact pressure history.

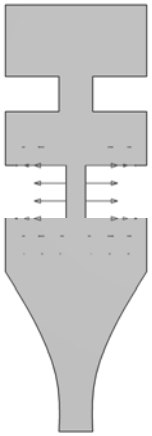

Figure 14.2.3–10 Symbol plot of the computed shape variation with respect to $t2$.

14.2.4 DESIGN SENSITIVITY ANALYSIS OF A RUBBER BUSHING

Products: Abaqus/Standard Abaqus/Design

This example demonstrates how design sensitivity analysis can be used to improve the design of a rubber bushing.

The objective is to alter the bushing geometry to lower the maximum axial stress, thus increasing the service life. Design sensitivity analysis provides a means of predicting the effect of a change in the geometry on the stress concentration, thereby aiding in identifying the important design parameters and determining an appropriate design change.

Geometry, model properties, and design parameters

The bushing consists of inner and outer steel tubes that are bonded to a central rubber cylinder (Figure 14.2.4–1). It is assumed that the outer perimeter of the bushing is fully fixed. The bushing is 457.2 mm (18.0 in) long, with an outside diameter of 508.0 mm (20.0 in) and an inside diameter of 228.6 mm (9.0 in). The steel is elastic with Young's modulus = 206.0 GPa (3.0×10^7 psi) and Poisson's ratio = 0.3. The rubber is modeled as a fully incompressible hyperelastic material that at all strain levels is relatively soft compared to the steel. The nonlinear elastic behavior of the rubber is described by a strain energy function that is a second-order polynomial in the strain invariants.

The model is discretized with standard axisymmetric elements since the axial loading results in pure axisymmetric deformation. CAX4 elements are used for the steel components, and CAX4H elements are used for the rubber component. Rigid elements (element type RAX2) are attached to the inside of the bushing in both models to represent the relatively stiff shaft. The use of these elements also simplifies the application of the loading conditions. The axisymmetric finite element mesh is shown in Figure 14.2.4–1. An axial force of magnitude 10675.0 N (2400.0 lbs) is applied to the rigid body reference node, while the outer steel tube is fully fixed.

Two design parameters are considered for the design sensitivity analysis: the thickness, t, and the fillet radius, r, of the rubber bushing at the top and bottom ends where it is bonded to the inner steel tube, which is shown in Figure 14.2.4–1. These parameters represent typical geometry properties that may be considered during design evaluation.

Design sensitivity analysis and design parameters

To carry out a design sensitivity analysis with respect to a shape design parameter, the gradients of the nodal coordinates with respect to the design parameter must be specified with parameter shape variation. One simple approach to obtaining these gradients is to perturb the shape design parameters r and t one at a time and to record the perturbed coordinates. The gradients are then found by numerically differencing the initial and perturbed nodal coordinates. In the current study the constraint is imposed that a change in the thickness causes the line of nodes connecting the thickness dimension to the fillet radius to rotate about the point of tangency of this line to the fillet radius. The Abaqus Scripting Interface command

`_computeShapeVariations()` provides a semi-automated facility to compute the shape variations (see "Design sensitivity analysis: overview," Section 14.1.1).

Results and discussion

The deformed mesh is shown in Figure 14.2.4–2. Figure 14.2.4–3 shows the contours of axial stress in the rubber part of the bushing at the end of the axisymmetric analysis. The maximum stress occurs near the top fillet close to the axis. Figure 14.2.4–4 and Figure 14.2.4–5 show the contours of the sensitivities of the axial stress for the shape design variables ***r*** and ***t***, respectively. Table 14.2.4–1 shows the normalized sensitivities of the maximum axial stress, $\sigma_{\max} = 0.17$ MPa (24.55 psi), with respect to the shape design variables. The normalization has been carried out by multiplying the sensitivities by a characteristic dimension (initial fillet radius $r_0 = 12.7$ mm (0.5 in) and initial thickness $t_0 = 15.24$ mm (0.6 in)) and dividing by the maximum stress. As can be inferred from this table, a change in the fillet radius influences the maximum stress to a larger extent than a change in the thickness of the rubber. Hence, it is desirable to change ***r*** to modify the stresses. To obtain approximately a 10% reduction in the maximum stress in the axial direction, the fillet radius is increased by

$$\Delta r = \frac{\Delta\sigma_{\max}}{\frac{d\sigma_{\max}}{dr}}.$$

Substituting $\Delta\sigma_{\max} = 0.1\sigma_{\max}$ and $d\sigma_{\max}/dr = 0.008$ MPa/mm (28.75 psi/in) (see Figure 14.2.4–4) gives $\Delta r = 2.25$ mm (0.09049 in). A reanalysis of the problem with the radius changed to $r_0 + \Delta r = 14.99$ mm (0.59049 in) yields a reduction of 8.8% in the maximum axial stress, which is slightly less than the goal of 10%. This is expected because of the nonlinearity of the problem; to achieve the 10% reduction, this process would have to be repeated, which is essentially an optimization problem.

Input files

bushing_cax4_axi_dsa.inp	Design sensitivity analysis for the axisymmetric model.
bushing_node.inp	Node definitions.
bushing_steel.inp	Element definitions for the steel.
bushing_rubber.inp	Element definitions for the rubber.
bushing_rigid.inp	Element definitions for the rigid body.

Table 14.2.4–1 Normalized sensitivities of the maximum stress.

Parameter	$\frac{r_0}{\sigma_{\max}}\frac{d\sigma_{\max}}{dr}$	$\frac{t_0}{\sigma_{\max}}\frac{d\sigma_{\max}}{dt}$
r	−0.58	—
t	—	−0.11

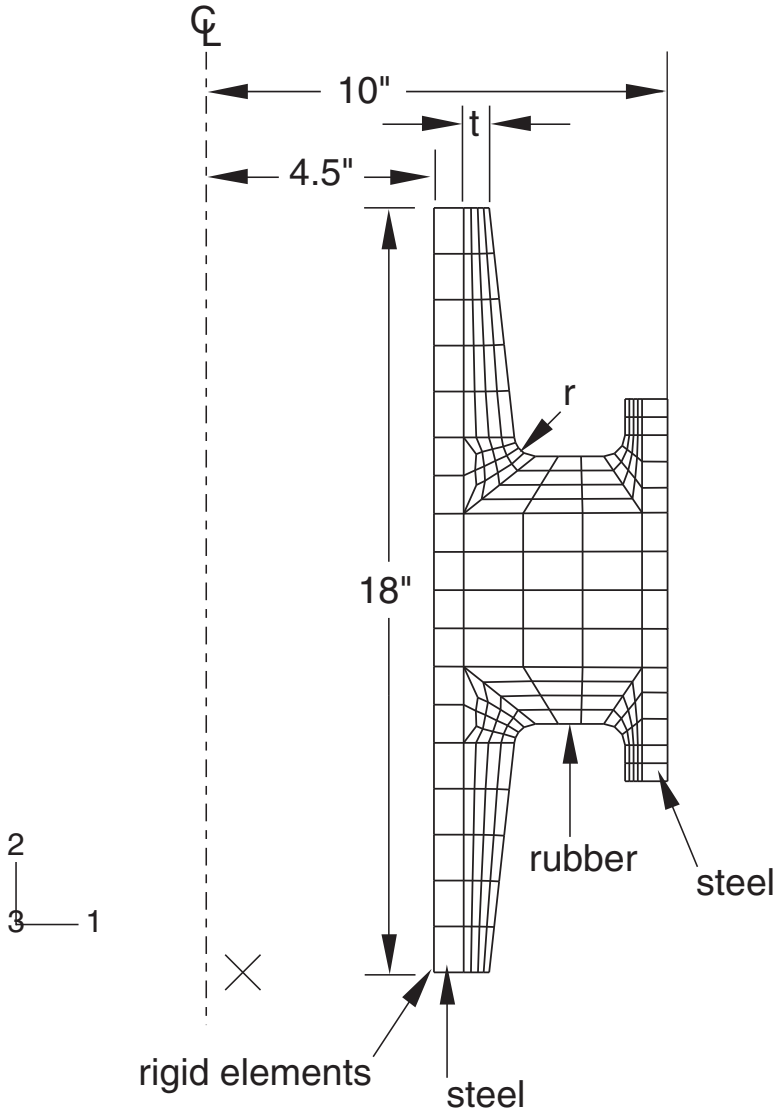

Figure 14.2.4–1 Axisymmetric cross-section.

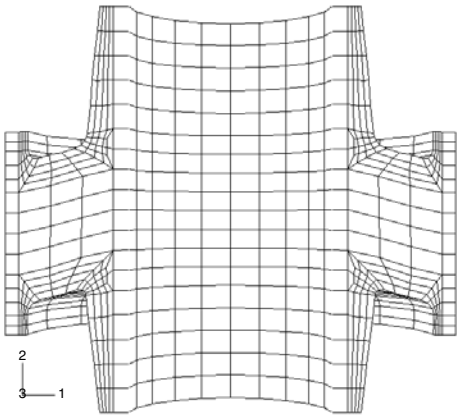

Figure 14.2.4–2 Deformed mesh after axial loading.

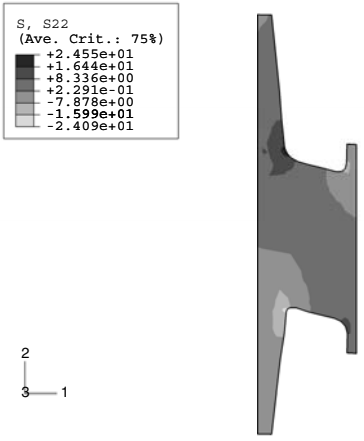

Figure 14.2.4–3 Variation of axial stress in the rubber after axial loading.

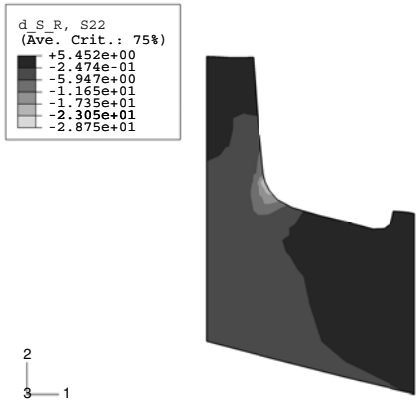

Figure 14.2.4–4 Variation of the sensitivity of the axial stress with respect to an increase in the radius of the fillet, r.

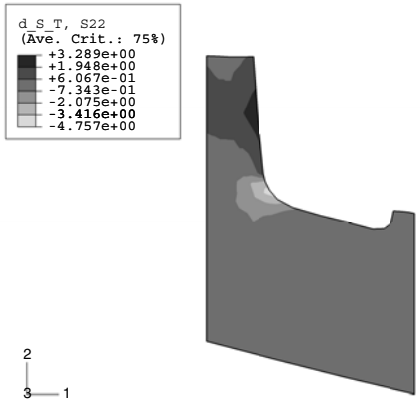

Figure 14.2.4–5 Variation of the sensitivity of the axial stress with respect to a decrease in the thickness of the rubber, t.

15. Postprocessing of Abaqus Results

- "Postprocessing examples," Section 15.1

15.1 Postprocessing examples

- "User postprocessing of Abaqus results files: overview," Section 15.1.1
- "Joining data from multiple results files and converting file format: FJOIN," Section 15.1.2
- "Calculation of principal stresses and strains and their directions: FPRIN," Section 15.1.3
- "Creation of a perturbed mesh from original coordinate data and eigenvectors: FPERT," Section 15.1.4
- "Output radiation view factors and facet areas: FRAD," Section 15.1.5
- "Creation of a data file to facilitate the postprocessing of elbow element results: FELBOW," Section 15.1.6
- "Translating Abaqus data to modal neutral file format for analysis in MSC.ADAMS," Section 15.1.7

15.1.1 USER POSTPROCESSING OF Abaqus RESULTS FILES: OVERVIEW

You can write and utilize postprocessing programs to manipulate data stored in the Abaqus results file.

The Abaqus results file is identified by the file extension **.fil** and contains results based on user-specified output requests; see "Output to the data and results files," Section 4.1.2 of the Abaqus Analysis User's Guide, for more information on the types of data that are written to the results file. The standard file format is binary, but it can be changed to ASCII format for each run by user request. Alternatively, it can be set to a default ASCII format during site installation. Abaqus uses Fortran unit **8** to communicate with the results file.

Sample postprocessing programs that perform commonly exercised tasks are presented in separate sections in this chapter. These include merging multiple results files and converting the resulting results file from binary format to ASCII, or vice-versa; computing principal values and directions of stress and strain; and computing a perturbed mesh for a collapse analysis by incorporating a user-specified geometric imperfection in the form of the critical buckling mode shape.

Each postprocessing program must be linked using the **make** parameter when running the Abaqus execution procedure (see "Making user-defined executables and subroutines," Section 3.2.18 of the Abaqus Analysis User's Guide). To link properly, the postprocessing program cannot contain a Fortran PROGRAM statement. Instead, the program must begin with a Fortran SUBROUTINE with the name ABQMAIN.

General programming concepts, Abaqus Fortran interfaces, and data processing concepts are described below. Refer to Chapter 5, "File Output Format," of the Abaqus Analysis User's Guide for additional information. The program listings in each section provide details on the program flow, how to interface with various computer platforms that use different operating systems and Fortran compilers, and how to interface with Abaqus subroutines to handle data files and records.

Refer to Chapter 9, "Using the Abaqus Scripting Interface to access an output database," of the Abaqus Scripting User's Guide or Chapter 10, "Using C++ to access an output database," of the Abaqus Scripting User's Guide for information on accessing data stored in the Abaqus output database.

Initialization

Details about the variables that are used in the postprocessing programs are discussed in "Accessing the results file information," Section 5.1.3 of the Abaqus Analysis User's Guide. Abaqus uses a 512-word buffer named **ARRAY** for the reading and writing of data on the results file. This is dimensioned as **ARRAY(513)**. The integer equivalent is **JRRAY(513)** for a 64-bit computer or **JRRAY(2,513)** for a 32-bit computer. The **EQUIVALENCE** statement is used to equivalence **ARRAY** and **JRRAY** to simplify manipulation of real and integer numbers in the data record stored in the buffer.

The information concerning the Fortran unit number and format of the results file that is read is defined in **LRUNIT(2,NRU)**, where **NRU** is the number of files to be processed. The Fortran unit number for the *n*th file is stored in **LRUNIT(1,*n*)**. The information about the file format is stored in **LRUNIT(2,*n*)**, which is initialized to 1 for ASCII format and to 2 for binary format. If a new results file is to be created by the postprocessing program, the file format of the output file is defined similarly via the variable **LOUTF**, which is also initialized to 1 for ASCII format and 2 for binary format. The

root file name for both input and output results files is defined through the character variable **FNAME**. The root file name case will be the same as the case in which **FNAME** is defined; Abaqus defines the file extensions to be lowercase letters. See "Accessing the results file information," Section 5.1.3 of the Abaqus Analysis User's Guide, for a discussion of the naming convention for the file extensions.

The final initialization phase is done internally by calling the Abaqus subroutines **INITPF** and **DBRNU**. The Fortran interfaces are

```
CALL INITPF(FNAME, NRU, LRUNIT, LOUTF)
CALL DBRNU (JUNIT)
```

where the arguments in the call to **INITPF** are as described above, and **JUNIT** is the Fortran unit number connecting the file.

These integer variables must be defined before the subroutines are called.

Data processing

Data manipulation requires knowledge of each data record. Details of these records are found in "Results file output format," Section 5.1.2 of the Abaqus Analysis User's Guide.

The data organization in the results file uses a sequential format. Each record must, therefore, be retrieved in a sequential manner via a call to **DBFILE** using the interface

```
CALL DBFILE(0, ARRAY, JRCD)
```

This call can be placed inside a **DO**-loop, and the loop count should exceed the number of records stored in the file. Alternatively, **DBFILE** can be called as long as **JRCD** is equal to **0**. The first argument, **0**, indicates that a record is to be read. Each record that is read is stored in the buffer **ARRAY** and returned to the calling program for manipulation. The last argument, **JRCD**, is a return code that is set to **0** unless an end-of-file condition or an incomplete record is processed, in which case **JRCD** is set to **1**.

If it is desirable to extract or modify certain records and save them in a new results file with the same data organization as an Abaqus-generated results file, then the subroutine **DBFILW** should be called with the interface

```
CALL DBFILW(1, ARRAY, JRCD)
```

The new results file will be written with the file extension **.fin**. Refer to "Utility routines for accessing the results file," Section 5.1.4 of the Abaqus Analysis User's Guide.

15.1.2 JOINING DATA FROM MULTIPLE RESULTS FILES AND CONVERTING FILE FORMAT: FJOIN

Products: Abaqus/Standard Abaqus/Explicit

This example illustrates how to use a Fortran program to extract specific data from different Abaqus results files and to join the data into a single results file. This program can also be used to convert the format of results files.

Postprocessing

Sometimes it is desirable to combine a number of results files into a single file or to create a new results file by retrieving selected data from different results files. The **abaqus append** utility joins two results files by stripping the header information from the second results file and appending the step information to the end of the first results file. See "Joining results (`.fil`) files," Section 3.2.15 of the Abaqus Analysis User's Guide, for more information on this utility.

This example postprocessing program demonstrates how a Fortran program can be used to extract specific information from results files created by separate analyses of the same model. In this example the stress and strain records in three analyses will be merged to create a new results file.

Programming details

The general discussion on programming concepts and Abaqus Fortran interfaces in "User postprocessing of Abaqus results files: overview," Section 15.1.1, should be reviewed before running or modifying this program. Review of the results file format in Chapter 5, "File Output Format," of the Abaqus Analysis User's Guide is also recommended.

The program `FJOIN` (named `fjoin.f` on the Abaqus release media) prompts for the values of `NRU`, `LRUNIT(1,NRU)`, `LRUNIT(2,NRU)`, and `FNAME`. Then subroutines `INITPF` and `DBNRU` are called to complete the necessary initializations and file connections. Data processing starts with a double `DO`-loop looping over all of the records to be read, one-by-one, via a call to `DBFILE`. A record can be skipped or written to the new results file with or without any modifications. Each record is identified by its record key, which is stored in the second entry of the record (see "Results file output format," Section 5.1.2 of the Abaqus Analysis User's Guide).

Each file contains a number of header records, `1900`-series. These records contain general information about the model. Different analyses using the same model place essentially the same information in these records. Hence, when combining results files from different analyses of the same model, all `1900`-series records from the first file that is processed should be kept. Similar records in subsequent files should be skipped to avoid duplication and confusion. However, the `1910`, `1911`, `1922`, and `1980` records should be kept. They are useful for processing results within a substructure, output requests, and natural frequency extraction results.

The data for each increment of an analysis begin with the increment start record, which is identified by record key `2000`. Record `2000` is followed by the records that correspond to the data requested

through file output options specified in the Abaqus input file. Record **1**, the element header record, is automatically written to the results file when element variables are requested. It is of interest when postprocessing since it contains important information about the element data, including the location of data within an element (i.e., whether data are written at the element integration points, the centroid, nodes, etc.). For this example, records **11** and **21** (the stress and strain records, respectively) are written to the results file since stress and strain were requested. The increment end record is identified by record key **2001**. When an end-of-file condition is encountered and the previously processed record is a **2001** record, a Fortran **CLOSE** is executed on the current Fortran unit number so that the processing of the next file can begin.

Program compilation and linking

The **abaqus make** utility is designed to compile and link this type of postprocessing program. It will also make the **aba_param.inc** file available during compilation. The command to compile and link the **FJOIN** program is as follows:

```
abaqus make job=fjoin
```

This command will have to be repeated if Fortran errors are discovered during the compilation or link. The commands used by the **abaqus make** utility can be changed if necessary. The Abaqus Installation and Licensing Guide lists the typical compile and link commands for each computer type.

Program execution

Before program execution, the analysis jobs must be run to generate results files to be read by the program. In this example three jobs are run. The input files for these analyses are **fjoin002.inp**, **fjoin003.inp**, and **fjoin004.inp**. The results files from these analyses are output in binary format and are called **fjoin002.fil**, **fjoin003.fil**, and **fjoin004.fil**.

The **FJOIN** program will read these files via Fortran units **2**, **3**, and **4**. The name of the new file will be **fjoinxxx**. Before running the program, the results files must be renamed to **fjoinxxx.002**, **fjoinxxx.003**, and **fjoinxxx.004**. Note that the root file names are the same (defined using **FNAME**), and that the extensions are set to the Fortran unit numbers used to open the files.

When the program is executed using the command **abaqus fjoin**, the first prompt will be

```
Enter the number of files to be joined:
```

Enter **3** to set **NRU=3**. The second prompt will be

```
Enter the unit number of input file # 1:
```

Enter **2** to define **LRUNIT(1,1)=2**. At the third prompt,

```
Enter the format of input file # 1 (1-ASCII, 2-binary):
```

enter **2**. This sets **LRUNIT(2,1)=2** and means that the file being read is binary. The second and third prompts are repeated for each additional file to be processed. The program will then ask whether the new results file should be written in ASCII or binary format,

```
Enter the format of the output file (1-ASCII, 2-binary):
```

Enter **2** to set **LOUTF=2**, which specifies that binary format has been chosen for the new results file. The format of the output file may be different from the format of the input files, so this program can also be used to convert the format of results files. Finally, when the program issues the prompt

```
Enter the name of the input files (w/o extension):
```

enter **fjoinxxx** to define **FNAME** (the input files must have been given the root file name **fjoinxxx**; the output file will be created as **fjoinxxx.fin**).

As soon as the *n*th file has been processed, the message **END OF FILE #** *n* is written to the terminal. After all files have been processed, the program stops and the new results file is created. The new results file created by this program contains stress and strain records at all integration points in each element and at all nodal points.

Analysis description

The structure is a 10 × 10 square plate with unit thickness. The plate lies in the *X*–*Y* plane such that its bottom edge coincides with the x-axis and the left edge coincides with the y-axis. The finite element model employs a 2 × 2 mesh of CPS8R elements. The material is linear elastic with Young's modulus = 30×10^6 and Poisson's ratio = 0.3. Three separate analyses are performed with displacement-controlled load steps.

In the first analysis (fjoin002.inp), the plate is subjected to biaxial tension by prescribing a vertical displacement of 0.25 along the top edge, a horizontal displacement of 0.25 along the right edge, and symmetry boundary conditions on the left and bottom edges.

In the second analysis (fjoin003.inp), the structure is forced to deform in simple shear by applying a horizontal displacement of 0.25 to the top edge while holding the bottom edge fixed and allowing the horizontal displacement to vary linearly with y along the left and right edges. The vertical displacement is zero everywhere.

In the third analysis (fjoin004.inp), the plate is subjected to uniaxial tension by applying a displacement of 0.25 in the y-direction to the nodes along the top edge and symmetry boundary conditions to the nodes along the x- and y-axes.

Results and discussion

Since the state of stress and strain is homogeneous, the integration point and nodal averaged values of stress and strain are identical everywhere. A typical record obtained at the end of each step is included below:

Analysis	σ_{xx}	σ_{yy}	σ_{xy}
fjoin002.inp	1.07×10^6	1.07×10^6	0.0
fjoin003.inp	0.0	0.0	2.88×10^5
fjoin004.inp	0.0	7.50×10^5	0.0

Analysis	ε_{xx}	ε_{yy}	ε_{xy}
fjoin002.inp	2.50×10^{-2}	2.50×10^{-2}	0.0
fjoin003.inp	0.0	0.0	2.50×10^{-2}
fjoin004.inp	-7.50×10^{-3}	2.50×10^{-2}	0.0

Input files

fjoin002.inp	First analysis file.
fjoin003.inp	Second analysis file.
fjoin004.inp	Third analysis file.
fjoin.f	Postprocessing program.

15.1.3 CALCULATION OF PRINCIPAL STRESSES AND STRAINS AND THEIR DIRECTIONS: FPRIN

Product: Abaqus/Standard

This example illustrates the use of a Fortran program to read stress and strain records from an Abaqus results file and to calculate principal stress and strain values and their directions.

General description

This program shows how to retrieve integration point and nodal averaged stress and strain components from an Abaqus results file and then compute principal values and directions using the Abaqus utility routine **SPRIND**. Usage of this utility routine is documented in the input file provided for this problem, and further details about the interface to this subroutine are discussed in "Obtaining stress invariants, principal stress/strain values and directions, and rotating tensors in an Abaqus/Standard analysis," Section 2.1.11 of the Abaqus User Subroutines Reference Guide. The results file created by the **FJOIN** program in "Joining data from multiple results files and converting file format: FJOIN," Section 15.1.2, is used here to verify that the records that have been put together are retrievable. The previously generated results file was named **fjoinxxx.fin**. To use it as an input file for postprocessing program **FPRIN**, the file extension must be changed. This program will assume that the results file has the default **.fil** extension, which corresponds to Fortran unit **8**.

Programming details

The user should first review the general discussion on programming concepts and Abaqus Fortran interfaces in "User postprocessing of Abaqus results files: overview," Section 15.1.1, and the detailed discussion of postprocessing given in Chapter 5, "File Output Format," of the Abaqus Analysis User's Guide.

When running program **FPRIN** (this program is named **fprin.f** on the Abaqus release media), the user will be prompted for the file name that initializes **FNAME**. Other variables, such as **LOUTF**, **NRU**, **LRUNIT(1,NRU)**, and **LRUNIT(2,NRU)**, are initialized inside the program. **INITPF** and **DBRNU** are then called to complete the neccesary initializations and file connections. Data processing starts with a double **DO**-loop over all the records to be read, one-by-one, via a call to **DBFILE**. Each record is identified by its record key, which is stored in the second entry of the record. When records **1922** and **2000** are processed by program **FPRIN**, the heading and the current step and increment numbers are written out so as to provide a way to recognize the beginning of data in each analysis. Record type **1** is then examined to determine the output location of stress and strain, the number of direct and shear stress and strain components, and either the element number or the node number for which the records are written. The stress and strain records (**11** and **21**, respectively) will be filtered out for processing by the Abaqus utility routine **SPRIND**. When a stress or strain record is passed into **SPRIND**, principal stresses or strains and the corresponding principal directions are calculated and returned in an unsorted order.

Program compilation and linking

Before program execution, the Fortran program has to be compiled and linked. Both operations, as well as the inclusion of the **aba_param.inc** file, are performed by a single execution of the **abaqus make** utility:

```
abaqus make job=fprin
```

This may have to be repeated until all Fortran errors are corrected. After successful compilation, the program's object code is automatically linked with the Abaqus object codes stored in the shared program library and interface library in order to build the executable program. Refer to Chapter 4, "Customizing the Abaqus environment," of the Abaqus Installation and Licensing Guide to see which compile and link commands are used for a particular computer.

Program execution

Before the program is executed, a results file must have been created. In this example the results file **fjoinxxx.fin** created by the **FJOIN** program discussed in "Joining data from multiple results files and converting file format: FJOIN," Section 15.1.2, is used. This file must be renamed to **fjoinxxx.fil** since Fortran unit **8** (which is associated with the **.fil** file extension) is used in the program to read the file. When the program is executed using the command **abaqus fprin**, the prompt

```
Enter the name of the input file (w/o .fil):
```

will appear. Enter **fjoinxxx** to define **FNAME**. The program processes the data and produces a file named **pvalue.dat**, which contains information about principal stresses and strains and their directions.

Results and discussion

The computed principal stress and strain values and their directions are tabulated below.

Analysis File	Principal Component	Stress × 10^5	Strain × 10^{-3}	Dir-1	Dir-2	Dir-3
fjoin002.inp	1	10.714	25.0	1.0	0.0	0.0
	2	10.714	25.0	0.0	1.0	0.0
	3	0.0	0.0	0.0	0.0	1.0
fjoin003.inp	1	−2.8846	−12.5	0.707	−0.707	0.0
	2	2.8846	12.5	0.707	0.707	0.0
	3	0.0	0.0	0.0	0.0	1.0

Analysis File	Principal Component	Stress × 10^{5}	Strain × 10^{-3}	Dir-1	Dir-2	Dir-3
fjoin004.inp	1	0.0	−7.5	1.0	0.0	0.0
	2	7.5	25.0	0.0	1.0	0.0
	3	0.0	0.0	0.0	0.0	1.0

Input file

fprin.f Postprocessing program.

15.1.4 CREATION OF A PERTURBED MESH FROM ORIGINAL COORDINATE DATA AND EIGENVECTORS: FPERT

Product: Abaqus/Standard

This example illustrates the use of a Fortran program to create a perturbed mesh by superimposing a small imperfection in the form of the weighted sum of several buckling modes on the initial geometry.

The program retrieves the original nodal coordinates and the desired eigenvectors from an Abaqus results file, then calculates new nodal coordinates for the perturbed mesh.

General description

Collapse studies of a structure's postbuckling load-displacement (Riks) behavior are often conducted to verify that the critical buckling load and mode predicted by an eigenvalue buckling analysis are accurate. They are also done to investigate the effect of an initial geometric imperfection on the load-displacement response. A typical assumption is that an imperfection made up of a combination of the eigenmodes associated with the lowest eigenvalues will be the most critical. One method of introducing an imperfection of this type into the model is by adding $\sum_{i=1}^{M} \alpha_i \mathbf{u}_i$ to the original mesh coordinates. In this case $\mathbf{u}_i$ is the ith eigenmode, α_i is a scaling factor of the ith eigenmode, and M is the total number of eigenmodes extracted in the buckling analysis. Since the eigenvector is typically normalized to a maximum absolute value of one, α_i is usually some fraction of a geometric parameter, such as the shell thickness. The postprocessing program described below can be used to introduce an imperfection of this type into a model.

The perturbation procedure is illustrated in "Buckling of a cylindrical shell under uniform axial pressure," Section 1.2.3 of the Abaqus Benchmarks Guide. An eigenvalue buckling analysis, **`fpert001`**, is run first. This analysis creates the results file, **`fpert001.fil`**, which contains the original nodal coordinates and the eigenvectors for the buckling modes. This results file is then used to generate a perturbed mesh for the postbuckling load-displacement analysis. The postprocessing program perturbs the original mesh using the relation

$$\mathbf{X}' = \mathbf{X} + \sum_{i=1}^{M} \alpha_i \mathbf{u}_i,$$

where $\mathbf{X}'$ is the vector containing the new global coordinates; $\mathbf{X}$ is the vector of original coordinates; M is the number of buckling modes; and α_i is the imperfection factor for the ith eigenvector, u_i. The new coordinates are written to the file **`fpert002.015`**, which is read by the load-displacement analysis **`fpert002`**.

Programming details

The general discussion on programming concepts and Abaqus Fortran interfaces in "User postprocessing of Abaqus results files: overview," Section 15.1.1, should be reviewed before running or modifying this

program. Review of the results file format in Chapter 5, "File Output Format," of the Abaqus Analysis User's Guide is also recommended.

The **FPERT** program (this program is named **fpert.f** on the Abaqus release media) makes some assumptions concerning the type of results file it will be reading. Variables **NRU**, **LRUNIT(1,NRU)**, and **LRUNIT(2,NRU)** are initialized within the program to **1**, **8**, and **2**. These values indicate that one file will be read, the Fortran unit used will be **8**, and the file type will be binary. See "Accessing the results file information," Section 5.1.3 of the Abaqus Analysis User's Guide, for more information on opening and initializing postprocessing files.

Once the file specification parameters are set, the **INITPF** and **DBNRU** subroutines are called to open and ready the file, whose name is stored in **FNAME**, for reading. The file to which the perturbed coordinates are to be written can be directly opened using a Fortran **OPEN** statement. The Abaqus file utilities are not necessary since the file is a plain text file.

The records with the original nodal coordinates are read using the **DBFILE** routine and stored in the local array **COORDS(3,8000)**. The first index of the **COORDS** array indicates the x-, y-, and z-coordinate of the node. The second index indicates the node number. The second dimension should be increased if there are more than 8000 nodes in a model.

Components of the eigenvector are stored in the local array **DISP(6,8000)**. This array holds up to 6 displacement terms for each node. The second dimension should be increased if there are more than 8000 nodes in a model. Subroutine **NODEGEN**, a subroutine local to this postprocessing program, is then called to compute the new nodal coordinates. Once all the requested mode shapes are computed, the new nodal coordinates are written to the plain text file opened earlier.

Program compilation and linking

The **abaqus make** utility is designed to compile and link this type of postprocessing program. It will also make the **aba_param.inc** file available during compilation. The command to compile and link the **FPERT** program is as follows:

```
abaqus make job=fpert
```

This command will have to be repeated if Fortran errors are discovered during the compilation or link. The commands used by the **abaqus make** utility can be changed if necessary. The Abaqus Installation and Licensing Guide lists the typical compile and link commands for each computer type.

Program execution

Before the program is executed, an eigenvalue buckling job must have been run with Abaqus. In this example the input file **fpert001.inp** is used to generate the results file **fpert001.fil**. When the **FPERT** program is executed using the command **abaqus fpert**, the first prompt will be

```
Enter the name of the results file (w/o .fil):
```

Enter **fpert001** to define **FNAME**. The second prompt will be

```
Enter the mode shape(s) to be used in calculating the perturbed
mesh (zero when finished):
```

Enter **1** followed by **0**, since this is the only eigenvector available in the results file for this example. At the third prompt,

```
Enter the imperfection factor to be introduced into the geometry
for this eigenmode:
```

enter **0.25**. This sets $\alpha = 0.25$, the shell thickness for this model. The program then processes the data and writes the nodal coordinates for the new mesh to **fpert002.015**.

Analysis description

For a full discussion of the analysis, refer to "Buckling of a cylindrical shell under uniform axial pressure," Section 1.2.3 of the Abaqus Benchmarks Guide. The input file **fpert001.inp** (same file as **bucklecylshell_s9r5_n3.inp**) contains a 2 × 20 mesh of S9R5 elements and data lines for a buckling analysis. The input file **fpert002.inp** contains data lines for a Riks analysis using a perturbed mesh. The source code for the **FPERT** program is in **fpert.f**.

Results and discussion

Plots produced by these analyses are shown in Figure 15.1.4–1 and Figure 15.1.4–2. Figure 15.1.4–1 is obtained from the eigenvalue buckling analysis and shows the original (cylindrical) mesh and the critical buckling mode. Figure 15.1.4–2 is generated when the load level has reached a local maximum (increment 8) in the Riks analysis using the perturbed mesh.

Input files

fpert001.inp	Eigenvalue buckling analysis.
fpert002.inp	Riks analysis using a perturbed mesh.
fpert.f	Postprocessing program.

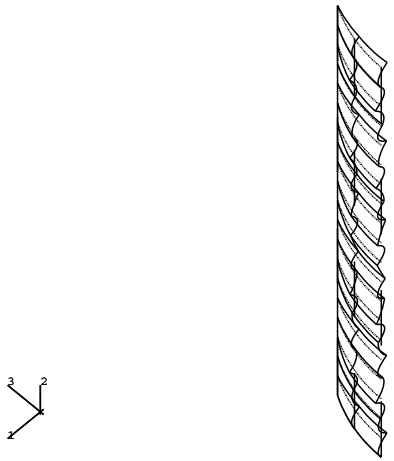

Figure 15.1.4–1 Undeformed shape and eigenvalue buckling mode.

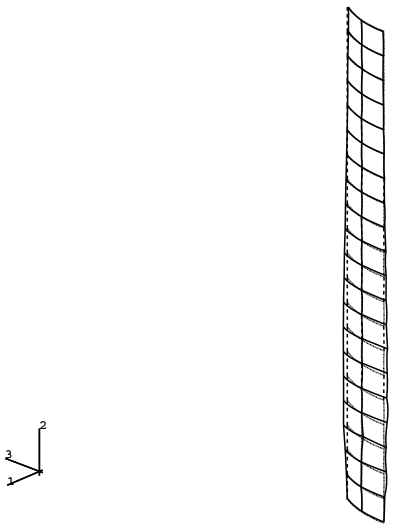

Figure 15.1.4–2 Deformed shape at first peak load in Riks analysis.

15.1.5 OUTPUT RADIATION VIEW FACTORS AND FACET AREAS: FRAD

Product: Abaqus/Standard

This example illustrates the use of a Fortran program to read the radiation view factors and the facet areas from the results file.

General description

The program shows how to retrieve the view factors and the facet areas from the results file. The results file created from the benchmark problem detailed in "Axisymmetric elemental cavity radiation view factor calculations," Section 1.6.6 of the Abaqus Benchmarks Guide, is used to verify that the output records have been read and output correctly. This program will assume that the results file has the default file extension, **`.fil`**, which corresponds to Fortran unit 8.

Programming details

Before proceeding, review the general discussion on programming concepts and Abaqus Fortran interfaces in "User postprocessing of Abaqus results files: overview," Section 15.1.1, and the detailed discussion of postprocessing given in Chapter 5, "File Output Format," of the Abaqus Analysis User's Guide.

When running the program **`FRAD`** (this program is named **`frad.f`** on the Abaqus release media), the user will be prompted for the file name that initializes **`FNAME`**. Other variables, such as **`LOUTF`**, **`NRU`**, **`LRUNIT(1,NRU)`**, and **`LRUNIT(2,NRU)`**, are initialized inside the program. **`INITPF`** and **`DBNRU`** are then called to complete the necessary initializations and file connections. By default, the results file is processed for all steps and increments in the results file. The user can restrict the output by setting **`LSTEPA`** and **`LINCA`** to the required step and increment and uncommenting the simple **`IF - END IF`** block. Data processing starts with a **`DO`**-loop over all the records to be read, one-by-one, by means of a call to **`DBFILE`**. Each record is identified by its record key, which is stored in the second entry of the record. When records **`1922`** and **`2000`** are processed by **`FRAD`**, the heading and the current step and increment numbers are written out so as to provide a way to recognize the beginning of data in each analysis. Record types **`1605`**, **`1606`**, **`1607`**, and **`1609`** are then read; and the desired output is written to the output file **`vfout`**.

Program compilation and linking

Before it can be executed, the Fortran program must be compiled and linked. Both operations, as well as the inclusion of the **`aba_param.inc`** file, are performed by a single execution of the **abaqus make** utility:

```
abaqus make job=frad
```

This procedure may have to be repeated until all Fortran errors are corrected. After successful compilation, the program's object code is linked automatically with the Abaqus object codes stored

in the shared program library and the interface library to build the executable program. Refer to the Abaqus Installation and Licensing Guide for information about the compile and link commands for a particular computer.

Program execution

Before the program is executed, a results file must have been created with the desired output being written to that file. In this example the results file **xrvda4n1.fil** created by running the input file **xrvda4n1.inp** discussed in "Axisymmetric elemental cavity radiation view factor calculations," Section 1.6.6 of the Abaqus Benchmarks Guide, is used. When the program is executed using the command **abaqus frad**, the prompt

```
Enter the name of the input file (w/o .fil):
```

will appear. Enter **xrvda4n1** to define **FNAME**. The program processes the data and produces a file named **vfout**, which contains the required information.

Results and discussion

The radiation view factors and facet areas are read and output to **vfout**. The output agrees with the expected results.

Input file

frad.f	Postprocessing program.

15.1.6 CREATION OF A DATA FILE TO FACILITATE THE POSTPROCESSING OF ELBOW ELEMENT RESULTS: FELBOW

Product: Abaqus/Standard

This example illustrates the use of a Fortran program to read selected element integration point records from an Abaqus results file to facilitate the postprocessing of elbow element results. *X–Y* data are created that are suitable for use with the *X–Y* plotting capability in Abaqus/CAE.

General description

This program shows how to retrieve integration point data for elbow elements from an Abaqus results file to visualize one of the following:

1. Variation of a variable along a line of elbow elements,
2. Variation of a variable around the circumference of a given elbow element, or
3. Ovalization of a given elbow element.

An ASCII file containing *X–Y* data is created that can be read into Abaqus/CAE for visualization purposes.

To execute option 1, the elbow elements must be numbered such that they increase monotonically within the range of elements considered; all elements in the desired range must be elbow elements. *X–Y* data will be created with the *X*-data being the distance along the line of elbow elements, measured along the elbow centerline and the *Y*-data being the variable value. The user must ensure that the integration point coordinates (COORD) are written to the results file if either option 2 or 3 is needed. For option 2 *X*-data are the distance around the circumference of the elbow element, measured along the middle surface, and *Y*-data are the variable value. For option 3 the *X–Y* data are the current coordinates of the middle-surface integration points around the circumference of the elbow element, projected to a local coordinate system in the plane of the deformed cross-section. The origin of the local system coincides with the center of the cross-section; the plane of the deformed cross-section is defined as the plane that contains the center of the cross-section and integration points 1 and 2.

Programming details

The user is prompted for the name of the results file (assumed to be binary) and the postprocessing option (1, 2, or 3). The user is then prompted for additional information depending on the option that was chosen; this information includes

- The range of element numbers (options 2 and 3 require only a single element number),
- The section point number (options 1 and 2 only),
- The integration point number (option 1 only),
- The element variable (options 1 and 2 only),

- The component of the variable (as defined in "Results file output format," Section 5.1.2 of the Abaqus Analysis User's Guide, options 1 and 2 only),
- The step number, and
- The increment number.

The data are processed in a double **DO**-loop over all records, via a call to **DBFILE**. The desired data are stored in variable **VAR**; the integration point coordinates are stored in **COORDS**. The program checks to make sure the requested data are available in the results file. An error is issued if the user tries to process data that are not found in the results file.

Program compilation and linking

Before program execution, compile and link the Fortran program by using the **abaqus make** utility:

```
abaqus make job=felbow
```

Repeat this command until all Fortran errors are corrected. After successful compilation, the program's object code is linked automatically with the Abaqus object codes stored in the shared program library and interface library to build the executable program. Refer to Chapter 4, "Customizing the Abaqus environment," of the Abaqus Installation and Licensing Guide to see which compile and link commands are used for a particular computer.

Program execution

Before executing the program, run an analysis that creates a results file containing the appropriate output. This analysis includes, for example, output for the elements in a given range and the integration point coordinates of the elements. When the program is executed using the command **abaqus felbow**, the prompt

```
Enter the name of the input file (w/o .fil):
```

will appear. Enter the name of the results file to define **FNAME**. The user is then prompted for other information, such as the desired postprocessing option, element number, etc. The program processes the data and produces a file named **output.dat** that contains the information required to visualize the elbow element results.

Results and discussion

"Elastic-plastic collapse of a thin-walled elbow under in-plane bending and internal pressure," Section 1.1.2, contains several figures created with the aid of this program. The output agrees with the expected results.

Input file

felbow.f	Postprocessing program.

15.1.7 TRANSLATING Abaqus DATA TO MODAL NEUTRAL FILE FORMAT FOR ANALYSIS IN MSC.ADAMS

Product: Abaqus/Standard

Objectives

This example shows how you can investigate the flexibility of a substructure in your model during a dynamic analysis.

The following **abaqus adams** translator features are demonstrated:

- creating Abaqus models of MSC.ADAMS components,
- converting the Abaqus results into an MSC.ADAMS modal neutral (`.mnf`) file, the format required by ADAMS/Flex, and
- displaying results of an ADAMS/Flex flexibility analysis.

Application description

The following cases are illustrated:

- A three-dimensional steel link substructure meshed with solid elements and with displacement degrees of freedom at its nodes, as shown in Figure 15.1.7–1. Multi-point constraints connect it to the other components in the model. The analysis includes two steps: an eigenfrequency extraction step and a substructure generation step defined for a flexible body.
- The same steel link meshed with beam elements. Because the beam elements have both displacement and rotational degrees of freedom at their nodes, no multi-point constraints are required to connect the substructure to the rest of the model. The analysis includes two steps: an eigenfrequency extraction step and a substructure generation step defined for a flexible body.

Abaqus modeling approaches and simulation techniques

Both cases described in this section share the same general approach:

1. Create an Abaqus model for each flexible component of the MSC.ADAMS model. Each component is modeled as an Abaqus substructure.
2. Run the Abaqus analysis.
3. Run the **abaqus adams** translator to read the Abaqus results from the SIM database produced by the analysis and to create the modal neutral (`.mnf`) file for MSC.ADAMS.
4. Read the modal neutral file into MSC.ADAMS. A separate modal neutral file must be created for each flexible part in MSC.ADAMS.

Summary of analysis cases

Case 1 Link modeled with solid elements.

Case 2 Link modeled with beam elements.

Case 1 Link modeled with solid elements

This example models a simple flexible link component using three-dimensional continuum elements.

Analysis types

The example includes an eigenfrequency extraction and a substructure generation analysis.

Mesh design

The link is modeled with 642 C3D10 tetrahedral solid elements (1368 nodes).

Material model

The steel used in this case has a Young's modulus of 2.07×10^{11} N/m^2 (3.0×10^7 lbf/in^2) and a Poisson's ratio of 0.29. The density of the model is 7.8×10^3.

Boundary conditions

The **RETNODES** node set is fixed in the 1- and 6-directions.

Constraints

This analysis includes two multi-point constraints: one applied to the **LEFTCYL** node set and the other applied to the **RIGHTCYL** node set.

Analysis steps

The analysis includes two steps: an eigenfrequency extraction step and a substructure generation analysis step.

Output requests

Element stiffness matrices and mass matrices are written to the SIM database for the element set **PROP1** as part of the substructure generation analysis step.

Run procedure

You can perform the analysis of the link with solid elements using the procedure shown below.

1. Enter the following commands to extract the input files from the compressed archive files provided with the Abaqus release:

```
abaqus fetch job=adams_ex1
abaqus fetch job=adams_ex1_nodes
abaqus fetch job=adams_ex1_elements
```

2. Enter the following command to execute the Abaqus analysis:

```
abaqus job=adams_ex1
```

3. Enter the following command to execute the **abaqus adams** translator and translate the results in a SIM database generated in the Abaqus analysis to a modal neutral file for use with ADAMS/Flex:

```
abaqus adams job=adams_ex1 substructure_sim=adams_ex1_Z1
```

Results and discussion

Because the solid elements have only displacement degrees of freedom at their nodes, multi-point constraints are used to provide a connection to the other components in the MSC.ADAMS model. Two nodes are added along the centerline of the beam at the centers of the hinge holes. The C3D10 nodes that lie on the faces of the hinge holes are connected to the extra nodes with BEAM-type multi-point constraints, allowing the nodes to transmit both forces and moments between the link and other MSC.ADAMS components.

The options used to define the single substructure are those described in "The Abaqus substructure model" in "Translating Abaqus data to MSC.ADAMS modal neutral files," Section 3.2.38 of the Abaqus Analysis User's Guide. Twenty fixed-interface vibration modes are computed to represent the dynamic behavior of the link.

MSC.ADAMS uses the fixed-interface vibration modes and the constraint modes to characterize the flexibility of the link. The eight lowest fixed-interface vibration frequencies computed by Abaqus are shown in Table 15.1.7–1. These frequencies are reported in the **adams_ex1.dat** file. The **abaqus adams** translator combines these fixed-interface modes with the static constraint modes to compute an equivalent modal basis to be used by ADAMS/Flex. The first six frequencies of this equivalent basis are approximately zero. The next eight frequencies for the unconstrained model are shown in Table 15.1.7–2. These frequencies are written to the screen when executing the **abaqus adams** translator.

Case 2 Link modeled with beam elements

This example models a simple flexible link component using three-dimensional beam elements.

Analysis types

As in Case 1, this example includes an eigenfrequency extraction and a substructure generation analysis.

Mesh design

The mesh for the beam model uses 10 B31 elements (11 nodes).

Material model

The steel material definition is the same as in Case 1.

Boundary conditions

The beam elements have both displacement and rotational degrees of freedom at their nodes.

Analysis steps

The analysis includes two steps: an eigenfrequency extraction step and a substructure generation analysis step.

Run procedure

You can perform the analysis of the link with beam elements using the procedure shown below.

1. Enter the following command to extract the input files from the compressed archive files provided with the Abaqus release:

   ```
   abaqus fetch job=adams_ex2
   ```

2. Enter the following command to execute the Abaqus analysis:

   ```
   abaqus job=adams_ex2
   ```

3. Enter the following command to execute the **abaqus adams** translator and translate the results in a SIM database generated in the Abaqus analysis to a modal neutral file for use with ADAMS/Flex:

   ```
   abaqus adams job=adams_ex2 substructure_sim=adams_ex2_Z1
   ```

Results and discussion

The primary difference between the beam model and the solid model is that the beam model uses only 10 B31 elements (11 nodes). Because the beam elements have both displacement and rotational degrees of freedom at their nodes, no multi-point constraints are needed to connect the link to other MSC.ADAMS components. The rest of the model is essentially identical to the solid model of the link.

The first eight nonzero frequencies for the unconstrained model are shown in Table 15.1.7–3. These frequencies are close to those of the solid model of the link. Although the computational cost in Abaqus is much less for this model than for the solid model, the computational costs in MSC.ADAMS for the two models are very similar because both models have 32 modes (12 constraint modes and 20 fixed-interface vibration modes).

Input files

Case 1 Link modeled with solid elements

adams_ex1.inp	Input file to analyze a link model subjected to a gravity load.

adams_ex1_nodes.inp	Node definitions for Case 1.
adams_ex1_elements.inp	Element definitions for Case 1.

Case 2 Link modeled with beam elements

adams_ex2.inp	Input file to analyze a link model subjected to a gravity load.

Reference

Abaqus Analysis User's Guide

- "Translating Abaqus data to MSC.ADAMS modal neutral files," Section 3.2.38 of the Abaqus Analysis User's Guide

Table 15.1.7–1 Fixed-interface vibration frequencies for the solid link model.

Frequency, Hz
206
391
570
1124
1228
1817
1879
2541

Table 15.1.7–2 Nonzero frequencies for the solid link model that are used by ADAMS/Flex.

Frequency, Hz
194
535
574
1055
1551
1762
1801
2653

Table 15.1.7–3 Nonzero frequencies for the beam link model that are used by ADAMS/Flex.

Frequency, Hz
205
555
610
1070
1618
1742
1775
2568

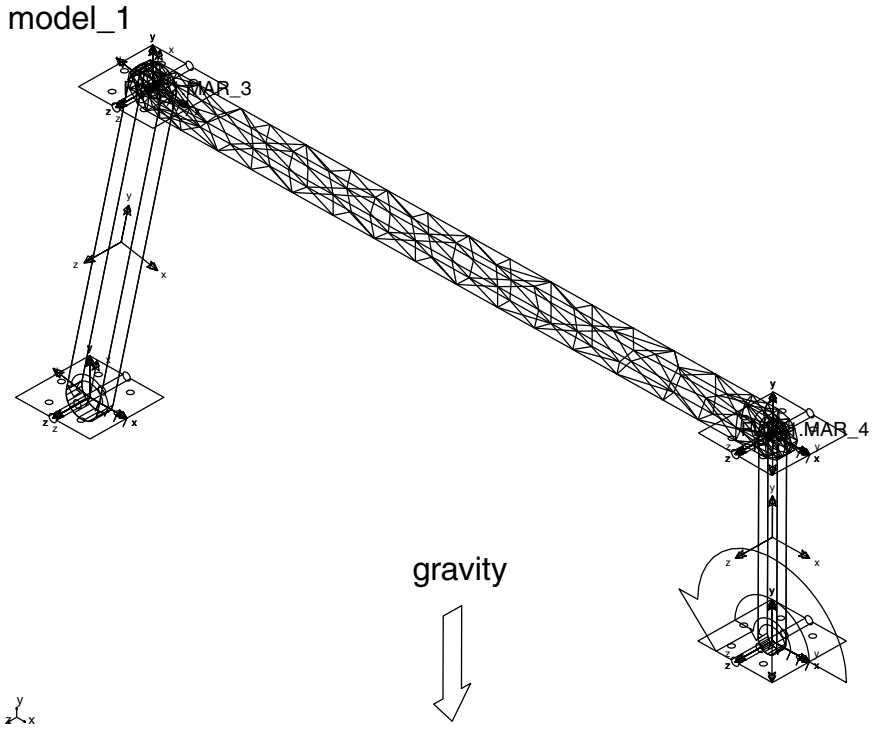

Figure 15.1.7–1 Solid link model.

I.1. Product Index

Abaqus/Standard

Section 1.1.1 Axisymmetric analysis of bolted pipe flange connections
Section 1.1.2 Elastic-plastic collapse of a thin-walled elbow under in-plane bending and internal pressure
Section 1.1.3 Parametric study of a linear elastic pipeline under in-plane bending
Section 1.1.4 Indentation of an elastomeric foam specimen with a hemispherical punch
Section 1.1.5 Collapse of a concrete slab
Section 1.1.6 Jointed rock slope stability
Section 1.1.7 Notched beam under cyclic loading
Section 1.1.8 Uniaxial ratchetting under tension and compression
Section 1.1.9 Hydrostatic fluid elements: modeling an airspring
Section 1.1.10 Shell-to-solid submodeling and shell-to-solid coupling of a pipe joint
Section 1.1.11 Stress-free element reactivation
Section 1.1.12 Transient loading of a viscoelastic bushing
Section 1.1.14 Damage and failure of a laminated composite plate
Section 1.1.15 Analysis of an automotive boot seal
Section 1.1.16 Pressure penetration analysis of an air duct kiss seal
Section 1.1.17 Self-contact in rubber/foam components: jounce bumper
Section 1.1.18 Self-contact in rubber/foam components: rubber gasket
Section 1.1.19 Submodeling of a stacked sheet metal assembly
Section 1.1.20 Axisymmetric analysis of a threaded connection
Section 1.1.21 Direct cyclic analysis of a cylinder head under cyclic thermomechanical loadings
Section 1.1.22 Erosion of material (sand production) in an oil wellbore
Section 1.1.23 Submodel stress analysis of pressure vessel closure hardware
Section 1.1.24 Using a composite layup to model a yacht hull
Section 1.1.25 Energy computations in a contact analysis
Section 1.2.1 Snap-through buckling analysis of circular arches
Section 1.2.2 Laminated composite shells: buckling of a cylindrical panel with a circular hole
Section 1.2.3 Buckling of a column with spot welds
Section 1.2.4 Elastic-plastic K-frame structure
Section 1.2.5 Unstable static problem: reinforced plate under compressive loads
Section 1.2.6 Buckling of an imperfection-sensitive cylindrical shell
Section 1.3.1 Upsetting of a cylindrical billet: quasi-static analysis with mesh-to-mesh solution mapping (Abaqus/Standard) and adaptive meshing (Abaqus/Explicit)
Section 1.3.2 Superplastic forming of a rectangular box
Section 1.3.3 Stretching of a thin sheet with a hemispherical punch

Section 1.3.4 Deep drawing of a cylindrical cup
Section 1.3.5 Extrusion of a cylindrical metal bar with frictional heat generation
Section 1.3.7 Axisymmetric forming of a circular cup
Section 1.3.16 Upsetting of a cylindrical billet: coupled temperature-displacement and adiabatic analysis
Section 1.3.17 Unstable static problem: thermal forming of a metal sheet
Section 1.3.18 Inertia welding simulation using Abaqus/Standard and Abaqus/CAE
Section 1.3.19 Moldflow translation examples
Section 1.4.1 A plate with a part-through crack: elastic line spring modeling
Section 1.4.2 Contour integrals for a conical crack in a linear elastic infinite half space
Section 1.4.3 Elastic-plastic line spring modeling of a finite length cylinder with a part-through axial flaw
Section 1.4.4 Crack growth in a three-point bend specimen
Section 1.4.5 Analysis of skin-stiffener debonding under tension
Section 1.4.6 Failure of blunt notched fiber metal laminates
Section 1.4.7 Debonding behavior of a double cantilever beam
Section 1.4.8 Debonding behavior of a single leg bending specimen
Section 1.4.9 Postbuckling and growth of delaminations in composite panels
Section 1.5.1 Springback of two-dimensional draw bending
Section 1.5.2 Deep drawing of a square box
Section 2.1.1 Nonlinear dynamic analysis of a structure with local inelastic collapse
Section 2.1.2 Detroit Edison pipe whip experiment
Section 2.1.6 Pressurized fuel tank with variable shell thickness
Section 2.1.7 Modeling of an automobile suspension
Section 2.1.15 Seismic analysis of a concrete gravity dam
Section 2.1.17 Impact analysis of a pawl-ratchet device
Section 2.2.1 Analysis of a rotating fan using substructures and cyclic symmetry
Section 2.2.2 Linear analysis of the Indian Point reactor feedwater line
Section 2.2.3 Response spectra of a three-dimensional frame building
Section 2.2.4 Brake squeal analysis
Section 2.2.5 Dynamic analysis of antenna structure utilizing residual modes
Section 2.2.6 Steady-state dynamic analysis of a vehicle body-in-white model
Section 2.4.1 Dynamic impact of a scooter with a bump
Section 3.1.1 Symmetric results transfer for a static tire analysis
Section 3.1.2 Steady-state rolling analysis of a tire
Section 3.1.3 Subspace-based steady-state dynamic tire analysis
Section 3.1.4 Steady-state dynamic analysis of a tire substructure
Section 3.1.5 Coupled acoustic-structural analysis of a tire filled with air
Section 3.1.7 Analysis of a solid disc with Mullins effect and permanent set
Section 3.1.8 Tread wear simulation using adaptive meshing in Abaqus/Standard
Section 3.1.9 Dynamic analysis of an air-filled tire with rolling transport effects
Section 3.1.10 Acoustics in a circular duct with flow

Section 3.2.1	Inertia relief in a pick-up truck
Section 3.2.2	Substructure analysis of a pick-up truck model
Section 3.2.3	Display body analysis of a pick-up truck model
Section 4.1.1	Resolving overconstraints in a multi-body mechanism model
Section 4.1.2	Crank mechanism
Section 4.1.3	Snubber-arm mechanism
Section 4.1.4	Flap mechanism
Section 4.1.5	Tail-skid mechanism
Section 4.1.7	Driveshaft mechanism
Section 4.1.8	Geneva mechanism
Section 4.1.9	Trailing edge flap mechanism
Section 4.1.10	Substructure analysis of a one-piston engine model
Section 4.1.11	Application of bushing connectors in the analysis of a three-point linkage
Section 5.1.1	Thermal-stress analysis of a disc brake
Section 5.1.2	A sequentially coupled thermomechanical analysis of a disc brake with an Eulerian approach
Section 5.1.3	Exhaust manifold assemblage
Section 5.1.4	Coolant manifold cover gasketed joint
Section 5.1.5	Conductive, convective, and radiative heat transfer in an exhaust manifold
Section 5.1.6	Thermal-stress analysis of a reactor pressure vessel bolted closure
Section 5.1.7	Coupled thermomechanical analysis of viscoelastic dampers
Section 6.1.1	Conjugate heat transfer analysis of a component-mounted electronic circuit board
Section 7.1.1	Eigenvalue analysis of a piezoelectric transducer
Section 7.1.2	Transient dynamic nonlinear response of a piezoelectric transducer
Section 7.2.1	Thermal-electrical modeling of an automotive fuse
Section 8.1.1	Hydrogen diffusion in a vessel wall section
Section 8.1.2	Diffusion toward an elastic crack tip
Section 9.1.1	Fully and sequentially coupled acoustic-structural analysis of a muffler
Section 9.1.2	Coupled acoustic-structural analysis of a speaker
Section 9.1.7	Coupled acoustic-structural analysis of a pick-up truck
Section 9.1.8	Long-duration response of a submerged cylinder to an underwater explosion
Section 10.1.1	Plane strain consolidation
Section 10.1.2	Calculation of phreatic surface in an earth dam
Section 10.1.3	Axisymmetric simulation of an oil well
Section 10.1.4	Analysis of a pipeline buried in soil
Section 10.1.5	Hydraulically induced fracture in a wellbore
Section 10.1.6	Permafrost thawing–pipeline interaction
Section 11.1.1	Topology optimization of an automotive control arm
Section 11.2.1	Shape optimization of a connecting rod
Section 11.3.1	Sizing optimization of a gear shift control holder
Section 11.3.2	Sizing optimization of a car door

Section 11.4.1 Bead optimization of a plate
Section 12.1.1 Jack-up foundation analyses
Section 12.1.2 Riser dynamics
Section 14.2.1 Design sensitivity analysis of a composite centrifuge
Section 14.2.2 Design sensitivities for tire inflation, footprint, and natural frequency analysis
Section 14.2.3 Design sensitivity analysis of a windshield wiper
Section 14.2.4 Design sensitivity analysis of a rubber bushing
Section 15.1.2 Joining data from multiple results files and converting file format: FJOIN
Section 15.1.3 Calculation of principal stresses and strains and their directions: FPRIN
Section 15.1.4 Creation of a perturbed mesh from original coordinate data and eigenvectors: FPERT
Section 15.1.5 Output radiation view factors and facet areas: FRAD
Section 15.1.6 Creation of a data file to facilitate the postprocessing of elbow element results: FELBOW
Section 15.1.7 Translating Abaqus data to modal neutral file format for analysis in MSC.ADAMS

Abaqus/Explicit

Section 1.1.3 Parametric study of a linear elastic pipeline under in-plane bending
Section 1.1.4 Indentation of an elastomeric foam specimen with a hemispherical punch
Section 1.1.5 Collapse of a concrete slab
Section 1.1.9 Hydrostatic fluid elements: modeling an airspring
Section 1.1.10 Shell-to-solid submodeling and shell-to-solid coupling of a pipe joint
Section 1.1.13 Indentation of a thick plate
Section 1.1.14 Damage and failure of a laminated composite plate
Section 1.1.17 Self-contact in rubber/foam components: jounce bumper
Section 1.1.18 Self-contact in rubber/foam components: rubber gasket
Section 1.2.3 Buckling of a column with spot welds
Section 1.3.1 Upsetting of a cylindrical billet: quasi-static analysis with mesh-to-mesh solution mapping (Abaqus/Standard) and adaptive meshing (Abaqus/Explicit)
Section 1.3.3 Stretching of a thin sheet with a hemispherical punch
Section 1.3.5 Extrusion of a cylindrical metal bar with frictional heat generation
Section 1.3.6 Rolling of thick plates
Section 1.3.7 Axisymmetric forming of a circular cup
Section 1.3.8 Cup/trough forming
Section 1.3.9 Forging with sinusoidal dies
Section 1.3.10 Forging with multiple complex dies
Section 1.3.11 Flat rolling: transient and steady-state
Section 1.3.12 Section rolling
Section 1.3.13 Ring rolling
Section 1.3.14 Axisymmetric extrusion: transient and steady-state
Section 1.3.15 Two-step forming simulation

Section 1.3.16 Upsetting of a cylindrical billet: coupled temperature-displacement and adiabatic analysis
Section 1.4.6 Failure of blunt notched fiber metal laminates
Section 1.4.7 Debonding behavior of a double cantilever beam
Section 1.4.8 Debonding behavior of a single leg bending specimen
Section 1.4.9 Postbuckling and growth of delaminations in composite panels
Section 1.5.1 Springback of two-dimensional draw bending
Section 1.5.2 Deep drawing of a square box
Section 2.1.3 Rigid projectile impacting eroding plate
Section 2.1.4 Eroding projectile impacting eroding plate
Section 2.1.5 Tennis racket and ball
Section 2.1.8 Explosive pipe closure
Section 2.1.9 Knee bolster impact with general contact
Section 2.1.10 Crimp forming with general contact
Section 2.1.11 Collapse of a stack of blocks with general contact
Section 2.1.12 Cask drop with foam impact limiter
Section 2.1.13 Oblique impact of a copper rod
Section 2.1.14 Water sloshing in a baffled tank
Section 2.1.15 Seismic analysis of a concrete gravity dam
Section 2.1.16 Progressive failure analysis of thin-wall aluminum extrusion under quasi-static and dynamic loads
Section 2.1.18 High-velocity impact of a ceramic target
Section 2.3.1 Rivet forming
Section 2.3.2 Impact of a water-filled bottle
Section 2.4.1 Dynamic impact of a scooter with a bump
Section 3.1.6 Import of a steady-state rolling tire
Section 3.1.7 Analysis of a solid disc with Mullins effect and permanent set
Section 3.2.4 Continuum modeling of automotive spot welds
Section 3.3.1 Seat belt analysis of a simplified crash dummy
Section 3.3.2 Side curtain airbag impactor test
Section 4.1.2 Crank mechanism
Section 4.1.4 Flap mechanism
Section 4.1.5 Tail-skid mechanism
Section 4.1.6 Cylinder-cam mechanism
Section 4.1.7 Driveshaft mechanism
Section 4.1.11 Application of bushing connectors in the analysis of a three-point linkage
Section 4.1.12 Gear assemblies
Section 5.1.1 Thermal-stress analysis of a disc brake
Section 6.1.1 Conjugate heat transfer analysis of a component-mounted electronic circuit board
Section 9.1.1 Fully and sequentially coupled acoustic-structural analysis of a muffler
Section 9.1.3 Analysis of a speaker using Abaqus-Dymola co-simulation

Section 9.1.4 Response of a submerged cylinder to an underwater explosion shock wave
Section 9.1.5 Convergence studies for shock analyses using shell elements
Section 9.1.6 UNDEX analysis of a detailed submarine model
Section 9.1.8 Long-duration response of a submerged cylinder to an underwater explosion
Section 9.1.9 Deformation of a sandwich plate under CONWEP blast loading
Section 13.1.1 Mixing of granular media in a drum mixer
Section 15.1.2 Joining data from multiple results files and converting file format: FJOIN

Abaqus/CFD

Section 6.1.1 Conjugate heat transfer analysis of a component-mounted electronic circuit board

Abaqus/CAE

Section 1.1.10 Shell-to-solid submodeling and shell-to-solid coupling of a pipe joint
Section 1.1.24 Using a composite layup to model a yacht hull
Section 1.2.3 Buckling of a column with spot welds
Section 1.3.1 Upsetting of a cylindrical billet: quasi-static analysis with mesh-to-mesh solution mapping (Abaqus/Standard) and adaptive meshing (Abaqus/Explicit)
Section 1.3.18 Inertia welding simulation using Abaqus/Standard and Abaqus/CAE
Section 1.4.2 Contour integrals for a conical crack in a linear elastic infinite half space
Section 2.3.1 Rivet forming
Section 5.1.6 Thermal-stress analysis of a reactor pressure vessel bolted closure
Section 6.1.1 Conjugate heat transfer analysis of a component-mounted electronic circuit board
Section 9.1.7 Coupled acoustic-structural analysis of a pick-up truck
Section 11.1.1 Topology optimization of an automotive control arm
Section 11.2.1 Shape optimization of a connecting rod
Section 11.3.1 Sizing optimization of a gear shift control holder
Section 11.3.2 Sizing optimization of a car door
Section 11.4.1 Bead optimization of a plate

Abaqus/Viewer

Section 1.1.24 Using a composite layup to model a yacht hull

Abaqus/AMS

Section 2.2.6 Steady-state dynamic analysis of a vehicle body-in-white model

Abaqus/Aqua

Section 12.1.1 Jack-up foundation analyses

Section 12.1.2 Riser dynamics

Abaqus/Design

Section 1.1.4 Indentation of an elastomeric foam specimen with a hemispherical punch
Section 14.2.1 Design sensitivity analysis of a composite centrifuge
Section 14.2.2 Design sensitivities for tire inflation, footprint, and natural frequency analysis
Section 14.2.3 Design sensitivity analysis of a windshield wiper
Section 14.2.4 Design sensitivity analysis of a rubber bushing

About SIMULIA

Dassault Systèmes SIMULIA applications, including Abaqus, Isight, Tosca, and Simulation Lifecycle Management, enable users to leverage physics-based simulation and high-performance computing to explore real-world behavior of products, nature, and life. As an integral part of Dassault Systèmes' **3D**EXPERIENCE platform, SIMULIA applications accelerate the process of making highly informed, mission-critical design and engineering decisions before committing to costly and time-consuming physical prototypes. **www.3ds.com/simulia**

Our **3D**EXPERIENCE Platform powers our brand applications, serving 12 industries, and provides a rich portfolio of industry solution experiences.

Dassault Systèmes, the **3D**EXPERIENCE Company, provides business and people with virtual universes to imagine sustainable innovations. Its world-leading solutions transform the way products are designed, produced, and supported. Dassault Systèmes' collaborative solutions foster social innovation, expanding possibilities for the virtual world to improve the real world. The group brings value to over 170,000 customers of all sizes in all industries in more than 140 countries. For more information, visit **www.3ds.com**.

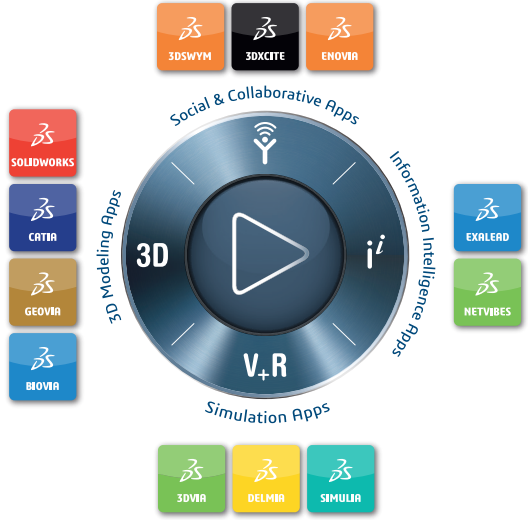

DASSAULT SYSTEMES | The **3D**EXPERIENCE® Company

Europe/Middle East/Africa
Dassault Systèmes
10, rue Marcel Dassault
CS 40501
78946 Vélizy-Villacoublay Cedex
France

Asia-Pacific
Dassault Systèmes K.K.
ThinkPark Tower
2-1-1 Osaki, Shinagawa-ku,
Tokyo 141-6020
Japan

Americas
Dassault Systèmes
175 Wyman Street
Waltham, Massachusetts
02451-1223
USA